Understanding the Cosmological Evolution of Galaxies with Intensity Mapping

Thesis by
Guochao Sun

In Partial Fulfillment of the Requirements for the
Degree of
Doctor of Philosophy

CALIFORNIA INSTITUTE OF TECHNOLOGY
Pasadena, California

2023
Defended July 11, 2022

Guochao Sun
ORCID: 0000-0003-4070-497X

ACKNOWLEDGEMENTS

Many years have passed since I opened that email titled "congratulations from caltech" during a physics lab in my senior year at UCLA. Yet more years have gone by since that story I wrote in my Caltech application, about a sweating but uplifted me cycling hard from bookstore to my TOEFL summer course with the book I just got in the backpack: *Astronomy: A Physical Perspective*. It was the textbook that introduced me to the exciting world of astrophysics.

Thinking back on these old memories on another (though not sultry anymore) summer day in Pasadena years after, all I feel is that I have been a fortunate person — someone who got to spend some time and effort, and received lots and lots of help and inspiration from the people around him, on his way to make a dream come true. It is also for those people that this thesis was written.

First, I am grateful to my advisor, Jamie Bock, who has led me on the journey of observational cosmology, ever since I joined the group as a SURF student, and provided me with an invaluable amount of guidance, understanding, and support. I am indebted to him for the great insights and rigorousness that he brought in to my PhD research and education, from which I will still benefit for sure in my future academic career. I am fortunate to have him as my advisor.

I am also grateful to Tzu-Ching Chang, who is one of the best and most considerate mentors and collaborators I could ever imagine. Whether it is a conundrum in research, a bold project idea, a down time in life, or a difficult choice about the future, she is always there to listen, help, and cheer me up. My sincere gratitude also goes to Olivier Doré, a truly insightful scientist and lovely person to chat with any time.

A special thanks of mine goes to Steve Furlanetto, who has been a close mentor/collaborator of mine, and my role model actually, since I was a young undergrad. His profound understanding and philosophy of astrophysical research have deeply shaped the growth of my mindset as a researcher. I am indebted to him for his continuous support, caring, and guidance of me, and it is my pleasure to be (and continue to be) a part of "Furlanetto's army".

I would like to acknowledge the rest of my thesis committee members: Gregg Hallinan, Lynne Hillenbrand, and Sunil Golwala for providing careful reviews and valuable feedback of my research. My gratitude also goes to other Caltech faculty members who contributed to my PhD education, staff members who made my life at Caltech easy and convenient, as well as my colleagues and fellow students in Caltech Astronomy and the ObsCos group, especially Cheng Zhang, Jon Hunacek, Lunjun (Simon) Liu, Shibo Shu, Yun-Ting Cheng, and Zucheng Gao for their friendship and help throughout the years.

Throughout my PhD studies, I have been particularly fortunate to have worked closely with a number of inspiring and helpful postdoc researchers on various projects, to whom I would like to express my deep gratitude as well. I would like to thank Jordan Mirocha for years of research camaraderie, lots of illuminating discussions and fruitful collaborations, and continuous help with my career development. I would like to thank Lluís Mas-Ribas for sharing lots of ups and downs with me on our LIMFAST adventure and teaching me the importance of thinking critically about research and writing. I would like to thank Brandon Hensley for being an extremely knowledgeable collaborator and showing me the attraction of small-scale physics of the ISM. I would like to thank Marco Viero and Lorenzo Moncelsi for developing some very cool ideas and sharing our critical views of the world together. Last but not least, I would like to thank Abby Crites and the entire TIME Collaboration for teaching me all different aspects about instrumentation and observational cosmology in general, creating lots of memorable moments in the lab, and providing valuable feedback of my research.

There are a few more people I would like to mention and thank here. I have been lucky enough to have met some lifelong friends in my life so far. My thanks goes to Jianfei Shen, Kaizheng Wang, Winson Lu, Xinnan Du, Xin Wang, Yu Lei, and Zuguang Gao for being caring, supportive, and inspiring friends all the time. I am also thankful to all my teachers in the past, especially my high school physics teacher, Yushui Wang, who impressed and convinced me with the simplicity and sheer beauty of physics — a key driver for my career choice.

Finally, I want to express my deepest gratitude to my family and loved ones. I am grateful for my parents, Xiaoru Yang and Dejin Sun, who inspired me to pursue a career in academia and always stand by me, my grandparents, Liru Meng and Zhihua Yang, who taught me how to be a loving person with their unreserved love for me, and my partner, Zhuyun Zhuang, who makes me a better person and always has a warmest place in my heart.

ABSTRACT

The intensity mapping (IM) technique has been proven to be a powerful addition to the toolkit for understanding the cosmology and astrophysics behind cosmic structure formation. From the nearby universe to the epochs of cosmic dawn and reionization, by mapping the large-scale structure traced by a certain intensity field, IM provides an economical and a holistic view of the formation and evolution of galaxies in the cosmological text, in a way that is highly complementary to traditional methods based on individual galaxy detections. In this thesis, I present a number of theoretical perspectives on how the IM technique, especially line intensity mapping (LIM), can help us better understand the cosmological evolution of galaxies — all the way to the intriguing era of first galaxy formation.

In the first part of this thesis, I use the Tomographic Ionized-carbon Mapping Experiment (TIME), a pathfinder for LIM observations of the 158 μm [C II] line emission from the epoch of reionization (EoR), as an example to demonstrate the aspects of high-redshift star-forming galaxies that can be practically studied with LIM. In Chapter 2, I elaborate the science cases of TIME for the investigations of the EoR using the redshifted [C II] line as a star formation rate tracer, and the cosmic molecular gas content near cosmic noon using CO rotational lines redshifted into the same observing bandpass. The results also guide the design of future phases of TIME. In Chapter 3, I introduce and demonstrate an effective masking strategy for the cleaning of line interlopers such as CO from the [C II] data TIME will measure. Using proxies of CO emitters built from stacking analysis of deep, near-infrared selected galaxies, it provides a practical solution to the notoriously challenging line confusion problem for LIM data analysis.

The second part of this thesis focuses on the concept of multi-tracer LIM, namely the synergies among LIM observations of multiple distinct tracers. Forward modeling and inference tools based on semi-analytic models and semi-numerical simulations are developed to explore and showcase the scientific potential of multi-tracer LIM. In Chapter 4, I describe a self-consistent, semi-analytic framework for modeling a variety of LIM signals from the multi-phase interstellar medium (ISM) of galaxies, and use it to illustrate the potential application of LIM to shed light on mean ISM properties of galaxies. In Chapters 5 and 6, I present a new semi-numerical simulation called LIMFAST that is developed for efficiently and self-consistently simulating a plethora of IM signals in the high-redshift universe. The LIMFAST

code is particularly tailored for revealing the connection between the EoR and the first galaxy formation with multiple cosmological probes.

Finally, in the last part of thesis, I show two example case studies where the IM technique is applied to investigate the astrophysics of star formation in galaxies. In Chapter 7, I present an updated analysis of the contributions from star-forming galaxies at $z \gtrsim 5$ to the observed cosmic near-infrared background. Imprints that reveal the formation histories of first stars, including the prospects for detecting them with the forthcoming space missions, are also studied. In Chapter 8, I describe a novel way to constrain the global star formation law of galaxies using LIM measurements of the baryonic acoustic oscillations.

As an emerging technique in observational cosmology, IM is no doubt still in its early days, promising exciting scientific returns while facing various practical challenges. Studies described in this thesis represent only a tiny fraction of the theoretical efforts from the community, but they pave the way for more follow-up investigations that will eventually turn IM into a truly rewarding endeavor.

PUBLISHED CONTENT AND CONTRIBUTIONS

Sun, G., Mas-Ribas, L., Chang, T.-C., et al. (2022). "LIMFAST. II. Line Intensity Mapping as a Probe of High-Redshift Galaxy Formation", preprint, arXiv:2206.14186. https://arxiv.org/abs/2206.14186.
G. Sun participated in the conception of the project, the scientific analysis, and the writing of the manuscript.

Mas-Ribas, L., Sun, G., Chang, T.-C., Gonzalez, M. O., Mebane, R. H. (2022). "LIMFAST. I. A Semi-Numerical Tool for Line Intensity Mapping", preprint, arXiv:2206.14185. https://arxiv.org/abs/2206.14185.
G. Sun participated in the conception of the project, the scientific analysis, and the writing of the manuscript.

Sun, G. (2022). "Cosmological Constraints on the Global Star Formation Law of Galaxies: Insights from Baryon Acoustic Oscillation Intensity Mapping", *Astrophysical Journal*, 931, L29. DOI: 10.3847/2041-8213/ac7138.
G. Sun conceived the project, carried out the scientific analysis, and wrote the manuscript.

Sun, G., Mirocha, J., Mebane, R. H., & Furlanetto, S. R. (2021). "Revealing the Formation Histories of the First Stars with the Cosmic Near-Infrared Background", *Monthly Notices of the Royal Astronomical Society*, 508, 1954. DOI: 10.1093/mnras/stab2697.
G. Sun participated in the conception of the project, carried out the scientific analysis, and wrote the bulk of the manuscript.

Sun, G., Chang, T.-C., Uzgil, B. D., et al. (2021). "Probing Cosmic Reionization and Molecular Gas Growth with TIME", *Astrophysical Journal*, 915, 33. DOI: 10.3847/1538-4357/abfe62.
G. Sun participated in the conception of the project, carried out the scientific analysis, and wrote the bulk of the manuscript.

Sun, G., Hensley, B. S., Chang, T.-C., Doré, O., & Serra, P. (2019). "A Self-Consistent Framework for Multi-Line Modeling in Line Intensity Mapping Experiments", *Astrophysical Journal*, 887, 142. DOI: 10.1042/BJ20150183.
G. Sun participated in the conception of the project, carried out the scientific analysis, and wrote the bulk of the manuscript.

Sun, G., Moncelsi, L., Viero, M. P., et al. (2018). "A Foreground Masking Strategy for [C II] Intensity Mapping Experiments Using Galaxies Selected by Stellar Mass and Redshift", *Astrophysical Journal*, 856, 107. DOI: 10.3847/1538-4357/aab3e3.
G. Sun participated in the conception of the project, carried out the scientific analysis, and wrote the bulk of the manuscript.

TABLE OF CONTENTS

LIST OF ILLUSTRATIONS

LIST OF TABLES

Chapter 1

INTRODUCTION

Understanding the formation and evolution of galaxies — from the cosmic dawn to the present day — is a recurring and all-important theme in astrophysics, which also plays a key role in the study of physical cosmology. Our knowledge of the universe has been repeatedly updated and revised by studying galaxies in the cosmological context. Major developments and achievements include the discovery of an expanding universe, the evidence for the existence of dark matter, and various tests of the general relativity, just to name a few. As one of the major frontiers in modern observational cosmology, surveys of the large-scale structure (LSS) using galaxies as tracers aim to perform stringent tests of the standard, ΛCDM cosmological model and thereby shed light on open questions in cosmology, such as the properties and origins of dark matter and dark energy. Beginning with the observations of large quasar groups, superclusters, and filamentary structures in the 1980s, a series of large galaxy redshift survey programs like the Two-Degree-Field Galaxy Redshift Survey (2dF) and the Sloan Digital Sky Survey (SDSS) have successfully depicted a magnificent, 3D picture of the structure of our universe in terms of matter distribution over the past several decades, using precise positional measurements of millions of galaxies in a huge, Gpc^3 cosmic volume.

Despite its immense contribution to our understanding of the observable universe, a few major limitations exist for the traditional galaxy redshift survey method, including the observational cost and systematic effects such as selection bias and incompleteness associated with the detection threshold of flux limited surveys. As an emerging technique in observational cosmology to study the LSS evolution, line intensity mapping (LIM) probes the LSS by tomographically measuring the emission (or absorption) of spectral lines from either galaxies or the intergalactic medium (IGM) permeating and making up the space among galaxies. LIM generalizes and extends the idea of mapping the continuum emission of cosmic background radiations, e.g., the cosmic microwave background (CMB), with a coarse beam that does not resolve individual sources. However, in this case, extra redshift information is available thanks to the spectral line of interest, which renders the 3D tomography possible. Compared with traditional galaxy surveys, an outstanding feature of LIM is that it provides an economical and holistic way to efficiently access the entire source population, including contributions from dwarf galaxies and the diffuse emission that typically fail to make the detection threshold of flux limited surveys. For these reasons, LIM is highly complementary to methods based on individual galaxy detection for the extraction of astrophysical and cosmological information from the LSS.

Significant theoretical and experimental progress has been made for the LIM technique since Madau et al. (1997) first proposed the concept of H I 21 cm tomography for the investigation of the IGM at high redshift. Chang et al. (2010) made the first detection of the large-scale 21 cm fluctuations through the cross-correlation with the distribution of galaxies at $z \approx 0.8$, whereas the scientific potential of LIM surveys with other spectral line tracers has drawn more and more attention, such as Lyα, [C II], and CO lines that generally trace the star-forming galaxies across cosmic times. Particularly, during the epoch of reionization (EoR); when the neutral IGM after recombination became ionized again by the strong UV radiation background accumulated through the formation of earliest galaxies, the complementarity between different probes such as 21 cm and [C II] lines can be leveraged to constrain the global history and detailed morphology of the reionization process. In the past decade, a number of LIM experiments operating at different wavelengths, such as CHIME, COMAP, CONCERTO, HERA, MWA, TIANLAI, and TIME, have either started scientific observations or yielded first results already in terms of detections/upper limits. Meanwhile, several new-generation experiments targeting at various different tracers have been planned to conduct LIM observations with space-borne/ground-based/balloon-borne telescopes, including SPHEREx, CCAT-prime/FYST, SKA, EXCLAIM, and TIM. Figure 1.1 summarizes the target signal, observing platform, current status, and geographic location of a selected number of recent LIM experiments and concepts. Over the next few years, exciting new data will flood in from LIM experiments at multiple wavelengths using multiple tracers, ushering in a golden age of multi-probe cosmology.

1.1 An Overview of the LIM Technique

Broadly speaking, LIM can be perceived as a direct generalization and extension (to the 3D space) of mapping the 2D, angular anisotropy of the continuum emission of cosmic background radiation, which is also referred to as the extragalactic background light (EBL). The best-known example of such continuum emission is the CMB, though similar studies have been conducted at all wavelengths, including X-ray, UV, optical, and infrared. Using the known wavelength of the target spectral

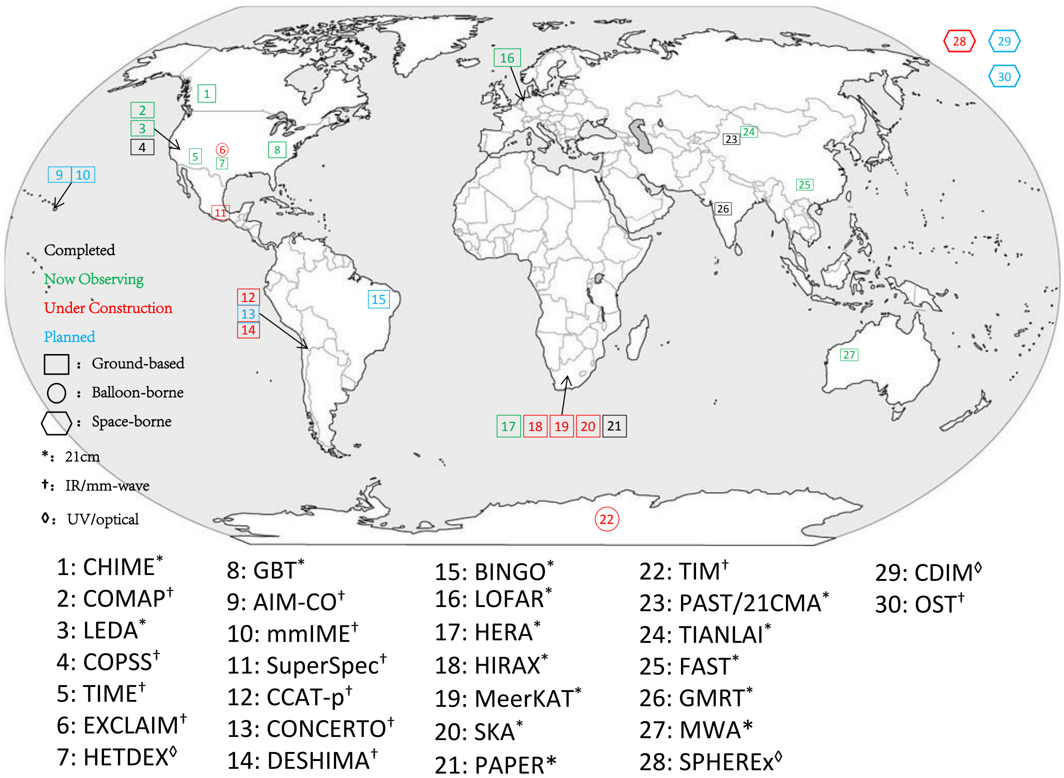

Figure 1.1: A world map of past, ongoing, and planned LIM experiments.

line emission, LIM can break the ubiquitous redshift degeneracy in 2D measurements by accessing the fluctuation signal along the line-of-sight (LOS) direction. This greatly facilitates the separation of different components (usually from different redshifts) in the observed signal, which is known to be a major challenge for interpreting purely angular fluctuations. The 3D line intensity field contains rich information not only about the abundance and spatial distribution of the source population, but also the statistics of emissivity for individual sources. Therefore, statistically studying the aggregate emission from all the unresolved sources with the LIM technique provides key evidence for the formation and evolution of cosmic structures over a huge dynamic range, probing physics ranging from sub-pc to Gpc scales.

As illustrated in Figure 1.2, LIM measures the 3D fluctuations of the target line signal by acting as an imaging spectrometer. Depending on the exact observing technique, measurements can be directly done either in real space by a single-dish antenna, or Fourier space with an interferometric array. The line intensity fluctuations are sampled to a minimum resolution unit called "voxel", which is defined by the spatial

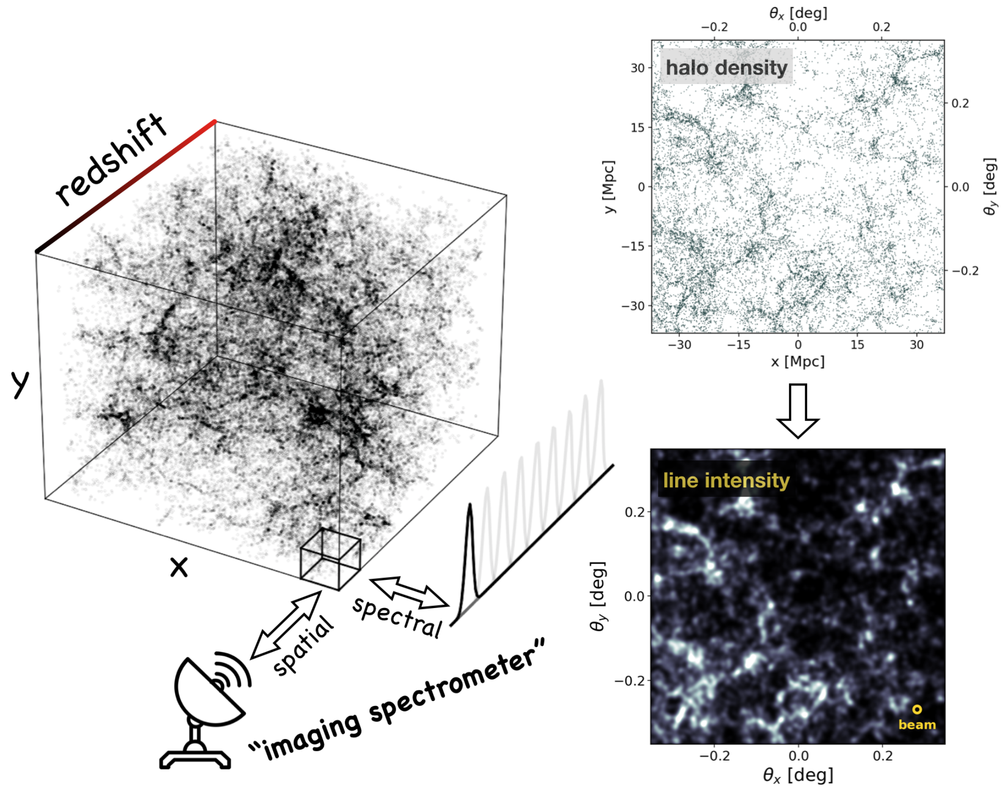

Figure 1.2: An illustration of the LIM concept as a powerful way to survey the LSS.

and spectral resolutions of the instrument in directions perpendicular and parallel to the LOS, respectively. The total cosmic volume mapped, on the other hand, is determined by the sky coverage and bandwidth of the survey. The resulting line intensity map provides a coarse-grained representation of the LSS, which is shown by the dark matter halo distribution in Figure 1.2. As a biased tracer of the underlying density field, the aggregate line emission from the entire halo population, including those too faint to be individually detected, is mapped with a coarse beam.

Given that no sources are resolved and thus the statistical nature of LIM data sets, the astrophysical and cosmological information contained must be extracted through analyses of summary statistics describing the line intensity fields. The power spectrum is the most commonly-used observable that quantifies the two-point statistics of LIM data. Spatial fluctuations on large and small scales can be quantified by the clustering power spectrum arising from source clustering and the shot-noise power spectrum arising from the Poisson distribution of discrete sources, respectively. While the power spectrum provides an intuitive and easy-to-calculate way to describe and interpret LIM data, it contains incomplete information when intensity fluctuations are non-Gaussian, which is indeed the case especially on smaller scales when astrophysical effects become increasingly predominant. Therefore, one-point statistics (Breysse et al. 2017; Kittiwisit et al. 2022) and higher-order statistics such as bispectrum and trispectrum are also widely considered to prevent the loss of information due to non-gaussianity. Similarly, alternative methods making use of Minkowski Functionals (Yoshiura et al. 2017; Chen et al. 2019) and wavelet scattering transform (Cheng et al. 2020a; Greig et al. 2022) have also been recently proposed to extract non-gaussian features of LIM data.

1.2 LIM: Scientific Applications

The scientific applications of the LIM technique can be roughly classified into three broad themes: late-time cosmology, galaxy assembly and evolution, and epochs of cosmic dawn and reionization.

Late-Time Cosmology

The cosmological application of the LIM technique involves measuring the large-scale matter distribution using the spectral line emission from low-to-intermediate redshifts as an alternative tracer to the spatial distribution of galaxies. Accurate measurements of the clustering of matter on different scales and the comparison to the prediction of the standard cosmological model can help address a wide range of open questions in modern cosmology, including dark matter, dark energy, modified gravity, neutrino masses, primordial non-gaussianity, etc. For instance, the level of small-scale clustering sensitive to the abundance of low-mass halos serves as a useful probe of dark matter models other than the cold dark matter (CDM), whereas measurements of the baryon acoustic oscillations (BAO) as a standard ruler can constrain the cosmic expansion history in general. Despite its great potential and promising future for studying cosmology, LIM obtains abundant information about the astrophysics of galaxies sourcing the line emission. For cosmology, the astrophysical information is an important nuisance to be marginalized over, but such information is of great scientific interest by itself to better understand galaxy formation and evolution.

Galaxy Assembly and Evolution

The investigation of the astrophysics of galaxies is an important and highly practical goal for LIM, especially in its current early days when most of the experiments can only cover a limited fraction of the sky. Tracers that probe different phases and physical conditions of the interstellar gas have been considered for LIM observations in both auto-correlations and cross-correlations with external tracers such as galaxies. For example, 21 cm line intensity mapping promises to directly constrain the H I gas content of galaxies (of various kinds presumably) at high accuracy in the post-reionization universe (e.g., Wolz et al. 2017a), whereas mm-wave IM observations of the 158 μm [C II] and CO rotational lines are pursued as a way to quantify the connection between star formation and the molecular gas supply in galaxies (e.g., Gong et al. 2012; Li et al. 2016). LIM data allow to statistically probe not only the global, macroscopic properties of galaxies such as the galaxy–halo connection, star formation efficiency, chemical enrichment, and feedback, but also the coarse-grain averaged, microscopic properties of the stellar population and the ISM with different spectral line diagnostics combined (e.g., Serra et al. 2016; Sun et al. 2019). Although it is sometimes challenging to uniquely constrain a specific physical process or quantity related to galaxy evolution by the statistical measurements, with appropriate model assumptions and reasonable combinations of different probes, LIM offers a powerful way to study the physics of galaxy assembly and evolution using large and complete samples.

Epochs of Cosmic Dawn and Reionization

Deciphering the still mysterious epochs of cosmic dawn and reionization is arguably the best suited for applying and showcasing the power of LIM, which turns out to be a main focus of this thesis. Given the intrinsic faintness and the huge luminosity distance of the sources of emission during these epochs, individual detections of sources like galaxies and quasars require long exposures that make a complete census of the ionizing source population prohibitively expensive. Meanwhile, the even much weaker emission of 21 cm and Lyα lines from the diffuse IGM will be entirely missed. LIM can resolve these issues altogether by mapping out the aggregate emission of lines tracing the IGM in different phases, thereby drawing a complete view of the reionization process including both the ionizing UV background and the neutral gas. Besides the 21 cm line as a neutral gas tracer, lines generally tracing star-forming galaxies contributing to the UV background, such as Lyα, [C II], and CO, as well as He II for likely less important contributors like Population III stars, are considered as ideal LIM targets. Joint analyses of these lines and the 21 cm signal can quantify the overall history and detailed morphology of reionization by answering open questions about the ionizing photon budget, bubble size distribution, anisotropies of the various relevant background radiations, and so forth, while also providing a way of measuring EoR signals less susceptible to observational systematics and the issue of foreground contamination. Moreover, 3D measurements of line intensity fluctuations may be cross-correlated as well with other EoR probes that are generally 2D, such as the patchy kinetic Sunyaev-Zel'dovich (kSZ) effect and the cosmic near-infrared background (NIRB), to further extract the physics of ionizing sources during the EoR (Fernandez et al. 2014; La Plante et al. 2020).

1.3 Thesis Outline

The structure of this thesis is as follows. In the first part of this thesis, I use the Tomographic Ionized-carbon Mapping Experiment (TIME), a pathfinder for LIM observations of the 158 μm [C II] line emission from the epoch of reionization (EoR), as an example to demonstrate the aspects of high-redshift star-forming galaxies that can be practically studied with LIM. In Chapter 2, I elaborate on the science cases of TIME for the investigations of the EoR using the redshifted [C II] line as a star formation rate tracer, and the cosmic molecular gas content near cosmic noon using CO rotational lines redshifted into the same observing bandpass. The results also guide the design of future phases of TIME. In Chapter 3, I introduce and demonstrate an effective masking strategy for the cleaning of line interlopers such as CO from the [C II] data TIME will measure. Using proxies of CO emitters built from stacking analysis of deep, near-infrared selected galaxies, it provides a practical solution to the notoriously challenging line confusion problem for LIM data analysis.

The second part of this thesis focuses on the concept of multi-tracer LIM, namely the synergies among LIM observations of multiple distinct tracers. Forward modeling and inference tools based on semi-analytic models and semi-numerical simulations are developed to explore and showcase the scientific potential of multi-tracer LIM. In Chapter 4, I describe a self-consistent, semi-analytic framework for modeling a variety of LIM signals from the multi-phase interstellar medium (ISM) of galaxies, and use it to illustrate the potential application of LIM to shed light on mean ISM properties of galaxies. In Chapters 5 and 6, I present a new semi-numerical simulation called LIMFAST that is developed for efficiently and self-consistently simulating a plethora of IM signals in the high-redshift universe. The LIMFAST code is particularly tailored for revealing the connection between the EoR and the first galaxy formation with multiple cosmological probes.

In the last part of thesis, I show two example case studies where the IM technique is applied to investigate the astrophysics of star formation in galaxies. In Chapter 7, I present an updated analysis of the contributions from star-forming galaxies at $z \gtrsim 5$ to the observed cosmic near-infrared background. Imprints that reveal the formation histories of first stars, including the prospects for detecting them with the forthcoming space missions, are also studied. In Chapter 8, I describe a novel way to constrain the global star formation law of galaxies using LIM measurements of the BAOs.

Finally, in Chapter 9, I briefly discuss the outlook for the IM concept in the era of upcoming cosmological surveys with multiple probes.

Chapter 2

PROBING COSMIC REIONIZATION AND MOLECULAR GAS GROWTH WITH TIME

Sun, G., Chang, T.-C., Uzgil, B. D., et al. (2021). "Probing Cosmic Reionization and Molecular Gas Growth with TIME", *Astrophysical Journal*, 915, 33. DOI: 10.3847/1538-4357/abfe62.

Abstract

Line intensity mapping (LIM) provides a unique and powerful means to probe cosmic structures by measuring the aggregate line emission from all galaxies across redshift. The method is complementary to conventional galaxy redshift surveys that are object-based and demand exquisite point-source sensitivity. The Tomographic Ionized-carbon Mapping Experiment (TIME) will measure the star formation rate (SFR) during cosmic reionization by observing the redshifted [C II] 158 μm line ($6 \lesssim z \lesssim 9$) in the LIM regime. TIME will simultaneously study the abundance of molecular gas during the era of peak star formation by observing the rotational CO lines emitted by galaxies at $0.5 \lesssim z \lesssim 2$. We present the modeling framework that predicts the constraining power of TIME on a number of observables, including the line luminosity function, and the auto- and cross-correlation power spectra, including synergies with external galaxy tracers. Based on an optimized survey strategy and fiducial model parameters informed by existing observations, we forecast constraints on physical quantities relevant to reionization and galaxy evolution, such as the escape fraction of ionizing photons during reionization, the faint-end slope of the galaxy luminosity function at high redshift, and the cosmic molecular gas density at cosmic noon. We discuss how these constraints can advance our understanding of cosmological galaxy evolution at the two distinct cosmic epochs for TIME, starting in 2021, and how they could be improved in future phases of the experiment.

2.1 Introduction

Marked by the emergence of a substantial hydrogen-ionizing background sourced by the first generations of galaxies, the epoch of reionization (EoR) at $6 \lesssim z \lesssim 10$ represents a mysterious chapter in the history of the universe (Barkana & Loeb 2001; Loeb & Furlanetto 2013; Stark 2016). How the formation and evolution of the first, star-forming galaxies explains the history of reionization is a key question to be addressed. The answer lies in the cosmic star formation history (SFH) required to complete reionization by $z \sim 6$, from which the net production and escaping of ionizing photons can be inferred. The study of the SFH also involves understanding how efficiently generations of stars formed out of the cold molecular gas supply regulated by feedback processes (Bromm & Yoshida 2011; Carilli & Walter 2013). A census of the molecular gas content across cosmic time offers a different perspective on the redshift evolution of cosmic star formation and is amenable to study at later times, including the pronounced peak (sometimes dubbed as the "cosmic noon") at $1 \lesssim z \lesssim 3$.

Over the past decades, our understanding of the EoR has deepened from advances in the observational frontier of galaxies in the early universe. Dedicated surveys of high-redshift galaxies using the *Hubble Space Telescope* (HST) have measured a large sample of galaxies out to redshift as high as $z \sim 8$ (Bouwens et al. 2015b; Finkelstein et al. 2015), which with the help of gravitational lensing has allowed the rest-frame ultraviolet (UV) galaxy luminosity function (LF) to be accurately constrained to a limiting magnitude of $M_{\rm UV}^{\rm AB} \gtrsim -15$ (Atek et al. 2015; Bouwens et al. 2017; Yue et al. 2018). It is expected that, by the advent of the *James Webb Space Telescope* (JWST), not only the currently limited sample size of $9 \lesssim z \lesssim 12$ galaxies and candidates (Ellis et al. 2013; Oesch et al. 2014, 2016, 2018), but also constraints on the faint-end slope evolution of the UVLF, will be considerably enhanced (Mason et al. 2015; Yung et al. 2019). Combined with the Thomson scattering optical depth $\tau_e = 0.055 \pm 0.009$ inferred from the CMB temperature and polarization power spectra by Planck Collaboration et al. (2016a), the SFH based on a plausible faint-end extrapolation of the luminosity function suggests that the global reionization history could be explained by the "known" high-z galaxy population. If the average escape fraction of their ionizing photons into the intergalactic medium (IGM) is in the range of 10–20% (e.g., Robertson et al. 2015; Bouwens et al. 2015a; Mason et al. 2015; Sun & Furlanetto 2016; Madau 2017; Naidu et al. 2020), there will be no need to invoke additional ionizing sources such as Population III stars and quasars. Nevertheless, the uncertainty associated with such an extrapolation indicates a fundamental limitation of surveys of individual objects—sources too faint compared with the instrument sensitivity, such as dwarf galaxies, are entirely missed by galaxy surveys, even though a significant fraction, if not the majority, of the ionizing photons are contributed by them (Wise et al. 2014, Trebitsch et al. 2018; but see also Naidu et al. 2020).

On the other hand, despite being subject to different sources of systematics (e.g., dust attenuation, source confusion, etc.), surveys at optical to far-infrared (FIR) wavelengths have revealed a general picture of the cosmic evolution of the star formation rate density (SFRD, e.g., Cucciati et al. 2012; Gruppioni et al. 2013; Bourne et al. 2017) and the stellar mass density (SMD, e.g., Hopkins & Beacom 2006; Pérez-González et al. 2008; Muzzin et al. 2013a). Since the onset of galaxy formation at $z \gtrsim 10$, the star formation in galaxies first increased steadily with redshift as a result of continuous accretion of gas and mergers. The SFRD then reached a peak at redshift $z \sim 2$ and declined by roughly a factor of 10 towards $z = 0$. Changes in the supply of cold molecular gas as the fuel of star formation may be responsible for the decline in the cosmic star formation at $z \lesssim 2$. The coevolution of the cosmic molecular gas density and the SFRD is therefore of significant interest (Popping et al. 2014; Decarli et al. 2016). Unfortunately, the faintness of cold ISM tracers, such as rotational lines of carbon monoxide (CO), has restricted observations to only the more luminous galaxies (Tacconi et al. 2013; Decarli et al. 2016; Riechers et al. 2019; Decarli et al. 2020). A census of the bulk molecular gas, however, requires a complete CO survey down to the very faint end of the line luminosity function (see e.g., Uzgil et al. 2019).

As an alternative method complementary to sensitivity-limited surveys of point sources, line intensity mapping (LIM) measures statistically the aggregate line emission from the entire galaxy population (Visbal & Loeb 2010), including those at the very faint end of the luminosity distribution that are difficult to detect individually. First pioneered in the deep survey of H I 21cm line at $z \sim 1$ to probe the baryon acoustic oscillation (BAO) peak as a cosmological standard ruler (Chang et al. 2008, 2010), LIM provides an economical way to survey large-scale structure (LSS) without detecting individual line emitters. Over the past decade, LIM has received increasing attention in a variety of topics in astrophysics and cosmology (see the recent review by Kovetz et al. 2017, and references therein).

In addition to the 21cm line, a number of other emission lines have also been proposed as tracers for different phases of the ISM and the IGM, including Lyα, Hα, [C II], CO and so forth. Among these lines, [C II] is particularly interesting for constraining the global SFH. Thanks to the abundance of carbon, its low ionization potential (11.3 eV), and the modest equivalent temperature of fine-structure splitting (91 K), the 157.7 μm $^2P_{3/2} \rightarrow {}^2P_{1/2}$ transition of [C II] is the major coolant of neutral ISM and can comprise up to 1% of the total FIR luminosity of galaxies.

As illustrated in Figure 2.1, a tight, nearly redshift-independent correlation between [C II] line luminosity and the SFR has been identified in both nearby galaxies (e.g., De Looze et al. 2011, 2014; Herrera-Camus et al. 2015) and distant galaxies at redshift up to $z \sim 5$ as revealed by deep ALMA observations (e.g., Capak et al. 2015; Matthee et al. 2019; Schaerer et al. 2020), which makes [C II] a promising SFR tracer. Even though some observations (Willott et al. 2015; Bradač et al. 2017) and semi-analytical models (Lagache et al. 2018) suggest a larger scatter in $L_{\mathrm{C\,II}}$–SFR relation at high redshifts, the general reliability of using [C II] to trace star formation has motivated a number of LIM experiments targeting at the redshifted [C II] signal from the EoR, including TIME (Crites et al. 2014), CONCERTO (CarbON C II line in post-rEionization and ReionizaTiOn epoch; Concerto Collaboration et al. 2020), the Cerro Chajnantor Atacama Telescope-prime (CCAT-prime; Stacey et al. 2018), and the Deep Spectroscopic High-redshift Mapper (DESHIMA; Endo et al. 2019). Meanwhile, on large scales [C II] intensity maps complement surveys of the 21cm line tracing the neutral IGM. The [C II]–21cm cross-correlation provides a promising means to overcome foregrounds of 21cm data and to measure the size evolution of ionized bubbles during reionization (e.g., Gong et al. 2012; Dumitru et al. 2019).

TIME is a wide-bandwidth, imaging spectrometer array (Crites et al. 2014; Hunacek et al. 2016, 2018) designed for simultaneously (1) conducting the first tomographic measurement of [C II] intensity fluctuations during the EoR, and (2) investigating the molecular gas growth at cosmic noon by measuring the intensity fluctuations of rotational CO lines, which also present a source of foreground contamination (Lidz & Taylor 2016; Cheng et al. 2016; Sun et al. 2018; Cheng et al. 2020b). TIME will operate at the ALMA 12-m Prototype Antenna (APA) at the Arizona Radio Observatory (ARO) in Kitt Peak, Arizona, for 1000 hours of winter observing time, starting in 2021. Meanwhile, the instrument may observe from the Leighton Chajnantor Telescope (LCT) in Chile in the future, enabling a significantly longer observing time and lower loading. We refer to this phase as TIME-EXT hereafter, which, as will be discussed in Section 7.3, represents a case where the constraining power from [C II] auto-power spectrum is pushed to the limit. In this chapter, we will describe in detail the modeling framework that allows us to demonstrate the science cases and forecast parameter constraints for the two important cosmic epochs.

The remainder of this chapter is structured as follows. In Section 2.2, we first provide an overview of the types of measurements TIME (and TIME-EXT) per-

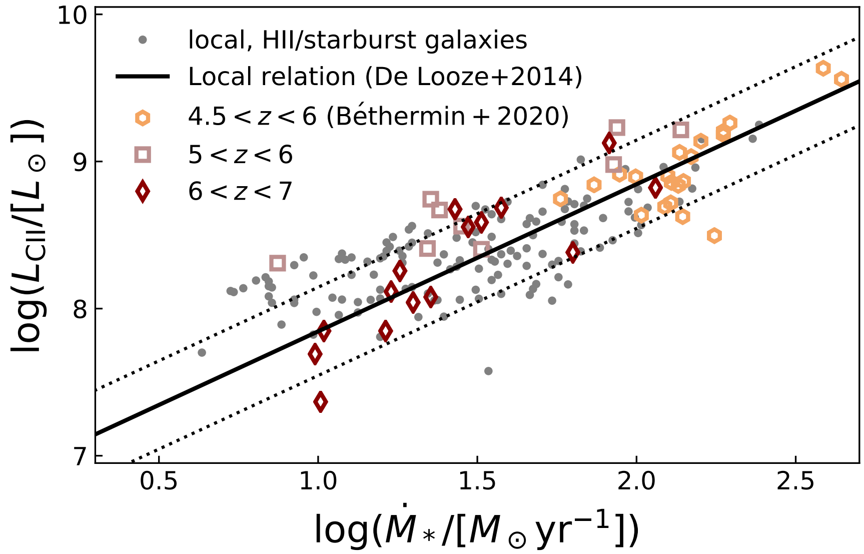

Figure 2.1: The observed correlation between [C II] luminosity and the total SFR (UV + IR) of galaxies in the local universe and $z \gtrsim 5$. Measurements from the ALPINE survey are shown by the hexagons for sources with dust continuum detection (Béthermin et al. 2020). Additional $z \gtrsim 5$ data shown by the squares and diamonds are compiled by Matthee et al. (2019). The solid line represents the best-fit relation to local, H II/starburst galaxies from De Looze et al. (2014), which has a scatter of about 0.3 dex as indicated by the dotted lines. Both the fitting relation and data points are homogenized to be consistent with the same Salpeter IMF assumed throughout this chapter.

forms, together with the corresponding observables. In Section 2.3, we describe the modeling framework for the various signals TIME will observe, which provide physical constraints on the galaxy evolution during reionization and the molecular gas growth history near cosmic noon. We then describe the survey strategy of TIME in Section 2.4. In Section 7.3 we present the predicted sensitivities to different observables as well as TIME's constraining power on various physical quantities. We elaborate the issue of foreground contamination and our mitigation strategies in Section 2.6. We discuss the implications and limitations of TIME(-EXT) measurements, and briefly describe the scientific opportunities for a next-generation experiment, TIME-NG, in synergy with other EoR probes in Section 6.5, before summarizing our main conclusions in Section 7.6. Throughout this chapter, we assume cosmological parameters consistent with recent measurements by Planck Collaboration XIII (Planck Collaboration et al. 2016b).

Table 2.1: Emission lines observable to TIME

Line	Wavelength, λ_{rf} (μm)	Observable z range	Intensity, $\bar{I}_{250\,\mathrm{GHz}}$ (Jy/sr)	$(K_{\perp,\mathrm{min}}, K_{\perp,\mathrm{max}})$ (h/Mpc)	$(K_{\parallel,\mathrm{min}}, K_{\parallel,\mathrm{max}})$ (h/Mpc)
[C II]	158	(5.29, 8.51)	384	(0.061, 5.471)	(0.023, 0.511)
[C I]	609	(0.63, 1.46)	198	(0.186, 16.78)	(0.005, 0.100)
CO(3–2)	867	(0.15, 0.73)	234	(0.535, 48.11)	(0.005, 0.100)
CO(4–3)	650	(0.53, 1.31)	510	(0.212, 19.12)	(0.004, 0.099)
CO(5–4)	520	(0.91, 1.88)	544	(0.144, 13.00)	(0.005, 0.103)
CO(6–5)	434	(1.29, 2.46)	482	(0.115, 10.38)	(0.005, 0.109)
CO(7–6)	372	(1.67, 3.04)	320	(0.099, 8.928)	(0.005, 0.116)

2.2 Observables for TIME

2.2.1 Observables Internal to TIME Datasets

The primary goal of TIME is to constrain the SFH during the EoR by measuring the spatial fluctuations of [C II] line intensity. In particular, we will extract physical information of interest from the two-point statistics of the [C II] intensity field, namely its auto-correlation power spectrum $P_{\mathrm{C\,II}}(k)$, which can be directly measured from TIME's data cube. Combining $P_{\mathrm{C\,II}}(k)$ measured by TIME with other observations such as the CMB optical depth, we are able to constrain the global history of reionization.

TIME will also measure the CO and [C I] emission from galaxy populations from intermediate redshifts ($0.5 \lesssim z \lesssim 2$). These signals are strong and will be interlopers from the standpoint of the extraction of the [C II] signal, but they are interesting in their own right as a constraint on the evolving molecular gas content in galaxies. Without relying on external data, we can distinguish these foreground lines from the [C II] signal by cross-correlating pairs of TIME bands that correspond to frequencies of two lines emitted from the same redshift (and thus tracing the same underlying LSS). In this case, [C II] emission only contributes to the uncertainty rather than the signal of the cross-correlation power spectra (see Section 2.4.2).

2.2.2 Observables Requiring Ancillary Data

In addition to observables that can be directly measured from TIME datasets, we also consider joint analysis with ancillary data, in particular cross-correlations with external tracers of the LSS at both low and high redshifts. Based on surveys of available LSS tracers, we investigate the prospects for (1) measuring the angular correlation function, $\omega_{\mathrm{C\,II}\times\mathrm{LAE}}$, between [C II] intensity and Lyα emitters (LAEs) identified from narrowband data at $z \sim 6$, and (2) measuring the cross-power spectra, $P_{\mathrm{CO}\times\mathrm{gal}}$, between foreground CO lines and near-IR selected galaxies at the same redshifts. These cross-correlation analyses will not only help us better distinguish the low-z and high-z signals, but also shed light onto physical conditions of the overlapping galaxy population traced by these emission lines.

2.3 Models

Following the introduction of observables for TIME, in this section we first describe our models for tracers of the LSS (Section 2.3.1), including [C II] emission from the EoR and foreground CO/[C I] lines internal to TIME data sets, and external tracers like low-z galaxies and high-z LAEs to be cross-correlated with TIME data sets.

We then present models for how these tracers can reveal about (1) the molecular gas content of galaxies near cosmic noon (Section 2.3.2), and (2) the SFH of EoR galaxies at $z \gtrsim 6$ and its implications for the EoR history as the primary goal of TIME experiment (Section 2.3.3).

2.3.1 Tracers of Large-Scale Structure

Our modeling framework of LSS tracers captures the two major line signals TIME will directly measure, namely the target [C II] line from the EoR and foreground CO lines from cosmic noon. It also predicts the statistics of high-redshift Lyα emitters (LAEs), whose spatial distribution can be cross-correlated with [C II] intensity maps to serve as an independent validation of the auto-correlation analysis, which is subject to more complicated foreground contamination. Because observational constraints on the mean emissivity of [C II]/CO emitters and their luminosity distributions are still limited, we adopt a phenomenological approach by connecting the [C II] and CO line intensities to the observed cosmic infrared background (CIB) and UV LFs, respectively, such that the model can be readily constrained by existing measurements while being flexible enough to explore the possible deviations from the fiducial case. Table 2.1 lists the emission lines observable to TIME, including their rest-frame wavelengths, mean intensities, together with their observable redshift and scale ranges (see Section 2.4.1 for details about the Fourier space that TIME measures).

2.3.1.1 Carbon Monoxide and Neutral Carbon Near Cosmic Noon

As summarized in Table 2.1, several low-redshift foreground emission lines are brighter than the EoR [C II] line, and can be blended with the [C II] signal in an auto-correlation analysis. On the contrary, in-band cross-correlations measure (the product of) two line intensities tracing the same LSS distribution at a given redshift. Because low-J CO line ratios are well known and CO correlates with molecular hydrogen, these population-averaged line strengths provide valuable insights into physical conditions of molecular gas clouds from which they originate.

To model the emission lines near cosmic noon, we first take a CIB model of the infrared luminosity, L_{IR}, of galaxies as a function of their host halo mass and redshift. In short, we fit a halo model (Cooray & Sheth 2002) that describes the clustering of galaxies, whose SEDs are assumed to resemble a modified black-body spectrum, to the CIB anisotropy observed in different FIR bands. The resulting best-fit model is characterized by spectral indices of modified black-body spectrum, the dust temperature, and factors of mass and redshift dependence. Given that it is a well-established model whose variations have been applied to numerous studies of the CIB (e.g., Shang et al. 2012; Wu & Doré 2017a,b), the CMB (e.g., Desjacques et al. 2015; Shirasaki 2019), and line intensity mapping (e.g., Cheng et al. 2016; Serra et al. 2016; Pullen et al. 2018; Switzer et al. 2019; Sun et al. 2019), we refrain from going into further details about the CIB model and refer interested readers to the aforementioned papers for more information. In this work, we adopt the CIB model described in Wu & Doré (2017b) and Sun et al. (2019).

Combining the total infrared luminosities derived from the CIB model and its correlation with the CO luminosity, we can express the CO luminosity as

$$\log\left[\frac{L'_{\mathrm{CO}(J\to J-1)}}{\mathrm{K\,km\,s^{-1}\,pc^2}}\right] = \alpha^{-1}\left[\log\left(\frac{L_{\mathrm{IR}}}{L_\odot}\right) - \beta\right] + \log r_J\,, \tag{2.1}$$

where we adopt $\alpha = 1.27$ and $\beta = -1.00$ (see Table 8.1) as fiducial values for CO(1–0) transition (Kamenetzky et al. 2016). Provided that the slope α does not evolve strongly with increasing J (e.g., Carilli & Walter 2013; Kamenetzky et al. 2016; but see also Greve et al. 2014), higher J transitions can be described by a fixed scaling factor r_J, whose values are determined from a recent study by Kamenetzky et al. (2016) about the CO spectral line energy distributions (SLEDs; also known as the CO rotational ladder) based on *Herschel*/SPIRE observations. Specifically, for the excitation of CO we take $r_3 = 0.73$, $r_4 = 0.57$, $r_5 = 0.32$, $r_6 = 0.19$, and terminate the J ladder at $r_7 = 0.1$ (Kamenetzky et al. 2016) as the contribution from higher J's becomes negligible. For simplicity, our model ignores the variation of the CO SLEDs among individual galaxies, which needs to be investigated in future work. Even though ratios of adjacent CO lines do not vary as much as the full CO rotational ladder, the diverse SLEDs observed (especially at higher J) will affect power spectral measurements and introduce additional systematics in the inference of molecular gas content from mid- or high-J CO observations (Carilli & Walter 2013; Narayanan & Krumholz 2014; Mashian et al. 2015a,b). As a compromise, we include a log-normal scatter, σ_{CO}, to describe the level of dispersion in the strengths of all CO lines independent of J. As discussed in Narayanan & Krumholz (2014) and Mashian et al. (2015a), such a common scatter in the CO excitation ladder might be attributed to the stochasticity in global modes of star formation, which can be characterized by the SFR surface density of galaxies. The CO luminosity can be converted from $L'_{\rm CO}$ (in $\rm K\,km\,s^{-1}\,pc^2$) to $L_{\rm CO}$ (in $L_\odot$) by

$$L_{{\rm CO}(J\to J-1)} = 3.2 \times 10^{-11} \left[\frac{\nu_{{\rm CO}(J\to J-1)}}{\rm GHz}\right]^3 L'_{{\rm CO}(J\to J-1)} \ . \tag{2.2}$$

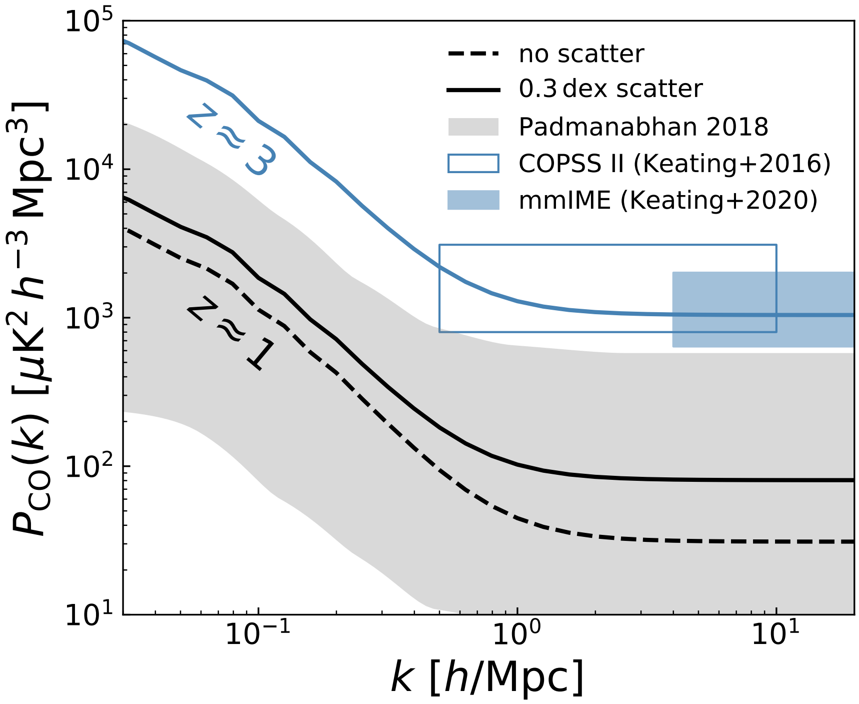

Figure 2.2: A comparison of the CO(1–0) auto-correlation power spectra predicted by our fiducial model with results in the literature. The COPSS II experiment (Keating et al. 2016) reported a marginal detection of CO shot-noise power spectrum $2000^{+1100}_{-1200}\,\mu{\rm K}^2h^{-3}{\rm Mpc}^3$ at $z \sim 3$ (from a refined analysis by Keating et al. 2020). Also shown is the independently measured shot-noise power $1140^{+870}_{-500}\,\mu{\rm K}^2h^{-3}{\rm Mpc}^3$ at $z \sim 3$ from mmIME (Keating et al. 2020). Padmanabhan (2018) fits an empirical model to a compilation of available observational constraints on CO line emissivities at different redshifts. The solid and dashed curves represent the power spectra with and without including a 0.3 dex lognormal scatter in the $L_{\rm CO}$–$L_{\rm IR}$ relation, respectively.

The fluctuations of CO emission can be written as the sum of a clustering term proportional to the power spectrum $P_{\delta\delta}$ of the underlying dark matter density fluctuations, and a scale-independent shot-noise term, [1]

$$P_{\rm CO}(k,z) = \bar{I}^2_{\rm CO}(z)\bar{b}^2_{\rm CO}(z)P_{\delta\delta}(k,z) + P^{\rm shot}_{\rm CO}(z) \ . \tag{2.3}$$

[1]For clarity, J is dropped in the expressions of CO power spectrum.

The mean CO intensity is defined as

$$\bar{I}_{\rm CO}(z) = \int {\rm d}M \frac{{\rm d}n}{{\rm d}M} \frac{L_{\rm CO}[L_{\rm IR}(M,z)]}{4\pi D_L^2} y(z) D_A^2 \,, \tag{2.4}$$

where the integration has a lower bound of $10^{10}\,M_\odot$ (Wu & Doré 2017b), below which the contribution to the total CO line intensity is expected to be negligible according to the CIB model, and an upper bound of $10^{15}\,M_\odot$. ${\rm d}n/{\rm d}M$ is the dark matter halo mass function (HMF), which is defined for the virial mass $M_{\rm vir}$ following Tinker et al. (2008) throughout this work. D_L and D_A are the luminosity and comoving angular diameter distances, respectively, and $y(z) \equiv d\chi/d\nu = \lambda_{\rm rf}(1+z)^2/H(z)$ maps the frequency into the line-of-sight (LOS) distance, where $\lambda_{\rm rf}$ is the rest-frame wavelength of the emission line. $\bar{b}_{\rm CO}(z)$ denotes the luminosity-averaged halo bias factor of CO as a tracer of the underlying dark matter density field, namely

$$\bar{b}_{\rm CO}(z) = \frac{\int {\rm d}M ({\rm d}n/{\rm d}M) b(M,z) L_{\rm CO}[L_{\rm IR}(M,z)]}{\int {\rm d}M ({\rm d}n/{\rm d}M) L_{\rm CO}[L_{\rm IR}(M,z)]} \,. \tag{2.5}$$

The shot-noise term is defined as

$$P^{\rm shot}_{\rm CO}(z) = \int {\rm d}M \frac{{\rm d}n}{{\rm d}M} \left\{ \frac{L_{\rm CO}[L_{\rm IR}(M,z)]}{4\pi D_L^2} y(z) D_A^2 \right\}^2 \,. \tag{2.6}$$

For simplicity, we neglect effects on the intensity fluctuations due to sub-halo structures such as satellite galaxies, which could be non-trivial at the redshifts from which CO lines are emitted. Nonetheless, a halo occupation distribution (HOD) formalism can be readily introduced in order to take into account such effects (Serra et al. 2016; Sun et al. 2019). We also note that the presence of the scatter $\sigma_{\rm CO}$ in $L_{\rm CO}$ for a given $L_{\rm IR}$ affects the clustering and shot-noise components differently. To account for such an effect, we adopt the same multiplicative factors $\mathcal{S}_I$ and $\mathcal{S}_{SN}$ ($\log \mathcal{S}_I = 0.5\sigma^2_{\rm CO} \ln 10$ for the mean intensity and $\log \mathcal{S}_{SN} = 2\sigma^2_{\rm CO} \ln 10$ for the shot-noise power, respectively) as presented in Sun et al. (2019) to scale the two components and obtain the correct form of power spectrum in the presence of scatter. Figure 2.2 shows how our model predictions with and without including a scatter of $\sigma_{\rm CO} = 0.3\,$dex compare to the constraints on CO(1–0) power spectrum at $z \sim 1$ derived from a compilation of observations by Padmanabhan (2018). Also shown in blue is a comparison between our model prediction and the 68% confidence intervals on CO(1–0) shot-noise power at $z \approx 3$ from a revised analysis of COPSS II (Keating et al. 2016) data, as well as a recent, independent measurement from the Millimeter-wave Intensity Mapping Experiment (mmIME) at 100 GHz by Keating et al. (2020).

Due to the resemblance in critical density, fine-structure lines of neutral carbon (C I) tightly correlate with CO lines independent of environment, as demonstrated by observations of molecular clouds in galaxies over a wide range of redshifts. The observed correlation and coexistence of C I and CO in molecular clouds can be explained by modern PDR models more sophisticated than simple, plane-parallel models (e.g., Bisbas et al. 2015; Glover et al. 2015). C I has therefore been recognized as a promising tracer of molecular gas in galaxies at both low and high redshift (Israel et al. 2015; Jiao et al. 2017; Valentino et al. 2018; Nesvadba et al. 2019). Both fine-structure transitions of C I at 492 GHz and 809 GHz are in principle detectable by TIME, but because the latter is from a much higher redshift and in fact spectrally blended with CO(7–6) transition, we will only consider [C I] $^3P_1 \rightarrow {}^3P_0$ transition at 492 GHz (609 μm) in this work and refer to it as the [C I] line henceforth for brevity. We also choose to not include CO(7–6) line (and higher-J transitions) in our subsequent analysis. Recent far-infrared observations suggest an almost linear correlation between [C I] and CO(1–0) luminosities (e.g., Jiao et al. 2017), so we empirically model the [C I] line luminosity by

$$\log\left[\frac{L'_{\mathrm{C\,I}}}{\mathrm{K\,km\,s^{-1}\,pc^2}}\right] = \alpha^{-1}\left[\log\left(\frac{L_{\mathrm{IR}}}{L_\odot}\right) - \beta\right] + \log r_{\mathrm{C\,I}}\,, \tag{2.7}$$

where α and β are set to the same values as in the CO case, while $r_{\mathrm{C\,I}} = 0.18$. Equation (2.7) provides a good fit to the observed $L_{\mathrm{C\,I}}$–L_{IR} relation covering a wide range of galaxy types and redshifts (Valentino et al. 2018; Nesvadba et al. 2019).

Table 2.2: Fiducial model parameters for sensitivity analysis

Parameter	Description	Value	Prior
α	L_{CO}–L_{IR} relation	1.27	$[0.5, 2]$
β	L_{CO}–L_{IR} relation	−1.00	$[-2, 0]$
σ_{CO}	scatter in $L_{\mathrm{CO}}(L_{\mathrm{IR}})$	0.3 dex	$[0, 1]$
a	$L_{\mathrm{C\,II}}$–L_{UV} relation	1.0	$[0.5, 2]$
b	$L_{\mathrm{C\,II}}$–L_{UV} relation	−20.6	$[-21.5, -19.5]$
$\sigma_{\mathrm{C,II}}$	scatter in $L_{\mathrm{C\,II}}(L_{\mathrm{UV}})$	0.2 dex	$[0, 1]$
ξ	SFE in low-mass halos	0	$[-0.5, 0.5]$
f_{esc}	escape fraction	0.1	$[0, 1]$

2.3.1.2 Low-z NIR-Selected Galaxies

Cross-correlating intensity fluctuations of aforementioned, low-redshift target lines for TIME with external tracers, such as galaxy samples, provides an independent measure of the line interlopers blended with the EoR [C II] signal. Therefore, we present an analytical description here to estimate how well TIME will be able to detect the cross-correlation between CO intensity maps and the distribution of near-IR (NIR) selected galaxies, whose redshifts are available from either spectroscopy ($\sigma_z/(1+z) \gtrsim 0.001$) or high-quality photometry ($\sigma_z/(1+z) \gtrsim 0.01$), such as those from the COSMOS/UVISTA survey (Laigle et al. 2016). As discussed in Sun et al. (2018), the same galaxy samples can be utilized to clean foreground CO lines following a targeted masking strategy.

Specifically, the total power spectrum of the galaxy density field is the sum of a clustering term and a shot-noise term

$$P_{\mathrm{gal}}(k,z) = P^{\mathrm{clust}}_{\mathrm{gal}}(k,z) + P^{\mathrm{shot}}_{\mathrm{gal}}(z) = \bar{b}^2_{\mathrm{gal}}(z) P_{\delta\delta}(k,z) + \frac{1}{n_{\mathrm{gal}}} \,. \tag{2.8}$$

The bias factor of galaxies can be derived from the halo bias via

$$\bar{b}_{\mathrm{gal}}(z) = \frac{\int_{>M_{\mathrm{crit}}} \mathrm{d}M (\mathrm{d}n/\mathrm{d}M) b(M,z) \left[N_{\mathrm{cen}} + N_{\mathrm{sat}}(M,z)\right]}{\int_{>M_{\mathrm{crit}}} \mathrm{d}M (\mathrm{d}n/\mathrm{d}M)} \,, \tag{2.9}$$

where M_{crit} is the halo mass corresponding to the critical stellar mass used for galaxy selection. N_{cen} and N_{sat} give the halo occupation statistics, namely the numbers of central galaxy and satellite galaxies per halo. For simplicity, we set N_{cen} to 1 for $M > 10^{10}\,M_{\odot}$ and zero otherwise, and ignore the presence of satellite galaxies by setting $N_{\mathrm{sat}} = 0$. Note that the denominator is simply the galaxy number density n_{gal}. The cross-power spectrum between the galaxy density and the CO intensity fields is therefore

$$P_{\mathrm{CO\times gal}}(k,z) = \bar{b}_{\mathrm{gal}}(z) \bar{b}_{\mathrm{CO}}(z) \bar{I}_{\mathrm{CO}}(z) P_{\delta\delta}(k,z) + \frac{\bar{I}_{\mathrm{CO,gal}}(z)}{n_{\mathrm{gal}}(z)} \,, \tag{2.10}$$

where $\bar{I}_{\mathrm{CO,gal}}$ represents the mean intensity of a given CO line attributed to the selected galaxy samples with halo mass $M > M_{\mathrm{crit}}$, which is an important quantity extractable from the cross shot-noise power as discussed in Wolz et al. (2017a). In the shot-noise regime, the cross-power spectrum effectively probes the mean CO line luminosity $\langle L_{\mathrm{CO}} \rangle_{\mathrm{g}}$ of individual galaxy samples, given prior information of their redshifts. The subscript g indicates the mean CO luminosity of the galaxy sample only. Figure 2.3 shows the cross-power spectrum together with the cross-correlation coefficient $r_{\mathrm{CO\times gal}}(k) = P_{\mathrm{CO\times gal}}(k)/\sqrt{P_{\mathrm{CO}}(k) P_{\mathrm{gal}}(k)}$ between the CO intensity maps TIME measures and galaxy distributions at $z \approx 0.4$ and $z \approx 0.9$.

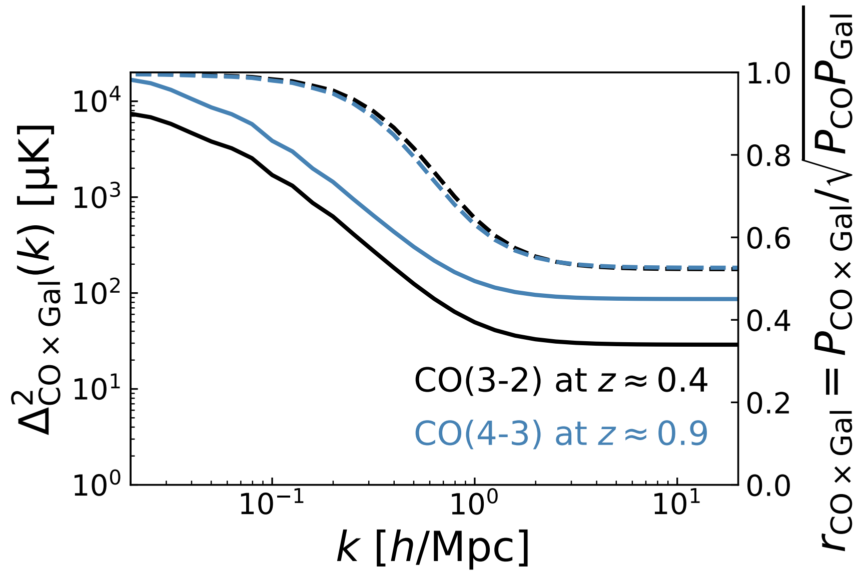

Figure 2.3: The cross-correlation between CO emission and galaxies. Predicted cross-power spectrum $P_{\mathrm{CO\times gal}}$ and cross-correlation coefficient $r_{\mathrm{CO\times gal}}(k)$ of CO(3-2) and CO(4-3) lines with galaxy distributions at $z \approx 0.4$ and $z \approx 0.9$, respectively. The partial correlation at large k is because the cross shot-noise term only probes CO emitters overlapped with the galaxy samples.

Both photometric redshift z_{phot} and spectroscopic redshift z_{spec} can be considered, as long as the corresponding n_{gal} allows a sufficiently large statistical sample to be selected. For photometric data, we examine two examples where galaxies are cross-correlated with CO(3-2) line and CO(4-3) line at $z \approx 0.4$ and $z \approx 0.9$, respectively. We set $M_{\mathrm{crit}} = 5\times10^{11}\,M_\odot$, which corresponds to a stellar mass of $M_* \gtrsim 2\times10^9\,M_\odot$ at $z \sim 1$ (Sun et al. 2018), comparable to the completeness limit of deep, near-IR selected catalogs like the COSMOS/UltraVISTA (Laigle et al. 2016). This implies a galaxy bias factor $\bar{b}_{\mathrm{gal}}$ of 1 (1.3) and a galaxy number density n_{gal} of 0.004 Mpc^{-3} (0.003 Mpc^{-3}) at $z \approx 0.4$ (0.9), corresponding to a total of approximately 50 (200) galaxies within TIME's survey volume. Alternatively, TIME CO maps may also be cross-correlated with spectroscopic galaxies such as samples from the DEEP2 survey (Mostek et al. 2013). Due to the limited survey area and spectral resolving power of TIME, it will not be a lot more beneficial to use spectroscopic galaxies, which have a significant lower number density. We therefore focus on the cross-correlation with photometric galaxies henceforth.

We follow Chung et al. (2019) to estimate the extent by which the redshift error de-correlates the cross-correlation signal. For a gaussian error σ_z around z_{phot}, the attenuation effect on the true power spectrum can be described by the filtering function

$$\begin{aligned}\mathcal{F}_z(k,z) &= \int_0^1 \mathrm{d}\mu \exp\left[-\frac{c^2k^2\mu^2\tilde{\sigma}_z^2}{H^2(z)}\right] \\ &= \frac{\sqrt{\pi}H(z)}{2ck\tilde{\sigma}_z}\mathrm{erf}\left(\frac{ck\tilde{\sigma}_z}{H(z)}\right)\,,\end{aligned} \tag{2.11}$$

where $\tilde{\sigma}_z = \sigma_z$ and $\sigma_z/\sqrt{2}$ for the galaxy auto and CO–galaxy cross-power spectra, respectively, and $\mu = k_{\|}/k$ is the cosine of the k-space polar angle. We note that $\mathcal{F}_z(k,z)$ is introduced here for illustrative purpose only. Because of the anisotropic Fourier space that TIME measures (to be discussed in Section 2.4), when estimating the observed 2D power spectrum we first account for the attenuation effect due to σ_z in the LOS direction, and then average the resulting power over the Fourier space sampled. Compared with TIME's modest spectral resolution, de-correlation is negligible on clustering scales for galaxies with spectroscopic redshifts, but has some effect for high-accuracy photometric redshifts.

2.3.1.3 Ionized Carbon During the EoR

A number of previous works have exploited galaxy evolution models derived from infrared observations to predict the strength of [C II] emission from the EoR (e.g., Silva et al. 2015; Cheng et al. 2016; Serra et al. 2016). However, tensions often exist between the modeled SFH and that inferred from deep, UV observations after correcting for dust attenuation. Such a discrepancy is not surprising, considering that FIR observations of EoR galaxies are still lacking and a fair comparison between the SFHs extrapolated from IR-based models and UV observations at $z \gtrsim 5$ is not necessarily guaranteed. In order to avoid such problems, here and in Section 2.3.1.4, we adopt an alternative approach based on UV observations to model the high-redshift [C II] and Lyα signals that TIME will directly measure in auto- and cross-correlations.

Our phenomenological model of [C II] emission assumes a correlation between the UV 1500–2800 Å continuum luminosity L_{UV} and the [C II] line luminosity $L_{\mathrm{C\,II}}$. As will be discussed below, L_{UV} is used only as a proxy for the SFR of galaxies. We choose to connect $L_{\mathrm{C\,II}}$ with L_{UV} instead of the SFR directly in order to model (1) the luminosity distribution of [C II] emitters and (2) their underlying SFH calibrated to the observed UV luminosity function of galaxies during reionization.

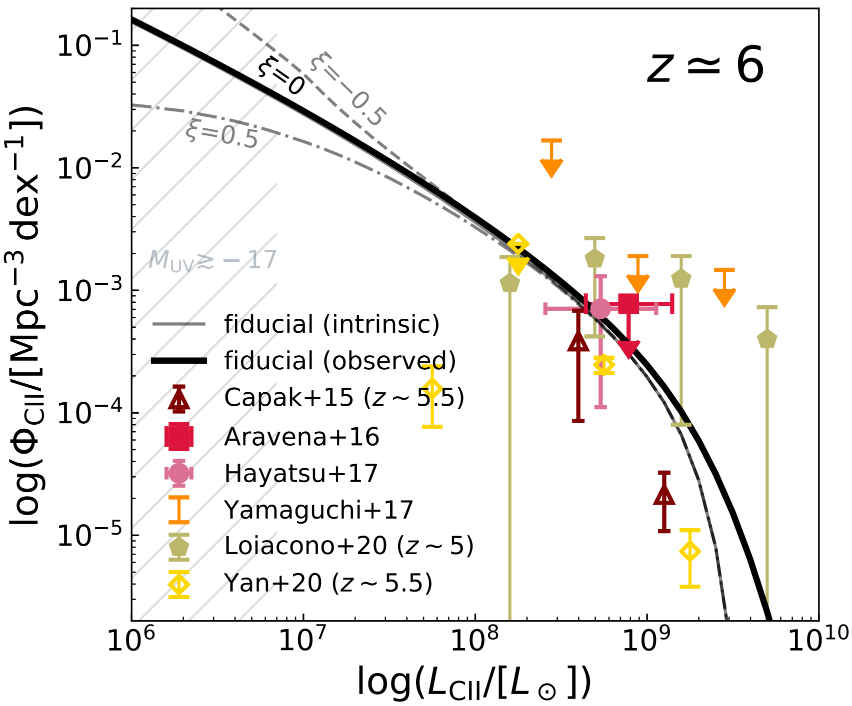

Figure 2.4: Comparison of [C II] luminosity functions. Our modeled [C II] luminosity function, $\Phi_{\mathrm{C\,II}}$, are compared with constraints from ALMA observations at $z \sim 6$, including both blind surveys (Aravena et al. 2016; Hayatsu et al. 2017; Yamaguchi et al. 2017; Loiacono et al. 2020) and those based on UV-selected samples (Capak et al. 2015; Yan et al. 2020), which will always underestimate $\Phi_{\mathrm{C\,II}}$. The black solid curve shows the observed luminosity function predicted by our fiducial [C II] model, which is related to the intrinsic one (gray solid curve) by the convolution described in Equation (2.15) assuming a scatter of $\sigma_{\mathrm{C\,II}} = 0.2\,\mathrm{dex}$. The dashed and dash-dotted curves in gray deviating at the faint end illustrate the dependence on the extrapolation of the star formation efficiency $f_*(M)$ at its low-mass end, as specified by the ξ parameter (see Appendix 2.9). The hatched region on the left shows the regime where in our model galaxies are fainter than $M_{\mathrm{UV}} = -17$, below current detection limit.

The correlation can be parameterized as

$$\log\left(\frac{L_{\mathrm{C\,II}}}{L_\odot}\right) = a \log\left(\frac{L_{\mathrm{UV}}}{\mathrm{erg\,s^{-1}\,Hz^{-1}}}\right) + b\,, \tag{2.12}$$

where $a = 1$ and $b = -20.6$ as listed in Table 8.1 are fiducial values that predict a reasonable [C II] luminosity function at $z \simeq 6$ consistent with existing observational constraints based on identified high-redshift [C II] emitters. We also consider a non-trivial scatter $\sigma_{\mathrm{C\,II}} = 0.2\,\mathrm{dex}$ which specifies a log-normal distribution of $L_{\mathrm{C\,II}}$

as a function of L_{UV}

$$P_{\mathrm{s}}(x)\mathrm{d}x = \frac{1}{\sqrt{2\pi}\sigma_{\mathrm{C\,II}}} \exp\left[-\frac{x^2}{2\sigma_{\mathrm{C\,II}}^2}\right]\mathrm{d}x\ , \tag{2.13}$$

where $x = \log L_{\mathrm{C\,II}} - \mu$ and $\mu = a \log L_{\mathrm{UV}} + b$. Under the assumption that a one-to-one correspondence exists between [C II]-emitting galaxies and their host dark matter halos, the intrinsic [C II] luminosity function can be simply obtained from the halo mass function $\mathrm{d}n/\mathrm{d}M$, connected via the UV luminosity, as

$$\Phi_{\mathrm{C\,II}}(L_{\mathrm{C\,II}}) = \frac{\mathrm{d}n}{\mathrm{d}\log M}\frac{\mathrm{d}\log M}{\mathrm{d}\log L_{\mathrm{UV}}}\frac{\mathrm{d}\log L_{\mathrm{UV}}}{\mathrm{d}\log L_{\mathrm{C\,II}}} = \frac{\mathrm{d}n}{a\mathrm{d}\log L_{\mathrm{UV}}}\ . \tag{2.14}$$

Following Behroozi et al. (2010), the observed luminosity function after accounting for the scatter is given by the convolution

$$\Phi_{\mathrm{C\,II}}^{\mathrm{obs}}(L_{\mathrm{C\,II}}) = \int_{-\infty}^{\infty} \Phi_{\mathrm{C\,II}}(10^x)P_{\mathrm{s}}(x - \log L_{\mathrm{C\,II}})\mathrm{d}x\ , \tag{2.15}$$

which effectively flattens the bright end of the luminosity function, since there are more faint sources being up-scattered than bright sources being down-scattered. Figure 2.4 shows a comparison between the [C II] luminosity function predicted by our fiducial model (as well as its variations) and constraints from a few recent high-redshift [C II] surveys with ALMA, based on either serendipitous (i.e., blindly detected) [C II] emitters (ASPECS, Aravena et al. 2016; Hayatsu et al. 2017; Yamaguchi et al. 2017; ALPINE, Loiacono et al. 2020) or observations of UV-selected targets (Capak et al. 2015; ALPINE, Yan et al. 2020), which are strictly speaking lower limits because [C II]-bright but UV-faint galaxies are potentially missing. We note that [C II] luminosity is known to be affected by physical conditions of the PDR in numerous ways (Ferrara et al. 2019). Theoretical models (e.g., Lagache et al. 2018) are in slight tension with existing constraints on the [C II] luminosity function. This may indicate problems with assumptions made about the PDR model, or failure to properly account for cosmic variance in estimates of the luminosity function (see e.g., Keenan et al. 2020, Trapp & Furlanetto 2020 and references therein, for recent studies about the impact of cosmic variance on high-redshift galaxy surveys and intensity mapping measurements).

The UV continuum luminosity is correlated with the SFR as

$$\dot{M}_* = \mathcal{K}_{\mathrm{UV}} L_{\mathrm{UV}}\ , \tag{2.16}$$

where the conversion factor is taken to be $\mathcal{K}_{\mathrm{UV}} = 1.15\times10^{-28}\ M_\odot\,\mathrm{yr}^{-1}/\mathrm{erg\,s}^{-1}\,\mathrm{Hz}^{-1}$, which is valid for stellar populations with a Salpeter IMF (Salpeter 1955) and a metallicity $Z \sim 0.05 Z_\odot$ during the EoR following Sun & Furlanetto (2016). The SFRD informed by UV data can then be expressed as

$$\dot{\rho}_*(z) = \int_{M_{\rm min}}^{M_{\rm max}} \mathrm{d}M \frac{\mathrm{d}n}{\mathrm{d}M} \dot{M}_*(M, z) \ , \tag{2.17}$$

where we choose $M_{\rm min} = 10^8\, M_\odot$, corresponding to the minimum halo mass for star formation implied by the atomic cooling threshold, and $M_{\rm max} = 10^{15}\, M_\odot$. As will be discussed in Section 2.3.3, the SFR, $\dot{M}_*$, as a function of halo mass and redshift can be specified by the star formation efficiency (SFE) and the rate at which halo mass grows. The shapes of both [C II] luminosity function and power spectrum are therefore affected by the halo mass dependence of these factors. Since the reionization history is irrelevant to star formation after reionization was complete, we do not match the SFRD inferred from UV observations to that obtained by extrapolating the CIB model to $z \gtrsim 5$, which is itself highly uncertain.

The spatial fluctuations of [C II] emission can be described by the [C II] auto-correlation power spectrum

$$P_{\rm C\,II}(k, z) = \bar{I}^2_{\rm C\,II}(z) \bar{b}^2_{\rm C\,II}(z) P_{\delta\delta}(k, z) + P^{\rm shot}_{\rm C\,II}(z) \ . \tag{2.18}$$

The mean [C II] intensity is

$$\bar{I}_{\rm C\,II}(z) = \int_{M_{\rm min}}^{M_{\rm max}} \mathrm{d}M \frac{\mathrm{d}n}{\mathrm{d}M} \frac{L_{\rm C\,II}[L_{\rm UV}(M, z)]}{4\pi D_L^2} y(z) D_A^2 \ , \tag{2.19}$$

and $\bar{b}_{\rm C\,II}(z)$ is the [C II] luminosity-averaged halo bias factor defined as

$$\bar{b}_{\rm C\,II}(z) = \frac{\int_{M_{\rm min}}^{M_{\rm max}} \mathrm{d}M (\mathrm{d}n/\mathrm{d}M) b(M, z) L_{\rm C\,II}[L_{\rm UV}(M)]}{\int_{M_{\rm min}}^{M_{\rm max}} \mathrm{d}M (\mathrm{d}n/\mathrm{d}M) L_{\rm C\,II}[L_{\rm UV}(M)]} \ . \tag{2.20}$$

The shot-noise term is

$$P^{\rm shot}_{\rm C\,II}(z) = \int_{M_{\rm min}}^{M_{\rm max}} \mathrm{d}M \frac{\mathrm{d}n}{\mathrm{d}M} \left\{ \frac{L_{\rm C\,II}[L_{\rm UV}(M, z)]}{4\pi D_L^2} y(z) D_A^2 \right\}^2 \ . \tag{2.21}$$

Similar to the CO case, we use the scaling factors given in Sun et al. (2019) to account for the effects of $\sigma_{\rm C\,II}$ on the [C II] power spectrum.

2.3.1.4 High-z LAEs

In order to estimate TIME's sensitivity to the cross-correlation between high-redshift [C II] emission and LAEs, we adopt a semi-analytical approach to paint [C II] and

Lyα emission onto the halo catalogs from the Simulated Infrared Dusty Extragalactic Sky (SIDES, Béthermin et al. 2017) simulation. Analytic models have been widely used to investigate physical properties of high-redshift LAEs (e.g., Samui et al. 2009; Jose et al. 2013; Mas-Ribas & Dijkstra 2016; Mas-Ribas et al. 2017a,b; Sarkar & Samui 2019). Here, to model Lyα luminosity of LAEs, we assume that Lyα photons are solely produced by recombinations under ionization equilibrium. As a result, for a given halo mass and redshift, it can be approximately related to the SFR by

$$L_{\mathrm{Ly}\alpha} = \frac{f_\gamma \dot{M}_*(M, z)/\eta}{m_\mathrm{p}/(1-Y)}(1 - f_\mathrm{esc}) f_\mathrm{esc}^{\mathrm{Ly}\alpha} f_{\mathrm{Ly}\alpha} E_{\mathrm{Ly}\alpha} \,, \tag{2.22}$$

where m_p is the mass of hydrogen atom. The ionizing photon produced per stellar baryon f_γ, the escape fraction of ionizing photons f_esc, the fraction of recombinations ending up as Lyα emission $f_{\mathrm{Ly}\alpha}$ and the helium mass fraction Y are taken to be $f_\gamma = 4000$ (typical for low-metallicity Pop II stars with a Salpeter initial mass function), $f_\mathrm{esc} = 0.1$, $f_{\mathrm{Ly}\alpha} = 0.67$ and $Y = 0.24$, respectively. The factors $(1 - f_\mathrm{esc})$ and $f_\mathrm{esc}^{\mathrm{Ly}\alpha}$ account for the fraction of ionizing photons failing to escape (and thus leading to recombinations) and the fraction of Lyα photons emitted that eventually reach the observer. Because the production of Lyα emission is also subject to local dust extinction, a scale factor $\log \eta = \langle A_\mathrm{UV} \rangle/2.5$, whose value is specified by the dust correction formalism described in Appendix 2.9, is included here to obtain the obscured star formation rate. As in cases of [C II] and CO emission, we consider a log-normal scatter $\sigma_{\mathrm{Ly}\alpha}$ around the mean $L_{\mathrm{Ly}\alpha}$–M relation above, which makes the observed LAE luminosity function a convolution of the intrinsic function with the log-normal distribution. In our model, we take $f_\mathrm{esc}^{\mathrm{Ly}\alpha} = 0.6$ and $\sigma_{\mathrm{Ly}\alpha} = 0.3\,\mathrm{dex}$, consistent with the observationally determined Lyα escape fraction (Jose et al. 2013) and the dispersion about the luminosity–halo mass relation (More et al. 2009), to obtain reasonably good fits to the luminosity functions measured by Konno et al. (2018), as shown in Figure 2.5. The luminosity–halo mass relation is then used to paint both [C II] and Lyα emission onto dark matter halos catalogued to obtain maps of LAE spatial distribution and [C II] intensity fluctuations.

The limiting magnitude $m_\mathrm{lim}^\mathrm{AB}$ of LAE surveys can be related to the line luminosity $L_{\mathrm{Ly}\alpha}$ of LAEs by $L_{\mathrm{Ly}\alpha} = 4\pi D_L^2 F_{\mathrm{Ly}\alpha}$ and

$$F_{\mathrm{Ly}\alpha} = 3 \times 10^{-5} \times \frac{10^{(8.90 - m_\mathrm{lim}^\mathrm{AB})/2.5} \Delta\lambda}{\lambda^2}\,\mathrm{erg\,s^{-1}\,cm^{-2}}\,,$$

where we take $\Delta\lambda = 131\,\text{Å}$ and $\lambda = 8170\,\text{Å}$ for $z = 5.7$ and $\Delta\lambda = 120\,\text{Å}$ and $\lambda = 9210\,\text{Å}$ for $z = 6.6$ as specified in Konno et al. (2018). Meanwhile, to generate

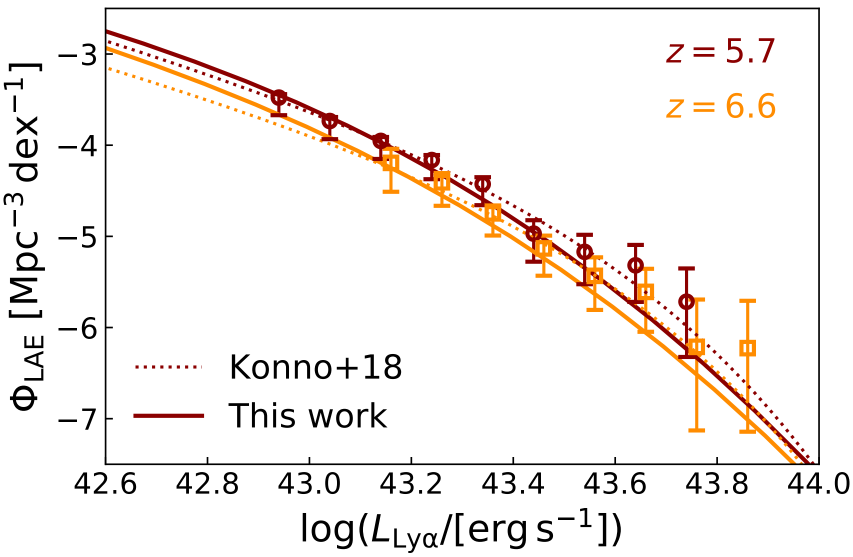

Figure 2.5: A comparison between modeled and observed LAE luminosity functions. The luminosity functions at $z = 5.7$ and $z = 6.6$ predicted by our analytical model (solid curves) are compared against the observed ones taken from Konno et al. (2018) (data points and dotted curves).

mock LAE catalogs we consider limiting magnitudes of the planned, ultra-deep (UD) survey of the HSC, namely $m_{\rm lim}^{\rm AB} = 26.5$ and 26.2 at $z = 5.7$ and 6.6, respectively, which correspond to minimum Lyα luminosities of $\log(L_{\rm Ly\alpha}/{\rm erg\,s^{-1}}) = 42.3$ and 42.4. For such survey depths, we predict the comoving number density of LAEs to be $n_{\rm LAE}^{z=5.7} = 1.4 \times 10^{-3}\,{\rm Mpc^{-3}}$ and $n_{\rm LAE}^{z=6.6} = 5.7 \times 10^{-4}\,{\rm Mpc^{-3}}$ by integrating the LAE luminosity functions our model implies. As a result, no more than a few LAEs are expected to exist in the survey volume of TIME due to its limited survey area of about $0.01\,{\rm deg^2}$. One caveat to our LAE model is that we ignore the impact of patchy reionization on the spatial distribution of LAEs through the Lyα transmission fraction, which is affected by, and thus informs, the growth of ionized bubbles around LAEs (e.g., Santos et al. 2016). We note, though, that for estimating the [C II]–LAE cross-correlation TIME will measure, our simple model calibrated against the LAE luminosity functions from the SILVERRUSH survey should suffice. In fact, thanks to the large survey areas covered (14 and 21 $\rm deg^2$ at $z = 5.7$ and 6.6, respectively), the patchiness effect is already captured, at least in part, by the observed LAE statistics. To fully address the suppression on the LAE number density due to patchy reionization, both numerical (e.g., McQuinn et al. 2007) and semi-analytical (e.g., Dayal et al. 2008) methods can be applied. We will explore how such effects may be probed by the [C II]–LAE cross-correlation in future work.

Therefore, we consider the measurement of two-point correlation function, instead of power spectrum, to maximally extract the information about large-scale correlation between distributions of LAEs and [C II] intensity. In general, for a given normalized selection function $\mathcal{N}(z)$, the angular correlation function is related to the spatial correlation function by the Limber equation

$$\omega(\theta, z) = \int \mathrm{d}z' \mathcal{N}(z') \int \mathrm{d}z'' \mathcal{N}(z'') \xi \left[r(\theta, z', z''), z \right] , \tag{2.23}$$

where we approximate $\mathcal{N}(z)$ by top-hat functions over $z = 5.67$–5.77 and $z = 6.52$–6.63 corresponding to the bandwidths of narrow-band filters used in the SILVER-RUSH survey (Ouchi et al. 2018; Konno et al. 2018). Specifically, the angular cross-correlation function between the [C II] intensity map measured by TIME and the LAE distribution is (in units of Jy/sr)

$$\omega_{\mathrm{C\,II \times LAE}}(\theta) \equiv \frac{\sum_{i}^{N(\theta)} \Delta I^{i}_{\mathrm{C\,II}}(\theta)}{N(\theta)} \approx b_{\mathrm{LAE}} \bar{b}_{\mathrm{C\,II}} \bar{I}_{\mathrm{C\,II}} \omega_{\mathrm{DM}}(\theta) , \tag{2.24}$$

where for the bin θ, $\Delta I^{i}_{\mathrm{C\,II}}(\theta) = I^{i}_{\mathrm{C\,II}}(\theta) - \bar{I}_{\mathrm{C\,II}}$ denotes the [C II] intensity fluctuation at pixel i, whereas $N(\theta)$ denotes the total number of LAE-pixel pairs. Determined from the LAE distributions generated with our semi-analytical approach, the LAE bias $b_{\mathrm{LAE}} \approx 6$ at both $z = 5.7$ and 6.6 is consistent with the upper limits on b_{LAE} estimated from the SILVERRUSH survey. The approximation is valid on large scales where the clustering of LAEs and [C II] emission are linearly biased tracers of the dark matter density field. The dark matter angular correlation function ω_{DM} is derived using Equation (2.23) from the spatial correlation function

$$\xi_{\mathrm{DM}}(r, z) = \frac{1}{2\pi^2} \int \mathrm{d}k \, k^2 P_{\delta\delta}(k, z) \frac{\sin(kr)}{kr} . \tag{2.25}$$

2.3.2 Molecular Gas Content

Over $0.5 \lesssim z \lesssim 2$, TIME can detect more than one CO rotational line over its 183–326 GHz bandwidth (see Table 2.3). Section 2.3.1.1. By cross-correlating a pair of adjacent CO lines emitted from galaxies at the same redshift, we are able to simultaneously constrain α, β, and σ_{CO} as defined in Eq. 2.1. As already mentioned in Section 2.3.1.1, provided that the CO SLED is known and does not appreciably vary over the galaxy population, we can place sensitive constraints on the luminosity density of CO(1–0) line using the intensity fluctuations of the higher-J CO transitions in TIME's spectral range. The cosmic molecular gas density can be consequently derived from the CO(1–0) line luminosity density as

$$\rho_{\mathrm{H}_2}(z) = \alpha_{\mathrm{CO}} \rho_{L'_{\mathrm{CO}}}(z) = \alpha_{\mathrm{CO}} \int \mathrm{d}M \frac{\mathrm{d}n}{\mathrm{d}M} L'_{\mathrm{CO}}[L_{\mathrm{IR}}(M, z)] \,, \tag{2.26}$$

where we adopt a universal CO-to-H_2 conversion factor $\alpha_{\mathrm{CO}} = 4.3\, M_\odot (\mathrm{K\,km\,s^{-1}\,pc^2})^{-1}$ for Milky Way-like environments, as given by Bolatto et al. (2013). One important caveat is that our model assumes the ratios of CO lines with different J's, as given by the excitation state of CO, are well-known. This is of course an oversimplification given the complexity of physical processes driving variations in the CO SLEDs in galaxies (Narayanan & Krumholz 2014), even though the variation in line ratios for adjacent CO lines tends to be small (e.g., Carilli & Walter 2013; Casey et al. 2014). The variation of α_{CO} serves as another source of uncertainty, but we note that it is a systematic uncertainty intrinsic to the usage of CO as tracer affecting nearly all measurements of the molecular gas content and a topic of extensive investigation at different redshifts (Bolatto et al. 2013; Amorín et al. 2016; Gong et al. 2018).

2.3.3 Reionization History

We embed our model of [C II] emission presented in Section 2.3.1.3 into a simple picture of reionization to demonstrate how TIME can probe the EoR. Our methods to model the production of [C II] emission and the progress of reionization are related to the cosmic SFH (see equations 2.17 and 2.30). TIME data constrain the SFRD during reionization, despite the uncertainty in the conversion from [C II] luminosity to star formation rate. In addition, if analyzed jointly with other observational constraints that probe different aspects of the EoR, such as quasar absorption spectra and the CMB optical depth, TIME observations can further improve our knowledge of key EoR parameters, including the escape fraction of hydrogen-ionizing photons f_{esc}.

Following Sun & Furlanetto (2016) and Mirocha et al. (2017), in this work we adopt a commonly-used, two-zone model of the IGM (Furlanetto 2006; Pritchard & Loeb 2010; Loeb & Furlanetto 2013) where the reionization history is characterized by the following set of differential equations that describe the redshift evolution of the H II-region filling factor $Q_{\mathrm{H\,II}}$ and the electron fraction x_e outside H II regions [2],

$$\frac{\mathrm{d}Q_{\mathrm{H\,II}}}{\mathrm{d}z} = \zeta \frac{\mathrm{d}f_{\mathrm{coll}}}{\mathrm{d}z} + \frac{C(z)\alpha_{\mathrm{B}}(T_e)}{H(z)}(1+z)^2 \bar{n}_{\mathrm{H}}^0 Q_{\mathrm{H\,II}} \tag{2.27}$$

[2] It is assumed that only X-ray photons can ionize the "cavities" of neutral gas between H II regions.

and

$$\frac{\mathrm{d}x_e}{\mathrm{d}z} = C_{\mathrm{ion}} f_{X,\mathrm{ion}}(x_e) \frac{\mathrm{d}f_{\mathrm{coll}}}{\mathrm{d}z} \approx 50.2 f_X f_{X,\mathrm{ion}}(x_e) \frac{\mathrm{d}f_{\mathrm{coll}}}{\mathrm{d}z} \,, \tag{2.28}$$

where $\bar{n}_{\mathrm{H}}^0$ is mean (comoving) number density of hydrogen. $C(z) \equiv \langle n_e^2 \rangle / \langle n_e \rangle^2$ defines the clumping factor of the IGM, whose globally-averaged value is approximately 3 as suggested by numerical simulations (Pawlik et al. 2009; Shull et al. 2012; D'Aloisio et al. 2020). $\alpha_{\mathrm{B}}(T_e)$ is the case-B recombination coefficient, and we take $T_e \sim 2 \times 10^4$ K valid for freshly reionized gas (Hui & Haiman 2003; Kuhlen & Faucher-Giguère 2012). The overall ionizing efficiency, ζ, is defined as the product of the star formation efficiency (SFE) f_*, the escape fraction of ionizing photons f_{esc}, the average number of ionizing photons produced per stellar baryon $f_\gamma = 4000$ and a correction factor $A_{\mathrm{He}} = 4/(4-3Y) = 1.22$ for the presence of helium, namely $\zeta = A_{\mathrm{He}} f_* f_{\mathrm{esc}} f_\gamma$. In our fiducial model, we set $f_{\mathrm{esc}} = 0.1$, which leads to a reionization history consistent with current observational constraints (see Figure 6.6). For simplicity, we only consider a population-averaged and redshift-independent escape fraction in this work, even though in practice it may evolve with halo mass and redshift (e.g., Naidu et al. 2020). In Equation (2.28), $f_{X,\mathrm{ion}}$ denotes the fractions of X-ray energy going to ionization, whose value is estimated by Furlanetto & Stoever (2010), and f_X is a free, renormalization parameter for the efficiency of X-ray production, which is set to 1 in our model. In order to solve Equations (2.27) and (2.28), we use COSMOREC (Chluba & Thomas 2011) to generate the initial conditions at $z = 30$.

The two differential equations above are closely associated with the redshift derivative of the collapse fraction of dark matter halos, $\mathrm{d}f_{\mathrm{coll}}/\mathrm{d}z$, which is always *negative* by definition (Furlanetto et al. 2017)

$$\bar{\rho} \frac{\mathrm{d}f_{\mathrm{coll}}}{\mathrm{d}z} \frac{\mathrm{d}z}{\mathrm{d}t} = \int_{M_{\mathrm{min}}}^{M_{\mathrm{max}}} \mathrm{d}M \frac{\mathrm{d}n}{\mathrm{d}M} \dot{M} + \left(\dot{M} M \frac{\mathrm{d}n}{\mathrm{d}M} \right) \Big|_{M_{\mathrm{min}}} \,, \tag{2.29}$$

where $\bar{\rho}$ is the mean matter density and the second term of Equation (2.29) describing the evolution due to mass growth at the boundary is subdominant at the redshifts of interest. Following Equations (2.27) and (2.29), the total ionization rate $\zeta \mathrm{d}f_{\mathrm{coll}}/\mathrm{d}z$ is related to the cosmic star formation rate density $\dot{\rho}_*(z)$ by

$$\begin{aligned} \zeta \frac{\mathrm{d}f_{\mathrm{coll}}}{\mathrm{d}z} &= \frac{A_{\mathrm{He}} f_{\mathrm{esc}} f_\gamma}{\bar{\rho}} \int_{M_{\mathrm{min}}}^{M_{\mathrm{max}}} \mathrm{d}M \frac{\mathrm{d}n}{\mathrm{d}M} \frac{\mathrm{d}t}{\mathrm{d}z} f_*(M,z) \dot{M} \\ &= \frac{A_{\mathrm{He}} f_{\mathrm{esc}} f_\gamma \Omega_{\mathrm{m}}}{\bar{\rho} \Omega_{\mathrm{b}}} \times \dot{\rho}_*(z) \times \frac{\mathrm{d}t}{\mathrm{d}z} \,, \end{aligned} \tag{2.30}$$

where the star formation rate of a given dark matter halo is $\dot{M}_*(M,z) = f_*(M,z)\Omega_\mathrm{b}/\Omega_\mathrm{m}\dot{M}(M,z)$. In order to find the SFE f_* and the growth rate of halo mass $\dot{M}$, we perform the halo abundance matching technique to the UV LF and halo mass function respectively, following Mirocha et al. (2017). In particular, the potential redshift evolution of f_*, likely driven by feedback processes such as supernova explosions, is assumed to be negligible so that it can be described by a modified double-power law in M. The dust correction uses the observed UV continuum slope (see Appendix 2.9 for details), although observed LFs are probably only modestly affected by dust extinction (Capak et al. 2015). As also elaborated in Appendix 2.9, to characterize the degeneracy between the abundance of faint sources and the minimum halo mass, we allow the low-mass end of $f_*(M)$ to deviate from a perfect power law, as shown by Equation (2.44). A modulation factor ξ is introduced to make $f_*(M)$ either asymptote to a constant floor value when $\xi < 0$ or decay exponentially when $\xi > 0$. As listed in Table 8.1, we set the fiducial value of ξ to 0 such that the low-mass end of $f_*(M)$ follows a power law implied by observed UV luminosity functions at $z \gtrsim 6$ (Mirocha et al. 2017).

Once the redshift evolutions of $Q_\mathrm{H\,II}$ and x_e have been solved, we can calculate the Thomson scattering optical depth for CMB photons as (Robertson et al. 2015; Sun & Furlanetto 2016)

$$\tau_e(z) = \frac{3H_0\Omega_\mathrm{b}c\sigma_\mathrm{T}}{8\pi G m_\mathrm{p}} \int_0^z \mathrm{d}z' \frac{\bar{x}_i(z')(1+z')^2(1-Y+\frac{N_\mathrm{He}Y}{4})}{\sqrt{\Omega_\mathrm{m}(1+z')^3+1-\Omega_\mathrm{m}}}\,, \tag{2.31}$$

where $\sigma_\mathrm{T} = 6.65\times10^{-25}\,\mathrm{cm}^2$ is the cross section of Thomson scattering, and $\bar{x}_i(z) = Q_\mathrm{H\,II}(z) + [1-Q_\mathrm{H\,II}(z)]x_e(z)$ is the overall ionized fraction. For simplicity, we further set N_He to 2 for $z < 3$ and 1 otherwise (i.e., instantaneous helium reionization at $z = 3$) to account for the degree of helium ionization (Furlanetto & Oh 2008). As will be discussed in Section 6.4.1, with $\bar{x}_i$ and τ_e in hand, we can constrain our model by combining the [C II] power spectra TIME measures with independent constraints on the IGM neutrality and CMB optical depth inferred from observations.

2.4 Mock Observations

Based on the survey strategy and sensitivity analysis to be described in the following sub-sections, we estimate TIME measurements in auto- and cross-correlations from the instrument parameters listed in Table 2.3, and use them to forecast constraints on physical quantities of interest relevant to the EoR and galaxy evolution (Section 7.3).

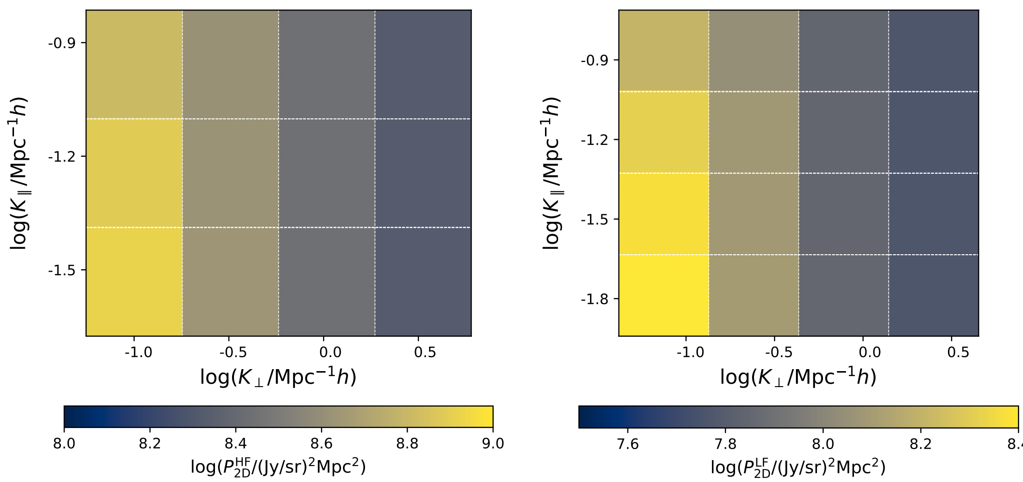

Figure 2.6: 2D binned [C II] auto-power spectra. The 2D power spectra are measured in TIME low-z/HF (left) and high-z/LF (right) sub-bands and binned in $K_\perp$ (perpendicular to the LOS) versus $K_\parallel$ (parallel to the LOS) space. The scale change between $K_\perp$ and $K_\parallel$ reflects the anisotropic Fourier space that TIME measures.

2.4.1 Survey Strategy

With a line scan design, TIME will directly observe a two-dimensional map of intensity fluctuations in instrument coordinates, namely a spatial coordinate defined by the angular position and spectral frequency. As a result, the two-point statistics are described by a 2D power spectrum defined in the observed comoving frame of the instrument, which relates to the theoretical 3D power spectrum defined in Equation (2.18) by the survey window function.

From the definition of window function $W_{ii}\left(k, \vec{K}_i\right)$ discussed in Appendix 2.10, we obtain an integral equation that maps the true 3D power spectrum $P(k)$ of a sky mode k to the observed 2D power spectrum $\mathcal{P}(K)$ of an instrument mode K

$$\mathcal{P}\left(\vec{K}_i\right) = L_x L_z \int_{-\infty}^{\infty} \mathrm{d}\ln k \Delta^2(k) W_{ii}\left(k, \vec{K}_i\right) , \tag{2.32}$$

where L_x and L_z measure dimensions of survey volume perpendicular and parallel to the LOS direction, respectively, and $\Delta^2(k) \equiv k^3 P(k)/2\pi^2$ is the dimensionless spatial power spectrum containing both the clustering and shot-noise terms. The window function W_{ii} describes the relationship between K and k, thereby acting as a kernel that projects the spatial power spectrum $P(k)$ into $\mathcal{P}(K)$ measured in the observing frame of TIME. A given instrument mode K can be further decomposed into two components parallel ($K_\parallel$) and perpendicular ($K_\perp$) to the LOS, respectively, with $K = \sqrt{K_\parallel^2 + K_\perp^2}$. In particular, the minimum accessible scales are defined by the survey size and bandwidth, whereas the maximum accessible scales are defined by the beam size and spectral resolution (Uzgil et al. 2019). By discretizing the linear integral equation above with a trapezoidal-rule sum, we can arrive at a simple matrix representation of Equation (2.32)

$$\vec{\mathcal{P}} = \mathbf{A}\vec{P}\,, \tag{2.33}$$

where $\mathbf{A}$ is an $m \times n$ transfer matrix, with each row summing up to unity, that converts a column vector $\vec{P}$, which represents the true power spectra $P(k)$ binned into n bins of k, into another column vector $\vec{\mathcal{P}}$, which represents the 2D power spectrum $\mathcal{P}(K)$ measured in m bins of K.

In practice, though, various foreground cleaning techniques such as voxel masking (Breysse et al. 2015; Sun et al. 2018) may be applied in order to remove contamination due to both continuum foregrounds (e.g., atmosphere, the CMB, etc.) and line interlopers. As a result, it is unlikely that the window function will have a simple analytic form. Therefore, it must be calculated numerically to account for the loss of survey volume and/or accessible k space due to foreground cleaning.

Table 2.3: Experimental parameters for TIME and TIME-EXT

Parameter	TIME	TIME-EXT
Number of spectrometers (N_{feed})	32	32
Dish size (D_{ap})	12 m	10 m
Beam size (θ_{FWHM})[a]	0.43 arcmin	0.52 arcmin
Spectral range (ν_{min}, ν_{max})[b]	183–326 GHz	183–326 GHz
Spectral bands	LF: 200–265 GHz HF: 265–300 GHz	LF: 200–265 GHz HF: 265–300 GHz
Resolving power (R)	90–120	90–120
Observing site	ARO	LCT
Noise equivalent intensity (NEI)	5 MJy sr^{-1} s$^{1/2}$	2.5 MJy sr^{-1} s$^{1/2}$
Total integration time (t_{obs})	1000 hours	3000 hours
Survey power[c]	1	12

[a] θ_{FWHM} is evaluated at 237 GHz, corresponding to $z_{\mathrm{C\,II}} = 7$.

[b] TIME has 44 (30+14 in LF and HF sub-bands, respectively) scientific spectral channels over 200–300 GHz, and 16 additional channels monitoring atmospheric water vapor.

[c] The survey power is defined to scale as $N_{\mathrm{feed}} t_{\mathrm{obs}}/\mathrm{NEI}^2$.

Using the mode counting method to be described in Section 2.4.2, we aim to determine a survey strategy that optimizes our [C II] auto-correlation measurements, while ensuring a reasonable chance for successfully detecting the cross-correlation signals. In particular, we consider two defining factors of the survey, namely its geometry (i.e., aspect ratio of the survey area) and depth. We find that while the scale-independent shot-noise component dominating the total S/N of the power spectrum is not sensitive to survey geometry, a line scan offers the most economical way to overlap large-scale $K_{\parallel}$ modes with $K_{\perp}$ modes—a desirable property that allows cross-check of systematics that manifest themselves differently in $K_{\parallel}$ and $K_{\perp}$ dimensions. It is also a favorable geometry of TIME, which has an instantaneous field of view (FOV) of 32×1 beams due to the arrangement of the grating spectrometer array in the focal plane. The length of the line scan, on the other hand, is set by the trade-off between accessing large scales (small $K_{\parallel}$) and maintaining a survey depth that ensures a robust [C II] detection. The resulting survey strategy after optimization is a line scan with 180×1 beams across, covering a total survey area of approximately $1.3 \times 0.007\,\mathrm{deg}^2$, which applies to all the analysis in the remainder of the chapter.

Figure 2.6 shows explicitly the Fourier space that TIME will sample via the line scan in its two sub-bands, a low-z/high-frequency (HF) sub-band with bandwidth 265–300 GHz ($5.3 < z_{C\,II} < 6.2$), and a high-z/low-frequency (LF) sub-band with bandwidth 200–265 GHz ($6.2 < z_{C\,II} < 8.5$). The 2D binned [C II] power spectrum is shown for each individual bin in $K_{\parallel}$ versus $K_{\perp}$ space. The line scan can access modes at scales $K_{\parallel} \sim K_{\perp} \sim 0.1\,h/\mathrm{Mpc}$, a regime where the power is dominated by the clustering component.

2.4.2 Sensitivity Analysis

As discussed in the previous section, the effect of the window function is non-trivial for the clustering signal, so it is most reasonable to estimate the measurement uncertainty first in the observing frame (i.e., instrument space) and then propagate it to obtain the uncertainty on the true power spectrum. Here, we follow Gong et al. (2012) to provide an overview of the sensitivity analysis based on the mode counting method.

Table 2.3 summarizes the instrument specifications for TIME and an extended version of the experiment, TIME-EXT, which may offer more than an order of magnitude improvement in survey power by combining (1) lower photon noise offered by a better-sited telescope with fewer mirrors like the LCT (S. Golwala, private communication)[3] and (2) longer integration time. For the observed [C II]

[3]See slides from the Infrared Science Interest Group (IR SIG) seminar given by Sunil Golwala, available at the time of writing at `https://fir-sig.ipac.caltech.edu/system/media_files/binaries/29/original/190115GolwalaLCTIRSIGWeb.pdf`

auto power spectrum after binning in K space, the uncertainty can be expressed as

$$\delta\mathcal{P}_{\mathrm{C\,II}}(K) = \frac{\mathcal{P}_{\mathrm{C\,II}}(K) + \mathcal{P}^{\mathrm{n}}_{\mathrm{C\,II}}}{\sqrt{N_{\mathrm{m}}(K)}} , \tag{2.34}$$

where the noise power $\mathcal{P}^{\mathrm{n}}$ is related to the noise equivalent intensity (NEI), angular sizes of the beam (Ω_{beam}) and the survey (Ω_{survey}), number of spectrometers N_{feed}, total observing time t_{obs}, and voxel volume V_{vox} by

$$\mathcal{P}^{\mathrm{n}} = \sigma^2_{\mathrm{n}} V_{\mathrm{vox}} = \frac{(\mathrm{NEI})^2 V_{\mathrm{vox}}}{N_{\mathrm{feed}}(\Omega_{\mathrm{beam}}/\Omega_{\mathrm{survey}}) t_{\mathrm{obs}}} . \tag{2.35}$$

For TIME, the NEI values assumed are 5 MJy sr^{-1} s$^{1/2}$ and 10 MJy sr^{-1} s$^{1/2}$ for the high-z/LF and low-z/HF sub-bands, respectively, which are estimated assuming operation at ARO with 3 mm perceptible water vapor (PWV) content. These numbers are assumed to be a factor of 2 smaller for TIME-EXT, since the LCT is better-sited and requires fewer number of coupling mirrors (Hunacek 2020). $N_{\mathrm{m}}(K)$ is the total number of independent Fourier modes accessible to the instrument, determined by both how the Fourier space is sampled by the instrument and the loss due to e.g., foreground cleaning. We conservatively assume the lowest $K_{\parallel}$ and $K_{\perp}$ modes are contaminated by scan-synchronous systematics, so they are rejected from our mode counting, which in turn affects the accessible K range for a given survey. It is also important to note that, due to the survey geometry of TIME, Fourier space is not uniformly sampled. Consequently, instead of managing to derive an analytical expression for $N_{\mathrm{m}}(K)$, we simply count the number of independent K modes in a discrete manner for any given binning scheme (see also Chung et al. 2020).

For the CO cross-power spectrum, the uncertainty can be similarly expressed as

$$\delta\mathcal{P}_{J\times J'} = \frac{\left[\mathcal{P}^2_{J\times J'} + \delta\mathcal{P}_J \delta\mathcal{P}_{J'}\right]^{1/2}}{\sqrt{2N_{\mathrm{m}}}} , \tag{2.36}$$

where $\delta\mathcal{P}_J(K) = \mathcal{P}_J(K) + \mathcal{P}^{\mathrm{n}}_J$. When evaluating $\delta\mathcal{P}_J$, we also include the expected [C II] auto power at the corresponding redshift and wavenumber[4] as an additional source of uncertainty for CO cross-correlation measurements that would not be removed by simple continuum subtraction. A clarification of the factor of 2 in the denominator is provided in Appendix 2.11. Similarly, the uncertainty on the

[4] Following assumptions made in Sun et al. (2018), we use the approximation $k_{\mathrm{C\,II}} \approx \sqrt{3} k_{\mathrm{CO}} / \sqrt{2(\chi_{\mathrm{C\,II}}/\chi_{\mathrm{CO}})^2 + (y_{\mathrm{C\,II}}/y_{\mathrm{CO}})^2}$ and the rescaling factor $P_{\mathrm{C\,II}}(k_{\mathrm{CO}})/P_{\mathrm{C\,II}}(k_{\mathrm{C\,II}}) = (\chi_{\mathrm{CO}}/\chi_{\mathrm{C\,II}})^2 y_{\mathrm{CO}}/y_{\mathrm{C\,II}}$ to project the [C II] power spectrum into the observing frame of CO.

CO–galaxy cross-power spectrum is

$$\delta\mathcal{P}_{\mathrm{CO}\times\mathrm{gal}} = \frac{\left[\mathcal{P}^2_{\mathrm{CO}\times\mathrm{gal}} + \left(\mathcal{P}_{\mathrm{CO}} + \mathcal{P}^{\mathrm{n}}_{\mathrm{CO}}\right)\left(\mathcal{P}^{\mathrm{clust}}_{\mathrm{gal}} + n^{-1}_{\mathrm{gal}}\right)\right]^{1/2}}{\sqrt{2N_{\mathrm{m}}}} . \tag{2.37}$$

We note that the finite spatial and spectral resolutions of the instrument will also affect the minimum physical scales, or equivalently $K_{\perp,\mathrm{max}}$ and $K_{\|,\mathrm{max}}$, that can be probed. In order to account for the reduction of sensitivity due to this effect, for $K_\perp$ and $K_\|$ modes we divide the thermal noise part of the uncertainty by scaling factors

$$\mathcal{R}_\perp(K_\perp) = e^{-K_\perp^2/K_{\perp,\mathrm{max}}^2} \tag{2.38}$$

and

$$\mathcal{R}_\|(K_\|) = e^{-K_\|^2/K_{\|,\mathrm{max}}^2} , \tag{2.39}$$

respectively, where $K_{\perp,\mathrm{max}} \approx 2\pi\left(\chi\Omega^{1/2}_{\mathrm{beam}}\right)^{-1}$ and $K_{\|,\mathrm{max}} \approx 2\pi\left(\delta\nu d\chi/\mathrm{d}\nu\right)^{-1}$ are characterized by the comoving radial distance χ, the angular size of the beam Ω_{beam}, and the spectral resolution $\delta\nu$.

These estimated uncertainties are combined with observables predicted by our fiducial model to generate mock data and allow parameter inference, which will be presented in the next section.

2.5 Results

Assuming a line scan optimized for reliably detecting the [C II] intensity fluctuations from the EoR as described in Section 2.4, we adopt the fiducial model parameters given in Table 8.1 and use the mode counting method discussed to create mock signals of the [C II], CO, and [C I] power spectra TIME will measure. We then implement a Bayesian analysis framework for parameter estimation and solve it with the affine-invariant Markov Chain Monte Carlo (MCMC) code EMCEE (Foreman-Mackey et al. 2013). For the inference of [C II], the calibration dataset for parameter fitting is taken to be the mock auto power spectra measured in two redshift bins by TIME, to be combined with independent constraints on the EoR history such as τ_e. For adjacent pairs of CO transitions and [C I], the calibration dataset is taken to be the mock cross-power spectra. The likelihood function for fitting mock observations can be expressed as

$$l\left(\hat{x}\middle|\hat{\theta}\right) = \prod_{i=0}^{N_z}\prod_{j=0}^{N_K} p_{ij}(K,z) , \tag{2.40}$$

where N_K (N_z) denotes the number of K (redshift) bins in which auto- or cross-power spectra are measured. The probability of the data vector $\hat{x}$ for a given set of model parameters $\hat{\theta}$ is assumed to be described by a normal distribution

$$p_{ij} = \frac{1}{\sqrt{2\pi}\sigma_{ij}(K,z)} \exp\left\{-\frac{\left[\mathcal{P}(K,z) - \mathcal{P}(K,z|\hat{\theta})\right]^2}{2\sigma_{ij}^2(K,z)}\right\}, \tag{2.41}$$

where σ_{ij} represents the gaussian error associated with the measurement. As specified in Table 8.1, broad, uniform priors on the model parameters are used. The bounds are chosen to ensure that parameter values suggested by observations in literature fall well within the prior ranges.

The predicted detectability of various target signals of TIME and TIME-EXT, together with the constraints to be placed on the key astrophysical parameters involved in our models, are summarized in Table 2.4. We note that for brevity TIME-EXT forecasts will be shown for [C II] measurements only. The detectability of low-z CO and [C I] lines with cross-correlation will also be improved, though by a significantly smaller amount, as these measurements are dominated by sample variance rather than instrument noise — the latter in general contributes less than half of the total power spectrum uncertainty in these cases.

2.5.1 Constraints on [C II] Intensity

Using the measured [C II] auto-correlation power spectra, we can quantify the strength of [C II] emission by simultaneously constraining parameters a, b, $\sigma_{\rm C\,II}$, and ξ related to the [C II] power spectrum in our model (see Section 2.3.1.3). Figure 2.7 shows the posterior distributions from the MCMC analysis, in which power spectrum templates specified by $\{a, b, \sigma_{\rm C\,II}, \xi\}$ are first projected into observing frame by the window function and then fit to the mock, observed 2D power spectra in the two sub-bands of TIME, which have a total S/N of 5.3 (HF) and 5.8 (LF), respectively. These numbers increase to 23 (HF) and 30 (LF) for TIME-EXT because of its enhanced survey power, as summarized in Table 2.3. Among the four parameters, constraining power is observed for a, $\sigma_{\rm C\,II}$, and ξ that affect (and therefore benefit from having access to) the full shape of the power spectrum, whereas b controls only the normalization of the power spectrum and is prior dominated. In particular, a clear anti-correlation between $\sigma_{\rm C\,II}$ and ξ exists because they have similar effects on the power spectrum shape — increasing $\sigma_{\rm C\,II}$ elevates the shot-noise power (2nd moment of luminosity function), while increasing ξ suppresses the star formation rate and [C II] emissivity of faint galaxies and therefore reduces the clustering power.

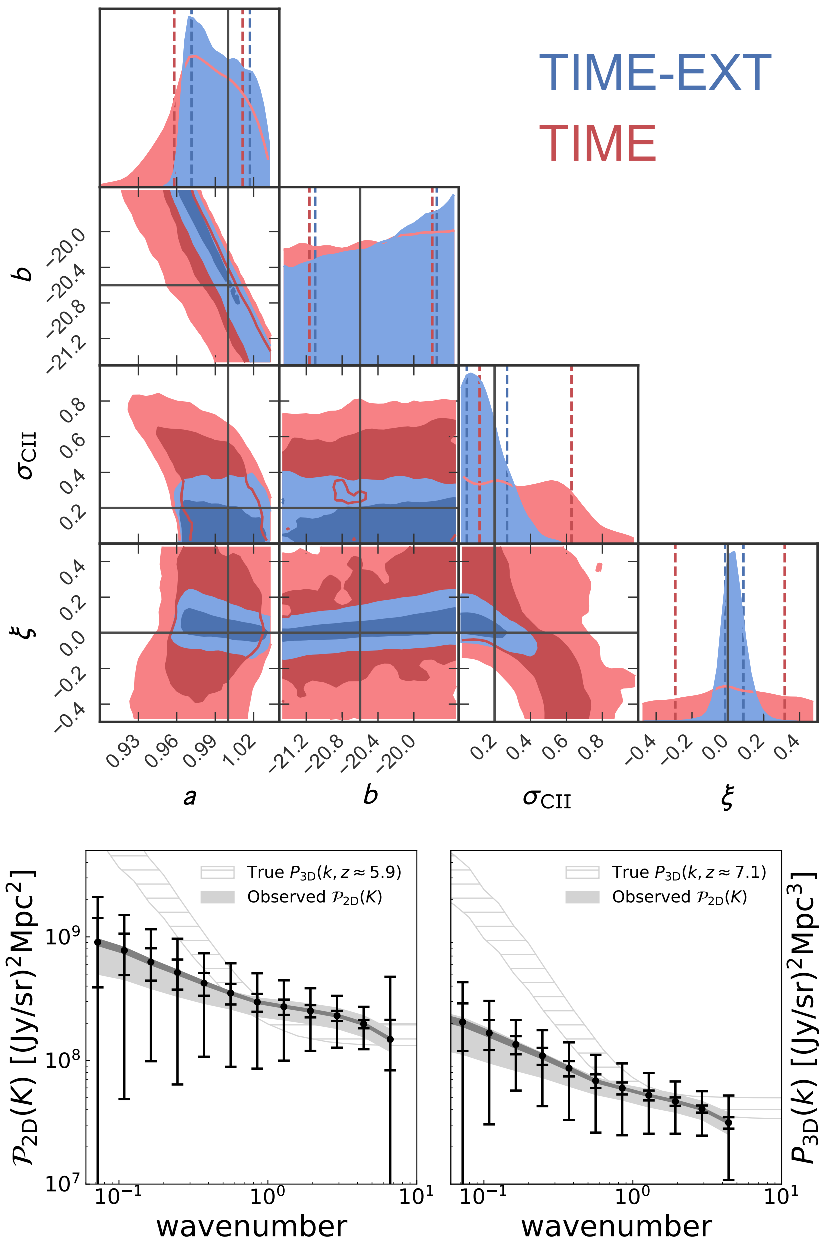

Figure 2.7: Posterior distributions of parameter from [C II] power spectrum constraints. Top: the joint posterior distribution of $\{a,\ b,\ \sigma_{\mathrm{C\,II}},\ \xi\}$ constrained by TIME (red) and TIME-EXT (blue). True values of parameters in our fiducial model are indicated by the solid lines in gray, whereas the 68% confidence intervals of marginalized distributions are shown by the vertical dashed lines. Bottom: constraining power of TIME's HF (low-z) and LF (high-z) bands on the [C II] power spectrum from a $1.3{\times}0.007$ deg^2 line scan. The data points denote TIME (outer) and TIME-EXT (inner) sensitivities to the binned, observed 2D power spectra $\mathcal{P}(K)$, estimated using the mode counting method described in Section 2.4.2. The light and dark shaded bands represent the 68% confidence intervals of the observed power spectra, inferred from the posterior distribution constrained by TIME and TIME-EXT, respectively. For reference, horizontally-hatched regions show the true, 68% confidence intervals of 3D power spectra $P(k)$ constrained by TIME.

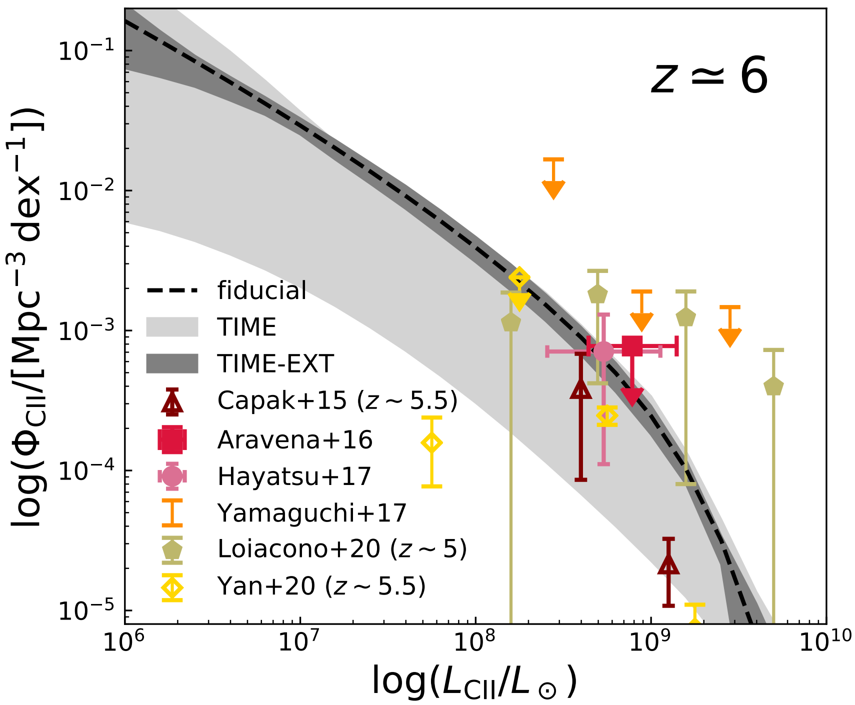

Figure 2.8: [C II] luminosity function constraints from TIME and TIME-EXT. Same as Figure 2.4, but with the light and dark shaded regions indicating the 68% confidence interval reconstructed from the joint posterior distribution of $\{a, b, \sigma_{\rm C\,II}, \xi\}$ constrained by TIME and TIME-EXT, respectively.

The shot-noise power, on the other hand, is dominated by bright sources and thus not much affected by the faint-end behavior controlled by ξ. Such a degeneracy can be greatly reduced by TIME-EXT thanks to its increased constraining power on ξ, which is more than a factor of 5 better than TIME. The weak anti-correlation between a and $\sigma_{\rm C\,II}$ or ξ (not obvious for TIME due to its low S/N) has a similar origin, since a steeper slope a also gives rise to a flatter [C II] power spectrum with fractionally higher shot-noise power.

From the joint posterior distribution, we are able to infer how accurately the [C II] luminosity function can be constrained by the measured power spectrum. As shown in Figure 2.8, the integral constraints from [C II] power spectrum allow us to determine the [C II] luminosity function to within a factor of a few for TIME and smaller than 50% for TIME-EXT. Even though the detailed shape determined from integral constraints is model dependent, such measurements provide unique information of the aggregate [C II] emission from galaxies, including the faintest [C II] emitters cannot be accessed by even the deepest galaxy observation to date. We can also determine the [C II] luminosity density evolution during the EoR. Figure 2.9 shows the level of constraint TIME is expected to provide on the [C II] luminosity density over $5 < z < 10$ assuming our fiducial [C II] model. We note that overall our fiducial model predicts lower [C II] luminosity density compared with the mean line brightness temperature in ALMA 242 GHz band measured by Carilli et al. (2016). The apparent discrepancy between the measurement and our model may be understood in two ways. First, the ALMA observation based on individual, blindly-detected line emitters shall be interpreted as a lower limit because contribution from galaxies too faint to be blindly detected is not included. That said, it may include a substantial contribution from emission lines such as CO and [C I] at lower redshifts, which typically requires near-IR counterparts to characterize (see also Decarli et al. 2020).

Combined with improved measurements of the total SFR based on both optical/near-IR and mm-wave data, TIME's measurements of the distribution and overall density of [C II] emission help narrow down the uncertainty exists in the connection between [C II] line luminosity and the SFR, particularly at high z. Physical processes that determine [C II] luminosity and its scatter in EoR galaxies, including the ISM properties (e.g., metallicity and the interstellar radiation field), feedback, as well as the impact of stochasticity, can be consequently studied.

2.5.2 EoR Constraints Inferred From [C II] Measurements

To illustrate the information TIME adds to our understanding of the EoR history, we consider two contrasting cases, namely whether or not to combine TIME data with other EoR constraints, including the integral constraint from Thomson scattering optical depth of CMB photons and constraints on the end of the EoR from quasar absorption spectra. Specifically, to include these observations as independent constraints in the MCMC analysis, we compare predictions of our reionization model (assuming Gaussian statistics) to $\tau_e = 0.055 \pm 0.009$ (Planck Collaboration et al. 2016a) and $1 - \bar{x}_i(z = 5.5) < 0.1$ that represents an up-to-date, though conservative, constraint on the IGM neutrality near the end of reionization from quasar observations at $z \lesssim 6$ (e.g., Fan et al. 2006b; McGreer et al. 2015; Davies et al. 2018).

Using these combined datasets, we simultaneously fit two EoR parameters of our model, namely the modulation factor ξ controlling the contribution from the faint galaxy population and the population-averaged escape fraction of ionizing photons $f_{\rm esc}$, using the MCMC method. Values of [C II] parameters (a, b, and $\sigma_{\rm C\,II}$) are fixed

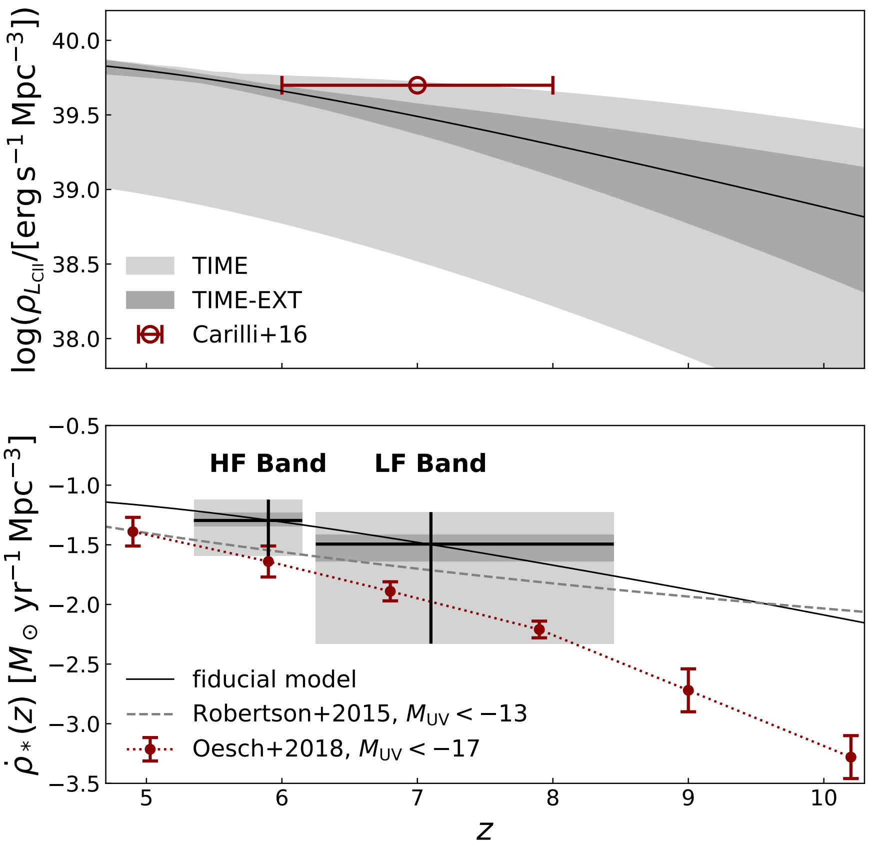

Figure 2.9: Constraints on [C II] luminosity density and the SFRD. Top: constraints (68% confidence interval) on the [C II] luminosity density, calculated from TIME and TIME-EXT measurements, compared against the mean line brightness temperature at 242 GHz measured from the ASPECS blind survey (Carilli et al. 2016). Bottom: constraints (68% confidence interval) on the cosmic SFRD provided by the low-z/HF and high-z/LF sub-bands of TIME and TIME-EXT. The solid curve shows our fiducial SFH assuming $\xi = 0$ and a minimum halo mass of $M_{\mathrm{min}} = 10^8\,M_\odot$. For comparison, the dashed line shows the best-fit cosmic SFRD integrated down to 0.001 $L_\star$ ($M_{\mathrm{UV}} < -13$ at $z \sim 7$) from Robertson et al. (2015), whereas the data points in red represent the observed SFRD from Oesch et al. (2018) after the dust correction and with a limiting magnitude of $M_{\mathrm{UV}} < -17$.

to their fiducial values in this exercise in order to better demonstrate the information contributed by a [C II] intensity mapping experiment. While fixing [C II] parameters is likely an oversimplified assumption given uncertainties associated with how well [C II] traces the SFR of EoR galaxies, future galaxy and LIM observations at mm/sub-mm wavelengths are expected to greatly improve the prior on the conversion from [C II] luminosity to the SFR. We therefore consider an idealized case of constraining

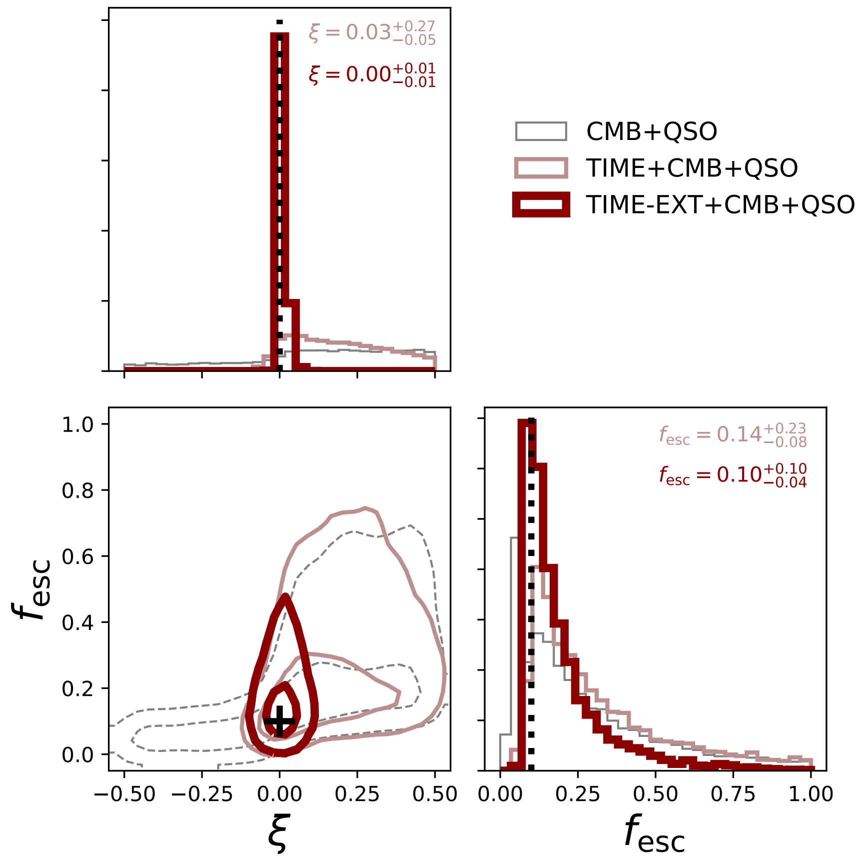

Figure 2.10: Posterior distribution of the escape fraction and faint-end slope. The parameter ξ measures the contribution to reionization from faint galaxies and $f_{\rm esc}$ is the escape fraction of ionizing photons. The black cross and dotted lines indicate the fiducial values. The comparison among contours and histograms of different colors illustrates the improvement thanks to the addition of TIME and TIME-EXT measurements to constraints from the CMB optical depth and quasar absorption spectra. The 68% confidence intervals (based on the highest posterior density) estimated from the marginalized distributions are quoted.

$f_{\rm esc}$ with TIME/TIME-EXT when this conversion is perfectly known, similar to what is routinely done when inferring $f_{\rm esc}$ from rest-frame UV observations of EoR galaxies (Robertson et al. 2015; Mason et al. 2015; Sun & Furlanetto 2016; Yue et al. 2018; Naidu et al. 2020). As a final note, we also verify that with the 5-parameter fitting the distributions of ξ and $f_{\rm esc}$ do not deteriorate catastrophically. The resulting posterior distributions of the parameters are shown in Figure 2.10, where cases combing both TIME and external data from the CMB and quasars are compared against the case without TIME shown in gray. From the marginalized distributions, we find an average escape fraction of ionizing photons $f_{\rm esc} = 0.14^{+0.23}_{-0.08}$ ($f_{\rm esc} = 0.10^{+0.10}_{-0.04}$) and a faint-end modulation factor $\xi = 0.03^{+0.27}_{-0.05}$ ($\xi = 0.00^{+0.01}_{-0.01}$) for TIME (TIME-EXT), where the uncertainties are quoted for a 68% confidence interval derived from the highest posterior density (HPD). By imposing a tight constraint on the faint-end slope of galaxy LF parameterized by ξ, TIME(-EXT) reduces the degeneracy between it and the escape fraction. An accurate measurement of ξ also informs how the ionization background built up during the EoR may have suppressed star formation in galaxies hosted by low-mass halos. Effects of stellar and reionization feedback on the faint-end of galaxy LF provide important information about the interplay between reionization and its driving forces (Furlanetto et al. 2017; Yue et al. 2018).

TIME also sheds light onto the global history of reionization by constraining the cosmic SFR with integrated [C II] emission. Figure 6.6 shows the reionization timeline inferred from a joint analysis of TIME, the CMB optical depth, and quasar absorption spectra. The left panel shows the constraints on the evolution of the mean IGM neutrality $1 - \bar{x}_i$, compared with estimates based on Lyα emission from Lyman Break galaxies (LBGs) (Mason et al. 2018, 2019) and damping wing signatures of quasars (Davies et al. 2018) at $z \gtrsim 7$. The reionization history implied by our fiducial model agrees reasonably well with the independent Lyα and quasar observations, which suggest that the IGM is about half ionized at $z \simeq 7$. The right panel shows the inferred Thomson scattering optical depth of CMB photons. We note that because TIME only directly constrains the SFRD, $1 - \bar{x}_i$ inferred this way is also subject to the uncertainty in τ_e, which is non-trivial compared with the fraction to be explained by hydrogen reionization at $z \gtrsim 6$ ($\Delta\tau_e \approx 0.02$). Nevertheless, the constraints from TIME are less susceptible to sample variance, and, in contrast to analyses of UV galaxies (e.g., Robertson et al. 2015; Mason et al. 2015; Sun & Furlanetto 2016), immune to the uncertainty associated with faint-end extrapolation.

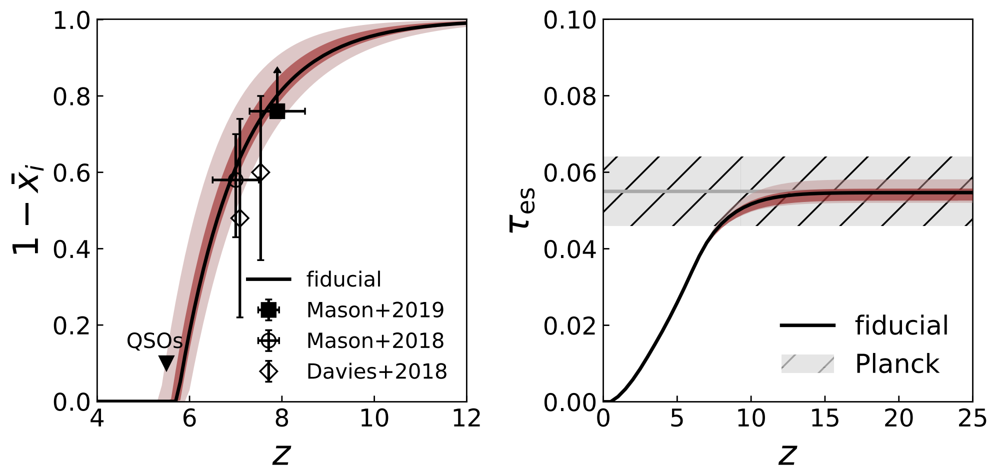

Figure 2.11: Constraints on the IGM neutral fraction and CMB optical depth. Left: the redshift evolution of the average IGM neutrality $1 - \bar{x}_i$ compared with the reionization timeline constraints from recent observations of LBGs and IGM damping wings of quasars at $z \gtrsim 7$. The dark (light) shaded region denotes the 68% confidence level inferred from the SFRD constrained by TIME (TIME-EXT), when f_{esc} is held fixed at 0.1. Right: the CMB electron-scattering optical depth inferred from TIME and TIME-EXT measurements compared with constraints from Planck (Planck Collaboration et al. 2016a).

2.5.3 [C II]–LAE Cross-Correlation

As discussed in Section 2.4.1, the survey strategy of TIME optimizes the detectability of large-scale modes. A line scan, however, limits the spatial overlap between [C II] data and LAEs available for a cross-power spectral analysis. Because the two-point correlation function in this case is computed as a function of angular distance, we can include LAEs that do not fall exactly along the scan path, thereby increasing the number of LAE–voxel pairs available for constraining [C II]–LAE angular clustering. Using Equation (2.24), we compute the angular correlation function between LAEs and the [C II] line intensity measured by TIME. To estimate the detectability of the cross-correlation signal, we first extract mock [C II] data in the TIME spectral channel corresponding to the redshift of LAEs identified by the Subaru HSC narrow-band filter. The [C II] data from a line scan of 180 beams wide is then cross-correlated with angular positions of LAEs simulated in a $1.4 \times 1.4 = 2\,\mathrm{deg}^2$ field.

Figure 2.12 shows the sensitivity of [C II]–LAE angular correlation function $\omega_{\mathrm{C\,II} \times \mathrm{LAE}}$ at $z = 5.7$ and 6.6, as predicted by our semi-analytical approach. For comparison, we also show the angular correlation function of dark matter (from linear theory) scaled by b^2_{LAE}. While only marginal detections of the angular correlation function are expected due to the limited survey size, upper limits inferred from this cross-correlation provide a valuable independent check against our [C II] auto-correlation analysis. Taking $b_{\mathrm{LAE}} = 6$ inferred from our simulated LAE distributions, which is broadly consistent with measurements from Ouchi et al. (2018), and restricting the fitting to linear scales with $r > 10\,\mathrm{Mpc}$, we obtain $b_{\mathrm{C\,II}}\bar{I}_{\mathrm{C\,II}} = 2700 \pm 3200\,\mathrm{Jy/sr}$ at $z = 5.7$ and $2600 \pm 2900\,\mathrm{Jy/sr}$ at $z = 6.6$, respectively. Because of the restricted number of LAE–voxel pairs given TIME's small survey area, sample variance contributes a significant fraction ($> 60\%$) of the uncertainty in $\omega_{\mathrm{C\,II}\times\mathrm{LAE}}$ measurements predicted above, which is estimated by bootstrapping 1000 randomized LAE catalogs. Thus, with the same survey area as TIME but lower instrument noise, TIME-EXT only slightly improves the detectability of $\omega_{\mathrm{C\,II}\times\mathrm{LAE}}$. Nevertheless, as will be discussed in Section 2.7.2, precise measurements of $\omega_{\mathrm{C\,II}\times\mathrm{LAE}}$ during the EoR will be one of the major targets for next-generation [C II] LIM experiments covering $\sim 10\,\mathrm{deg}^2$ of sky.

2.5.4 Probing Physics of Molecular Gas Growth with CO and [C I] Intensities

Here, we consider two potential applications of in-band cross-correlation to measure the strengths of CO and [C I] lines from $0.5 \lesssim z \lesssim 2$. The mean intensities of these lines extracted from cross-power spectra reveal physical information about molecular gas in galaxies near cosmic noon. In the first scenario, we assume a fixed CO rotational ladder, with the line ratios to CO(1–0) specified by the scaling factors provided in Section 2.3.1.1, and constrain the molecular gas density evolution by converting luminosities of higher-J CO lines into CO(1–0) luminosity (see Section 2.3.2). We relax our assumption that the CO rotational ladder is known in the second scenario, and use the cross-correlations of three pairs of CO and [C I] lines to determine their individual strengths.

2.5.4.1 Cross-correlating high-J CO lines at $0.5 \lesssim z \lesssim 2$

By cross-correlating intensity maps measured at frequencies corresponding to a pair of adjacent CO lines emitted at the same redshift, TIME can measure the intensity product of two CO lines. Thanks to the wide bandwidth of TIME, we are able to detect multiple CO transitions over $0 < z < 2$ and thereby determine the evolution of molecular gas content. In order to quantify how well TIME constrains $\rho_{\mathrm{H_2}}$, we create mock CO data with our fiducial model outlined in Section 2.3.1.1 and apply an MCMC analysis in a similar manner to the [C II] case. Specifically, we consider measuring the cross-power spectra of CO(3–2) $\times$ CO(4–3) at $z \approx 0.6$

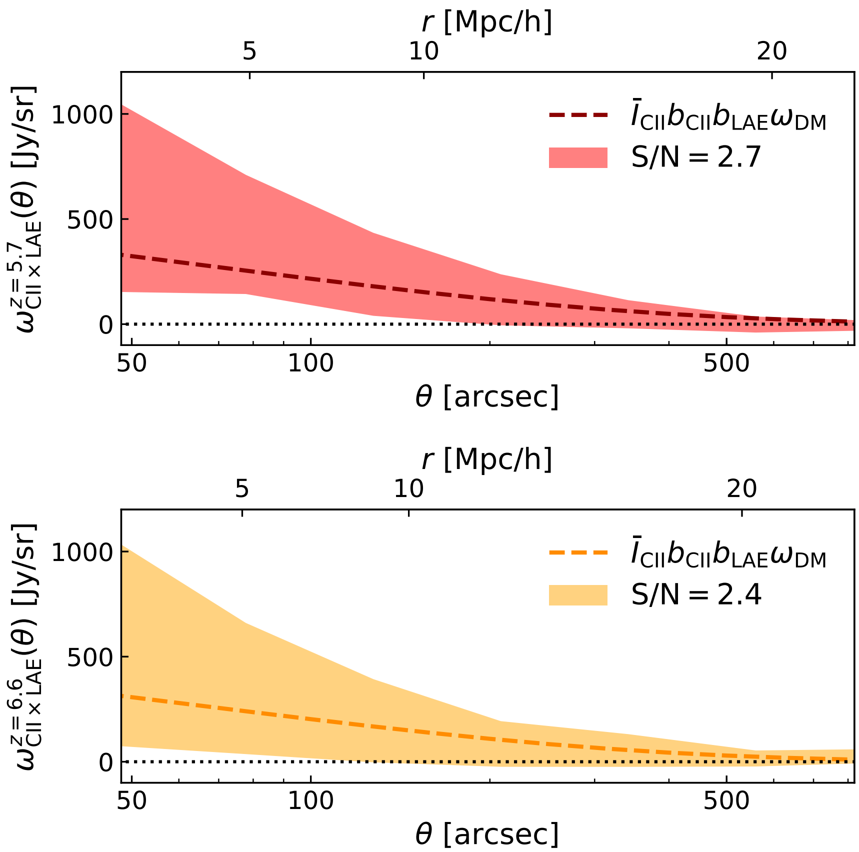

Figure 2.12: Sensitivity to the [C II]–LAE angular cross-correlation function. The correlation between the [C II] line intensity and LAEs surveyed by Subaru HSC at $z = 5.7$ and 6.6 are considered. The dashed lines show analytical approximations $\omega_{\rm C\,II \times LAE} \approx b_{\rm LAE} \bar{b}_{\rm C\,II} \bar{I}_{\rm C\,II} \omega_{\rm DM}$ scaled from the angular correlation function of dark matter. The shaded region indicates the 68% confidence interval from measurements of TIME, estimated by bootstrapping 1000 randomized LAE catalogs.

($0.53 < z < 0.73$), CO(4–3) × CO(5–4) at $z \approx 1.1$ ($0.90 < z < 1.31$), and CO(5–4) × CO(6–5) at $z \approx 1.6$ ($1.29 < z < 1.88$), which end up using 13, 21, and 25 TIME spectral channels, respectively.

The resulting posterior distributions of our CO model parameters $\{\alpha, \beta, \sigma_{\rm CO}\}$ are shown in Figure 4.11, in tandem with the reproduced cross-power spectra of CO(3–2) × CO(4–3), CO(4–3) × CO(5-4) and CO(6–5) × CO(5–4). As is the case of [C II], the slope α anti-correlates with the intercept β of the log-log relation specifying the line luminosity. However, an anti-correlation between the slope α and scatter $\sigma_{\rm CO}$ is not observed, as the CO slope is always greater than unity and thus only weakly affects the shape of the power spectrum. The constraints on the cosmic evolution of

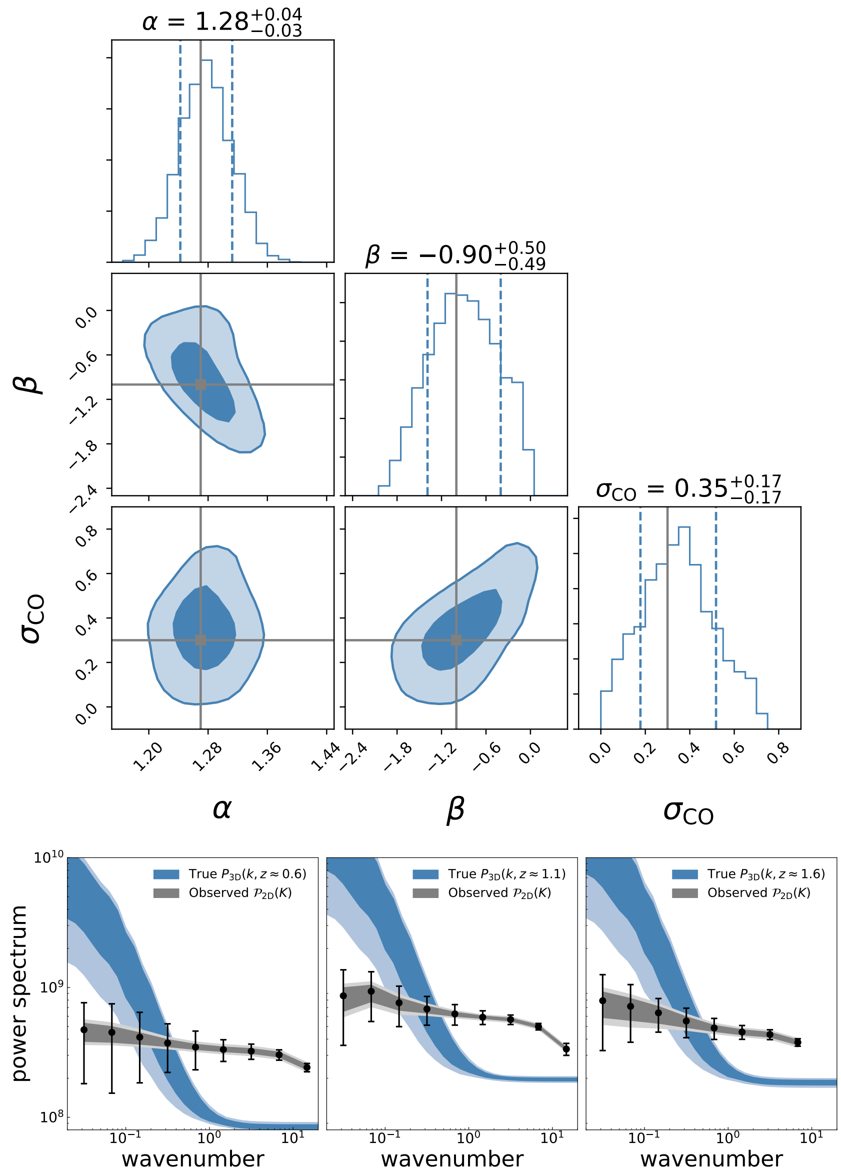

Figure 2.13: Posterior distributions of CO parameters from CO cross-power spectra. Top: joint posterior distributions of the free parameters of our CO model inferred from cross-correlating pairs of adjacent CO rotational lines over $0.5 \lesssim z \lesssim 2$ observable by TIME. Bottom: TIME constraints on the cross-correlation power spectra of CO(3–2)×CO(4–3) at $z \approx 0.6$, CO(4–3)×CO(5–4) at $z \approx 1.1$ and CO(5–4)×CO(6–5) at $z \approx 1.6$. 68% and 95% confidence intervals of the cross-power spectra, derived from 1000 random samples of the posterior distribution, are shown.

molecular gas density ρ_{H_2} inferred from MCMC analysis of the cross-power spectra are shown in Figure 4.4 as boxes in various shades of blue, indicating the pairs of CO lines being cross-correlated at different redshift intervals. These constraints

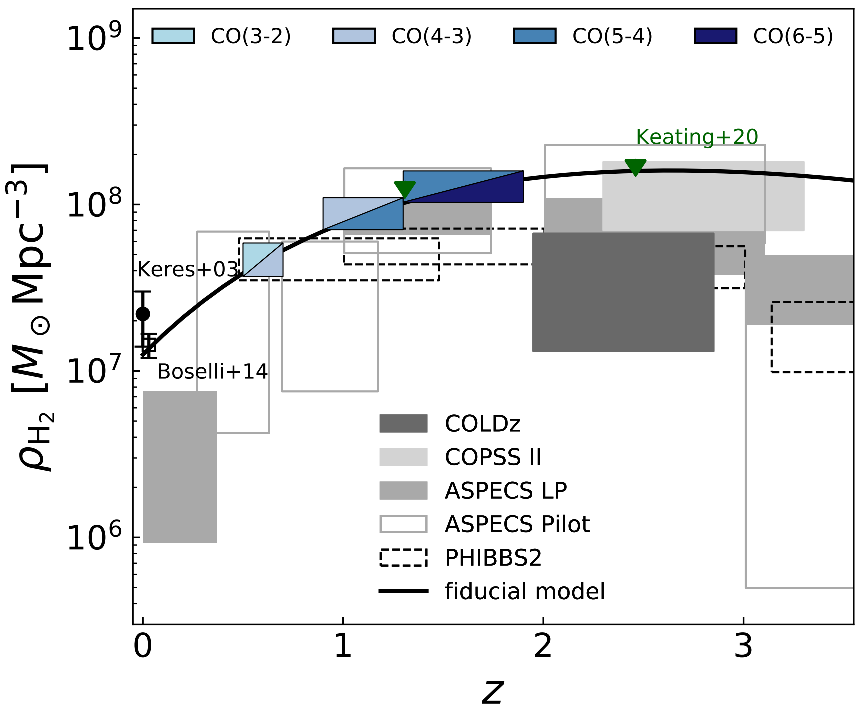

Figure 2.14: Constraints on the molecular gas density from TIME and the literature. The evolution of molecular gas density over $0 < z < 3.5$, compared with several molecular line observations showing a wide range of variation, as indicated by the data from COLDz (Riechers et al. 2019), COPSS II (Keating et al. 2016), mmIME (Keating et al. 2020), ASPECS Pilot (Decarli et al. 2016), ASPECS large program (Decarli et al. 2019), PHIBBS2 (Lenkić et al. 2020), and near $z = 0$ by Keres et al. (2003) (filled circle) and Boselli et al. (2014) (open square). Boxes in blue denote the constraints TIME is expected to provide by cross-correlating pairs of adjacent CO lines emitted from the same redshift, assuming our fiducial CO model (black curve).

are competitive compared with a collection of estimates from existing molecular line observations (Keres et al. 2003; Boselli et al. 2014; Keating et al. 2016, 2020; Riechers et al. 2019; Decarli et al. 2016, 2019). While interpreting the CO signal requires common assumptions about the CO excitation and the relation between CO luminosity and H_2 mass as discussed in Section 2.3.2, overall TIME complements other CO surveys by providing high-significance (S/N $\gtrsim$ 5 in each redshift bin) constraints on the cosmic molecular gas density evolution near cosmic noon.

By quantifying the volume-averaged depletion timescale of cold molecular gas, which can be defined as $\langle t_{\mathrm{depl}} \rangle = \rho_{\mathrm{H_2}}/\dot{\rho}_*$, these $\rho_{\mathrm{H_2}}$ measurements from TIME provide important information for understanding the nearly factor-of-10 decline of cosmic SFRD over this redshift range (see also Walter et al. 2020; Decarli et al. 2020).

2.5.4.2 Cross-correlating CO and [C I] lines at $z \approx 1.1$

In addition to measuring pairs of adjacent CO transitions at different redshift, TIME can simultaneously observe the CO(4–3), CO(5–4) and [C I] lines emitted by the same sources at $0.9 \lesssim z \lesssim 1.3$. Provided that these three lines are perfectly correlated (as assumed in our model), their mutual cross-correlations can uniquely determine the mean emission from each individual line, while being immune to bright line interlopers (Serra et al. 2016; Beane et al. 2019). We note that although CO and [C I] lines can be similarly related to the total infrared luminosity by empirical scaling relations described in Section 2.3.1.1, in practice [C I] is likely not perfectly correlated with CO(4–3) or CO(5–4) line due to source-to-source variations such as the gas excitation state, galaxy type, [C I] abundance, and so forth. The resulting de-correlation, quantifiable by measuring the [C I] auto-power spectrum, needs to be taken into account in actual data analysis, but is ignored here for simplicity.

To illustrate the constraining power TIME will offer on these line strengths, we fit templates of cross-power spectrum specified by a set of four free parameters $\{\sigma, r_{43}, r_{54}, r_{\mathrm{C\,I}}\}$, to mock observations created assuming their fiducial values as specified in Section 2.3.1.1 and Table 8.1 with the MCMC technique. Uninformative priors over [0,1] are assumed. Figure 2.15 shows the posterior distributions of the free parameters constrained by the mock observed cross-power spectra $\mathcal{P}_{\mathrm{CO(4-3)\times CO(5-4)}}$, $\mathcal{P}_{\mathrm{CO(4-3)\times C\,I}}$, and $\mathcal{P}_{\mathrm{CO(5-4)\times C\,I}}$, which are measured at S/N = 26, 18, and 13, respectively. Under the assumption that all these lines are proportional to CO(1–0) line and share the same log scatter σ, values of r_{43}, r_{54}, and $r_{\mathrm{C\,I}}$ and σ can be determined at 3-sigma level from the mutual cross-correlations. The anti-correlation between the scaling factors and σ is because increasing σ will increase the overall amplitudes of all the cross-power spectra.

These measurements of [C I]-to-CO line ratios provide direct constraints on the mass fraction of neutral atomic carbon $f_{\mathrm{C\,I}} = M_{\mathrm{C\,I}}/M_{\mathrm{C}}$ across the entire galaxy population at $z \sim 1$, which can be compared against the values ($\lesssim 10\%$) derived from ALMA observations of individual main-sequence galaxies at similar redshift (e.g., Valentino et al. 2018) to better understand how different phases of carbon co-exist in PDRs and molecular clouds.

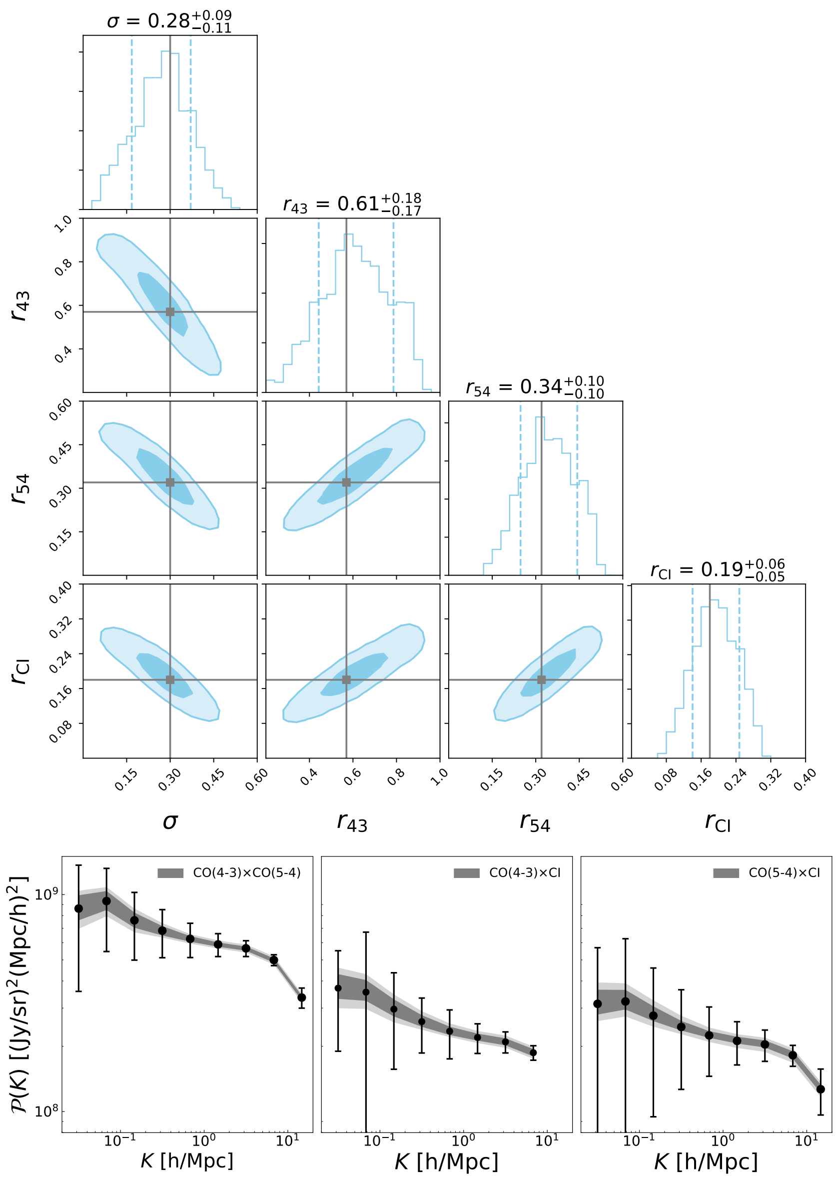

Figure 2.15: Posterior distributions of parameters from mutual cross-correlations of CO and [C I] lines. Top: joint posterior distributions of the free parameters inferred from cross-correlating the CO(4–3), CO(5–4), and [C I] lines at $z \sim 1.1$. Assuming all three lines are proportional to CO(1–0) line by some unknown scaling factors and a common log scatter σ, values of r_{43}, r_{54}, $r_{\rm C\,I}$, and σ can be determined at 3-sigma level from the mutual cross-correlations. Bottom: the constraining power of TIME on the mutual cross-power spectra. 68% and 95% confidence intervals of the cross-power spectra, derived from 1000 random samples of the posterior distribution, are shown.

2.5.5 CO–Galaxy Cross-Correlation

As discussed in Section 2.3.1.2, the cross-correlation between TIME maps of low-redshift CO lines with the galaxy density field serves as an important check for

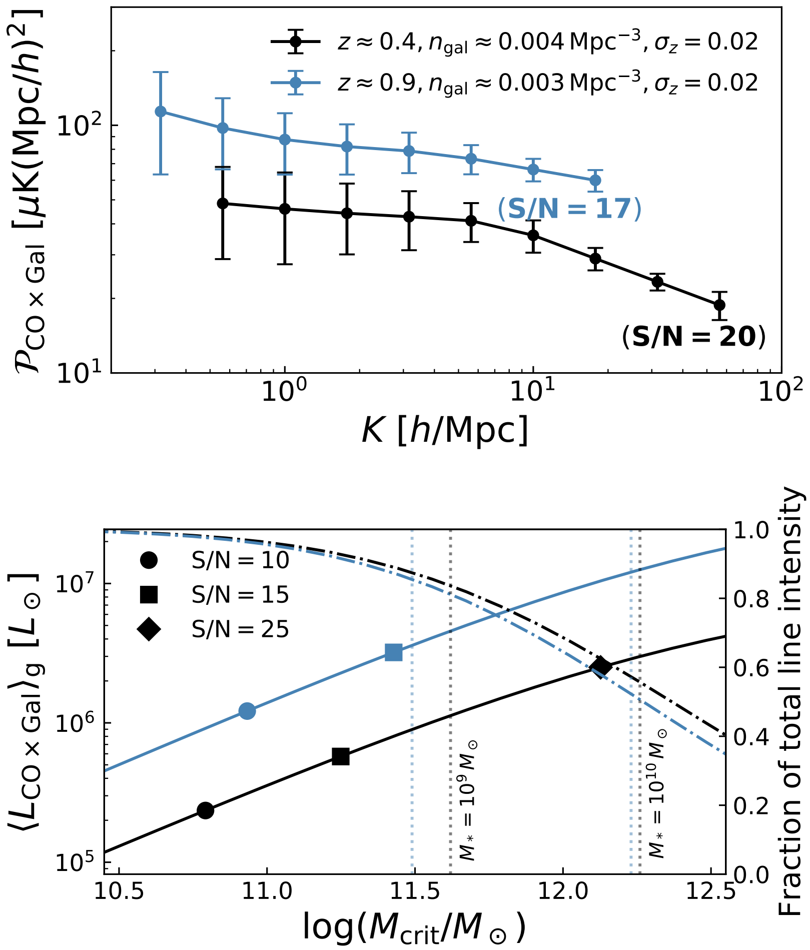

Figure 2.16: Sensitivity to and mean CO luminosities inferred from CO–galaxy cross-power spectra. Top: predicted TIME sensitivities to the CO–galaxy cross-power spectra at $z \approx 0.4$ and 0.9 for CO(3–2) and CO(4–3) lines, respectively. Bottom: mean CO line luminosity of individual galaxy samples measurable from the cross shot power (left axis) and the fraction of total CO line intensity consisting of the galaxy samples (right axis) as a function of selection threshold, measured in critical halo mass M_{crit} or stellar mass M_* (dotted lines).

separating line foregrounds and a useful probe of CO emission associated with the selected galaxy population. Despite the small survey volume of TIME, a significant number of photometric/spectroscopic galaxies are still expected to be incorporated, allowing a meaningful measurement of the cross-power spectrum at $z \sim 1$. The top panel of Figure 2.16 shows the predicted detectability of CO–galaxy cross-power spectrum by TIME, as described in Equation (2.10) and projected into the observing frame of TIME by the corresponding window function. We consider two examples in which TIME maps of CO(3-2) and CO(4-3) lines are cross-correlated with photometric galaxies ($\sigma_z^{\rm phot} \approx 0.02$) at $z \approx 0.4$ and 0.9, respectively. As summarized in Table 2.4, these cross-power measurements allow us to infer the mean CO intensity $\bar{I}_{\rm CO,gal}$ attributed to the overlapped galaxy sample from the shot-noise component, which dominates the total power spectrum. The product of mean CO bias and intensity $\bar{b}_{\rm CO}\bar{I}_{\rm CO}$ may also be weakly constrained by the clustering component, which is only marginally detected due to the limited survey size of TIME.

The amplitude and detectability of the CO–galaxy shot power is sensitive to the selection threshold of galaxy samples. As demonstrated in the bottom panel of Figure 2.16, as the selection threshold (measured in critical halo mass or stellar mass) increases, galaxies selected approach the brighter end of the CO luminosity function. This in turn enhances the overall detectability of the cross shot power, though at the expense of probing a less representative sample of CO-emitting galaxies, as indicated by the right axis, which shows the fraction of total CO line emission associated with the galaxies selected. Given prior information on galaxy redshifts, we can probe the shape of the CO luminosity function by measuring this cross-shot power for galaxy samples with varying critical mass.

2.6 Foreground Contamination and Mitigation Strategies

To reach the full scientific potential of TIME as outlined in previous sections, systematic effects in the measurement must be carefully controlled and mitigated. Among the culprits, the astrophysical and atmospheric foreground emissions are major challenges for a line intensity mapping experiment. The astrophysical foregrounds include continuum emission such as the CMB, the CIB, and spectral line interlopers such as the low-z CO rotational transition lines contaminating the high-z [C II] signals.

2.6.1 Continuum Emission

The primary and secondary CMB temperature fluctuations as well as the CIB fluctuation arising from aggregate dusty galaxy emission, are spectrally smooth with well-measured spectral characteristics (Planck Collaboration et al. 2020), and are thus distinct from the spectral line fluctuations TIME aims to measure. This is analogous to the component separation problem in 21cm cosmology where the spectrally smooth synchrotron foreground emission dominates over the 21cm line fluctuation, except that the foreground-to-signal ratio for TIME is more forgiving by about one to two orders of magnitudes in intensity as a function of scales. At

Table 2.4: Predicted constraints on astrophysical parameters from different TIME observables

Observable	TIME (TIME-EXT) S/N	Parameter	TIME (TIME-EXT) Constraint
$P_{\mathrm{C\,II}}$	HF: 5.3 (23.1), LF: 5.8 (29.9)	a	$0.98^{+0.03}_{-0.03}$ $(0.99^{+0.02}_{-0.02})$
		b	$-20.46^{+0.67}_{-0.70}$ $(-20.36^{+0.62}_{-0.74})$
		$\sigma_{\mathrm{C\,II}}$	$0.44^{+0.24}_{-0.27}$ $(0.14^{+0.13}_{-0.09})$
		ξ	$-0.01^{+0.31}_{-0.30}$ $(0.03^{+0.06}_{-0.04})$
		$\bar{b}_{\mathrm{C\,II}}\bar{I}_{\mathrm{C\,II}}$ [Jy/sr]	HF: 3260^{+480}_{-850} (3970^{+130}_{-200})
			LF: 1580^{+560}_{-390} (1870^{+170}_{-110})
$P_{\mathrm{C\,II}}$ (with τ_e and QSOs)	HF: 5.3 (23.1), LF: 5.8 (29.9)	ξ	$0.03^{+0.27}_{-0.05}$ $(0.00^{+0.01}_{-0.01})$
		f_{esc}	$0.14^{+0.23}_{-0.08}$ $(0.10^{+0.10}_{-0.04})$
$\omega_{\mathrm{C\,II}\times\mathrm{LAE}}$	$z = 5.7$: 2.7, $z = 6.6$: 2.4	$\bar{b}^{z=5.7}_{\mathrm{C\,II}}\bar{I}^{z=5.7}_{\mathrm{C\,II}}$ [Jy/sr]	2700 ± 3200
		$\bar{b}^{z=6.6}_{\mathrm{C\,II}}\bar{I}^{z=6.6}_{\mathrm{C\,II}}$ [Jy/sr]	2600 ± 2900
$P_{\mathrm{CO(3-2)\times CO(4-3)}}$ at $z \sim 0.6$, $P_{\mathrm{CO(4-3)\times CO(5-4)}}$ at $z \sim 1.1$, $P_{\mathrm{CO(5-4)\times CO(6-5)}}$ at $z \sim 1.6$	20, 26, 22	α	$1.28^{+0.04}_{-0.03}$
		β	$-0.90^{+0.50}_{-0.49}$
		σ	$0.35^{+0.17}_{-0.17}$
$P_{\mathrm{CO(4-3)\times C\,I}}$, $P_{\mathrm{CO(5-4)\times C\,I}}$, $P_{\mathrm{CO(4-3)\times CO(5-4)}}$ at $z \sim 1.1$	18, 13, 26	σ	$0.28^{+0.09}_{-0.11}$
		r_{43}	$0.61^{+0.18}_{-0.17}$
		r_{54}	$0.34^{+0.10}_{-0.10}$
		$r_{\mathrm{C\,I}}$	$0.19^{+0.06}_{-0.05}$
$P_{\mathrm{CO(3-2)\times gal\ (phot)}}$ at $z \sim 0.4$	20	$\bar{b}_{\mathrm{CO}}\bar{I}_{\mathrm{CO}}$ [μK]	$0.087^{+0.236}_{-0.068}$
		$\bar{I}_{\mathrm{CO,gal}}$ [μK]	$0.102^{+0.005}_{-0.005}$
$P_{\mathrm{CO(4-3)\times gal\ (phot)}}$ at $z \sim 0.9$	17	$\bar{b}_{\mathrm{CO}}\bar{I}_{\mathrm{CO}}$ [μK]	$0.129^{+0.372}_{-0.105}$
		$\bar{I}_{\mathrm{CO,gal}}$ [μK]	$0.229^{+0.011}_{-0.015}$

this level, several techniques including the principal component analysis (PCA) or the independent component analysis (ICA) have been demonstrated with data to effectively separate the continuum foreground from line emission at minimum loss of signal (Chang et al. 2010; Switzer et al. 2013; Wolz et al. 2017b).

We model atmospheric emission based on data taken at Mauna Kea at 143 and 268 GHz (Sayers et al. 2010), and scale it to the typical atmosphere opacity values for Kitt Peak. We note that the TIME spectrometer covers the full 183 GHz to 326 GHz band, while only the 201 GHz to 302 GHz sub-band is used for science. The other channels at the high- and low-frequency edges (a total of 16) serve as atmospheric monitors (Hunacek et al. 2016). Because they access the water lines, they combine to provide greater sensitivity to the PWV fluctuations than the combined science band channels, allowing effective tracking removal of the water vapor fluctuations to below the instrumental noise levels. Given that the PWV fluctuations amount to a time-dependent amplitude modulation of the emission constant across frequency, the same PCA-based removal techniques may be used for mitigation.

We simulate the above astrophysical and atmospheric continuum foregrounds and add their contribution to a simulated TIME signal light cone based on the SIDES simulation (Béthermin et al. 2017) to investigate the de-contamination strategy. A detailed analysis will be described in future TIME publications, and we summarize here that with a PCA-based foreground removal technique, the CMB, CIB, and atmospheic emissions can be removed to high fidelity with minimum loss of spectral line signals. As noted previously, we approximate continuum foreground removal by removing the largest spatial and spectral modes from our analysis.

2.6.2 Spectral Line Interlopers

As noted earlier, the low-redshift CO rotational lines present a rich science opportunity to probe the molecular gas growth in the universe and to trace the LSS. They however can be confused with the high-z [C II] line emission at the same observed frequencies, and present a challenge as spectral line interlopers. Several mitigation strategies have been proposed, including the usage of cross-correlation (Silva et al. 2015), masking (Breysse et al. 2015; Sun et al. 2018), anisotropic power spectrum effect (Lidz & Taylor 2016; Cheng et al. 2016), as well as map-space de-blending techniques involving deep learning (Moriwaki et al. 2020) and spectral template fitting with sparse approximation (Cheng et al. 2020b).

For TIME, for the purpose of [C II] measurement we plan to follow the targeted masking strategy laid out in Sun et al. (2018) using an external galaxy catalog to identify and mask bright low-z CO emitters. As elucidated in Sun et al. (2018), using the total IR luminosity as a proxy for CO emission in NIR-selected galaxies, we can clean CO interlopers to a level sufficient for a robust [C II] detection by masking no more than 10% of the total voxels. Because of the small masking fraction required and that CO foregrounds are not spatially correlated with [C II] emission from much higher redshift, masking only causes a modest reduction of survey sensitivity[5] and does not bias the [C II] measurement itself. The coupling between Fourier modes arising from the survey volume lost to extra real-space filtering (i.e., masking) can be corrected by inverting the mode-coupling matrix, $\mathbf{M}_{KK'}$, which can be directly calculated from the masked data cube by generalizing the window function calculation presented in Appendix 2.10. Nevertheless, CO residuals may lead to an actual loss of sensitivity, although methods such as cross-correlation can be used to quantify the residual line-interloper contamination. A detailed presentation of how to correct for the mode coupling due to foreground cleaning and estimate the level of residuals is beyond the scope of this work. We therefore postpone a more thorough analysis of these issues to future publications.

2.7 Discussion

2.7.1 Implications and Limitations of Power Spectral Constraints from TIME and TIME-EXT

Due to their distinct physical origins, clustering (proportional to the square of the first luminosity moment) and shot-noise (proportional to the second luminosity moment) components of the power spectrum have different sensitivities to different populations of line emitters. For this reason, while astrophysical parameters may still be constrained by measuring only one single component such as the shot noise, it is favorable to access the full power spectrum at different scales in order to maximize the effectiveness of parameter estimation (Yue & Ferrara 2019). Given the projection effect of its line-scan geometry, TIME and TIME-EXT will directly measure a 2D power spectrum much less scale-dependent compared with the true 3D power spectrum, as shown in Figure 2.7, and any particular observed mode K results from a non-trivial mixing of sky modes k described by the window function $W_{ii}\left(k, \vec{K}_i\right)$. The connection between parameter constraints and observed modes is therefore less straightforward. Nevertheless, although the shot noise dominates

[5] The power spectrum S/N roughly scales as the square root of survey volume via $\sqrt{N_\mathrm{m}}$, so masking $< 10\%$ of voxels for removing CO interlopers only moderately changes the sensitivity.

large $K \gtrsim 1\ h/\mathrm{Mpc}$ modes for both [C II] and CO signals, the access to the clustering component at smaller K's helps lift the degeneracy among parameters affecting the shape of the power spectrum differently. For instance, the faint-end modulation factor ξ has a minute effect on the shot-noise power dominated by bright sources. Hence, it can be most easily constrained by measuring the clustering component with higher significance, as indicated by the comparison between TIME and TIME-EXT in the top panel of Figure 2.7.

For TIME, our fiducial model predicts that the uncertainties in the [C II] auto-power spectra and CO cross-power spectra are dominated by the instrument noise and sample variance, respecitively. Therefore, with the same survey strategy but more than 10 times greater survey power, TIME-EXT is expected to outperform TIME by measuring the [C II] auto-power spectrum at a high significance of S/N>20. This allows the [C II] parameters to be constrained to a level limited by their intrinsic degeneracies, which have to be broken by additional observables such as the one-point statistics (Breysse et al. 2017) and/or data sets such as independent constraints from galaxy detection. Further insights into [C II] line emission from the EoR can be obtained from LIM measurements beyond the auto-correlation, such as the cross-correlation of [C II] with other EoR probes, some examples of which are discussed in the next sub-section.

2.7.2 Next-generation [C II] LIM Experiment

So far, we have outlined the rich and diverse science enabled by TIME and TIME-EXT, as two distinct phases of a first-generation [C II] LIM experiment. In the future, we anticipate the sensitivity, in part limited by the number of spectrometers on TIME, can be advanced by the development of a more densely populated focal plane empowered by on-chip mm-wave spectrometers (Redford et al. 2018; Endo et al. 2019; Karkare et al. 2020). A next-generation TIME experiment, TIME-NG, can have an increased number of spectrometers by at least a factor of 10. Combined with a lower atmospheric loading from a better observing site and with a dedicated telescope, TIME-NG can achieve at least three times lower NEI level compared to TIME, and expect a few thousands of hours of integration time. All these factors can result in another order of magnitude improvement in survey power to measure the [C II] power spectrum compared with TIME-EXT.

The high-significance measurements of the [C II] statistical properties will not only characterize the science cases summarized in this paper with higher precision,

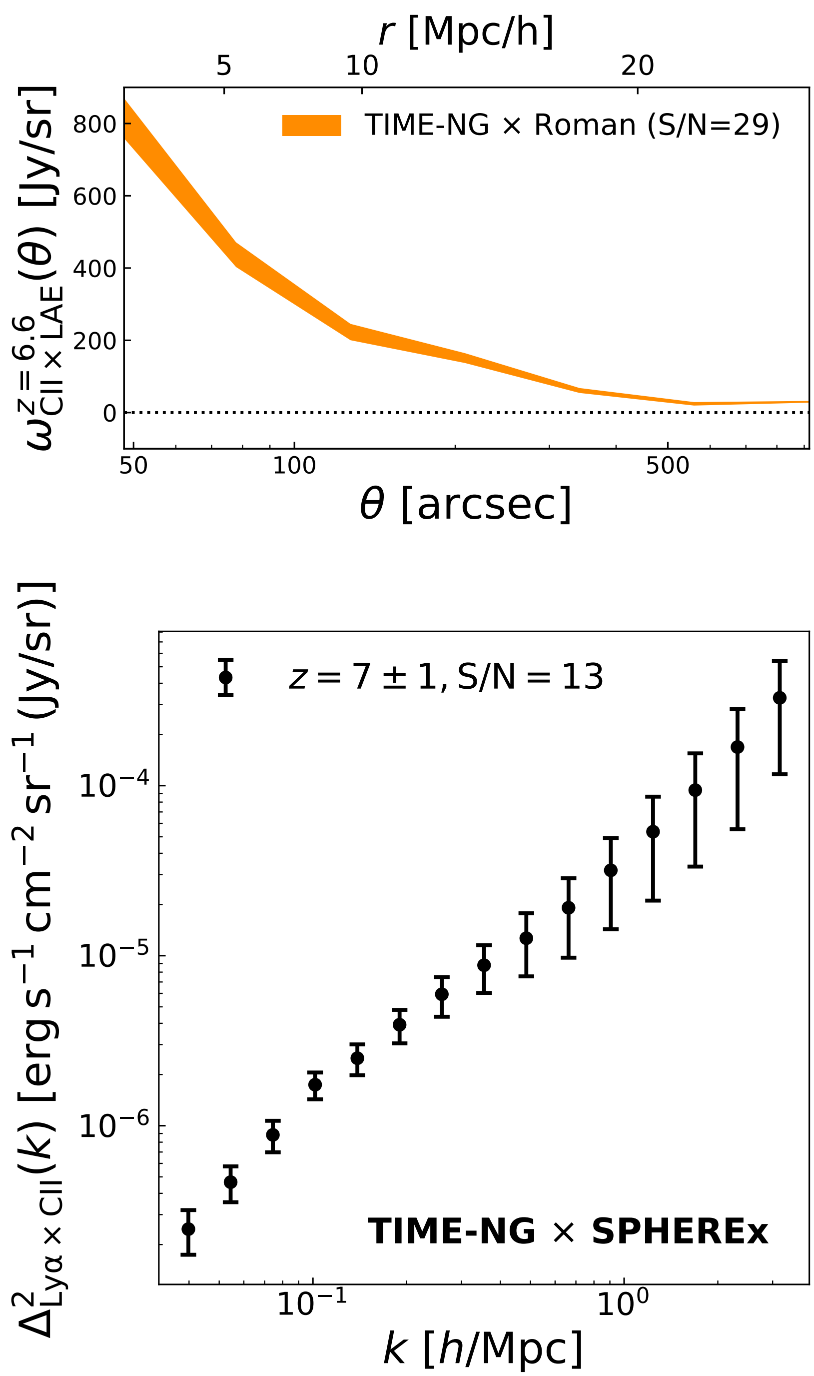

Figure 2.17: Synergies between TIME-NG and surveys of LAEs and Lyα intensity fluctuations. Measurement uncertainties quoted assume an overlapped survey area of 10 deg^2 and a factor of 120 improvement in survey power from TIME to TIME-NG. Top: predicted angular cross-correlation function at $z = 6.6$ between [C II] intensity measured by TIME-NG and LAEs observed with a Roman Space Telescope GO survey reaching a minimum Lyα luminosity of $\log(L_{\mathrm{Ly}\alpha,\mathrm{min}}/\mathrm{erg\,s^{-1}}) = 42.7$ (or $m^{\mathrm{AB}}_{\mathrm{lim}} = 25.5$, which implies $n_{\mathrm{LAE}} \simeq 10^{-4}\,\mathrm{Mpc^{-3}}$). Bottom: predicted dimensionless cross-power spectrum at $z \approx 7$ between [C II] intensity measured by TIME-NG and Lyα intensity measured in SPHEREx deep field (with a 1-σ surface brightness sensitivity level of 10^3 Jy/sr).

but more significantly, enrich the multi-tracer probe of reionization in the coming decade to further our understanding of reionization beyond presented here (e.g., Chang et al. 2019). The improved sensitivity of TIME-NG will make possible a variety of cross-correlation analyses between [C II] and other tracers of the EoR, including LAEs and LBGs to be surveyed by the Nancy Grace Roman and Euclid Telescopes in the near future, as well as emission lines from other LIM experiments such as the Lyα diffuse emission from SPHEREx (Doré et al. 2014, 2016), and the 21cm emission from HERA (DeBoer et al. 2017) and the SKA (Koopmans et al. 2015). Using models [C II] and LAEs presented in this work together with physical models of Lyα and 21cm line motivated by observations (e.g., Gong et al. 2012; Chang et al. 2015; Heneka et al. 2017; Dumitru et al. 2019), we estimate that, for a $10\,\mathrm{deg}^2$ survey and a TIME-NG-like capability with 3000 hours of integration, the [C II]-LAE cross-correlation with an anticipated Roman General Observer (GO) survey (Spergel et al. 2015) of the same size and a depth of $m_{\rm lim}^{\rm AB} = 25.5$ can be measured at high significance, as shown in the top panel of Figure 2.17 and elaborated in the caption. In addition, the [C II]–Lyα and [C II]–21cm cross-power spectra at $z \sim 7$, with SPHEREx and SKA, respectively, can both be solidly detected at an S/N $\gtrsim 5$. The bottom panel of Figure 2.17 shows the [C II]–Lyα cross-power spectrum estimated based on the Lyα power spectrum from Heneka et al. (2017). We expect a significant detection by overlapping TIME-NG with SPHEREx deep field, whose surface brightness sensitivity level is taken to be 10^3 Jy/sr[6]. Subsequent multi-tracer analyses, based on detecting these cross-correlations at circum-galactic to inter-galactic scales during reionization, will provide a comprehensive view of how ionized bubbles grew out of the production and escape of ionizing photons from galaxies.

2.8 Conclusions

Complementary to conventional galaxy surveys, intensity mapping of the redshifted [C II] and CO lines from the reionization era and the epoch of peak star formation reliably probes aggregate line emission, offering invaluable insight into the total cosmic star formation and the evolution of the molecular gas content of galaxies during those epochs.

We presented a modeling framework that self-consistently models the target signals

[6]See the public file containing the forecasted surface brightness sensitity level of SPHEREx at `https://github.com/SPHEREx/Public-products/blob/master/Surface_Brightness_v28_base_cbe.txt`.

of TIME and predicts its capability of constraining a series of physical quantities of interest. Using forecasts based on realistic TIME instrument specifications and our fiducial model informed by observations available to date, we identified a line-scan survey geometry optimized for measuring of [C II] intensity fluctuations from the EoR.

Starting from the optimized line survey, we generate mock power spectra of our [C II] signal as well as line interlopers including rotational CO and [C I] line from lower redshifts. We then analyzed results within a Bayesian inference framework to forecast parameter constraints, given the sensitivity levels of TIME and TIME-EXT (the extended TIME survey from the LCT). Based on our analysis, we expect TIME(-EXT) to measure the [C II] power spectrum during reionization with a total S/N greater than 5 (20) and thereby provide robust constraints on the [C II] luminosity density and the cosmic SFRD over $6 \lesssim z \lesssim 9$. Combining such measurements with the Thomson scattering optical depth of CMB photons and quasar absorption spectra, we also expect to constrain the population-averaged escape fraction of ionizing photons to the level of $f_{\rm esc} \approx 0.1^{+0.2}_{-0.1}$ and $f_{\rm esc} \approx 0.1^{+0.10}_{-0.05}$ respectively for the two phases of TIME experiment. Such measurements are independent of the faint-end extrapolation of galaxy LF, which will be robustly constrained by TIME-EXT.

Through in-band cross-correlations, we predict that TIME and TIME-EXT will measure the cross-power spectra of interloping CO and [C I] lines at $0.5 \lesssim z \lesssim 2$ with high significance (S/N>10). Thanks to the wide bandwidth, these cross-correlation measurements can be used to infer the cosmic molecular gas density near cosmic noon assuming prior knowledge of the CO rotational ladder, whereas the mutual cross-correlations among CO(4–3), CO(5–4), and [C I] lines at $z \sim 1.1$ can extract the individual line strengths, shedding light on the excitation state of CO and the relation with neutral carbon in the ISM, averaged over the entire galaxy population.

The synergy of TIME maps and external galaxy surveys serves as a useful sanity check of foreground removal, while also providing additional astrophysical information about the overlapping galaxy population. We therefore analyze the prospects for cross-correlating TIME [C II] maps with narrow-band selected LAEs at $z = 5.7$ and $z = 6.6$ from the Subaru HSC survey. Due to TIME's limited survey size, only upper limits can be extracted on $\bar{b}_{\rm C\,II}\bar{I}_{\rm C\,II}$ from the angular cross-correlation function of [C II] and LAEs. At lower redshifts, we expect significant detections of the cross-power spectra between TIME CO maps and galaxies with known redshifts.

From these shot-noise-dominated measurements, we placed stringent constraints on the mean CO intensity attributed to the galaxy sample of interest.

Finally, we discuss that a next-generation [C ii] experiment, TIME-NG, can map [C ii] intensity fluctuations during the EoR with high significance on $\sim 10\,\mathrm{deg}^2$ scales, opening exciting opportunities for multi-tracer analyses based on cross-correlating [C ii] maps with other EoR probes such as LAEs, Lyα, and the 21cm line.

Acknowledgments

We would like to thank the anonymous referees for their comments that improved the manuscript. We are indebted to Lluis Mas-Ribas for helpful comments on an early version of the paper and Lin Yan for discussion about the [C ii] luminosity function measured from the ALPINE survey. We are also grateful for Garrett (Karto) Keating for compiling the observational constraints on molecular gas density. TCC and GS acknowledge support from the JPL Strategic R&TD awards. AC acknowledges support from NSF AST-1313319 and 2015-2016 UCI Office of Research Seed Funding Award. DPM and RPK were supported by the National Science Foundation through CAREER grant AST-1653228. RPK was supported by the National Science Foundation through Graduate Research Fellowship grant DGE-1746060. ATC was supported by a KISS postdoctoral fellowship and a National Science Foundation Astronomy and Astrophysics Postdoctoral Fellowship under Grant No. 1602677. This work is supported by National Science Foundation award number 1910598. Part of the research described in this paper was carried out at the Jet Propulsion Laboratory, California Institute of Technology, under a contract with the National Aeronautics and Space Administration.

2.9 Appendix: Modeling the Star Formation Efficiency

2.9.1 Dust Correction

Following Sun & Furlanetto (2016) and Mirocha & Furlanetto (2019), we derive the dust extinction correction at any given magnitude M_{UV} by combining the Meurer et al. (1999) relation between the dust extinction (evaluated at 1600 Å) A_{UV} and the slope of UV continuum β,

$$A_{\mathrm{UV}} = 4.43 + 1.99\beta \geq 0\,, \tag{2.42}$$

with the β–M_{UV} relation, which is modeled by Bouwens et al. (2014) as a linear relation with a constant gaussian error $\sigma_\beta = 0.34$. The correction factor averaged

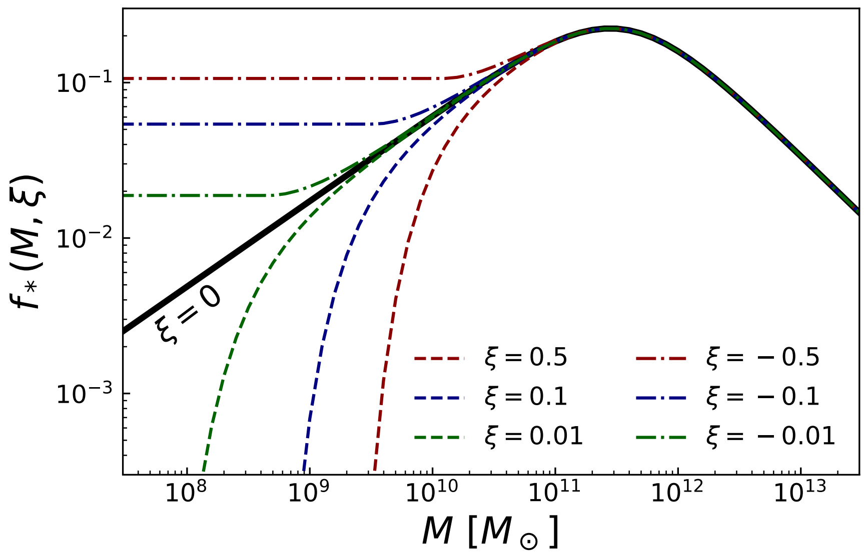

Figure 2.18: The star formation efficiency f_* as a function of halo mass. Curves corresponding to different choices of ξ, as defined in Equation (2.43), are shown to illustrate how our model captures the uncertainty in the mass dependence at the low-mass end.

over the β-distribution, $\langle A_{\rm UV} \rangle$, is then applied to obtain the dust-corrected UVLFs from the observed ones, and consequently define the SFRs with and without the dust correction.

2.9.2 The Star Formation Efficiency as a Function of Halo Mass

As discussed in Section 2.3.3, the SFE f_*, which together with the mass accretion rate of dark matter halos determine the SFH, is an essential quantity in our modeling framework. The low-mass end behavior of f_* is particularly important because, in the context of luminosity function, the cosmic star formation rate and therefore the total budget of ionizing photons are determined by both the steepness of the faint-end slope and the cutoff luminosity. As a result, our f_* model aims to maximize the flexibility to explore the degeneracy between these two quantities by extending the low-mass end unconstrained by abundance matching differently, ranging from an asymptote to a constant value to an exponential decay. Specifically, we define a redshift-independent SFE that can be expressed as

$$f_*(M) = \frac{f_{*,0}}{\left(\frac{M}{M_{\rm p}}\right)^{\gamma_{\rm lo}(M)} + \left(\frac{M}{M_{\rm p}}\right)^{\gamma_{\rm hi}}}\,, \tag{2.43}$$

where $f_{*,0} = 0.22$ is twice the maximum possible SFE peaking at $M_\mathrm{p} = 3.6 \times 10^{11}\,M_\odot$, and $\gamma_\mathrm{hi} = 0.77$ specifies the mass dependence of the high-mass end. The low-mass end is allowed to deviate from perfect power law by

$$\gamma_\mathrm{lo}(M) = -0.55 \times 10^{\xi/(M/M_\mathrm{c})} \,, \tag{2.44}$$

where $M_\mathrm{c} = 3 \times 10^9\,M_\odot$ is the characteristic halo mass for a deviation from power law at the low-mass end. ξ is a free parameter defining the level of deviation, with $\xi = 0$ corresponding to the best-fit double power-law model of f_* calibrated against the observed UVLFs at $5 < z < 9$ after the dust correction (see also Mirocha et al. 2017). Note that when $\xi < 0$, we impose a ceiling on f_* such that it asymptotes to a constant value rather than blowing up. A few sample $f_*(M)$ curves with different choices of ξ are shown in Figure 6.2.

2.10 Appendix: Window Function

Following Dodelson (2003), we can express the *dimensionless* covariance matrix of a pair of instrument modes, whose wavenumbers are denoted by $\vec{K}_i$ and $\vec{K}_j$ to distinguish from the wavenumber $\vec{k}$ of the sky mode before being filtered by the survey geometry, as

$$\begin{aligned} C^S_{ij}\left(\vec{K}_i, \vec{K}_j\right) &= \langle \delta^*_{\mathbf{K}_i} \delta_{\mathbf{K}_j} \rangle \\ &= \int \frac{\mathrm{d}k\mathrm{d}\theta\mathrm{d}\phi}{(2\pi)^3}\, k^2 \sin\theta P(k) \tilde{\psi}_i \tilde{\psi}^*_j \\ &= \int \mathrm{d}k \frac{k^2}{2\pi^2} P(k) W_{ij}\left(k, \vec{K}_i, \vec{K}_j\right) \,, \end{aligned} \tag{2.45}$$

where the weighting function $\tilde{\psi}(k)$ is the Fourier transform of the real-space selection function $\psi(x)$ which describes the actual geometry with survey volume $V_S = \int \mathrm{d}^3x = L_x L_y L_z$ and satisfies $\int \mathrm{d}^3x \psi(x) = 1$. Note that for simplicity we have assumed the actual fluctuations on sky to be isotropic such that we can replace sky modes $\vec{k}$ with k. We consequently define the window function W_{ij} to be the angular average of the inner product of two weighting functions, $\tilde{\psi}_i \tilde{\psi}^*_j$, which satisfies $V_S \int \mathrm{d}k k^2 W_{ij}(k)/2\pi^2 = 1$ for a 3D survey due to the unitarity of Fourier transform. Effectively, Equation (2.45) can be interpreted as a projection from the sky frame to the observing frame that results in mode mixing, where W_{ij} serves as the projection kernel.

For a line intensity mapping experiment like TIME, the survey volume within which fluctuations of the intensity field are measured can be effectively approximated with a three-dimensional box of dimensions L_x, L_y and L_z. Specifically, in the case of a 2D line scan, we require that $L_y \ll L_x, L_z$. The corresponding selection function can be specified by a product of top-hat functions, which implies a weighting function in k space of the form

$$\begin{aligned}
\tilde{\psi}_i\left(\vec{k}, \vec{K}_i\right) &= \int \mathrm{d}^3 x e^{i(\vec{K}_i - \vec{k})\cdot\vec{x}} \psi\left(\vec{x}\right) \\
&= \int \mathrm{d}^3 x e^{i(\vec{K}_i - \vec{k})\cdot\vec{x}} \prod_{m=x,y,z} \frac{1}{L_m} \Theta\left(\frac{L_m}{2} \pm m\right) \\
&= j_0\left(q_x L_x/2\right) j_0\left(q_y L_y/2\right) j_0\left(q_z L_z/2\right) \ ,
\end{aligned} \tag{2.46}$$

where $\vec{K}_i = (K_{i,x}, 0, K_{i,z})$, $q_m = K_{i,m} - k_m$ and $j_0(x) = \sin(x)/x$ is the spherical Bessel function of the first kind. The covariance matrix C^S_{ij} is thus related to the observed 2D power spectrum (in units of area) by

$$\mathcal{P}\left(\vec{K}_i\right) = L_x L_z C^S_{ii}\left(\vec{K}_i\right) \ , \tag{2.47}$$

where we only consider the diagonal terms assuming the correlation between different instrument modes are negligible. We note that for the line scan considered, we must normalize Equation (2.47) by dividing it with $V_S \int \mathrm{d}k k^2 W_{ii}(k)/2\pi^2 < 1$ to account for the difference between 2D and 3D power.

2.11 Appendix: Uncertainties of Auto- and Cross-Power Spectra

Here we present a derivation of the errors on auto and cross-power spectra, which is a simplified version of that given by Visbal & Loeb (2010). For the cross-power spectrum of two real fields f_1 and f_2, we define the estimator to be the *real part* of the inner product of their Fourier transforms $\tilde{f}_1$ and $\tilde{f}_2$, namely

$$\hat{P}_{1,2} = \frac{V}{2}\left(\tilde{f}_1 \tilde{f}_2^* + \tilde{f}_1^* \tilde{f}_2\right) \tag{2.48}$$

and its variance can be consequently written as

$$var\left(\hat{P}_{1,2}\right) = \delta\hat{P}^2_{1,2} = \langle \hat{P}^2_{1,2} \rangle - \langle \hat{P}_{1,2} \rangle^2 \ , \tag{2.49}$$

where $\langle ... \rangle$ stands for averaging over the statistical ensemble. Expanding the above expression with Equation (2.48), we have

$$\begin{aligned}
\delta P^2_{1,2} = \langle \hat{P}^2_{1,2} \rangle - \langle \hat{P}_{1,2} \rangle^2 &= \left\langle \frac{V^2}{4}\left(\tilde{f}_1 \tilde{f}_2^* + \tilde{f}_1^* \tilde{f}_2\right)^2 \right\rangle - P^2_{1,2} \\
&= \frac{V^2}{2}\left\langle \tilde{f}_1 \tilde{f}_1 \tilde{f}_2^* \tilde{f}_2^* \right\rangle + \frac{V^2}{2}\left\langle \tilde{f}_1 \tilde{f}_1^* \tilde{f}_2 \tilde{f}_2^* \right\rangle - P^2_{1,2} \ .
\end{aligned} \tag{2.50}$$

We now use Wick's theorem to rewrite the four-term product as the sum of three cross products

$$\left\langle \tilde{f}_1\tilde{f}_1\tilde{f}_2^*\tilde{f}_2^*\right\rangle = \left\langle \tilde{f}_1\tilde{f}_1\right\rangle\left\langle \tilde{f}_2^*\tilde{f}_2^*\right\rangle + 2\left\langle \tilde{f}_1\tilde{f}_2^*\right\rangle^2 = 2\left\langle \tilde{f}_1\tilde{f}_2^*\right\rangle^2 , \tag{2.51}$$

and

$$\begin{aligned}\left\langle \tilde{f}_1\tilde{f}_1^*\tilde{f}_2\tilde{f}_2^*\right\rangle &= \left\langle \tilde{f}_1\tilde{f}_2\right\rangle\left\langle \tilde{f}_1^*\tilde{f}_2^*\right\rangle + \left\langle \tilde{f}_1\tilde{f}_1^*\right\rangle\left\langle \tilde{f}_2\tilde{f}_2^*\right\rangle + \left\langle \tilde{f}_1\tilde{f}_2^*\right\rangle\left\langle \tilde{f}_1^*\tilde{f}_2\right\rangle \\ &= \left\langle \tilde{f}_1\tilde{f}_1^*\right\rangle\left\langle \tilde{f}_2\tilde{f}_2^*\right\rangle + \left\langle \tilde{f}_1\tilde{f}_2^*\right\rangle\left\langle \tilde{f}_1^*\tilde{f}_2\right\rangle .\end{aligned} \tag{2.52}$$

Note that for the Fourier transform $\tilde{f}$ of a real field f, the first terms in the two expressions above vanish because of the Hermitianity condition $\tilde{f}^*(k) = \tilde{f}(-k)$ and the fact that different k modes are statistically independent. For the ensemble average, we should have $\left\langle \tilde{f}_1\tilde{f}_2^*\right\rangle = \left\langle \tilde{f}_1^*\tilde{f}_2\right\rangle$. As a result, the variance becomes

$$\begin{aligned}\delta P_{1,2}^2 &= \frac{V^2}{2}\left\langle \tilde{f}_1\tilde{f}_1\tilde{f}_2^*\tilde{f}_2^*\right\rangle + \frac{V^2}{2}\left\langle \tilde{f}_1\tilde{f}_1^*\tilde{f}_2\tilde{f}_2^*\right\rangle - P_{1,2}^2 \\ &= \frac{3V^2}{2}\left\langle \tilde{f}_1\tilde{f}_2^*\right\rangle^2 + \frac{V^2}{2}\left\langle \tilde{f}_1\tilde{f}_1^*\right\rangle\left\langle \tilde{f}_2\tilde{f}_2^*\right\rangle - P_{1,2}^2 .\end{aligned} \tag{2.53}$$

Using the definitions of auto- and cross-power spectra (as the ensemble average of the Fourier pair product), we finally obtain

$$\delta P_{1,2}^2 = \frac{3}{2}P_{1,2}^2 + \frac{1}{2}P_1P_2 - P_{1,2}^2 = \frac{1}{2}\left(P_{1,2}^2 + P_1P_2\right) . \tag{2.54}$$

For the auto power spectrum, the variance given by Equation (2.50) simply becomes

$$\delta P_1^2 = V^2\left\langle \tilde{f}_1\tilde{f}_1\tilde{f}_1^*\tilde{f}_1^*\right\rangle - P_1^2 = 2V^2\left\langle \tilde{f}_1\tilde{f}_1^*\right\rangle^2 - P_1^2 = P_1^2 . \tag{2.55}$$

Chapter 3

A FOREGROUND MASKING STRATEGY FOR [C II] INTENSITY MAPPING EXPERIMENTS USING GALAXIES SELECTED BY STELLAR MASS AND REDSHIFT

Sun, G., Moncelsi, L., Viero, M. P., et al. (2018). "A Foreground Masking Strategy for [C II] Intensity Mapping Experiments Using Galaxies Selected by Stellar Mass and Redshift", *Astrophysical Journal*, 856, 107. DOI: 10.3847/1538-4357/aab3e3.

Abstract

Intensity mapping provides a unique means to probe the epoch of reionization (EoR), when the neutral intergalactic medium was ionized by the energetic photons emitted from the first galaxies. The [C II] 158μm fine-structure line is typically one of the brightest emission lines of star-forming galaxies and thus a promising tracer of the global EoR star-formation activity. However, [C II] intensity maps at $6 \lesssim z \lesssim 8$ are contaminated by interloping CO rotational line emission ($3 \leq J_{\mathrm{upp}} \leq 6$) from lower-redshift galaxies. Here we present a strategy to remove the foreground contamination in upcoming [C II] intensity mapping experiments, guided by a model of CO emission from foreground galaxies. The model is based on empirical measurements of the mean and scatter of the total infrared luminosities of galaxies at $z < 3$ and with stellar masses $M_* > 10^8\, M_\odot$ selected in K-band from the COSMOS/UltraVISTA survey, which can be converted to CO line strengths. For a mock field of the Tomographic Ionized-carbon Mapping Experiment (TIME), we find that masking out the "voxels" (spectral-spatial elements) containing foreground galaxies identified using an optimized CO flux threshold results in a z-dependent criterion $m_{\mathrm{K}}^{\mathrm{AB}} \gtrsim 22$ (or $M_* \gtrsim 10^9\, M_\odot$) at $z < 1$ and makes a [C II]/$\mathrm{CO_{tot}}$ power ratio of $\gtrsim 10$ at $k = 0.1\, h$/Mpc achievable, at the cost of a moderate $\lesssim 8\%$ loss of total survey volume.

3.1 Introduction

The formation of stars in the first generations of galaxies is closely associated with the Epoch of Reionization (EoR) occurring at $6 \lesssim z \lesssim 10$, during which Lyman continuum photons ionized the mostly neutral intergalactic medium (IGM) after recombination ($z \sim 1100$). Advances in surveys of individual high-redshift galaxies at both near-infrared (e.g., Ellis et al. 2013; Bouwens et al. 2015b; Oesch et al. 2015; Livermore et al. 2017) and millimeter/sub-millimeter wavelengths (e.g., Capak et al. 2015; Carilli et al. 2016), together with constraints on the global ionization history from the cosmic microwave background (Planck Collaboration et al. 2016c) and a variety of spectroscopic diagnostics of the evolving IGM neutrality (see Robertson et al. 2015 for a compilation), have greatly deepened our understanding of the reionization era over the past several years. However, none of these observables directly probes the entire ionizing photon budget responsible for reionization — even for a typical "ultra-deep" survey with the most powerful telescopes like JWST, limitations on the sensitivity may result in missing up to 50% of the total star formation inside galaxies at $z > 8$, given the steep faint-end slope of the galaxy luminosity function implied by current observations (Sun & Furlanetto 2016; Furlanetto et al. 2017).

An alternative to galaxy counting is to measure the aggregate emission from all galaxies through line intensity mapping. In this approach, an imaging spectrometer is used to map the surface brightness of the Universe as a function of position on the sky and frequency. A bright emission line creates structure in the resulting 3D map due to the cosmic matter distribution; this structure is analyzed in the Fourier domain, i.e., with a power spectrum. In particular, the variance on large scales carries information about the total line emission from all galaxies, integrated over the full luminosity function, including all faint sources (Visbal & Loeb 2010; Visbal et al. 2011).

[C II] is a particularly promising probe for line intensity mapping of the reionization epoch (e.g., Gong et al. 2012; Silva et al. 2015; Yue et al. 2015; Breysse et al. 2015; Serra et al. 2016). As the dominant coolant of the cold, neutral interstellar medium (ISM), the [C II] 157.7μm fine-structure line is among the strongest emission lines in aggregate galaxy spectra and it is found to be a reliable tracer of the star formation activity of typical star-forming galaxies (De Looze et al. 2011; Herrera-Camus et al. 2015). Observationally, [C II] is redshifted into the 200–300 GHz atmospheric window, which is relatively accessible from even modest millimeter-wave sites.

However, extracting signals from EoR galaxy populations in intensity mapping experiments is challenging because these galaxies are typically not the dominant source of fluctuations in a map. EoR signals suffer from both a small luminosity density and the $1/D_L^2$ cosmological dimming relative to the later-time emission when luminosity density was at its peak. Specifically, for an intensity mapping experiment at $\sim$ 250 GHz, the EoR [C II] signal will be confused by the CO rotational lines emitted by foreground galaxies ($3 \leq J_{\rm upp} \leq 6$, at $0 < z < 2$) and redshifted into the same frequency band, in addition to the continuum sources that make up the cosmic infrared background (CIB). As a result, an accurate measurement of the EoR [C II] power spectrum requires that foreground contamination can either be appropriately identified and subtracted, or masked.

A variety of foreground removal techniques for general line intensity mapping experiments have been proposed for continuum foregrounds and/or line interlopers. Treatments of continuum emission are especially well-studied for extracting the cosmological 21cm signal and often exploit spectral smoothness, which allows a suite of subtraction or avoidance techniques (e.g., Furlanetto et al. 2006; McQuinn et al. 2006; Harker et al. 2009; Liu & Tegmark 2011; Parsons et al. 2012; Chapman et al. 2016). As the continuum-to-line brightness in [C II] measurements is smaller by orders of magnitude, we expect these 21cm methods will prove effective.

Line interlopers, such as the CO signal in the [C II] EoR band, on the other hand, are different in that they are truly 3D signals. Therefore they require different cleaning techniques. One approach is cross-correlating the target line with an alternative tracer of the same cosmic volume such as galaxy surveys (Visbal & Loeb 2010; Gong et al. 2012, 2014; Silva et al. 2015). Another promising approach is "line de-confusion", introduced by Visbal & Loeb (2010) and studied in detail recently by Lidz & Taylor (2016) and Cheng et al. (2016), which uses the fact that the CO foreground power spectra projected onto the [C II] coordinate system are highly anisotropic between the directions perpendicular and parallel to the light of sight.

In this chapter we focus on what is arguably the simplest approach that works in real space: voxel masking. The masking approach consists of identifying foreground galaxies in 3D using external galaxy catalogs and removing the corresponding voxels from the survey. This "guided" masking approach is fundamentally different from the blind, bright-voxel masking approach discussed in Gong et al. (2014) and Breysse et al. (2015), which works well only when the bright end of the voxel intensity distribution is dominated by the foreground, while all the signal is at the faint end (see Figure 9 of Gong et al. 2014). However, while we expect that some of the foreground sources will be bright and directly detectable, faint sources likely contribute a large fraction of the CO foreground, based on the observed shape of CO luminosity function (e.g., Walter et al. 2014). For example, the expected CO clustering signal at 250 GHz may be 2–10 times larger than the [C II] signal, so up to

99% of the integrated CO luminosity function needs to be masked out. This implies that a blind, bright-voxel masking approach will be insufficient, as found by Breysse et al. (2015), and therefore foreground sources must be traced and masked down to a greater depth to ensure a sufficient reduction.

The voxels containing CO-emitting sources must be identified a priori so that they can be masked from the [C II] survey. Using CO measurements directly is currently impractical because CO line surveys of individual galaxies are extremely time-consuming and may be feasible for only the brightest galaxies, while accurately measuring CO power spectra at intermediate redshifts is still an emerging field (e.g., Walter et al. 2014; Keating et al. 2016; Decarli et al. 2016). We do note that some blind, deep CO surveys are underway with ALMA (PIs: Walter, Decarli), but even these do not scale to the cosmic volume (area and spectral range) required for the first-stage [C II] EoR intensity mapping experiments.

Alternatively, ancillary datasets (i.e., CO proxies) can be used to model both the position and brightness of foreground CO sources, in which case the masking depth required to sufficiently remove the foreground will depend on the uncertainty in the CO flux estimated with the proxy. A potential proxy for CO emission is the total infrared luminosity, believed to be proportional to star formation rate through the Kennicutt (1998) relationship. Strong correlations are measured between the luminosities of various CO transitions and the total infrared luminosity for both local system and at $z \sim 1$–2, albeit for relatively luminous galaxies (Carilli & Walter 2013). The limitation though comes from the lack of direct far-IR data to the required depth. For example, Spitzer MIPS serves as an excellent tracer of total infrared luminosity at $0.5 < z < 2$ (Bavouzet et al. 2008). However, the source density required to sufficiently reduce the CO foreground, which we estimate to be $\sim 10^5\,\mathrm{deg}^{-2}$, is about twice as high as that of the deepest MIPS catalog.

Fortunately, recent deep near-IR catalogs do have sufficient source density to potentially identify CO emitters down to the required depth. The challenge is to understand the degree to which the near-IR measurements can serve as a proxy for CO emission; this is the major thrust of this work. Our approach is to start from ultra-deep, near-infrared selected source catalogs and cross-correlate them with far-infrared/sub-millimeter maps via stacking analysis to measure the mean infrared luminosities of galaxies (Viero et al. 2013a; Schreiber et al. 2015; Viero et al. 2015) as well as the scatter in their population. The multi-wavelength coverage of these catalogs allows for high-quality photometric redshifts, which we use to position the foreground galaxies into our voxel space.

To estimate the CO foreground level — complete with mean and scatter — and explore the effects that different levels of masking have on the resulting power spectrum, we first model the mean total infrared luminosity ($L_{\mathrm{IR}[8-1000\mu\mathrm{m}]}$, or simply L_{IR} hereafter) as a function of stellar mass and redshift, and then exploit the empirical relationship between L_{IR} and L'_{CO} to convert L_{IR} to CO luminosities, after including the scatters in both the $L_{\mathrm{IR}}(M_*, z)$ and the L_{IR}–L'_{CO} correlation. Finally, as an application of our method, we use the CO power spectrum to determine the degree of masking necessary to significantly detect the [C II] power spectrum with the Tomographic Ionized-carbon Mapping Experiment (TIME, Crites et al. 2014) at the angular scales of interest. It is important to note that our proxy-based method always allows for "over-masking", namely removing foreground galaxies that do not emit appreciable CO by discarding more voxels than is necessary, without biasing the EoR signal. This relies on the fact that the CO emission is uncorrelated with the target [C II] emission from the masked voxels, and that effects of masking such as mode mixing can be appropriately corrected (e.g., Zemcov et al. 2014).

This chapter is arranged as follows. In Section 2, we model the mean total infrared luminosity of galaxies as a function of stellar mass and redshift with the simultaneous stacking formalism and algorithm developed by Viero et al. (2013a) called SIMSTACK[1]. We also describe in detail the innovative technique of thumbnail stacking on residual maps, used to characterize the scatter in L_{IR}. We discuss the observational implications for the masking strategy of [C II] intensity mapping experiments in Section 3 and briefly conclude in Section 4. Throughout this chapter, we assume a Chabrier (2003) initial mass function (IMF) and a flat, ΛCDM cosmology consistent with the most recent measurement by the Planck Collaboration et al. (2016d).

3.2 Methods for Modeling Infrared Galaxies as CO Proxies

We model both the mean and variance of the galaxy total infrared luminosity in galaxy samples binned in redshift and stellar mass. We measure these quantities using an extension of the SIMSTACK method introduced by Viero et al. (2013a). The modeled L_{IR} can then be related to the strength of CO emission from foreground galaxies. The results presented in this work are performed on the COSMOS field (Scoville et al. 2007) by combining a catalog derived using the imaging described

[1]https://web.stanford.edu/~viero/downloads.html

in Laigle et al. (2016) but processed by the Muzzin et al. (2013b) pipeline, with maps spanning the full far-infrared/sub-millimeter (FIR/sub-mm) spectral range of the thermal spectral energy distribution (SED) from interstellar dust. Note that, in addition to the maps used in Viero et al. (2013a), we use maps at 450μm and 850μm from deep SCUBA-2 observations made available by Casey et al. (2013), which provide critical constraints on the low-energy end of the SED (for details on the fitting routine, see Moncelsi et al. 2011; Viero et al. 2012). The full dataset including the maps and catalog used is summarized in Table 3.1 (see also Laigle et al. 2016) and will be described in detail in Viero et al. (in prep.).

3.2.1 Estimating the Mean $L_{\rm IR}(M_*, z)$ with SIMSTACK

SIMSTACK is an algorithm that takes galaxy positions from an external catalog, splits them into subsets (typically, but not necessarily, by stellar mass and redshift), and generates mock map layers that are *simultaneously* regressed with the real sky map to estimate the mean flux density of each subset. Formally, it is an extension of simple thumbnail stacking (Marsden et al. 2009), the difference being that the off-diagonal entries in the subsets covariance matrix are not assumed to be zero, so as to account for galaxy clustering. The simultaneous fitting provides a solution to the limitations of stacking in highly confused maps (i.e., biased flux density estimates due to the clustering of sources at angular scales comparable to that of the FIR/sub-mm beam), such that in the theoretical limit where the catalog is complete it naturally leads to a completely unbiased estimator (see Appendix 3.5 for some justification). Viero et al. (2013a) show that SIMSTACK yields unbiased results at any beam size, while conventional thumbnail stacking (e.g., “median” or “mode” stacking, etc.), without additional corrections, inevitably leads to wavelength-dependent biases, in the presence of galaxy clustering.

The first step in measuring $L_{\rm IR}(M_*, z)$ is to split the catalog into subsets of star-forming and quiescent galaxies based on their $U - V$ vs. $V - J$ colors (UVJ, e.g., Williams et al. 2009), and then again into bins of stellar mass (5 and 3 layers for star-forming and quiescent galaxies, respectively) and redshift (8 layers), determined by their optical and near-infrared photometry. We developed an algorithm to calculate the optimized locations of the $5 \times 8 + 3 \times 8 = 64$ stellar-mass/redshift bins so that each bin contains at least 100 (10) star-forming (quiescent) galaxies, as illustrated in Figure 3.1.

Next, the average FIR/sub-mm flux density for each bin and at each wavelength is

MAPS		
Instrument/Telescope	**Wavelength** [μm]	**1-σ sensitivity**[a] [mJy/beam] literature (measured)
MIPS/*Spitzer*	24	0.06[b] (0.08)
	70	1.7[c] (2.85)
PACS/*Herschel*	100	5[d] (3.1)
	160	10[d] (7.4)
SPIRE/*Herschel*	250	†5.8[e] (6.8)
	350	†6.3[e] (7.4)
	500	†6.8[e] (7.7)
SCUBA–2/*JCMT*	450	†4.7[f] (4.5)
	850	†0.8[f] (1.5)
AzTEC/*JCMT*	1100	†1.3[g] (1.6)

CATALOG (COSMOS/UVISTA DR2)		
Instrument /Telescope	**Filter /Central** λ [Å]	**3-σ depth**[h] ±0.1
GALEX	NUV / 2.3139×10^3	25.5
MegaCam/CFHT	u^* / 3.8233×10^3	26.6
Suprime-Cam/Subaru	B / 4.4583×10^3	27.0
	V / 5.4778×10^3	26.2
	r / 6.2887×10^3	26.5
	i^+ / 7.6839×10^3	26.2
	z^{++} / 9.1057×10^3	25.9
	$IA427$ / 4.2634×10^3	25.9
	$IA464$ / 4.6351×10^3	25.9
	$IA484$ / 4.8492×10^3	25.9
	$IA505$ / 5.0625×10^3	25.7
	$IA527$ / 5.2611×10^3	26.1
	$IA574$ / 5.7648×10^3	25.5
	$IA624$ / 6.2331×10^3	25.9
	$IA679$ / 6.7811×10^3	25.4
	$IA709$ / 7.0736×10^3	25.7
	$IA738$ / 7.3616×10^3	25.6
	$IA767$ / 7.6849×10^3	25.3
	$IA827$ / 8.2445×10^3	25.2
	$NB711$ / 7.1199×10^3	25.1
	$NB816$ / 8.1494×10^3	25.2
VIRCAM/VISTA	Y / 1.0214×10^4	25.3
	J / 1.2535×10^4	24.9
	H / 1.6453×10^4	24.6
	K / 2.1540×10^4	24.7
IRAC/*Spitzer*	ch1 / 3.5634×10^4	25.5
	ch2 / 4.5110×10^4	25.5
	ch3 / 5.7593×10^4	23.0
	ch4 / 7.9595×10^4	22.9

[a] † means the sensitivity is confusion-limited. Parenthesized values are estimated from maps.
[b] Sanders et al. (2007)
[c] Frayer et al. (2009)
[d] Table 3.1, `http://herschel.esac.esa.int/Docs/Herschel/html/ch03s02.html`
[e] Nguyen et al. (2010)
[f] Chen et al. (2013)
[g] Scott et al. (2008)
[h] Limiting magnitudes are calculated from variance map in 2" aperture on PSF-matched images.

Table 3.1: Map and catalog information.

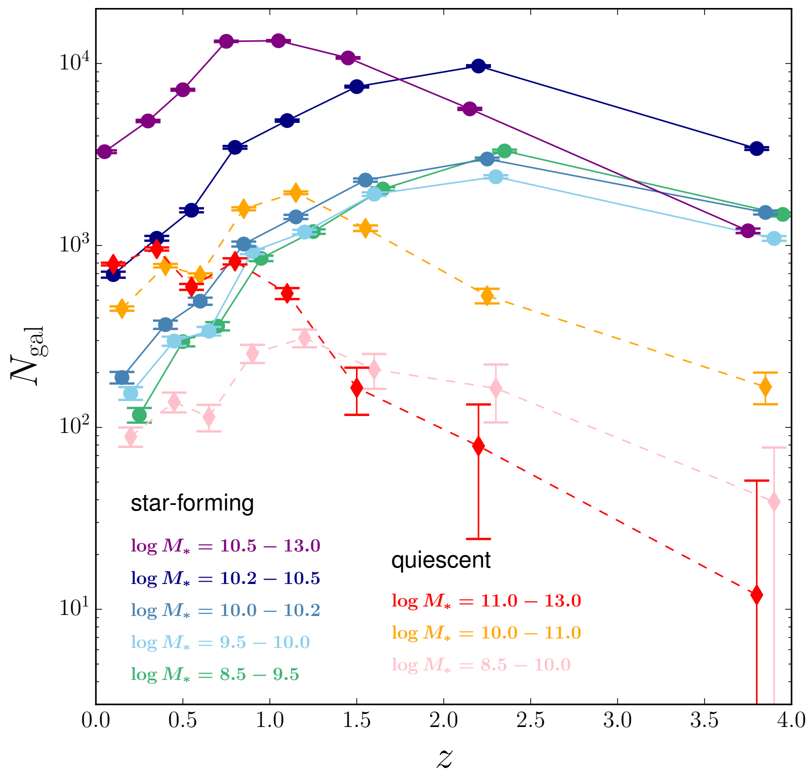

Figure 3.1: Numbers of star-forming or quiescent galaxies in bins of stellar mass and redshift. The binning is optimized to have more than 100 (10) star-forming (quiescent) galaxies in each bin and be approximately uniform in lookback time. The error bars show the square roots of the numbers of galaxies, which are Poisson distributed.

estimated with SIMSTACK. Uncertainties on the mean flux densities are estimated with an extended bootstrap technique which takes into account the uncertainties in the photometric redshift and stellar-mass estimates of individual sources. $L_{\rm IR}$ for each bin is estimated by first fitting a modified blackbody (or graybody) with emissivity index $\beta = 2$, and the Wien side approximated as a power-law with slope $\alpha = -2$ (Blain et al. 2002), to the full spectrum of intensities $\nu I_\nu(\lambda)$, and then integrating under the best-fit graybody from $\lambda_{\rm rf} = 8$ to $1000\,\mu$m. The final step is to fit the full set of mean $L_{\rm IR}$'s with multiple linear regression as described by Viero et al. (2013a):

$$\log L_{\rm IR}(M_*, z) = \sum_{p=0}^{n} \left\{ \left[\sum_{q=0}^{n} A_{p,q} \left(\log M_*\right)^q \right] z^p \right\}, \tag{3.1}$$

where $n = 2$ and 1 for star-forming and quiescent galaxies, respectively. The coefficient matrices $A_{p,q}$ are found to be

$$A^{\rm sf}_{p,q} = \begin{pmatrix} 2.417 & 0.733 & 0.004 \\ -38.84 & 8.080 & -0.406 \\ 4.947 & -1.223 & 0.069 \end{pmatrix} \tag{3.2}$$

and

$$A^{\rm qt}_{p,q} = \begin{pmatrix} 0.845 & 0.820 \\ 4.556 & -0.354 \end{pmatrix}. \tag{3.3}$$

Figure 3.2 shows two sample SED fittings to the stacked fluxes, together with the best-fit polynomials to the mean $L_{\rm IR}(M_*, z)$ relations of star-forming and quiescent galaxies separately. As demonstrated in Viero et al. (2012), the modified blackbody approximation produces mean SEDs consistent with best-fit templates such as Chary & Elbaz (2001) and the derived mean $L_{\rm IR}$ is largely insensitive to the exact choice of the Wien side slope α.

3.2.2 Characterization of the Scatter in $L_{\rm IR}(M_*, z)$

At this point, we have modeled the mean infrared luminosity as a function of stellar mass and redshift, but naturally we expect $L_{\rm IR}$ of individual galaxies to depart from this model, with some characteristic scatter. The question we aim to answer now is what is the degree of scatter of the full ensemble of sources?

The answer lies in the standard deviation of the *residual map* (see Table 3.2 for the definition), which is the difference between the real sky map at each wavelength and a synthetic map made by applying the $L_{\rm IR}(M_*, z)$ model to the original catalog (i.e., the actual stellar masses, redshifts, and sky positions). In a universe where (i) objects are perfectly described by the mean model with no scatter, (ii) catalogs are 100% complete, and (iii) maps have no noise, the residual map would be completely blank. In practice, the actual residual map will have structure due to the intrinsic stochasticity of the galaxy populations, catalog incompleteness, as well as instrumental noise.

We now introduce a method to formally characterize the scatter about the mean $L_{\rm IR}(M_*, z)$ relation by leveraging the structure in the residual map. Although our method has similarities with the "scatter stacking" method described in Schreiber et al. (2015), our use of residual maps — estimated by taking the difference with "base" maps generated with SIMSTACK-derived luminosities — makes us less susceptible to clustering contamination, and provides a more robust estimate of the

TERM	DESCRIPTION	REFERENCE
Bins	Stellar mass or redshift intervals used to divide galaxies into sub-populations for stacking analysis.	S2.1
Layer	A subset of a real/mock sky image (or map) attributed to only the sources in the corresponding stellar mass or redshift bin.	S2.1, S2.2
Scatter	In this chapter, we exclusively define “scatter” as the standard deviation of flux density or luminosity in the source population, which is characterized and represented by σ_S in equation 3.4.	S2, App.A, Eq. 3.4
(Un)perturbed	Fluxes being assigned to the sources in a specific layer are drawn from a distribution with the mean equal to the best-fit value given by SIMSTACK and some (zero) nonzero width defined by the scatter.	S2.2, App.A, Eq. 3.4
Real/Mock	“Real” refers to the actual sky image, whereas “mock” refers to the image reconstructed using source locations and perturbed mean fluxes from SIMSTACK. More specifically, in our analysis we construct the mock sky image by merging 1) a layer of interest perturbed according to a distribution with a tunable scatter and 2) background layers perturbed by a distribution with a fiducial scatter of 0.3 dex.	S2.2, Eq. 3.5, 3.6
Base	The “base” map, different from the mock image, is obtained by merging 1) an unperturbed layer of interest and 2) background layers perturbed by a distribution with a fiducial scatter of 0.3 dex.	S2.2, Eq. 3.5, 3.6
Residual	The difference between the real or noise-added mock sky image and a “base” one.	S2.2, Eq. 3.5, 3.6
$\mathbf{D}_{\mathrm{real}}$, $\mathbf{D}_{\mathrm{mock}}$	A small cutout image a few pixels by side, where each pixel measures the standard deviation of a data cube obtained by thumbnail-stacking the residual map at the positions of the sources in each $i,\ j$ layer.	S2.2, Eq. 3.5, 3.6

Table 3.2: A summary of the terms used in our discussion of methodology. A summary of the terms used in our discussion of methodology in Section 2 and 3.

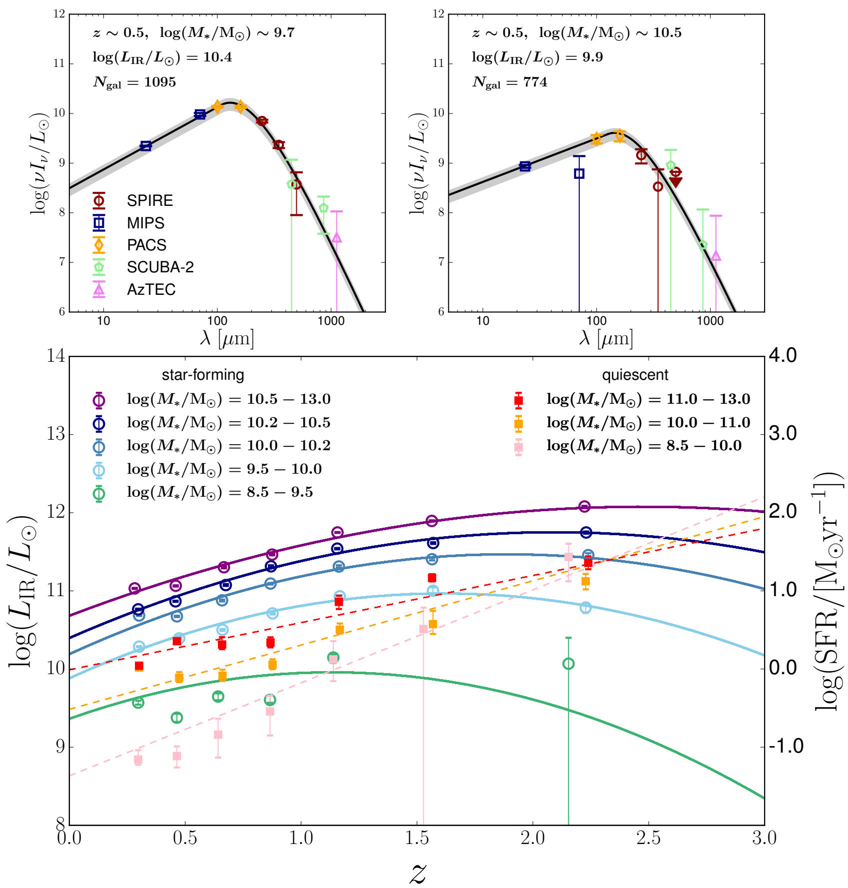

Figure 3.2: Sample fittings to the SED and mean IR luminosity as a function of stellar mass and redshift. Top: Sample best-fit SEDs of star-forming (left) and quiescent galaxies (right). Bottom: Polynomial fits to the mean $L_{IR}(M_*, z)$ estimated from the stacked fluxes and best-fit, modified graybody spectra. Open (filled) markers show the measured luminosities in individual (M_*, z) bins for star-forming (quiescent) galaxies, while the solid (dashed) curves represent the corresponding best-fit curves.

scatter in each (M_*, z) bin, validated through an extensive set of end-to-end simulations (see Section 3.5). Due to the layered structure of our maps, the interplay between individual layers (often with a root-mean-square, or rms, amplitude below the confusion limit of the real map) must be investigated through simulations to estimate the scatter in each layer. For simplicity, we assume that the scatter is dominated by the stochasticity of the star-formation activity and therefore is independent of wavelength. We perform the scatter calibration with the 250μm

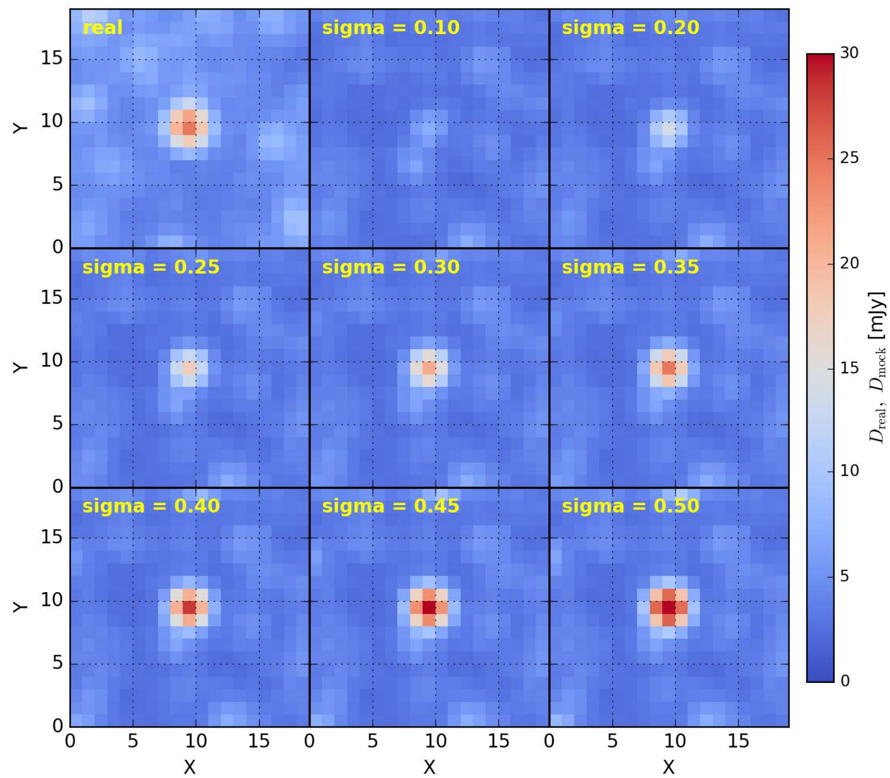

Figure 3.3: Standard deviation in thumbnail stacks that illustrates the scatter characterization method. The top left panel shows the standard deviation in the real residual (real map minus “base” using the mean relation). The other panels show mock residuals with various levels of log scatter (per equation 3.4) artificially incorporated. This figure refers to a single bin: $0 < z < 0.3$, $\log M_* = 10.5$–13. The central pixels show the standard deviation due to source variance – a value of $\sigma_S \sim 0.35$ best reproduces the measured variance in the map.

SPIRE/HerMES (Griffin et al. 2010; Oliver et al. 2012) map which covers the entire COSMOS/UltraVISTA field.

We assume that for a given redshift z_i and stellar mass $M_{*,j}$, the actual flux density S (and therefore the total infrared luminosity) is log-normally distributed about the mean value with a scatter σ_S, an assumption that is motivated by the observed scatter in the star-formation main sequence (SFMS, e.g., Sargent et al. 2012). Namely,

$$P\left(x|\mu,\sigma_S\right) = \frac{1}{\sigma_S\sqrt{2\pi}}\exp\left(-\frac{(x-\mu)^2}{2\sigma_S^2}\right), \tag{3.4}$$

where $\mu = \log\langle S(M_*, z)\rangle$ is the log of the mean flux density measured by SIMSTACK.

Intuitively, σ_S can be estimated by examining the statistics of source fluxes (e.g., standard deviation) in each stellar-mass/redshift bin of interest. However, for the highly-confused far-IR maps we use, clustering could render measured statistics biased by the contribution from sources in other bins, whose scatter must also be properly accounted for.

Therefore we assign a fiducial scatter to the "background" sources. As will be shown in Section 3.2, the actual scatter can be measured without bias using our method, as long as it is not drastically different from the fiducial value. In particular, the scatter being investigated here is analogous to that of the SFMS, which can be explained as an application of the central limit theorem (Kelson 2014) and is measured to be around ~ 0.3 dex (Behroozi et al. 2013; Sparre et al. 2015). We therefore adopt 0.3 dex as the fiducial population scatter for the "background" sources in our mock maps and demonstrate in Section 3 that it is indeed a reasonable choice.

We hereafter refer to the actual sky image as the "real map" and the synthetic map based on the $L_{\rm IR}$ model as the "mock map". In addition, we call a layer unperturbed when the flux density of its sources is constant and equal to the average value μ found using SIMSTACK, while a layer is perturbed when each source has been assigned a flux density according to a log-normal distribution of mean μ and scatter σ_S. Finally, as anticipated before, the residual map is either a real or mock map from which the "base" map (the layer of interest, unperturbed, plus the background layers perturbed with the fiducial scatter) is subtracted. This nomenclature is summarized in Table 3.2.

The crucial step of the algorithm is that we take the standard deviation $D^k_{\rm real}$, computed over the positions of all cataloged sources in the (M_*, z) bin of interest, of the residual real map, and compare it to its counterpart $D^k_{\rm mock}$, which is the standard deviation of a residual mock map obtained by adding up all perturbed layers, plus noise floor (e.g., Nguyen et al. 2010).

Mathematically, at a given pixel of interest k, we have

$$D^k_{\rm real} = {\rm SD}\left[S^k_{\rm real} - \sum_{i,j} S^k_{\rm base}(z_i, M_{*,j})\right] \tag{3.5}$$

and

$$D^k_{\rm mock} = {\rm SD}\left[\sum_{i,j} S^k_{\rm mock}(z_i, M_{*,j}) + S^k_{\rm noise} - \sum_{i,j} S^k_{\rm base}(z_i, M_{*,j})\right], \tag{3.6}$$

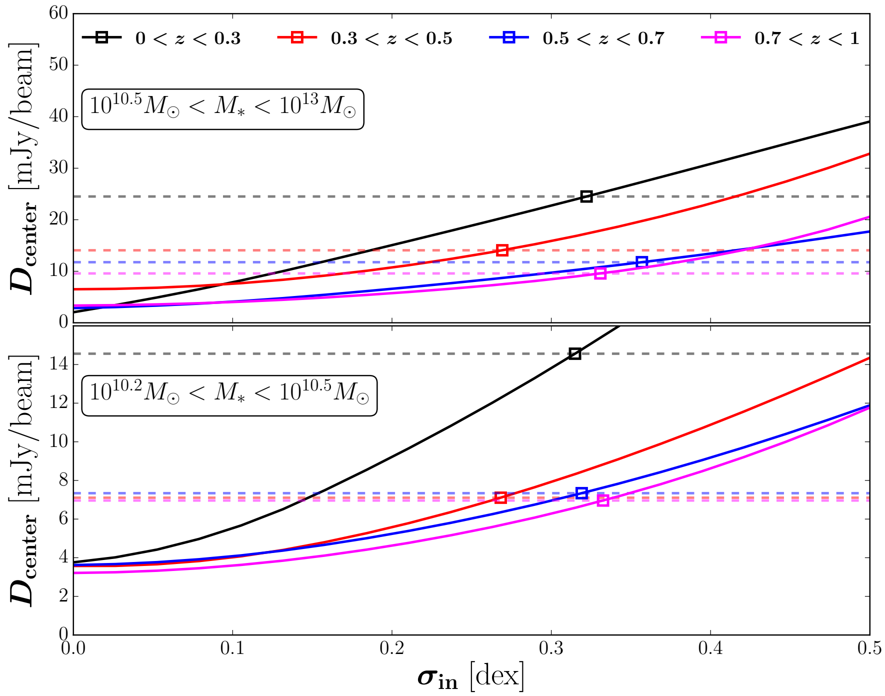

Figure 3.4: Calibration curves for the scatter in the derived $L_{\rm IR}(M_*, z)$ relation at 250 μm. The top and bottom panels correspond to galaxies with stellar mass $10^{10.2}$–$10^{10.5}$ $M_\odot$ and $10^{10.5}$–10^{13} $M_\odot$, respectively, in four redshift bins. The x-axis is the level of input scatter injected into the mock maps (labeled "sigma" in the panels of Figure 3.3), and the y-axis is the measured standard deviation level in the residual real/mock maps (illustrated by the color bar in Figure 3.3). The horizontal, dashed lines are the measured standard deviation levels in the residual real data cubes. The solid curves are the measured output standard deviation levels, with increasing input scatter, of the thumbnail-stacked residual cubes. The intersecting squares indicate the estimated level of scatter in the real sky images.

where SD stands for taking the standard deviation of the thumbnail-stacked cube at each pixel k, and i, j are the indices of redshift and stellar-mass bins (see Table 3.2 for a reminder of the definitions).

Note that the layer of interest in the mock map is perturbed with different, adjustable levels of σ_S (while all other layers are perturbed with the constant, fiducial value 0.3 dex) to provide a "calibration curve" to compare with the real map. The idea is that the mock map is our best representation of the real map, including the positional source clustering and the scatter in luminosity that may be present in the actual galaxy populations, as well as instrument and confusion noise. From each of these, we want to subtract our best estimate of the average flux density in each layer, i.e., the *unperturbed* SIMSTACK values. At this point, the residual real map

	Number of Galaxies (N_{gal}), Luminosity ($\log[L_{IR}/L_{\odot}]$), and Scatter (σ_L [dex])			
	$0 < z < 0.3$	$0.3 < z < 0.5$	$0.5 < z < 0.7$	$0.7 < z < 1$[a]
		Star-forming Galaxies		
$10^{10.5} < M_*/M_{\odot} < 10^{13}$	$117, 10.94^{+0.01}_{-0.01}, 0.33$	$296, 11.04^{+0.01}_{-0.01}, 0.34$	$360, 11.25^{+0.01}_{-0.01}, 0.35$	$849, 11.42^{+0.01}_{-0.01}, 0.33$
$10^{10.2} < M_*/M_{\odot} < 10^{10.5}$	$154, 10.78^{+0.01}_{-0.01}, 0.35$	$298, 10.84^{+0.01}_{-0.01}, 0.29$	$338, 11.11^{+0.01}_{-0.02}, 0.34$	$926, 11.29^{+0.01}_{-0.02}, 0.35$
$10^{10} < M_*/M_{\odot} < 10^{10.2}$	$188, 10.64^{+0.01}_{-0.01}, 0.37$	$367, 10.68^{+0.02}_{-0.02}, 0.33$	$494, 10.90^{+0.01}_{-0.02}, 0.33$	$1018, 11.08^{+0.02}_{-0.01}, 0.42$
$10^{9.5} < M_*/M_{\odot} < 10^{10}$[b]	$691, 10.28^{+0.01}_{-0.01}, 0.44$	$1095, 10.43^{+0.02}_{-0.02}, 0.43$	$1561, 10.61^{+0.02}_{-0.03}, \lesssim 0.6$	$3461, 10.69^{+0.02}_{-0.02}, \lesssim 0.7$
		Quiescent Galaxies		
$10^{11} < M_*/M_{\odot} < 10^{13}$	$89, 10.08^{+0.05}_{-0.04}$, –	$138, 10.26^{+0.07}_{-0.06}$, –	$114, 10.33^{+0.05}_{-0.05}$, –	$255, 10.36^{+0.09}_{-0.06}$, –
$10^{10} < M_*/M_{\odot} < 10^{11}$	$450, 10.00^{+0.03}_{-0.03}$, –	$774, 9.85^{+0.09}_{-0.07}$, –	$684, 9.96^{+0.10}_{-0.09}$, –	$1591, 10.00^{+0.05}_{-0.08}$, –

[a] Redshift bins are only shown up to $z \sim 1$ where the majority of CO foreground comes from.

[b] The lowest-mass layers of faint star-forming and quiescent galaxies are not shown here as their mean and variance are less well-constrained.

Table 3.3: The number of galaxies, mean total infrared luminosity, and scatter. The number of galaxies, the mean total infrared luminosity and the scatter about the mean. The scatters of faint, star-forming galaxies in the two low-mass, high-redshift bins are shown as upper limits since in these cases the noise floor (both instrument and confusion) dominates the variance of the residual data cube.

will contain, at the positions of the sources in the layer of interest, information on the layer's intrinsic scatter in flux density. The magnitude of this scatter is then simply measured by gauging which level of σ_S in the residual mock map matches the scatter in the residual real map. This is illustrated in Figure 3.3, where we show how the thumbnail-stacked mock data cube, $D^k_{\rm mock}$, compares to the real one, $D^k_{\rm real}$, as we tune up the level of the scatter σ_S. For the purpose of measuring the scatter, we focus only on the central pixel of $D^k_{\rm mock}$ and $D^k_{\rm real}$.

As shown in Figure 3.4, the standard deviation in the mock thumbnail cubes gradually increases with increasing input scatter. The horizontal, dashed line represents the standard deviation measured in the real map. The scatter in the real maps can be consequently inferred from the intersection points, marked as squares in the figure. Since the maps are confusion-noise limited, the calibration curves do not start at zero, but rather at some noise floor equivalent to the standard deviation obtained by thumbnail stacking on random, non-source positions. A more detailed justification of this method based on end-to-end simulations is provided in Appendix 3.5.

Table 3.3 lists the results of our extended SIMSTACK procedure, i.e., the number of galaxies in each bin, their mean total infrared luminosity and their scatter about the mean. In particular, we find an average logarithmic scatter, of $\langle\sigma_{\rm L}\rangle \sim 0.35$ dex, with no evidence for systematic dependence on redshift or stellar mass, which is consistent with both observations (e.g. Whitaker et al. 2012) and theoretical expectations (e.g. Kelson 2014; Sparre et al. 2015) of the dispersion about the SFMS. Dutton et al. (2010) investigate the origin of such small, roughly constant scatter in the SFMS using a semi-analytic model for disk galaxies based on smooth mass accretion onto dark matter halos and show that the scatter is mainly dominated by the variations in the gas accretion history and therefore does not evolve strongly with time or mass. Note that the method fails to give a reliable estimate of the scatter when the source population's flux density is too close to the noise floor.

3.3 Evaluating the Masking Strategy of [C II] Intensity Mapping Experiments

We will use the proposed configuration of TIME (Crites et al. 2014) as an example to demonstrate that the CO foreground can be efficiently removed by masking the contaminated voxels traced by infrared galaxies. Specifically, we apply our estimates of the mean and scatter in the $L_{\rm IR}(M_*, z)$ relation to model CO emission in the $z < 2$ sky to guide foreground masking. Based on our fiducial model, a robust detection of the [C II] signal can be achieved by masking galaxies using an evolving mass cut

TIME Instrument Parameters	
Dish size	12 m
Instantaneous FOV	$14' \times 0.43'$
Survey area	$1.3^\circ \times 0.43'$ (1×180 beams)
Number of spectrometers	32: 16 per polarization
Spectral range	183–326 GHz
Spectral resolution	90–120
Survey volume	153 Mpc×1.1 Mpc×1240 Mpc

Table 3.4: TIME specifications.

(roughly tracing a constant CO flux), which results in a moderate 4%–8% loss of the total survey volume.

3.3.1 Experiment Overview

TIME is a high-throughput millimeter-wave imaging spectrometer array, designed to measure the 3D [C II] power spectrum. The clustering amplitude constrains the aggregate luminosity of [C II] emission from EoR galaxies. The instrument parameters of the proposed experiment are summarized in Table 3.4.

3.3.2 Power Spectrum of CO Foreground

CO emission is derived for each object in the catalog by converting infrared luminosity to CO line strength with the well-established $L_{\rm IR}$–$L'_{\rm CO}$ correlation (e.g., Carilli & Walter 2013, hereafter CW13; Greve et al. 2014, hereafter G14; Dessauges-Zavadsky et al. 2015). We can then use the measured stellar mass functions of galaxies at $0 < z < 2$ to calculate the power of CO line foregrounds, with the ability of monitoring different subsets (e.g., different stellar mass bins, quiescent vs star-forming galaxies, etc.) Now the total mean intensity of CO contamination can be expressed as

$$\begin{aligned}\bar{I}_{\rm CO} = \sum_J \int_{M_*^{\rm min}}^{M_*^{\rm max}(z)} & {\rm d}M_* \Phi(M_*, z) \\ & \times \frac{L_{\rm CO}^J\left(L_{\rm IR}(M_*, z)\right)}{4\pi D_L^2} y^J(z) D_A^2, \end{aligned} \tag{3.7}$$

where $M_*^{\rm min} = 1.0 \times 10^8\, M_\odot$, $3 \leq J_{\rm upp} \leq 6$, representing all CO transitions acting as foregrounds and $\Phi(M_*, z)$ being the stellar mass function measured by the COSMOS/UltraVISTA Survey (Muzzin et al. 2013a). $M_*^{\rm max}(z)$ represents an evolving mass cut that measures the depth of foreground masking (see Section 4.3 for a de-

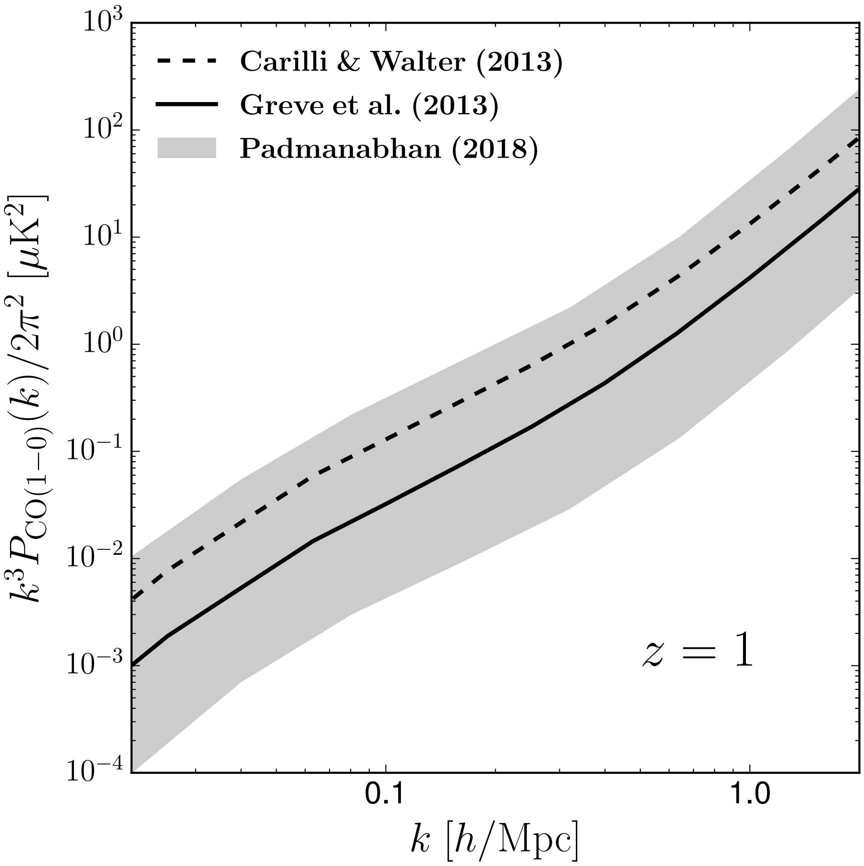

Figure 3.5: CO(1–0) power spectra predicted by our models. Predictions assuming prescriptions of CW13 and G14 are compared with that of the best-fit model calibrated to the observed CO luminosity function by Padmanabhan (2018).

tailed discussion) and is set to $M_{*,0}^{\max} = 1.0 \times 10^{13}\, M_\odot$ when no masking is applied. The factor $y^J(z) = \mathrm{d}\chi/\mathrm{d}\nu_{\mathrm{obs}}^J = \lambda_{\mathrm{rf}}^J (1+z)^2/H(z)$ accounts for the mapping of frequency into distance along the line of sight (Visbal & Loeb 2010). The comoving radial distance χ, the comoving angular diameter distance D_A and the luminosity distance D_L are related by $\chi = D_A = D_L/(1+z)$. In the presence of scatter (as is always the case), the expectation value of a function $\mathcal{F}$ of CO luminosity at a best-fit $L_{\mathrm{IR}}(M_*, z)$ given by SIMSTACK can be written as

$$E\left[\mathcal{F}\left(L_{\mathrm{CO}}^J\right)\right] = \int_{-\infty}^{\infty} \mathrm{d}x \mathcal{F}\left(10^x\right) P\left(x|\log L_{\mathrm{IR}}\right), \tag{3.8}$$

and

$$P\left(x|\log L_{\mathrm{IR}}\right) = \frac{1}{\sigma_{\mathrm{tot}}\sqrt{2\pi}} \exp\left(-\frac{(x-\mu)^2}{2\sigma_{\mathrm{tot}}^2}\right), \tag{3.9}$$

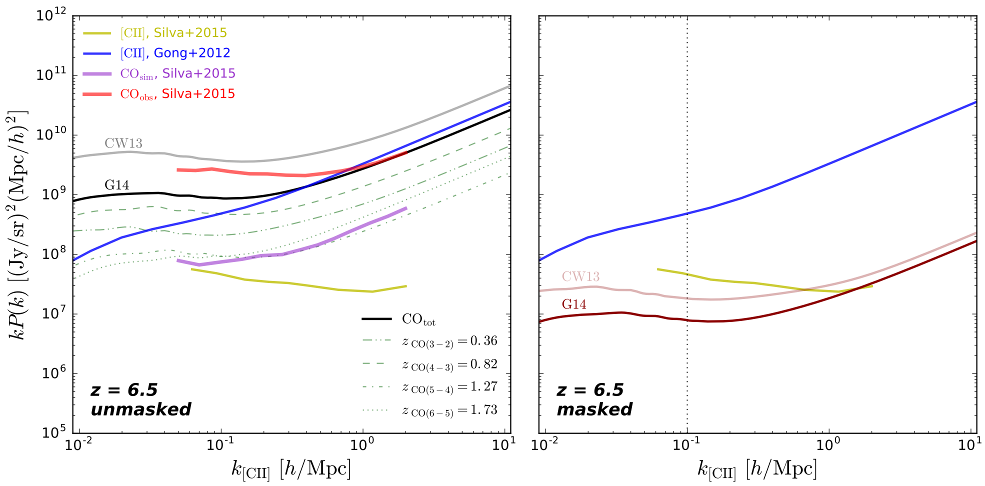

Figure 3.6: Comparison of masked and unmasked projected CO power spectra. Left: a comparison of the projected power spectra of unmasked CO emission lines and [C II] at $\nu_{obs} \sim 250$ GHz ($z_{C\,II} \sim 6.5$). Our model illustrates the relative contribution to the total CO power spectrum (gray and black solid lines, respectively, for the two L_{IR}–L'_{CO} prescriptions, CW13 & G14) from different CO transitions (green lines, just for G14), with a simulated input scatter of $\sigma_{tot} = 0.5$ dex. Also shown are two CO models from Silva et al. (2015): the first based on simulated $L^J_{CO} - M_{halo}$ relations (purple line labeled 'sim'); and the second from scaling the observed infrared luminosity function (red line labeled 'obs'). [C II] signals predicted by Gong et al. (2012) and Silva et al. (2015, "m2" model), shown as blue and yellow lines, respectively, highlight the large range of existing [C II] predictions. Right: the same comparison as in the left panel, but after masking bright galaxies down to an evolving stellar mass cut (see Section 3.3.3), which results in a ~8% (G14) and ~18% (CW13) loss of the total survey volume.

where

$$\mu = \log L^J_{CO}(\log L_{IR}) = \alpha^{-1}(\log L_{IR} - \beta) + \log r_J \tag{3.10}$$

is derived from the best-fit L'_{CO}–L_{IR} correlation, with r_J being some scaling factor for different J's. Consequently, in the presence of scatter, Equation 3.7 becomes $\langle \bar{I}_{CO} \rangle \equiv E\left[\bar{I}_{CO}(L^J_{CO})\right]$, which describes the expectation value of the total CO mean intensity, averaged over the probability distribution of L^J_{CO} as specified by μ and σ_{tot}. In our calculation, we consider two prescriptions: (i) CW13, who give $\alpha = 1.37 \pm 0.04$, $\beta = -1.74 \pm 0.40$, and scaling relations appropriate for sub-millimeter galaxies which are used to convert to transitions higher than $J = 1 \to 0$, and (ii) G14, who provide α and β coefficients for each individual J transition (i.e., $r_J = 1$) based on samples of low-z ultra luminous infrared galaxies (ULIRGs) and high-z dusty star-forming galaxies (DSFGs) comparable to CW13. Since the total

CO foreground consists of multiple J transitions, we deem the G14 prescription more appropriate for our purposes, because it treats both the slope and intercept as free parameters when fitting to galaxies observed in different J's. Henceforth, we present our results based on the G14 model unless otherwise stated.

It is worth noting that the L'_{CO}–L_{IR} relation is usually determined using a compilation of galaxy samples which collectively spans the stellar mass range $\log_{10}(M_*)$ ~9.5-11.5. Simply extrapolating this relation to lower stellar masses without considering possible changes in the ISM in this regime likely overestimates the predicted CO emission, as observations suggest that local galaxies with $M_* < 10^9 M_\odot$ are deficient in CO, due to lower molecular gas contents and low metallicities (e.g., Bothwell et al. 2014). Dessauges-Zavadsky et al. (2015) find a 0.38 dex scatter in L_{IR} for a given $L'_{\mathrm{CO(1-0)}}$, which corresponds to 0.32 dex scatter when converting infrared luminosity into CO luminosity. Comparable levels of scatter have also been identified by CW13 and G14 using galaxy samples of similar types. We note that different from our assumption in Equation 3.9, Li et al. (2016) re-normalize the log-normal distribution so that the *linear* mean remains constant and that the level of scatter only affects the shot-noise component of the power spectrum. Instead, we choose to fix the *logarithmic* mean in this work to best represent the distribution about the best-fit line for the observed $\log L_{\mathrm{IR}}$-$\log L'_{\mathrm{CO}}$ correlation. Also, for simplicity, we ignore any potential correlation between the ~0.3 dex scatter intrinsic to the total infrared luminosity and the comparable ~0.3 dex scatter in the IR-to-CO conversion [2] and combine them orthogonally (i.e., adding in quadrature, see also Li et al. 2016), yielding a total scatter of $\sigma_{\mathrm{tot}} \sim 0.5$ dex, which is what our reference model assumes hereafter.

Figure 3.5 shows the CO(1–0) power spectra predicted by our CO model at $z = 1$, compared with the best-fit model from Padmanabhan (2018) which is derived from abundance matching the halo mass function to the CO luminosity function observed at $0 < z < 3$. The overall power spectrum of the CO foreground can be written as the sum of the clustering and shot noise terms

$$P_{\mathrm{CO}}^{\mathrm{tot}}(z_f, k_f) = P_{\mathrm{CO}}^{\mathrm{clust}}(z_f, k_f) + P_{\mathrm{CO}}^{\mathrm{shot}}(z_f, k_f), \tag{3.11}$$

where the clustering component can be derived from the mean intensity I_{CO}, the average bias $\bar{b}_{\mathrm{CO}}(z)$ (Visbal & Loeb 2010) and the nonlinear matter power spectrum

[2] This is a somewhat arbitrary choice given the potentially similar physics (star formation, dust attenuation, etc.) that leads to the observed scatters in both cases. As it is difficult to accurately determine this potential correlation, we simply assume here that 0.5 dex is a relatively conservative estimate of the total scatter.

$P^{\rm nl}_{\delta\delta}$ (computed with the `CAMB`-based `HMFcalc` code, Murray et al. 2013) as

$$P^{\rm clust}_{\rm CO}(z_f, k_f) = \sum_J \bar{b}^2_{\rm CO} \left(\bar{I}^J_{\rm CO}\right)^2 P^{\rm nl}_{\delta\delta}(z_f, k_f), \tag{3.12}$$

and the shot noise or Poisson component is given by

$$\begin{aligned} P^{\rm shot}_{\rm CO}(z_f) = & \sum_J \int_{M_*^{\rm min}}^{M_*^{\rm max}(z)} {\rm d}M_* \Phi(M_*, z_f) \\ & \times \left\{ \frac{L^J_{\rm CO}\left(L_{\rm IR}(M_*, z_f)\right)}{4\pi D_L^2} y^J(z_f) D_A^2 \right\}^2 . \end{aligned} \tag{3.13}$$

Estimating the CO contamination for any given observed [C II] power spectrum also requires scaling (i.e., projecting) the corresponding CO comoving power spectrum at low redshift to the redshift of [C II]. Following Visbal & Loeb (2010) and Gong et al. (2014), the projected CO power spectrum can be written as

$$P^J_{\rm obs,CO}(z_s, \boldsymbol{k}_s) = P^J_{\rm CO}(z_f, \boldsymbol{k}_f) \times \left(\frac{\chi(z_s)}{\chi(z_f)}\right)^2 \frac{y^J(z_s)}{y^J(z_f)}, \tag{3.14}$$

where $|\boldsymbol{k}_f| = \sqrt{(\chi(z_s)/\chi(z_f))^2 k_\perp^2 + (y^J(z_s)/y^J(z_f))^2 k_\parallel^2}$ is the 3D k vector at the redshift of CO foreground. Here we assume $k_\perp = \sqrt{k_1^2 + k_2^2}$ and $k_1 = k_2 = k_\parallel$ for the 3D k vector $|\boldsymbol{k}_s| = \sqrt{k_\perp^2 + k_\parallel^2}$ at the redshift of [C II] signal.

The left panel of Figure 3.6 shows our predicted CO power spectra projected into the frame of [C II] at redshift $z = 6.5$ or an equivalent observing frequency of $\nu_{\rm obs} = 250$ GHz. Contributions from different CO transitions (green curves) to the total CO power (gray and black solid curves) are shown by different line styles. For comparison, we also show two alternative CO models from Silva et al. (2015). The simulation-based model (purple line) is derived from fitting to the simulated $L^J_{\rm CO} - M_{\rm halo}$ relations (Obreschkow et al. 2009a,b), whereas the observational CO model (red line) is based on rescaling the observed infrared luminosity function (Sargent et al. 2012) with the ratios given by CW13. Finally, we note that Breysse et al. (2015) assume "Model A" of Pullen et al. (2013), which models the CO luminosity at a given dark matter halo mass with a simple scaling relation and predict a much higher level of CO foreground for the [C II] signal given by the "m2" model of Silva et al. (2015). However, we note that the Pullen et al. (2013) "Model A" is only optimized for observations at $z \sim 2$ and fails to capture the transition to sub-linear scaling of the $L_{\rm CO}$–$M_{\rm halo}$ relation at halo masses $M_{\rm halo} > 10^{11} M_\odot$.

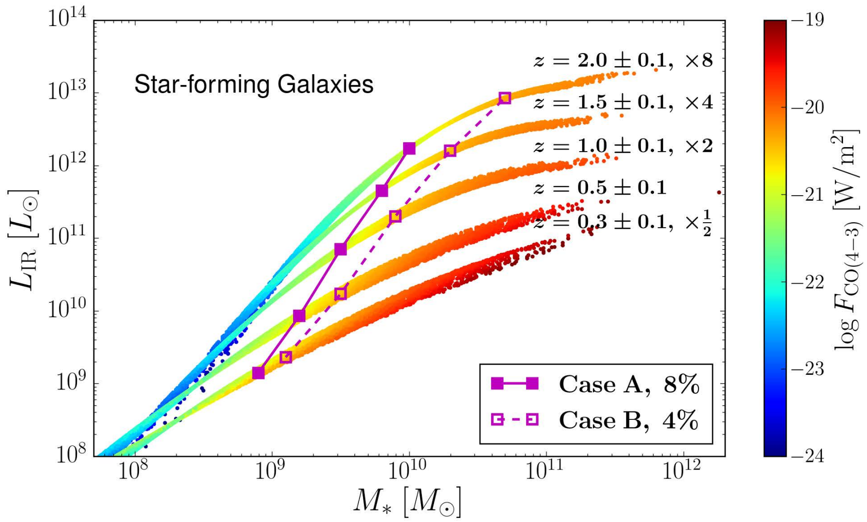

Figure 3.7: $L_{\rm IR}(M_*, z)$ model predictions in five narrow redshift intervals. $L_{\rm IR}(M_*, z)$ predictions are color-coded by the derived CO(4–3) flux in [W/m^2], assuming the G14 prescription. Each (M_*, z) point is taken directly from the UVISTA-DR2 catalog. Note that some bands are shifted vertically for visual clarity (the multiplicative factors are reported in the legend). The magenta curves are two examples of constant CO flux, or equivalently evolving stellar mass cut, corresponding to a total masked fraction of 8% (Case A, extensive) and 4% (Case B, moderate), respectively.

The variation in modeling the [C II] intensity is illustrated by the predicted signals from Gong et al. (2012) and Silva et al. (2015, "m2" model), shown as blue and yellow lines, respectively. Recent ALMA observations of several typical star-forming galaxies at $5 \lesssim z \lesssim 8$ have tentatively suggested a high [C II]-to-IR luminosity ratio (Capak et al. 2015; Aravena et al. 2016). The [C II] luminosity function derived from these observations is similar to that of Gong et al. (2012), implying a high clustering amplitude. In terms of the cumulative number density of $z \sim 6$ galaxies, the Gong et al. (2012) model is also supported by recent observations (Aravena et al. 2016; Hayatsu et al. 2017), which suggest a cumulative number density more than 10 times higher for galaxies with $L_{\rm [C\,II]} > 2\times10^8 L_\odot$ compared to Silva et al. (2015).

3.3.3 Masking Strategy

3D positional information (RA, Dec, z) from the galaxy catalog allows us to remove spectral-spatial elements (voxels) in the survey. Namely, after a 3D intensity map consisting $\sim$ 8000 voxels has been measured, we discard the voxels contaminated by at least one foreground CO line falling into TIME's spectral range. We specifically

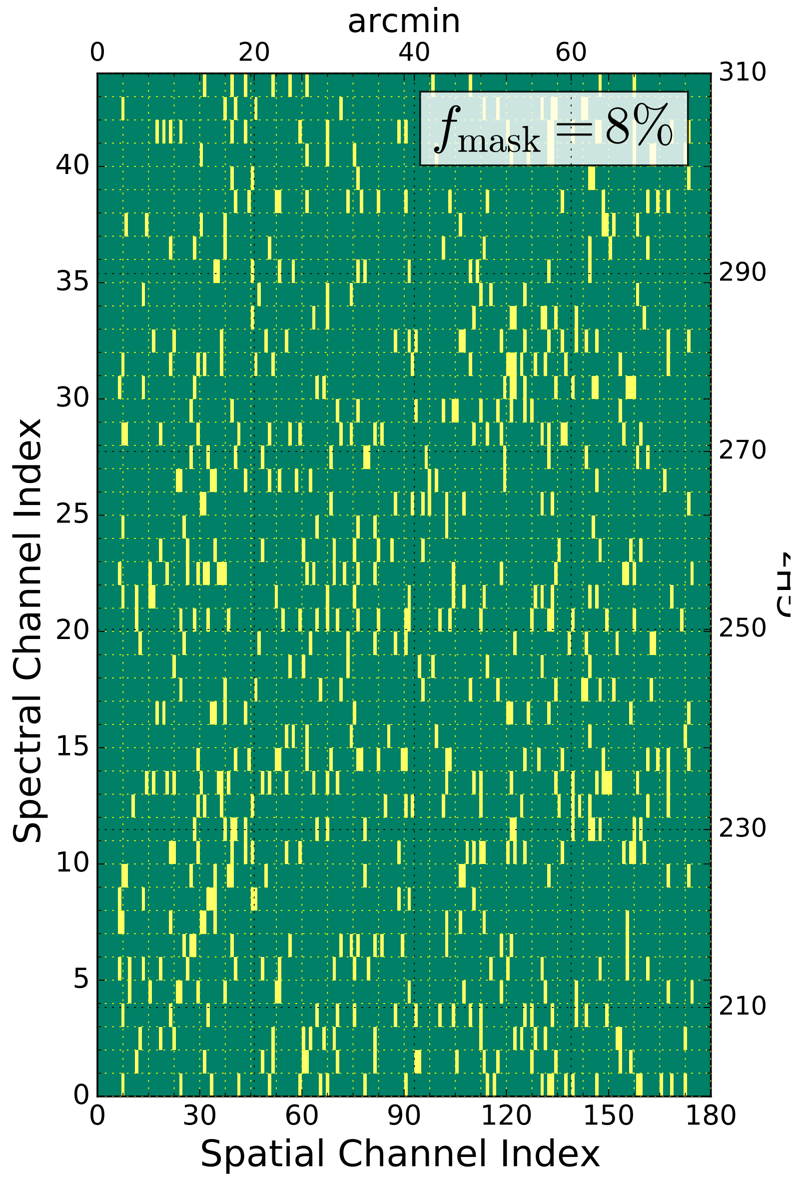

Figure 3.8: Voxel masking as a method of attenuating the CO foreground.. By masking all the voxels that are contaminated by CO emission lines ($3 \leq J_{\mathrm{upp}} \leq 6$) from low-redshift galaxies with stellar mass higher than the evolving mass cut (two examples are shown in Figure 3.7), we lose only a moderate fraction ($\lesssim 8\%$) of our survey volume. The exact voxels being masked are illustrated in terms of their channel indices (44 spectral and 180 spatial channels) and are calculated from a mock TIME field chosen in the COSMOS/UltraVISTA field. Note that the spectral-to-spatial aspect ratio of the voxels here is set to 10 for visual clarity, while TIME's will be roughly 20.

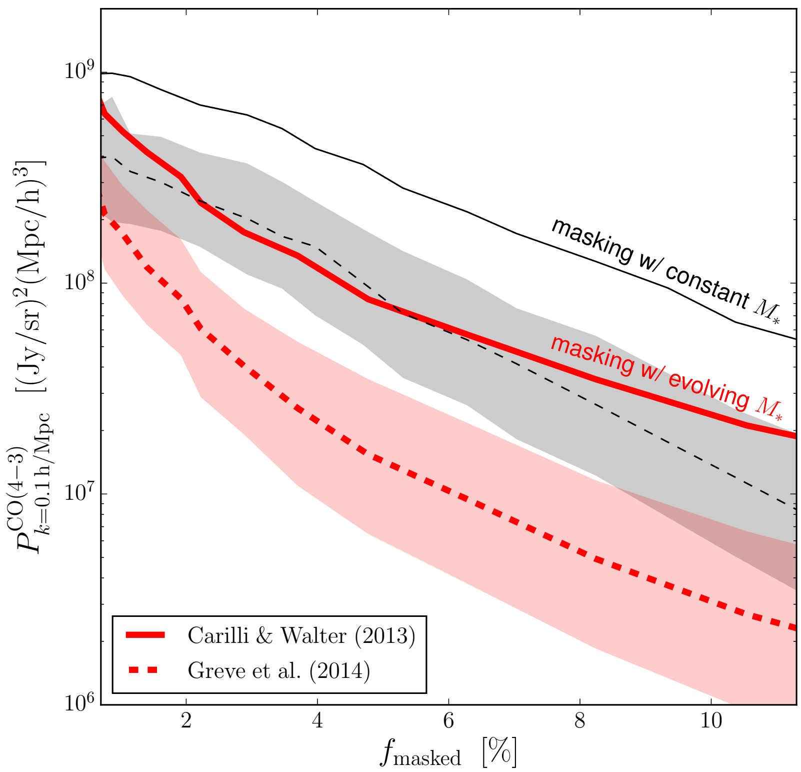

Figure 3.9: The predicted CO(4–3) power spectrum after projection as a function of voxel masking fraction. The predicted CO(4–3) power spectrum at $k = 0.1$ h/Mpc (after scale-projecting into the frame of [C II] at $z \sim 6.5$), as a function of voxel masking fraction for the two different masking strategies (constant, thin lines, vs. evolving M_*, thick lines; see text), and for the two different L_{IR}–L'_{CO} prescriptions considered in this work (CW13 and G14), showing that the evolving mass cut is more effective. The shaded bands represent the typical uncertainty in the inferred masking fraction due to fitting errors of the L'_{CO}–L_{IR} relation (only shown for G14 for clarity).

use stellar mass as a measure of the masking depth because it is directly provided by the galaxy catalog and CO power spectra are conveniently parameterized in terms of it. This approach is different from the blind, bright-voxel masking approach (e.g. Breysse et al. 2015), which does not exploit spectral information to identify and mask the voxels contaminated by faint CO sources, and thus fails to reduce the CO foreground sufficiently.

Provided that the catalog is complete between the integration limits (i.e., $M_*^{\mathrm{min}} < M_* < M_*^{\mathrm{max}}$), it is possible to estimate the loss of survey volume at a given masking depth by simply counting the number of voxels contaminated by the CO lines emitted from galaxies to be masked. Laigle et al. (2016) lists the 90% completeness levels for the COSMOS/UltraVISTA (UltraDeep, or "UD") catalog under consideration here (also shown in Figure 3.1); the stellar mass limits are $M_*^{90\%} \leq 10^{8.9}\,M_\odot$ for all CO transitions of interest. Since galaxies with $M_* \leq 10^{8.9}\,M_\odot$ contribute a negligible fraction ($\lesssim 0.5\%$) of the total CO power, the loss fraction is essentially dominated by the choice of masking strategy.

We optimize the masking sequence using an "evolving mass" cut, as shown in Figure 3.7. Instead of masking galaxies with a simple, universal stellar-mass cut, which results in removing more voxels containing higher-redshift, relatively faint CO-emitters, in order to mask equally-massive, lower-redshift, CO-bright counterparts, we define a function $M_*^{\max}(z) \leq M_{*,0}^{\max} = 1.0 \times 10^{13}\,M_\odot$ that is designed to follow a threshold of constant CO(4–3) flux (in W/m^2, assuming G14). Motivated by the range of uncertainty in [C II] models, we show two examples here corresponding to an extensive masking scheme (Case A) for the Silva et al. (2015) model as well as a moderate masking scheme (Case B) for the Gong et al. (2012) model. Masking essentially reduces the amplitude of CO power spectrum by varying the integration limit of the first and second CO-luminosity moments of the stellar mass function $\Phi(M_*)$, which correspond to the mean intensity and shot-noise power, respectively. Namely,

$$\frac{\langle \bar{I}_{\mathrm{CO}} \rangle_{\mathrm{m}}}{\langle \bar{I}_{\mathrm{CO}} \rangle_{\mathrm{um}}} = \frac{E\left[\int_{M_*^{\min}}^{M_*^{\max}(z)} L_{\mathrm{CO}}(M_*)\Phi(M_*)\mathrm{d}M_*\right]}{E\left[\int_{M_*^{\min}}^{M_{*,0}^{\max}} L_{\mathrm{CO}}(M_*)\Phi(M_*)\mathrm{d}M_*\right]} \tag{3.15}$$

and

$$\frac{\langle P_{\mathrm{CO}}^{\mathrm{shot}} \rangle_{\mathrm{m}}}{\langle P_{\mathrm{CO}}^{\mathrm{shot}} \rangle_{\mathrm{um}}} = \frac{E\left[\int_{M_*^{\min}}^{M_*^{\max}(z)} L_{\mathrm{CO}}^2(M_*)\Phi(M_*)\mathrm{d}M_*\right]}{E\left[\int_{M_*^{\min}}^{M_{*,0}^{\max}} L_{\mathrm{CO}}^2(M_*)\Phi(M_*)\mathrm{d}M_*\right]}, \tag{3.16}$$

where the angle brackets indicate that values are averaged over the log-normal distribution described by Equations 3.8 and 3.9.

The constant vs. evolving stellar-mass cut approaches are explicitly compared in Figure 3.9, where we show the predicted CO(4–3) power at $k = 0.1\ h$/Mpc (after scale-projecting into the frame of [C II] at $z \sim 6.5$) for the two different masking strategies, and for the two different L_{IR}–L'_{CO} prescriptions considered in this work, namely CW13 and G14. One can see that there is a clear advantage in using the evolving mass cut strategy, yielding a CO contamination almost an order of magnitude lower than the constant mass cut (at equal masking fractions). We show

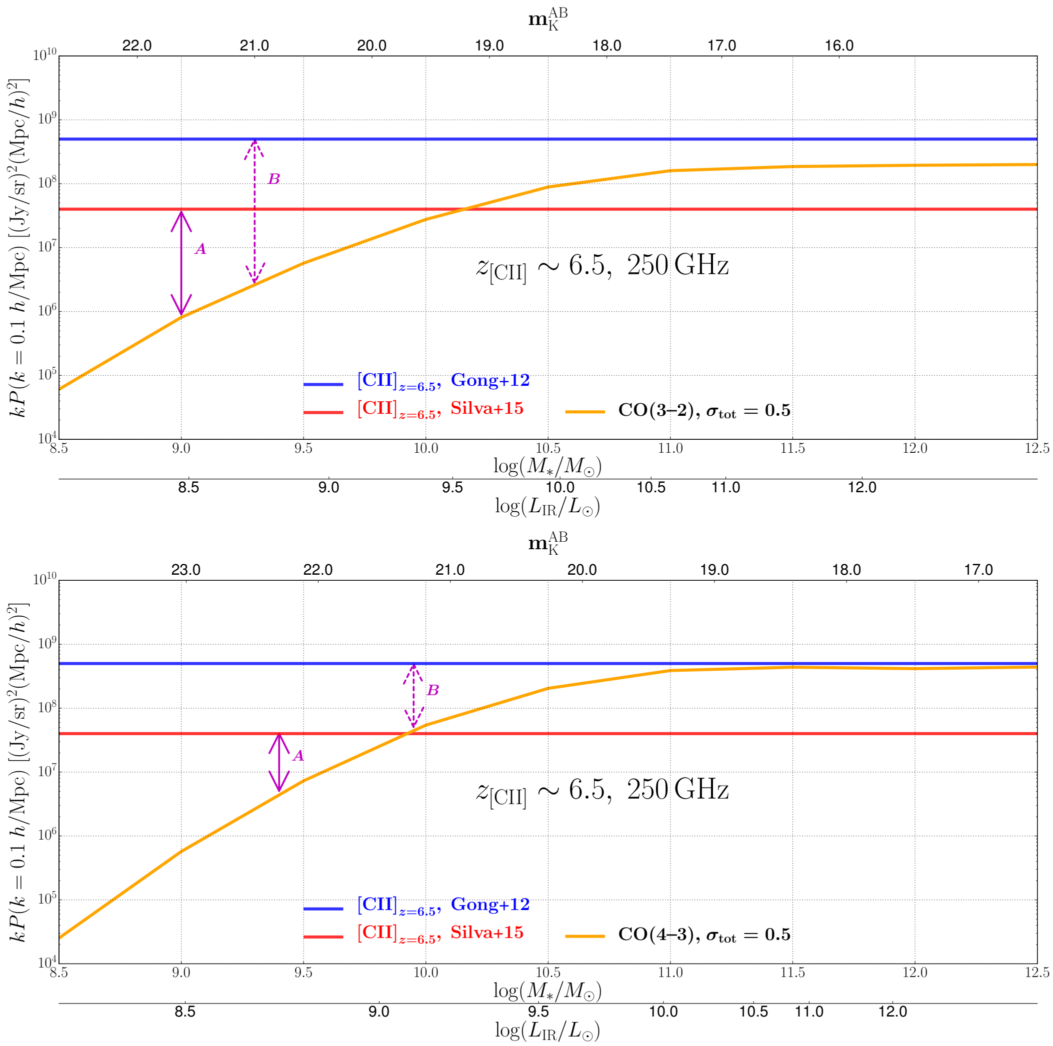

Figure 3.10: The predicted power of CO(3–2), CO(4–3), and [C II] at $z = 6.5$. Multiple x-axes are shown to illustrate how the masking depth in K-band AB magnitude projects to L_{IR}, stellar mass M_*, and mask fraction f_{mask}. Note that the $m_{\mathrm{K}}^{\mathrm{AB}}$ and L_{IR} scales differ from top to bottom panels because the interloping lines in the top and bottom panels originate from different redshifts: $z = 0.36$ and 0.82 for CO(3–2) and CO(4–3), respectively. Solid horizontal lines represent model predictions from Gong et al. (2012, blue) and Silva et al. (2015, "m2", red). The orange curve represents the CO power level vs. masking fraction assuming a scatter of $\sigma_{\mathrm{tot}} = 0.5$ dex. The solid (dashed) arrow indicates the evolving masking depth of Case A (Case B) considered in Figure 3.7, which yields a [C II]-to-CO(3–2) power ratio of 50 (200) and a [C II]-to-CO(4–3) power ratio of 10 (10).

this masking scheme for TIME voxels individually in Figure 3.8, where they are positioned according to their spatial (x-axis) and spectral channel (y-axis) indices. For the more extensive Case A masking, of which the depth decreases from $\sim 10^9\ M_\odot$

at $z \sim 0.3$ to $\sim 10^{10}\,M_{\odot}$ at $z \sim 2$, about 8% of voxels need to be masked, as indicated by the yellow stripes.

In the right panel of Figure 3.6, we show how this masking strategy can effectively bring down the CO contamination to levels that are sub-dominant to the clustering [C II] power. The power of total CO emission is calculated only from unmasked galaxies with an evolving stellar-mass cut, which results in a ~8% loss of the total survey volume (Case A). We note that although our analysis disfavors a total scatter larger than ~ 0.5 dex, the uncertainty in the scaling relations of different rotational J transitions among galaxy populations may also affect the predictions of CO power. Such uncertainty can be readily absorbed into the total scatter in our model by examining a broader range of scatter.

The effect of voxel masking on the [C II] power spectrum is to essentially remove a small fraction of voxels from the survey volume in a nearly random (i.e., uncorrelated) pattern. In Appendix 3.6, we demonstrate using a simulated light cone that simply discarding the CO-contaminated voxels would only cause a change in the raw, measured [C II] power spectrum of the order of the masked fraction ($\lesssim 10\%$), which is already small compared to the expected measurement uncertainty and thus will not affect our predictions for the [C II]/CO power ratio.

In order to obtain the true power spectrum though, one must correct for the artifact arising from the coupling between Fourier modes due to windowing (i.e., masking) in real space (Hivon et al. 2002; Zemcov et al. 2014). Specifically, individual k modes are propagated through the mask to characterize how their powers are mixed into other modes k'. A mode-coupling matrix $M_{kk'}$ can be constructed consequently, whose inverse provides the appropriate transformation from a masked power spectrum to an unmasked one. Provided that mode mixing and other systematics such as instrument beam and experimental noise are properly corrected, the [C II] power spectrum should be measured in an unbiased way in the presence of voxel masking. Alternatively, the correlation information can also be extracted from the two-point correlation function (2PCF), which is formally the Fourier transform of the power spectrum. It has the advantage of being less affected by the complicated survey geometry and incomplete sky coverage due to masking, albeit making the theoretical interpretation less straightforward. A detailed discussion of such corrections and alternatives is beyond the scope of this paper and thus left for future work.

We show in Figure 3.10 the evolution of CO power at scale $k = 0.1\,h/\mathrm{Mpc}$, where the clustering term dominates, with the masking depth expressed in K-band magnitude

$m_{\mathrm{K}}^{\mathrm{AB}}$, infrared luminosity L_{IR} and stellar mass M_*. Two dominant CO transitions are displayed separately here because the conversion between different masking depth expressions is redshift dependent. For our reference model, masking out voxels containing galaxies with $m_{\mathrm{K}}^{\mathrm{AB}} \lesssim 22$ at $z < 1$ renders a total CO power small enough compared with the [C II] clustering power with a moderate $\sim 8\%$ loss of total survey volume.

The accuracy of masking depends on the error in photometric redshift estimates with respect to instrument spectral resolution; for COSMOS DR2, $\sigma_z^{\mathrm{phot}}/(1+z^{\mathrm{phot}})$ is less than 1% (Laigle et al. 2016), comparable to TIME's typical voxel size in redshift space. While for simplicity the presented masked fractions are calculated assuming the maximum-likelihood photometric redshift, one may perform an even more conservative masking by accounting for the 68% confidence interval of the photometric redshift distribution, which would approximately *double* the masking fraction. Compared with the uncertainty in masking fraction due to fitting errors in the CO–IR relation shown in Figure 3.9, photometric redshift errors would likely dominate the uncertainty in the predicted masking fraction.

As illustrated in Figure 3.8, we expect to be masking at most $\sim$ 700 voxels at $0 < z < 2$ to reduce the level of CO contamination to a level required for a solid [C II] detection; hence, a follow-up campaign to measure spectroscopic redshifts is straightforward, if deemed necessary. For moderate masking (Case B; $\sim$ 350 voxels), a typical $z \sim 1$ star-forming galaxy close to our masking threshold $m_{\mathrm{K}}^{\mathrm{AB}} \sim 21$ requires about 3 hours of integration to obtain a robust spectroscopic redshift measurement with a multi-object spectrometer like MOSFIRE, which amounts to a total exposure time of about 30 hours for all $\sim$ 200 galaxies[3] that need to be masked within TIME's survey volume. For the more extensive masking (Case A; down to $m_{\mathrm{K}}^{\mathrm{AB}} \sim 22$), spectroscopic confirmation becomes more costly (> 60 hours), so the masking of these fainter sources will be guided solely by photometric redshifts.

Finally, we note that this masking formalism is flexible enough so that it can be further optimized in multiple ways. First of all, stacking using more information of the sources (e.g., by including dust extinction, see Viero et al., in prep) than the mass-redshift plane could improve the total infrared luminosity model by reducing the scatter. Moreover, although here the masking depth is chosen quite arbitrarily to roughly trace a constant level of observed CO flux, it can be more formally optimized

[3]Note that the number of galaxies to follow up is lower than the number of voxels to be masked due to multiple CO transitions from the same source that fall within TIME's observing band.

based on the properties of the foreground emitters, including the level of scatter.

3.3.4 Residual Foreground Tracers

Given the uncertainties in the strength of the [C II] signal and the CO contamination (see Figure 3.6), it is desirable to probe the level of remaining CO foreground after the voxel masking technique is applied in order to determine whether the foreground has been removed sufficiently. Silva et al. (2015) discuss the usefulness of cross correlation as a way to constrain the degree of post-masking foreground. Specifically, cross correlation can be done either between a foreground CO line and another dark matter tracer (e.g. a known population of galaxies) at the same redshift, or between two foreground CO lines (e.g. $J = 4 \rightarrow 3$ and $J = 3 \rightarrow 2$) emitted from the same redshift but contaminating the intensity maps observed at two different frequencies. The CO–galaxy cross-correlation requires an external dataset like COSMOS. The correlation can be checked as the masking depth increases. The CO–CO cross-correlation can be done within the experiment's own dataset, albeit at the expense of a potentially lower sensitivity after masking. The cross power in this case serves as a tracer of the degree of contamination as a function of masking depth. Since [C II] signals from different redshifts are uncorrelated, they do not contribute to the overall cross-correlation power. It is worth noting that these methods can test whether the CO foreground has been removed satisfactorily, although without indicating which sources must be further removed. In Appendix 3.7, we present a more detailed discussion of the usefulness of cross-correlating CO lines from the same redshift, including how it can be used to measure CO lines themselves and thus constrain the cosmic molecular gas content.

3.4 Conclusions

We presented a method to estimate the mean and scatter of CO line emission from measurements of the total infrared luminosity, L_{IR}, and showed how it can be applied as a foreground removal strategy for [C II] intensity mapping experiments. We optimized the trade-off between the relative strength of CO/[C II] power and the loss of survey volume. We found that even in the most conservative scenario, by progressively masking galaxies above a stellar mass cut increasing with redshift — which approximately amounts to K-band magnitudes of $m_K^{\mathrm{AB}} \lesssim 22$ at $z < 1$, or ~8% of all voxels — a [C II]/CO power ratio $\gtrsim 10$ is achievable in the clustering amplitude.

Acknowledgments

The authors would like to thank the anonymous referee for valuable suggestions. The authors also acknowledge Ryan Quadri and Adam Muzzin for the continued support of our stacking program and the valuable insights from the near-infrared community. T.-C. C. acknowledges MoST grant 103-2112-M-001-002-MY3 and JPL R&TD Award 01STCR - R.17.226.063. JH is supported by the National Science Foundation Graduate Research Fellowship under Grant No. DGE-1144469. AC was supported by a KISS postdoctoral fellowship and is now supported by the National Science Foundation Astronomy and Astrophysics Postdoctoral Fellowship under Grant No. 1602677. MBS acknowledges the Netherlands Foundation for Scientific Research support through the VICI grant 639.043.006. MPV acknowledges support by the US Department of Energy through a KIPAC Fellowship at Stanford University.

3.5 Appendix: Validation of the Stacking Method

In order to demonstrate the validity of our methods for estimating the mean and scatter of source populations, and to identify any potential bias due to galaxy clustering, we apply the procedures from the previous section to simulated maps, whose input mean flux densities and their scatter are known. We base our simulations on the COSMOS catalog which inherently contains the positional information about source clustering and defer a more thorough analysis involving a varying degree of clustering to future work.

Simulated FIR/sub-mm maps are generated in the same way as the mock maps for scatter characterization, as described in Section 3.2.2. We note that different realizations of random flux assignments ensure that we obtain distinct maps with similar statistics. Flux densities are assigned to sources in each individual (M_*, z) bin according to a log-normal distribution, with scatter $\sigma_{\rm in}$ and mean $\langle S_{\rm in}\rangle$.

We further verify that SIMSTACK estimates are robust for subsets with different levels of scatter. As shown in Figure 3.11, flux densities $\langle S_{\rm out}\rangle$ estimated with or without a 0.3 dex scatter (solid line) are consistent with their respective mean inputs (circles) for a simulated map. Note that in these simulations we only perturb a subset of bins (indicated by the filled circles), in order to test the interplay between perturbed and unperturbed layers in the mock maps. Additionally, we test that SIMSTACK estimates are unbiased for perturbations of up to 0.5 dex on different combinations of bins (not shown), which provides confidence that the mean flux density distribution in the actual ~ 0.35 dex measurement is correctly estimated.

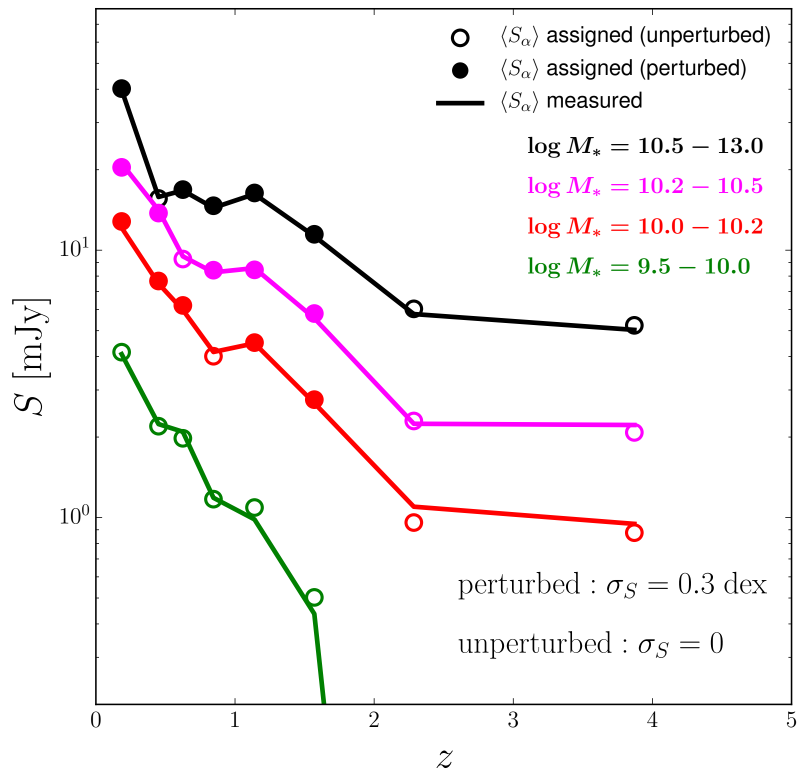

Figure 3.11: Robustness of measuring the mean flux densities with SIMSTACK. When a simulated map is created, sources in a selected number of bins are assigned flux densities according to a log-normal distribution with a fiducial scatter of 0.3 dex (i.e., sources are perturbed by 0.3 dex of scatter), whose means are calculated and represented by the filled circles. Sources in other bins are simply assigned a fixed flux density with zero scatter (i.e., sources are unperturbed) and their means are represented by the open circles. SIMSTACK measurements of the constructed simulated map shown by the solid lines are then compared with both the filled and open circles, indicating a good agreement between the assigned fluxes (both perturbed and unperturbed) and the measured ones at all redshifts and flux levels.

As a final validation test, we estimate the scatter in simulated maps. Figure 3.12 shows the ratio of measured scatter (σ_{o}) to the assigned scatter (σ_{i}), for different stellar mass/redshift bins. The error bars indicate the 68% confidence intervals estimated from many map realizations. We investigate the robustness of this method with two simple tests: (i) a given bin is assigned a scatter different from the fiducial value (0.3 dex), but still within the range (0.2–0.4 dex) observed, and (ii) a different fiducial scatter within the observed range is assigned to the "background" sources.

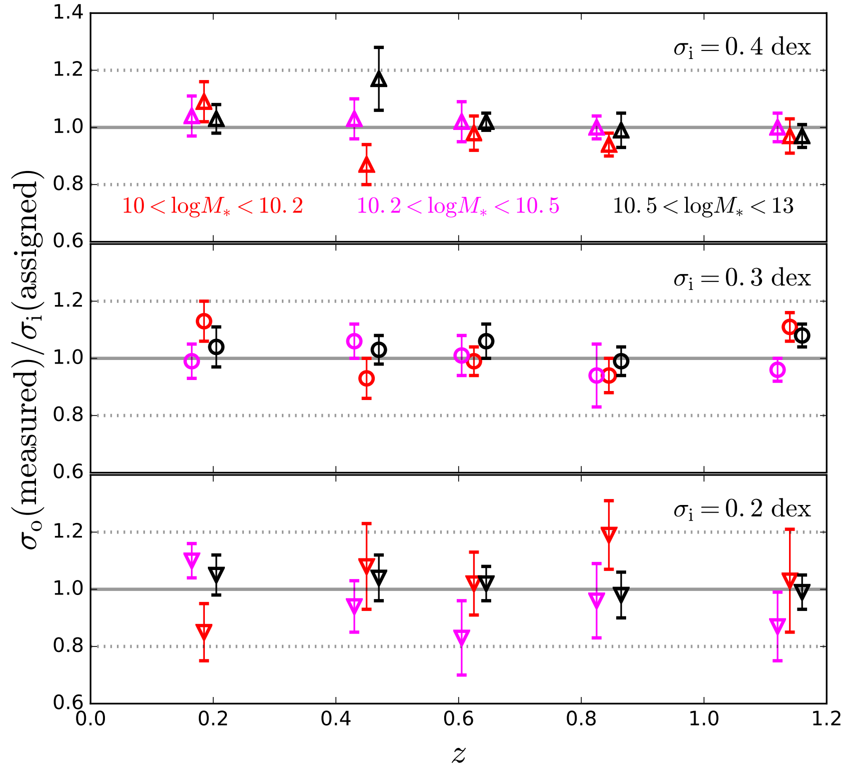

Figure 3.12: Comparison between the measured and assigned levels of scatter as a validation of the scatter measurements. A ratio of 1 stands for a perfect agreement. The middle panel shows the ratio of the scatter measured by our thumbnail stacking formalism to that assumed by the distribution of fluxes (0.3 dex) to generate simulated maps. This ratio of recovered to assigned scatters ($\sigma_{\rm o}/\sigma_{\rm i}$) is evaluated for different stellar mass and redshift bins, as indicated by the x-axis and marker colors. For comparison, the top and bottom panels show the cases where, only in the bin under examination, the fluxes assigned to the galaxies are drawn from a log-normal distribution with a different scatter (0.4 and 0.2 dex, respectively). Sources not in the bin under examination are varied by 0.3 dex in all three cases. Note that the data points are slightly shifted along the x-axis for visual clarity.

The first test is shown in the top and bottom panels of Figure 3.12, where the bins under examination are perturbed by $\sigma_{\rm i}$ = 0.2 and 0.4 dex respectively, along with the case shown in the middle panel where all bins have the same 0.3 dex scatter. Our method recovers the input scatter to within ~ 10%, typically, and 20% at worst. For the second case, we find that, on average, varying the fiducial scatter between 0.2 and 0.4 dex introduces less than 10% uncertainty in the recovered scatter, comparable to the level of statistical error. Therefore, although a fiducial scatter must be assigned to properly account for the flux variance due to "background" sources in a confusion-limited map, our method is generally insensitive to its exact value, at least within the range of the observed scatter in the SFMS.

3.6 Appendix: Effect of masking on the [C II] power spectra

Intensity maps of [C II] emission from the EoR will be contaminated by emission from several CO transitions at low redshifts whose signal is expected to be higher than that of the target [C II] line. Masking voxels contaminated by strong CO emission has been shown to significantly reduce the foreground lines signal.

During the CO masking process, a fraction of the [C II] signal will be inevitably removed. Given that CO and [C II] emissions are originated from different volumes in space, they will be observed as uncorrelated both in angular position and in the observed frequency. Therefore, the percentage of reduction of the [C II] intensity due to the masking procedure should be of the order of the percentage of pixels masked, while the CO intensity of emission will be substantially reduced as long as the bright CO galaxies are correctly identified. The masked pixels can also be seen as a loss in volume of the observed field and the [C II] corrected for masking such as is done in CMB studies. This correction will be done for observational data allowing for the recovery of the target signal as long as the masked percentage is not very high. For this study we are however not going to discuss the possible algorithms that can be used to correct for this masking since even without the correction the target signal would be reasonably well recovered for the discussed masking percentages.

We simulate the masking procedure using a CO signal characterized by the Greve et al. (2014) model and for two models of [C II] emission. The CO and [C II] lines are then masked according to a cut in stellar mass corresponding to the Case A masking described in this paper. This corresponds to a masking of about 10% of the simulated volume.

The line signals are obtained by post processing galaxy data from the EAGLE simulation (Schaye et al. 2015; McAlpine et al. 2016; Crain et al. 2017) using semi-analytic models. The stellar masses predicted by this simulation differ from that of the COSMOS/UltraVISTA survey as shown in Figure 1 from Furlong et al. (2015). However, the qualitative conclusions that can be taken from this exercise are valid anyway.

The IR luminosities of CO emitting galaxies are obtained using Equation 3.1 (where

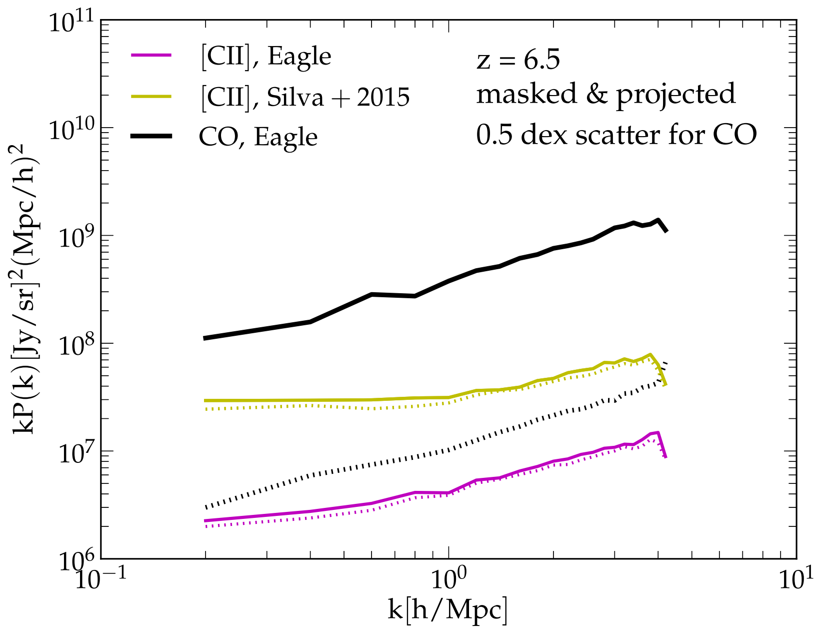

Figure 3.13: Simulated effects of masking on power spectra. Power spectra of CO (projected) and [C II] emission computed from simulated intensity maps before (solid) and after (dotted) Case A masking as illustrated in Figure 3.7.

passive galaxies were identified as galaxies with $\dot{M}_* = 0\,M_\odot\,\mathrm{yr}^{-1}$). Note that given the resolution of the EAGLE simulation, the star formation rate (SFR) is only resolved for $\dot{M}_* > 2\times10^{-3}\,\mathrm{M_\odot yr^{-1}}$. Therefore, in this simulation some galaxies might have been considered as having a quenched SFR while still having some star formation. The CO luminosities are then derived from the IR luminosities using the relations by Greve et al. (2014) and assuming a total scatter of 0.5 dex in this relation.

We model the [C II] luminosities assuming the following relation:

$$\frac{L_{[\mathrm{C\,II}]}}{L_\odot} = \frac{9.22\times10^6\dot{M}_*}{M_\odot\,\mathrm{yr}^{-1}}. \tag{3.17}$$

The [C II] signal is calculated assuming the relation between SFR and halo mass from Silva et al. (2015) (where the halo masses were taken from the EAGLE simulation) or directly assuming the SFRs from the Eagle simulation. These two models span the expected uncertainty on the [C II] signal during the EoR (more precisely at $z = 6.5$) due to the uncertainty on the SFR powering these emissions. Another important source of uncertainty on the amplitude of the [C II] signal is the evolution of the ratio between IR luminosity and [C II] luminosity towards high redshifts, which is however beyond the scope of this paper.

Figure 3.13 shows the effect of masking pixels on the CO and on the [C II] power spectra. According to these CO/[C II] models, the masking described in this paper would reduce the CO signal efficiently. The relative amplitude of the masked [C II] signal to the CO signal will mainly depend on the initial relation between the amplitude of the two signals.

3.7 Appendix: Cross Correlating [C II] + CO Maps

As mentioned in Section 3.3.4, the cross correlation between maps of [C II]+CO emission can be used to test if the masking procedure effectively decreased the signal of some of the line contaminants. Moreover, without masking, this cross correlation can be used to get an independent measurement of the intervening CO lines themselves.

In the frequency range covered by TIME surveys there are a few sets of two observing frequencies which contain emission from two or more adjacent CO lines originating from the same redshift. As an example the [C II] intensity maps at $z = 7.8$ and 5.6 will be respectively contaminated by CO(3–2) and CO(4–3) lines emitted from $z \sim 0.6$. Since only two lines emitted from the same redshift will be correlated, this cross correlation in principle only measures the CO foreground.

In terms of a tracer of residual CO emission, the amplitude of the cross correlation of the two *masked* signals will be proportional to the product of the residual signals from the two CO lines. The shape of the cross correlation power spectra, between the two masked signals, will be correlated and uncorrelated at different scales if masking has reduced the CO foreground sufficiently. This lack of correlation is a strong indication that the masked maps are dominated by the [C II] emission. In this case, the nonzero power is due to the self correlations of the emission within individual simulation boxes, which can be understood as high-order terms in the cross correlation. Figure 3.14 shows this cross correlation power spectra made with the simulations described in Section 3.5.

On the other hand, the cross correlation of the two *unmasked* signals will result in the product of the signals from the two CO lines and serve as a probe of CO intensities, which can also be further converted into H_2 mass to infer the molecular gas content of galaxies. It should be noted, however, that certain assumptions of CO excitation have to be made in order to understand the correlation factors (i.e.,

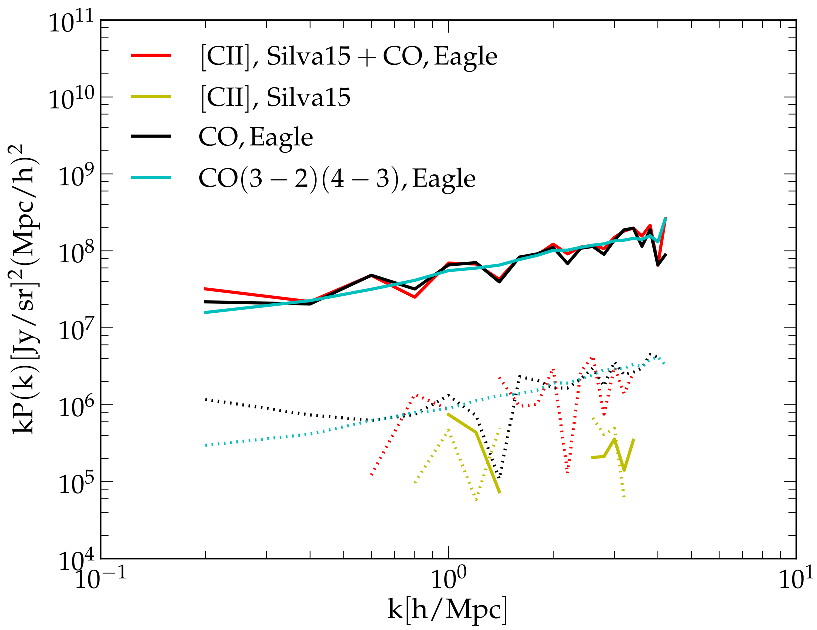

Figure 3.14: Quantifying residual foregrounds with cross-correlation. Cross-power spectra between observed intensity maps at frequencies 216.1 GHz ($z_{\mathrm{C\,II}} = 7.8$) and 288.2 GHz ($z_{\mathrm{C\,II}} = 5.6$), corresponding to the observed frequencies of CO(3–2) and CO(4–3) lines emitted from $z \sim 0.6$. The solid and dashed lines represent power spectra before and after masking respectively. Different colors indicate cases where the simulated intensity maps contain different combinations of signal and foreground lines.

line ratios) of different CO transitions and therefore interpret the cross correlation measurements of adjacent CO lines. Fortunately, existing observations suggest rather small variations in the line ratios of adjacent CO lines (e.g., Carilli & Walter 2013), allowing [C II] experiments like TIME to make reliable measurements of CO lines by cross-correlating within the dataset.

Chapter 4

A SELF-CONSISTENT FRAMEWORK FOR MULTI-LINE MODELING IN LINE INTENSITY MAPPING EXPERIMENTS

Sun, G., Hensley, B. S., Chang, T.-C., Doré, O., & Serra, P. (2019). "A Self-Consistent Framework for Multi-Line Modeling in Line Intensity Mapping Experiments", *Astrophysical Journal*, 887, 142. DOI: 10.1042/BJ20150183.

Abstract

Line intensity mapping (LIM) is a promising approach to study star formation and the interstellar medium (ISM) in galaxies by measuring the aggregate line emission from the entire galaxy population. In this work, we develop a simple yet physically-motivated framework for modeling the line emission as would be observed in LIM experiments. It is done by building on analytic models of the cosmic infrared background that connect total infrared luminosity of galaxies to their host dark matter halos. We present models of the H I 21 cm, CO(1–0), [C II] 158 μm, and [N II] 122 and 205 μm lines consistent with current observational constraints. With four case studies of various combinations of these lines that probe different ISM phases, we demonstrate the potential for reliably extracting physical properties of the ISM, and the evolution of these properties with cosmic time, from auto- and cross-correlation analysis of these lines as measured by future LIM experiments.

4.1 Introduction

Line intensity mapping (LIM) is an emerging observational technique developed to statistically measure the intensity field fluctuations of a given spectral line (see Kovetz et al. 2017 for a recent review). While traditional galaxy surveys are restricted by the detection limit of individual sources, LIM is sensitive to the emission from all galaxies, providing a complementary probe of faint objects. Due to its statistical nature, LIM is most effective at constraining how average physical properties, including the star formation rate, ISM conditions, luminosity function, spatial distribution, etc., of the source galaxy population evolve over cosmic time (Serra et al. 2016, hereafter S16; Kovetz et al. 2017; Chang et al. 2019).

LIM was first pioneered with the redshifted H I 21 cm line signal. It serves as a probe of both the matter density distribution as traced by the atomic hydrogen gas in the interstellar medium (ISM), for example, the baryon acoustic oscillation (BAO) feature in galaxy power spectrum (Chang et al. 2010; Switzer et al. 2013), and the structure of neutral intergalactic medium (IGM) at high redshift, in particular during cosmic reionization (Madau et al. 1997; Furlanetto et al. 2004, 2006; Pritchard & Loeb 2012). Recently, the application of LIM to other emission lines has gained increasing attention, including CO rotational lines (Pullen et al. 2013; Breysse et al. 2014; Mashian et al. 2015b; Li et al. 2016), far-infrared (FIR) fine-structure lines of C II, N II, O I and others (Gong et al. 2012; Uzgil et al. 2014; Silva et al. 2015; Yue et al. 2015; S16), and bright optical/UV emission lines such as Lyα and Hα (Silva et al. 2013; Pullen et al. 2014; Comaschi & Ferrara 2016; Gong et al. 2017; Silva et al. 2018).

Substantial theoretical and experimental efforts have been devoted to the detection and interpretation of LIM signals of individual lines. However, a simple, physical model that allows multiple line signals, presumably originating from and thus probing different ISM phases, to be modeled in a self-consistent manner is still lacking. The goal of this work is to develop such a self-consistent framework for determining the integrated line intensities of galaxies observed in the intensity mapping regime. This framework is intended to bridge the gap between commonly-used approaches anchored on scaling relations empirically determined from observations (e.g., Visbal & Loeb 2010; Pullen et al. 2013; Silva et al. 2015; Li et al. 2016; S16) and sophisticated simulations of galaxy-scale hydrodynamics and radiative transfer (e.g., Pallottini et al. 2019; Popping et al. 2019). More specifically, it should be sophisticated enough to capture the relevant ISM physics and employ meaningful physical parameters, yet simple enough to interpret the auto/cross-correlation of the intensities of various lines observed in the intensity mapping regime in terms of coarse-grained galactic ISM properties. Some examples include the mass fraction of different ISM phases, as well as quantities like the photoelectric (PE) heating efficiency and the CO-to-H_2 ratio, which are closely related to exact physical conditions of the ISM (e.g., temperature, density, radiation field) and therefore of particular interest to LIM surveys of the corresponding lines. Furthermore, this analytical framework should also allow mock signal maps to be readily constructed from given information about the position and physical properties of source populations, thereby enabling straightforward implementation in semi-analytic models of the LIM signals.

We build such a formalism using the information from the cosmic infrared background (CIB). The CIB has, on account of sensitive FIR observations from experiments like *Planck* (Planck Collaboration XXX 2014) and *Herschel* (Viero et al. 2013b), been the subject of detailed modeling efforts. In particular, analytic models connecting the infrared (IR) luminosity of galaxies to the mass and redshift of their host halos have been successful in reproducing the statistical properties of the CIB (e.g., Shang et al. 2012; S16; Wu & Doré 2017b). In this work, we follow and extend the ideas presented in S16 by employing the CIB model as a starting point for models of both line and continuum emission from galaxies as a function of redshift and halo mass. Taken at face value, the IR luminosities assumed in these models imply a corresponding dust mass, gas mass, and metallicity, which in turn can inform predictions of emission from various interstellar lines, including H I, [C II], [N II] and CO(1–0). We work through these consequences, with an eye toward testable predictions from upcoming intensity mapping experiments of these lines.

This paper is organized as follows. In Section 4.2, we present a simple analytic model that describes a variety of physical properties of dark matter halos hosting the line-emitting galaxies, such as their star formation rate, dust mass, metallicity and so forth. We then discuss in Section 4.3 how we model the emission of H I, [C II], [N II] and CO lines as tracers of different phases of the ISM, based on our model of halo properties. In Section 4.4, we review the theoretical framework of estimating the power spectrum signal of intensity mapping experiments, as well as the uncertainty associated with the measurements. We compare the predicted strengths of different lines to constraints from the literature in Section 7.3. We then present four case studies in Section 4.6 to demonstrate how physical conditions of multi-phase ISM may be probed by and extracted from with intensity mapping experiments. We outline prospects for further improving and extending our simple modeling framework, before briefly concluding in Section 4.7. Throughout the paper, we assume a flat, ΛCDM cosmology consistent with the measurement by the Planck Collaboration XIII (2016).

4.2 A Simple Analytic Model of Mean Halo Properties

An important criterion for choosing first targets for LIM surveys is the overall brightness of the spectral line, which is determined by many different factors, including abundance, excitation potential, critical density, destruction and/or scattering, and so forth. In many cases, nevertheless, the line signal either directly traces the star-forming activity (e.g., [C II], [N II]) or indirectly probes the gas reservoir closely associated with star formation (e.g., H I, CO). Therefore, it is critical to understand and model the star formation of galaxies well enough in order to properly estimate the production of lines in LIM.

The majority of starlight from young stars at optical/UV wavelengths is absorbed and reprocessed into IR radiation by interstellar dust, naturally giving rise to the connection between IR observations of galaxies and their star formation rate. Because the fraction of spatially resolved galaxies decreases rapidly with increasing wavelength in the IR/sub-millimeter regime, the observed CIB mean intensity and fluctuations provide a useful probe of global star-forming activities. Combining the halo model formalism describing the clustering of galaxies at different angular scales (Cooray & Sheth 2002) and the observed angular anisotropy of the CIB, Shang et al. (2012) developed a simple parametric form for the infrared luminosity of galaxies as a function of halo mass and redshift, which has been successfully applied to reconstruct the observed angular CIB auto- and cross-power spectra (Planck Collaboration XXX 2014; S16; Wu & Doré 2017b). In this section, we extend the discussion in S16 and present a simple, CIB-based model for the mean properties of dark matter halos, such as their infrared luminosity, dust and gas mass, metallicity, etc., which are essential ingredients for the line emission models in this work.

Table 4.1: Fiducial Parameters of CIB Model

Parameter	Description	Value	Reference
L_0	$L_{\rm IR}$ normalization	$0.0135\,L_\odot/M_\odot$	Eq. 4.1
s	z evolution of $L_{\rm IR}$	3.6	Eq. 4.2
T_0	$T_{\rm dust}$ at $z=0$	24.4 K	Eq. 4.4
α	z evolution of $T_{\rm dust}$	0.36	Eq. 4.4
β	RJ-side index	1.75	Eq. 4.5
γ	Wien-side index	1.7	Eq. 4.5, 4.6
$M_{\rm eff}$	effective halo mass	$10^{12.6}\,M_\odot$	Eq. 4.8
$\sigma_{L/M}$	log scatter	0.5	Eq. 4.8

4.2.1 IR luminosity

We work in the aforementioned framework of the halo model for CIB anisotropies introduced by Shang et al. (2012), which has been exploited in various contexts, including the modeling of high-redshift emission lines (e.g., Planck Collaboration XXX 2014; S16; Wu & Doré 2017b; Pullen et al. 2018). In this model, the specific luminosity emitted by a galaxy hosted by a halo of mass M at redshift z at the observed frequency ν is given by

$$L_{\mathrm{IR},(1+z)\nu}(M,z) = L_{\mathrm{IR},0}\Phi(z)\,\Sigma(M)\,\Theta\left[(1+z)\,\nu\right] \ , \tag{4.1}$$

where $L_{\mathrm{IR},0}$ is a normalization constant (see Table 4.1 for a summary of fiducial parameter values taken for the CIB model), whereas $\Phi(z)$, $\Sigma(M)$, and $\Theta\left[(1+z)\,\nu\right]$ are functions to be specified. $\Phi(z)$ governs the evolution of the luminosity–mass relation with redshift, driven, e.g., by an increase in the star formation rate at fixed halo mass with increasing redshift. This is modeled as a power law

$$\Phi(z) = (1+z)^{s} \ , \tag{4.2}$$

where Wu & Doré (2017b) found a best-fit value of $s = 3.6$. However, we note that the exact value of s is not well-constrained by the integrated CIB intensity and less steep slopes have indeed been suggested by some other CIB analyses and galaxy evolution models (see discussion in S16).

$\Theta\left[(1+z)\,\nu\right]$ describes the frequency dependence of the dust emission as a function of redshift. Over most of the FIR frequency range, the dust emission in a galaxy is modeled as a modified blackbody of temperature T_{d} and spectral index β,

$$I_\nu \propto \nu^{\beta}\, B_\nu\left[T_{\mathrm{d}}(z)\right] \ , \tag{4.3}$$

where $B_\nu\left[T_{\mathrm{d}}(z)\right]$ is the Planck function at a dust temperature

$$T_{\mathrm{d}}(z) = T_0(1+z)^{\alpha} \ , \tag{4.4}$$

where $T_0 = 24.4\,\mathrm{K}$ is the typical dust temperature in a star-forming galaxy at $z = 0$, and the redshift dependence is taken to be $\alpha = 0.36$ following Planck Collaboration XXX (2014) and Wu & Doré (2017b). The high frequency component is modeled as a power law to account for emission from small, stochastically-heated grains. The full SED is given by

$$\Theta\left[(1+z)\,\nu\right] = A(z) \times \begin{cases} \nu^{\beta}\, B_\nu\left[T_{\mathrm{d}}(z)\right] & \nu < \nu_0 \\ \nu^{-\gamma} & \nu \geq \nu_0 \end{cases} \ , \tag{4.5}$$

where the frequency ν_0 at any given redshift is determined by having

$$\frac{d\,\ln\left\{\nu^{\beta} B_\nu\left[T_{\mathrm{d}}(z)\right]\right\}}{d\,\ln\nu} = -\gamma \tag{4.6}$$

satisfied at $\nu = \nu_0$. We adopt $\beta = 1.75$ and $\gamma = 1.7$ (Planck Collaboration XXX 2014; Wu & Doré 2017b), which yield $\nu_0 = 3.3, 2.1, 1.6$ and $1.3\,\mathrm{THz}$ or wavelength equivalents 92, 143, 185, and 222 μm at redshifts $z = 0, 1, 2$ and 3, respectively. The redshift-dependent normalization factor $A(z)$ is defined such that

$$\int \Theta(\nu, z)\ d\nu = 1 \tag{4.7}$$

for all z.

$\Sigma(M)$ links the IR luminosity to the halo mass and is modeled as a log-normal relation:

$$\Sigma(M) = M\frac{1}{\sqrt{2\pi\sigma_{L/M}^2}}\exp\left[-\frac{(\log_{10}M - \log_{10}M_{\rm eff})^2}{2\sigma_{L/M}^2}\right], \tag{4.8}$$

where $M_{\rm eff}$ describes the most efficient halo mass at hosting star formation, and $\sigma_{L/M}$ accounts for the range of halo masses mostly contributing to the infrared luminosity. This functional form captures the fact that the star formation efficiency is suppressed for halo masses much lower or much higher than $M_{\rm eff}$ (Mo et al. 2010; Furlanetto et al. 2017; Kravtsov et al. 2018), due to various feedback mechanisms such as input from supernova explosions and active galactic nuclei (AGNs). The total infrared luminosity (8–1000 μm) is then

$$L_{\rm IR}(M, z) = \int_{300\,\rm GHz}^{37.5\,\rm THz} {\rm d}\nu L_{(1+z)\nu}(M, z)\ . \tag{4.9}$$

4.2.2 Star Formation History

From the total infrared luminosity, it is straightforward to derive the star formation rate as a function of halo mass and redshift thanks to the well-established correlation between them (Kennicutt 1998; Madau & Dickinson 2014). In this work, we simply take

$$\dot{M}_\star(M, z) = \mathcal{K}_{\rm IR} L_{\rm IR}\ , \tag{4.10}$$

where $\mathcal{K}_{\rm IR} = 1.73 \times 10^{-10}\, M_\odot\, {\rm yr}^{-1}\, L_\odot^{-1}$, consistent with a stellar population with a Salpeter initial mass function (IMF) and solar metallicity. The star formation rate density (SFRD) can consequently be written as

$$\dot{\rho}_\star(M, z) = \int_{M_{\rm min}}^{M_{\rm max}} \frac{{\rm d}N}{{\rm d}M}\dot{M}_\star(M, z)\ , \tag{4.11}$$

where ${\rm d}N/{\rm d}M$ is the dark matter halo mass function defined for the virial mass $M_{\rm vir}$ (Tinker et al. 2008). Figure 4.1 shows a comparison between cosmic SFRDs predicted by the adopted CIB model and those from the literature. The data points represent estimated SFRDs based on both dust-corrected UV observations (Cucciati

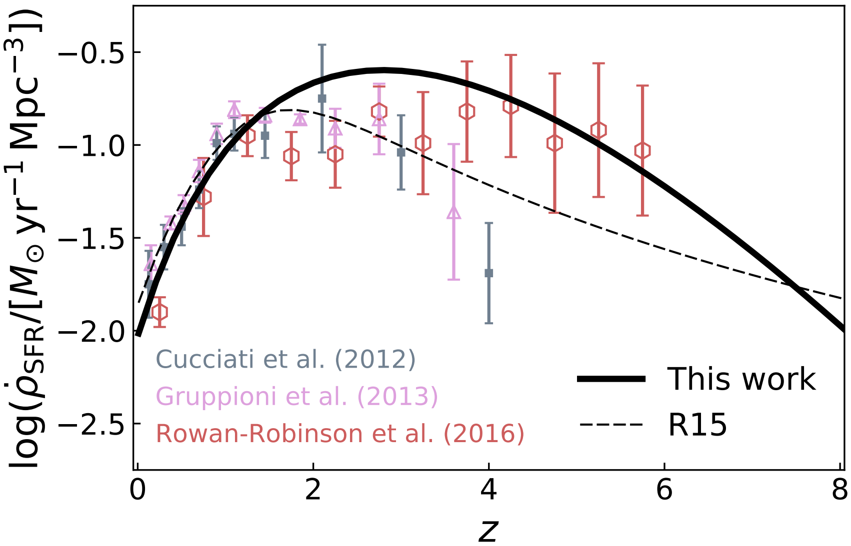

Figure 4.1: Cosmic star formation history from the CIB model and the literature. The SFRD implied by our CIB model is compared with those inferred from UV (Cucciati et al. 2012) and IR (Gruppioni et al. 2013; Rowan-Robinson et al. 2016) data. Also shown for comparison is the maximum-likelihood model from Robertson et al. (2015), which is a fit to the SFRD estimates based on IR and (primarily) optical/UV data.

et al. 2012) and infrared/sub-millimeter observations of obscured star formation (Gruppioni et al. 2013; Rowan-Robinson et al. 2016). Also shown is the maximum-likelihood model of cosmic SFRD from Robertson et al. (2015) based on extrapolating the galaxy IR and UV luminosity functions down to $10^{-3}\,L_\star$. The agreement between the CIB-derived SFRD and the optical/UV-derived SFRD may be improved with different modeling choices (e.g., Maniyar et al. 2018). However, this comes at the expense of phenomenological parameterizations of the effective bias factor of dusty galaxies, and we therefore do not follow that approach here.

4.2.3 Dust Mass

Since we have specified both the dust luminosity and the dust temperature from the CIB model, it is possible to estimate the implied dust mass. Assuming that the dust mass is dominated by larger grains whose emission can be described by a modified blackbody with a single dust temperature, the dust luminosity, mass, and temperature can be related via

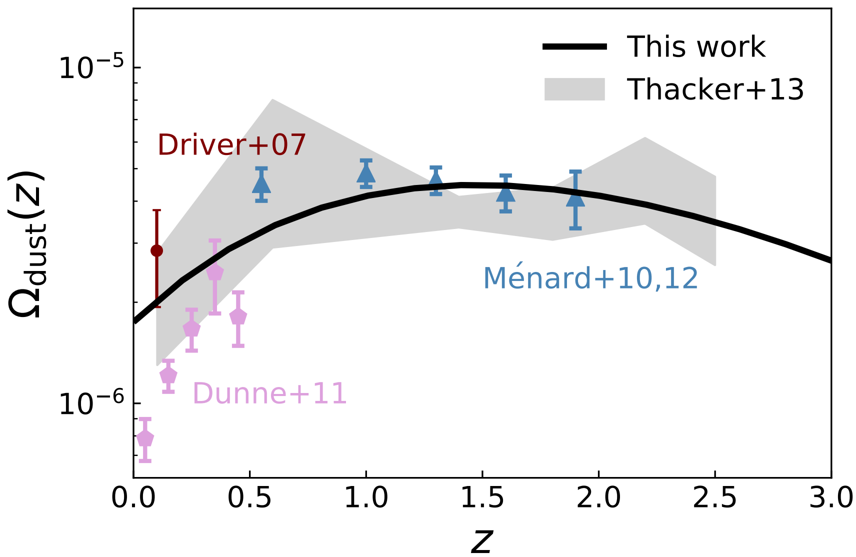

Figure 4.2: The redshift evolution of the dust density parameter Ω_d. Our model prediction is compared with various dust abundance constraints from the literature (Driver et al. 2007; Dunne et al. 2011; Ménard et al. 2010; Ménard & Fukugita 2012; Thacker et al. 2013).

$$L_{\mathrm{IR}}\left(M, z\right) = P_0 M_\mathrm{d}\left(M, z\right)\left[\frac{T_\mathrm{d}(z)}{T_0}\right]^{4+\beta} , \tag{4.12}$$

where the normalization constant P_0 is the power emitted per mass of dust at temperature T_0.

To estimate P_0, we note that Planck Collaboration Int. XVII (2014) found the Galactic H I-correlated dust emission to be well-described by Equation 4.3 with $T_\mathrm{d} \simeq 20\,\mathrm{K}$ and $\beta \simeq 1.6$. Further, they derived an 857 GHz dust emissivity per H of $\epsilon_{857} = 4.3 \times 10^{-21}\,\mathrm{MJy\,sr^{-1}\,cm^2\,H^{-1}}$. Thus,

$$P_0 = 4\pi\epsilon_{857}\frac{M_\mathrm{H}}{M_\mathrm{d}}\frac{1}{m_\mathrm{p}}\int\left(\frac{\nu}{857\,\mathrm{GHz}}\right)^{1.6}\frac{B_\nu\left(20\,\mathrm{K}\right)}{B_{857}\left(20\,\mathrm{K}\right)}\,\mathrm{d}\nu \simeq 110\,L_\odot/M_\odot\,, \tag{4.13}$$

where we have assumed a gas-to-dust mass ratio of 100 (Draine et al. 2007). By using this formalism to estimate the dust mass, we are implicitly assuming that physical properties (e.g., composition) of dust grains do not evolve systematically with redshift or metallicity, only their abundance per H atom.

Because Θ is normalized to unity (see Equation 4.5), the redshift dependence of $L_{\rm IR}$ is determined entirely by $\Phi(z)$, and thus

$$M_{\rm d} \propto \Sigma(M)(1+z)^{s-\alpha(4+\beta)} \,. \tag{4.14}$$

The implied cosmic density of dust, $\Omega_{\rm d}$, as a function of redshift is

$$\Omega_{\rm d}\,(z) = \frac{1}{\rho_{\rm crit,0}} \int {\rm d}M \frac{{\rm d}N}{{\rm d}M} M_{\rm d}(M,z) \,, \tag{4.15}$$

where $\rho_{\rm crit,0}$ denotes the critical density of the universe at the present time. In Figure 4.2, we plot the redshift evolution of the dust density parameter $\Omega_{\rm d}$, which is compared with a compilation of previous dust abundance measurements by Thacker et al. (2013), including constraints from integrating low-z dust mass functions (Dunne et al. 2011), extinction measurements from the Sloan Digital Sky Survey[1] (Ménard et al. 2010; Ménard & Fukugita 2012) and 2dF (Driver et al. 2007), and cosmic far-infrared background anisotropy (Thacker et al. 2013).

4.2.4 Hydrogen Mass

Insofar as gas and dust are well mixed, $\Phi\Sigma$ encodes the total hydrogen mass in the halo. However, the correspondence is not direct since the dust luminosity depends on not only the amount of dust present but also the dust temperature, which is assumed to evolve with redshift (see Equation 4.5). We therefore introduce the modification

$$M_{\rm H}(M,z) = K(z)\Sigma(M)\Phi(z) \,, \tag{4.16}$$

where $K(z) = \zeta(1+z)^{\xi}$ is a normalization factor that sets the total amplitude of $M_{\rm H}$. The amplitude and redshift dependence of K are determined by approximately matching the hydrogen–halo mass relation over $0 < z < 3$ predicted by Popping et al. (2015) as shown in Figure 4.3, while at the same time yielding a gas metallicity of approximately $Z_{\odot}$ at $z = 0$ (discussed in next section). For our fiducial model, we take $\zeta = 0.005$, $\xi = -1$ for $0 < z < 1$ and $\zeta = 0.0025$, $\xi = 0$ otherwise. These values are chosen such that the overall redshift dependence of $M_{\rm H}$ roughly agrees with the product of inferred growth rate of halo mass, which scales as $(1+z)^{1.5}$ at $z \lesssim 1$ and $(1+z)^{2.5}$ at higher redshifts (McBride et al. 2009), and the average star formation efficiency, which may carry an extra factor of $(1+z)^{1-1.5}$ depending

[1]The combined data set from Thacker et al. (2013) is adopted here, which assumes that the halo dust content does not evolve significantly with redshift.

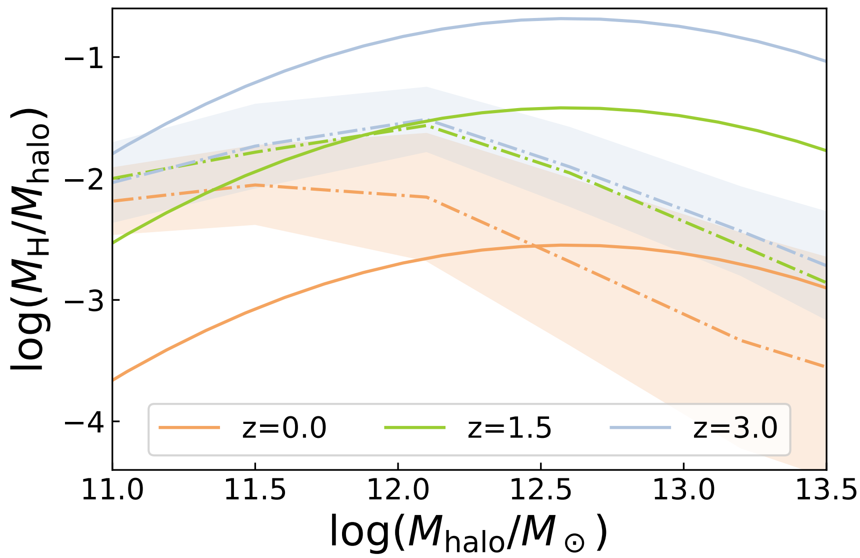

Figure 4.3: Hydrogen–halo mass relation at different redshifts. Hydrogen–halo mass relation predicted by our $K\Sigma(M)\Phi(z)$ parameterization at different redshifts (solid curves), compared with the semi-empirical estimates from Popping et al. (2015) shown by the dash-dotted curves and shaded bands (at $z = 0$ and 3 only, 95% confidence intervals).

on the exact physical mechanisms coupling the stellar feedback (e.g., supernova explosions) to galaxies (Sun & Furlanetto 2016; Furlanetto et al. 2017). Indeed, the gas-to-stellar mass ratio of $M > 10^{11}\ M_\odot$ halos of interest has been found to be only weakly dependent on redshift (Popping et al. 2015). The mass dependence, on the other hand, is motivated since the same physical mechanisms preventing star formation at both ends of halo masses also play a role in regulating the hydrogen mass in a galaxy.

The total mass of hydrogen in our model can be written as

$$M_{\rm H} = M_{\rm H\,I} + M_{\rm H_2} + M_{\rm H\,II}\ . \tag{4.17}$$

If we express the fractions of molecular and ionized hydrogen as $f_{\rm H_2}$ and $f_{\rm H\,II}$ respectively, then the masses of hydrogen in three different phases become

$$M_{\rm H_2}(M,z) = f_{\rm H_2} M_{\rm H}(M,z)\ , \tag{4.18}$$

$$M_{\rm H\,II}(M,z) = f_{\rm H\,II} M_{\rm H}(M,z)\ , \tag{4.19}$$

$$M_{\rm H\,I}(M,z) = (1 - f_{\rm H_2} - f_{\rm H\,II}) M_{\rm H}(M,z)\ . \tag{4.20}$$

As a fiducial value, we set $f_{\rm H_2} = 0.2$, typical for most galaxies up to $z \sim 1$ and the most massive ones up to $z \sim 2$ (see, e.g., Popping et al. 2012). Likewise, we adopt

$f_{\mathrm{H\,II}} = 0.1$, based on the estimated masses of different ISM phases from Tielens (2005). We note that a factor of 1.36 accounting for the helium abundance is needed to connect the total hydrogen mass to the total gas mass, i.e., $M_{\mathrm{gas}} = 1.36M_{\mathrm{H}}$ (Draine et al. 2007).

Using Eq. 4.16 and the fiducial molecular gas fraction $f_{\mathrm{H_2}} = 0.2$, we can also obtain the cosmic evolution of the molecular gas density $\rho_{\mathrm{H_2}}$, whose comparison against the cosmic SFRD (especially the peak of star formation at $z \sim 2$) provides vital information about the fueling and regulation of star formation by cold gas. Constraints on $\rho_{\mathrm{H_2}}$ have so far been placed primarily by observations of the CO rotational transitions. Figure 4.4 shows how $\rho_{\mathrm{H_2}}$ as a function of redshift, computed with our fiducial choice of $f_{\mathrm{H_2}} = 0.2$, compares with constraints derived from various CO LIM experiment and deep galaxy surveys, including COLDz (Riechers et al. 2019), COPSS II (Keating et al. 2016), ASPECS Pilot (Decarli et al. 2016) and ASPECS large program (Decarli et al. 2019). Planned LIM experiments such as COMAP (Li et al. 2016) and TIME (Crites et al. 2014) and next-generation Very Large Array (ngVLA) concepts (Walter et al. 2019) are expected to greatly reduce the substantial uncertainties present in current limits.

4.2.5 Metallicity

If the dust-to-metals ratio is assumed to be constant, the metallicity Z of interstellar gas in our model can be expressed as a function of the dust mass as

$$\frac{Z}{Z_{\odot}}(z) \sim 100\frac{M_{\mathrm{d}}(M,z)}{M_{\mathrm{H}}(M,z)}\ . \tag{4.21}$$

Recent hydrodynamic galaxy formation simulations have indeed found little variation in the dust-to-metals ratio with redshift or metallicity above $0.5Z_{\odot}$ (Li et al. 2019).

Our simple model of the gas-phase metallicity gives no halo mass dependence, which is likely an oversimplification given that effects like galactic winds regulating the metallicity of galaxies may evolve with halo mass in a non-trivial way. Nevertheless, as shown in Figure 4.5, our predicted redshift evolution of metallicity is broadly consistent with that estimated semi-analytically by Fu et al. (2013), using the Millennium-II Simulation (Boylan-Kolchin et al. 2009) combined with an H_2 prescription specified by the gas surface density, metallicity, and a constant clumping factor (Krumholz et al. 2009; McKee & Krumholz 2010). We note that Z only evolves moderately for $M > 10^{11.5}\,M_{\odot}$, a halo mass range that our CIB model is

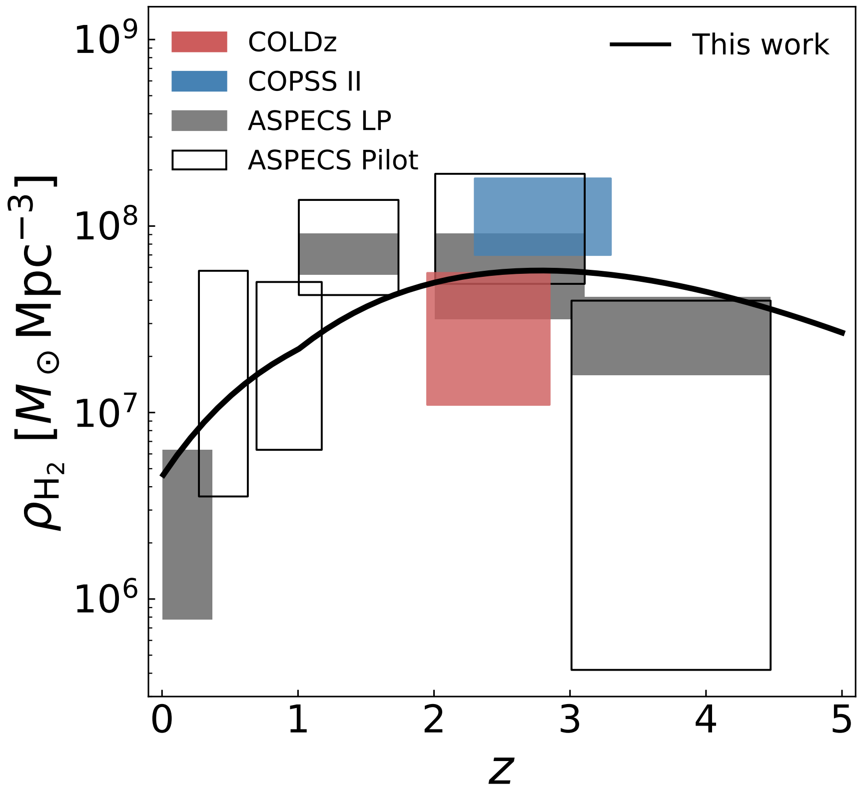

Figure 4.4: Cosmic evolution of the molecular gas density ρ_{H_2}. The prediction of our reference model with $f_{H_2} = 0.2$ is compared with observational constraints from COLDz (Riechers et al. 2019), COPSS II (Keating et al. 2016), ASPECS Pilot (Decarli et al. 2016) and ASPECS large program (Decarli et al. 2019).

calibrated and most sensitive to. Therefore, in the context of the CIB model a mass-independent gas metallicity is likely a fair approximation. Figure 4.5 also shows the cosmic metallicity evolution inferred from gamma-ray burst (GRB) observations for comparison. By analogy to damped Lyα (DLA) systems of quasars, Savaglio (2006) uses strong absorption lines due to the intervening neutral gas to estimate the metallicity evolution of GRB-DLA systems and compare it with the average metallicity derived for a sample of GRB hosts at $z < 1$.

4.3 Models of Emission Lines

Based on the mass and redshift dependencies of a wide range of halo properties derived in Section 4.2, we construct a model of the emission lines that trace star formation and the ISM in galaxies. In this section, we present our line emission models of the H I 21 cm line, [C II] 158 μm line, the 122 and 205 μm [N II] lines, and the CO(1–0) 2.6 mm line. Each of these lines probes a somewhat different

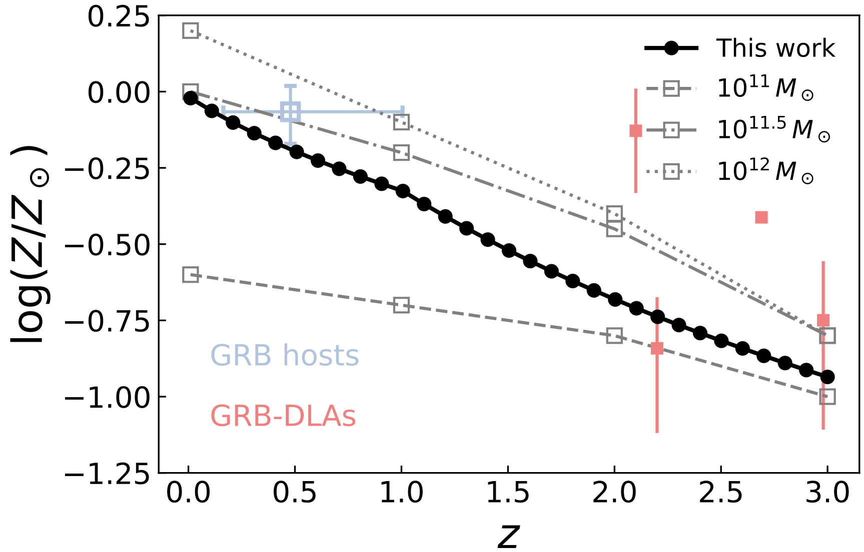

Figure 4.5: The redshift evolution of the metallicity Z. The Z evolution derived from our model is compared with semi-analytic estimates of gas-phase Z from Fu et al. (2013), evaluated at different halo masses ranging from 10^{11} to $10^{12}\,M_{\odot}$. Also shown are inferred metallicities of the warm ISM of $z < 1$ GRB host galaxies and the neutral ISM of GRB-DLAs from Savaglio (2006).

phase of the ISM, ranging from the coldest molecular gas to the warm ionized medium (WIM). As such, their joint analysis can reveal rich information about the multi-phase ISM, as will be illustrated in the following sections.

Figure 4.6 illustrates how our modeling framework connects the emission from each of these lines to the phases of the ISM. Young stars formed in dense regions of a giant molecular cloud (GMC) are surrounded by H ii regions ionized by UV radiation, whose physical conditions may be probed by FIR [N ii] and [C ii] lines. Photodissociation regions (PDRs) occupy the interface of H ii regions and cold molecular gas traced by CO lines and produce the majority of [C ii] emission, which is the main cooling mechanism balancing the photoelectric heating by dust grains. Together molecular gas clouds compose roughly half of the total ISM mass, whereas warm/cold atomic gas contributing most of the H i mass is responsible for the remaining half.

4.3.1 H i 21cm Line

The hyperfine structure H i 21 cm line serves as a direct probe of the atomic hydrogen content of galaxies, so its abundance and clustering properties can be straightfor-

Table 4.2: Physical Parameters of the Reference ISM Model.

Signal	Parameter	Symbol	Value
–	Molecular gas fraction*	$f_{\mathrm{H_2}}$	0.2
–	Ionized gas fraction*	$f_{\mathrm{H\,II}}$	0.1
CO	L–M conversion*	α_{CO}	$\frac{4.4\,M_\odot}{\mathrm{K\,km\,s^{-1}\,pc^2}}$
	Excitation temperature	T_{exc}	10 K
	H_2 number density	$n_{\mathrm{H_2}}$	$2\times10^3\,\mathrm{cm^{-3}}$
[C II]	PE efficiency*	ϵ_{PE}	5×10^{-3}
[N II]	Gas temperature*	$T_{\mathrm{gas,H\,II}}$	10^4 K
	Electron number density*	$n_{e,\mathrm{H\,II}}$	$10^2\,\mathrm{cm^{-3}}$

* Varied as free parameters in the case studies presented in Section 4.6.

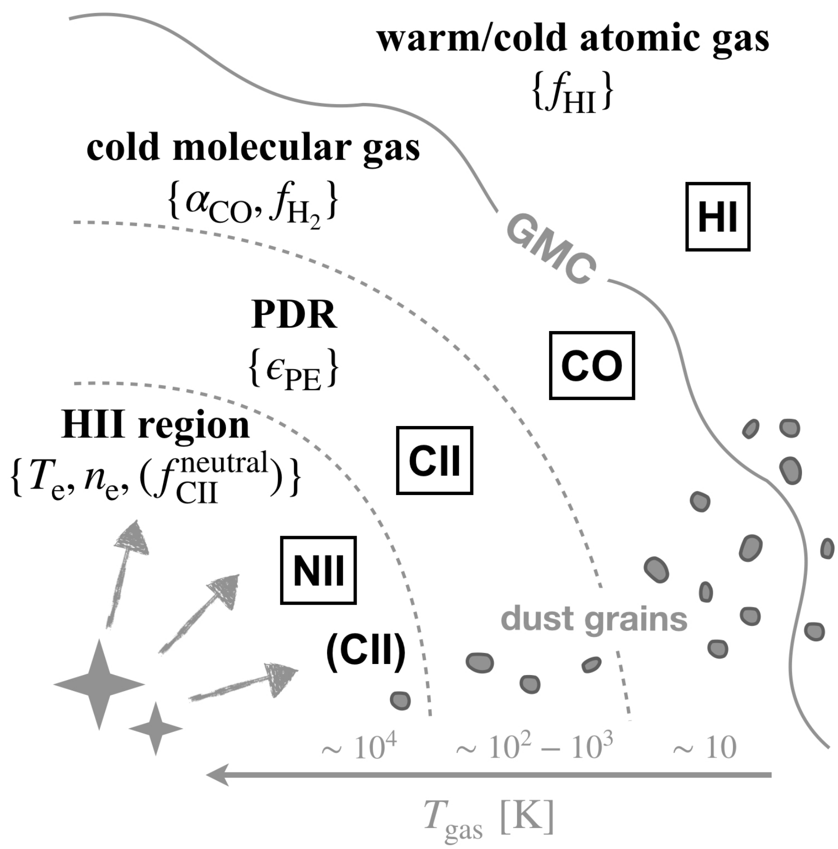

Figure 4.6: Cartoon illustration of lines and associated parameters from the ISM.

wardly modeled with the H I–halo mass relation derived. The H I mass is related to the mean brightness temperature, the relevant observable for H I maps, via (e.g., Bull et al. 2015; Wolz et al. 2017a)

$$\bar{T}_{\mathrm{H\,I}} = C_{\mathrm{H\,I}}\bar{\rho}_{\mathrm{H\,I}}(z) = \frac{3hc^3A_{21}}{32\pi k_{\mathrm{B}} m_{\mathrm{p}} \nu_{21}^2}\frac{(1+z)^2}{H(z)}\bar{\rho}_{\mathrm{H\,I}}(z) \,, \tag{4.22}$$

where $C_{\mathrm{H\,I}}$ is the conversion factor from the mean H I density to the mean brightness temperature and $A_{21} = 2.88 \times 10^{-15}\,\mathrm{s}^{-1}$ is the Einstein coefficient corresponding to the 21 cm line. The mean H I mass density is expressed as (Padmanabhan et al. 2017)

$$\bar{\rho}_{\mathrm{H\,I}}(z) = \int \mathrm{d}M \frac{\mathrm{d}N}{\mathrm{d}M} M_{\mathrm{H\,I}}(M, z) \,. \tag{4.23}$$

4.3.2 [CII] 158 μm Line

The 158 μm [C II] line is one of the most important metal cooling lines in the interstellar medium and can alone account for $\sim 0.1\%$ of the total FIR emission of a galaxy (Stacey et al. 1991; Malhotra et al. 1997). Empirically, the emission in the [C II] line correlates with both FIR dust emission (Crawford et al. 1985; Wright et al. 1991) and star formation (Stacey et al. 1991; De Looze et al. 2014).

The strong correlation between the [C II] and IR luminosity can be understood with a model in which the cooling of interstellar gas is dominated by [C II] emission and the heating is dominated by photoelectric emission from dust grains. If the dust converts a fraction $\epsilon_{\mathrm{PE}} \ll 1$ of UV and optical radiation absorbed into photoelectric heating and the remainder into infrared emission, then the total heating rate is proportional to $\epsilon_{\mathrm{PE}} L_{\mathrm{IR}}$. We can therefore approximate

$$L_{[\mathrm{C\,II}]} = \left(1 - f_{\mathrm{H_2}}\right) \epsilon_{\mathrm{PE}} L_{\mathrm{IR}} \,, \tag{4.24}$$

where the factor $\left(1 - f_{\mathrm{H_2}}\right)$ accounts for the fact that dust is present and will radiate in molecular clouds where there is little atomic C. ϵ_{PE} is taken to be a free parameter in the model with a fiducial value of 5×10^{-3}, which yields an $L_{[\mathrm{C\,II}]}/L_{\mathrm{IR}}$ ratio consistent with that estimated from observations of the LMC (e.g., Rubin et al. 2009) and nearby galaxies (e.g., De Looze et al. 2014). We note that the observed proportionality between SFR and $L_{[\mathrm{C\,II}]}$ is reproduced here since SFR is correlated with L_{IR} (Equation 4.10).

A number of simplifications are inherent in this prescription. For instance, other cooling lines (e.g., [O I]) can be important relative to [C II] (Tielens & Hollenbach 1985; Young Owl et al. 2002). Second, the photoelectric efficiency of dust grains is a function of the grain charge. As gas density and radiation intensity increase, ϵ_{PE}

is expected to decrease (Bakes & Tielens 1994), and so we might expect systematic changes in the $L_{\rm IR}$–$L_{\rm [C\,II]}$ relation with galaxy properties just from this effect. Finally, unlike the dust emission, the [C II] line can saturate at high gas temperatures and radiation intensities, breaking the linear correlation (Muñoz & Oh 2016; Rybak et al. 2019). These effects are most pronounced in gas of extreme density and temperature and may account for the breakdown of the $L_{\rm IR}$–$L_{\rm [C\,II]}$ correlation in luminous and ultraluminous galaxies. We do not incorporate these effects into our model at this time, but we discuss potential implementation in Section 4.7.

4.3.3 [N II] 122 and 205μm Lines

The emission from singly ionized nitrogen, which has an ionization potential of 14.53 eV, traces H II regions (see Figure 4.6). When the density is lower than the critical density, collisional de-excitation can be neglected and the luminosity of the [N II] 122 and 205 μm lines can be approximated by the balance between the rates of collisional excitation and radiative de-excitation. For an ionized gas cloud of volume V,

$$L_{\rm [N\,II]} \simeq n_{e,{\rm H\,II}} n_{\rm N^+} q_\nu h\nu_{\rm [N\,II]} V \,, \tag{4.25}$$

where q_ν denotes the collisional excitation coefficient, with $q_{122} = 2.57{\times}10^{-8}\,{\rm cm^3\,s^{-1}}$ and $q_{205} = 6.79 \times 10^{-8}\,{\rm cm^3\,s^{-1}}$ (e.g., Herrera-Camus et al. 2016). Meanwhile, the ionization equilibrium of H II regions gives

$$Q_0 = n_{e,{\rm H\,II}} n_{\rm H^+} \alpha_{\rm B} \left(T_{\rm gas,H\,II}\right) V \,, \tag{4.26}$$

where Q_0 is the rate of hydrogen photoionization sourced by UV photons from O and B stars and $\alpha_{\rm B} = 2.6 \times 10^{-13} \left(T_{\rm gas,H\,II}/10^4\,{\rm K}\right)^{-0.76} {\rm cm^3\,s^{-1}}$ is the case B recombination coefficient, a reasonable assumption for typical H II regions where the mean free path of ionizing photons is small. For Population II stars with a Salpeter IMF, each stellar baryon produces $N_{\rm ion} \simeq 4000$ ionizing photons on average (Loeb & Furlanetto 2013), in which case Q_0 can be related to the star formation rate by

$$Q_0(M,z) = \frac{N_{\rm ion}\dot{M}_\star}{m_{\rm p}/(1-Y)} \simeq 1.14 \times 10^{53} \left[\frac{\dot{M}_\star(M,z)}{M_\odot/{\rm yr}}\right] {\rm s^{-1}} \,, \tag{4.27}$$

where we take the helium mass fraction to be $Y = 0.25$. The ionization rate can then be related to the luminosity of [N II] lines by

$$L_{\rm [N\,II]} \simeq \frac{q_\nu h\nu_{\rm [N\,II]}}{\alpha_{\rm B}\left(T_{\rm gas,H\,II}\right)} \frac{n_{\rm N^+}}{n_{\rm H^+}} \frac{N_{\rm ion}\dot{M}_\star}{m_{\rm p}/(1-Y)} \tag{4.28}$$

which gives

$$L^{\rm tot}_{\rm [N\,II]} = 9\times10^6 L_\odot \left(\frac{T_{\rm gas,H\,II}}{10^4\,{\rm K}}\right)^{0.76} \times \frac{\dot{M}_\star}{M_\odot/{\rm yr}} \times \frac{Z}{Z_\odot}\,, \tag{4.29}$$

where $n_{\rm N^+}/n_{\rm H^+}$, under the assumption that the second ionization of nitrogen ($\rm N^+ \rightarrow N^{++}$) with a potential of 29.6 eV is negligible, can be approximated by the N/H ratio $\rm N/H = (N/H)_\odot \times [Z(z)/Z_\odot] \simeq 7.4\times10^{-5}\,[Z(z)/Z_\odot]$ (Asplund et al. 2009).

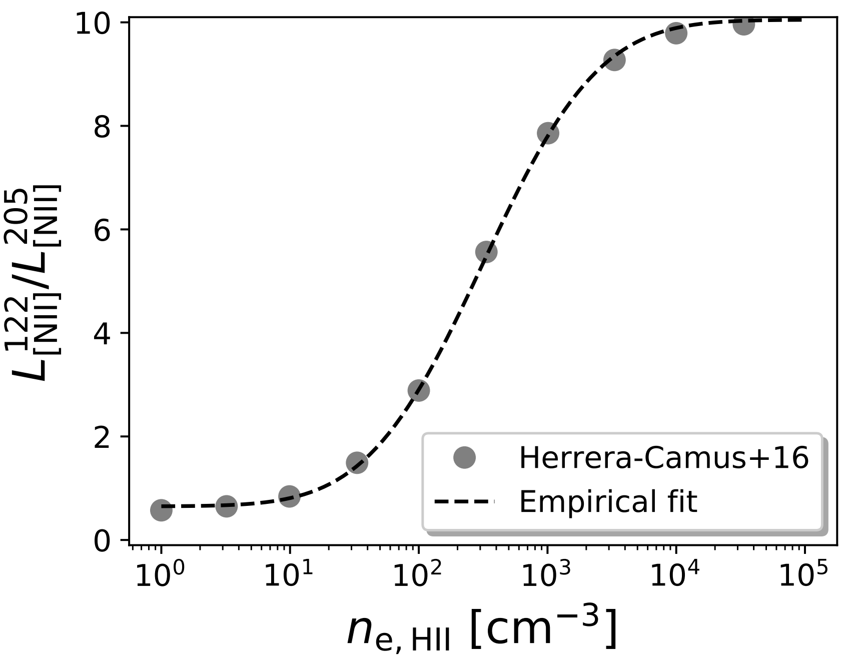

Figure 4.7: Line ratio of [N II] lines as a function of electron number density. The dashed line shows our model parameterization given by Equation 4.30.

In order to model the impact of electron number density $n_{e,\rm H\,II}$ on the strength of [N II] line emissions, we exploit a simple parameterization of the [N II] 122 μm/205 μm line ratio as a function of $n_{e,\rm H\,II}$

$$R'_{\rm [N\,II]} = R_{\rm [N\,II]} + A_R \times \left\{1 + {\rm erf}\left[\frac{\log(n_{e,\rm H\,II}/n^0_{e,\rm H\,II})}{\sigma_R}\right]\right\}\,, \tag{4.30}$$

where $R_{\rm [N\,II]} = L^{122}_{\rm [N\,II]}/L^{205}_{\rm [N\,II]} \sim 0.65$ is the line ratio in the low-density limit discussed above. We further take the normalization factor A_R to be 4.7, the characteristic density $n^0_{e,\rm H\,II}$ to be $10^{2.5}$ cm^{-3} and the transition width σ_R to be 1, in order to obtain a good fit to the results from Herrera-Camus et al. (2016) over

$1\,\mathrm{cm}^{-3} \lesssim n_{e,\mathrm{H\,II}} \lesssim 10^5\,\mathrm{cm}^{-3}$, as illustrated in Figure 4.7. Meanwhile, there is also a non-trivial evolution of the total [N II] luminosity with the electron number density (or effectively $R'_{[\mathrm{N\,II}]}$) owing to the increasingly important collisional de-excitation at higher densities, whose effect can be approximated by

$$L'^{\mathrm{tot}}_{[\mathrm{N\,II}]} \simeq L^{\mathrm{tot}}_{[\mathrm{N\,II}]}\left(T_{\mathrm{gas,H\,II}}\right) \times 10^{0.12\left[R_{[\mathrm{N\,II}]}-R'_{[\mathrm{N\,II}]}(n_{e,\mathrm{H\,II}})\right]} . \tag{4.31}$$

The resulting [N II] line luminosities depend on both the temperature and the density of H II regions:

$$L'^{205}_{[\mathrm{N\,II}]} = \frac{1}{1+R'_{[\mathrm{N\,II}]}(n_{e,\mathrm{H\,II}})} \times L'^{\mathrm{tot}}_{[\mathrm{N\,II}]}\left(T_{\mathrm{gas,H\,II}}, n_{e,\mathrm{H\,II}}\right) , \tag{4.32}$$

and

$$L'^{122}_{[\mathrm{N\,II}]} = \frac{R'_{[\mathrm{N\,II}]}(n_{e,\mathrm{H\,II}})}{1+R'_{[\mathrm{N\,II}]}(n_{e,\mathrm{H\,II}})} \times L'^{\mathrm{tot}}_{[\mathrm{N\,II}]}\left(T_{\mathrm{gas,H\,II}}, n_{e,\mathrm{H\,II}}\right) . \tag{4.33}$$

In our model of [N II] emission, we set the gas temperature to be $T_{\mathrm{gas,H\,II}} \simeq 10^4\,\mathrm{K}$, which is a characteristic temperature of H II regions where ionized nitrogen is expected to be found (e.g., Goldsmith et al. 2015; Herrera-Camus et al. 2016). Meanwhile, it is important to note that, alternatively to the empirical prescription presented, the dependence of [N II] line ratio on $n_{e,\mathrm{H\,II}}$ may also be derived ab initio from the transition rates of collisionally coupled states of [N II] (see, e.g., Goldsmith et al. 2015).

4.3.4 CO(1–0) Line

The CO(1–0) rotational transition ($\lambda = 2.6\,\mathrm{mm}$) is a powerful tracer of the molecular gas content of both individual molecular clouds and of galaxies (e.g., Solomon et al. 1987; Dame et al. 2001; Ivison et al. 2011; Saintonge et al. 2011). In molecular clouds, the CO(1–0) line is generally optically thick, and so the line luminosity L_{CO} is independent of the CO abundance. For a virialized molecular cloud, it can be shown that L_{CO} is proportional to the cloud mass (e.g., Draine 2011; Bolatto et al. 2013), with the constant of proportionality designated α_{CO}. Even in this idealized case of a homogeneous cloud, α_{CO} depends on the precise conditions within the cloud. Draine (2011) derives the dependence of α_{CO} on the excitation temperature T_{exc} and molecular gas density $n_{\mathrm{H_2}}$ as

$$\alpha_{\mathrm{CO}} = 4.2\left(\frac{n_{\mathrm{H_2}}}{10^3\,\mathrm{cm}^{-3}}\right)^{1/2}\left(e^{5.5\,\mathrm{K}/T_{\mathrm{exc}}}-1\right)\frac{M_\odot}{\mathrm{K\,km\,s^{-1}\,pc^2}} , \tag{4.34}$$

where we have adopted a factor of 1.36 to convert from hydrogen mass to total gas mass, which accounts for the abundance of He (Bolatto et al. 2013). We note that for a density $n_{\mathrm{H}_2} = 2 \times 10^3\,\mathrm{cm}^{-3}$, typical of GMCs, $T_{\mathrm{exc}} = 10\,\mathrm{K}$ implies a CO-to-H_2 conversion factor of $\alpha_{\mathrm{CO}} \approx 4.4\,M_{\odot}(\mathrm{K\,km\,s^{-1}\,pc^2})^{-1}$, consistent with the value inferred from observations (Bolatto et al. 2013).

A population of virialized molecular clouds will likewise have a linear relationship between the total molecular gas mass and the integrated CO(1–0) line luminosity provided that the covering factor is low enough just that the CO emission from one cloud is unlikely to be absorbed by another cloud (Dickman et al. 1986; Bolatto et al. 2013).

Under these assumptions, we can write the CO luminosity directly in terms of the molecular gas mass $M_{\mathrm{H}_2} \equiv f_{\mathrm{H}_2} M_{\mathrm{H}}$ as

$$L_{\mathrm{CO}}\,(M, z) = \alpha_{\mathrm{CO}}^{-1} f_{\mathrm{H}_2} M_{\mathrm{H}}\,(M, z)\ . \tag{4.35}$$

We treat α_{CO} as a parameter to be fit. While there are indications that α_{CO} may vary systematically with other galaxy properties, e.g., metallicity (Genzel et al. 2012; Bolatto et al. 2013; Sandstrom et al. 2013), we do not consider such variations here.

4.4 Intensity Mapping Framework

4.4.1 Modeling the Fluctuation Signals

In this section, we introduce a simple, generic halo occupation distribution (HOD) model, which is used to compute the power spectra that describe the spatial fluctuations of various signals emitted from discrete galaxies. Incorporating the correlation of subhalo structure (e.g., satellite galaxies) via such an HOD model is non-trivial, since both observational and theoretical studies have shown that massive dark matter halos tend to host more than one galaxy at low redshifts (e.g., Gao et al. 2011; McCracken et al. 2015), with a peak in subhalo abundance for a given halo mass at $z \sim 2 - 3$ as found by Wetzel et al. (2009). The original HOD model describes the occupation of halos by central and satellite galaxies (Kravtsov et al. 2004). Here, we generalize it to describe the fluctuations in line signals associated with the clustering of both central and satellite galaxies by weighting the galaxy number counts by a measure of the signal strength S_ν at observed frequency ν for a given halo mass and redshift, which means slightly differently for different signals (see later text). In particular, we define the number-count-weighted signal strengths of central and satellite galaxies,

$$f_\nu^{\mathrm{cen}}(M, z) = N_{\mathrm{cen}} S_\nu(M, z)\ , \tag{4.36}$$

and

$$f_\nu^{\rm sat}(M,z) = \int_{M_{\rm min}}^{M} {\rm d}m \frac{{\rm d}n}{{\rm d}m}(m,z|M) S_\nu(m,z) \ , \tag{4.37}$$

where $N_{\rm cen}$ is the number of central galaxies in a halo, which is equal to 1 for $M > M_{\rm min} = 10^{10}\, M_\odot$ and 0 otherwise (Wu & Doré 2017b), and ${\rm d}n/{\rm d}m$ represents the subhalo mass function, for which we adopt the fitting function in Tinker & Wetzel (2010). We consequently define the mean radiation strength as

$$\bar{j}_\nu(z) = \int_{M_{\rm min}}^{M_{\rm max}} {\rm d}M \frac{{\rm d}N}{{\rm d}M} \left[f_\nu^{\rm cen}(M,z) + f_\nu^{\rm sat}(M,z) \right] \ . \tag{4.38}$$

We note that in our expression, for different signals, $\bar{j}_\nu$ represents slightly different physical quantities and thus carries different units by convention. Specifically, $\bar{j}_\nu$ denotes the mean *volume emissivity*, *intensity*, and *brightness temperature* for the CIB,[2] [C II]/[N II]/CO lines and H I 21cm line, respectively. For the signals under consideration, we have

$$S_\nu(M,z) = \frac{L_{(1+z)\nu}\,(M,z)}{4\pi} \quad \text{(CIB)} \ , \tag{4.39}$$

$$S_\nu(M,z) = \frac{L_{\rm line}(M,z)}{4\pi D_L^2} y(z) D_A^2 \quad \text{([C II], [N II] and CO)} \ , \tag{4.40}$$

$$S_\nu(M,z) = C_{\rm H\,I} M_{\rm HI}(M,z) \quad \text{(H I)} \ , \tag{4.41}$$

where the units of signal strengths are ${\rm erg\,s^{-1}\,Hz^{-1}\,sr^{-1}}$, ${\rm cm\,erg\,s^{-1}\,Hz^{-1}\,sr^{-1}}$, and ${\rm mK\,cm^3}$, respectively. The mapping from frequency to line-of-sight distance is given by $y(z) = {\rm d}\chi/{\rm d}\nu = c(1+z)/[\nu H(z)]$, where χ denotes the comoving radial distance.

Generally, the power spectrum of a pair of signals at frequencies ν and ν' (auto-correlation if $\nu = \nu'$ and cross-correlation otherwise) can be expressed as the sum of one-halo, two-halo, and shot-noise components, namely

$$P_{\nu\nu'}(k,z) = P_{{\rm 1h},\nu\nu'}(k,z) + P_{{\rm 2h},\nu\nu'}(k,z) + P_{{\rm SN},\nu\nu'}(k,z) \ . \tag{4.42}$$

The one-halo term characterizes the contribution to the fluctuations from emitters residing in the same halo. Assuming that the occupation statistics of central and

[2] This shows how the HOD formalism is originally defined in the CIB anisotropy model, provided here for completeness and better illustrating our generalization.

satellite galaxies are independent and that the latter is Poissonian, we have

$$P_{1\mathrm{h},\nu\nu'}(k,z) = \int_{M_{\min}}^{M_{\max}} \mathrm{d}M \frac{\mathrm{d}N}{\mathrm{d}M} \times \Big[f_{\nu}^{\mathrm{cen}}(M,z) f_{\nu'}^{\mathrm{sat}}(M,z) u(k|M,z) + f_{\nu'}^{\mathrm{cen}}(M,z) f_{\nu}^{\mathrm{sat}}(M,z) u(k|M,z) + f_{\nu}^{\mathrm{sat}}(M,z) f_{\nu'}^{\mathrm{sat}}(M,z) u^2(k|M,z) \Big] , \tag{4.43}$$

where $u(k|M,z)$ is the normalized Fourier transform of the halo density profile (Navarro et al. 1997; Bhattacharya et al. 2013). The two-halo component describes the contribution from emitters residing in different halos,

$$P_{2\mathrm{h},\nu\nu'}(k,z) = D_{\nu}(k,z) D_{\nu'}(k,z) P_{\delta\delta}(k,z) , \tag{4.44}$$

where $P_{\delta\delta}(k,z)$ is the dark matter power spectrum and

$$D_{\nu}(k,z) = \int_{M_{\min}}^{M_{\max}} \mathrm{d}M \frac{\mathrm{d}N}{\mathrm{d}M} b(M,z) u(k|M,z) \times \left[f_{\nu}^{\mathrm{cen}}(M,z) + f_{\nu}^{\mathrm{sat}}(M,z) \right] , \tag{4.45}$$

with $b(M,z)$ being the halo bias factor (Tinker et al. 2008). Finally, the shot-noise component describes the self-correlation of emitters due to their discrete nature,

$$P_{\mathrm{SN},\nu\nu'}(z) = \int_{M_{\min}}^{M_{\max}} \mathrm{d}M \frac{\mathrm{d}N}{\mathrm{d}M} f_{\nu}^{\mathrm{cen}}(M,z) f_{\nu'}^{\mathrm{cen}}(M,z) , \tag{4.46}$$

which can be considered as the $k \to 0$ limit of the one-halo term in the absence of satellite galaxies (see, e.g., Wolz et al. 2017a).

Finally, following Sun et al. (2018), in order to take into account of the stochasticity of individual galaxies, we introduce a simple parameterization of a log-normal distribution of line brightness below for a given halo mass and redshift. The probability density can be expressed as

$$P\left(x|\mu_{\nu},\sigma_{\nu}\right) = \frac{1}{\sqrt{2\pi}\sigma_{\nu}} \exp\left[-\frac{(x-\mu_{\nu})^2}{2\sigma_{\nu}^2} \right] , \tag{4.47}$$

where $\mu_{\nu} = \log[S_{\nu}(M,z)]$ is the aforementioned mean line strength and $\sigma_{\nu} = 0.3$ dex is our fiducial level of scatter reflecting the typical galaxy-to-galaxy variation in line production. It is straightforward to show that the power spectrum averaged over the log-normal distribution is essentially a scaling of the power spectrum without scatter, specified by the additive correction factors in the following relations:

$$\langle \mu_{\nu} \rangle = \mu_{\nu} + \frac{\sigma_{\nu}^2}{2} \ln 10 , \tag{4.48}$$

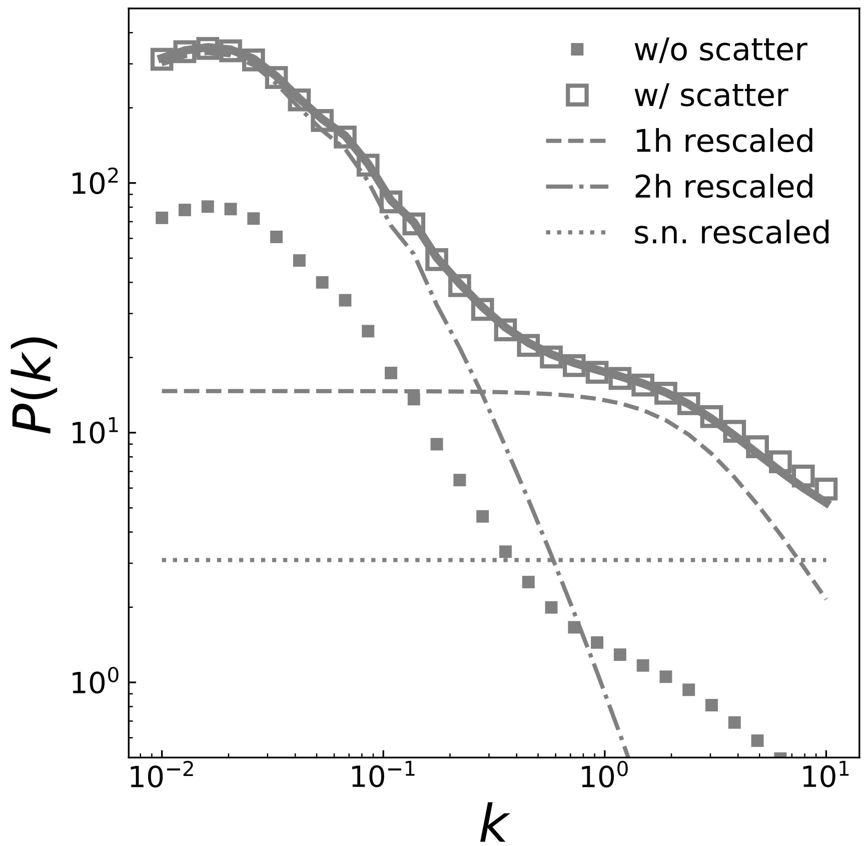

Figure 4.8: The effect of scatter on the power spectrum. The two-halo (dash-dotted curve) term is rescaled by the correction factor defined by Eq. 4.48, whereas the one-halo (dashed curve) and shot-noise (dotted curve) terms are rescaled by the correction factor defined by Eq. 4.49. The total power spectrum (solid curve) rescaled from the one without scatter (filled squares) matches well with that derived from averaging over 1000 random realizations (open squares).

which applies to the two-halo term of power spectrum scaling as the square of the first luminosity moments, and

$$\langle 2\mu_\nu \rangle = 2\mu_\nu + 2\sigma_\nu^2 \ln 10 \,, \tag{4.49}$$

which applies to the one-halo and shot-noise terms of power spectrum scaling as the second luminosity moment. Figure 4.8 shows how the power spectrum is affected by the above correction factors in the presence of a non-trivial scatter σ_ν. For comparison, the open squares indicate the average of power spectra directly drawn from 1000 random realizations of the log-normally distributed $S_\nu(M, z)$ relation, which agrees well with the one analytically derived using $\langle \mu_\nu \rangle$ and $\langle 2\mu_\nu \rangle$ as shown by the solid curve (a sum of rescaled one-halo, two-halo, and shot-noise components). In our power spectrum analysis, we include these correction factors to obtain constraints on the log-normal scatter together with physical properties of the ISM. We further assume, for simplicity, that similar physical processes (e.g., regulations of galaxy evolution by star formation, outflows and interactions, variations of stellar population and ISM properties) give rise to the stochasticity for a given halo mass and redshift, and therefore line luminosities considered in this work all share the same log-normal scatter σ.

4.4.2 Sensitivity Analyses

In this section, we describe the formalism to forecast the sensitivity to the power spectrum signal, assuming a given experimental setup. For a three-dimensional survey of volume $V_{\mathrm{s}} = L_x L_y L_z$, the observed 3D power spectrum $\mathcal{P}(K)$ for a given mode K in the Fourier space of the observing frame is related to the true, spherically-averaged power spectrum $\Delta^2(k) = k^3 P(k)/2\pi^2$ by

$$\mathcal{P}(K) = V_{\mathrm{s}} \int_{-\infty}^{\infty} \mathrm{d}\ln k \Delta^2(k) W(k, K) \,, \tag{4.50}$$

where $W(k, K)$ is a convolution kernel commonly referred to as the "window function," which is determined by the survey geometry. Here we only consider the simple situation that the survey volume is large enough such that $W(k, K)$ can be well-approximated by a function sharply peaking at $k \sim K$, which yields $\mathcal{P}(K) \approx P(k)$. Following S16, we write the uncertainty of the power spectrum $P(k)$ as the sum of a sample variance (i.e., cosmic variance) term and a thermal noise term. In particular, for the auto power spectrum $P_{\nu\nu}(k)$, we have

$$\delta P_{\nu\nu}(k) = \frac{P_{\nu\nu}(k) + P^{\mathrm{noise}}_{\nu\nu}(k)}{G(k)\sqrt{N_{\mathrm{modes}}(k)}} \,, \tag{4.51}$$

where $G(k)$ denotes a smoothing factor due to finite spatial and spectral resolutions, which attenuates the power spectrum at large k values beyond resolvable scales and is defined as (Li et al. 2016)

$$G(k) = e^{-k^2\sigma_\perp^2} \int_0^1 e^{-k^2(\sigma_\parallel^2 - \sigma_\perp^2)\mu^2} \mathrm{d}\mu \,, \tag{4.52}$$

where $\mu = \cos\theta$ is the cosine of the angle a given k vector makes with respect to the line of sight. For any given frequency channel width δ_ν, the spatial and spectral resolutions in physical units are given by $\sigma_\parallel(z) = k^{-1}_{\parallel,\mathrm{max}}(z) = y(z)\delta_\nu$ and $\sigma_\perp(z) = k^{-1}_{\perp,\mathrm{max}}(z) = \chi(z)\sqrt{\Omega_{\mathrm{beam}}}$, respectively. For the cross power spectrum

Table 4.3: Reference Instrumental Parameters for Case Studies

Parameter Units	t_{obs} [hr]	D_{ap} [m]	Ω_{survey} [deg^2]	N_{feeds}	$\{\nu_{\mathrm{min}}, \nu_{\mathrm{max}}\}$ [GHz]	Δz	δ_ν [GHz]	V_{vox} [Mpc^3]	NEFD (T_{sys}) [mJy s$^{1/2}$] ([K])	SNR$_{\mathrm{tot}}$
Case I: $P_{\mathrm{H\,I}}$ and P_{CO} at $z = 2$										
H I	2000	1000	1	100	{0.44, 0.52}	±0.25	0.003	22.8	(50)	7.6
CO	500	10	1	100	{35, 42}	±0.25	0.05	7.11	(40)	7.7
Case II: $P_{\mathrm{C\,II}}$, $P_{\mathrm{H\,I}}$, P_{CO}, $P_{\mathrm{C\,II,H\,I}}$ $P_{\mathrm{H\,I,CO}}$, and $P_{\mathrm{C\,II,CO}}$ at $z = 2$										
H I	2000	1000	1	100	{0.44, 0.52}	±0.25	0.003	22.8	(50)	7.6, H I×[C II]: 5.0
[C II]	1000	12	1	100	{585, 691}	±0.25	2	0.04	50	8.0, H I×[C II]: 6.6
CO	500	10	1	100	{35, 42}	±0.25	0.05	7.11	(40)	7.7, H I×CO: 5.1
Case III: $P^{\mathrm{N\,II}}_{122}$, $P^{\mathrm{N\,II}}_{205}$ and $P^{\mathrm{N\,II}}_{122\times205}$ at $z = 2$										
[N II] 122	2000	10	1	400	{757, 894}	±0.25	1	0.02	10	5.2
[N II] 205	2000	10	1	400	{450, 531}	±0.25	1	0.07	10	4.7, cross: 6.7
Case IV: $P_{\mathrm{C\,II}}$ and $P^{\mathrm{N\,II}}_{205}$ at $z = 2$										
[C II]	1000	12	1	100	{585, 691}	±0.25	2	0.04	50	8.0
[N II] 205	2000	10	1	400	{450, 531}	±0.25	1	0.07	10	4.7

$P_{\nu\nu'}(k)$, we have

$$\delta P_{\nu\nu'}(k) = \frac{\left[P^2_{\nu\nu'}(k) + \delta P_\nu(k)\delta P_{\nu'}(k)\right]^{1/2}}{G(k)\sqrt{2N_{\mathrm{modes}}(k)}} , \tag{4.53}$$

where

$$\delta P_\nu(k) = P_{\nu\nu}(k) + P^{\mathrm{noise}}_{\nu\nu}(k) . \tag{4.54}$$

The (averaged) power spectrum of thermal noise is scale-independent and can be expressed as

$$P^{\mathrm{noise}}_{\nu\nu} = \sigma^2_{\mathrm{noise}} V_{\mathrm{vox}} . \tag{4.55}$$

Using the radiometer equation, we can compute the on-sky sensitivity from the noise equivalent flux density (NEFD) or system temperature T_{sys}, the beam size

$$\Omega_{\mathrm{beam}} = \left(\frac{\theta_{\mathrm{FWHM}}}{2.355}\right)^2 = \left(\frac{1.15\lambda_{\mathrm{obs}}/D_{\mathrm{ap}}}{2.355}\right)^2 , \tag{4.56}$$

and the observing time per voxel

$$t_{\mathrm{obs}} = \left(N_{\mathrm{feeds}}\Omega_{\mathrm{beam}}/\Omega_{\mathrm{survey}}\right) t_{\mathrm{survey}} \tag{4.57}$$

as

$$\sigma_{\mathrm{noise}} = \frac{\mathrm{NEFD}}{\Omega_{\mathrm{beam}}\sqrt{t_{\mathrm{obs}}}} = \frac{T_{\mathrm{sys}}}{\sqrt{\delta_\nu t_{\mathrm{obs}}}} , \tag{4.58}$$

where D_{ap} and N_{feeds} represent the instrument's effective aperture size and number of feeds (i.e., the number of spatial channels or spectrometers simultaneously on sky), respectively; the radio astronomy convention is adopted in the second equality. The voxel size can be derived from the spectral and angular resolutions as

$$V_{\mathrm{vox}} = \sigma^2_\perp \sigma_\parallel = \chi(z)^2 \Omega_{\mathrm{beam}} y(z) \delta_\nu . \tag{4.59}$$

As long as the survey has proper spectral and angular resolutions to sample the k space in a roughly isotropic manner, the number of (independent) modes N_{modes} can be calculated as (e.g., Furlanetto & Lidz 2007; Li et al. 2016; S16)

$$N_{\mathrm{modes}}(k) = \frac{1}{2} \times 4\pi k^2 \Delta k \frac{V_{\mathrm{s}}}{(2\pi)^3} = \ln(10) k^3 \Delta \log k \frac{V_{\mathrm{s}}}{4\pi^2} , \tag{4.60}$$

where the factor of $1/2$ comes from the fact that the power spectrum is the Fourier transform of a real-valued function and thus only half of the Fourier plane contains independent information. The total signal-to-noise ratio (S/N) of a measured power spectrum is then defined to be (Gong et al. 2012; Li et al. 2016)

$$\mathrm{SNR}_{\mathrm{tot}} = \sqrt{\sum_{k \text{ bins}} \left[\frac{P(k)}{\delta P(k)}\right]^2} . \tag{4.61}$$

The values of relevant instrumental parameters, adopted to guarantee significant detections of the LIM signals with comparable total S/N in our analysis, are summarized in Table 7.2 for each of the four case studies to be discussed in Section 4.6. We note that certain requirements presented exceed the scope of planned surveys and better resemble future mission concepts, for instance, a 10 m class, FIR telescope in space like the *Origins Space Telescope (OST)* for measuring [C II] and [N II] at intermediate redshifts, as well as the large number of feeds that will be enabled by the successful deployment of broadband, on-chip spectrometers like SuperSpec (Hailey-Dunsheath et al. 2014) and DESHIMA (Endo et al. 2019). Meanwhile, the detector noise levels assumed for some signals (e.g., [N II]) are substantially more optimistic than what may be achieved from the ground, and therefore require observations in space, in which case an NEFD of order of 10 mJy $\mathrm{s}^{1/2}$, corresponding to a noise equivalent power (NEP) of a few times $10^{-19}\,\mathrm{W\,Hz}^{-1/2}$, is achievable (Bradford et al. 2008, 2018). Even though we make no effort to carefully build these case studies on existing or planned experiments, auto-/cross-correlation opportunities based on real experiments in similar contexts will be described.

4.5 Comparison to Existing Observational Constraints

From LIM observations of the large-scale distribution of neutral hydrogen, constraints have been placed on the H I density parameter, defined as the ratio of the H I density to the critical density of the universe at $z = 0$, namely, $\Omega_{\mathrm{H\,I}} = \rho_{\mathrm{H\,I}}/\rho_{\mathrm{c},0}$ or equivalently the mean H I brightness temperature $\bar{T}_{\mathrm{H\,I}}$ as defined in Equation 4.22. The top two panels of Figure 4.9 show the product of H I density parameter and bias factor, degenerate when constrained by the large-scale clustering of H I, and the mean 21cm brightness temperature predicted by our model, respectively, which are found to be in good agreement with observed values at $z \sim 0.8$ (Chang et al. 2010; Switzer et al. 2013). The corresponding H I power spectra $\Delta^2_{\mathrm{H\,I}}$ derived from our HOD model at $z = 0, 0.8$ and 1 are shown in the bottom panel of Figure 4.9, together with the deep-field results (detections only) from Switzer et al. (2013). While the detections shall be interpreted as upper limits since residual, correlated foregrounds are very likely present, predictions by our reference ISM model are still broadly consistent with H I observations available to date.

The top panel of Figure 4.10 shows the $L_{[\mathrm{C\,II}]}$–SFR relations derived from our model assuming different photoelectric heating efficiency (from bottom to top, $\epsilon_{\mathrm{PE}} = 3\times10^{-4}, 1\times10^{-3}, 3\times10^{-3}, 1\times10^{-2}$ and 3×10^{-2}) and how they compare with the best-fit relation to a large sample of galaxies of various populations (starburst

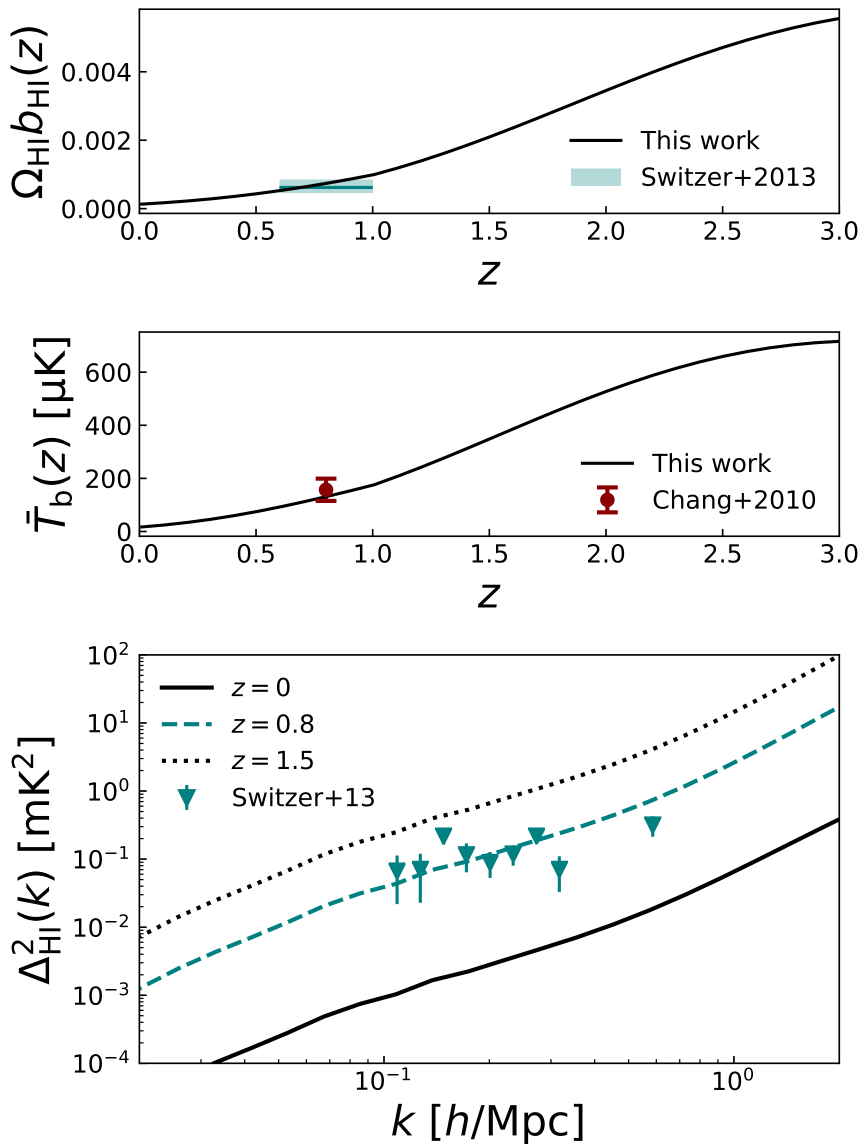

Figure 4.9: Observational constraints on H I density, temperature, and power. Top: observational constraints from the literature (Switzer et al. 2013) on the product $\Omega_{\rm H\,I} b_{\rm H\,I}$ of H I density parameter and bias factor at $z \sim 0.8$, compared with our model prediction. Middle: redshift evolution of H I brightness temperature, compared with the constraint from Chang et al. (2010) at $z \sim 0.8$. Bottom: H I power spectrum at different redshifts predicted by our HOD model. For comparison, deep-field results from Switzer et al. (2013) are shown by the teal triangles, which shall be interpreted as upper limits when residual foreground is present. All the data from observations are shown with their 68% confidence level.

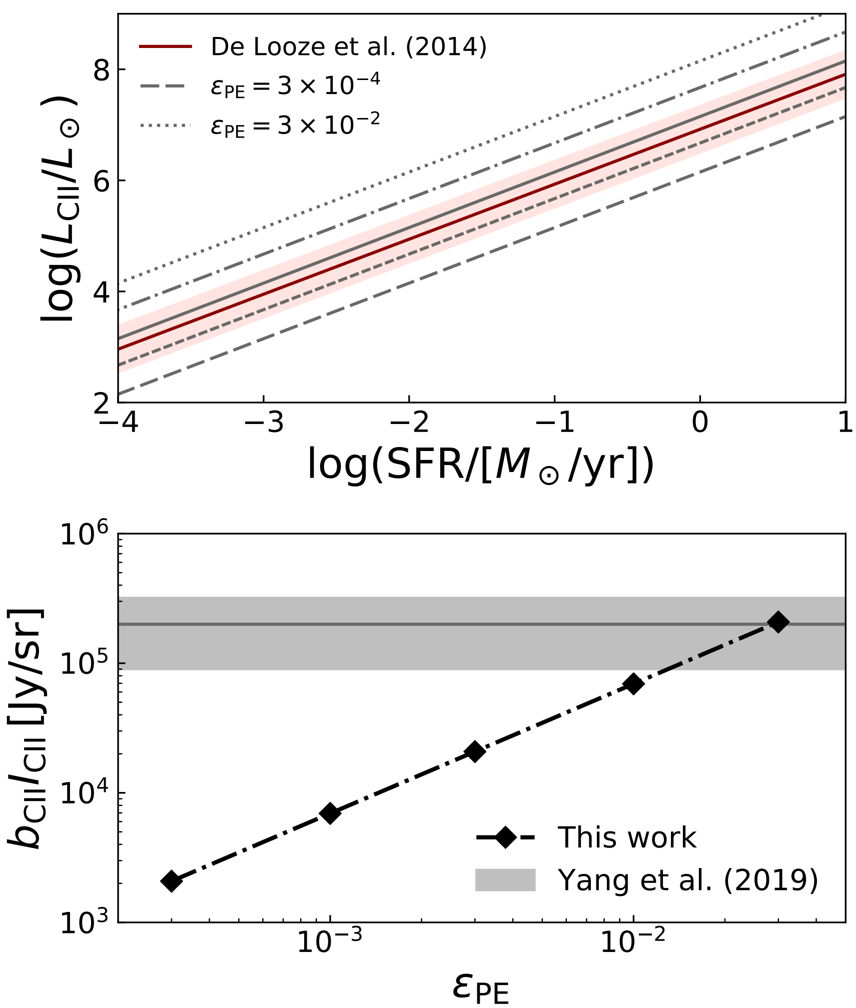

Figure 4.10: The effect of photoelectric heating efficiency on the [C II] signal. Top: $L_{C\,II}$–SFR relation from our model evaluated at different values of the photoelectric heating efficiency (from bottom to top, $\epsilon_{PE} = 3 \times 10^{-4}, 1 \times 10^{-3}, 3 \times 10^{-3}, 1 \times 10^{-2}$ and 3×10^{-2}), compared with the best-fit relation with a 0.4 dex scatter to the entire galaxy sample from De Looze et al. (2014). Bottom: products of the mean [C II] intensity and the bias factor $b_{[C\,II]} I_{[C\,II]}$ predicted by our model at $z \sim 2.6$ for the five different values of ϵ_{PE}. The latest observational constraint on $b_{[C\,II]} I_{[C\,II]}$ (95% confidence level) inferred from the cross-correlation between Planck maps and galaxy surveys (Yang et al. 2019).

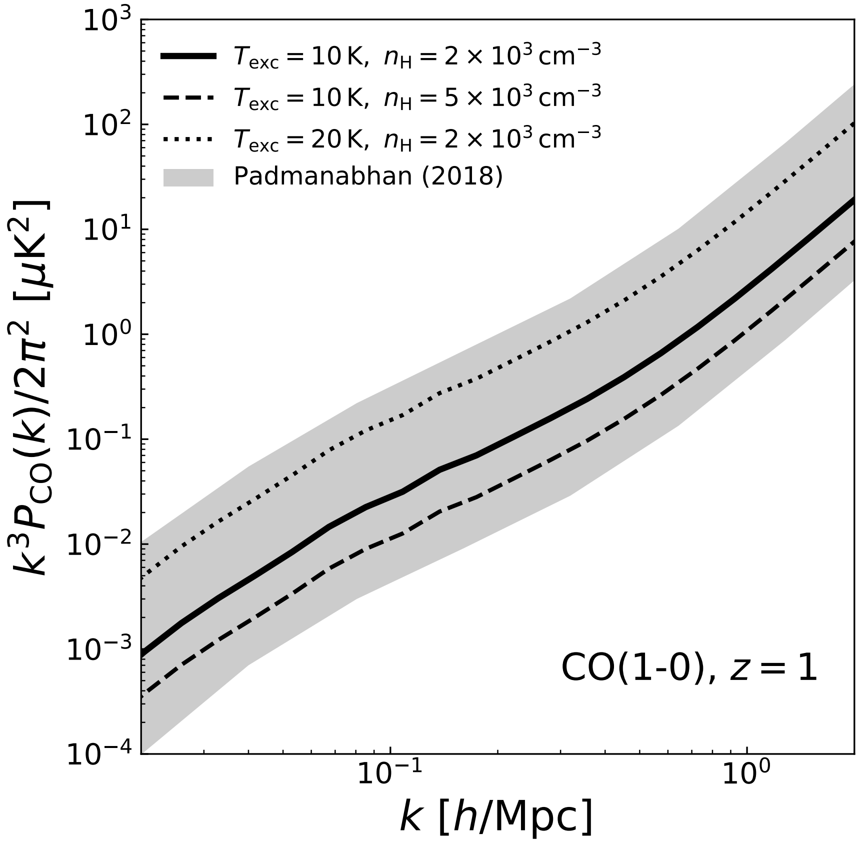

Figure 4.11: Effects of gas density and excitation temperature on the CO(1–0) signal. Power spectra of CO(1–0) emission at $z = 1$ for different values of the molecular gas density n_{H_2} and the excitation temperature T_{exc} as predicted by our HOD model. Constraints (68% confidence level) from a compilation of observations by Padmanabhan (2018) are also shown by the shaded region for comparison.

galaxies, dwarfs, ULIRGs, AGNs, high-z galaxies, etc.) taken from De Looze et al. (2014). Recently, Pullen et al. (2018) and Yang et al. (2019) report a tentative detection of excess emission in the 545 GHz Planck map that can be attributed to redshifted [C II] line emission. From angular cross-power spectra of high-frequency Planck maps with BOSS quasars and CMASS galaxies, a joint constraint on the product of mean [C II] intensity and bias factor $b_{[\mathrm{C\,II}]} I_{[\mathrm{C\,II}]} = 2.0^{+1.2}_{-1.1} \times 10^5\ \mathrm{Jy\,sr^{-1}}$ is inferred at 95% confidence level. In the bottom panel of Figure 4.10, we compare our model predictions at the five different ϵ_{PE} values against the measurement from Yang et al. (2019). We note that a relatively high ϵ_{PE} is required to match the measured level of $b_{[\mathrm{C\,II}]} I_{[\mathrm{C\,II}]}$, which may lead to tension with the observed $L_{[\mathrm{C\,II}]}$–

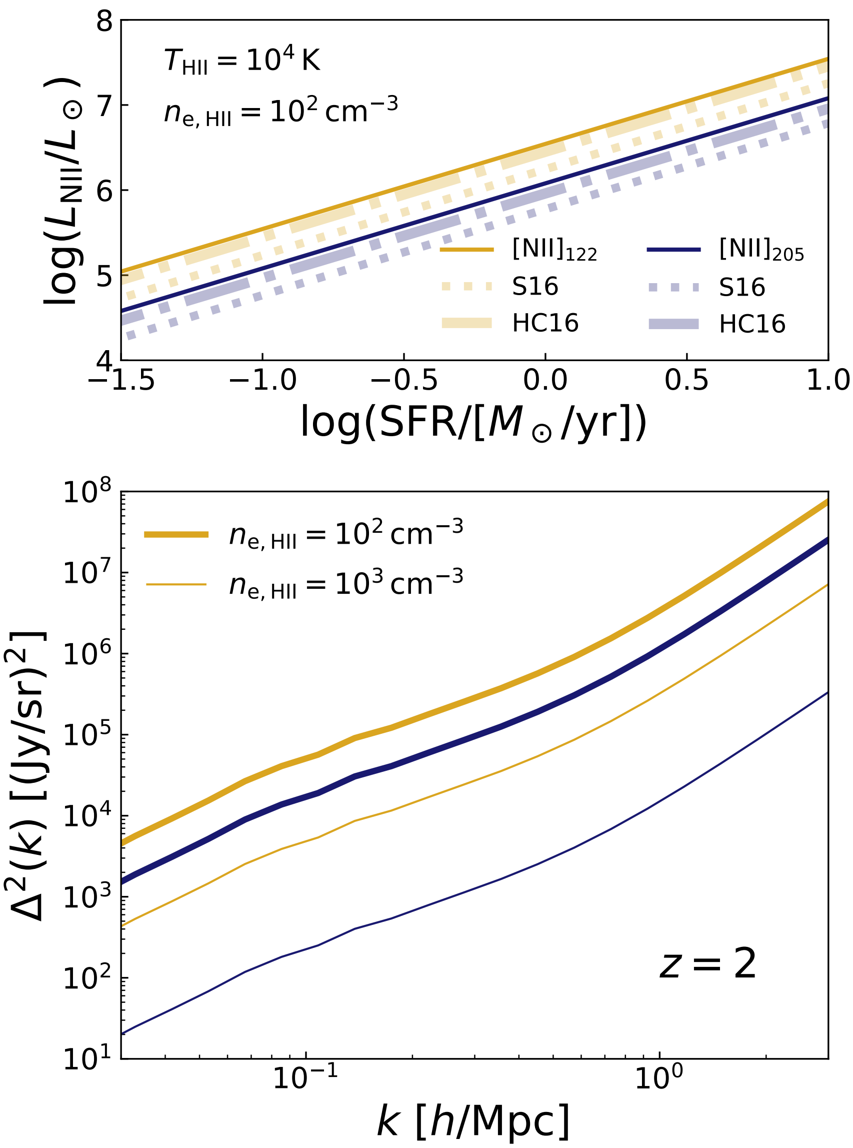

Figure 4.12: The effect of electron number density on signals of [N II] lines. Top: correlations between [N II] 122μm and 205μm line luminosities and the star formation rate, compared with those taken from S16 and Herrera-Camus et al. (2016). Fiducial values of H II region temperature and electron density from the reference ISM model are assumed. Bottom: [N II] power spectra at $z = 2$ predicted by our HOD model. Two sets of curves with different thicknesses are shown to illustrate the density effect on the ratio of [N II] lines.

SFR relation. Such a discrepancy is also observed by Pullen et al. (2018) and Yang et al. (2019) when comparing against phenomenological models (e.g., Gong et al. 2012; Silva et al. 2015) based on local observations. While it is possible that the

L_{IR}–$L_{[\mathrm{C\,II}]}$ relation is different at these redshifts, in which case a deviation from the proportionality $L_{[\mathrm{C\,II}]} \propto \mathrm{SFR}$ may be implied (see, e.g., the data-driven model of [C II] emission presented by Padmanabhan 2019), the observed excess may also be produced by non-[C II] factors such as interloper lines or redshift evolution of CIB parameters. Future, high-resolution [C II] LIM surveys will help clarify this discrepancy.

Measuring CO power spectrum from dedicated LIM experiments, such as COPSS II (Keating et al. 2016), COMAP (Li et al. 2016) and Y. T. Lee Array (Ho et al. 2009), or galaxy surveys (e.g., Uzgil et al. 2019) is an emerging field. In Figure 4.11, we show our model predictions of the CO(1–0) power spectrum at $z = 1$, evaluated for three pairs of excitation temperature T_{exc} and molecular gas density n_{H_2} to illustrate how sensitive CO power spectrum is to these gas properties. For comparison, the best estimate from an empirical model fit to a compilation of existing observations, including constraints on CO luminosity function and power spectrum obtained at redshifts $0 < z < 3$, taken from Padmanabhan (2018) is shown by the shaded band. The prediction of our reference ISM model is in good agreement with the observational constraints.

As there has not been any LIM measurement of [N II] lines because of their faintness, in Figure 4.12 we only compare our reference $L_{[\mathrm{N\,II}]}$-L_{IR} model against results from the literature and then present the [N II] power spectra it predicts. The top panel of Figure 4.12 shows the relations between [N II] line luminosities and the star formation rate predicted by our reference ISM model assuming $T_{\mathrm{H\,II}} = 10^4\,\mathrm{K}$ and $n_{e,\mathrm{H\,II}} = 10^2\,\mathrm{cm}^{-3}$. Estimates from previous work are shown for comparison, including scaling relations (Spinoglio et al. 2012; S16)[3] based on a sample of local galaxies observed with the *ISO*-LWS spectrometer (Clegg et al. 1996) and compiled by Brauher et al. (2008), and relations derived by Herrera-Camus et al. (2016) based on an observationally-motivated prescription assuming a uniform $n_{e,\mathrm{H\,II}} = 10^2\,\mathrm{cm}^{-3}$. Given the relatively large dispersion that exists in the existing data (see, e.g., Spinoglio et al. 2012), our simple model is deemed satisfactory despite the fact that it may slightly overestimate the local [N II] luminosities. The bottom panel of Figure 4.12 shows the power spectra of [N II] 122 μm and 205 μm lines, evaluated at $z = 2$ for two different values of the H II region electron number density to illustrate the density effect on the [N II] line ratio.

[3] The scaling relation for [N II] 205μm is not provided by Spinoglio et al. (2012), for which we assume a line ratio of $L^{122}_{[\mathrm{N\,II}]}/L^{205}_{[\mathrm{N\,II}]} = 3$ following S16 (corresponding to $n_{e,\mathrm{H\,II}} \sim 100\,\mathrm{cm}^{-3}$, as can be seen from Figure 4.7).

4.6 Inferring ISM Properties from Auto/Cross-Correlations

Both auto-correlation and cross-correlation analyses serve as a powerful tool to study the ISM physics when LIM data sets of multiple lines are available. The latter, however, has the advantage of avoiding contamination from uncorrelated foregrounds (line and continuum), which are usually a few orders of magnitude brighter than and/or spectrally blended with the signal of interest, therefore presenting a great challenge to reliably measuring the line intensity fluctuations (Lidz et al. 2009; Pullen et al. 2013; Silva et al. 2015; S16; Beane et al. 2019; see also Switzer et al. 2019). In the rest of this section, we present several case studies in order to demonstrate how the population-averaged physical properties of different ISM phases, such as their gas temperature and density, might be reliably extracted by auto/cross-correlating the intensity fields of different tracers.

We adopt a Bayesian analysis framework and fit parameters of ISM properties with the affine-invariant Markov Chain Monte Carlo (MCMC) code `emcee` (Foreman-Mackey et al. 2013). The likelihood function for fitting the mock power spectra can be expressed as

$$l\left(\hat{x}\middle|\hat{\theta}\right) = \prod_{i=0}^{N_s} \prod_{j=0}^{N_k} p_{ij}(k)\,, \tag{4.62}$$

where N_k is the number of k bins in which auto or cross power spectra are measured and N_s represents the number of auto/cross-correlation surveys being included. The probability of the data vector $\hat{x}$ is described by a normal distribution

$$p_{ij} = \frac{1}{\sqrt{2\pi}\sigma_{ij}(k)} \exp\left\{-\frac{\left[P(k) - P(k|\hat{\theta})\right]^2}{2\sigma_{ij}^2(k)}\right\}\,, \tag{4.63}$$

where σ_{ij} represents the gaussian error associated with the measurement. Broad, uninformative priors on the model parameters $\hat{\theta}$ are used, whose values are to be stated below for each individual case study. Furthermore, for all the following case studies, we adopt the same range and binning scheme for k which yield 15 bins evenly-spaced in $\log k$ over $-1.5 < \log[k/(h/\mathrm{Mpc})] < 1$. We stress that while all four case studies presented below are evaluated at $z \sim 2$ for a redshift interval of $\Delta z = \pm 0.25$, the same exercise could be repeated at different redshifts in order to study the redshift evolution of different ISM properties, which is one of the most important applications of the modeling framework presented.

It is also important to point out that our model implicitly enforces a linear relation between line luminosity and halo mass, which is likely an oversimplification given the complicated physics involved in line production. The only physical parameter that modifies the shape of line luminosity function (and therefore the shape of power spectrum) is the log scatter σ_ν. Consequently, whether the constraining power comes from the clustering or shot-noise regime of the power spectrum only makes a moderate difference in our analysis, as will be shown in Case I. The scale dependence of constraining power in a power spectrum analysis without such simplification can be found in recent studies (e.g., Yue & Ferrara 2019).

4.6.1 Case I: Multi-Phase Diagnosis with H I and CO

As the first example, we investigate how the multi-phase ISM may be probed by a combination of H I and CO LIM observations, which trace atomic and molecular hydrogen, respectively. Because the total gas mass is constrained implicitly by the CIB, the H I measurement constrains both the atomic and molecular gas fraction. The CO measurement can then in principle break the degeneracy between the total amount of molecular gas and α_{CO}.

We consider two independent, mock measurements of H I and CO auto power spectra, generated at $z \sim 2$ assuming the reference ISM model described in Table 4.2 and experimental setups specified in Table 7.2, which yield a total S/N of approximately 8 for each signal[4]. Forthcoming single-dish/interferometric suveys, including FAST (Bigot-Sazy et al. 2016), CHIME (Bandura et al. 2014) and SKA (Dewdney et al. 2013) for H I and COMAP (Li et al. 2016; Chung et al. 2019) and mmIME (Keating et al. in preparation) for CO, will carry out these auto-correlation measurements directly, even though in both cases the signal is expected to be heavily contaminated by line/continuum foregrounds. Broad, flat priors over $0 < f_{\mathrm{H_2}} < 0.5$, $0 < f_{\mathrm{H\,II}} < 0.5$, $10^1 < n_{\mathrm{H_2}}/\mathrm{cm}^{-3} < 10^5$ and $0 < \sigma < 1$ are assumed for the MCMC analysis. The MCMC sampling is constructed with 60 walkers, 500 burn-in steps—well above the estimated autocorrelation time (~ 50 steps) `emcee` returned, and another 500 steps for sampling.

The left panel of Figure 4.13 shows mock observed power spectra of H I 21cm and CO auto-correlation signals at $z \sim 2$, where the error bars are calculated from the assumed instrument parameters. The joint and marginalized posterior distributions of free parameters constrained by the mock auto power spectra under the MCMC framework are shown in the right panel of Figure 4.13. Note that we have converted the posterior of $n_{\mathrm{H_2}}$ into the more commonly seen α_{CO} factor using the assumed

[4] Summed over all k bins; see Equation (4.61)

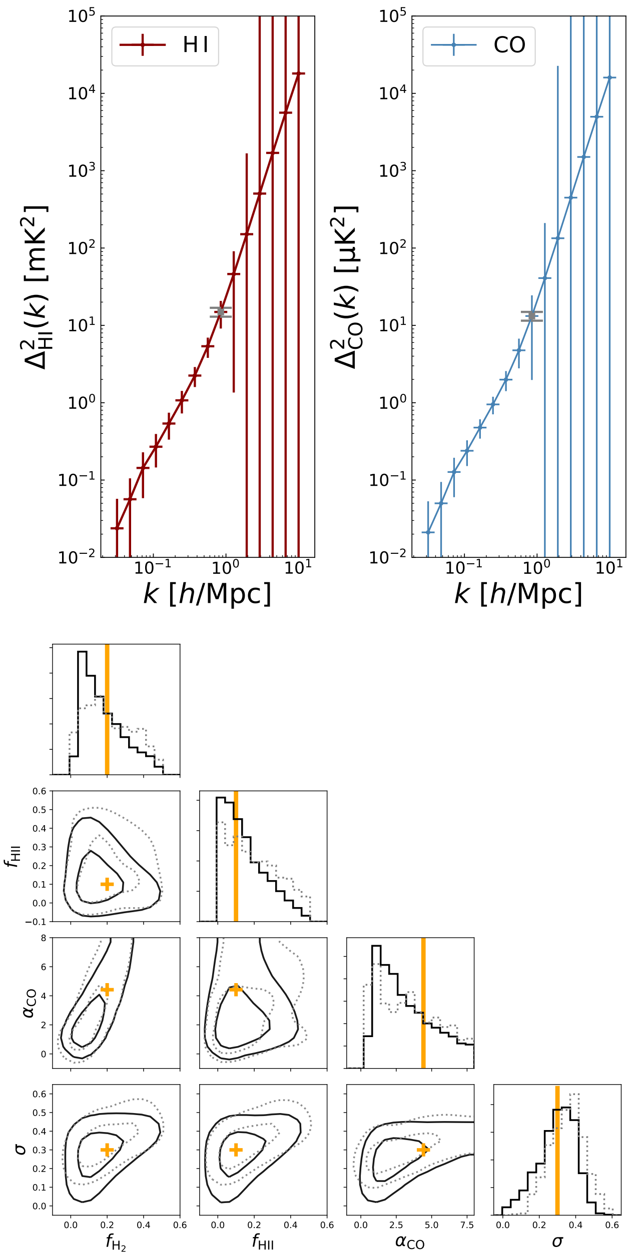

Figure 4.13: Parameter constraints from mock H I and CO data sets. Left: mock data sets of the observed H I and CO auto power spectra at $z \sim 2$. The error bars are calculated via mode counting assuming the Case I experimental setups specified in Table 7.2. The gray error bar at $k \approx 1\ h/\mathrm{Mpc}$ indicates the shot-noise-only measurement with the same overall S/N. Right: joint posterior distributions of the molecular gas fraction $f_{\mathrm{H_2}}$, the ionized gas fraction $f_{\mathrm{H\,II}}$, the molecular gas density $n_{\mathrm{H_2}}$ and the scatter σ, shown for 68% and 95% confidence levels. The solid and dotted contours represent the constraints from measurements of the full power spectrum and only the shot noise, respectively. The true values in our reference ISM model used to generate mock observations are indicated by the orange plus signs. Diagonal panels show the marginalized distributions of each individual parameter.

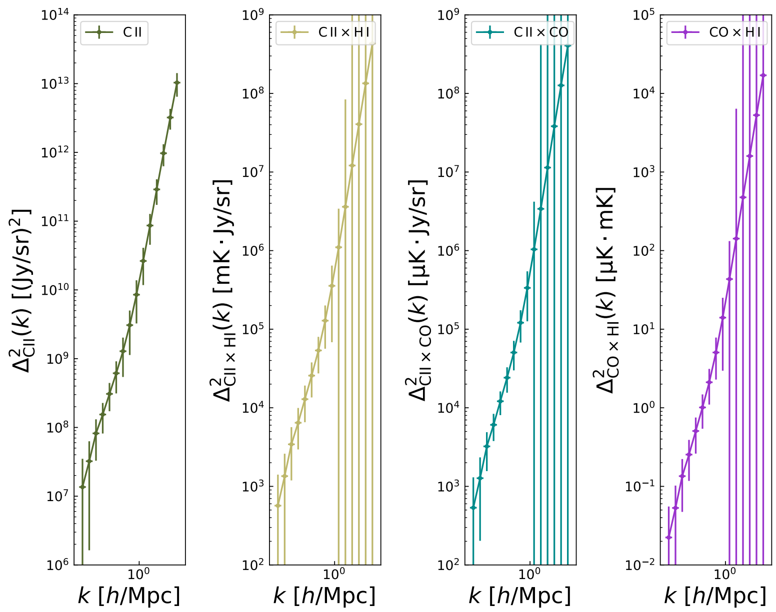

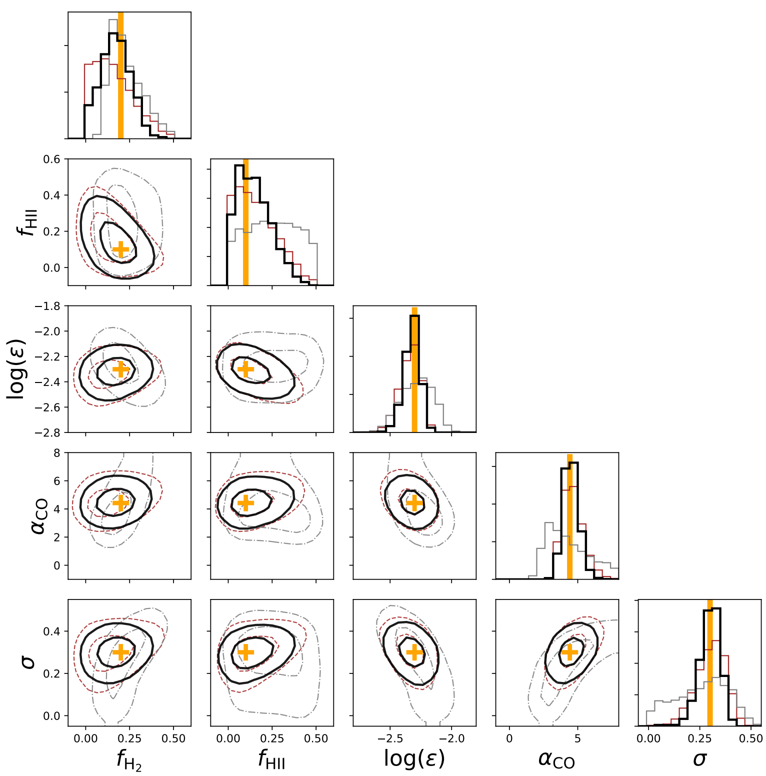

Figure 4.14: Parameter constraints on mock [C II], CO, and H I data sets. Left: mock data sets of the observed [C II] auto power spectrum and [C II] × H I, [C II] × CO and CO × H I cross power spectra at $z \sim 2$. The error bars are calculated via mode counting assuming the Case II experimental setups specified in Table 7.2. Right: joint posterior distributions of the molecular gas fraction $f_{\mathrm{H_2}}$, the ionized gas fraction $f_{\mathrm{H\,II}}$, the photoelectric heating efficiency ϵ_{PE}, the molecular gas density $n_{\mathrm{H_2}}$ and the scatter σ, shown for 68% and 95% confidence levels as constrained by the auto-correlation (dashed contours), cross-correlation (dashed-dotted contours) and auto-and-cross combined data (solid contours). The true values in our reference ISM model used to generate mock observations are indicated by the orange plus signs. Diagonal panels show the marginalized distributions of each individual parameter.

$T_{\mathrm{exc}} = 10\,\mathrm{K}$.

From the comparison between posterior distributions and true values (orange plus signs), as well as the fact that none of them are prior dominated, constraining power on all four parameters is observed. Even f_{H_2} and α_{CO}, though still strongly correlated, are individually constrained in this analysis. However, more precise estimation of the molecular gas content of galaxies from CO power spectrum measurements is conditional on how well α_{CO} can be reliably determined, even if additional information about the atomic hydrogen content from H I LIM is available. In practice, the exact value of α_{CO} could vary in a non-trivial way with physical conditions of molecular gas in galaxies, especially the gas temperature distribution and metallicity. As a result, how LIM might be exploited to better determine its value is an interesting topic to be explored (see Section 4.7 for further discussion).

In addition to the default scenario using the full power spectrum in all k bins, we consider an alternative scenario, where only the shot-noise power can be measured, while holding the overall S/N fixed. This resembles deep, targeted observations by, e.g., ALMA, from which information about large-scale intensity fluctuations is not available. As indicated by the gray error bars in the left panel of Figure 4.13, we assume two $\mathrm{S/N} \sim 8$ measurements of H I and CO power spectrum at $k \approx 1\,h/\mathrm{Mpc}$ where shot noise is dominant. Due to the implicitly assumed linearity between line luminosity and halo mass, similar constraining power on the parameter space is observed, except that the measured log scatter σ_ν becomes biased, which can be easily understood given that in our model it is the only parameter sensitive to the shape of the power spectrum.

4.6.2 Case II: Multi-Phase Diagnosis with H I, [C II] and CO

Given the observed degeneracy between f_{H_2} and α_{CO} in the previous case study, which introduces ambiguity to the interpretation of CO LIM results in terms of a molecular gas census, we investigate in this case how the inclusion of [C II] data, an indirect tracer of the molecular hydrogen fraction as indicated by Equation (4.24), may help alleviate such a degeneracy. Additionally, we investigate how the constraining power on the parameter space may differ between using the three separate auto power spectra and using the $3(3-1)/2 = 3$ cross-correlation measurements available, which has the advantage of being immune to contamination from uncorrelated foregrounds as suggested in S16.

Mock data sets of LIM observations are again created assuming the reference ISM model parameters and instrument parameters listed in Table 4.2 and Table 7.2, respectively. We note that when accounting for the effect of finite beam size in the cross-correlation sensitivity analysis, we conservatively evaluate for the coarser beam throughout our calculations. The overall S/N of cross-correlation data ($\mathrm{SNR}_{\mathrm{tot}} \sim 5$ for each cross signal) is consequently lower than that of auto-correlation data. At intermediate redshifts, experiments like EXCLAIM (Switzer 2017) and TIM (Aguirre & STARFIRE Collaboration 2018) will measure [C II] in tomography, which, when spatially overlapped, may be combined with the H I and CO surveys mentioned in the previous case to obtain their mutual cross-correlations. Broad, flat priors over $0 < f_{\mathrm{H_2}} < 0.5$, $0 < f_{\mathrm{H\,II}} < 0.5$, $10^{-4} < \epsilon_{\mathrm{PE}} < 10^{-1}$, $10^1 < n_{\mathrm{H_2}}/\mathrm{cm^{-3}} < 10^5$ and $0 < \sigma < 1$ are assumed for the MCMC analysis. The MCMC sampling is constructed with 50 walkers, 500 burn-in steps—sufficiently larger than the estimated autocorrelation time (~ 60 steps)—and another 500 steps for sampling.

In the left panel of Figure 4.14, we show the mock power spectrum data sets in addition to what has been shown in Figure 4.13, including auto-correlation of [C II] and mutual cross-correlations of the three lines considered, all evaluated at $z \sim 2$. The corresponding constraining power on the parameter space of our mock auto-correlation (brown dashed contours) and cross-correlation (gray dashed-dotted contours) and auto/cross-correlation-combined (black solid contours) data sets is presented in the right panel of Figure 4.14 as joint and marginalized posterior distributions.

From the posterior constrained by auto-correlations, which becomes less biased from the true value after including [C II] data, it is clear that the degeneracy between $f_{\mathrm{H_2}}$ and α_{CO} has been substantially reduced, although considerable uncertainty is still associated with $f_{\mathrm{H_2}}$. Other parameters, including α_{CO}, ϵ_{PE} and σ, are well constrained by the auto-correlations from their marginalized posteriors, except for $f_{\mathrm{H\,II}}$ which is not directly traced by any of the lines. The constraining power from cross-correlations, on the other hand, is not as good—particularly for $f_{\mathrm{H\,II}}$ of which the constraint is prior dominated—yet still significant in general. While formally when $N \geq 3$, perfectly correlated lines are present, the mean line intensities shall be constrained equally well by their mutual cross-correlations; the poorer performance can be largely explained by the lower overall S/N of cross-correlation data. For completeness, we show also the total constraining power combining both auto-correlation and cross-correlation data sets, even though it is only slightly improved

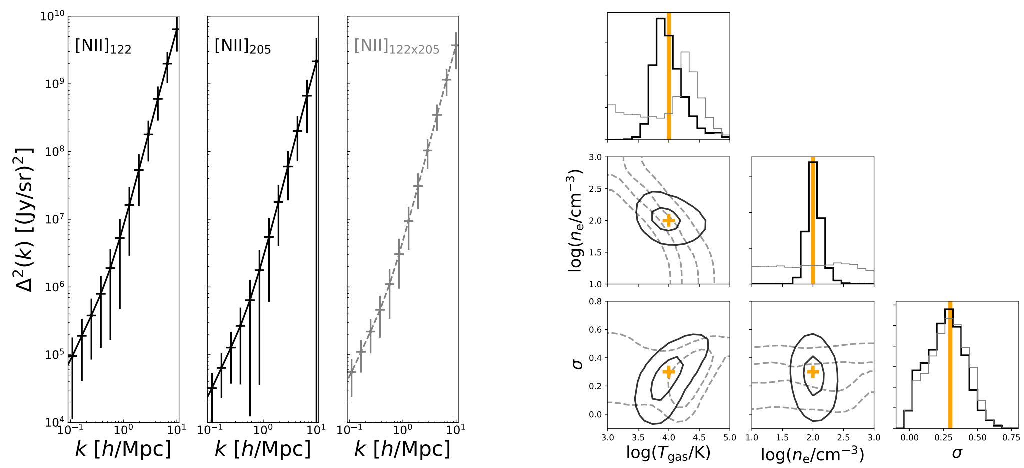

Figure 4.15: Parameter constraints from mock [N II] data sets. Left: mock data sets of the observed auto (solid) and cross (dashed) power spectra of [N II] 122 μm and 205 μm lines at $z \sim 2$. The error bars are calculated via mode counting assuming the Case III experimental setups specified in Table 7.2. Right: posterior distributions of the gas density $n_{e,\mathrm{H\,II}}$ and temperature $T_{\mathrm{gas,H\,II}}$ in H II regions, constrained by the cross power spectrum $P_{122\times205}$ (gray dashed contours) and the auto power spectra P_{122} and P_{205} (black solid contours), respectively. The inner and outer contours represent the 68% and 95% confidence intervals. The true values in our reference ISM model used to generate mock observations are indicated by the orange plus signs. Diagonal panels show the marginalized distributions of each individual parameter.

compared with the auto-only case. Both kinds of measurement are subject to realistic but different limitations — while analysis based on auto correlations tends to be more foreground-contaminated in general, it has the advantage of not requiring the experiments to be spatially overlapped, as long as the cosmic variance of individual surveys can be properly accounted for.

4.6.3 Case III: Probing H II Regions with [N II] Lines.

Another straightforward application of our line model is to use the two [N II] lines to constrain the state of ionized ISM, especially its electron number density $n_{e,\mathrm{H\,II}}$ directly probed by the [N II] fine-structure line ratio (see, e.g., Goldsmith et al. 2015 and Díaz-Santos et al. 2017 for applications of the $[\mathrm{N\,II}]_{205}/[\mathrm{N\,II}]_{122}$ ratio as a diagnostic of $n_{e,\mathrm{H\,II}}$ to the Galactic plane and local galaxies). Here, we consider two types of measurements, namely, the cross power spectrum of the two [N II] lines and their respective auto power spectra.

Mock data sets of LIM observations are created assuming the reference ISM model ($n_{e,\mathrm{H\,II}} = 100\,\mathrm{cm}^{-3}$, $T_{\mathrm{gas,H\,II}} = 10^4$ K and $\sigma = 0.3$ dex), together with experimental setups specified in Table 7.2. We note that while [N II] lines tend to be spectrally covered by [C II]-targeted experiments like EXCLAIM and TIM, at intermediate redshifts the required specifications in this (and the next) case study for a detection may only be achievable for next-generation space missions like *OST* owing to the faintness of [N II] emission. Broad, flat priors over $1 < n_{e,\mathrm{H\,II}}/\mathrm{cm}^{-3} < 10^5$, $10^3 < T_{\mathrm{gas,H\,II}}/\mathrm{K} < 10^5$ and $0 < \sigma < 1$ are assumed for the MCMC analysis. The MCMC sampling in either case is done with 100 walkers, 1000 burn-in steps—well above the estimated autocorrelation time ($\sim$ 100 steps)—and another 1000 steps for sampling.

Figure 4.15 shows the posterior distributions of the electron number density $n_{e,\mathrm{H\,II}}$, the gas temperature $T_{\mathrm{gas,H\,II}}$ and the lognormal scatter in line intensity σ, as constrained by the two types of observations, respectively. With the assumed model and survey parameters, the auto and cross power spectra $P_{122}^{[\mathrm{N\,II}]}$, $P_{205}^{[\mathrm{N\,II}]}$ and $P_{122\times205}^{[\mathrm{N\,II}]}$ are measured at a total S/N of $\mathrm{SNR_{tot}} \sim 5.2$, 4.7 and 6.7, respectively. Both methods are able to determine the density and temperature without significant bias. Nevertheless, the auto power spectra of both [N II] lines together are much more effective than the just the cross power at breaking the degeneracy between the density and temperature as probed by the line ratio (see Figure 4.7). We note that the difference in the constraining power between these two contrasting cases serves as an example of the importance of determining the amplitude of each individual tracer, through measurements of either the individual auto power spectra, or all mutual cross power spectra when $N \geq 3$ lines are detected, as suggested in S16 and demonstrated in the previous case study.

4.6.4 Case IV: Dissecting [C II] Origin with [C II]–[N II] 205μm Line Ratio

While in Section 4.3.2 we have assumed that the [C II] line is solely attributed to the atomic gas in the PDRs so as to keep the line model simple, a small yet non-trivial fraction of the observed [C II] emission may actually originate in ionized gas phases as suggested by several recent studies (Hughes et al. 2015; Croxall et al. 2017; Cormier et al. 2019). Therefore, in this final example we consider a slight extension of the [C II] model presented: we rewrite the total [C II] emission observed with LIM as $L_{[\mathrm{C\,II}]}^{\mathrm{tot}} = L_{[\mathrm{C\,II}]}/f_{[\mathrm{C\,II}]}^{\mathrm{neutral}}$, where $L_{[\mathrm{C\,II}]} = (1 - f_{\mathrm{H_2}})\epsilon_{\mathrm{PE}} L_{\mathrm{IR}}$ is the contribution from the neutral ISM (PDRs) defined in Section 4.3.2 and $f_{[\mathrm{C\,II}]}^{\mathrm{neutral}}$ is an extra parameter introduced here to describe the fraction of [C II] emission contributed by the neutral ISM. Following Croxall et al. (2017), we use the ratio of [C II]/[N II] 205 μm lines, whose critical densities for electron collisions are very similar ($n_{[\mathrm{C\,II}]}^{\mathrm{crit}} \sim 45\,\mathrm{cm}^{-3}$ and

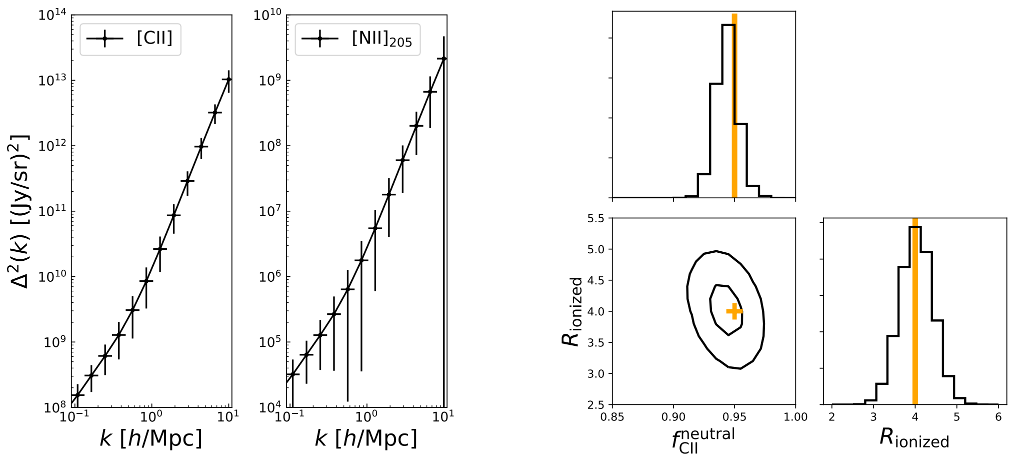

Figure 4.16: Parameter constraints from mock [C II] and [N II] data sets. Left: mock data sets of the [C II] and [N II] 205 μm auto power spectra at $z \sim 2$. The error bars are calculated via mode counting assuming the Case IV experimental setups specified in Table 7.2. Right: joint posterior distribution of the neutral-phase contribution, $f_{\mathrm{[C\,II]}}^{\mathrm{neutral}}$, to the total [C II] line emission and the [C II]/[N II] line ratio, R_{ionized}, inferred from collision rates, shown for 68% and 95% confidence levels. The (equivalent) true values $f_{\mathrm{[C\,II]}}^{\mathrm{neutral}} \approx 0.95$ and $R_{\mathrm{ionized}} \approx 4$ in our reference ISM model used to generate mock observations are indicated by the orange plus sign. Diagonal panels show the marginalized distributions of each individual parameter.

$n_{\mathrm{[N\,II],205}}^{\mathrm{crit}} \sim 32\,\mathrm{cm}^{-3}$), as a diagnostic of $f_{\mathrm{[C\,II]}}^{\mathrm{neutral}} = 1 - R_{\mathrm{ionized}} L_{\mathrm{[N\,II],205}}/L_{\mathrm{[C\,II]}}$, where $R_{\mathrm{ionized}} \approx 4$ denotes the ionized gas [C II]/[N II] ratio implied by their respective collision rates with electrons (Blum & Pradhan 1992; Tayal 2008, 2011), assuming Galactic gas-phase abundances.

Figure 4.16 demonstrates the constraining power on the neutral-phase contribution $f_{\mathrm{[C\,II]}}^{\mathrm{neutral}}$ to the observed [C II] emission, estimated from the line ratio $L_{\mathrm{[N\,II],205}}/L_{\mathrm{[C\,II]}}$ inferred from mock LIM observations at $z \sim 2$ (left panel). For the MCMC analysis, we assume a gaussian prior $\mathcal{N}(4, 0.4)$ for R_{ionized}, whereas a broad, flat prior is used for $f_{\mathrm{[C\,II]}}^{\mathrm{neutral}}$. The sampling is done with 100 walkers, 500 burn-in steps—sufficiently large compared with the estimated auto-correlation time ($\sim$ 30 steps)—and another 500 steps for sampling.

Our reference ISM model assumes a high $f_{\mathrm{[C\,II]}}^{\mathrm{neutral}} \sim 0.9$ (orange plus sign), consistent with the finding that [C II] emission arises mostly from the neutral ISM. For the survey specifications given in Table 7.2, we find that a population-averaged, neutral-phase contribution $f_{\mathrm{[C\,II]}}^{\mathrm{neutral}}$ can be robustly determined by simultaneously observing [C II] and [N II] 205 μm lines with LIM. We note that, in principle, the simple diagnostic described may be subject to density effects on the [C II]/[N II] line ratio and R_{ionized}, although in both cases the dependence on n_e is found to be weak (Croxall et al. 2017).

4.7 Discussion and Conclusion

We have presented a simple analytical framework to self-consistently model the production of emission lines in the multi-phase ISM, based on the mean dark matter halo properties derived from a model fit to the observed CIB anisotropy. The redshift evolution of cosmic star formation, dust mass, gas (total and molecular) mass, gas-phase metallicity, and the strengths of H I, [C II], [N II] and CO lines predicted by our model have been compared with observations, showing that our model, despite its simplicity, can describe the production of lines in the ISM in a physically-motivated way. We have illustrated how this modeling framework can be used to reconstruct the average properties of different ISM phases, such as the mass fractions and densities of neutral and ionized gas, the photoelectric heating efficiency in the PDRs, and so forth, over a wide range of redshifts from multi-tracer LIM observations.

Our analysis underscores the importance of cross-correlation analyses. While equivalent information may be obtained from the auto-correlation of respective tracers, cross-correlation analysis in the same cosmological volume is minimally susceptible to foreground contamination. With the large number of upcoming LIM experiments targeting lines produced in different ISM phases, e.g., CCAT-Prime (Stacey et al. 2018), CHIME (Bandura et al. 2014), COMAP (Li et al. 2016), CONCERTO (Lagache 2018), HIRAX (Newburgh et al. 2016), SKA (Santos et al. 2015), SPHEREx (Doré et al. 2014), Tianlai (Xu et al. 2015), TIM (Aguirre & STARFIRE Collaboration 2018) and TIME (Crites et al. 2014), our understanding of the ISM evolution and physical processes dominating line emission over cosmic time is expected to be greatly deepened by the coarse-grained view built up from LIM surveys with multiple tracers.

The simplicity and modularity of the model presented here lends itself to straightforward improvements and extensions to incorporate more sophisticated treatments of both galaxy evolution and ISM physics motivated by observational and theoretical studies. For instance, to more reliably apply this framework to galaxies at higher redshifts, including the reionization era, it would be valuable to introduce additional calibrations and constraints from data sets at other wavelengths. Currently the star formation history is anchored only to FIR emission constrained by the CIB anisotropy, which is sensitive mostly to galaxies at redshift $z \lesssim 3$ (e.g., Viero et al. 2013a). However, much of the information about the galaxy–halo connection, feedback-regulated galaxy and ISM evolution, and so forth, is encoded in data at shorter wavelengths, e.g., the galaxy UV luminosity function (UVLF). We therefore expect the exact mass and redshift dependence of mean halo properties (see Section 4.2) to be better constrained out to the epoch of reionization by combining IR and UV data, which will be explored in future work.

Given the necessarily coarse-grained picture of galactic ISM properties painted by LIM, we have employed physically-motivated but ultimately simple prescriptions for the line emission physics. Particularly as new observations yield more model constraints, the line physics can be refined. Notably, our prescription for the [C II] emission does not account for the deficit relative to L_{IR} observed in luminous and ultraluminous galaxies (e.g., Malhotra et al. 1997). It should be explored whether this can be recovered within the modeling framework by introducing the effect of dust charging on ϵ_{PE} (Bakes & Tielens 1994) and the saturation of [C II] at high gas temperatures (Muñoz & Oh 2016). Further, given that this effect appears to be a strong function of galaxy luminosity, this may have important testable implications for the predicted [C II] power spectra.

Another important caveat to our simple prescription lies in the interpretation of LIM signals in terms of globally-averaged ISM properties. In reality, the ensemble of gas clouds within a galaxy, while all contributing to the same line emission, may have a wide distribution of physical properties (e.g., H_2 gas temperature). Likewise, these distributions may vary significantly among different galaxy populations. As a result, interpreting LIM data in terms of a single "mean" property is an oversimplification. A more robust extraction of ISM physics from LIM data sets could be achieved by modeling these distributions directly, perhaps incorporating prior information about ISM conditions that are known to vary systematically in different galaxy populations, as well as how the line production is coupled to these distributions through radiative processes. Such modeling is beyond the scope of this paper and will be the subject of future investigation.

Finally, in this work we selected a small subset of available lines to illustrate the power of LIM to probe the multi-phase ISM. However, the model is readily extensible to other lines. For instance, the [O I] 63 μm and [O III] 88 μm lines are also important cooling lines, and so the sum of emission from these lines and [C II] may yield a more robust correlation with $L_{\rm IR}$ (De Looze et al. 2014), with their relative importance as a function of redshift and galaxy properties providing constraints on the physical state of the emitting gas. Simultaneous measurements of multiple CO rotational lines are both a powerful probe of the physics of molecular gas and a means of validation since the CO lines should be spatially correlated. In addition to CO, H_2 rotational lines can be used to constrain the molecular gas content of galaxies, meanwhile shedding light on the gas temperature distribution (Pereira-Santaella et al. 2014; Togi & Smith 2016). Optical and UV lines of hydrogen such as Lyα, Hα, and Hβ are also being actively pursued by LIM experiments and should be incorporated, particularly given their potential to probe metal-poor environments in the very high redshift universe.

Acknowledgments

We would like to thank the anonymous referee for comments that helped improve this paper. We would like to thank Hao-Yi (Heidi) Wu for helpful discussion on the CIB model, as well as Garrett (Karto) Keating and Ryan Keenan for compiling and sharing the constraints on cosmic molecular gas content. We are also grateful to Jamie Bock, Matt Bradford, Patrick Breysse, Paul Goldsmith, Adam Lidz, Lunjun Liu, Lluis Mas-Ribas, and Anthony Pullen for constructive discussion and comments on this work. Part of the research described in this paper was carried out at the Jet Propulsion Laboratory, California Institute of Technology, under a contract with the National Aeronautics and Space Administration.

Chapter 5

LIMFAST. I. A SEMI-NUMERICAL TOOL FOR LINE INTENSITY MAPPING

Mas-Ribas, L., Sun, G., Chang, T.-C., Gonzalez, M. O., Mebane, R. H. (2022). "LIMFAST. I. A Semi-Numerical Tool for Line Intensity Mapping", preprint, arXiv:2206.14185. https://arxiv.org/abs/2206.14185.

Abstract

We present LIMFAST, a semi-numerical code for computing the progress of reionization and line intensity mapping signals self-consistently, over large cosmological volumes and in short computational times. LIMFAST builds upon and extends the 21cmFAST code by implementing modern galaxy formation and evolution models. Furthermore, LIMFAST makes use of pre-computed stellar synthesis and photoionization results to obtain ensemble ionizing and line emission fields on large scales that vary with redshift, following the evolution of galaxy properties. We show LIMFAST calculations for the redshift evolution of the cosmic star formation rate, hydrogen neutral fraction, and metallicity in galaxies during reionization, which agree with current observational constraints. We also display the average signal with redshift, as well as the auto-power spectra at various redshifts, for the 21 cm line, the Lyα intergalactic and background emission, and the Lyα, Hα, Hβ, [O II] 3727 Å, and [O III] 5007 Å line emission from star formation. Overall, the LIMFAST results agree with calculations from other intensity mapping models, especially with those that account for the contribution of small halos during reionization. We further discuss the impact of considering redshift-space distortions, the use of local luminosity and star formation relations, and the dependence of line emission on the ionization parameter value. LIMFAST aims at being a resourceful tool for a broad range of intensity mapping studies, enabling the exploration of a variety of galaxy and reionization scenarios and frequencies over large volumes in a short time scale.

5.1 Introduction

Line intensity mapping (LIM) provides a statistical approach to the study of the formation and evolution of galaxies and large-scale structure in the universe. Compared to more traditional observational techniques that are limited to the individually detectable bright sources, LIM takes into account the emission produced by all the star formation present in large areas of the sky; its data, therefore, contains information of the entire galaxy population (Madau et al. 1997; Suginohara et al. 1999; Visbal & Loeb 2010; Kovetz et al. 2019). This characteristic is especially relevant for high redshift studies, including the epochs of reionization and cosmic dawn. The LIM approach can prove beneficial here because the faint end of the galaxy population may have played a major role during these early times, but this is difficult to explore directly (e.g., Fontanot et al. 2012; Choudhury & Ferrara 2007; Robertson et al. 2015; Yue et al. 2018).

A number of emission lines resulting from different radiative processes and environments are taken into account for LIM studies, the usual ones being the [C ii] line at 158 μm (e.g., Gong et al. 2012; Silva et al. 2015; Yue et al. 2015; Dumitru et al. 2019; Yue & Ferrara 2019; Sun et al. 2021b), those of the CO molecule (e.g., Righi et al. 2008; Gong et al. 2011; Lidz et al. 2011; Pullen et al. 2013; Li et al. 2016; Chung et al. 2019; Ihle et al. 2019), the hydrogen 21cm spin-flip transition (e.g., Scott & Rees 1990; Madau et al. 1997; Furlanetto et al. 2006; Chang et al. 2008; Visbal et al. 2009; Chang et al. 2010; Pritchard & Loeb 2012; Switzer et al. 2013; Liu & Shaw 2020), and the potentially bright rest-frame optical, ultraviolet lines such as Hα, Hβ, Lyα, He 2, [O ii], and [O iii] among others (e.g., Silva et al. 2013; Pullen et al. 2014; Visbal et al. 2015; Comaschi & Ferrara 2016; Heneka et al. 2017; Gong et al. 2017; Visbal & McQuinn 2018; Mas-Ribas & Chang 2020; Heneka & Cooray 2021; Kannan et al. 2022b; Padmanabhan et al. 2021; Parsons et al. 2021).

Numerically modeling LIM data is of major importance to guide future missions and experiments, but it is computationally challenging because the statistical power of LIM resides in the analysis of emission over large areas of the sky and at several frequencies that are sensitive to small-scale physics. Simulations need to include both, detailed processes related to star formation, as well as the emission and transport of radiation in large cosmological volumes. This combination of a broad range of dynamical scales and redshifts is demanding: numerical simulations accounting for resolved galaxy physics typically only allow for the simulation of a small number of galaxies (e.g., Hopkins et al. 2018; Katz et al. 2019; Pallottini et al. 2019; Kannan et al. 2020). On the other hand, simulations covering large volumes typically lack numerical precision at the smallest scales, and the processes connected to star formation are often modeled by means of sub-grid prescriptions (e.g., Vogelsberger et al. 2014; Eide et al. 2018, 2020; Shen et al. 2020; Kannan et al. 2022a,b; Lewis et al. 2022; Shen et al. 2022, and the review by Vogelsberger et al. 2020). Overall, in all cases these simulations typically require very long running times (and/or the need of super computers), on the order of weeks or months and, therefore, they are not well-suited for an exploration of parameter values or of different scenarios in a very short time scale.

With these limitations and constraints in mind, we present here LIMFAST, a semi-numerical tool designed for flexible high-redshift intensity mapping modeling. LIMFAST aims at self-consistently simulating line emission from galaxies and the intergalactic medium, over scales of several hundreds of Mpc and spanning the epoch of cosmic reionization, in a matter of hours with a current personal computer. The fast calculations are possible by using analytical prescriptions and pre-computed radiative processes, and they allow the user to perform large-scale computations following different parameterizations and scenarios in a short time.

As discussed in more detail below, LIMFAST builds upon and uses the 21cmFAST code (Mesinger & Furlanetto 2007; Mesinger et al. 2011) to compute the underlying large-scale structure in large volumes of the universe. This computational step is rapidly achieved because 21cmFAST uses perturbation theory and analytical approaches to the evolution of the density field and formation of collapsed objects. LIMFAST will then inherit this collapsed structure and will apply the modern galaxy formation and evolution models of Furlanetto (2021) to it to ultimately compute the radiation fields for a number of emission lines, in addition to the original 21cm emission from 21cmFAST. The progress of reionization is simultaneously computed also following the approach in 21cmFAST, but with extensions that self-consistently include the ionizing emission from galaxy populations that co-evolve with redshift.

This paper introduces and details the main structure of the LIMFAST code, and it is the first of a series that will implement further extensions and use LIMFAST to address science questions related to the epoch of cosmic reionization. For example, the second paper, Sun et al. (2022; Paper II hereafter) presents the computations to include the [C II] 158 μm and CO line emission, and explores the effects of different feedback and star-formation models beyond the fiducial signals presented here. Furthermore, a progenitor version of LIMFAST was presented and used to address the use of intensity mapping to measure the average He 2/Hα line ratio for inferring the initial mass function of Population III stars in Parsons et al. (2021). That code is publicly available under request to the authors. The structure of this present paper is as follows: the models and calculations of LIMFAST are detailed in Section 5.2, and the fiducial results are shown in Section 7.3. In Section 7.5 we discuss and compare the LIMFAST results with those from the literature. We finally summarize and conclude in Section 5.5.

We assume a flat, ΛCDM, $h = 67.8$ cosmology consistent with recent measurements by Planck Collaboration XIII (Planck Collaboration et al. 2016b) throughout.

5.2 LIMFAST: the Code

We detail the LIMFAST code below, after a brief description of 21cmFAST. In Section 5.2.1 we present the galaxy model by Furlanetto (2021) and its implementation in LIMFAST. We next describe in Section 5.2.2 the usage of `BPASS` to create the stellar spectra, and the photoionization calculations with `Cloudy` to obtain the nebular radiation. The details of the ionization computations in the intergalactic medium are presented in Section 5.2.3, and the calculations of the intergalactic and background Lyα, as well as the 21 cm emission, are presented in Sections 5.2.4, 5.2.5, and 5.2.6, respectively. Finally, Section 5.2.7 describes the inclusion of redshift-space distortions in the calculations.

LIMFAST builds upon and extends 21cmFAST (Mesinger & Furlanetto 2007; Mesinger et al. 2011) after inheriting the density and velocity fields computed by the later at each simulated cell. In detail, 21cmFAST computes evolving density and velocity fields from a set of initial conditions and first-order perturbation theory (Zel'Dovich 1970). Then, the code makes use of the conditional Press-Schechter formalism (Lacey & Cole 1993; Somerville & Kolatt 1999) to obtain the collapsed mass field. As described in the next section, LIMFAST makes use of the Sheth-Tormen (ST) halo mass function (HMF) to connect and derive the properties of galaxies from halos at each cell, following the prescriptions in Furlanetto (2021). We stress that in 21cmFAST, this approach corresponds to the 'matter density field' case, where individual halos are not resolved nor identified in the simulation; at each cell, the distribution of halo masses follows the ST HMF, and the total number of halos depends on the value of the matter overdensity and the collapsed fraction in that region.

After the collapsed mass field is obtained, 21cmFAST computes the ionization state of the baryonic intergalactic gas via the comparison of the cumulative number of ionizing photons from sources and the number of neutral hydrogen atoms and recombinations in spherical regions, from large to small volumes. This method, first proposed by Furlanetto et al. (2004), is analogous to the excursion-set formalism and it allows for scenarios of inhomogeneous reionization. Finally, the code computes the X-ray and Lyα radiation background fields, and uses them to derive the spin and brightness temperature of the 21 cm emission. In the following sections, we will discuss the extensions and variations of these calculations in LIMFAST, and refer the interested reader to Mesinger & Furlanetto (2007) and Mesinger et al. (2011) for more details on 21cmFAST.

5.2.1 Galaxy Formation and Evolution Model

We summarize next how the properties of galaxies are derived following the galaxy formation prescriptions by Furlanetto (2021).

In the Furlanetto (2021) model, galaxies evolve due to the interplay between star formation and feedback. Star formation is fueled by a smooth accretion of mass onto the dark matter halo, and it is at the same time regulated by the feedback that governs the ejection of material outside the galaxy. In this scenario, the production of gas, stars (i.e., the star-formation rate), and metals are described by

$$\dot{M}_{\rm g} = f_b \dot{M} - (\mathcal{R} + \eta)\dot{M}_* \,, \tag{5.1}$$

$$\dot{M}_* = M_{\rm g}/t_{\rm sf} \,, \tag{5.2}$$

and

$$\dot{M}_Z = -(1+\eta) Z \dot{M}_* + y_Z \dot{M}_* \,. \tag{5.3}$$

In Eq. 5.1 above, $f_b = \Omega_b/\Omega_m \approx 1/6$ is the baryon fraction, $\dot{M}$ is the mass accretion rate of the halo, $\mathcal{R} \approx 0.75$ denotes the fraction of mass available for star formation that resides in stars, and $\eta \gg 1$ accounts for the amount of mass ejected out of the galaxy by stellar feedback. In Eq. 5.2, $t_{\rm sf} = t_{\rm orb}/\epsilon$ denotes the star-formation timescale, where $t_{\rm orb} \sim 18 \left(\frac{7}{1+z}\right)^{3/2}$ Myr is the orbital timescale, and ϵ characterizes the temporal star formation efficiency per orbital timescale. In Eq. 5.3, $Z \equiv M_Z/M_{\rm g}$ denotes the metallicity, and $y_Z = 0.03$ (Benson 2010) is the fraction of stellar mass returned to the ISM in the form of metals.

Now writing $M_{\rm g}$ as a fraction of the total accreted mass $M_a = f_b M$, one can define $X_{\rm g} \equiv M_{\rm g}/M_a$ as the gas retention factor (Dekel & Mandelker 2014), and similarly $X_* \equiv M_*/M_a$. The previous equations can then be rewritten in terms of the dimensionless quantity $\tilde{M} \equiv M/M_0$, where M_0 denotes the halo mass at some initial redshift z_0, and taking derivatives with respect to redshift instead of time, namely $\tilde{M}' = d\tilde{M}/dz$. With these substitutions, the system of differential equations describing the halo, gas, and stellar mass evolution with redshift finally equates

$$\frac{\tilde{M}'}{\tilde{M}} = -|\tilde{M}_0'| \,, \tag{5.4}$$

$$\frac{\tilde{M}_{\rm g}'}{\tilde{M}_{\rm g}} = -|\tilde{M}_0'| \left[X_{\rm g}^{-1} - \frac{\epsilon(\mathcal{R}+\eta)}{|\tilde{M}_0'| C_{\rm orb}} \left(\frac{1+z_0}{1+z} \right) \right] \,, \tag{5.5}$$

$$\tilde{M}_*' = -\mathcal{R}\tilde{M}_{\rm g} \left[\frac{\epsilon}{C_{\rm orb}} \left(\frac{1+z_0}{1+z} \right) \right] \,, \tag{5.6}$$

$$\frac{\tilde{M}_Z'}{\tilde{M}_Z} = \mathcal{R}\left(-1-\eta+y_Z Z^{-1}\right) \left[\frac{\epsilon}{C_{\rm orb}} \left(\frac{1+z_0}{1+z} \right) \right] \,. \tag{5.7}$$

Here, $C_{\rm orb} = (1+z_0)t_{\rm orb}H(z)$ characterizes the parameter dependence of the orbital timescale, and $H(z)$ is the Hubble parameter at redshift z.

In order to solve the above equations, the parameters denoting the feedback model, η and ϵ, also need to be specified. For the fiducial LIMFAST case introduced here, we adopt the momentum-driven feedback model by Furlanetto et al. (2017), and present detailed dependencies on feedback prescriptions, as well as other star-formation recipes, in Paper II. In the momentum-driven feedback case, we set $\epsilon = 0.015$, and compute the term denoting the relation between the rate of gas expelled from the galaxy and the star-formation rate as

$$\eta(M,z) = C\left(\frac{10^{11.5}}{M}\right)^{\xi}\left(\frac{9}{1+z}\right)^{\sigma} \,, \tag{5.8}$$

where we have adopted the parameter values $C = 5$, $\xi = 1/3$, and $\sigma = 1/2$, consistent with the findings by Sun & Furlanetto (2016).

For the implementation of this galaxy model in LIMFAST, we have solved the above equations considering an initial redshift of $z = 30$ and tabulated the results as a function of halo mass and redshift. These tables cover the redshift range between $z = 5$ and $z = 30$ in steps of $dz = 0.1$, and the halo masses range from $M = 10^7\,M_\odot$ to $M = 10^{16}\,M_\odot$ in 900 evenly distributed bins in logarithmic space. LIMFAST then interpolates the tables to obtain the result for any combination of mass and redshift within these ranges.

Once the above quantities are calculated, we can derive two other important observables: the star formation rate density and the metallicity. The star formation rate density in a simulation cell is obtained by integrating the star formation rate per halo over the halo mass function (HMF) of the cell as

$$\dot{\rho}_*(z) = \int dn/dM(M,z)\, \dot{M}_*(M,z)\, dM\ , \tag{5.9}$$

where $\mathrm{d}n/\mathrm{d}M(M,z)$ denotes the HMF in 21cmFAST, consistent with the Sheth-Tormen (Sheth & Tormen 1999) formalism with the correction by Jenkins et al. (2001). For an individual halo, the metallicity at a given redshift is simply defined as $Z(M,z) \equiv M_Z(M,z)/M_{\mathrm{g}}(M,z)$, but for a cell the metallicity is computed as the ratio of total metal mass to total gas mass in such a cell as

$$Z(z) = \frac{\int dn/dM(M,z)\, M_Z(M,z)\, dM}{\int dn/dM(M,z)\, M_{\mathrm{g}}(M,z)\, dM}\ . \tag{5.10}$$

This calculation differs from that of the star formation rate because the metallicity is not an additive quantity and, therefore, one cannot integrate the metallicity per halo over the HMF. However, one may want to perform the metallicity per halo integration, and then divide it by the total number density of halos in the respective cell, to obtain the average metallicity per halo in such a volume. The integrals in the above two equations are performed from a minimum halo mass denoted by the atomic cooling halo mass at a virial temperature of $T_{\mathrm{vir}} = 10^4$ K in 21cmFAST. This halo mass value depends on redshift and extends from $\sim 10^7\, M_\odot$ at $z = 20$ to $\sim 10^8\, M_\odot$ at $z = 5$. Considering the atomic cooling threshold here is valid because we do not account for Population III star formation in this work; one may want to include smaller halo masses corresponding to molecular cooling when accounting for that stellar population (see, e.g., Mebane et al. 2018; Parsons et al. 2021, and references therein for further discussions). The upper limit of the integrals extends to infinity but, in practice, we limit it to a halo mass of $M_{\mathrm{max}} = 10^{16}\, M_\odot$.

Finally, we can also define the comoving luminosity density from halos in a cell as

$$\rho_l(z) = \int dn/dM(M,z)\, l(M,z)\, dM\ , \tag{5.11}$$

where $l(M,z)$ is the luminosity of a halo at a given redshift detailed in the next section, and with the same integration limits as before[1]. Then, the observed specific intensity is derived from the luminosity density as

$$I_\nu(z) = \frac{c}{4\pi} \frac{\rho_l(z)}{\nu_0\, H(z)}\ , \tag{5.12}$$

[1] We do not account for scatter in the relation between luminosity and halo mass in this work. This could be incorporated by considering a distribution of luminosity values instead of a single value in Eq. 5.11.

where ν_0 is the rest-frame frequency of the emission line of interest, c is the speed of light, and $H(z)$ is the Hubble parameter at redshift z.

In further sections we will refer to the mean value of these quantities to assess their redshift evolution. These mean values are obtained by taking the mean cell value over the entire simulation box at the redshift of interest.

5.2.2 Stellar and Nebular SEDs

As mentioned before, in this work we account only for normal (Population II) stellar populations, and leave the inclusion of Population III stars to future implementations (see, e.g., Mebane et al. 2018; Qin et al. 2020a, 2021b; Parsons et al. 2021; Tanaka & Hasegawa 2021; Muñoz et al. 2022, for previous work on implementations of Population III stars in 21cmFAST).

The original 21cmFAST code considers one single redshift-independent stellar SED describing the Pop II stellar population, and uses its properties for the calculations of the ionization of the intergalactic medium (IGM) and the Lyα background radiation field. The SED used by 21cmFAST assumes a Scalo IMF (Scalo 1998), with a metallicity of 1/20 with respect to the solar metallicity, and continuous star formation for 100 Myr (Barkana & Loeb 2005). LIMFAST replaces this SED by a set of 13 metal-dependent stellar SEDs, and uses them to compute the ionization-state of the IGM, the Lyα background and the nebular line emission. This parameterization allows us to connect the processes of galaxy evolution and reionization consistently by using different SEDs that trace the evolution of metallicity with redshift.

The stellar SEDs used by LIMFAST are computed by using `BPASS` v2.1 (Eldridge et al. 2017), assuming a single-star and constant star formation modes over 100 Myr, and a Salpeter (Salpeter 1955) initial mass function with stellar masses within the range $0.5 - 100\,M_\odot$. The 13 SEDs differ from each other by their metallicity value, and they respectively account for the default absolute `BPASS` metallicity values of $Z_\star = [10^{-5}, 10^{-4}, 10^{-3}, 2\times10^{-3}, 3\times10^{-3}, 4\times10^{-3}, 6\times10^{-3}, 8\times10^{-3}, 10^{-2}, 1.4\times10^{-2}, 2\times10^{-2}, 3\times10^{-2}, 4\times10^{-2}]$. `BPASS` provides this range of metallicities that is well suited to reach the low metallicity values that may occur at the redshifts of reionization, as well as the possible higher values in massive objects. The number of ionizing photons per stellar baryon in these SEDs spans the range $\sim 2500 - 6000$, where higher numbers are for more metal-poor SEDs. For comparison, the single value for the number of ionizing photons used in 21cmFAST is 4361, which is in between our maximum and minimum values.

For the calculation of the nebular line emission, we use our stellar SEDs as the incident spectrum in the photoionization code `Cloudy` (version 17.02, Ferland et al. 2017), and the following quantities describing the nebular medium; we consider a gas density of $n_{\rm H} = 10^2$ cm^{-3}, a distance between the radiation source and the medium of $r = 10^{19}$ cm, and the ionization parameter values $\log_{10} U = [-4, -3.5, -3, -2.5, -2, -1.5, -1]$. Changing the value of the ionization parameter with the other quantities fixed would imply that the number of ionizing photons also changes. In practice, however, the number of photons is fixed by the intrinsic SEDs, so we renormalize the resulting nebular emission by the corresponding default number of photons in the SEDs in all cases. In other words, this approach would be equivalent to vary the value of r or $n_{\rm H}$ to obtain different ionization parameter values while keeping a constant number of photons (see similar procedures in Byler et al. 2017, and Xiao et al. 2018). For each SED case, we assume the gas and the SED (the stars) to have the same metallicity. We then perform photoionization calculations combining these metallicity and ionization parameter values and tabulate the emission results in units of luminosity per unit of star formation rate. For a given pair of metallicity and ionization parameter values describing a halo, LIMFAST will then linearly interpolate the tabulated results to derive the luminosity per star formation rate in that halo, $l(M, z)$.

We do not consider dust in these calculations and leave its implementation to future versions of the code. Not including dust implies that the default escape fraction of nebular radiation in LIMFAST is 100%, where we have presently also neglected the effect of neutral hydrogen on the escape and transfer of Lyα emission. In other words, the line emission presented here is the intrinsic one. However, the calculation of the intrinsic emission allows the user to apply desired custom attenuation effects a posteriori at a cell level, e.g., applying analytical extinction prescriptions that depend on redshift or other parameters, or treating the scattering of Lyα emission with the intergalactic H I. Alternatively, one could implement the effects of dust directly on the SEDs (e.g., through a wavelength-dependent attenuation curve) resulting in attenuated nebular spectra, or by linking the dust properties to the halo metallicities resulting from the LIMFAST simulations.

Finally, the default calculations assume a constant escape fraction of ionizing photons of 8% throughout. This value is chosen such that the resulting reionization history is broadly consistent with current constraints as further discussed in Section 7.3. In practice, one can obtain different reionization histories in LIMFAST by

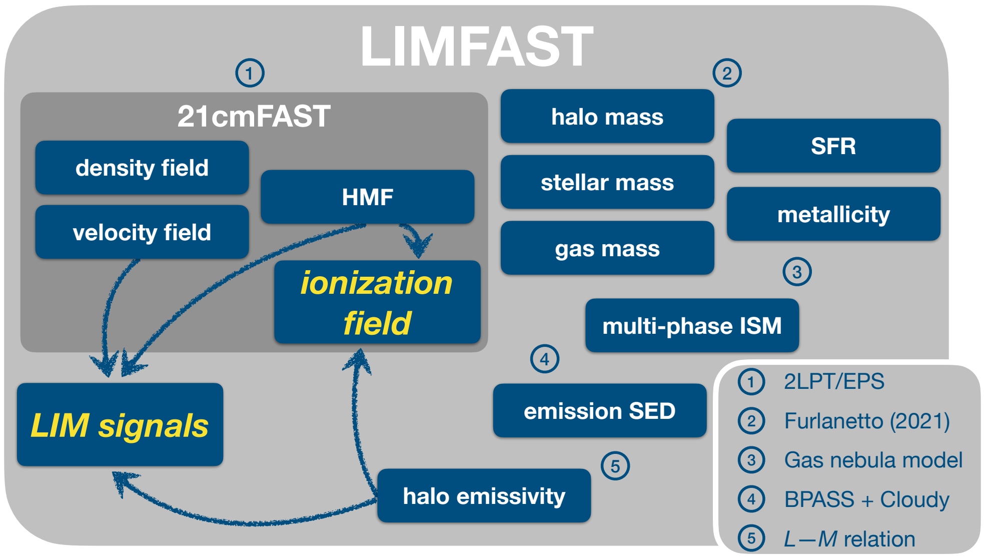

Figure 5.1: The core structure of LIMFAST. Starting from the metal, stellar and gas mass of a given halo of mass M at redshift z arising from the Furlanetto (2021) galaxy models, the halo star formation rate and the metallicity are derived. These last two parameters, combined with the tabulated stellar and nebular SEDs and luminosities computed with `BPASS` and `Cloudy`, then yield to the amount of line and ionizing emission from the halo. The luminosities of all halos in a given cell are integrated with the halo mass function computed by 21cmFAST from the density field and the collapse of structure. Finally, the ionizing radiation is used for the calculation of the ionization of the intergalactic medium and the progress of reionization.

changing the value of the escape fraction, as well as by varying the star formation parameters, such as feedback mode, star formation law, or the minimum halo mass able to host star formation, in the above galaxy model. We explore the impact of some of these variations on the neutral fraction evolution in Paper II.

5.2.3 Ionization Calculation

As mentioned in the previous section, 21cmFAST uses a fix value of 4361 ionizing photons per stellar baryon describing the Pop II stellar population in the ionization calculations at all redshifts. Following our approach of metallicity-dependent SEDs, LIMFAST instead computes a number of ionizing photons that depends and evolves with metallicity. In detail, LIMFAST computes the number of ionizing photons for a halo of a given metallicity by linearly interpolating the number of ionizing photons from the two SEDs with metallicities closer to that of the halo. Then the code integrates the contribution from all the halos in the volume considered, and applies the resulting number of ionizing photons to the ionization calculations in that simulated region. Therefore, because the metallicity of the halos changes with time, the number of ionizing photons also evolves with redshift. Finally, we have not considered radiation transfer effects that may produce further spatial variations in the ionization calculations (see, e.g., Davies & Furlanetto 2022, for a recent discussion on the propagation of ionizing radiation and its effects on 21cmFAST, and Lewis et al. 2022).

Figure 5.1 summarizes the basic parts of the LIMFAST code. Starting from the metal, stellar and gas mass of a given halo of mass M arising from the Furlanetto (2021) galaxy models, the halo star formation rate and the metallicity are derived. These last two parameters, combined with the tabulated stellar and nebular SEDs and luminosities computed with `BPASS` and `Cloudy`, then yield the amount of line and ionizing emission from the halo. The luminosities of all halos in a given cell are integrated with the halo mass function computed by 21cmFAST from the density field and the collapse of structure. Finally, the ionizing radiation is used for the calculation of the ionization of the intergalactic medium and the progress of reionization.

5.2.4 IGM Lyα Emission

The IGM Lyα emission denotes here the Lyα radiation produced in situ in the intergalactic medium due to the recombination of ionized gas leading to the formation of H I. We ignore collisional effects that may also lead to the production of Lyα because these are expected to be subdominant compared to recombination (see further discussions in Silva et al. 2013 and Comaschi & Ferrara 2016).

The comoving Lyα luminosity density from the recombination of IGM gas in a cell can be expressed as

$$\rho^{\rm IGM}_{\rm Ly\alpha,\,rec}(z) = f_{\rm rec}\, E_{\rm Ly\alpha}\, \dot{n}_{\rm rec}(z)\, n_{\rm H\,I}(z)\ , \tag{5.13}$$

where $f_{\rm rec} = 0.66$ denotes the fraction of recombinations producing Lyα photons, $E_{\rm Ly\alpha} = 1.637 \times 10^{-11}$ erg is the energy of the Lyα transition, and $\dot{n}_{\rm rec}(z)$ represents the recombination rate computed by the original 21cmFAST code. The last term above equates

$$n_{\rm H\,II}(z) = [1 - x_{\rm H\,I}(z)]\, n_{\rm b}\, [1 + \delta(z)]\ , \tag{5.14}$$

and it describes the comoving number density of ions in the IGM. Here, $x_{\rm H\,I}(z)$ denotes the neutral hydrogen fraction, $\delta(z)$ corresponds to the matter overdensity, and $n_{\rm b}$ is the present day comoving number density of baryons. The comoving luminosity density can be finally converted to the observed intensity by means of Equation 5.12 as above.

Although the recombination process may lead to the production of other hydrogen lines, we ignore here their contribution. Other than Lyα, Hα would be the brightest of these hydrogen lines, but given the value of its recombination coefficient and the transition probabilities between the atomic energy level of the hydrogen atom, the expected luminosities for Hα are expected to be around one order of magnitude fainter than those of Lyα.

5.2.5 Lyα Background

Another component contributing to the Lyα radiation field is that produced by the scattering of high energy UV photons that, while traveling through the IGM, redshift into the frequency of the Lyman series lines in the rest frame of the IGM gas. When these initially high energy photons reach the frequencies of the Lyman lines they are susceptible to be absorbed by the neutral H I and they can subsequently lead to the processes of resonant scatter or a down-cascade by the electron in the atom that may ultimately produce Lyα radiation.

We follow the calculation of the Lyα background in 21cmFAST, but we use our set of SEDs consistently instead of the single SED used by 21cmFAST. In detail, each of the 13 stellar SEDs is tabulated to account for the number of photons in between the first 23 energy levels of the hydrogen atom as in 21cmFAST (see details of this calculation in Barkana & Loeb 2005 and Mesinger et al. 2011). Then, interpolation is used to find the photon number corresponding to metallicities within those of the two nearest SEDs as done for the line and ionizing emission.

With the Lyα background calculated by 21cmFAST in the frame of the gas in units of photon rate per unit frequency, area and steradian, J_α, the observed intensity can be obtained as (Silva et al. 2013)

$$I = \frac{6\,E_{\rm Ly\alpha}}{(1+z)^4} J_\alpha \,, \tag{5.15}$$

where the term in the denominator accounts for the redshift dimming of the surface brightness.

5.2.6 21 cm Signal

The 21 cm signal sourced by the neutral hydrogen in the intergalactic medium is often expressed as a differential brightness temperature that can take a positive or negative sign depending on whether the gas is emitting or absorbing 21 cm radiation. This differential brightness temperature can be written as (Furlanetto et al. 2006)

$$\delta T_b(z) \approx 27\, x_{\mathrm{H\,I}}(z)\, [1+\delta(z)] \left| 1 + \frac{1+z}{H(z)} \frac{dv_{\parallel}}{dr_{\parallel}} \right|^{-1} \times \left[1 - \frac{T_\gamma(z)}{T_S(z)} \right] \left[\frac{1+z}{10} \frac{0.15}{\Omega_m h^2} \right] \left[\frac{\Omega_b h^2}{0.023} \right] \mathrm{mK}\,. \tag{5.16}$$

Here, T_γ and T_S denote the temperature of the cosmic microwave background (CMB) radiation and the spin temperature of the intergalactic neutral hydrogen, respectively. The term $dv_{\parallel}/dr_{\parallel}$ represents the peculiar velocity gradient of the gas along the line of sight, and it is responsible for introducing redshift-space distortions as detailed in the next section.

The spin temperature term in the above equation traces the CMB temperature and the thermal history of the IGM via different coupling mechanisms. These include the collisional (thermal) coupling of the intergalactic gas, as well as radiative coupling effects through CMB and Lyα photons. The coupling through resonant scattering of Lyα photons is known as the Wouthuysen-Field (WF) effect, and it is sourced by the cosmic soft-UV Lyα background described in the previous section. Taking into account these processes, the offset $1 - T_\gamma/T_S$ can then be expressed as

$$1 - \frac{T_\gamma}{T_S} = \frac{x_c + x_\alpha}{1 + x_c + x_\alpha} \left(1 - \frac{T_\gamma}{T_K} \right)\,, \tag{5.17}$$

where T_K is the kinetic temperature of the intergalactic gas, and x_c and x_α are the collisional and WF radiative coupling coefficients, respectively. While the Lyα background is the responsible for the WF coupling as mentioned above, the heating of the intergalactic gas is mostly dominated by the X-ray background field.

For the calculation of the 21 cm signal, LIMFAST follows the methodology developed in 21cmFAST, except for the Lyα background derivation. As mentioned in the previous section, for the Lyα background we adopt our metallicity-dependent SEDs, which results in a varying Lyα background due to the evolution of metallicity, in addition to that of star formation, with redshift. For the X-ray background, we use the prescriptions relating luminosity and star formation adopted by Park et al. (2019). Finally, for both radiation background calculations, we have modified the original code to take into account our star formation formalism.

5.2.7 Redshift-Space Distortions

We briefly revisit here the formalism of redshift-space distortions (RSD), and show its application to LIM observations targeting 21 cm and other emission lines. Our discussion is based on that in Mao et al. (2012), to which we refer the interested reader for details.

The observation of line emission at a specific frequency and along the line of sight indicates, in principle, the position in redshift space of the sources producing such a line. In reality, however, the observed redshift can be different from the real cosmological one because not only the Hubble expansion determines its value; the line-of-sight peculiar velocity of the sources affects the value of the observed frequency via the Doppler effect which, in turn, results in deviations from the true redshift[2]. Because the peculiar velocities of the sources are typically unknown in observations, the redshift space information is the only one that is observable. Therefore, to predict observed quantities from our simulations, we need to account for the effect of peculiar velocities on the real space calculations. We use the term redshift-space distortions here to refer to the change in apparent position induced by the peculiar velocity of the sources (see Hamilton 1998, for a review on RSD).

As detailed in section 4 in Mao et al. (2012), deriving the cosmological radiative transfer equations for radiation emitted from sources with peculiar velocity, and considering an optically thin medium along the line of sight, one finds that the observed specific intensity can be written as (equation 12 in Mao et al. 2012)

$$I_{\nu_{\rm obs}} = \frac{c L_{\nu_0}\, a\, \nu_{\rm obs}^2}{4\pi \nu_0^3 H(a)} \frac{n'}{\left|1 + \frac{1}{aH(a)}\frac{dv_\parallel}{dr_\parallel}\right|} \ . \tag{5.19}$$

Here, c denotes the speed of light, L_{ν_0} is the rest-frame luminosity of the sources, $H(a)$ represents the Hubble parameter at a scale factor value a, and ν_0 and $\nu_{\rm obs}$ are the rest-frame and observed frequencies of the emission, respectively. The rightmost term denotes the apparent change in the number density of sources due to their peculiar velocities, where n' is the *proper* number density of sources in real space, and $dv_\parallel/dr_\parallel$ is the velocity gradient along the line of sight. Expressing now the

[2]Quantitatively, when peculiar velocities along the line of sight, $v_\parallel$, are present, the position $\boldsymbol{r}$ of a source in real space appears to a position $\boldsymbol{s}$ in redshift space through the expression

$$\boldsymbol{s} = \boldsymbol{r} + \frac{1+z_{\rm obs}}{H(z_{\rm obs})} v_\parallel \hat{r} \ . \tag{5.18}$$

Here, $1 + z_{\rm obs} = (1+z)(1 - v_\parallel/c)^{-1}$, the term $\hat{r}$ is the unit vector along the line-of-sight direction, and $z_{\rm obs}$ and z are the observed and cosmological redshifts, respectively.

observed frequency in terms of the rest-frame one via $\nu_{\rm obs} = \nu_0(1+z)^{-1}(1-v_{\parallel}/c)$, transforming the scale factor to its redshift equivalent, and considering the *comoving* number density of sources, n, we can rewrite the previous equation as

$$\begin{aligned} I_{\nu_{\rm obs}} &= \frac{cL_{\nu_0}(1-v_{\parallel}/c)^2}{4\pi\nu_0 H(z)} \frac{n}{\left|1+\frac{1+z}{H(z)}\frac{dv_{\parallel}}{dr_{\parallel}}\right|} \\ &\simeq \frac{I_\nu(z)}{\left|1+\frac{1+z}{H(z)}\frac{dv_{\parallel}}{dr_{\parallel}}\right|} \,. \end{aligned} \tag{5.20}$$

The last expression above highlights the fact that the observed intensity considering RSD is simply roughly equivalent to the specific intensity computed by LIMFAST (Equation 5.12), with a velocity gradient correction denoted by the denominator. Here, we have omitted the correction term $(1 - v_{\parallel}/c)^2$ in the numerator because its effect is much smaller than that from the denominator. The correction shown in the last term of Equation 5.20 is the one that we will apply to the intensity of the optical and ultraviolet lines computed by LIMFAST. This is the same correction as for the 21 cm radiation field shown in Equation 5.16, but there the 21 cm signal is expressed as a differential brightness temperature instead of as an intensity.

As mentioned before, the above derivation considers an optically thin medium. This assumption is valid for all optical and ultraviolet emission lines accounted for in our work except for Lyα. The reason for this difference is that Lyα is severely affected by the neutral hydrogen gas, both within halos and in the intergalactic medium, due to its resonant nature (see a review on the physics of Lyα in Dijkstra 2017)[3]. For simplicity, we do not address further corrections for Lyα here, but we refer the interested reader to Zheng et al. (2011) for an investigation of the impact of Lyα radiative transfer to RSD.

Finally, the observable of interest that is sensitive to RSD is the power spectrum. Thus, it is also useful to write the intensity and brightness temperature in terms of fluctuations to visualize the impact from the clustering bias of the sources and from RSD when comparing the power spectra of different emission lines. For the intensity case and considering linear scales, this can be expressed as

$$I_{\nu_{\rm obs}} = \bar{I}_\nu(z)\,\frac{1+b\,\delta_{\rm DM}(\boldsymbol{r})}{|1+\delta_{\partial_r v}(\boldsymbol{r})|}\,, \tag{5.21}$$

and substituting the intensity by the differential brightness temperature when taking into account the 21 cm emission. Here, $\bar{I}_\nu(z)$ is the cosmic mean intensity of a given

[3]See a discussion about the optically thin assumption and its validity for 21 cm emission in Mao et al. (2012).

emission line, $\delta_{\rm DM}(\boldsymbol{r})$ denotes the fluctuations of the dark matter density field, and $\delta_{\partial_r v}(\boldsymbol{r}) = \frac{1+z}{H(z)}\frac{dv_\parallel}{dr_\parallel}$, with all three quantities considered in real space. The term b denotes the bias factor of the line emission with respect to the dark matter field, where we assume this emission bias to be the same as that of the sources since we ignore radiative transfer effects. Overall, Equation 5.21 readily shows the known result that the impact of RSD effects will be more significant when the sources of radiation are less biased. This case corresponds to emission sourced by the intergalactic gas, i.e., 21 cm and IGM Lyα[4], while emission from star formation tracing more biased galaxies will be less sensitive to the impact of RSD as shown in the next sections.

The computations of RSD in LIMFAST follows that of 21cmFAST, as described in Mesinger et al. (2011), and includes the numerical approach to transform the data from real to redshift space outlined by Jensen et al. (2013). This method divides each simulation cell into sub-cells of equal intensity and computes their new position according to the peculiar velocities. Then, the sub-cells are re-grid to the original resolution (see section 3.1.2 in Jensen et al. 2013). Finally, for the calculation of intensities with RSD, we use the default 21cmFAST cut-off velocity gradient value of $dv_\parallel/dr_\parallel = 0.2\,H(z)$. This limit is set to avoid extremely large intensities when the velocity gradient presents large values. The exact value for this cut-off is arbitrary but Mao et al. (2012) found that values around the default one used here do not produce extreme departures from the true results (their section 9), although this depends on the specific simulation and case. We have tested that using values $dv_\parallel/dr_\parallel = 0.1\,H(z)$ and $dv_\parallel/dr_\parallel = 0.3\,H(z)$ does not change significantly our results. This cut-off, however, is not required and, therefore, used in the calculations of the 21 cm emission. This is because the full radiative transfer derivation ignoring the optically thin assumption in 21 cm results in terms that go to zero instead of infinity (see section 5.1.1 in Mao et al. 2012). In principle, a similar full derivation would be possible for other lines, but this requires accounting for the specific radiative processes affecting each line of interest. We leave these calculations to future work and here simply use the cut-off method for the optical and ultraviolet lines.

[4] We remind here that we do not account for the Lyα radiative transfer (scattering) that can also affect the fluctuations of this emission line.

5.3 Results

We present here the results from LIMFAST runs considering simulation boxes of 0.5 comoving Gpc and cell size of 2.5 comoving Mpc on a side[5], and from redshift $z = 15$ to $z = 5$[6] the 21cm line, the Lyα IGM and background radiation fields, and the Lyα, Hα, Hβ, [O II] 3727 Å, and [O III] 5007 Å line emission arising from star formation. In Paper II we present the extensions to include CO and [C II] 158 μm emission. We adopt the value $\log_{10} U = -2$ as the fiducial choice in all our calculations, but we will discuss later the impact of changing this ionization parameter value on the oxygen lines. The aforementioned computations require a time of about 5-6 hours in a regular laptop computer. The number of optical or UV emission line calculations has a small impact on the running times, but changes in box or cell sizes can have a major effect on the speed of the calculations, the exact number depending on the specific case. The reasonably short computing time required with our choice of parameters allows the user to explore multiple scenarios via parameter variations and it is one of the major strengths of LIMFAST.

In Section 5.3.1 we present the results for the redshift evolution of some quantities of interest and for the line emission. Section 5.3.2 shows calculations of the power spectra for the line emission at various redshifts. In both cases we also display results from the literature for comparison.

5.3.1 Redshift Evolution

We show below the redshift evolution of the box-averaged star formation rate density, the metallicity and the neutral fraction of intergalactic gas, as well as the evolution of the line emission.

5.3.1.1 Star Formation Rate Density

The black line in Figure 5.2 displays the evolution of the cosmic star formation rate density computed by LIMFAST with the fiducial parameter values described in previous sections. The colored lines denote results from the simulation 2 by Silva et al. 2013, Park et al. (2019), the Pop II-only case of Muñoz et al. (2022), the `THESAN` 1 and 2 simulations by Kannan et al. (2022a), and the analytical Furlanetto et al.

[5] Cosmological distances in the simulation are quoted without the reduced Hubble parameter. We use k [h/Mpc] for the power spectra results to facilitate comparisons with other works.

[6] The galaxy model allows calculations of halos up to $z = 30$, but we here present results below $z = 15$ when the neutral fraction is clearly below 1, and taking into account that our adopted stellar age is 100 Myr. These runs include the calculations of the ionization field, as well as a number of the brightest ultraviolet and optical lines and emission.

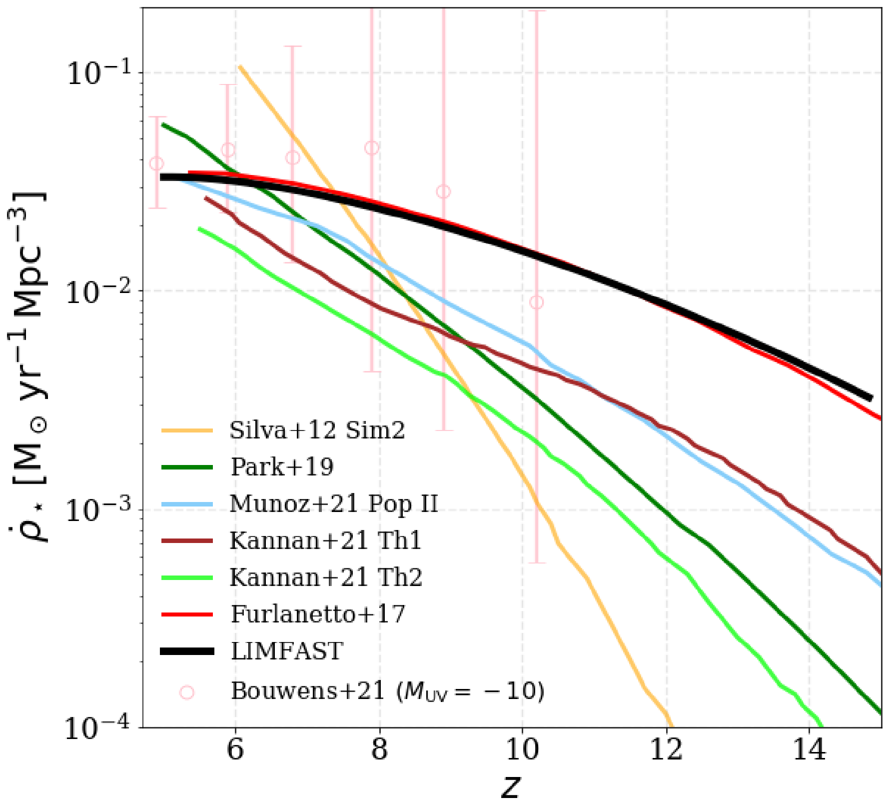

Figure 5.2: Cosmic star formation rate density from LIMFAST. For comparison, we plot also the evolutions from other works as solid colored lines, and the data from Bouwens et al. (2021) extrapolating their luminosity functions to a magnitude $M_{\mathrm{UV}} = -10$.

(2017) galaxy model with momentum-regulated feedback. The data points represent the data from Bouwens et al. (2021), extrapolating their luminosity functions to a magnitude $M_{\mathrm{UV}} = -10$. This magnitude value broadly corresponds to the minimum halo masses considered in our calculations, and the error bars represent the maximum and minimum values allowed by the combination of parameter uncertainties in the Bouwens et al. (2021) luminosity functions; they do not correspond to the 1σ uncertainties.

Overall, the LIMFAST star formation rate density evolution in Figure 5.2, $\dot{\rho}_\star(z)$, broadly agrees with the extrapolated data from Bouwens et al. (2021), although a large range of $\dot{\rho}_\star(z)$ values are allowed by the data beyond $z \sim 6$. Compared to the trends from the literature, the $\dot{\rho}_\star(z)$ derived by LIMFAST is generally higher than that of other works, except for the Furlanetto et al. (2017) case, because we allow star formation to occur down to the atomic cooling halo mass threshold. We discuss

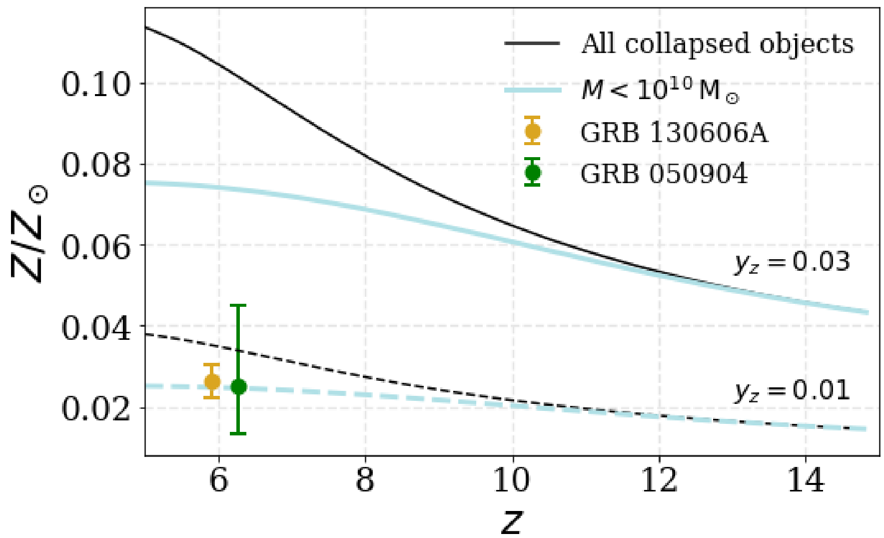

Figure 5.3: Metallicity evolution of the collapsed structure from LIMFAST. The dashed lines represent the alternate case using a value of metal yield, y_Z, three times smaller than the fiducial one. The data points represent the metallicity estimates of the two highest redshift gamma-ray burst (GRB) hosts with confident metal detections to date. The blue lines show the metallicity evolution considering halos of masses $M < 10^{10}$ $M_\odot$, which may be hosts of GRBs. See main text for details.

these comparisons further in Section 7.5.

5.3.1.2 Metallicity

The solid black line in Figure 5.3.1.1 shows the mean metallicity evolution of the collapsed structure, as derived from Equation 5.10 and over the entire simulation box. Specifically, these metallicity values represent the mean metallicity of stars and gas in the simulated cells at the corresponding redshift, but they should not be confused with the mean halo metallicity. For comparison, the dashed black line denotes an alternative case that uses a value of metal yield, y_Z, three times smaller than the fiducial one. For completeness, we show two data points that represent the metallicity estimates of the two highest redshift gamma-ray burst (GRB) hosts with confident metal detections to date. We adopted the metallicity values from Thöne et al. (2013) and Bolmer et al. (2019) for GRB 050904 and GRB 130606, respectively. Because GRBs may preferentially reside and represent the interstellar medium of low mass (i.e., low metallicity) galaxies (e.g., Graham & Fruchter 2017; Palmerio et al. 2019, and references therein), we also show the metallicity evolution considering only halos with masses $M < 10^{10}$ $M_\odot$ as blue lines. Despite the only two data points at these high redshifts and considering the uncertainties associated to metallicity determinations in GRBs and the properties of their host halos (see, e.g., Metha et al. 2021, and references therein), we find broad agreement between these data and our mean values.

5.3.1.3 Neutral Fraction

Figure 5.4 shows the evolution of the gas neutral fraction with redshift computed by LIMFAST, considering the fiducial ionizing escape fraction value of 8%. The colored data represents constraints from McGreer et al. (2015), Davies et al. (2018), Greig et al. (2016), Greig et al. (2019), Mason et al. (2019), Whitler et al. (2020), and Hoag et al. (2019) for comparison. In general, there is broad agreement between the LIMFAST results and the estimates from the literature, and we have tested that ionizing escape fraction values between $\sim$ 6–10% also produce reasonable neutral fraction evolutions. For completeness, the solid lines represent other results from 21cmFAST used in (Mesinger et al. 2016, for their bright and faint galaxies cases) and Park et al. (2019). Although there are differences in the evolution for different cases, all models were tuned to be consistent with the concurrent average electron optical depth values inferred from the cosmic microwave background.

5.3.1.4 Line Emission

To qualitatively illustrate the output of LIMFAST, Figure 5.5 displays LIMFAST light cones for various quantities, where the redshift-slice maps are interpolated to show a continuous evolution of such quantities with redshift. In this case, the light cones cover the redshift range $5 \leq z \leq 15$. From top to bottom, the signals correspond to the hydrogen neutral fraction, the brightness temperature of the 21cm radiation, the star formation rate density, the metallicity of collapsed structure, and the intensity of Lyα emission, arising from star formation and recombination in the intergalactic medium, as well as the intensity of the O II 3727Å line emission. Figure 5.5 allows to easily visualize qualitative correlations between quantities. For example, beyond the well-studied correlation of the 21cm signal with the hydrogen neutral fraction, Figure 5.5 illustrates the increase of metallicity and Lyα emission from star formation with the corresponding evolution of the star formation rate density. Very similar evolutions not displayed here are also found for the Hα and Hβ signals. This similarity arises from the fact that all these lines mostly depend on the number of ionizing photons that is produced, which in turn is proportional to

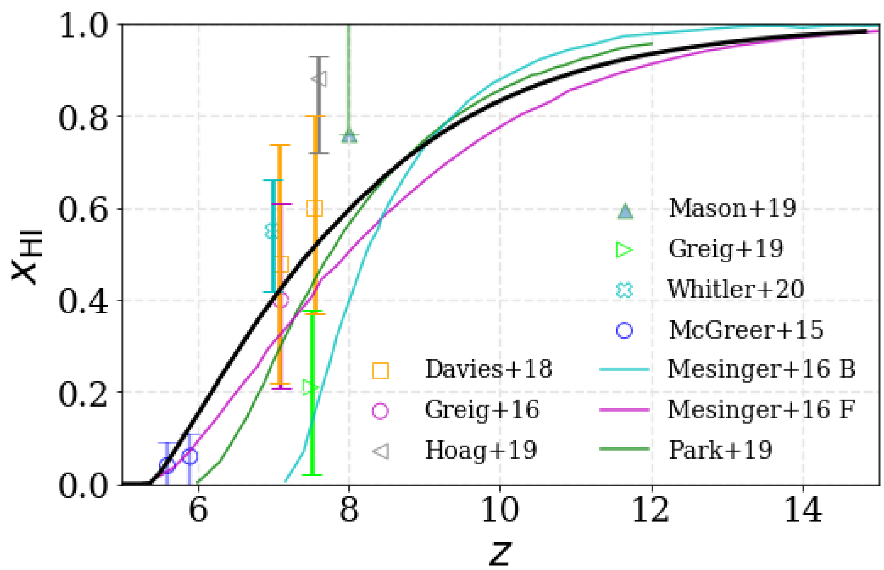

Figure 5.4: IGM neutral fraction evolution as computed by LIMFAST. Evolution of the gas neutral fraction with redshift as computed by LIMFAST with an 8% ionizing escape fraction value (black solid line). For comparison, the colored data show constraints from the literature. Furthermore, the solid lines represent the evolution resulting from other works using 21cmFAST and that match the concurrent average electron optical depth inferred from the cosmic microwave background.

the star formation, and that is also dependent on the specific SED via the metallicity value. However, over the redshift range here considered, the metallicity varies across roughly one order of magnitude, while the star formation rate changes by around six decades, thus making the later quantity the major driver of the signal evolution. The bottom two panels, on the other hand, highlight the strong dependence of the intergalactic Lyα emission on the ionization state of the gas and less on the specific star formation value. For the case of the O II 3727Å signal, its panel shows a steeper evolution of the intensity with redshift compared to that of Lyα from star formation, indicated by the different color gradient in the respective panels. This difference in evolution is driven by the higher sensitivity of the O II 3727Å emission to metallicity compared to Lyα from star formation (we discuss this point further below).

We turn now to a more quantitative analysis of the intensity results and perform comparisons with other works. The solid black lines in Figure 5.6 display the redshift evolution of the line emission brightness computed by LIMFAST. From top to bottom and left to right, the panels show the differential brightness temperature of the 21cm line emission, where negative values denote absorption, the intensity values of Lyα from star formation, Lyα from recombination in the IGM, the Lyα

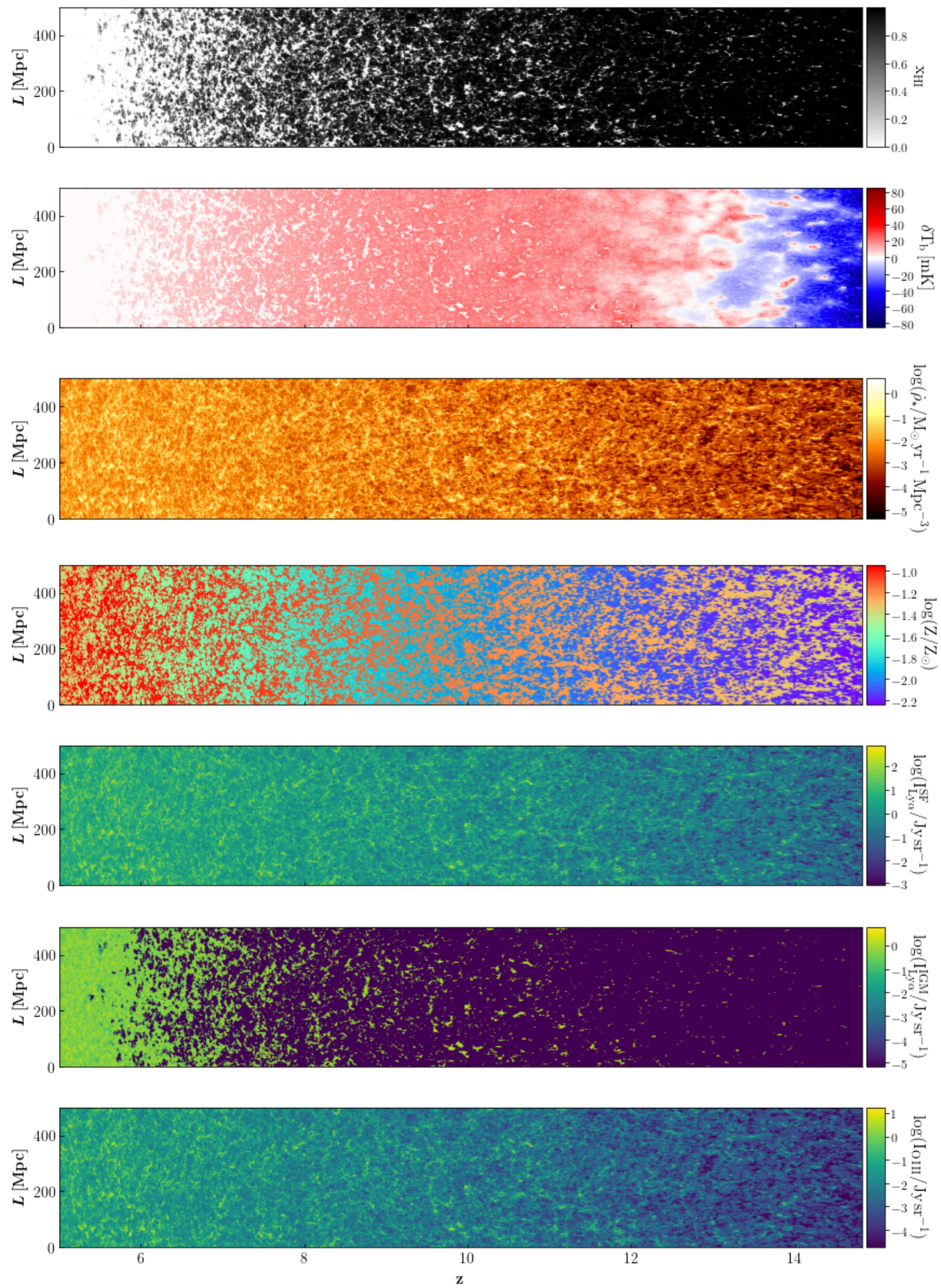

Figure 5.5: LIMFAST light cones covering the redshift range $5 \leq z \leq 15$. From top to bottom, the signals correspond to the hydrogen neutral fraction, the brightness temperature of the 21cm radiation, the star formation rate density, the metallicity of collapsed structure, and the intensity of Lyα emission, arising from star formation and recombination in the intergalactic medium, as well as the intensity of the O II at 3727 Å line emission.

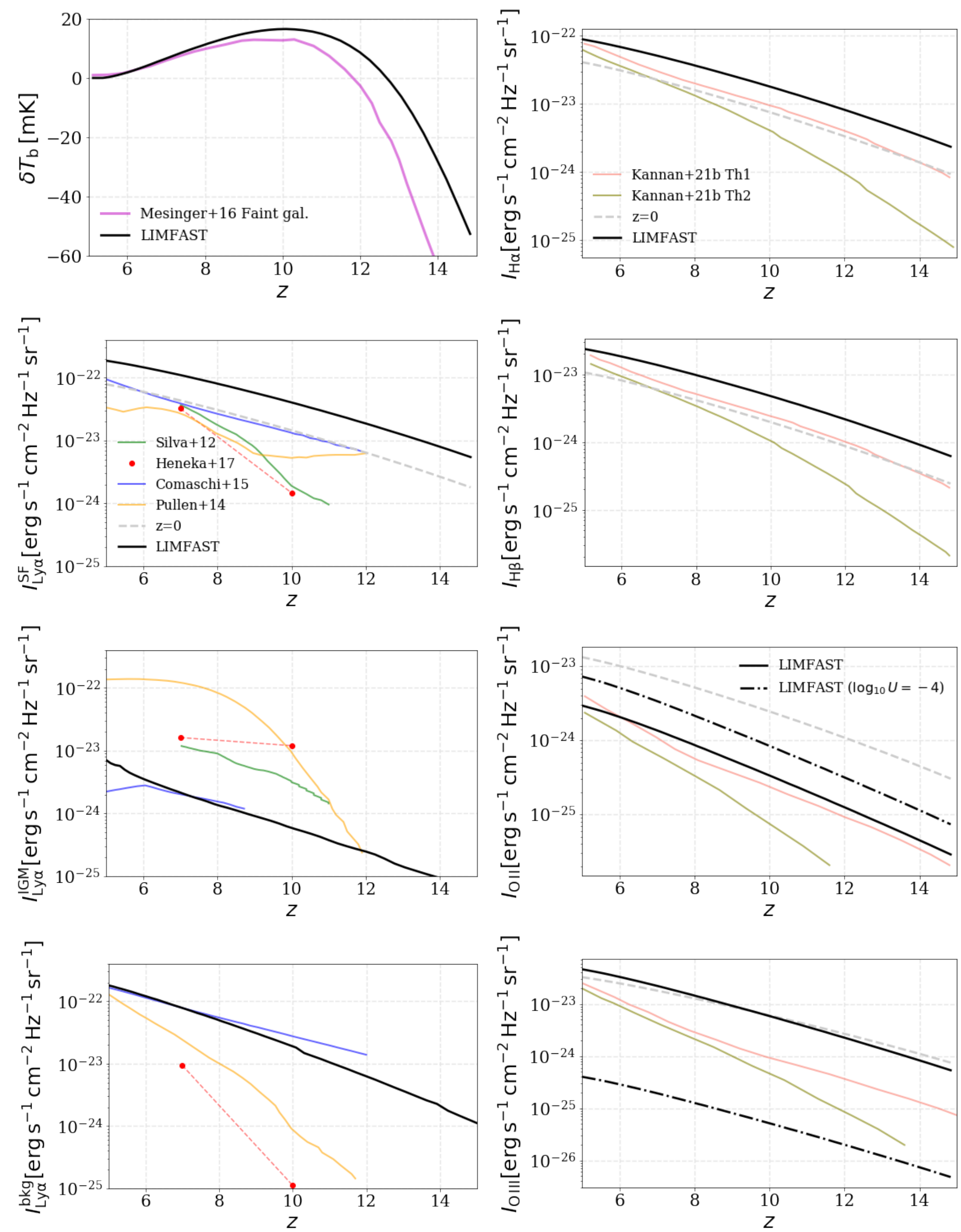

Figure 5.6: Redshift evolution of the emission line brightness from LIMFAST. The colored solid lines represent results from the literature. For the oxygen lines, the dash-dotted black lines denote the LIMFAST results considering an ionization parameter value of $\log U = -4$, instead of the fiducial value of $\log U = -2$ to highlight the sensitivity of the line emission to this parameter value. The gray dashed lines show calculations assuming (local) relations between star formation and luminosity often used in other works.

background, Hα, Hβ, [O II] at 3727 Å, and [O III] at 5007 Å rest frame. The colored solid lines represent results from the works by (Mesinger et al. 2016, their faint galaxies case), Silva et al. (2013), Heneka et al. (2017), Comaschi & Ferrara (2016), Pullen et al. (2014), and the `THESAN` 1 and 2 simulations by Kannan et al. (2022a). For the oxygen lines, the dash-dotted black lines denote the LIMFAST results considering an ionization parameter value of $\log U = -4$, instead of the fiducial value of $\log U = -2$. The gray dashed lines denote calculations assuming relations between star formation and luminosity that are sometimes considered in other intensity mapping works for comparison. These relations, however, are usually derived from local observations and they may not be valid to represent high-redshift galaxies. Considering a relation between luminosity and star formation rate of the form $L = C\,\dot{M}_\star$, the gray dashed lines represent the cases adopting the values of $C = 1.26 \times 10^{41}\,\mathrm{erg\,s^{-1}}\,\dot{M}_\star^{-1}$ for Hα (Kennicutt 1998), $C = 1.3 \times 10^{42}\,\mathrm{erg\,s^{-1}}\,\dot{M}_\star^{-1}$ for Lyα, assuming a factor of 8.7 times more emission for Lyα than that of Hα (Osterbrock 1989), $C = 4.41 \times 10^{40}\,\mathrm{erg\,s^{-1}}\,\dot{M}_\star^{-1}$ for Hβ, arising from the relation Hα/Hβ = 2.86, $C = 7.14 \times 10^{40}\,\mathrm{erg\,s^{-1}}\,\dot{M}_\star^{-1}$ for [O II] from the relation [O II]/Hα = 0.57 (Kennicutt 1998), and $C = 1.32 \times 10^{41}\,\mathrm{erg\,s^{-1}}\,\dot{M}_\star^{-1}$ for [O III] (Ly et al. 2007).

For the case of emission from star formation, the fiducial LIMFAST signal is generally higher than that of other works, driven by the higher average star formation rate density shown in Figure 5.2, and by the fact that we have not applied any attenuation to the emission, contrary to most results from the literature. For the hydrogen lines, this signal is also higher than that derived with local relations because the lower metallicity of high redshift galaxies compared to the local ones results in higher emissivities of ionizing photons and, in turn, recombination emission. For the oxygen lines, however, the emission is very sensitive to the metallicity and ionization parameter values, and it can thus appear to be higher or lower than that from local relations (e.g., Kewley et al. 2019). This highlights the sensitivity of the brightness of the oxygen lines to the value of the ionization parameter, which is of notable importance although typically not taken into account in the intensity mapping modeling literature (but see a discussion on the relevance of this parameter when accounted for in Silva et al. 2017). Figure 5.9 in Section 5.6 shows the relation between luminosity and metallicity at various ionization parameter values for the star-formation emission lines discussed in this work for completeness.

Figure 5.6 overall highlights the plethora of results from various works, where differences between models sometimes exceed one order of magnitude or more.

These differences further increase by their squared power when considering their power spectra, which implies the same level of differences in detectability estimates. This comparison therefore emphasizes the dramatic dependence of detectability estimates and constraints on the models and assumptions, most times disregarded in the literature. We discuss differences between models further in Section 7.5.

5.3.2 Power Spectra

Figure 5.7 shows the power spectra of intrinsic line emission at redshifts $z = 7$, $z = 10$, $z = 12$, with the vertical axes covering different ranges of values for different lines, and where each step (tick) represents a variation of one dex. The solid black lines denote the default LIMFAST calculations, and the dashed gray ones the results considering the local relations between star formation and luminosity introduced in the previous section. For the oxygen lines, the dot-dashed lines represent the alternate case with an ionization parameter value of $\log U = -4$. The black dotted lines illustrate the angle-averaged power spectra for the default calculations, but including the effect of RSD. The colored lines show results from the literature. In detail, the light green lines represent the Silva et al. (2013) results for their total galaxy signal including shot noise (their figure 6), and the dark green lines show the simulated galaxy, intergalactic medium and background results from figure 10 in Silva et al. (2013). The red lines show the results from Heneka et al. (2017), the brown ones from Heneka & Cooray (2021), the yellow ones represent the calculations by Pullen et al. (2014), and the blue ones those by Comaschi & Ferrara (2016). Finally, for the Hα and [O III], the salmon and olive color lines denote the `THESAN` 1 and 2 simulations from Kannan et al. (2022b). For the the 21 cm, the salmon lines represent the data from Kannan et al. 2022a (the right panel in their figure 18), where we have adopted their 10%, 20%, and 60% ionized fraction curves in our $z = 12$, $z = 10$, and $z = 7$ panels, respectively. While these ionization fractions match well our values in Figure 5.4 for $z = 7$ and $z = 10$, we see differences between the curves at $z = 12$ that likely arise from the fact that our ionization fraction values at that redshift are lower than the minimum 10% value in the plot by Kannan et al. 2022a. Figure 5.10 in Section 5.7 displays the same power spectra for the optical and ultraviolet lines, but with the same range of values in all vertical axes for comparison.

As mentioned in the previous section, the differences observed earlier for the evolution of line emission between models are amplified by the squared of the respective values when considering the power spectra. In general, the LIMFAST results in

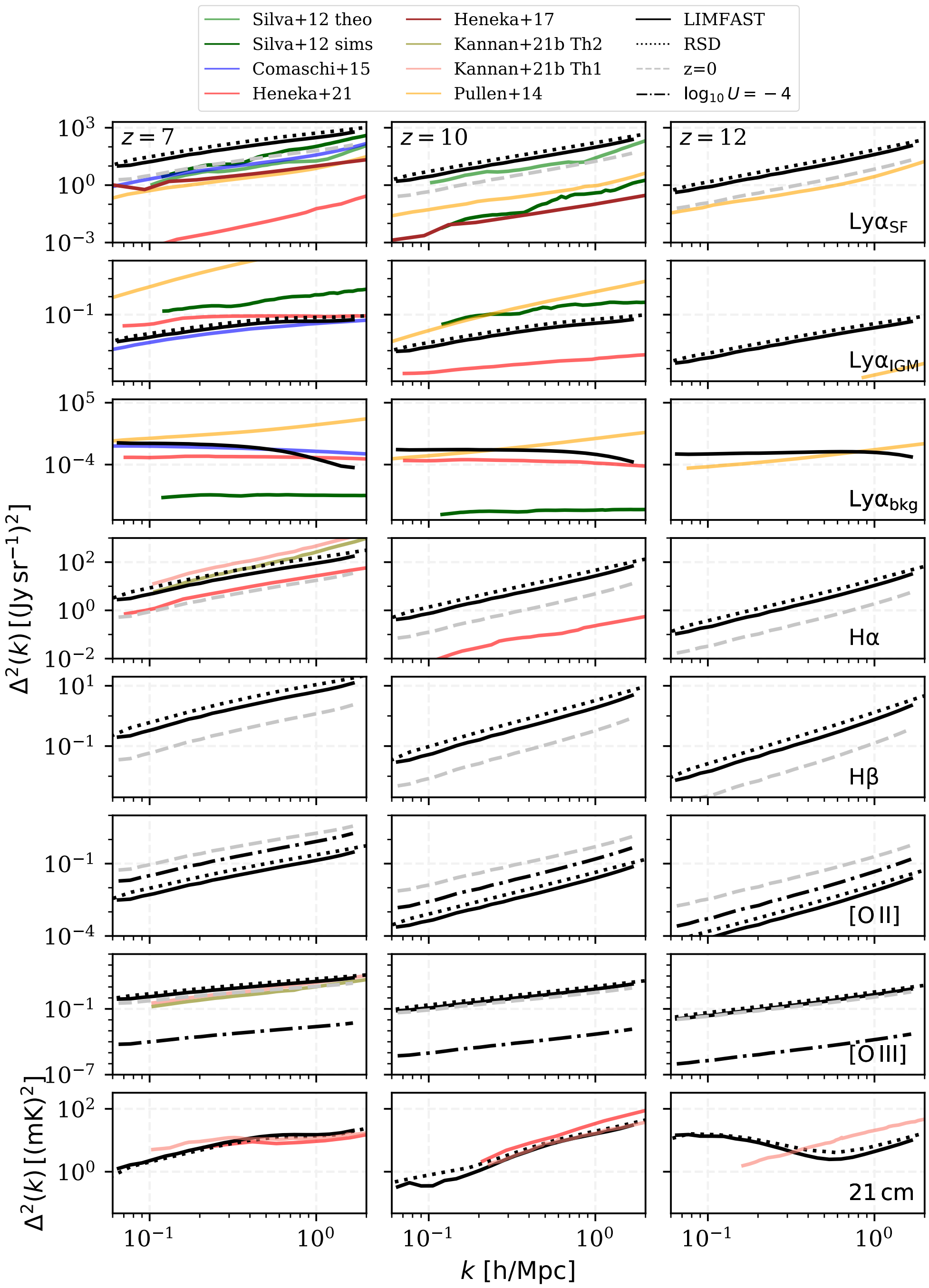

Figure 5.7: Power spectra of intrinsic line emission at $z = 7$, 10, and 12. The solid black lines denote the fiducial LIMFAST calculations, and the dashed gray ones the results considering the local relations between star formation and luminosity introduced in the previous section. For the oxygen lines, the dot-dashed lines represent the alternate case with an ionization parameter value of $\log U = -4$. Finally, the dotted lines denote the angle-averaged power spectra of the fiducial calculations considering the redshift-space distortions produced by peculiar velocities along the line of sight, and the colored lines show results from the literature as detailed in the main text.

Figure 5.7 are in broad agreement with some of the previous works despite the fact that we here present the intrinsic (unattenuated) line emission. However, differences between models in some cases are as large as several orders of magnitude, which again argues in favor of adopting physical and/or observational constraints from individual works with care due to the sensitivity of the results on the modeling. Of most importance are also the differences between the two ionization parameter values for the oxygen lines, which result in one and four order of magnitude differences in the power spectra of [O II] and [O III], respectively. Works modeling these lines should pay attention to this strong dependence. Finally, the comparison between the full LIMFAST calculations and those using the local relations presents power spectrum differences of about one dex for the hydrogen lines. For the case of the oxygen lines, the differences between the two approaches again depend strongly on the ionization parameter considered in the photoionization calculations. Considering RSD in the angle-averaged power spectra has a little effect on the results since RSD impact the line-of-sight direction. In Figure 5.11 in the appendix, we show the two-dimensional power spectra for some of the lines, at redshifts $z = 5.5$, $z = 10$ and $z = 14.5$, where the RSD effect is more discernible. Overall, as mentioned before, the largest impact of RSD along the line-of-sight appears for the 21 cm and Lyα emission sourced by the intergalactic medium (without considering Lyα scattering effects). This is because the intergalactic gas has a small clustering bias and, therefore, the RSD effect is more relevant, as indicated by Equation 5.21. For the case of emission sourced by galaxies, the differences between the results with and without RSD are small since the clustering bias plays the dominant role in driving the distribution of intensities.

5.4 Comparison to Previous Work

Below, we highlight the origin of the main differences between the LIMFAST results and those from the literature. Our goal here is not to detail the specific individual calculations but to identify the parameters that generally play a major role on the results in intensity mapping modeling and that are relevant to LIMFAST.

5.4.1 Comparing Star Formation Results

A significant difference between LIMFAST and other works observed in the previous section is the higher star formation rate density of LIMFAST at redshifts $z \gtrsim 7$. This difference mostly arises from assuming the atomic cooling threshold (10^4 K neutral gas) for hosting star formation in halos, which results in evolving minimum halo mass values from $\log{(M/M_{\odot})} \sim 7$ at $z \sim 20$ to $\log{(M/M_{\odot})} \sim 8$ at $z \sim 5-6$. At the lowest redshifts here explored, the minimum halo mass considered has little effect on the star formation rate because the latter is dominated by massive halos of mass $\log{(M/M_{\odot})} \gtrsim 10-12$. However, at the highest redshifts most halos have small masses and, therefore, the resulting star formation is very sensitive to the minimum halo mass adopted. Some of the other works consider minimum halo masses above the atomic cooling threshold because in these small systems feedback effects may suppress star formation (e.g., Yue et al. 2014; Yue et al. 2018).

We show how changing the minimum halo mass parameter in LIMFAST affects the star formation rate density in Figure 5.8. The solid black line is the fiducial star formation rate density shown in Figure 5.2, which considers all halos above the atomic cooling threshold. The black dotted and dashed curves represent the star formation assuming minimum halos masses of $\log{(M/M_{\odot})} = 8$ and the contribution from halos in the range of masses $8 \leq \log{(M/M_{\odot})} < 10$, respectively. The brown lines show the results from the `THESAN` 1 simulations by Kannan et al. 2022a (their figure 12), where the brown solid line is the total and the dashed one illustrates the contribution from halos of mass $\log{(M/M_{\odot})} = 10$. Furthermore, the dotted brown line denotes the contribution from halos in the mass range $8 \leq \log{(M/M_{\odot})} < 9$, showing that these mass range drives the total values at the highest redshifts. The other colored lines represent the same lines as in Figure 5.2 for comparison. Overall, the value adopted for the minimum halo mass hosting star formation at high redshift has a strong impact in the star formation rate and, in turn, it affects the level of emission when this is proportional to the star formation of the halos. However, visible differences are still present between LIMFAST and `THESAN`, especially regarding the contribution from small halos. Although the upper mass limit in the two respective ranges is different, the impact from halos of mass $\log{(M/M_{\odot})} \leq 8$ is notable as visible by the difference between the solid and dotted black lines at $z \gtrsim 8$. We attribute the differences between the two codes to the different star formation prescriptions used in each case.

5.4.2 Comparing Line Emission and Power Spectra Results

A fundamental distinction between the LIMFAST and literature results for line emission in Figure 5.6 is that we have presented the intrinsic emission instead of the attenuated one. The effect of dust and gas attenuation can be treated on-the-fly or post-processed, analytically or numerically, and can be linked to the properties of the simulated gas or simply accounted for in the photoionization calculations

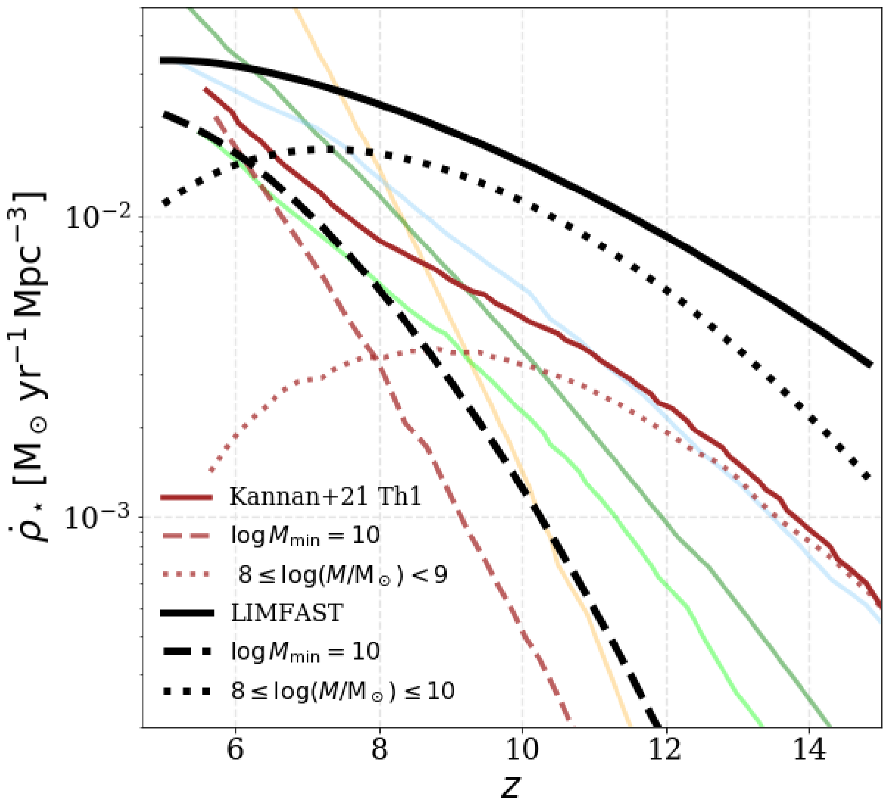

Figure 5.8: Contributions to the cosmic star formation rate density. The different line types consider different minimum halo masses and halo mass ranges able to host star formation. The other colored lines represent the results from other works as in Figure 5.2.

as a property of the nebular gas. Because of these different approaches, we leave the implementation of attenuation effects to future work, but it is still important to compare the evolution of the line emission. The left panels in Figure 5.6 for Lyα from star formation show good agreement in the shape of the evolution between the LIMFAST and the Comaschi & Ferrara (2016) results, arising from the fact that both calculations assume the atomic cooling threshold as the limiting halo mass to host star formation. Generally, other works show a steeper decrease towards high redshift because of the impact of a lower number of small halos as discussed above. Similarly, the slope of the LIMFAST evolution for other lines matches well that from the THESAN 1 simulations. There is no such a match for the THESAN 2 case because these simulations do not resolve the small halos that drive the signal at high redshift, resulting in a steeper evolution (Kannan et al. 2022a). Finally, once again we emphasize the differences in amplitude arising from the usage or not of local relations, and from different ionization parameter values on the oxygen lines, a resource that can be exploited to retrieve information about the physical properties of the interstellar medium (Silva et al. 2017).

In some cases, very large differences exist between some works, especially for the Pullen et al. (2014) and Heneka et al. (2017) results for the intergalactic and background Lyα compared to LIMFAST and Comaschi & Ferrara (2016). We have tested that using a minimum halo mass for star formation of $\log(M/M_{\odot}) = 10$ produces Lyα background signals closer to those of Pullen et al. (2014) and Heneka et al. 2017 (not shown), and we ascribe further differences between Heneka et al. (2017) and LIMFAST to the respective modeling and simulations. Finally, we note that Comaschi & Ferrara (2016) pointed to an inaccurate treatment of the ionization history of the IGM in Pullen et al. (2014), which may contribute to the observed signals.

As mentioned before, the differences observed for line emission roughly increase by their squared value when comparing the power spectra. The exact value also depends on the specific clustering bias parameter used in different works, but we find no extraordinary behaviors when comparing these results. Perhaps most significant are the differences between theory and simulations in the Silva et al. (2013) work, highlighting the model sensitivity, and the strong decrease of between three and five orders of magnitude for the star formation Lyα signal (both at $z = 7$ and $z = 10$; see Figure 5.7 and also Figure 5.10) between Heneka et al. (2017) and Heneka & Cooray (2021) with the same simulations and modeling.

5.5 Conclusion

In this paper we have introduced LIMFAST, a semi-numerical code to perform the modeling of line emission in the intensity mapping regime at the redshifts of reionization and in short time scales. LIMFAST implements the modern galaxy formation and evolution models by Furlanetto (2021) on the underlying large scale structure computed by 21cmFAST, and makes use of pre-computed stellar synthesis and photoionization results from `BPASS` and `Cloudy` to obtain line emission. In Section 5.2 we have detailed the galaxy model and the calculation of 13 stellar and nebular spectral energy distributions (SEDs) covering the metallicity range $0.5 \gtrsim \log(Z/Z_{\odot}) \gtrsim -3$, and for different values of the ionization parameter. These SEDs are used self-consistently at each redshift step, following the evolution of stellar and gas metallicity with time, for the calculations of halo line emission, the ionizing background that drives the progress of reionization and the Lyα background relevant to the 21 cm spin-flip temperature of the intergalactic gas. We have presented the results from LIMFAST runs in simulation boxes of 0.5 comoving Gpc side with cell sizes of 2.5 Mpc side in Section 7.3. These runs require about 5-6 hours in a regular laptop computer and they consider the evolution of galaxies and the intergalactic medium from redshift $z = 15$ to $z = 5$. The runs include the calculations of the ionization field, the 21cm line, the Lyα IGM and background radiation fields, and the Lyα, Hα, Hβ, [O II] 3727Å, and [O III] 5007Å line emission arising from star formation. We have compared our results with a number of previous works from the literature, discussing the main aspects of the discrepancies in Section 7.5. Our main findings are as follows:

1. The average star formation rate density computed by LIMFAST appears higher than most works at redshifts $z \gtrsim 8$ because LIMFAST considers the atomic cooling threshold for the minimum halo mass able to host star formation (Figure 5.2). However, the LIMFAST prediction is broadly consistent with the values allowed by extrapolating the luminosity function results by Bouwens et al. (2021) down to a magnitude $M_{\rm UV} = -10$, and with the analytical calculations of Furlanetto et al. (2017). Changing the minimum halo mass in the code to higher values such as $\log(M/M_\odot) \sim 9$–10 allows the user to obtain star formation histories that match those of other works (Figure 5.8).

2. LIMFAST produces a neutral fraction evolution of the intergalactic gas that is broadly consistent with reionization constraints from the literature, considering a fiducial ionizing escape fraction value of 8% (Figure 5.4).

3. The redshift evolutions and the power spectra of line emission from LIMFAST are in broad agreement with other works in the literature (Figures 5.6 and 5.7). In particular, the redshift evolution of line emission matches well — those from works that consider the contribution of small halos at high redshifts. In some particular cases, however, large differences with LIMFAST or with other works exist, which stresses the sensitivity of the results and, more importantly, the inferred constraints on the specific modeling. Redshift-space distortion effects on the power spectra appear to be small when considering the emission produced by galaxies, due to the large bias of these sources. However, when the radiation originates in the IGM, such as the 21 cm line or Lyα emission

from recombination of the intergalactic gas, redshift-space distortions can have a larger impact on the signals (Figure 5.11).

4. We have also shown that the luminosity and star formation relations derived from observations in the local universe that are often used in the literature are not well suited for studies during reionization, owing to the dependence of the emission on metallicity. Finally, the choice of the ionization parameter value has a dramatic impact on the amplitude of the [O II] 3727Å and [O III] 5007Å line emission, and it should be carefully accounted for in the modeling of these lines.

In this first paper of the LIMFAST series we have introduced the general structure of LIMFAST and some capabilities and calculations. In Paper II, we take into account the modeling of photodissociation regions (PDRs) for the inclusion of the [C II] 158 μm and CO lines. We anticipate further implementations such as the aforementioned inclusion of attenuation effects from gas and dust, or the treatment of Population III star formation, as well as the calculation of continuum emission to address questions related to the cosmic infrared background. LIMFAST enables calculations over large volumes and for a variety of frequencies in a short time scale, and it is therefore a useful complement to more complex numerical simulations that resolve the smaller scales, such as the recently presented `THESAN` simulations by Kannan et al. (2022a), to advance on the modeling of intensity mapping signals.

Acknowledgement

We thank Steven Furlanetto, Adam Trapp and Fred Davies for useful discussions and comments during this project. We acknowledge support from the JPL R&TD strategic initiative grant on line intensity mapping. This research was carried out at the Jet Propulsion Laboratory, California Institute of Technology, under a contract with the National Aeronautics and Space Administration.

5.6 Appendix: Luminosity Dependence on U and Z

Figure 5.9 shows the dependence of the luminosity of emission lines arising from star formation on metallicity and ionization parameter. The luminosity of the oxygen lines changes by orders of magnitude when varying the metallicity, while the changes in hydrogen line emission are of a factor of a few. Furthermore, varying the ionization parameter also has a major impact on the oxygen lines, with an opposite effect for the O II and O III ions.

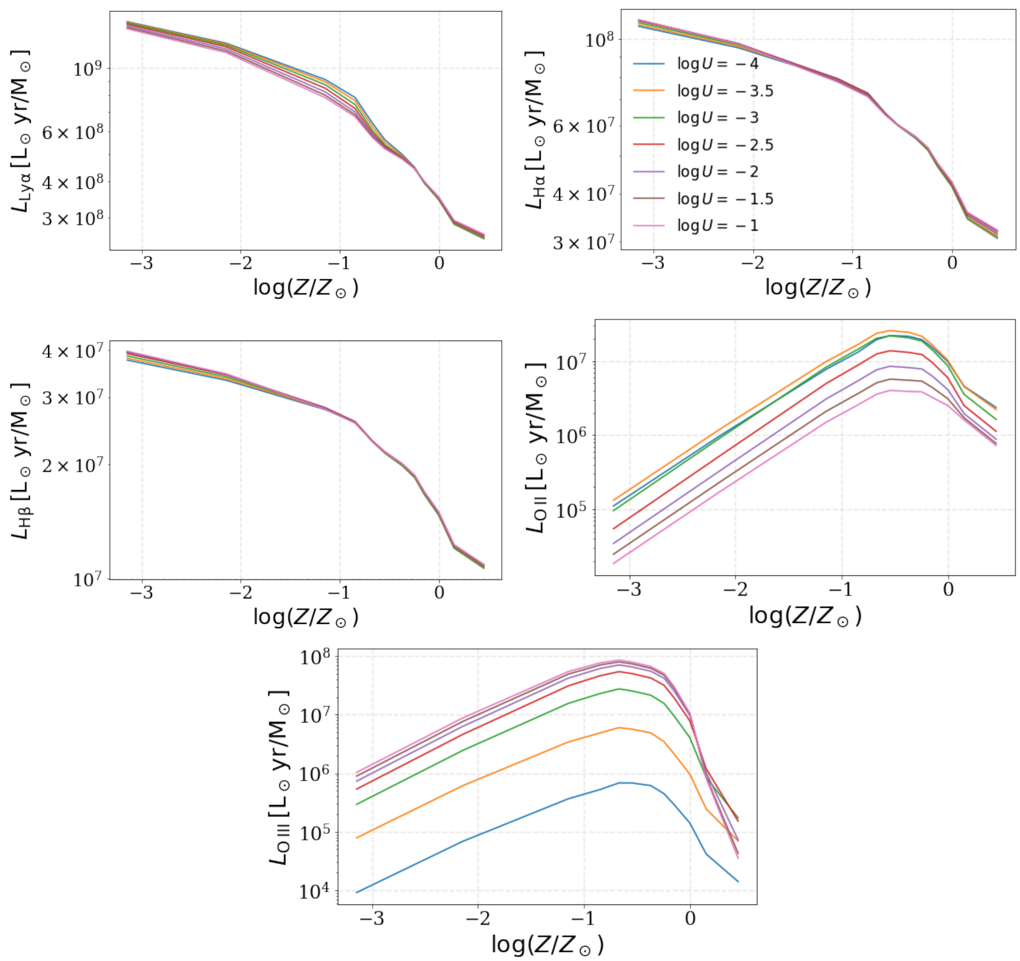

Figure 5.9: Dependence of star-formation line luminosities on metallicity and ionization parameter. Note that scales in the vertical axes vary for different lines.

5.7 Appendix: Power Spectra of Optical and UV Line Emission

Figure 5.10 shows the same power spectra in Figure 5.7 but focusing on the optical and ultraviolet lines that have been implemented in LIMFAST and with the same range of values in all vertical axes for comparison. Here the vertical range spans 12 orders of magnitude and highlights some large differences between models. Of notable relevance are the differences in the power spectra of the [O III] emission between the default $\log U = -2$ and alternate $\log U = -4$ cases due to the sensitivity of this line to the ionization parameter.

5.8 Appendix: 2D Power Spectra with Redshift-Space Distortions

Figure 5.11 displays the two dimensional power spectra for a selection of lines simulated by LIMFAST when including RSD, at redshifts (from left to right) $z = 5.5$,

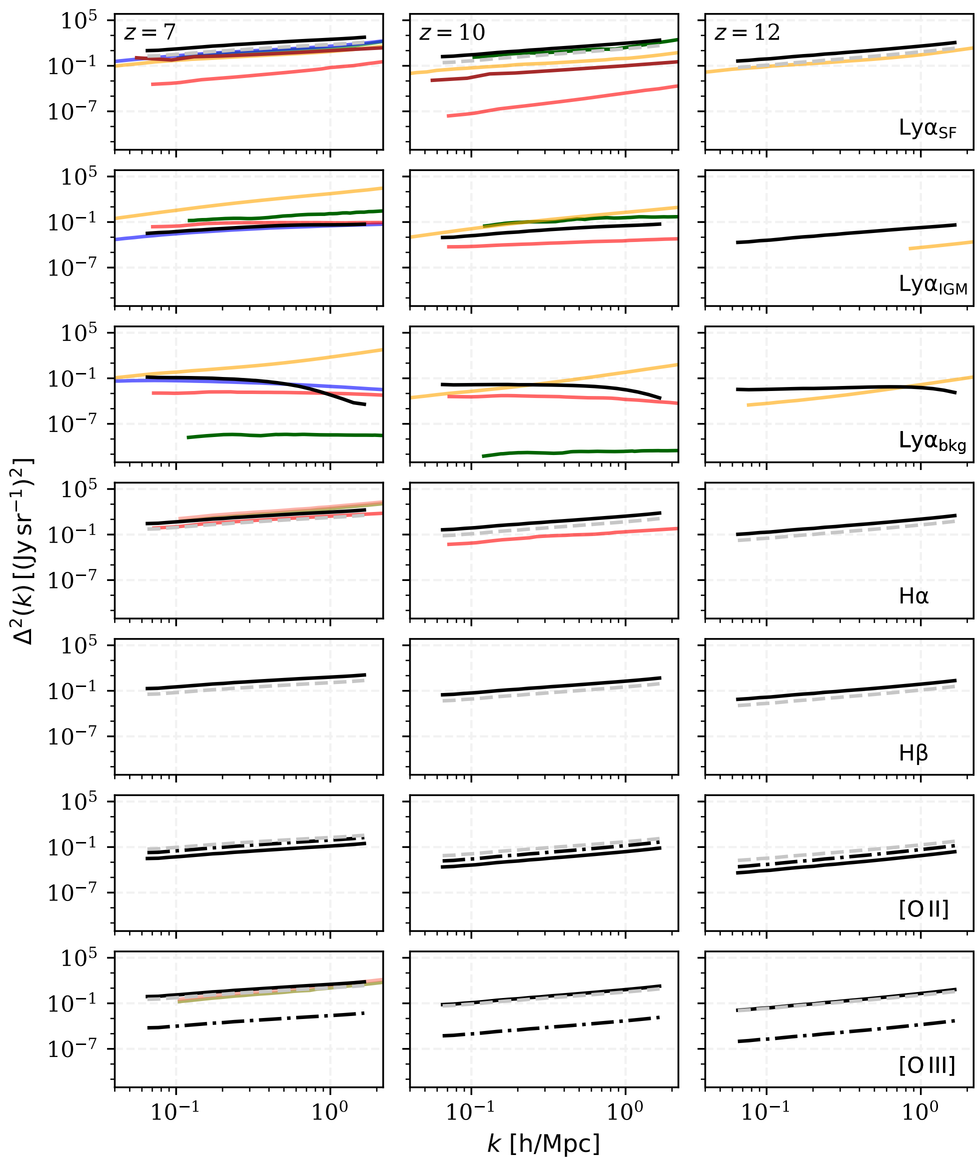

Figure 5.10: Same as Figure 5.7, but with same vertical axis ranges.

$z = 10$ and $z = 14.5$. The colorbars cover different scales to facilitate visualization, where the quoted values express power, i.e., I_ν^2/V, with the specific intensity in cgs units and the volume in Mpc. Due to the large effect of RSD for the case of 21 cm emission, we here used an arbitrary normalization and range of values for visualization. The case of intergalactic Lyα emission at $z = 14.5$ is not displayed because the ionized regions that produce the emission are small enough at this redshift that the plot appears as single colored. The overlaid contour plots denote the power for the non-RSD case in black and for the RSD case in red for comparison. Some contour lines in the top right corner of the plots may appear spurious due to the small number of points for their calculation in that region. Overall, the RSD effect along the line of sight is most visible for lines that trace and are sourced by the intergalactic gas, i.e., the 21 cm line and the intergalactic Lyα radiation. When the clustering bias of the sources is large, as it is the case of halos, the RSD impact is less important than for the intergalactic gas case, as indicated by Equation 5.21.

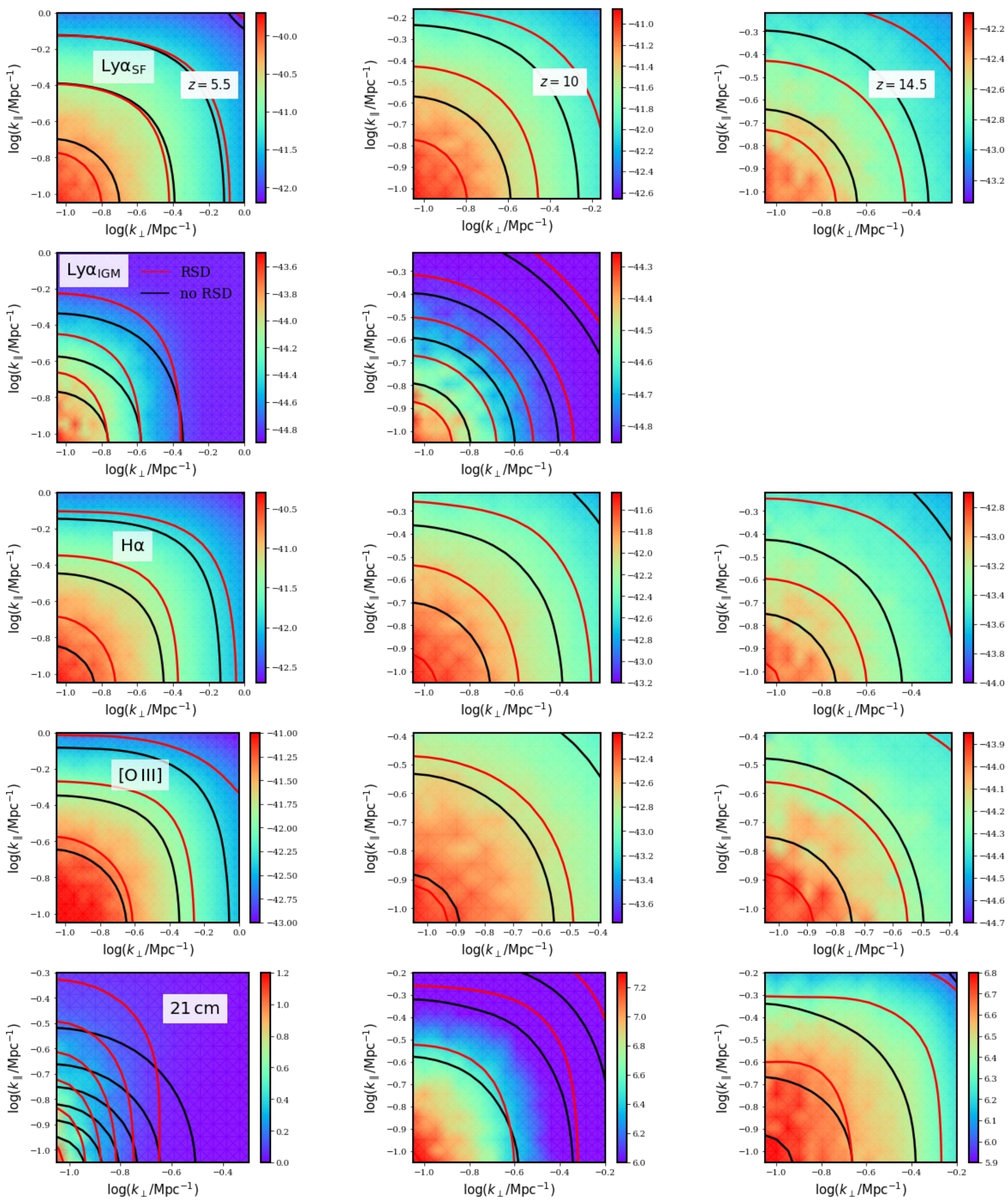

Figure 5.11: 2D power spectra simulated by LIMFAST taking into account RSD. The case of intergalactic Lyα emission at $z = 14.5$ is not displayed because the ionized regions that produce the emission are small enough at this redshift that the plot appears as single colored. The overlaid contour plots denote the power for the non-RSD case in black and for the RSD case in red for comparisons. As noted in the main text, the impact of RSD is more significant for those lines that trace the bulk of the intergalactic gas (i.e., 21 cm and Lyα from the IGM) instead of for those from the more biased halos.

Chapter 6

LIMFAST. II. LINE INTENSITY MAPPING AS A PROBE OF HIGH-REDSHIFT GALAXY FORMATION

Sun, G., Mas-Ribas, L., Chang, T.-C., et al. (2022). "LIMFAST. II. Line Intensity Mapping as a Probe of High-Redshift Galaxy Formation", preprint, arXiv:2206.XXXXX. https://arxiv.org/abs/2206.XXXXX.

Abstract

The epoch of reionization (EoR) offers a unique window into the dawn of galaxy formation, through which high-redshift galaxies can be studied by observations of both themselves and their impact on the intergalactic medium. Line intensity mapping (LIM) promises to explore cosmic reionization and its driving sources by measuring intensity fluctuations of emission lines tracing the cosmic gas in varying phases. Using LIMFAST, a novel semi-numerical tool designed to self-consistently simulate LIM signals of multiple EoR probes, we investigate how building blocks of galaxy formation and evolution theory, such as feedback-regulated star formation and chemical enrichment, might be studied with multi-tracer LIM during the EoR. On galaxy scales, we show that the star formation law and the feedback associated with star formation can be indicated by both the shape and redshift evolution of LIM power spectra. For a baseline model of metal production that traces star formation, we find that lines highly sensitive to metallicity are generally better probes of galaxy formation models. On larger scales, we demonstrate that inferring ionized bubble sizes from cross-correlations between tracers of ionized and neutral gas requires a detailed understanding of the astrophysics that shape the line luminosity–halo mass relation. Despite various modeling and observational challenges, wide-area, multi-tracer LIM surveys will provide important high-redshift tests for the fundamentals of galaxy formation theory, especially the interplay between star formation and feedback by accessing statistically the entire low-mass population of galaxies as ideal laboratories, complementary to upcoming surveys of individual sources by new-generation telescopes.

6.1 Introduction

The enormous amount of observational and modeling efforts over the past two decades have revealed an increasingly detailed and precise picture of the epoch of reionization (EoR). Following the onset of the first galaxy formation at $z > 10$ (Oesch et al. 2016; Naidu et al. 2020; Bouwens et al. 2021; Harikane et al. 2022) and being completed by $z \approx 5$–6 (McGreer et al. 2015; Becker et al. 2021; Cain et al. 2021), the neutral intergalactic medium (IGM) after cosmic recombination was ionized again by an accumulating background of energetic UV photons emerged from the evolving populations of early star-forming galaxies (Fan et al. 2006a; Stark 2016; Dayal & Ferrara 2018; Robertson 2021; but see also e.g., Qin et al. 2017 for alternative sources like quasars).

An emerging technique in observational cosmology, line intensity mapping (LIM) has been widely recognized as a powerful method to study the co-evolution of galaxies and the IGM during the EoR (Kovetz et al. 2017; Chang et al. 2019). Particularly, the prospects of synergies among LIM surveys targeting at different (and usually complementary) tracers have attracted considerable attention in recent years, as more and more target lines being identified and observed at wavelengths across the electro-magnetic spectrum. Substantial theoretical effort has been made in recent years to investigate the scientific potentials of multi-tracer LIM. One important objective is to employ the large-scale complementarity between tracers of ionized and neutral regions in the IGM to tomographically measure the reionization history (e.g., Lidz et al. 2011; Gong et al. 2012; Heneka et al. 2017; Dumitru et al. 2019; Kannan et al. 2022b). Such joint analyses can trace the growth of ionized regions and alleviate observational challenges like systematics and foreground contamination. Another major objective is to infer physical properties of the source population through simultaneous diagnosis of multiple spectral lines emitted from the multi-phase interstellar medium (ISM) and/or IGM (e.g., Heneka et al. 2017; Sun et al. 2019; Yang et al. 2021; Schaan & White 2021; Bethermin et al. 2022). Even though the coarse-grain averaged nature of these statistical measurements makes the interpretation challenging in many circumstances, these efforts have showcased the richness of astrophysical information about the EoR to be gleaned from multi-tracer LIM datasets.

Nevertheless, the majority of modeling efforts in the LIM context can be broadly considered as "semi-empirical", which leverage a small number of simple, observationally-motivated trends to describe the source population and create mock LIM signals.

Although these models provide quantitative expectations of LIM signals anchored to observations, clear physical connections among properties of the source population and different observables are often missing (but see Kannan et al. 2022b, who employ fully-detailed, radiation-magneto-hydrodynamic simulations of reionization with photoionization and radiative transfer modeling to study multi-tracer LIM). Relatively little effort has been devoted so far to the development of physical yet efficient modeling frameworks that capture the essential astrophysical information, while being flexible enough to allow model testing and inference from multi-tracer LIM datasets. For these reasons, we have developed LIMFAST, a semi-numerical toolkit for self-consistently simulating a multitude of LIM signals during the EoR, as introduced in detail in Mas-Ribas et al. (2022, henceforth Paper I). LIMFAST extends the 21cmFAST code, and implements significantly improved models of galaxy formation and line emission in the high-z universe.

In this work, we present a generalization and applications of the basic framework of LIMFAST introduced in Paper I, by considering physically-motivated variations of stellar feedback and star formation law prescriptions. Given the important consequences these variations have on galaxy and IGM evolution during the EoR, we investigate their implications for a number of promising LIM targets for probing the EoR, including the 21 cm line of H I and nebular lines at optical/UV (e.g., Hα, Lyα) and far-infrared (e.g., [C II], [O III], CO) wavelengths. Such a generalization allows us to relate specific LIM observables to a fundamental picture of high-z galaxy formation described by a balance maintained by star formation from the ISM and stellar feedback typically from supernovae (Furlanetto et al. 2017; Furlanetto 2021). By characterizing how these astrophysical processes impact the summary statistics of different LIM signals, especially the auto- and cross-power spectra, we investigate how the underlying astrophysics of feedback-regulated star formation can be better understood from future LIM observations combining different line tracers.

The remainder of this paper is structured as follows. In Section 6.2, we briefly review LIMFAST, including its basic code structure and functionalities. In Section 8.2, we specify key features of the galaxy formation model and its variations considered in this work, namely prescriptions for stellar feedback and the star formation law. We also introduce a supplement to the baseline nebula model discussed in Paper I, which allows us to model lines emitted from the photodissociation regions (PDRs) and molecular gas irradiated by the interstellar radiation field sourced by star formation. In Section 7.3, we present the main quantitative results of this work about how variations of the galaxy model affect the reionization history, followed by how distinct forms of feedback and the star formation law may be revealed by multi-tracer LIM observations. We compare our results with previous work, discuss some limitations and caveats of the analyses presented, and outline several possible extensions of the current framework in Section 6.5, before summarizing our main conclusions in Section 7.6. Throughout the paper, we assume cosmological parameters consistent with recent measurements by Planck Collaboration XIII (Planck Collaboration et al. 2016b).

6.2 The LIMFAST Code

In Paper I, we describe in detail the general features and applications of the LIMFAST code. Here, we only briefly review the key features of LIMFAST and refer interested readers to the paper for further details.

Built on top of the 21cmFAST code (Mesinger et al. 2011; Park et al. 2019), LIMFAST shares with it the efficient, semi-numerical configuration adopted to approximate the formation of the large-scale structure and the partitioning of mass into dark matter halos. Specifically, the evolution of density and velocity fields is calculated with the Lagrangian perturbation theory, whereas the hierarchical formation of structures and the growth of ionized regions are described by the excursion set formalism (Lacey & Cole 1993; Mesinger & Furlanetto 2007), without resolving individual halos. Using the overdensity field derived, LIMFAST replaces the simplistic galaxy formation model used in 21cmFAST by a quasi-equilibrium model of high-z, star-forming galaxies introduced by Furlanetto et al. (2017) and Furlanetto (2021), which predicts a range of physical properties important for LIM studies, including the gas mass, stellar mass, star formation rate (SFR), metallicity, and so on. The line intensity fields of interest are then computed by integrating emissivities predicted by the photoionization and radiative transfer simulation code, Cloudy (Ferland et al. 2017), over the halo mass function conditional on the local overdensity. Following Mesinger et al. (2011), we normalize integrals of the subgrid conditional halo mass function in the Press-Schechter formalism (Bond et al. 1991) to match the mean values from the Sheth-Tormen formalism.

LIMFAST coherently simulates a variety of LIM signals that trace the reionization and the underlying galaxy formation histories. In Paper I, the simulated cosmic star formation rate density and the IGM neutral fraction evolution are verified by comparing against latest observations of high-z galaxies/quasars and the cosmic microwave background (CMB), whereas LIM statistics of a suite of (mainly optical/UV) nebular lines typically from H 2 regions (e.g., Lyα, Hα, [O II], and [O III]) are compared with other high-z model predictions in the literature. Extensions and variations of the baseline model presented in Paper I, including an extended model of emission lines that predominantly originate from the neutral ISM (e.g., [C II] and CO), are introduced in this work to facilitate the analysis.

6.3 Models

To understand the connection between astrophysics of galaxy formation and LIM signals originating from different environments, especially the multi-phase ISM, and demonstrate the astrophysical applications of multi-tracer LIM studies, we need to consider some plausible variations of the galaxy formation model, and preferably a large set of line signals sensitive to the variations and different gas phases. In what follows, we will describe how the baseline LIMFAST simulation presented in Paper I is extended for such purposes.

6.3.1 Models of Galaxy Formation and Evolution

Following the galaxy formation model described in Paper I based on Furlanetto et al. (2017) and Furlanetto (2021), the star formation and chemical evolution of individual halos can be described by a set of simple, coupled ordinary differential equations.

Expressing any given mass in terms of the dimensionless quantity $\tilde{M} \equiv M/M_0$, where M_0 denotes the halo mass at some initial redshift z_0, and taking derivatives with respective to redshift for the time evolution (i.e., $\tilde{M}' = d\tilde{M}/dz$), we can express the evolution of halo mass, gas mass, stellar mass, and metal mass as

$$\frac{\tilde{M}'}{\tilde{M}} = -|\tilde{M}_0'| \, , \tag{6.1}$$

$$\frac{\tilde{M}_g'}{\tilde{M}_g} = -|\tilde{M}_0'| \left[X_g^{-1} - \frac{\epsilon(\mathcal{R}+\eta)}{|\tilde{M}_0'| C_{\rm orb}} \left(\frac{1+z_0}{1+z} \right) \right] \, , \tag{6.2}$$

$$\tilde{M}_*' = -\mathcal{R} \tilde{M}_g \left[\frac{\epsilon}{C_{\rm orb}} \left(\frac{1+z_0}{1+z} \right) \right] \, , \tag{6.3}$$

$$\frac{\tilde{M}_Z'}{\tilde{M}_Z} = \mathcal{R} \left(-1 - \eta + y_Z Z^{-1} \right) \left[\frac{\epsilon}{C_{\rm orb}} \left(\frac{1+z_0}{1+z} \right) \right] \, , \tag{6.4}$$

where $C_{\rm orb} = (1 + z_0) A_{\rm dyn} \Delta_{\rm vir}^{-1/2}$ characterizes the parameter dependence of the orbital timescale, which is set by some normalization factor $A_{\rm dyn}$ and the virial overdensity of a collapsed halo $\Delta_{\rm vir} = 18\pi^2$. A constant return fraction $\mathcal{R} = 0.25$ is taken to describe the fraction of stellar mass recycled back to the star-forming gas due to stellar evolution (Benson 2010; Tacchella et al. 2018). A metal yield $y_Z = 0.03$ is adopted, which is appropriate for metal-poor, Population II (Pop II) stars with a typical initial mass function (Benson 2010).

To investigate what astrophysics of galaxy formation may be inferred from LIM data, we consider a total of 6 model variations involving different assumptions for the underlying feedback mode and star formation law, which are described by the value (or functional form) of the mass loading factor, η, and the temporal efficiency factor, ϵ, respectively. Our baseline model assumes that stellar feedback is momentum-driven ($\eta \propto M^{-2/3}(1 + z)^{-1}$) and sets ϵ to a fiducial value of 0.015 consistent with local observations (Krumholz et al. 2012), which is referred to as Model Ia. A set of feedback variations are considered, where we explore a range of feedback modes leading to different star formation efficiency (SFE), especially in low-mass halos, while fixing ϵ. In Model II, we consider energy-driven feedback ($\eta \propto M^{-1/3}(1 + z)^{-1/2}$), whereas in Model III (IV) we envisage a more extreme scenario where the coupling between stellar feedback and the star-forming gas is weaker (stronger) than the momentum-driven (energy-driven) case. Specifically, a weak coupling in Model III assumes $\eta \propto M^{1/6}$, whereas a strong coupling in Model IV assumes $\eta \propto M$, with the redshift dependence being dropped in both cases for simplicity.

On the other hand, a set of star formation law variations are explored in Models Ib and Ic for momentum-driven feedback, where we further allow ϵ to vary moderately with the gas mass and thus yield star formation surface density–gas surface density relations corresponding to those implied by observations and/or theoretical predictions. In Model Ib, we adopt $\epsilon \propto M_g^{0.2}$ which reproduces the well-known Kennicutt-Schmidt law (Kennicutt 1998) with a power-law index of 1.4, whereas in Model Ic we adopt $\epsilon \propto M_g^{0.4}$ to approximate the star formation law with a power-law index of 2 as suggested by Faucher-Giguère et al. (2013), where the gas disc is assumed to be entirely turbulence-supported by stellar feedback.

Solving Equations (6.1)–(6.4), we obtain the growth histories of stellar and gas masses in dark matter halos as they continuously accrete from an initial redshift of $z_i = 30$. Figure 6.1 shows the growth histories of gas, stellar, and metal masses for

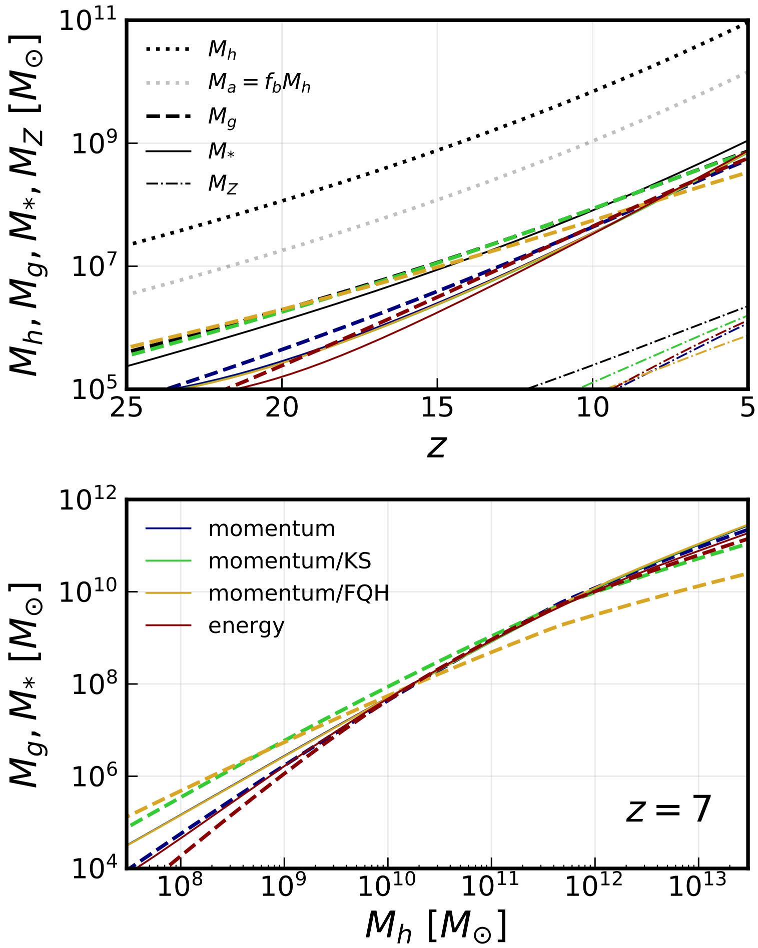

Figure 6.1: Halo properties derived from the galaxy model used in LIMFAST. Top: the mass growth histories of a sample halo reaching $M \approx 10^{11}\ M_\odot$ at $z = 5$ calculated by solving the system of differential equations from $z_i = 30$. The black set of curves show halo properties calculated by the bathtub model with constant $\eta = 10$ and $\epsilon = 0.015$. The sets of curves in blue, green, yellow, and red show the results of models "momentum" (Model Ia), "momentum/KS" (Model Ib), "momentum/FQH" (Model Ic), and "energy" (Model II), respectively. For reference, the dotted curve in grey indicates the total accreted baryonic mass, which is more than 10 times larger than the mass of gas and stars formed as a result of strong feedback regulation. Bottom: the gas/stellar mass–halo mass relations at $z = 7$ predicted by different choices of the feedback mode and star formation law.

a sample dark matter halo with $M \approx 10^{11}\ M_\odot$ at $z = 5$, derived from models with different feedback and star formation law combinations considered in this work. An averaged star formation efficiency (SFE) can be defined consequently as the stellar mass–halo mass ratio, namely $\tilde{f}_* = M_*/M_a$, which can be interpreted as

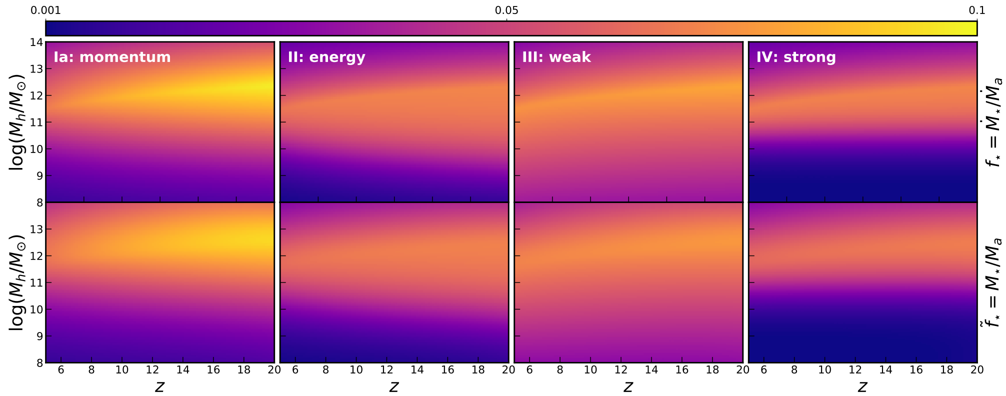

Figure 6.2: The star formation efficiency. The mass and redshift dependence of the instantaneous (top row) and time-averaged (bottom row) star formation efficiencies calculated using different feedback prescriptions.

Table 6.1: Specifications of the baseline model and its variations. Specifications of the baseline model and its variations considered for LIM power spectrum analyses. The adopted value of the escape fraction is varied accordingly to ensure that the reionization completes by $z \approx 5.5$.

Model	Feedback Mode	Star Formation Law	f_{esc}
Ia	momentum	$\epsilon = 0.015$	10%
Ib	momentum	KS	10%
Ic	momentum	FQH	10%
II	energy	$\epsilon = 0.015$	12.5%
III	weak	$\epsilon = 0.015$	5%
IV	strong	$\epsilon = 0.015$	30%

the time-integrated value of the instantaneous SFE $f_* = \dot{M}_*/\dot{M}_a$ — both are often derived in the literature with halo abundance matching (HAM), namely by matching the halo number density described by the halo mass function to the galaxy number density described by the galaxy UV luminosity function (e.g., Mason et al. 2015; Mashian et al. 2016; Sun & Furlanetto 2016; Furlanetto et al. 2017; Tacchella et al. 2018; Behroozi et al. 2019). For simplicity, we limit the stellar population resulting from our star formation prescriptions to Pop II stars only, and defer a systematic introduction of Population III (Pop III) stars to future studies (see Section 6.5.4). Figure 6.2 shows the instantaneous and time-averaged SFEs derived in different feedback prescriptions as a function of halo mass and redshift. The steepness of the color gradient indicates how strongly the fraction of accreted gas turned into stars is regulated by stellar feedback.

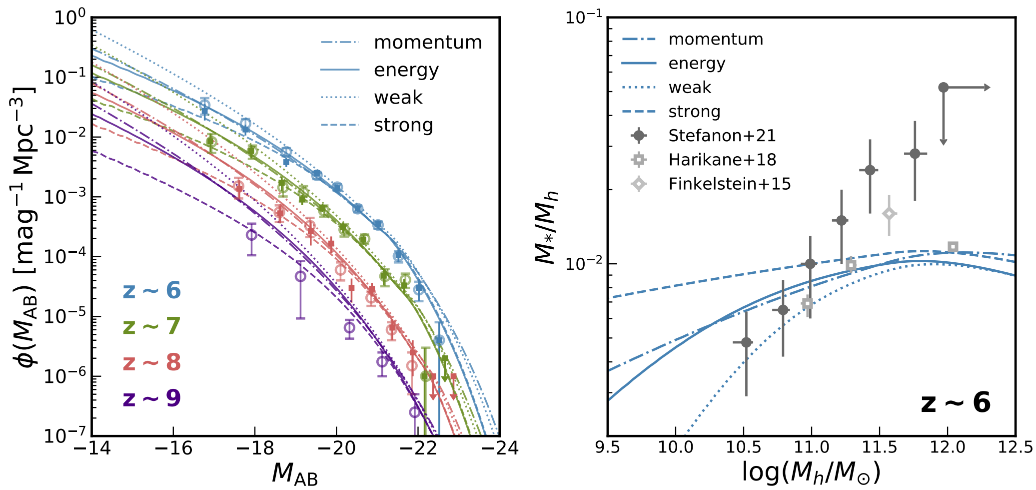

Figure 6.3: Galaxy luminosity function and stellar-to-halo mass relation from LIM-FAST. Left: galaxy rest-frame UV luminosity functions under different feedback assumptions. The predicted luminosity functions are compared against the observational constraints from Bouwens et al. (2015b) and Bouwens et al. (2021), as represented by the filled squares and empty circles, respectively. The $z = 6$, $z = 8$ and $z = 9$ luminosity functions are offset vertically by a multiplicative factor of 2, 0.5 and 0.25, respectively, for ease of comparison. Right: comparison of the galaxy stellar-to-halo mass ratios implied by different feedback assumptions to the latest estimates from observations based on clustering analysis (Harikane et al. 2018) and HAM (Finkelstein et al. 2015; Stefanon et al. 2021).

In Figure 6.3, we show a comparison between the observed galaxy UV luminosity functions and stellar-to-halo mass relation (SHMR) and our model predictions at $z \gtrsim 6$. As illustrated in the left panel, we verify that luminosity functions implied by the four feedback prescriptions considered are all reasonably well-consistent with constraints on the faint end from the Hubble Space Telescope (HST) data (Bouwens et al. 2015b, 2021). In the right panel, we show that the SHMRs predicted by our model variations are roughly consistent with observations in the low-mass regime. At the high-mass end, our predictions only agree well with estimates based on the galaxy clustering (Harikane et al. 2018), but not those based on HAM (Finkelstein et al. 2015; Stefanon et al. 2021), which are a factor of 2–3 larger. We note that lots of these uncertainties associated with EoR galaxies will be greatly reduced by new-generation telescopes like the James Webb Space Telescope (JWST), but as will be illustrated in what follows the information from multi-tracer LIM observations, which cover much wider areas wherein the entire galaxy population is accessed, will still be extremely valuable and complementary.

6.3.2 A Multi-Phase Extension of the Nebula Model

As described in Paper I, the numerical photoionization code Cloudy (version 17.02, Ferland et al. 2017) is supplemented to galaxy properties predicted by the galaxy formation model in LIMFAST to simulate the production of various emission lines as target LIM signals. Here, we extend the baseline nebular model introduced in Paper I, which mainly accounts for lines produced in H 2 regions, to include bright emission lines of particular interest to LIM studies from the neutral (atomic/molecular) ISM, such as [C II] 158 μm, and CO(1–0) 2601 μm lines. We note that because any legitimate nebular model based on Cloudy can be used as the input of LIMFAST, in what follows we do not repeat the analysis of optical/UV lines discussed in Paper I with the new nebular model. For Hα, Lyα, and [O III] 88 μm lines considered in this work, we simply reuse the results from Paper I, although in principle they can be captured together with lines originating from the neutral ISM by a generalized nebular model.

For lines emitted from atomic or molecular gas, namely in PDRs or H_2 cores of gas clouds, because their strengths depend on the gas content, we define an equivalent surface area $\mathcal{S}$ according to the distribution of gas density in giant molecular clouds (GMCs) following the prescription from Vallini et al. (2018). For simplicity, the gas mass M_g of a given halo is assumed to be evenly distributed among the population of GMCs with the same fixed mass $M_{\rm GMC}$, such that the total line luminosity can be simply scaled from that of one single GMC. Specifically, to describe the internal structure of GMCs, we first define a volumetric distribution of gas density ρ that follows a log-normal probability distribution function (PDF), as suggested by models of isothermal, non-self-gravitating, turbulent gas (e.g., Passot & Vázquez-Semadeni 1998; Padoan & Nordlund 2002). Namely,

$$P_V(\rho) \propto \frac{1}{\sqrt{2\pi}\sigma} \exp\left[-\frac{(\ln(\rho/\rho_0) - \langle \ln(\rho/\rho_0)\rangle)^2}{2\sigma^2}\right], \tag{6.5}$$

where $\rho_0 = \mu m_{\rm p} n_{\rm H,0}$ is the mean gas density of the GMC, with $n_{\rm H,0} = 100\,{\rm cm}^{-3}$ and $\mu = 1.36$ accounting for helium. The logarithmic scatter σ satisfies $\langle \ln(\rho/\rho_0)\rangle = -\sigma^2/2$, maintaining a fixed expectation of $\ln(\rho/\rho_0)$ as σ varies. The distribution of σ depends on the turbulence level characterized by the Mach number $\mathcal{M}$ through

$$\sigma^2 = \ln(1 + b^2\mathcal{M}^2)\,, \tag{6.6}$$

where $b = 0.3$ describes the efficiency of turbulence production and we take $\mathcal{M} = 5$, a plausible value for high-redshift galaxies that tend to have more supersonic structures (see discussion in e.g., Safarzadeh & Scannapieco 2016). Since in this work we focus on lines with low to intermediate critical densities (rather than e.g., high-J CO lines tracing the densest regions in GMCs), we ignore self-gravity, which has the critical effect of modifying the density distribution into a power law at high enough densities. The PDF is normalized such that its integral over gas density gives the total volume of the GMC,

$$V_{\rm GMC}^{\rm tot} = \int dV = \int P_V(\rho|\mathcal{M}) d\rho = \frac{4\pi}{3} R_{\rm GMC}^3 , \tag{6.7}$$

where $R_{\rm GMC} = 15\,{\rm pc}$ specifies the size of one GMC, implying a mass of $M_{\rm GMC} = \rho_0 V_{\rm GMC}^{\rm tot} = 4.7 \times 10^4\,M_\odot$. This allows one to conveniently define a characteristic length scale corresponding to each density ρ,

$$r(\rho) = \left[\int_{\rho-\delta\rho}^{\rho+\delta\rho} P_V(\rho'|\mathcal{M}) d\rho' \right]^{1/3} , \tag{6.8}$$

with which an equivalent surface area $\mathcal{S} = 4\pi r^2$ can be defined for the cumulative line flux $f_{\rm line} = 4\pi j_{\rm line}$ in units of ${\rm erg\,s^{-1}\,cm^{-2}}$. The line luminosity density (i.e., $l_{\rm line} \equiv dL_{\rm line}/dV$) can be then expressed as

$$l_{\rm line}(\rho) = \frac{4\pi r^2(\rho)}{V_{\rm GMC}^{\rm tot}} f_{\rm line}(\rho, Z_g, U) , \tag{6.9}$$

where $f_{\rm line}(\rho, Z_g, U)$ means that the line luminosity is a function of gas density, gas metallicity, and ionization parameter in Cloudy. Figure 6.4 shows the cumulative emissivities of the three FIR/mm-wave lines considered in this work, for a gas density of $n_{\rm H,0} = 100\,{\rm cm}^3$ and an interstellar radiation field (ISRF) of strength $G_0 = 10^3$ in units of the Habing flux, which we adopt as fiducial parameters in our model, consistent with observations of the ISM at high redshifts (Gullberg et al. 2015; Wardlow et al. 2017). The line luminosity of the GMC is consequently given by

$$\mathcal{L}_{\rm line}^{\rm tot} = \int l_{\rm line}(\rho) P_V(\rho|\mathcal{M})\, d\rho . \tag{6.10}$$

Finally, to arrive at the total line luminosity of a halo of gas mass M_g, we simply scale $\mathcal{L}_{\rm line}^{\rm tot}$ by

$$L_{\rm line}^{\rm tot} = \mathcal{L}_{\rm line}^{\rm tot} M_g / M_{\rm GMC} . \tag{6.11}$$

Figure 6.5 shows the luminosity–star formation rate relations for [O III], [C II], and CO lines from $z = 6$ (solid) and $z = 8$ (dashed) galaxies as predicted by our galaxy models. For comparison, we also plot empirical representations of the observed

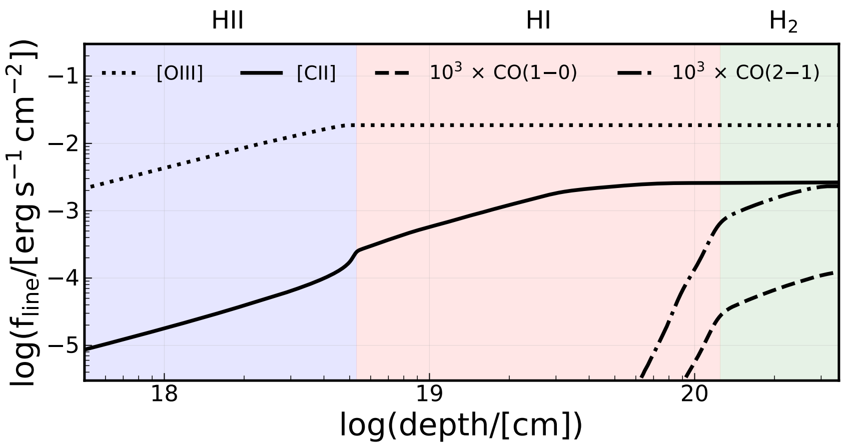

Figure 6.4: Line emissivities predicted by the Cloudy model in LIMFAST. Cumulative emissivities of [O III] 88 μm, [C II] 158 μm, CO(1–0) 2601 μm, and CO(2–1) 1300 μm lines calculated with Cloudy assuming a gas cloud with density $n_{\rm H}$ = 100 cm^3 and metallicity Z = 0.002 illuminated by the interstellar radiation field $G_0 = 10^3$ in the Habing flux. Note that CO lines are enlarged by 1000 times for the ease of comparison. Background colors indicate different ISM phases where the lines predominantly originate from, with the boundaries corresponding to where sharp changes in the gas kinetic temperature profile occur.

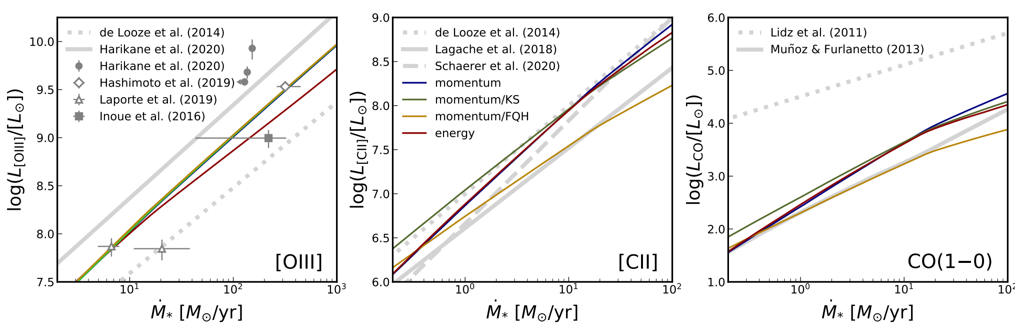

Figure 6.5: The line luminosity–star formation rate relations. The luminosity–star formation rate relations of [O III], [C II], and CO(1–0) lines at $z \sim 6$ predicted by LIMFAST assuming different stellar feedback and star formation law prescriptions. Empirical fittings to observations of nearby/low-z galaxies (Lidz et al. 2011; De Looze et al. 2014) and high-z galaxies (Harikane et al. 2020; Schaerer et al. 2020), as well as predictions from physically-motivated high-z ISM models (Lagache et al. 2018; Muñoz & Furlanetto 2013) from the literature are shown by the gray lines. Because of the relatively dearth of high-z [O III] emitters observed, a selected number of recent [O III] observations at $z > 6$ are also shown for comparison (Inoue et al. 2016; Hashimoto et al. 2019; Laporte et al. 2019; Harikane et al. 2020).

luminosity–star formation rate relations for low-z galaxies (Lidz et al. 2011; De Looze et al. 2014), together with high-z fitting relation (Harikane et al. 2020) and predictions based on physically-motivated ISM models (Muñoz & Furlanetto 2013; Lagache et al. 2018). For [C II] emission, recent observations of $4 \lesssim z \lesssim 6$ galaxies (e.g., Schaerer et al. 2020) suggest a lack of evolution in the $L_{[\mathrm{CII}]}$–SFR relation from that in the local universe (De Looze et al. 2014), which slightly disfavors some theoretical predictions derived from a combination of semi-analytical models of galaxies and photoionization simulations (Lagache et al. 2018).

6.3.3 Emission Lines From the IGM

Besides nebular emission lines produced in the multi-phase ISM, for the IGM emission LIMFAST also inherits and improves on the detailed 21 cm calculations from 21cmFAST, while adopting a simple prescription for recombination emission from the diffuse, ionized IGM in Lyα. As detailed in Sections 2.5 and 2.6 of Paper I, where interested readers are referred to for a complete description, the modeling of these emission lines from the IGM is also fully coupled with the galaxy formation model and its variations implemented in LIMFAST. This allows the influence of galaxy astrophysics on the statistics of 21 cm and IGM Lyα emission to be studied self-consistently with other emission lines from the ISM as tracers of the galaxy distribution.

6.4 Results

In this section, we present the main quantitative results of this paper derived from the set of model variations specified in Table 8.1. We first show the global reionization histories implied by models with varying feedback prescriptions (Section 6.4.1), which supplements the model predictions presented in Paper I based on Model Ia only, and then present how the corresponding sky-averaged signals of various lines are sensitive to the changes in feedback. Next, we demonstrate how variations of the feedback mode (Section 6.4.3) and the star formation law (Section 6.4.4) in play affect summary statistics, namely the auto- and cross-correlation power spectra of tracers of neutral and ionized IGM. By examining the shape and amplitude evolution of power spectra, we elaborate on how astrophysical information about ionizing sources and the IGM may be extracted in turn from joint analyses of multi-tracer LIM observations. For clarity, all results presented in the remainder of this section are shown in real space, without considering observational effects such as redshift space distortions (RSDs), whose treatment in LIMFAST is elaborated in

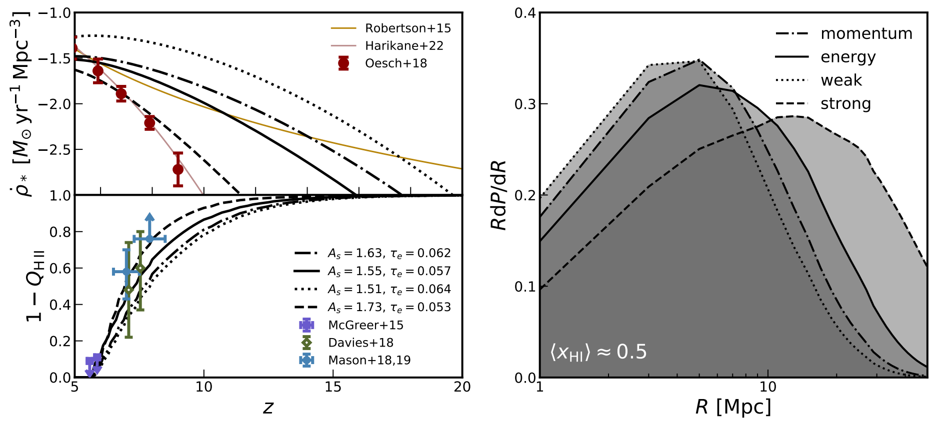

Figure 6.6: Cosmic SFRD, IGM neutrality, and ionized bubble size distribution from LIMFAST in different feedback modes. Left: the redshift evolution of the cosmic SFRD (top) and the mean neutrality of the IGM (bottom) simulated by LIMFAST models with different feedback assumptions. Also shown in the top panel are observational constraints on the SFRD from Oesch et al. (2018) integrated down to $M_{\rm UV} = -17$, along with empirical fits from Robertson et al. (2015) and Harikane et al. (2022) assuming different amounts of extrapolation for the faint populations. Observational constraints on the mean IGM neutral fraction from the dark fraction in the Lyα and Lyβ forests (McGreer et al. 2015), IGM damping wing signatures in quasar spectra (Davies et al. 2018), and Lyα emission from Lyman-break galaxies (Mason et al. 2018, 2019) are shown in the bottom panel. Curves of different feedback mode are also labeled by an asymmetry measure, $A_{\rm s}$, of the EoR history, and the implied CMB electron scattering optical depth, τ_e, which is verified to be consistent with the latest observational constraints (Pagano et al. 2020; Qin et al. 2020b). Right: the bubble size distribution derived with the "mean free path" approach when the IGM is approximately half-ionized.

Section 2.7 of Paper I.

6.4.1 Reionization Histories

Effects of feedback regulation on star-forming galaxies as ionizing sources can be revealed by both the global history and the detailed morphology of reionization. Figure 6.6 shows two important measures of the reionization, the volume-averaged neutral fraction and the ionized bubble size distribution (BSD), simulated by LIMFAST assuming different feedback prescriptions, which yield the different redshift evolution of the cosmic SFRDs shown in the upper left panel. Notably, the cosmic SFRD directly relates to the strength of stellar feedback through the SFE in low-mass halos. As illustrated in Figure 6.2, more efficient feedback coupling results in a steeper SFE gradient with halo mass, implying less efficient star formation

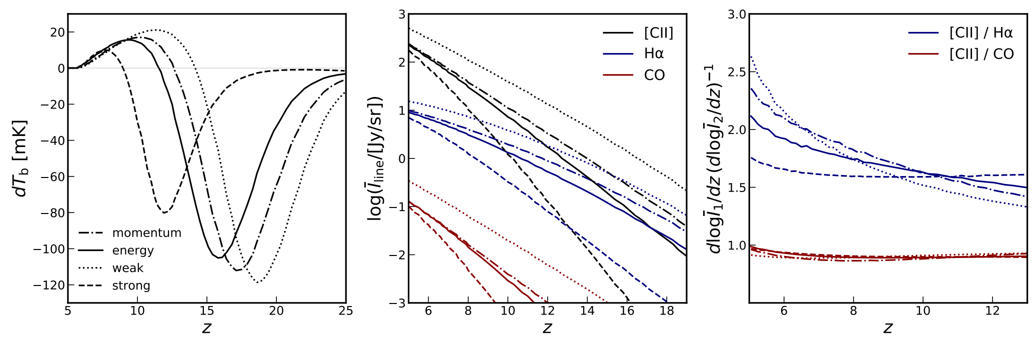

Figure 6.7: Sky-averaged line signals. The redshift evolution of the sky-averaged (global) 21 cm different brightness temperature (left) and intensities of [C II], Hα and CO lines (middle) under different feedback assumptions. Also shown in the right panel is the ratio of redshift dependence of different line intensities, which serves as a measure of the feedback-sensitive metal enrichment history.

in low-mass halos and thus an overall lower and steeper cosmic SFRD dominated by massive halos. The SFRDs predicted by our momentum- and energy-regulated models are comparable to the extrapolation to observations from Robertson et al. (2015) out to $z \sim 15$ (despite the opposite curvature), whereas stronger or weaker feedback can result in SFRDs close to or substantially higher (> 1 dex) than the observational constraints available to date (Oesch et al. 2018; Harikane et al. 2022). Since we tune $f_{\rm esc}$ such that the reionization completes roughly at the same time at $z \approx 6$ in each feedback scenario (see Table 8.1), a steeper SFRD corresponds to an overall more rapid and asymmetric reionization history, as measured by the factor $A_{\rm s} \equiv (z_{05} - z_{50})/(z_{50} - z_{95})$ which uses the reionization midpoint z_{50} and 5% (95%) completion point z_{05} (z_{95}) to characterize the asymmetry of the full extent of the EoR (Trac 2018).

The impact of stellar feedback on the size of ionized regions is illustrated in the right panel of Figure 6.6, which shows the BSD in different feedback modes when the IGM is about half-ionized. Following the "mean free path" method introduced by Mesinger & Furlanetto (2007), we describe the BSD with the probability density function of the logarithmic bubble radius R, which is calculated by repeatedly sampling the size of H 2 regions from random ionized points and in random directions with a Monte Carlo process. At a fixed neutral fraction $\langle x_{\rm H\,I} \rangle$, the BSD shifts towards larger bubble radius when the feedback regulation is stronger. As will be shown in what follows, cross-correlations between the 21 cm signal and tracers of star-forming galaxies turn out to be sensitive probes of the typical bubble size encoded by the BSD, even though the exact correspondence relies on a good understanding of the astrophysics.

6.4.2 Sky-Averaged Line Intensities

The sky-averaged intensity of spectral line emission, especially that of the 21 cm line (often referred to as the global 21 cm signal), as a spatial monopole measurement is known to be a useful probe of the EoR history and source population (Mirocha et al. 2015, 2017; Cohen et al. 2017; Mirocha & Furlanetto 2019; Park et al. 2019). Figure 6.7 shows the redshift evolution of the sky-averaged signals of various lines and their ratios. For the 21 cm global signal, $\delta\bar{T}_\mathrm{b}(z)$, as revealed by the timing and strength of its extrema, a stronger feedback implies delayed Lyα coupling and heating, which lead to an overall smaller signal amplitude in both absorption ($\delta\bar{T}_\mathrm{b} < 0$) at cosmic dawn and emission ($\delta\bar{T}_\mathrm{b} > 0$) during cosmic reionization. The absorption trough varies between $z \sim 12$ and 18 in the central redshift and between $\delta\bar{T}_\mathrm{b} = -80$ and $-120\,\mathrm{mK}$ in the depth for the four feedback modes considered, suggesting an intimate connection between feedback-regulated star formation in the first galaxies and the 21 cm spin temperature evolution during cosmic dawn. The is consistent with the overall shift of the 21 cm global signal towards lower redshift/higher frequency, as projected by the recent literature taking into account of the observed UV luminosity function at $z \gtrsim 6$ (Mirocha et al. 2017; Park et al. 2019; but see also Cohen et al. 2017).

The middle panel of Figure 6.7 shows the mean intensities of line tracers of galaxies [C II], Hα, and CO, whose redshift evolution is largely driven by that of the SFRD. Nonetheless, the subtle difference in the steepness of redshift evolution, caused by the different metallicity dependence of these tracers, serves as a potential probe of feedback through the implicit metal enrichment history. The effect is illustrated in the right panel of Figure 6.7, where ratios of slopes $\bar{I}^{-1}d\bar{I}/dz$ as a function of redshift are contrasted with each other. Clearly, the slope ratio of lines with high contrast in metallicity dependence (e.g., [C II] and Hα) is sensitive to feedback, with less efficient feedback producing a slope ratio with stronger redshift evolution, whereas the slope ratio of lines with similar metallicity dependence (e.g., [C II] and CO) is largely a constant insensitive to the exact feedback mechanism. Such sensitivity to feedback is not surprising though, given that the mean intensity evolution is mainly driven by the much more abundant low-mass galaxies that are most feedback-sensitive and least metal-enriched. In the case of very strong feedback, there are too few low-mass galaxies to make a significant variation in the slope ratio, and thus it

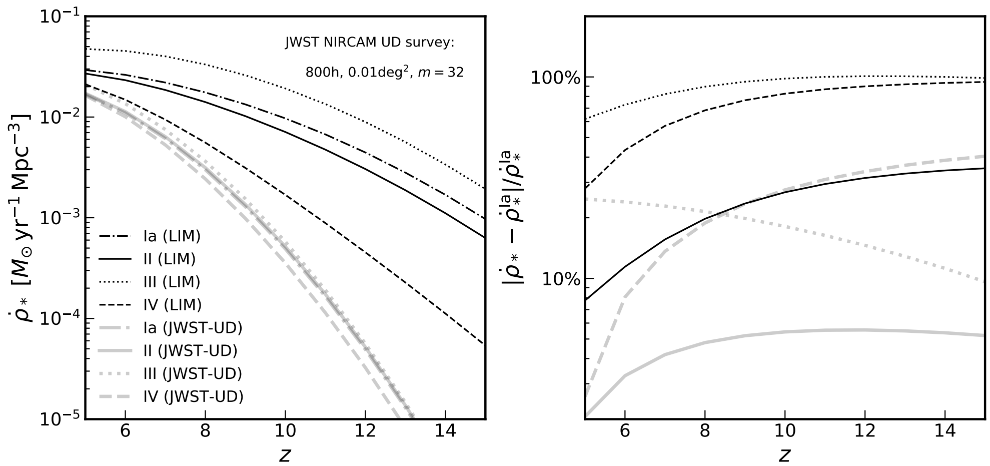

Figure 6.8: Comparison of SFRD estimates from LIM and JWST. Left: a comparison between the cosmic SFRD attributed to galaxies measurable by LIM experiments and a nominal JWST/NIRCAM ultra-deep survey reaching a limiting magnitude of $m \approx 32$ with four 200 h pointings covering a total area of $\approx 0.01\,\mathrm{deg}^2$. The thick and thin sets of curves represent LIM- and JWST-detectable galaxies, respectively. Right: the fractional SFRD deviation from the fiducial momentum-driven feedback model (Model Ia) in other feedback models.

remains roughly constant with redshift.

Measurements of the mean intensity evolution of spectral line tracers of galaxies, especially SFR tracers like Hα and [C II], can often be translated into constraints on the SFRD, provided that the L–SFR relation can be reliably determined. This in turn provides an angle to compare the information from LIM observations to what will be available from forthcoming surveys of individual high-z sources by new-generation telescopes like the JWST. In Figure 6.8, we illustrate a simple comparison between the distinguishing power on the cosmic SFRD in different feedback modes available from JWST and LIM observations in general. As an example, we consider an potential ultra-deep (UD) configuration for a galaxy dropout survey with JWST/NIRCAM that reaches a limiting magnitude of $m \approx 32$, similar to the strategies considered in Mason et al. (2015) and Furlanetto et al. (2017)[1]. As shown in the left panel of Figure 6.8, a JWST UD survey will likely still miss a considerable fraction ($\gtrsim 50\%$) of the total star formation in galaxies at $z \gtrsim 6$, unless the SFRD declines steeply with redshift due to a shallow faint-end slope of the galaxy luminosity function, a likely result of very efficient stellar feedback. On

[1]Even though more realistic survey plans are now available (see e.g., Williams et al. 2018; Robertson 2021), the approximate configuration, as presented, is sufficient for our purpose.

the contrary, the statistical nature of LIM makes the measurements sensitive to the collective star formation activity sourcing the aggregate line emission, although in some cases the conversion between line luminosity and the SFR can be sophisticated.

To further contrast the two types of measurements in the context of probing stellar feedback, we show in the right panel of Figure 6.8 the fractional deviation of the total, *measurable* SFRD in other feedback modes from that in the fiducial, momentum-driven case of feedback. Namely, $|\dot{\rho}_* - \dot{\rho}_*^{\rm Ia}|/\dot{\rho}_*^{\rm Ia}$ reflects how easily one might disprove a simple momentum-driven feedback model using deviations (if any) of the observed SFRD from the expected one. Due to the insufficient sensitivity of galaxy surveys to faint objects, for which the effect of feedback regulation is most pronounced, a JWST UD survey tends to have less distinguishing power than LIM observations especially towards higher redshift. The exception, again, is when comparing a very strong feedback to Model Ia, in which case the difference in distinguishing power decreases with increasing redshift as galaxies to which LIM is uniquely sensitive diminish rapidly, although LIM observations still offer more distinguishing power. We note that the example presented here only represents an extremely-simplified, special case of inferring stellar feedback from the SFRD evolution. In practice, the individual source detection and LIM methods further complement each other by the different quantities that are directly probed (e.g., the luminosity function vs. moments of the luminosity function) and the different sources of uncertainty involved (e.g., cosmic variance and the dust correction vs. foreground contamination and the L–SFR relation), and thus are both valuable probes of galaxy formation and evolution in the high-z universe.

6.4.3 Characterizing Stellar Feedback With LIM

In the left panel of Figure 6.9, we show slices of δT_b fluctuations in different feedback scenarios at various stages of reionization, when the average IGM neutral fraction is $\langle x_{\rm HI} \rangle = 0.2$, 0.5, and 0.8, respectively. It is obvious that at a given stage, the typical size of ionized regions is on average larger with stronger feedback. This is because under stronger feedback regulation, star formation tends to occur in more massive halos, which are more clustered and have a higher ionization rate to ionize a larger volume of gas thanks to their higher SFR. Note that although across each row the volume filling factor of fully ionized regions appears higher in the case of a stronger feedback, the volume-averaged neutral fraction $\langle x_{\rm HI} \rangle$ of individual simulated boxes are in fact comparable — because the *product* of ionization efficiency ζ and local collapse fraction $f_{\rm coll}(x, z, R)$ is more evenly distributed when feedback is less effi-

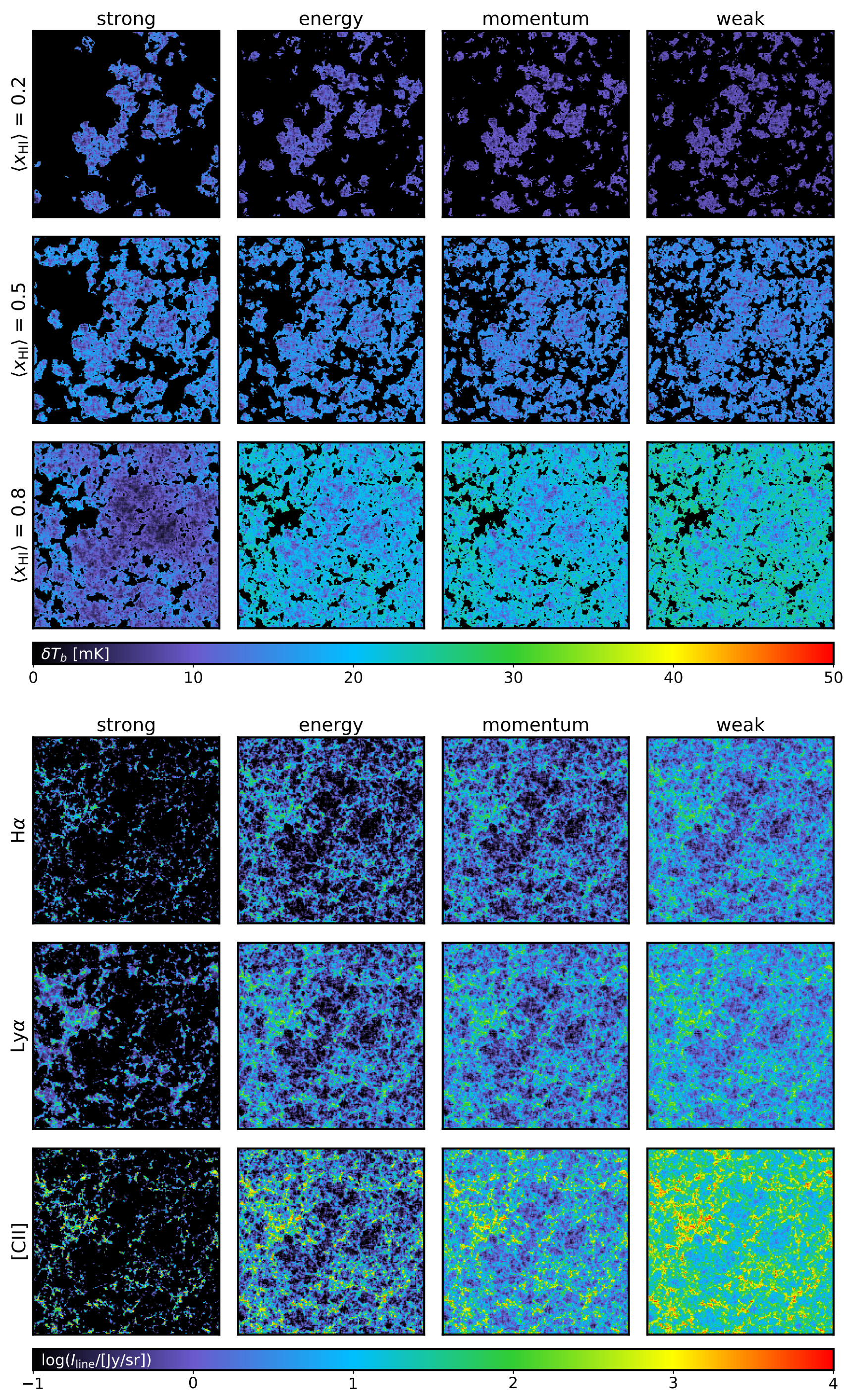

Figure 6.9: Snapshots of 21 cm signals in different feedback modes, and the corresponding Hα, Lyα, and [C II] line intensity maps. Left: slices of 21 cm differential brightness temperature δT_b fields at various stages of reionization ($\langle x_{\mathrm{HI}} \rangle \approx 0.2$, 0.5, and 0.8, respectively) simulated by LIMFAST, assuming different stellar feedback prescriptions as specified in Table 8.1. Right: slices of Hα, Lyα, and [C II] line intensity fields at $z \approx 7$ (when $\langle x_{\mathrm{HI}} \rangle \approx 0.5$) simulated by LIMFAST. Note that the Lyα intensity fields displayed have contributions from both Lyα emitters and recombinations in the diffuse ionized IGM, though without accounting for the damping wing absorption due to the intervening neutral IGM. Each slice is 256 Mpc on a side and 1 Mpc thick.

cient, more partially ionized cells with ionized fraction equal to $\zeta^{-1} f_{\rm coll}(x, z, R_{\rm cell})$ are allowed to exist (Mesinger et al. 2011), which compensate for the deficit in fully ionized regions.

In Section 6.4.2, we have demonstrated the impact of feedback on the history of cosmic dawn and reionization eras as revealed by the 21 cm global signal from the neutral IGM. Using LIMFAST, we supplement such a picture with the complementary LIM signals of UV/optical and far-infrared nebular emission lines tracing star-forming galaxies, which are considered to provide the majority of ionizing photons required to complete the reionization by $z \approx 5.5$ (Robertson et al. 2015; Naidu et al. 2020).

The right panel of Figure 6.9 shows slices through the boxes of Hα, Lyα, and [C II] intensity fluctuations simulated by LIMFAST when $\langle x_{\rm HI} \rangle \approx 0.5$ in different feedback scenarios, color-coded by the logarithmic line intensity in units of Jy/sr. In contrast to maps of the 21 cm signal, these line intensity maps generally trace the ionizing sources residing in overdense regions, whose spatial anti-correlation with the 21 cm signal is clearly visible on scales larger than the typical size of ionized regions. On finer scales, information about sources of line emission and the luminosity distribution of the source population is encoded in detailed features of the intensity fluctuations. For Lyα, a spatially-extended component is apparent, especially in the case of a strong feedback, which is sourced by recombinations in the diffuse ionized IGM surrounding ionizing sources.

On the other hand, the fact that the [C II] intensity field shows a larger spatial gradient compared with that of Hα indicates that the former is preferentially sourced by more massive and therefore more biased sources. This results from the difference in the luminosity–halo mass (L–M) relation of the two lines. As demonstrated in Appendix 6.7, where we contrast the L–M relation of several nebular lines under varying assumptions of the metallicity dependence, [C II] luminosity is a steeper function of halo mass compared with lines like Hα due to its much stronger metallicity dependence. The paucity of contribution from low-mass halos not only leads to a steep $\bar{I}(z)$ evolution shown in Figure 6.7, but also implies that [C II] intensity fluctuations will be more dominated by the Poisson noise from rare [C II]-bright sources, as can be shown by the power spectrum. As we will see, a sensitive luminosity–halo mass relation makes statistical measurements of lines like [C II] and CO promising ways of testing models of galaxy formation involving different feedback assumptions.

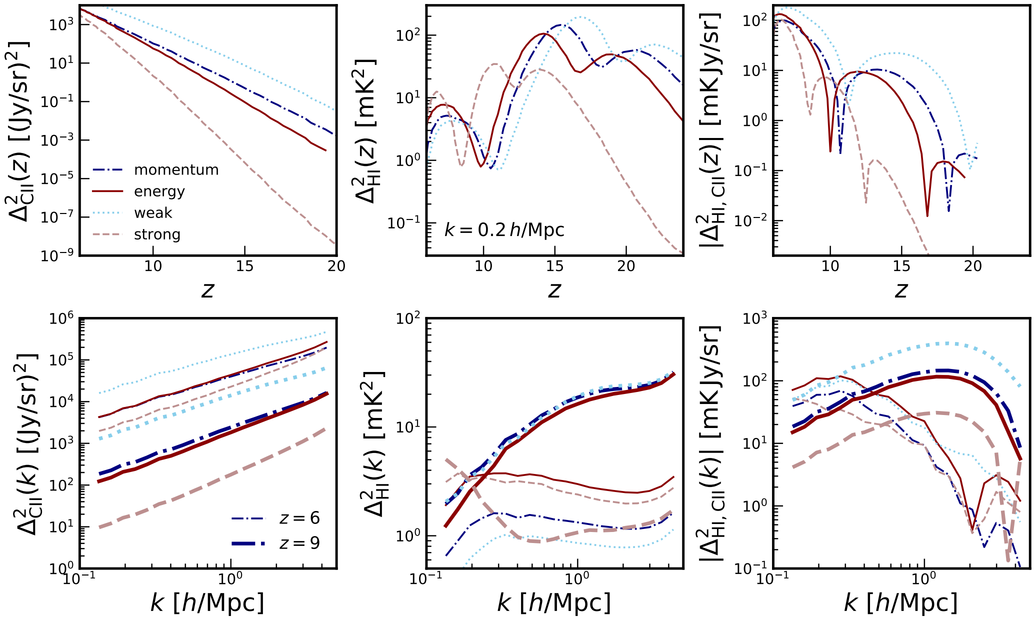

Figure 6.10: Evolution of multi-tracer power spectra. The redshift evolution at a fixed comoving scale of $k = 0.2\,h/\mathrm{Mpc}$ (top) and scale dependence (bottom) of auto- and cross-power spectra (absolute value) between [C II] emission from galaxies and the 21 cm line in different feedback models. The cross-power spectrum changes sign from negative on large scales to positive on small scales at $k_{\rm trans} \sim 2\,h/\mathrm{Mpc}$.

6.4.3.1 Information From Auto-Power Spectra

The statistical information about spatial fluctuations of a given LIM signal is directly available from its auto-power spectrum. As an example, we illustrate in Figure 6.10 the power spectra of 21 cm and [C II] lines, whereas similar illustrations for the power spectra of other nebular lines considered (and their cross-correlations with the 21 cm line) are provided in Appendix 6.8. The left two columns of Figure 6.10 show the shape and redshift evolution of [C II] and H 1 21 cm power spectra calculated from simulations boxes in the four cases of feedback considered. Even though the power spectrum only partially describes these potentially highly non-gaussian fields, it is encouraging to see that useful information about the feedback mode in play can be probed by either the shape or amplitude evolution of the auto-power spectrum.

From the redshift evolution of the power spectrum at $k = 0.15\,h/\mathrm{Mpc}$ shown in the top row, it is evident that the amplitude of large-scale fluctuations encapsulates statistics of the key drivers for the sky-averaged signal evolution. In the case of 21 cm power spectrum amplitude, the three characteristic peaks (from high z to low z) corresponds to the eras of Lyα coupling, X-ray heating, and reionization, when high-amplitude fluctuations in δT_{b} are concurrent with rapid changes (i.e., steep slopes) in the 21 cm global signal as shown in Figure 6.7. Different feedback prescriptions modulate these peaks in significantly different ways, with strong feedback yielding peaks later and more squeezed in redshift and less contrasted in amplitude.

The redshift evolution of [C II] power spectrum amplitude, on the other hand, largely reflects the sky-averaged intensity $\bar{I}(z)$ evolution of the signal, which in turn traces the cosmic SFRD evolution as discussed in Section 6.4.2. Thanks to the quadratic dependence $\Delta^2(k) \propto \bar{I}^2$, different feedback modes become more distinguishable, provided that the power spectrum amplitude can be monitored over a wide enough redshift range.

From the shape of power spectra at $z = 6$ and 9 shown in the bottom row, it is also straightforward to see the modulation effect by feedback. For 21 cm power spectrum, the impact of feedback on the ionized bubble size is manifested by the shift of the scale at which the power spectrum peaks, which is most discernible at $z = 6$ ($k \sim 0.1\,h/\mathrm{Mpc}$ for the "strong" model and $k \sim 0.3\,h/\mathrm{Mpc}$ for the "weak" model) when different feedback models predict similar $\langle x_{\mathrm{HI}} \rangle$ but different BSDs. The difference appears to be a lot smaller at $z = 9$ when the remains close to high, except for the case of very strong feedback which shows a qualitative difference from other cases. This is because the 21 cm spin temperature field is dominated by highly-biased, massive sources in the presence of strong feedback, thereby showing a distinctive large-scale power excess at $k \sim 0.1\,h/\mathrm{Mpc}$ due to the source clustering. The generally much lower amplitude on smaller scales in case, compared with other feedback cases, is due to the delayed reionization by strongly-suppressed cosmic star formation.

The shape evolution of [C II] power spectrum is much more subtle in the plot, although the effect of feedback can still be inferred from the shape contrast between two redshifts. Overall, stronger feedback leads to both a steeper $\Delta^2_{\mathrm{CII}}(k)$ that is more dominated by the small-scale Poisson noise and a stronger shape evolution. Considering a metric of the power spectrum shape contrast, $\mathcal{X}(k_1, z_1, k_2, z_2) = \Delta^2(k_1, z_2)/\Delta^2(k_2, z_2) - \Delta^2(k_1, z_1)/\Delta^2(k_2, z_1)$, which characterizes the change in the dominance of small-scale Poisson noise in the power spectrum between two redshifts z_1 and z_2, we find $\mathcal{X}_{\mathrm{CII}}(3\,h/\mathrm{Mpc}, 6, 0.1\,h/\mathrm{Mpc}, 9) = 20$, 40, 65, and 140 for the "weak", "momentum", "energy", and "strong" models, respectively. Here

$k = 3$ and $0.1\ h/\mathrm{Mpc}$ roughly correspond to the smallest and largest scales accessed by our simulation, and a larger, positive $\mathcal{X}$ indicates that from $z = 6$ to 9 the "strong" model implies a larger increase in the dominance of the Poisson noise contribution. Such a correlation between $\mathcal{X}$ and the feedback strength is insensitive to factors that only affect the power spectrum normalization, and thus marks a potentially useful application of auto-correlation analysis to the understanding of galaxy formation physics.

6.4.3.2 Information From Cross-Power Spectra

In practice, measurements of the auto-power spectrum are often unfortunately complicated by a variety of astrophysical and instrumental effects. One of the main obstacles is foreground contamination, which can overwhelm the target LIM signal by several orders of magnitude. Even though a multitude of cleaning techniques have been devised to remove foreground contamination of various origins, cross-correlating signals with uncorrelated foregrounds still has its unique advantages. Therefore, it is interesting to understand how cross-correlations between different lines, especially the 21 cm line and nebular lines tracing ionizing sources, may be leveraged to characterize the effect of feedback in high-z galaxy formation.

In the rightmost column of Figure 6.10, we compare different feedback models by showing how their predicted 21 cm–[C II] cross-power spectra evolve with redshift in their amplitude and shape. From the redshift evolution, the strength of feedback determines how rapidly the cross-power amplitude evolves. Moreover, thanks to the counteractive evolution of 21 cm and [C II] amplitudes with redshift, the peaks intrinsic to the 21 cm contribution become broadened for $\Delta^2_{\mathrm{H\,I,C\,II}}(z)$ compared with $\Delta^2_{\mathrm{H\,I}}(z)$ (especially for the peak due to X-ray heating), and the extent of the broadening depends on how long the counteractive effect persists. Different feedback modes are therefore easier to be distinguished by $\Delta^2_{\mathrm{H\,I,C\,II}}(z)$, wherein less rapid evolution with broad, flattened, and later peaks in redshift corresponding to weaker feedback. From the shape of the cross-power spectrum, on the other hand, the most pronounced feature is the dependence of the scale at which the cross-power changes sign on the feedback mode in play. As will be shown next, both feedback and the physics of line emission affect the interpretation of such a characteristic scale, which has been perceived as an indicator of the typical size of ionized bubbles during the EoR.

We further inspect the effect of feedback on the cross-correlation signals in Figure 6.11 by comparing the cross-correlation coefficient $r_{1\times2}(k) = P_{1\times2}(k)/\sqrt{P_1(k)P_2(k)}$

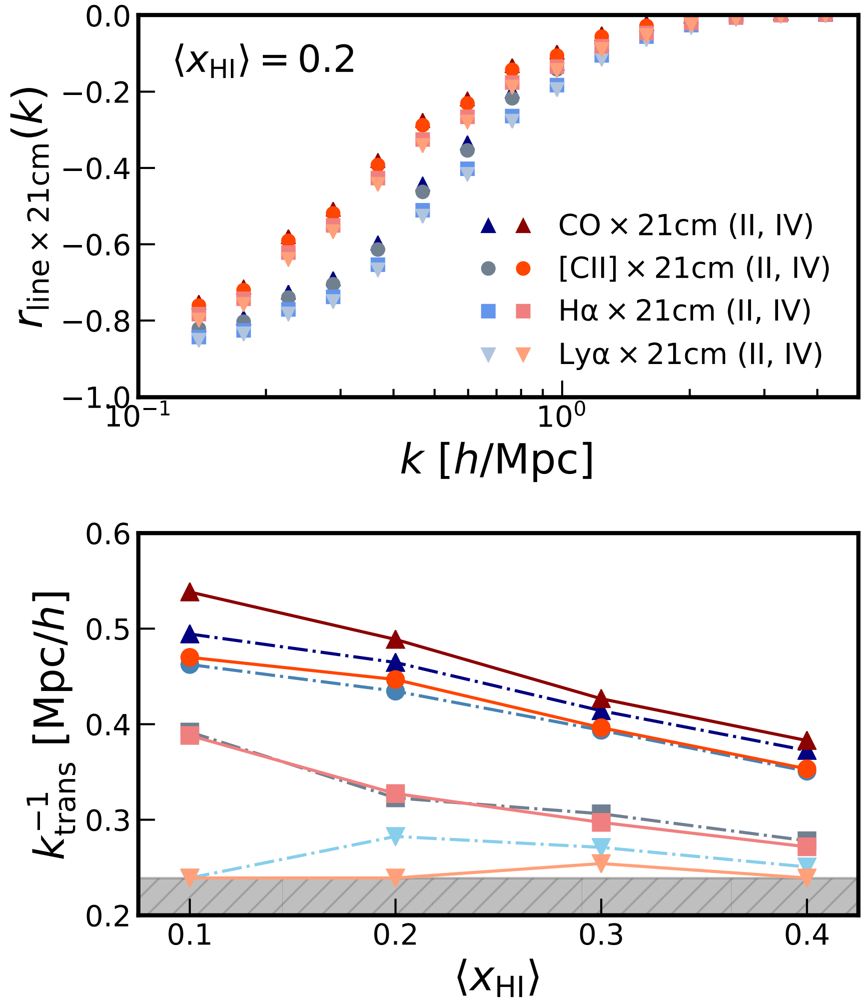

Figure 6.11: Cross-correlations between 21 cm line and galaxy tracers in different feedback modes. Top: cross-correlation coefficients between the 21 cm line and Hα, Lyα, [C II], and CO lines derived from the maps simulated by LIMFAST at $\langle x_{\rm H\,I}\rangle \approx 0.2$, assuming energy-driven (Model II, blue set of points) and strong (Model IV, red set of points) feedback. Bottom: the evolution of the comoving transition scale, at which $r_{\rm line\times21cm}(k_{\rm trans}) = 0$, with the mean IGM neutral fraction. Scales inaccessible by our simulation outputs of limited resolution are greyed out, and $k^{-1}_{\rm trans}$ values below which are marked and interpreted as upper limits.

of the 21 cm signal with a variety of emission-line tracers of galaxies, including Hα, Lyα, [C II], and CO lines. In particular, we focus on how the scale dependence of $r(k)$ differs for different cross-correlations assuming different feedback assumptions, especially the transition scale $k_{\rm trans}$ where $r(k_{\rm trans}) = 0$. In the top panel of Figure 6.11, $r(k)$ of different feedback models and line tracers when $\langle x_{\rm H\,I}\rangle \approx 0.2$ are shown in different hues and tints, respectively. The fact that, at a fixed stage (i.e.,

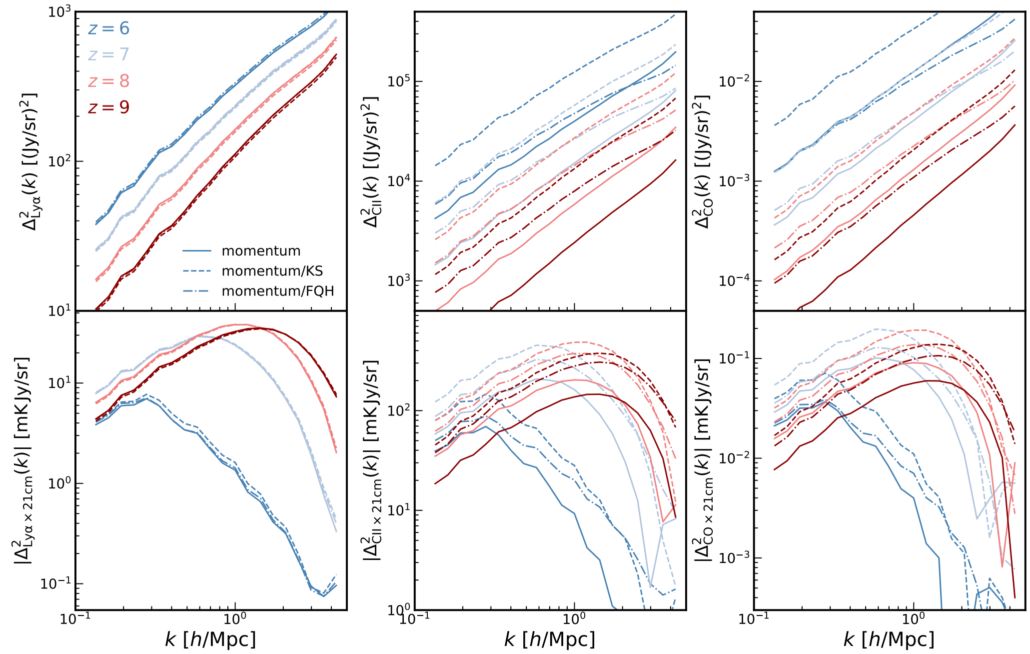

Figure 6.12: Effects of star formation law on multi-tracer power spectra. Power spectra of auto-correlations (top row) of Lyα, [C II], and CO lines, as well as their cross-correlations with the H 1 21 cm signal (bottom row) during the EoR predicted by the three LIMFAST models assuming the same momentum-driven feedback but different star formation laws.

$\langle x_{\mathrm{HI}}\rangle$) of reionization, stronger feedback predicts faster de-correlation between 21 cm and nebular lines as k increases (e.g., from 0.1 h/Mpc to 1 h/Mpc) is consistent with the more "top-heavy" BSD skewed towards larger bubble sizes expected in this case. Nonetheless, in the bottom panel of Figure 6.11, we show that k_{trans} is only modestly sensitive to feedback (and thus the BSD) for a given line tracer, although, as expected, it indeed traces the macroscopic progress of reionization described by $\langle x_{\mathrm{HI}}\rangle$.

Another noteworthy feature in Figure 6.11 is the discrepancies in the individual cross-correlations for a given feedback mode. Unlike naively expected, there are non-trivial differences in both $r(k)$ and k_{trans} among different line tracers of galaxies. Lines like [C II] and CO tracing the neutral ISM, whose luminosities evolve steeply with mass due to e.g., their strong dependence on the gas metallicity, exhibit a modestly lower level of (negative) correlation with the 21 cm line, when compared with tracers of the ionized ISM less sensitive to metallicity, such as Hα and Lyα. This, in turn, makes k_{trans} vary among different nebular lines with essentially different effective bias factors for a fixed feedback/reionization scenario. For example, $k_{\rm trans}^{-1}$, as a proxy for the bubble size, can differ by more than 50% at $\langle x_{\rm H\,I} \rangle \sim 0.3$ depending on whether Hα or CO is cross-correlated with the 21 cm line. Similar effects have been noted previously by several other authors (Dumitru et al. 2019; Kannan et al. 2022b; Cox et al. 2022), despite using less explicit formulations of the connection between nebular line emission and galaxy formation. Finally, for Lyα, we note that a qualitatively different trend appears for $k_{\rm trans}^{-1}$ as a function of $\langle x_{\rm H\,I} \rangle$, which is caused by the additional diffuse component from recombinations in the diffuse ionized IGM (see Figure 6.9) that can strongly modulate $k_{\rm trans}^{-1}$ especially towards the end of the EoR.

6.4.4 Characterizing the Star Formation Law With LIM

Besides stellar feedback, the other way that the astrophysics of galaxy formation can affect the luminosity–halo mass relation of nebular lines is through the star formation law. In particular, because the star formation law only alters the relative gas content of galaxies instead of the amount of star formation, as illustrated in Figure 6.1, lines originating from the neutral ISM are most sensitive to changes in the star formation law.

Figure 6.12 shows the auto-power spectra of Lyα, [C II], and CO lines and their cross-power spectra with the 21 cm signal during the EoR. Clearly, the statistics of Lyα, whose luminosity simply scales with the star formation rate, are little affected by using different forms of the star formation law (Models Ia, Ib, and Ic). On the contrary, given the substantial difference in the luminosity–halo mass (or SFR) relation caused by the gas mass dependence (see Figure 6.5), [C II] and CO lines have power spectra varying significantly with the assumed star formation law in both the shape and amplitude. Models implying more efficient star formation out of the gas reservoir and therefore a shallower luminosity–SFR relation, e.g., Model Ic, tend to yield auto-power spectra less dominated by the Poisson noise and evolving less rapidly with redshift — an unsurprising result given that large-scale fluctuations are mainly contributed by the more abundant fainter sources, whereas the small-scale Poisson fluctuations dominating are mainly contributed by the very rare and bright sources. For reference, we find $\mathcal{X}_{\rm CII}(3\,h/{\rm Mpc}, 6, 0.1\,h/{\rm Mpc}, 9) = 41$, 25, 17, and $\mathcal{X}_{\rm CO}(3\,h/{\rm Mpc}, 6, 0.1\,h/{\rm Mpc}, 9) = 55$, 36, 26 for Model Ia, Ib, and Ic, respectively, suggesting that indeed Model Ic assuming the FQH13 star formation law predicts power spectra the least Poisson noise-dominated.

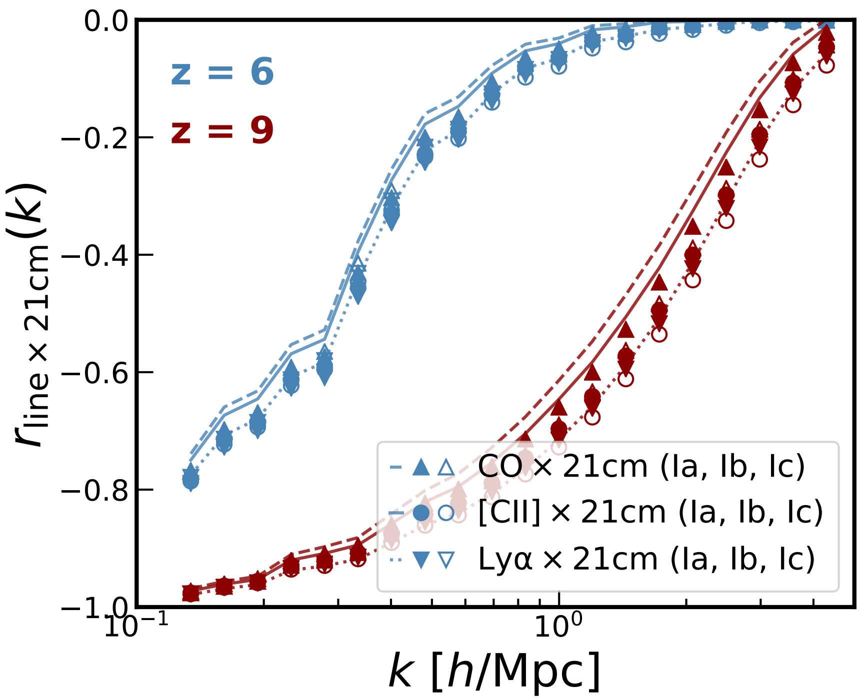

Figure 6.13: Cross-correlations between 21 cm line and galaxy tracers in different star formation laws. Cross-correlation coefficients between the 21 cm line and Lyα, [C II], and CO lines and derived from the maps simulated by LIMFAST assuming the default (lines, Model Ia), KS (filled markers, Model Ib), and FQH13 (empty markers, Model Ic) star formation law.

The cross-power spectrum between the 21 cm and [C II] or CO lines also exhibits a clear dependence on the star formation law assumed, even though the reionization scenario is largely independent of it. With a steeper star formation law (i.e., more efficient gas to stellar mass conversion), the intensity field of [C II] or CO becomes less dominated by bright sources and therefore de-correlates with the 21 cm field at smaller scales, causing a noticeable shape difference potentially useful for testing star formation law models. Moreover, the FQH13 model (Model Ic) predicts the strongest redshift evolution of the cross-power amplitude over $6 < z < 9$, again due to the weaker counteractive evolution of 21 cm and [C II] or CO lines in the case of a steeper star formation law.

In Figure 6.13, we show the cross-correlation coefficients, $r(k)$, between Lyα, [C II], CO lines and the 21 cm line at $z = 6$ and $z = 9$ under various assumptions of the star formation law. Since the reionization scenario is nearly insensitive to changes in the star formation law, any difference in $r(k)$ shown in this figure is due to the nebular line intensity signal rather than the 21 cm signal. Several interesting features are noteworthy. First, as expected, $r_{\mathrm{Ly}\alpha\times 21\mathrm{cm}}(k)$ remains almost unchanged in different star formation law models because Lyα only depends on the SFR. Second, similar to what is shown in Figure 6.11, for either [C ii] or CO line the level of (negative) correlation at a given scale depends moderately on the star formation law assumed, with steeper star formation law yielding a less rapid de-correlation as k increases. Lastly, a change in the relative order of $r(k)$ for Lyα, [C ii], and CO lines is observed by contrasting Model Ib with Model Ic, which may be utilized for star formation law model selection. Similar to stellar feedback, the star formation law also serves as a source of complications in the interpretation of typical ionized bubble size from $r(k)$ or k_{trans}.

6.5 Discussion

In what follows, we compare the results and their implications from this work against some previous literature, and discuss potential caveats and limitations of our methods. In addition, we also outline several promising directions to extend the current framework of LIMFAST in the future.

6.5.1 Comparison to Previous Work

A number of studies have previously studied and demonstrated the huge potential of LIM observations targeting at different tracers for understanding the cosmic dawn and reionization eras. As presented in Paper I and this work, with LIMFAST we provide an efficient modeling framework to self-consistently simulate a large number of LIM signals during the EoR that have been investigated individually (or in small subsets) before by different authors, such as Hα (e.g., Heneka et al. 2017; Silva et al. 2018; Heneka & Cooray 2021), Lyα (e.g., Silva et al. 2013; Pullen et al. 2014; Heneka et al. 2017), [C ii] (e.g., Gong et al. 2012; Chung et al. 2020; Sun et al. 2021b), [O iii] (e.g., Padmanabhan et al. 2021), and CO (e.g., Lidz et al. 2011; Mashian et al. 2015b; Breysse et al. 2021). Overall, the qualitatively good agreement between LIMFAST predictions and results in literature is encouraging. It suggests that target LIM signals during the EoR differing in both the natal phase of gas and the connection to galaxy properties may be well-described by a unified picture of high-z galaxy formation. Nonetheless, non-trivial offsets exist between our results and other individual, line-specific models involving vastly varying assumptions of the galaxy population and spectral line production. Thus, coherently modeling the otherwise disconnected physical conditions of multi-line emission and galaxy evolution with tools like LIMFAST is imperative to understand and exploit the multi-tracer LIM technique for studying the EoR.

On the usage of the scale $k_{\rm trans}$ at which the cross-correlation coefficient between the 21 cm signal and a given galaxy tracer changes sign, our findings are qualitatively similar to previous analyses by Lidz et al. (2011), Dumitru et al. (2019), and most recently Kannan et al. (2022b). Put briefly, the general redshift evolution of $k_{\rm trans}$ does reflect the overall progress of the reionization as measured by $\langle x_{\rm H\,I} \rangle$, but such evolution is complicated by uncertainties of the source population that affect signals of both tracers being cross-correlated. Specifically, at any given $\langle x_{\rm H\,I} \rangle$, variations of our galaxy model in either feedback or the star formation law can modulate $k_{\rm trans}$ through of the BSD and/or the effective bias of the galaxy tracer. While previous analyses often adopt a sharp dichotomy of halo emissivities in terms of ionizing photon production to distinguish between reionization scenarios dominated by faint vs. bright sources (e.g., Dumitru et al. 2019; Kannan et al. 2022b), our model allows galaxies of different luminosities to more smoothly impact both the neutral gas and line intensity distributions in a consistent manner. Such smooth transitions in the contribution from different sources to signatures of reionization are not merely more realistic, but also essential for shedding light on how high-z galaxies driving the reionization might be shaped by the balance between star formation and feedback.

6.5.2 Limitations of the Galaxy Formation Model

In LIMFAST, we have implemented and leveraged the simple, quasi-equilibrium model of high-z galaxy formation described in Furlanetto et al. (2017) and Furlanetto (2021) to study the impact of the astrophysics of galaxies on various target LIM signals. Although it already represents an improvement over the source modeling in the latest release of 21cmFAST (Murray et al. 2020) in aspects such as the physical connection between star formation and feedback regulation, some intrinsic limitations of the method need to be noted and are likely worthy of further exploration in future work.

A key assumption made in our galaxy formation model is that in the high-z universe a quasi-equilibrium state can already be established by proto-galaxies in the form of a settled disc where stars steadily form. Making this assumption provides a neat way to describe the formation of EoR galaxies by analogy to their low-z counterparts, though one may question how valid such a scenario can be in the highly dynamic and uncertain stage of early galaxy formation. Recently studies, including a follow-up study to the Furlanetto (2021) model, have shown that star formation might be highly bursty during the early phase of galaxy formation, before some critical mass is reached and stars can steadily form. For example, Furlanetto & Mirocha (2022) generalize the quasi-equilibrium disc model by introducing a non-trivial perturbation arising from the time delay between star formation and stellar feedback at high redshifts. Numerical simulations also find strong evidence for strongly time-variable star formation in early, low-mass galaxies before a rotationally-supported ISM emerges from a rapid process of disc settling (Gurvich et al. 2022), which turns out to be supported by Galactic archaeology of the in situ, metal-poor component of the Milky Way's stellar halo (Belokurov & Kravtsov 2022), indicating a potential requirement for full, non-equilibrium approaches. Given the intimate connection between star formation and spectral line emission in galaxies, as demonstrated in this work, it is crucial to quantify in future studies the effects of highly time-variable star formation on multi-tracer LIM observations of the EoR.

Even if the quasi-equilibrium model indeed approximates the formation and evolution of high-z star-forming galaxies well, it is admittedly simplistic in many ways, some of which are closely related to subgrid modeling that will be detailed in the next sub-section. One important simplification is associated with the diversity of galaxy formation histories. As demonstrated by Mirocha et al. (2021), simple subgrid, HAM-based models tend to produce biased signatures of the reionization process, when compared against fully numerical methods accounting for both halo mergers and the stochasticity of the halo mass accretion rate. A hybrid or numerically-calibrated approach will therefore be useful for further improvements in the model accuracy (see also Section 6.5.4). Relatedly, we have also neglected the scatter in astrophysical parameters of our galaxy formation model, which can impact LIM signals of interest in a non-trivial way (Shekhar Murmu et al. 2021; Reis et al. 2022) and therefore should be taken into account in future development of LIMFAST by e.g., cell-level stochastic sampling of astrophysical parameters. Pop III stars are another missing piece of the current model that can have non-trivial effects on the EoR, whose physical properties and formation histories may be studied either through their influence on the 21 cm signal (Mirocha et al. 2018; Mebane et al. 2020; Qin et al. 2021b; Muñoz et al. 2022) or by mapping the emission of nebular lines characteristic of Pop III stars, such as the He 2 1640 Å line (Visbal et al. 2015; Parsons et al. 2021). While extensions of 21cmFAST-like, semi-numerical simulations have attempted to self-consistently model the formation of Pop III and Pop II stars altogether (e.g., Tanaka & Hasegawa 2021; Muñoz et al. 2022), observational constraints, either direct or indirect, are pivotal to the down-selection of the poorly constrained model space (see e.g., Mirocha et al. 2018; Sun et al. 2021a).

6.5.3 Uncertainties With Subgrid Astrophysics

We note that a range of simplifications and model assumptions are made for the subgrid astrophysics of galaxy formation and evolution, which are essential for the application of LIMFAST to the EoR science, but in the meantime serve as important sources of uncertainty. For instance, the galaxy properties captured by our quasi-equilibrium model are highly simplified, which in turn limits how closely galaxy formation and the spectral line emission can be modeled coherently. In particular, several physical conditions of the stellar population and the ISM must be specified manually, including the star formation history of galaxies, the gas density, the interstellar radiation field strength, and dust properties, all of which are likely influential for the modeling of both galaxy formation and the variety of radiation fields of interest (e.g., Lagache et al. 2018; Mirocha 2020; Mirocha et al. 2021; Yang et al. 2021). Insights from observations and theoretical modeling on connections (and the mechanisms behind) among different ingredients of subgrid astrophysics, such as the co-evolution of gas, metals, and dust across cosmic time (Li et al. 2019) and the causal relation between the ionization parameter and metallicity (Ji & Yan 2022), will be extremely valuable for further improvements of the source modeling in LIMFAST simulations.

6.5.4 Extension of the Current Framework

In Paper I and this work, we present the current structure and functionalities of LIMFAST focusing on its capability of forward modeling the multi-tracer LIM observations of the EoR. It is useful to note that the current framework may be readily extended in various promising ways and applied to a broader range of EoR studies, thanks to the modular nature of LIMFAST.

First, additional probes of the EoR can be incorporated into the same modeling framework in a consistent manner similar to the existing ones. For instance, several authors have demonstrated that semi-numerical simulations are ideal tools for studying the kinetic Sunyaev-Zel'dovich (kSZ) effect from patchy reionization and its synergy with the 21 cm signal for constraining the reionization history (Battaglia et al. 2013; La Plante et al. 2020; Gorce et al. 2022). Cross-correlating the kSZ signal derived from the simulated ionization and velocity fields with line tracers of galaxies provides the redshift information missing in kSZ measurements. Similar ideas can be applied to other types broad-band, two-dimensional datasets such as the CMB lensing and the cosmic near-infrared background, through the large-scale fluctuations of which rich information about the population of ionizing sources may be extracted (Helgason et al. 2016, Maniyar et al. 2022, Sun et al. 2021a, Mirocha et al. in prep). Furthermore, as demonstrated already in the low-z universe, three-dimensional Lyα forest tomography serves as a promising probe of the large-scale distribution of the neutral IGM (Lee et al. 2018; Newman et al. 2020), which can be ideally suited for studying the late stages of the reionization process by itself or in combination with LIM datasets (Qin et al. 2021a). It is interesting to implement these additional observables into LIMFAST to quantitatively assess their potential for probing the EoR, especially when jointly analyzed with LIM observations, and examine methods required for overcoming observational challenges like foreground contamination (e.g., Zhu et al. 2018; Gagnon-Hartman et al. 2021).

Besides taking into account extra probes of the EoR, it is also of interest to extend LIMFAST further into the post-reionization universe ($0 < z < 5$). Galaxies during this age of active assembly and evolution are not only interesting by themselves but also important witnesses of the impact of reionization on galaxy formation, which will be studied by a number of forthcoming LIM surveys of galaxies at low-to-intermediate redshift, such as COMAP (Cleary et al. 2021), EXCLAIM (Cataldo et al. 2020), SPHEREx (Doré et al. 2018), and TIM (Vieira et al. 2020). That said, despite showing great promise, the low-z extension of LIMFAST faces two main challenges. First, at lower redshift, the halo occupation distribution (HOD) becomes more sophisticated due to the increased population of satellite galaxies (Kravtsov et al. 2004; Bhowmick et al. 2018; Behroozi et al. 2019), and quenching becomes a more and more important process in galaxy formation and evolution (Tal et al. 2014; Brennan et al. 2015; Donnari et al. 2021). Both factors call for more detailed subgrid models for the luminosity–halo mass relation. Meanwhile, accurately modeling the partitioning of mass into halos becomes more challenging at lower redshift due to the increased importance of halo mergers. LIMFAST inherits the formulation of large-scale structure and radiation field approximation from 21cmFAST, where the generation of halo source fields by a halo finding algorithm is bypassed. To properly account for halo merger histories in the low-z extension, an explicit halo finding algorithm, with either an extended dynamic range to resolve small halos at the cooling threshold, or an enhanced subgrid modeling of halo source fields involving merger trees and a stochastic population of simulation cells with unresolved halos, will be required at the cost of extra RAM capacity and a slower speed (see discussion in, e.g., Mesinger & Furlanetto 2007; Mesinger et al. 2011, and references therein).

6.6 Conclusions

Using simulations generated by the LIMFAST code introduced in Paper I, we have presented in this paper a unified picture of how the astrophysics of high-z galaxy formation affect and therefore can be reveal by multi-tracer LIM observations of the EoR. We investigate the impact of different stellar feedback and star formation law prescriptions on a variety of signatures of reionization, including the 21 cm signal and LIM signals of nebular emission lines from the multi-phase ISM, such as Hα, Lyα, [O III], [C II], and CO. Our main findings can be summarized as follows:

1. Because the cosmic star formation history is sensitive to feedback-regulated star formation in individual galaxies, the efficiency of stellar feedback directly impacts the history and thus signatures of the reionization. The star formation law, on the other hand, only affects tracers of the neutral ISM of galaxies as indirect probes of the reionization.

2. The redshift evolution of multiple sky-averaged line signals already serves as a useful probe of the astrophysics of high-z galaxy formation. Timings of the extrema in the 21 cm global signal are tightly connected to the feedback efficiency through radiation fields scaling with the cosmic SFRD. Due to the strong metallicity dependence of metal cooling lines like [C II], a comparison between their sky-averaged signal evolution and that of hydrogen lines like Hα can inform the (cosmic mean) stellar feedback strength.

3. Rich information about the reionization and its driving sources can be extracted from the auto- and cross-power spectra of multi-tracer LIM datasets. Both feedback and the star formation law can modulate the shape and amplitude of power spectra and their time evolution. A multi-tracer power spectral analysis therefore allows cross-checks and the separation of effects due to the reionization itself and those associated with galaxy formation and evolution.

4. The cross-correlation between the 21 cm line and a spectral line tracer of galaxies is particularly useful for tracing the overall progress of the EoR. However, even though the transition scale k_{trans} roughly probes the neutral fraction evolution, the exact interpretation and implications of it are subject to complications due to astrophysics of galaxy formation, and thus dependent on the line tracer considered. Multi-tracer LIM makes it possible to better

understand how LIM signals are influenced by astrophysical processes such as feedback and the star formation law, on which the usage of k_{trans} or the cross-correlation analysis in general is premised.

5. By accessing a larger fraction of the faint galaxy population than individual source detection, LIM surveys can use the inferred SFRD to offer more sensitive tests for processes central to galaxy formation like the stellar feedback. This makes LIM a highly complementary method for studying high-z galaxy formation even in the era of new-generation telescopes.

In summary, there is great potential for multi-tracer LIM to transform our understanding of cosmic reionization and the formation and evolution of high-z galaxies that drive the reionization process. In spite of the various challenges that commonly exist in practice for different tracers, such as the mismatch of scales and issues of foreground contamination (see the review e.g., Liu & Shaw 2020), careful coordination and optimization for future multi-tracer synergies will eventually allow the invaluable astrophysical information to be extracted and applied to tests of the galaxy formation theory at high redshift. Reliable semi-numerical simulations like LIMFAST, in its current and future forms, are essential tools for accurately modeling and analyzing the observational signals to come.

Acknowledgments
We would like to thank Fred Davies, Adam Lidz, Jordan Mirocha, Yuxiang Qin for helpful discussions and comments that helped improve this paper, as well as Mauro Stefanon for sharing the data of the stellar-to-halo mass ratios. We acknowledge support from the JPL R&TD strategic initiative grant on line intensity mapping. Part of this work was done at Jet Propulsion Laboratory, California Institute of Technology, under a contract with the National Aeronautics and Space Administration.

6.7 Appendix: Luminosity–Halo Mass Relation

The L–M relation directly dictates the way the underlying matter density field is traced by the line intensity map observed, as has been discussed in previous studies (e.g., Kannan et al. 2022b). Varying behaviors of the L–M relation are therefore essential for understanding the properties and statistics of the spectral line tracer in different variations of the galaxy model.

Figure 6.14 shows a comparison of the L–M relation of different lines, assuming either a fixed metallicity or a varying metallicity as predicted by our galaxy model.

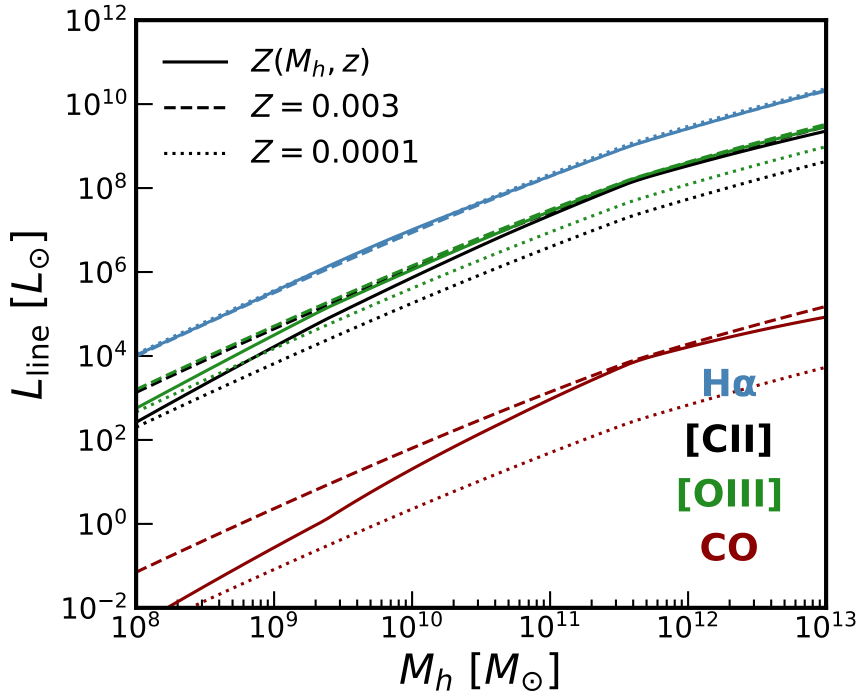

Figure 6.14: The luminosity–mass relations of different lines in LIMFAST. The L–M relations of Hα, [C II], [O III], and CO(1–0) lines assuming different metallicity values. The solid curve assumes a varying metallicity predicted by our galaxy model (Model Ia), whereas the dashed and dotted curves assume fixed metallicity values of $Z = 0.003$ and $Z = 0.0001$, respectively.

The similar shapes of curves with a fixed metallicity suggests that the scaling with the SFR (e.g., Hα and [O III]) or the gas mass (e.g., [C II] and CO) barely affects the L–M relation in the case of the simple star formation law assumed for Model Ia (and Models II–IV). It is really the metallicity dependence and evolution that result in different L–M relations of hydrogen and metal lines, which in turn lead to the different effective bias factors of these spectral line tracers. It is also interesting to note that the L–M relation is coupled to the metallicity not only through the metal content of the ISM, but also through the metallicity dependence of the ISRF, whose synthetic spectrum from BPASS v2.1 (Eldridge et al. 2017) is supplied to the Cloudy simulations (see Paper I). For instance, a more ionizing ISRF for a lower metallicity produces modestly brighter Hα emission, and partially counteracts the effect of a more metal-poor ISM towards lower halo masses for metal lines highly sensitive to the ionizing radiation like [O III].

6.8 Appendix: Power Spectra of Nebular and 21 cm Lines With Varying Feedback

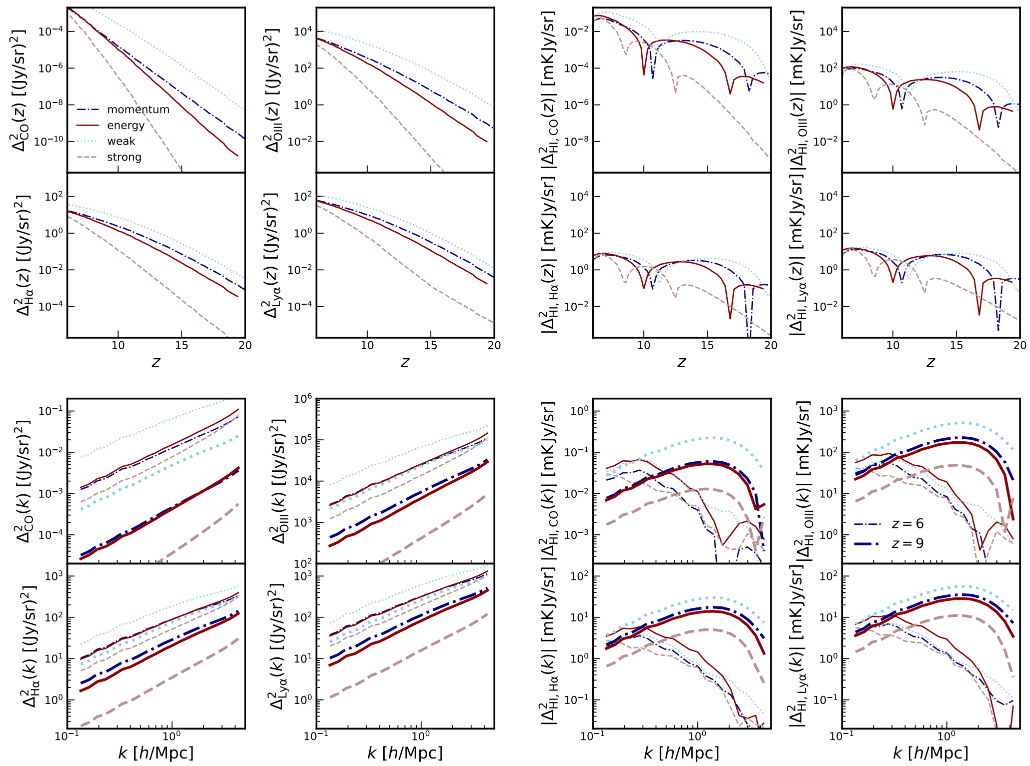

Figure 6.15: Same as Figure 6.10, but for CO(1–0), [O III], Hα, and Lyα lines.

Supplementing Figure 6.10 which uses [C II] and 21 cm lines to exemplify the ways feedback affects the redshift evolution and scale dependence of LIM power spectra, we further in Figure 6.15 similar results for other nebular lines considered in this work, including [O III], CO(1–0), Hα, and Lyα (sum of star formation and IGM contributions). Comparing the evolution with redshift and scale of different tracers shows interesting (though in some cases subtle) trends that inform about how these lines are sensitive to different aspects of the galaxy evolution such as the gas content and metallicity, which may be systematically probed by multi-tracer LIM surveys.

Chapter 7

REVEALING THE FORMATION HISTORIES OF THE FIRST STARS WITH THE COSMIC NEAR-INFRARED BACKGROUND

Sun, G., Mirocha, J., Mebane, R. H., & Furlanetto, S. R. (2021). "Revealing the Formation Histories of the First Stars with the Cosmic Near-Infrared Background", *Monthly Notices of the Royal Astronomical Society*, 508, 1954. DOI: 10.1093/mnras/stab2697.

Abstract

The cosmic near-infrared background (NIRB) offers a powerful integral probe of radiative processes at different cosmic epochs, including the pre-reionization era when metal-free, Population III (Pop III) stars first formed. While the radiation from metal-enriched, Population II (Pop II) stars likely dominates the contribution to the observed NIRB from the reionization era, Pop III stars — if formed efficiently — might leave characteristic imprints on the NIRB thanks to their strong Lyα emission. Using a physically-motivated model of first star formation, we provide an analysis of the NIRB mean spectrum and anisotropy contributed by stellar populations at $z > 5$. We find that in circumstances where massive Pop III stars persistently form in molecular cooling haloes at a rate of a few times $10^{-3}\,M_\odot\,\mathrm{yr}^{-1}$, before being suppressed towards the epoch of reionization (EoR) by the accumulated Lyman-Werner background, a unique spectral signature shows up redward of $1\,\mu$m in the observed NIRB spectrum sourced by galaxies at $z > 5$. While the detailed shape and amplitude of the spectral signature depend on various factors including the star formation histories, IMF, LyC escape fraction and so forth, the most interesting scenarios with efficient Pop III star formation are within the reach of forthcoming facilities such as the Spectro-Photometer for the History of the Universe, Epoch of Reionization and Ices Explorer (SPHEREx). As a result, new constraints on the abundance and formation history of Pop III stars at high redshifts will be available through precise measurements of the NIRB in the next few years.

7.1 Introduction

Population III (Pop III) stars are believed to form in primordial, metal-free gas clouds cooled via molecular hydrogen (H_2) at very high redshift, well before metal-poor, Population II (Pop II) stars typical for distant galaxies started to form. These first generation of stars at the so-called cosmic dawn were responsible for the onset of cosmic metal enrichment and reionization, and their supernova remnants may be the birthplaces of supermassive black holes observed today (see recent reviews by Bromm 2013; Inayoshi et al. 2020). Despite their importance in understanding the cosmic history of star formation, Pop III stars are incredibly difficult to directly detect, even for the upcoming generation of telescopes like the *James Webb Space Telescope* (JWST) as discussed in Rydberg et al. (2013) and Schauer et al. (2020a), and thus constraints on their properties remain elusive. Nevertheless, the formation and physical properties of Pop III stars have been investigated in detail with theoretical models over the past few decades, and several promising observing methods have been proposed to discover them in the near future.

Theoretical models of Pop III stars come in many forms, including simple analytical arguments (e.g., McKee & Tan 2008), detailed numerical simulations (e.g., Abel et al. 2002; Wise & Abel 2007; O'Shea & Norman 2007; Maio et al. 2010; Greif et al. 2011; Safranek-Shrader et al. 2012; Stacy et al. 2012; Xu et al. 2016a), and semi-analytic models that balance computational efficiency and physical accuracy (e.g., Trenti & Stiavelli 2009; Trenti et al. 2009; Crosby et al. 2013; Jaacks et al. 2018; Mebane et al. 2018; Visbal et al. 2018; Liu & Bromm 2020) These theoretical efforts reveal a detailed, though still incomplete, picture of how the transition from Pop III to metal-enriched, Pop II star formation might have occurred. Minihaloes above the Jeans/filtering mass scale set by some critical fraction of H_2 (Tegmark et al. 1997) and below the limit of atomic hydrogen cooling are thought to host the majority of Pop III star formation since $z \gtrsim 30$, where the rotational and vibrational transitions of collisionally-excited H_2 dominate the cooling of primordial gas[1]. The lack of efficient cooling channels yields a Jeans mass of the star-forming region as high as a few hundred $M_\odot$, producing very massive and isolated Pop III stars in the classical picture (Bromm & Larson 2004). However, simulations indicate that even modest initial angular momentum of the gas in minihaloes could lead to fragmentation of the protostellar core and form Pop III binaries or even multiple systems (e.g., Turk et al. 2009; Stacy et al. 2010; Sugimura et al. 2020), which further complicates the Pop III initial mass function (IMF). Several physical processes contribute to the transition to Pop II star formation. The feedback effect of the Lyman-Werner (LW) radiation

[1]Stars formed out of primordial gas in these molecular cooled haloes are sometimes referred to as Pop III.1 stars, whereas stars formed in atomic cooling haloes that are primordial but affected by previously-generated stellar radiation are referred to as Pop III.2 stars.

background built up by the stars formed is arguably consequential for the formation of Pop III stars. LW photons ($11.2\,\mathrm{eV} < h\nu < 13.6\,\mathrm{eV}$) can regulate Pop III star formation by photo-dissociating H_2 through the two-step Solomon process (Stecher & Williams 1967) and thereby setting the minimum mass of minihaloes above which Pop III stars can form (Haiman et al. 1997; Wolcott-Green et al. 2011; Holzbauer & Furlanetto 2012; Stacy et al. 2012; Visbal et al. 2014; Mebane et al. 2018), although some recent studies suggest that H_2 self-shielding might greatly alleviate the impact of the LW background (see e.g., Skinner & Wise 2020). Other important factors to be considered in modelling the transition include the efficiency of metal enrichment (i.e., chemical feedback) from Pop III supernovae (Pallottini et al. 2014; Sarmento et al. 2018), the X-ray background sourced by Pop III binaries that might replenish H_2 by catalyzing its formation (Haiman et al. 2000; Hummel et al. 2015; Ricotti 2016), and the residual streaming velocity between dark matter and gas (Tseliakhovich & Hirata 2010; Naoz et al. 2012; Fialkov et al. 2012; Schauer et al. 2020b). In spite of all the theoretical efforts, substantial uncertainties remain in how long and to what extent Pop III stars might have coexisted with their metal-enriched descendants, leaving the timing and duration of the Pop III to Pop II transition largely unconstrained.

Direct constraints on Pop III stars would be made possible by detecting their emission features. One such feature is the He II $\lambda1640$ line, which is a strong, narrow emission line indicative of a very hard ionizing spectrum typical for Pop III stars (Schaerer 2003). The association of the He II $\lambda1640$ line with Pop III stars has been pursued in the context of both targeted observations (e.g., Nagao et al. 2005; Cai et al. 2011; Mas-Ribas et al. 2016) and statistical measurements via the line-intensity mapping technique (e.g., Visbal et al. 2015). While possible identifications have been made for objects such as "CR7" (Sobral et al. 2015), the measurements are controversial and a solid He II $\lambda1640$ detection of Pop III stars may not be possible until the operation of next-generation ground-based telescopes such as the E-ELT (Grisdale et al. 2021). A number of alternative (and often complementary) probes of Pop III stars have therefore been proposed, including long gamma-ray bursts (GRBs) associated with the explosive death of massive Pop III stars (Mészáros & Rees 2010; Toma et al. 2011), caustic transits behind lensing clusters (Windhorst et al. 2018), the cosmic near-infrared background (NIRB, Santos et al. 2002; Kashlinsky et al. 2004; Fernandez & Zaroubi 2013; Yang et al. 2015; Helgason et al. 2016; Kashlinsky et al. 2018), and spectral signatures in the global 21-cm signal (Thomas & Zaroubi 2008; Fialkov et al. 2014; Mirocha et al. 2018; Mebane et al. 2020) and 21-cm power spectrum (Fialkov et al. 2013, 2014; Qin et al. 2021b).

Pop III stars have been proposed as a potential explanation for the observed excess in the NIRB fluctuations (Salvaterra & Ferrara 2003; Kashlinsky et al. 2004, 2005), which cannot be explained by the known galaxy populations with sensible faint-end extrapolation (Helgason et al. 2012), and their accreting remnants provide a viable explanation for the coherence between the NIRB and the soft cosmic X-ray background (CXB) detected at high significance (Cappelluti et al. 2013). However, subsequent studies indicate that, for Pop III stars to source a considerable fraction of the observed NIRB, their formation and ionizing efficiencies would need to be so extreme that constraints on reionization and the X-ray background are likely violated (e.g., Madau & Silk 2005; Helgason et al. 2016). Consequently, some alternative explanations have been proposed, such as the intrahalo light (IHL) radiated by stars stripped away from parent galaxies during mergers (Cooray et al. 2012b; Zemcov et al. 2014), with a major contribution from sources at $z < 2$, and accreting direct collapsed black holes (DCBHs) that could emit a significant amount of rest-frame, optical–UV emission at $z \gtrsim 12$ due to the absorption of ionizing radiation by the massive accreting envelope surrounding them (Yue et al. 2013b).

Pop III stars alone are likely insufficient to fully explain the source-subtracted NIRB fluctuations observed and separating their contribution to the NIRB from other sources, including Pop II stars that likely co-existed with Pop III stars over a long period of time, will be challenging. Nevertheless, there is continued interest in understanding and modelling potential signatures of Pop III stars in the NIRB (e.g., Kashlinsky et al. 2004, 2005; Yang et al. 2015; Helgason et al. 2016), which is one of only a few promising probes of Pop III in the near term. In particular, Fernandez and Zaroubi (2013, hereafter FZ13) point out that strong Lyα emission from Pop III stars can lead to a "bump" in the mean spectrum of the NIRB, a spectral signature that can reveal information about physical properties of Pop III stars and the timing of the Pop III to Pop II transition. The soon-to-be-launched satellite Spectro-Photometer for the History of the Universe, Epoch of Reionization and Ices Explorer (SPHEREx; Doré et al. 2014) has the raw sensitivity to detect the contribution of galaxies during the epoch of reionization (EoR) to the NIRB at high significance (Feng et al. 2019), making it possible, at least in principle, to detect or rule out such spectral features. However, despite significant differences in detailed predictions, previous modelling efforts (e.g., Fernandez & Komatsu 2006; Cooray et al. 2012a; Yue et al. 2013a; Helgason et al. 2016) have suggested that first galaxies during and before the EoR may only contribute to approximately less than 1% of both the source-subtracted NIRB mean intensity and its angular fluctuations, as measured from a series of deep imaging surveys (e.g., Kashlinsky et al. 2012; Zemcov et al. 2014; Seo et al. 2015). A challenging measurement notwithstanding, unprecedented NIRB sensitivities of space missions like SPHEREx and the Cosmic Dawn Intensity Mapper (CDIM; Cooray et al. 2019a) urge the need for an improved modelling framework to learn about the first galaxies from future NIRB measurements.

In this work, we establish a suite of NIRB predictions that are anchored to the latest constraints on the high-z galaxy population drawn from many successful *Hubble Space Telescope* (HST) programs, such as the Hubble Ultra Deep Field (Beckwith et al. 2006), CANDELS (Grogin et al. 2011), and Hubble Frontier Fields (Lotz et al. 2017). We employ a semi-empirical model to describe the known galaxy population, and then add in a physically-motivated, but flexible, model for Pop III stars that allow us to explore a wide range of plausible scenarios. This, in various aspects, improves over previous models, which, e.g., parameterized the fraction of cosmic star formation in Pop III haloes as a function of redshift only and/or employed simpler Pop II models calibrated to earlier datasets (e.g., Cooray et al. 2012a; FZ13; Helgason et al. 2016; Feng et al. 2019). These advancements not only allow more accurate modelling of the contribution to the NIRB from high-z galaxies, but also provide a convenient physical framework to analyse and interpret datasets of forthcoming NIRB surveys aiming to quantify the signal level of galaxies during and before reionization.

This chapter is organized as follows. In Section 7.2, we describe how we model the spatial and spectral properties of the NIRB associated with high-z galaxies, using a simple, analytical framework of Pop II and Pop III star formation in galaxies at $z > 5$. We present our main results in Section 7.3, including the predicted NIRB signals, potential spectral imprints due to Pop III star formation, and sensitivity estimates for detecting Pop II and Pop III signals in future NIRB surveys. In Section 7.4, we show implications for other observables of high-z galaxies that can be potentially drawn from NIRB observations. We discuss a few important caveats and limitations of our results in Section 7.5, before briefly concluding in Section 7.6. Throughout this chapter, we assume a flat, ΛCDM cosmology consistent with the results from the Planck Collaboration XIII (2016).

Table 7.1: Parameter values in the reference models of Pop II and Pop III star formation.

Symbol	Parameter	Reference	Model I	Model II	Model III	Model A	Model B	Model C	Model D
		Pop II stars							
f_*	star formation efficiency	equation (7.2)	dpl	steep	floor				
Z	stellar metallicity	Section (7.2.2.1)	0.02	0.02	0.02				
$f_{\rm esc}^{\rm II}$	LyC escape fraction	equation (7.18)	0.1	0.1	0.1				
$f_{\rm esc,LW}^{\rm II}$	LW escape fraction	Section (7.2.1.2)	1	1	1				
		Pop III stars							
$Q(\rm H)$ [s^{-1}]	H photoionization rate	equation (7.5)				10^{50}	10^{51}	10^{50}	10^{51}
$\dot{M}_*^{\rm III}$ [$M_\odot\,\rm yr^{-1}$]	SFR per halo	equation (7.4)				1×10^{-3}	2×10^{-4}	3×10^{-6}	1×10^{-5}
$\mathcal{T}_c$ [Myr]	critical time limit	Section (7.2.1.2)				25	0	0	250
$\mathcal{E}_c$ [erg]	critical binding energy	Section (7.2.1.2)				3×10^{52}	8×10^{51}	1×10^{52}	5×10^{52}
$f_{\rm esc}^{\rm III}$	LyC escape fraction	Fig. (7.3)				0.05/0.2	0.05/0.2	0.05/0.2	0.05/0.2
$f_{\rm esc,LW}^{\rm III}$	LW escape fraction	Section (7.2.1.2)				1	1	0	1

7.2 Models

7.2.1 Star formation history of high-redshift galaxies

7.2.1.1 The formation of Pop II stars

Following Mirocha et al. (2017), we model the star formation rate density (SFRD) of normal, high-z galaxies as an integral of the star formation rate (SFR) per halo $\dot{M}_*(M_h)$ over the halo mass function $n(M_h)$ (see also Sun & Furlanetto 2016; Furlanetto et al. 2017)

$$\begin{aligned}\dot{\rho}_*^{\mathrm{II}}(z) &= \int_{M_{h,\mathrm{min}}^{\mathrm{II}}} n(M_h)\dot{M}_*(M_h, z)dM_h \\ &= \int_{M_{h,\mathrm{min}}^{\mathrm{II}}} n(M_h) f_*(M_h, z)\frac{\Omega_b}{\Omega_m}\dot{M}_h(M_h, z)dM_h \ , \end{aligned} \tag{7.1}$$

where $M_{h,\mathrm{min}}^{\mathrm{II}}$ is generally evaluated at a virial temperature of $T_{\mathrm{vir}} = 10^4\,\mathrm{K}$, a free parameter in our model above which Pop II are expected to form due to efficient cooling via neutral atomic lines (Oh & Haiman 2002), namely $M_{h,\mathrm{min}}^{\mathrm{II}} = M_{h,\mathrm{max}}^{\mathrm{III}}$. $\dot{M}_*(M_h)$ is further specified by a star formation efficiency (SFE), f_*, defined to be the fraction of accreted baryons that eventually turn into stars, and the mass growth rate, $\dot{M}_h$, of the dark matter halo. We exploit the abundance matching technique to determine the mean halo growth histories by matching halo mass functions at different redshifts. As illustrated in Furlanetto et al. (2017) and Mirocha et al. (2020), the abundance-matched accretion rates given by this approach are generally in good consistency with results based on numerical simulations (Trac et al. 2015) for atomic cooling haloes at $5 \lesssim z \lesssim 10$ (but see Schneider et al. 2021 for a comparison with estimates based on the extended Press-Schechter formalism). Even though effects like mergers and the stochasticity in $\dot{M}_h$ introduce systematic biases between the inferences made based on merger trees and abundance matching, such biases can be largely eliminated by properly normalizing the nuisance parameters in the model (Mirocha et al. 2020). By calibrating to the latest observational constraints on the galaxy UV luminosity function (UVLF), Mirocha et al. (2017) estimate f_* to follow a double power-law in halo mass (the `dpl` model)

$$f_*^{\mathrm{dpl}}(M_h) = \frac{f_{*,0}}{\left(\frac{M_h}{M_{\mathrm{p}}}\right)^{\gamma_{\mathrm{lo}}} + \left(\frac{M_h}{M_{\mathrm{p}}}\right)^{\gamma_{\mathrm{hi}}}} \ , \tag{7.2}$$

with no evident redshift evolution, in agreement with other recent work (e.g., Mason et al. 2015; Tacchella et al. 2018; Behroozi et al. 2019; Stefanon et al. 2021). The evolution of f_* for low-mass haloes is however poorly constrained by the faint-end slope of the UVLF, and can be highly dependent on the regulation of feedback processes (Furlanetto et al. 2017; Furlanetto 2021) and the burstiness of star formation (Furlanetto & Mirocha 2022). Therefore, in addition to the baseline `dpl` model, we consider two alternative parameterization — one suggested by Okamoto et al. (2008) that allows a steep drop of f_* for low-mass haloes (the `steep` model)

$$f_*^{\rm steep}(M_h) = \left[1 + \left(2^{\mu/3} - 1\right)\left(\frac{M_h}{M_{\rm crit}}\right)^{-\mu}\right]^{-3/\mu}, \tag{7.3}$$

and the other that imposes a constant floor on the SFE of 0.005 (the `floor` model). In this work, we take the same best-fit parameters as those given by Mirocha et al. (2017) to define the two reference Pop II models, namely $f_{*,0} = 0.05$, $M_{\rm p} = 2.8 \times 10^{11}$, $\gamma_{\rm lo} = 0.49$, $\gamma_{\rm hi} = -0.61$, with $\mu = 1$ and $M_{\rm crit} = 10^{10}\,M_\odot$ for the `steep` model[2]. With the three variants of our Pop II SFE model, we aim to bracket a reasonable range of possible low mass/faint-end behaviour, and emphasize that future observations by the JWST (e.g., Furlanetto et al. 2017; Yung et al. 2019) and line-intensity mapping surveys (e.g., Park et al. 2020; Sun et al. 2021b) can place tight constraints on these models.

7.2.1.2 The formation of Pop III stars

While the star formation history of Pop II stars may be reasonably inferred by combing existing observational constraints up to $z \sim 10$ with physically-motivated extrapolations towards higher redshifts, the history of Pop III stars is only loosely constrained by observations. Several recent studies (e.g., Visbal et al. 2014; Jaacks et al. 2018; Mebane et al. 2018; Sarmento et al. 2018; Liu & Bromm 2020) investigate the formation of Pop III stars under the influence of a variety of feedback processes, including the LW background and supernovae. In general, these models find that Pop III SFRD increases steadily for approximately 200 Myr since the onset of Pop III star formation at $z \gtrsim 30$, before sufficiently strong feedback effects can be established to regulate their formation. In detail, however, the predicted Pop III SFRDs differ substantially in both shape and amplitude. Massive Pop III star formation can persist in minihaloes for different amounts of time depending on factors such as the strength of LW background and the efficiency of metal enrichment (which, in turn, depends on how metals can be produced, retained, and mixed within minihaloes).

[2]The SFE parameters taken are fit to the observed UVLFs measured by Bouwens et al. (2015b) at $6 < z < 8$, which agree reasonably well with the most recent measurements in, e.g., Bouwens et al. (2021).

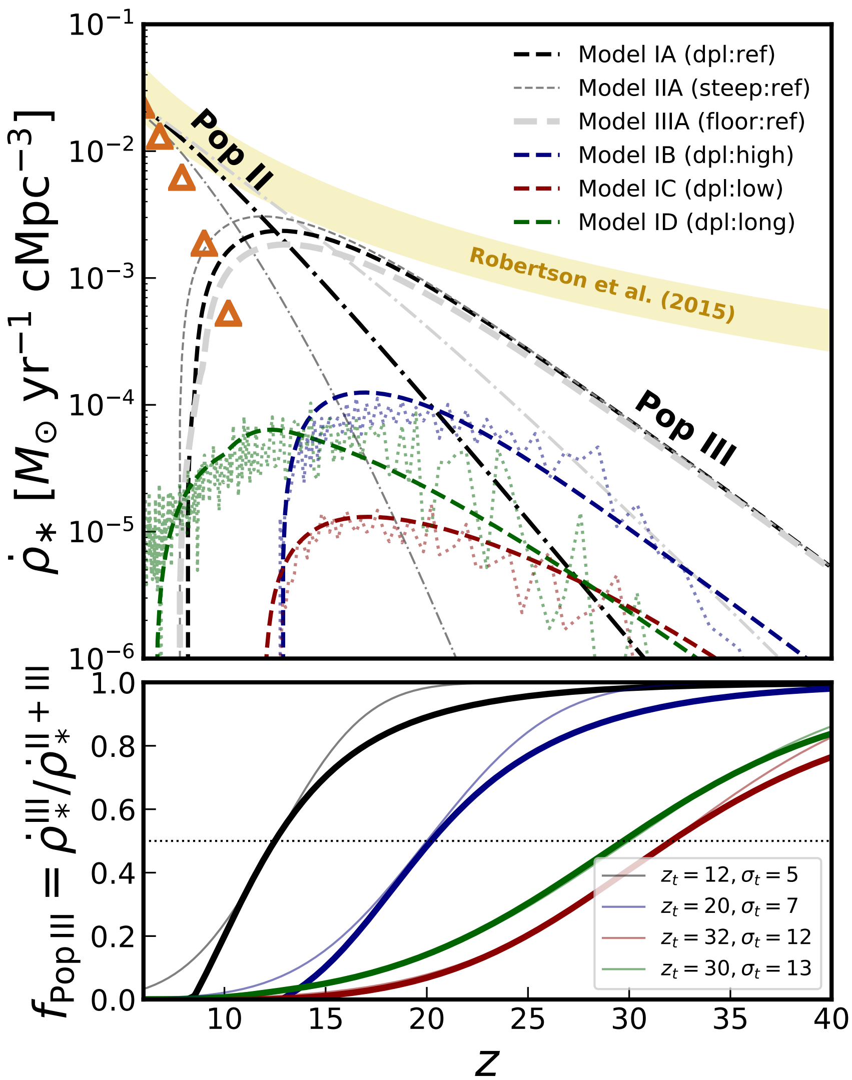

Figure 7.1: Star formation histories. Pop II and Pop III star formation histories in different models considered in this work, as specified in Table 8.1. *Top:* SFRDs of Pop II (dash-dotted) and Pop III (dashed) stars. The black curves represent our reference model (Model IA), with the thin dark grey curve and the thick light grey curve representing variations where the Pop II SFE follows the `steep` (Model II) and `floor` (Model III) models, respectively. The bottom set of three dotted curves show the Pop III histories derived with the semi-analytical approach in Mebane et al. (2018), to which Models IB, IC, and ID are calibrated. The shaded region and open triangles represent the cosmic SFRD inferred from the maximum-likelihood model by Robertson et al. (2015) and the observed SFRD (integrated to a limiting SFR of 0.3 $M_\odot\ \mathrm{yr}^{-1}$) up to $z = 10$ determined by Oesch et al. (2018), respectively. *Bottom:* the stellar population transition represented by the ratio of Pop III and total SFRDs. For comparison, approximations made with the functional form $f_{\mathrm{Pop\ III}}(z) = 1/2 + \mathrm{erf}[(z - z_t)/\sigma_t]/2$ are shown by the thin curves.

Consequently, the formation of Pop III stars can either terminate as early as $z > 10$ in some models, or remain a non-negligible rate greater than $10^{-4}\,\mathrm{M}_\odot\,\mathrm{yr}^{-1}\,\mathrm{Mpc}^{-3}$ through the post-reionization era in others. Given the large uncertainty associated with the Pop III SFRD, we follow Mirocha et al. (2018) and account for the Pop III to Pop II transition with a simple descriptive model, which offers a flexible way to simultaneously capture the physics of Pop III star formation and encompass a wide range of possible scenarios. We defer the interested readers to that paper and only provide a brief summary here.

We assume that Pop III stars can only form in minihaloes with halo mass between $M_{h,\mathrm{min}}^{\mathrm{III}}$ and $M_{h,\mathrm{max}}^{\mathrm{III}}$ at a constant rate $\dot{M}_*^{\mathrm{III}}$ per halo, in which case the Pop III SFRD can be written as

$$\dot{\rho}_*^{\mathrm{III}}(z) = \dot{M}_*^{\mathrm{III}} \int_{M_{h,\mathrm{min}}^{\mathrm{III}}}^{M_{h,\mathrm{max}}^{\mathrm{III}}} n(M_h) dM_h \ . \tag{7.4}$$

The minimum mass, $M_{h,\mathrm{min}}^{\mathrm{III}}$, of Pop III star-forming haloes is set by the threshold for effective H_2 cooling, regulated in response to the growing LW background following Visbal et al. (2014). The maximum mass, $M_{h,\mathrm{max}}^{\mathrm{III}}$, of Pop III star-forming haloes is controlled by two free parameters, which set the critical amount of time individual haloes spend in the Pop III phase, $\mathcal{T}_c$, as well as a critical binding energy, $\mathcal{E}_c$, at which point haloes are assumed to transition from Pop III to Pop II star formation. The first condition effectively results in a fixed amount of stars (and metals) produced per halo in our model, and thus serves as a limiting case in which the Pop III to Pop II transition is governed by the *production* of metals. The second condition enforced by $\mathcal{E}_c$ provides a contrasting limiting case, in which the transition from Pop III to Pop II is instead governed by metal *retention*. In practice, $\mathcal{E}_c$ may range from as small as the typical energy output of a supernova ($\sim 10^{51}$ erg) to a few hundred times larger[3]. It is worth noting that, rather than quantifying the impact of metal enrichment on Pop III star formation and the corresponding NIRB signal through a global volume-filling factor of metal-enriched IGM due to galactic outflows (see e.g., Yang et al. 2015), we use $\mathcal{T}_c$, and $\mathcal{E}_c$ to control the Pop III to Pop II transition. Although this approach does not invoke the metallicity of halos explicitly, it is flexible enough to produce SFRDs that are in good agreement with more sophisticated models, which do link the Pop III to Pop II transition to halo metallicity (e.g., Mebane et al. 2018). Finally, for simplicity, we assume blackbody spectrum for Pop III stars and scale

[3]As discussed in Mirocha et al. (2018), it is likely that $\dot{M}_*^{\mathrm{III}}$, $\mathcal{T}_c$, and $\mathcal{E}_c$ are actually positively-correlated with each other in reality, but we ignore such subtleties here to maximally explore the possible scenarios.

the ionizing flux with the parameter $Q(\mathrm{H})$, which we describe in more detail in Section 7.2.2.2.

Fig. 7.1 shows the star formation histories of Pop II and Pop III stars calculated from a collection of models we consider in this work. Values of key model parameters adopted are summarized in Table 8.1. Specifically, three different cases (all permitted by current observational constraints, see e.g., Mirocha et al. 2017) of extrapolating Pop II star formation down to low-mass, atomic-cooling haloes unconstrained by the observed UVLFs are referred to as Model I (`dpl`, see equation 7.2), Model II (`steep`, see equation 7.3), and Model III (`floor`), respectively. f_{esc} and $f_{\mathrm{esc,LW}}$ represent the escape fractions of Lyman continuum (LyC) and LW photons, respectively. Four Pop III models with distinct SFRDs resulting from different combinations of $\dot{M}_*^{\mathrm{III}}$, $\mathcal{T}_c$, and $\mathcal{E}_c$ are considered. Model A represents an optimistic case with extremely efficient formation of massive, Pop III stars that leads to a prominent signature on the NIRB. To form $100\,M_\odot$ Pop III stars that yields $Q(\mathrm{H}) \sim 10^{50}\,\mathrm{s}^{-1}$ at a rate as high as $\dot{M}_*^{\mathrm{III}} \sim 10^{-3}\,M_\odot\,\mathrm{yr}^{-1}$ in minihaloes with a typical baryonic mass accretion rate of 10^{-3}–$10^{-2}\,M_\odot\,\mathrm{yr}^{-1}$(e.g., Greif et al. 2011; Susa et al. 2014), the star formation efficiency must be exceedingly high and even close to unity over long timescales. This, in turn, requires a relatively inefficient coupling between the growth of Pop III stars and the radiative and mechanical feedback. Models B, C, and D are our model approximations to Pop III histories derived with the semi-analytical approach described in Mebane et al. (2018). Similar to Model A, all these models yield Pop III SFRDs regulated by LW feedback associated with Pop II and/or Pop III stars themselves, as controlled by the parameters $f^{\mathrm{II}}_{\mathrm{esc,LW}}$ and $f^{\mathrm{III}}_{\mathrm{esc,LW}}$. We note that setting $f^{\mathrm{III}}_{\mathrm{esc,LW}}$ to zero (as in Model C) is only meant to turn the LW feedback off, since in reality the escape fraction of LW photons tends to be order of unity in the far-field limit (see e.g., Schauer et al. 2017). Besides the LW feedback that sets the end of the Pop III era, the amplitude of the Pop III SFRD is also determined by the prescription of Pop III star formation. Among the three models, Model C approximates the scenario where Pop III stars with a normal IMF form at a low level of stellar mass produced per burst, which yields NIRB signals likely inaccessible to upcoming observations, whereas Models B and D approximate scenarios where Pop III stars form more efficiently and persistently, respectively, and if massive enough ($M_* \sim 500\,M_\odot$), can leave discernible imprints on the NIRB. For comparison, two additional cosmic SFRDs are shown: (i) that inferred from Robertson et al. (2015) by integrating the UVLFs down to $L_{\mathrm{UV}} \sim 0.001\,L_*$ (yellow band), and (ii) that reported in Oesch et al. (2018) which includes observed galaxies with

$\dot{M}_* \gtrsim 0.3\, M_\odot \mathrm{yr}^{-1}$ (open triangles).

To put things into the context of the literature, we show in the lower panel of Fig. 7.1 the fraction of stars that are Pop III at each redshift. Predictions from our models are shown together with approximations made using the functional form $f_{\rm Pop\ III}(z) = 1/2 + \mathrm{erf}[(z - z_t)/\sigma_t]/2$, which is frequently adopted in the literature to estimate the Pop III contribution (e.g., Cooray et al. 2012a; Fernandez & Zaroubi 2013; Feng et al. 2019). It can be seen that, compared with the phenomenological description using the error function, our physical models imply a more extended early phase with the Pop II SFRD gradually catching up. The late-time behaviour is characterized by how sharply the Pop III phase terminates, which in turn depends on whether $\mathcal{T}_c$ or $\mathcal{E}_c$ is in operation.

7.2.2 Spectra of high-z galaxies

In this section, we introduce our approach to modelling the spectral energy distribution (SED) of high-z galaxies. An illustrative example is shown first in Fig. 7.2, which includes Pop II and Pop III spectra, with and without the additional contribution from nebular emission. Each component of the SED is described in more detail in Section 7.2.2.1–7.2.2.4. We note that for the NIRB contribution from nebular line emission we only include hydrogen lines like Lyα, the strongest emission line from high-z galaxies in the near-infrared, even though lines such as the He II λ1640 line (for Pop III stars) could also be interesting — in the sense of both their contributions to the NIRB and their spatial fluctuations that can be studied in the line-intensity mapping regime. In the following subsections, we specify the individual components of the NIRB according to how they are implemented in ARES[4] (Mirocha 2014), which was used to conduct all the calculations in this work.

7.2.2.1 Direct stellar emission

The direct stellar emission from the surfaces of Pop II and Pop III stars is the foundation upon which the full SED of high-z galaxies is built in our models. It depends in general on the stellar IMF, metallicity, and assumed star formation history of galaxies. For the SED of Pop II stars, we adopt the single-star models calculated with the stellar population synthesis (SPS) code BPASS v1.0 (Eldridge & Stanway 2009), which assume a Chabrier IMF (Chabrier 2003) and a metallicity of

[4] https://github.com/mirochaj/ares

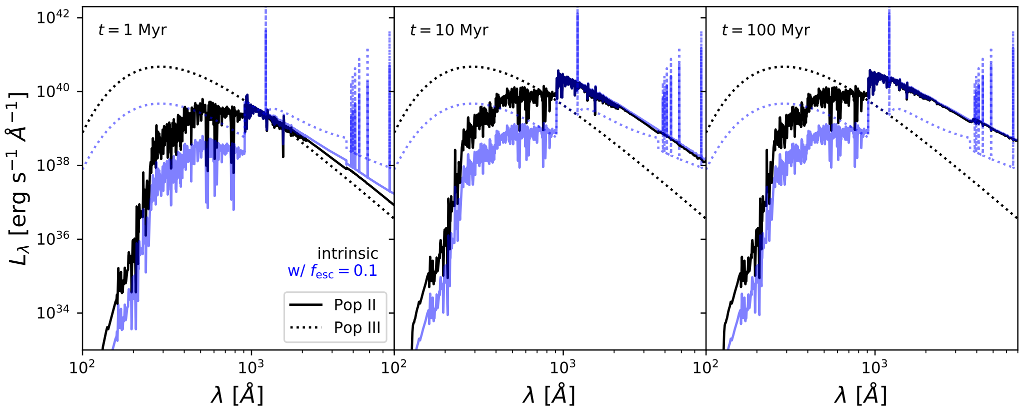

Figure 7.2: Example spectra of stellar populations employed in this work. In each panel, black curves show the intrinsic Pop II (solid) and Pop III (dotted) stellar continuum. For Pop II, we show models that assume a constant SFR of 1 $M_\odot$ yr^{-1} with ages of 1, 10, and 100 Myr (left to right). Pop III models are the same in each panel, and assume a single star with ionizing luminosity of 10^{48} photons s^{-1}. Blue lines show the nebular continuum and nebular line emission (see Section 7.2.2.2-7.2.2.4), powered by the absorption of Lyman continuum photons assuming an escape fraction of 10%. We adopt the $t = 100$ Myr models (right-most panel) throughout, a timescale on which the rest-UV spectrum will asymptote to a constant level. The early time evolution is included to demonstrate the nebular continuum treatment.

$Z = 0.02$[5] in the default case. As is common in many semi-empirical models, we further assume a constant star formation history, for which the rest-UV spectrum evolves little after $\sim$ 100 Myr. We therefore adopt 100 Myr as the fiducial stellar population age, as in Mirocha et al. (2017, 2018), which is a reasonable assumption for high-z galaxies with high specific star formation rates (sSFRs) of the order 10 Gyr^{-1} (e.g., Stark et al. 2013). For Pop III stars, the SED is assumed to be a 10^5 K blackbody for simplicity, which is appropriate for stars with masses $\gtrsim$ 100 $M_\odot$ (e.g., Tumlinson & Shull 2000; Schaerer 2002). We further assume that Pop III stars form in isolation, one after the next, which results in a time-independent SED.

7.2.2.2 Lyα emission

The full spectrum of a galaxy must also account for reprocessed emission originating in galactic HII regions. The strongest emission line is Lyα — because Lyα emission is mostly due to the recombination of ionized hydrogen, a simple model for its line

[5]While it is plausible to assume sub-solar metallicity for galaxies during and before reionization given the rate of metal enrichment expected (Furlanetto et al. 2017), the exact value of Z is highly uncertain and lowering it by 1 or 2 dex does not change our results qualitatively.

luminosity can be derived assuming ionization equilibrium and case-B recombination. Specifically, the photoionization equilibrium is described by defining a volume $V_{\rm S}$ within which the ionization rate equals the rate of recombination

$$\alpha_{\rm B} n_e^{\rm neb} n_{\rm H\,II}^{\rm neb} V_{\rm S} = Q({\rm H}) \, , \tag{7.5}$$

where $\alpha_{\rm B} = \alpha_{2^2{\rm P}}^{\rm eff} + \alpha_{2^2{\rm S}}^{\rm eff}$ is the total case-B recombination coefficient as the sum of effective recombination coefficients to the 2^2P and 2^2S states, and $Q({\rm H})$ is the photoionization rate in $\rm s^{-1}$. It is important to note that, in previous models of the NIRB, an additional factor $(1 - f_{\rm esc})$ is often multiplied to $Q_{\rm H}$. It is intended to roughly account for the fraction of ionizing photons actually leaking into the intergalactic medium (IGM), and therefore not contributing to the absorption and recombination processes that source the nebular emission. We have chosen not to take this simple approximation in our model, but to physically connect $f_{\rm esc}$ with the profile of ionizing radiation instead (see Section 7.2.4). The Lyα emission ($2^2P \rightarrow 1^2S$) is associated with the recombination of ionized hydrogen to the 2^2P state, so its line luminosity can be written as

$$l^{{\rm Ly}\alpha} = h\nu_{{\rm Ly}\alpha} \alpha_{2^2{\rm P}}^{\rm eff} n_e^{\rm neb} n_{\rm H\,II}^{\rm neb} V_{\rm S} = \frac{Q({\rm H}) h\nu_{{\rm Ly}\alpha} \alpha_{2^2{\rm P}}^{\rm eff}}{\alpha_{\rm B}} \, , \tag{7.6}$$

or in the volume emissivity $\epsilon_\nu^{{\rm Ly}\alpha}$

$$\epsilon_\nu^{{\rm Ly}\alpha} V_{\rm S} = Q({\rm H}) f_{{\rm Ly}\alpha} h\nu_{{\rm Ly}\alpha} \phi(\nu - \nu_{{\rm Ly}\alpha}) \, , \tag{7.7}$$

where $f_{{\rm Ly}\alpha} = \alpha_{2^2{\rm P}}^{\rm eff}/\alpha_{\rm B} \approx 2/3$ is the fraction of recombinations ending up as Lyα radiation and $\phi(\nu - \nu_{{\rm Ly}\alpha})$ is the line profile, which we assume to be a delta function in our model.

Now, with ϵ_b being the number of ionizing photons emitted per stellar baryon, which we derive from the stellar spectrum generated with BPASS (see Section 7.2.2.1), we can write

$$Q({\rm H}) \approx \epsilon_b \dot{\rho}_* V_{\rm S}/m_p \, , \tag{7.8}$$

where m_p is the mass of the proton. The volume emissivity of Lyα photons is then

$$\bar{\epsilon}_\nu^{{\rm Ly}\alpha} {\rm d}\nu = \frac{\dot{\rho}_*}{m_p} f_{{\rm Ly}\alpha} \epsilon_b h\nu_{{\rm Ly}\alpha} \phi(\nu - \nu_{{\rm Ly}\alpha}) d\nu \, . \tag{7.9}$$

It is also important to note that the above calculations assume Lyα emission is completely described by the case-B recombination of hydrogen, which only accounts for the photoionization from the ground state. In practice, though, additional effects such as collisional excitation and ionization may cause significant departures from the case-B assumption. These effects have been found to be particularly substantial for metal-free stars, which typically have much harder spectra than metal-enriched stars (see e.g., Raiter et al. 2010 and Mas-Ribas et al. 2016 for details). Due to the deficit of cooling channels, low-metallicity nebulae can have efficient collisional effects that induce collisional excitation/ionization and ionization from excited levels[6], which all lead to a higher Lyα luminosity than expected under the case-B assumption. This enhancement is found to scale with the mean energy of ionizing photons. Meanwhile, density effects can mix 2^2S and 2^2P states, thus altering the relative importance of Lyα and two-photon emission. This is determined simply by $\alpha^{\rm eff}_{2^2{\rm P}}$ and $\alpha^{\rm eff}_{2^2{\rm S}}$ in the low-density limit. When density effects are nontrivial as n_e becomes comparable to the critical density $n_{e,\rm crit}$ (at which $2^2{\rm S} \rightarrow 2^2{\rm P}$ transition rate equals the radiative decay rate), collisions may de-populate the 2^2S state of hydrogen before spontaneous decay occurs. In this case, Lyα is further enhanced at the expense of two-photon emission.

For simplicity, in our model we introduce an ad hoc correction factor $\mathcal{D}_{\rm B}$ to account for the net boosting effect of Lyα emission from Pop III star-forming galaxies. Throughout our calculations, we use a fiducial value of $\mathcal{D}_{\rm B} = 2$ for Pop III stars, a typical value for very massive Pop III stars considered in this work, and $\mathcal{D}_{\rm B} = 1$ for Pop II stars. The volume emissivity after correcting for case-B departures is then

$$\bar{\epsilon}_\nu^{\rm Ly\alpha} d\nu = \frac{\dot{\rho}_*(z)}{m_p} \epsilon_b h\nu_{\rm Ly\alpha} \mathcal{D}_{\rm B} \phi(\nu - \nu_{\rm Ly\alpha}) d\nu \ . \tag{7.10}$$

We also note that, by default, our nebular line model also includes Balmer series lines, using line intensity values from Table 4.2 of Osterbrock & Ferland (2006).

7.2.2.3 Two-photon emission

For two-photon emission ($2^2S \rightarrow 1^2S$), the probability of transition producing *one* photon with frequency in range $\mathrm{d}x = \mathrm{d}\nu/\nu_{\rm Ly\alpha}$ can be modelled as (Fernandez & Komatsu 2006)

$$P(x') = 1.307 - 2.627x'^2 + 2.563x'^4 - 51.69x'^6 \ , \tag{7.11}$$

[6]Mas-Ribas et al. (2016) find the column density and optical depth of hydrogen atoms in the first excited state to be very small in their photoionization simulations using Cloudy (Ferland et al. 2013), meaning that the photoionization from $n = 2$ is likely inconsequential for the boosting.

where $x' = x - 0.5$. Note that $P(x')$ is symmetric around $x = 0.5$ as required by energy conservation and is normalized such that $\int_0^1 P(x)dx = 1$. By analogy to L$y\alpha$ emission, the two-photon volume emissivity under the case-B assumption can be written as

$$\bar{\epsilon}_\nu^{2\gamma} d\nu = \frac{\dot{\rho}_*(z)}{m_p}(1 - f_{\mathrm{Ly}\alpha})\epsilon_b \frac{2h\nu}{\nu_{\mathrm{Ly}\alpha}} P(\nu/\nu_{\mathrm{Ly}\alpha}) d\nu \ . \tag{7.12}$$

7.2.2.4 Free-free & free-bound emission

The free-free and free-bound (recombination to different n levels of hydrogen) emission also contribute to the nebular continuum. The specific luminosity and the volume emissivity are related by

$$l_\nu = \frac{\epsilon_\nu Q_{\mathrm{H}}}{n_e n_p \alpha_{\mathrm{B}}} \ , \tag{7.13}$$

where α_{B} as a function of gas temperature T_g is given by

$$\alpha_{\mathrm{B}} = \frac{2.06 \times 10^{-11}}{T_g^{1/2}} \phi_2(T_g) \sim \frac{2.06 \times 10^{-11}}{T_g^{1/2}} \,\mathrm{cm}^3\,\mathrm{s}^{-1} \ , \tag{7.14}$$

where $\phi_2(T_g)$ is a dimensionless function of gas temperature that is of order unity for a typical temperature of H II regions $T_g \approx 2 \times 10^4$ K. We take the following expression given by Dopita & Sutherland (2003) for the volume emissivity including both free-free and free-bound emission

$$\epsilon_\nu^{\mathrm{free}} = 4\pi n_e n_p \gamma_{\mathrm{c}}(\nu) \frac{e^{-h\nu/kT_g}}{T_g^{1/2}} \,\mathrm{erg\,cm^{-3}\,s^{-1}\,Hz^{-1}} \ , \tag{7.15}$$

where a continuous emission coefficient, $\gamma_{\mathrm{c}}(\nu)$, in units of $\mathrm{cm^3\,erg\,s^{-1}\,Hz^{-1}}$ is introduced to describe the strengths of free-free and free-bound emission. Values of γ_{c} as a function of frequency are taken from Table 1 of Ferland (1980), which yield a nebular emission spectrum in good agreement with the reprocessed continuum predicted by photoionization simulations. We can then write the emissivity as

$$\bar{\epsilon}_\nu^{\mathrm{free}} d\nu = \frac{4\pi}{2.06 \times 10^{-11}} \frac{\dot{\rho}_*(z)}{m_p} \epsilon_b e^{-h\nu/kT} \gamma_c(\nu) d\nu \ . \tag{7.16}$$

Note that the volume emissivities shown above with an overbar can be considered as the first moment of luminosity, namely averaging the luminosity per halo over the halo mass function

$$\bar{\epsilon}_\nu^i(z) = \int n(M_h) l_\nu^i(M_h, z) dM_h \ , \tag{7.17}$$

where $l_\nu^i(M_h, z)$ is the specific luminosity of component i as a function of halo mass and redshift, which can be obtained by simply replacing the SFRD, $\dot{\rho}_*$, in equation (7.16) with the star formation rate, $\dot{M}_*$.

7.2.3 Mean NIRB intensity

For a given source population, the mean intensity at an observed frequency ν_0 of the NIRB can be described by evolving the volume emissivity through cosmic time (i.e., the solution to the cosmological radiative transfer equation)

$$J_{\nu_0}(z) = \frac{1}{4\pi}\int_{z_0}^{z} dz' \frac{d\ell}{dz'}\frac{(1+z_0)^3}{(1+z')^3}\bar{\epsilon}_{\nu'}^{\mathrm{prop}}(z')e^{-\tau_{\mathrm{HI}}(\nu,z_0,z')} , \tag{7.18}$$

where $d\ell/dz' = c/[H(z')(1+z')]$ is the proper line element and $\nu' = \nu_0(1+z')/(1+z_0)$. For $z_0 = 0$, the average, comoving volume emissivity is related to the proper volume emissivity by $\bar{\epsilon}_\nu(z) = \bar{\epsilon}_\nu^{\mathrm{prop}}(z)/(1+z)^3$. If one assumes the IGM is generally transparent to NIRB photons from high redshifts, then the mean intensity can be simplified to (e.g., Fernandez et al. 2010; Yang et al. 2015)

$$J_\nu \equiv \bar{I}_\nu = \frac{c}{4\pi}\int dz \frac{\bar{\epsilon}_{\nu'}(z)}{H(z)(1+z)} , \tag{7.19}$$

or the per logarithmic frequency form (e.g., Cooray et al. 2012a),

$$\nu\bar{I}_\nu = \frac{c}{4\pi}\int dz \frac{\nu'\bar{\epsilon}_{\nu'}(z)}{H(z)(1+z)^2} . \tag{7.20}$$

However, the IGM absorption may not be negligible for certain NIRB components, such as the highly resonant Lyα line, in which case the radiative transfer equation must be solved in detail. To approximate the attenuation by a clumpy distribution of intergalactic H I clouds, we adopt the IGM opacity model from Madau (1995). In ARES, equation (7.19) is solved numerically following the algorithm introduced in Haardt & Madau (1996).

7.2.4 NIRB fluctuations

Using the halo model established by Cooray & Sheth (2002), we can express the three-dimensional (3D), spherically-averaged power spectrum of the NIRB anisotropy associated with high-z galaxies as a sum of three terms

$$P_{\mathrm{NIR}}(k,z) = P_{\mathrm{2h}}(k,z) + P_{\mathrm{1h}}(k,z) + P_{\mathrm{shot}}(z) , \tag{7.21}$$

where each term is composed of direct stellar emission and/or nebular emission. In our model, we divide the emission from a galaxy into two components: (1) a discrete, point-source-like component sourced by direct stellar emission and contributing to the two-halo and shot-noise terms, and (2) a continuous, spatially-extended component sourced by nebular emission from the absorption of ionizing photons in the circumgalactic medium (CGM) or IGM by neutral gas and contributing to the two-halo and one-halo terms.

Specifically, the two-halo term is proportional to the power spectrum of the underlying dark matter density field

$$P_{2\mathrm{h}}(k) = \left[\int n(M_h) b(M_h) \sum_i l_\nu^i(M_h) u_i(k|M_h) dM_h\right]^2 P_{\delta\delta}(k), \tag{7.22}$$

where the summation is over the stellar and nebular components of galactic emission and $u(k)$ is the normalized Fourier transform of the halo flux profile. $P_{\delta\delta}$ is the dark matter power spectrum obtained from CAMB (Lewis et al. 2000). We take $u_*(k) = 1$ for the halo luminosity of direct stellar emission (l_ν^*) and derive the functional form $u_\mathrm{n}(k)$ for the halo luminosity of nebular emission ($l_\nu^{\mathrm{Ly}\alpha}$, $l_\nu^{2\gamma}$, $l_\nu^{\mathrm{ff+fb}}$) using the profile of ionizing flux emitted from the galaxy. Because the one-halo term is only sourced by nebular emission, it can be expressed as

$$P_{1\mathrm{h}}(k) = \int n(M_h) \left[\sum_j l_\nu^j(M_h) u_\mathrm{n}(k|M_h)\right]^2 dM_h\ , \tag{7.23}$$

where the summation is over the different types of nebular emission described in Sections 7.2.2.2–7.2.2.4. Finally, the scale-independent shot-noise term is solely contributed by direct stellar emission, namely

$$P_\mathrm{shot} = \int n(M_h) \left[l_\nu^*(M_h)\right]^2 dM_h\ . \tag{7.24}$$

For simplicity, we ignore the stochasticity in luminosity–halo mass relations for the ensemble of galaxies. Its effect on the shape of $P_\mathrm{NIR}(k)$ may be quantified by assuming a probability distribution function (e.g., Sun et al. 2019), but is likely subdominant to (and degenerate with) the systematic uncertainties associated with the relations themselves.

7.2.4.1 The radial profile of nebular emission

We stress that in our model, the nebular emission is assumed to be smooth and thus contributes to $P_{2\mathrm{h}}$ and $P_{1\mathrm{h}}$ only. In addition, rather than treating f_esc as a completely free parameter, we determine its value from the profile of ionizing flux, which in turn depends on the neutral gas distribution surrounding galaxies. This effectively renders $f_{\rm esc}$ and the shape of the one-halo term, which is captured by $u_{\rm n}(k|M)$, dependent on each other.

To derive $u_{\rm n}(k|M)$, we consider the scenario in which ionizing photons are radiated away from the centre of galaxy under the influence of neutral gas distribution in the CGM. While ionizing photons escaped into the IGM can also in principle induce large-scale fluctuations of the types of nebular emission considered in this work, especially Lyα, their strengths are found to be subdominant to the emission close to galaxies (e.g., Cooray et al. 2012a). For the CGM, since a substantial overdensity of neutral hydrogen exists in the circumgalactic environment in the high-redshift universe, the extended Lyα (and other nebular) emission is primarily driven by the luminosity of the ionizing source and the distribution of neutral gas clumps surrounding it. Here we only provide a brief description of the neutral gas distribution models adopted and refer interested readers to Mas-Ribas & Dijkstra (2016) and Mas-Ribas et al. (2017b) for further details. For the Lyα flux resulting from the fluorescent effect in the CGM, the radial profile at a proper distance r scales as

$$\mathrm{d}F_{\mathrm{Ly}\alpha}(r) \propto -r^{-2} f_{\rm c}(r) f_{\rm esc}(r) dr \ , \tag{7.25}$$

where r^{-2} describes the inverse-square dimming and $f_{\rm esc}(r) = \exp -[\int_0^r f_{\rm c}(r')dr']$ represents the fraction of ionizing photons successfully escaped from the ionizing source at distance r. $f_{\rm c}(r)$ is the *differential*, radial covering fraction of H I clumps, whose line-of-sight integral gives the total number of clumps along a sight line, analogous to the number of mean free path lengths. The product $f_{\rm c} f_{\rm esc}$ can be interpreted as the chance that an ionizing photon gets absorbed by a clump of H I cloud and thus gives rise to a Lyα photon. The resulting flux profile can then be expressed as

$$F_{\mathrm{Ly}\alpha}(r) \propto \int_r^\infty r'^{-2} f_{\rm c}(r') f_{\rm esc}(r') dr' \ , \tag{7.26}$$

given the boundary condition $F_{\mathrm{Ly}\alpha} = 0$ as $r \rightarrow \infty$.

Various CGM models have been proposed for high-z galaxies, from which the H I covering fraction $f_{\rm c}(r)$ can be obtained. However, due to the paucity of observational constraints especially in the pre-reionization era, it is impractical to robustly determine which one best describes the nebular emission profile of high-z galaxies relevant to our model. As a result, we follow Mas-Ribas et al. (2017b) and consider two CGM models that predict distinct H I spatial distributions surrounding galaxies, leading to high and low escape fractions of ionizing photons, respectively. We

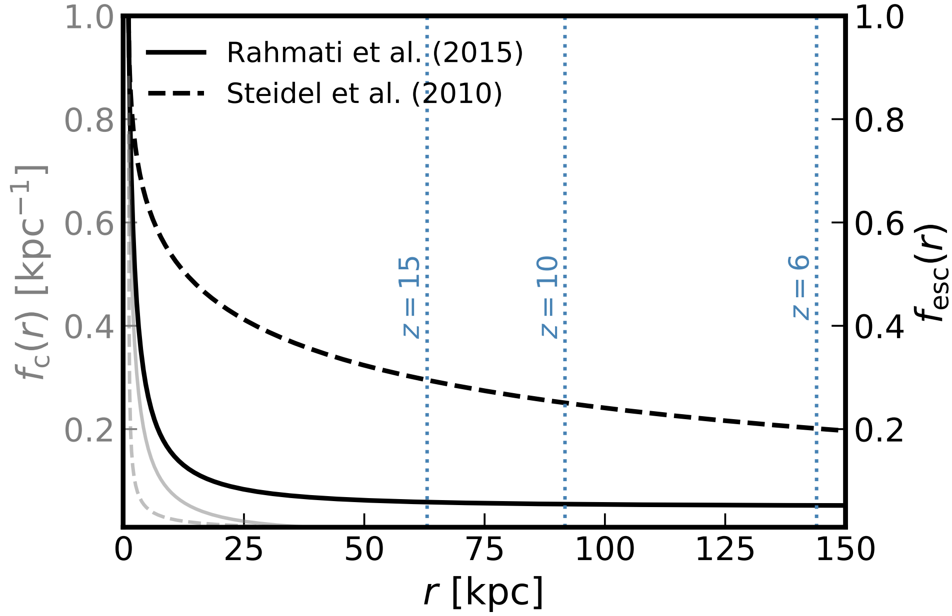

Figure 7.3: Radial profiles of the H I covering fraction and the escape fraction of ionizing photons. The radial profiles of the H I covering fraction f_c (grey, left axis) and the escape fraction of ionizing photons f_{esc} (black, right axis) as functions of the radial distance r away from the galaxy, derived from two CGM models by Rahmati et al. (2015) and Steidel et al. (2010). The virial radius of a $10^{14}\,M_\odot$ halo, which defines an upper bound on the scale relevant to ionizing photons escaping into the IGM, is quoted at $z = 6$, 10, and 15 (dotted vertical lines).

caution that the two profiles are explored here only to demonstrate the connection between $f_{esc}(r)$ and small-scale fluctuations. Exact escape fractions they imply are assessed with other observational constraints, such as the CMB optical depth, and therefore some tension may exist for a subset of our Pop III models. We will revisit this point in Section 7.4.1.

The low-leakage model is based on the fitting formula (see equation 17 of Mas-Ribas & Dijkstra 2016) for the area covering fraction of Lyman limit systems (LLSs), $\mathcal{F}_{\rm LLS}$, inferred from the EAGLE simulation (Rahmati et al. 2015). It has been successfully applied to reproduce the observed stacked profile of extended Lyα emission from Lyman-alpha emitters (LAEs) out to $z = 6.6$. Specifically, the radial covering fraction f_c is related to the area covering fraction $\mathcal{F}_{\rm LLS}(b)$, defined for a total area of $2\pi b db$ at the impact parameter b, by an inverse Abel transformation

$$f_c(r) = -\frac{1}{\pi}\int_r^\infty \frac{dN_{\rm clump}}{dy}\frac{dy}{\sqrt{y^2 - r^2}}\,, \tag{7.27}$$

where the number of gas clumps encountered is given by $N_{\rm clump}(b) = -\ln\left[1 - \mathcal{F}_{\rm LLS}(b)\right]$. The high-leakage model is proposed by Steidel et al. (2010) to provide a simple explanation to interstellar absorption lines and Lyα emission in the observed far-UV spectra of Lyman break galaxies (LBGs) at $z \lesssim 3$. It describes a clumpy outflow consisting of cold H I clumps embedded within a hot medium accelerating radially outward from the galaxy. The radial covering fraction $f_{\rm c}$ in this case can be written as (Dijkstra & Kramer 2012)

$$f_{\rm c}(r) = n_{\rm c}(r)\pi R_{\rm c}^2\,, \tag{7.28}$$

where $n_{\rm c}(r)$ is the number density of the H I clumps that is inversely proportional to their radial velocity $v(r)$ determined from the observed spectra, and the clump radius $R_{\rm c} \propto r^{-2/3}$ under pressure equilibrium.

Fig. 7.3 shows a comparison between radial profiles of $f_{\rm c}$ and $f_{\rm esc}$ in the two CGM models considered. The higher H I covering fraction in the Rahmati et al. (2015) model results in an $f_{\rm esc}$ profile which declines more rapidly with r than that from the Steidel et al. (2010) model. Given the potentially large uncertainties associated with the exact mapping between the $f_{\rm esc}$ profile and the average escape fraction $\bar{f}_{\rm esc}$ that matters for reionization, we refrain from defining $\bar{f}_{\rm esc}$ at the virial radius of a halo that hosts a typical EoR galaxy, as done by Mas-Ribas et al. (2017b). Instead, we quote the value of $f_{\rm esc}$ as predicted by the two CGM models at a proper distance $r = 150\,$kpc, sufficiently large compared to the virial radii of the largest relevant haloes ($10^{14}\,M_{\odot}$) as shown by the vertical dotted lines in Fig. 7.3. This allows us to effectively define *lower bounds* on the average escape fraction $\bar{f}_{\rm esc} = 0.05$ and 0.2 corresponding to the Rahmati et al. (2015) and Steidel et al. (2010) models, respectively, which in turn set *upper bounds* on the nebular emission signal allowed in the two cases. We note, nevertheless, that both CGM models predict only modest evolution of $f_{\rm esc}(r)$ beyond a few tens kpc — the size range of more typical haloes hosting ionizing sources. The exact choice of $\bar{f}_{\rm esc}$ value is thus expected to have only a small impact on the NIRB signal predicted, whereas the corresponding reionization history is more sensitive to this choice, as will be discussed in Section 7.4.1. To simplify the notation, in what follows we will drop the bar and use $f_{\rm esc}$ to denote the lower bound on $\bar{f}_{\rm esc}$ inferred from the CGM model chosen. As summarized in Table 8.1, in our models we set $f_{\rm esc}^{\rm III} = 0.05$ or 0.2 for Pop III stars according to the two CGM models, whereas for Pop II stars we adopt an intermediate profile that yields $f_{\rm esc}^{\rm II} = 0.1$. With reasonable faint-end extrapolations as in our model, an escape fraction of 10% is proven to yield a reionization history consistent with current observations without the presence of unknown source populations like Pop III stars.

7.2.4.2 The angular power spectrum

Following Fernandez et al. (2010) and Loeb & Furlanetto (2013), we can derive the angular power spectrum from the 3D power spectrum. With an observed frequency ν, equation (7.19) gives the NIRB intensity, which can be expressed as a function of direction on the sky $\hat{\mathbf{n}}$

$$I_\nu(\hat{\mathbf{n}}) = \frac{c}{4\pi} \int_{z_{\min}}^{z_{\max}} \frac{\epsilon_{\nu'}[z, \hat{\mathbf{n}} r(z)]}{H(z)(1+z)} dz \,, \tag{7.29}$$

where $\nu' = (1+z)\nu$ and $r(z)$ is the comoving radial distance out to a redshift z. Spherical harmonics decomposing $I_\nu(\hat{\mathbf{n}})$ gives

$$I_\nu(\hat{\mathbf{n}}) = \sum_{\ell,m} a_{\ell m} Y_\ell^m(\hat{\mathbf{n}}) \,, \tag{7.30}$$

with the coefficient

$$a_{\ell m} = \frac{c}{4\pi} \int \frac{dz \int d\hat{\mathbf{n}} \int \frac{d^3\mathbf{k}}{(2\pi)^3} \epsilon_{\nu'}(z, \mathbf{k}) e^{-i\mathbf{k}\cdot\hat{\mathbf{n}} r(z)} Y_{\ell m}^*(\hat{\mathbf{n}})}{H(z)(1+z)} \,. \tag{7.31}$$

Using Rayleigh's formula for $e^{-i\mathbf{k}\cdot\hat{\mathbf{n}} r(z)}$, we have

$$a_{\ell m} = \int \frac{c(-1)^\ell dz}{H(z)(1+z)} \int \frac{d^3\mathbf{k}}{(2\pi)^3} \tilde{\epsilon}_{\nu'}(z, \mathbf{k}) j_\ell[kr(z)] Y_{\ell m}^*(\hat{\mathbf{k}}) \,. \tag{7.32}$$

The angular power spectrum is consequently defined as the ensemble average $C_\ell = \langle |a_{\ell m}|^2 \rangle$. For a pair of observed frequencies ν_1 and ν_2, it can be written as (assuming Limber's approximation, which is valid for the range of $\ell \gg 1$ considered in this work)

$$C_\ell^{\nu_1\nu_2} = \frac{c}{(4\pi)^2} \int \frac{P_{\rm NIR}^{\nu_1\nu_2}\left[\nu_1(1+z), \nu_2(1+z), \ell/r(z)\right] dz}{H(z) r^2(z)(1+z)^2} \,, \tag{7.33}$$

where $P_{\rm NIR}^{\nu_1\nu_2}$ is the 3D NIRB power spectrum defined in equation 7.21.

Alternatively, a *band-averaged* intensity may be defined, in which case a factor of $(1+z)$ must be introduced to account for the cosmological redshift (Fernandez et al. 2010). Namely, in contrast to equation 7.29, we have

$$\begin{aligned} I(\hat{\mathbf{n}}) &= \frac{1}{\Delta\nu} \int_{\nu_1}^{\nu_2} d\nu I_\nu(\hat{\mathbf{n}}) \\ &= \frac{c}{4\pi\Delta\nu} \int dz \frac{\int_{\nu_1(1+z)}^{\nu_2(1+z)} d\tilde{\nu} \epsilon_{\tilde{\nu}}[z, \hat{\mathbf{n}} r(z)]}{H(z)(1+z)^2} \\ &= \frac{c}{4\pi\Delta\nu} \int dz \frac{\rho_L^{\rm em}[z, \hat{\mathbf{n}} r(z)]}{H(z)(1+z)^2} \,, \end{aligned} \tag{7.34}$$

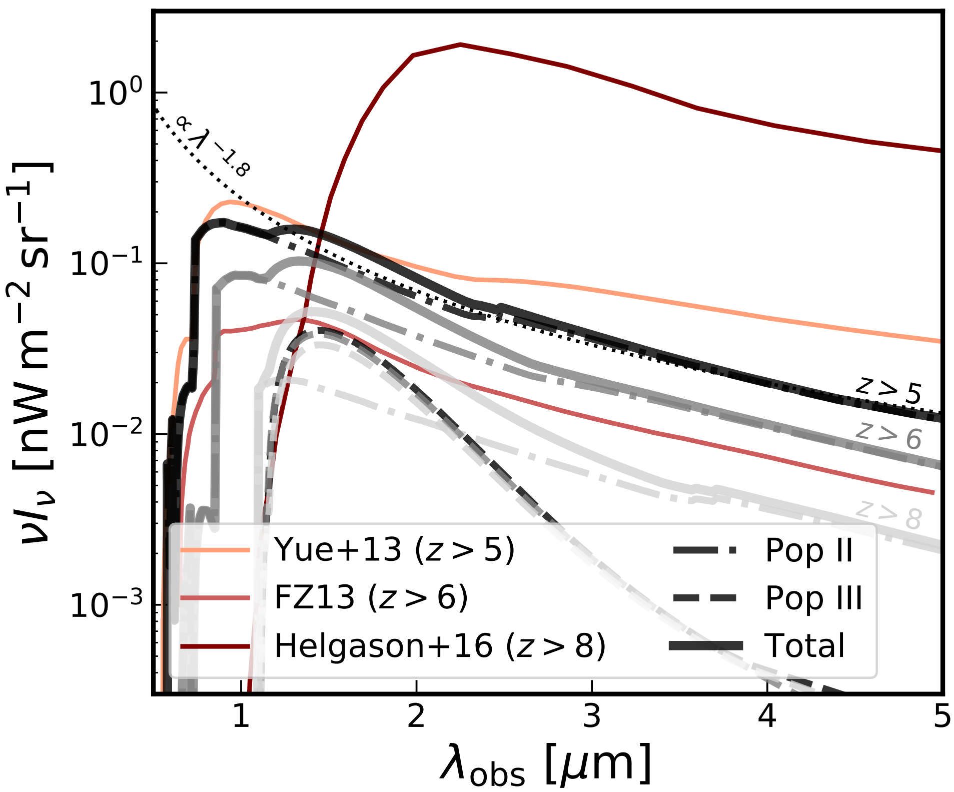

Figure 7.4: Spectra of NIRB mean intensity. The spectra of NIRB mean intensity $\nu \bar{I}_\nu$ sourced by Pop II (dash-dotted) and Pop III (dashed) star-forming galaxies at different redshifts, predicted by Model IA. The Pop II contribution can be approximated by $\lambda^{-1.8}$. For comparison, we show in color a few model predictions in the literature that include contributions from both Pop II and Pop III stars (Yue et al. 2013a; FZ13; Helgason et al. 2016). The impact of the Pop III to Pop II transition, which varies significantly among these models, can be seen from the shape and amplitude of NIRB spectrum. A spectral peak redward of 1 micron is characteristic of a significant Lyα contribution to the NIRB intensity due to the efficient formation of massive, Pop III stars.

where $\rho_L^{\rm em}$ represents the luminosity density emitted over some frequency band at the corresponding redshift. The band-averaged angular power spectrum is then

$$C_\ell = \frac{c}{(4\pi\Delta\nu)^2} \int \frac{dz}{H(z) r^2(z) (1+z)^4} P_L^{\rm NIR} \left[k = \ell / r(z), z\right] \ . \tag{7.35}$$

7.3 Results

In this section, we show the high-z NIRB signals sourced by galaxies at $z > 5$, with the emphasis on the potential contribution of Pop III stars. We first present a general picture expected given our reference model which combines a semi-empirical description of the known, Pop II star-forming galaxies and an optimistic model of Pop III star formation, characterized by high Pop III SFR with relatively inefficient chemical feedback (Section 7.3.1). Then, by exploring a range of plausible Pop III star formation histories, we focus on how spectral signatures of Pop III stars on the NIRB connect to their properties (Section 7.3.2). Finally, we estimate the sensitivities of two future instruments, SPHEREx and CDIM, to the high-z NIRB signals (Section 7.3.3).

7.3.1 The NIRB from star-forming galaxies at $z > 5$

To provide a general picture of the NIRB signal associated with first galaxies, we define our reference model to be Model IA, as specified in Table 8.1. The SFE of Pop II stars f_* follows a double power-law in mass fit to the observed galaxy UVLFs over $5 < z < 10$, and the Pop III SFRD is tuned such that the total cosmic SFRD roughly matches the maximum-likelihood model from Robertson et al. (2015) based on the electron scattering optical depth τ_e of CMB photons from Planck. A set of variations around this baseline case will be considered in the subsections that follow.

In Fig. 7.4, we show the mean intensity spectra of the NIRB over 0.75–5 μm, calculated from Model IA with different redshift cutoffs. For comparison, results from the literature that account for both Pop II and Pop III stars with similar cutoffs are also displayed. The sharp spectral break at the Lyα wavelength redshifted from the cutoff is caused by the IGM attenuation as described by Madau (1995), which serves as a characteristic feature that distinguishes the high-z component from low-z ones. From our model, the NIRB spectrum associated with Pop II stars without being blanketed by H I blueward of Lyα is predominantly sourced by direct stellar emission, and it can be well described by a power law that scales as $\lambda^{-1.8}$. This roughly agrees with the Pop-II-dominated prediction from Yue et al. (2013a), who find a slightly shallower slope that might be attributed to different assumptions adopted in the SED modelling and the SFH assumed. Unlike Pop II stars, massive Pop III stars contribute to the NIRB mainly through their nebular emission, especially in Lyα. The resulting NIRB spectrum therefore has a much stronger wavelength dependence that traces the shape of the Pop III SFRD. Similar to FZ13, our reference model suggests that strong Lyα emission from Pop III stars may lead to a spectral "bump" in the total NIRB spectrum, which causes an abrupt change of spectral index over 1–1.5 μm. We will discuss the implications of such a Pop III signature in detail in Section 7.3.2. We also compare our Pop III prediction based on physical arguments of different feedback mechanisms, to an extreme scenario from Helgason

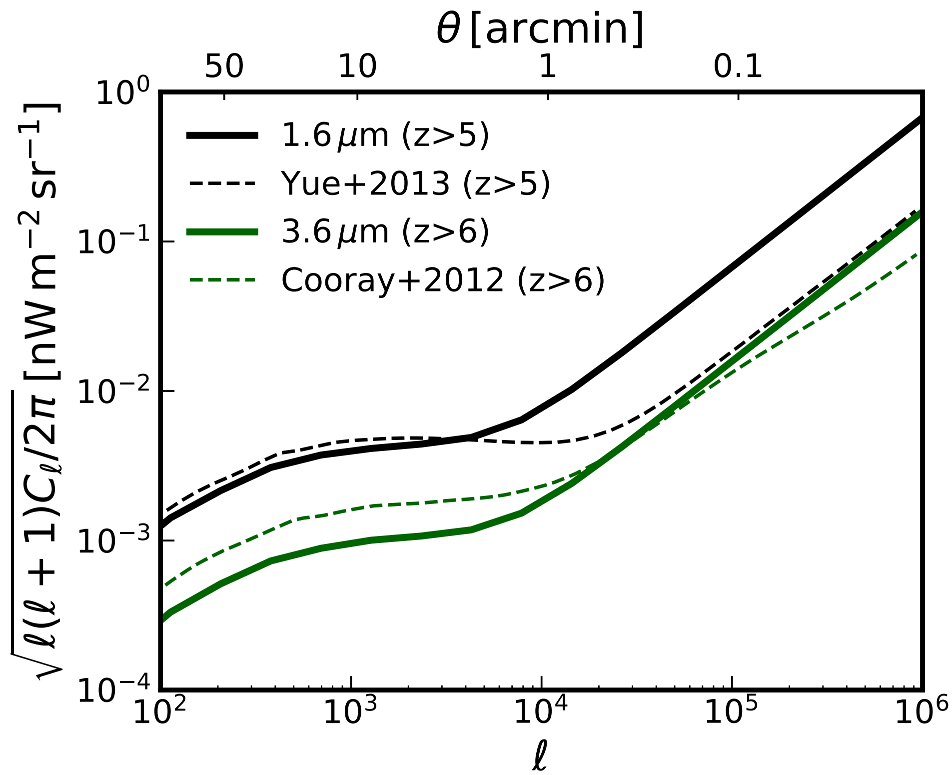

Figure 7.5: Comparison of the NIRB angular power spectra. Comparison of the NIRB angular power spectra associated with Pop II and Pop III stars over different bands and redshift ranges. As opposed to Cooray et al. (2012a) and Yue et al. (2013a), our model predicts a higher shot-noise power due to the inefficient star formation in low-mass haloes as described by the mass-dependent f_*.

et al. (2016) attempting to explain the entire observed, source-subtracted NIRB fluctuations with the Pop III contribution. The fact that our reference model, which already makes optimistic assumptions about the efficiency of Pop III star formation, predicts more than an order of magnitude lower NIRB signal corroborates the finding of Helgason et al. (2016). Pop III stars alone are unlikely to fully account for the observed NIRB excess without violating other observational constraints such as the reionization history — unless some stringent requirements on the physics of Pop III stars are met, including their ionizing and metal production efficiencies.

Fig. 7.5 shows predicted the angular intensity fluctuations $\delta F = \sqrt{\ell(\ell+1)C_\ell/2\pi}$ of the NIRB by our reference model at two wavelengths, 1.6 and 3.6 μm. Compared with predictions at the same wavelengths from Cooray et al. (2012a) and Yue et al. (2013a), our model produces similar (within a factor of 2) large-scale clustering amplitudes. On small scales, our model predicts significantly higher shot-noise amplitudes. Such a difference in the shape of angular power spectrum, C_ℓ, underlines the importance of properly accounting for the contribution from the population of faint/low-mass galaxies loosely constrained by observations. While all these models assume that haloes above a mass $M_{\rm min} \sim 10^8\,M_\odot$ can sustain the formation of Pop II stars (which dominates the total NIRB fluctuations) through efficient atomic cooling of gas, our model allows f_* to evolve strongly with halo mass. As demonstrated in a number of previous works (Moster et al. 2010; Mirocha et al. 2017; Furlanetto et al. 2017), the observed UVLFs of galaxies at $z > 5$ can be well reproduced by f_* as a double power-law in halo mass, consistent with simple stellar and AGN feedback arguments that suppress star formation in low-mass and high-mass haloes, respectively. Consequently, low-mass haloes in our model, though still forming stars at low levels, contribute only marginally to the observed NIRB fluctuations, especially on small scales where the Poissonian distribution of bright sources dominates the fluctuations. The resulting angular power spectrum has a shape different from those predicted by Cooray et al. (2012a) and Yue et al. (2013a), with fractionally higher shot-noise amplitude. Measuring the full shape of C_ℓ from sub-arcminute scales (where the sensitivity to f_* maximizes) to sub-degree scales (where the high-z contribution maximizes) with future NIRB surveys can therefore place interesting integral constraints on the effect of feedback regulation on high-z, star-forming galaxies, complementary to measuring the faint-end slope of the galaxy UVLF.

7.3.2 Spectral signatures of first stars on the NIRB

As shown in Fig. 7.4, a characteristic spectral signature may be left on the NIRB spectrum in the case of efficient formation of massive Pop III stars. Details of such a feature, however, depend on a variety of factors involving the formation and physical properties of both Pop II and Pop III stars. Of particular importance is when and for how long the transition from Pop III stars to Pop II stars occurred, which can be characterized by the ratio of their SFRDs, even though stellar physics such as age and the initial mass function (IMF) also matter and therefore serve as potential sources of degeneracy. FZ13 studies the NIRB imprints in this context using a simple phenomenological model for the Pop III to Pop II transition, without considering detailed physical processes that drive the transition. In this subsection, we investigate the effects of varying the Pop II and Pop III SFHs separately on the NIRB signal from high-z galaxies, exploring a set of physically-motivated model variations specified in Table 8.1.

7.3.2.1 Effects of variations in the Pop II SFH

To explore a range of plausible Pop II SFHs, we consider two alternative ways of extrapolating the low-mass end of f_* — beyond the mass range probed by the observed UVLFs but still within the constraints of current data — which are labeled as `steep` and `floor`, respectively, in Table 8.1 following Mirocha et al. (2017).

In Fig. 7.6, we show how the level of NIRB intensity fluctuations δF and the Pop III signature $\mathcal{R}_{\delta F} = \delta F_{\mathrm{Pop\ III}}/\delta F_{\mathrm{Pop\ II}}$ evolve with wavelength, as predicted by the three different combinations of our Pop II SFE models and the reference Pop III model, namely Model IA, Model IIA, and Model IIIA. Values of $\delta F_{\mathrm{Pop\ II}}$ and $\delta F_{\mathrm{Pop\ III}}$ are quoted at the centres of the nine SPHEREx broadbands for multipoles $500 < \ell < 2000$ to facilitate a comparison with the 1σ surface brightness uncertainty of SPHEREx in each band, as illustrated by the staircase curve in tan (see Section 7.3.3 for a detailed discussion of SPHEREx sensitivity forecasts). Overall, the imprint of Pop III stars on the NIRB is connected to (and thus traces) their SFRD evolution through the strong Lyα emission they produced, with a peak/turnover at the wavelength of Lyα redshifted from the era when Pop III star formation culminated/ended. Near the peak in the 1.5 μm band, the NIRB fluctuations contributed by Pop III stars can be up to half as strong as the Pop II contribution. Note that in practice the contribution of high-z star-forming galaxies will be blended with other NIRB components from lower redshifts. Separation techniques relying on the distinction in the spectral shape of each component have been demonstrated in e.g., Feng et al. (2019). For reference, we show in Fig. 7.6 the remaining fluctuation signal associated with low-z ($z \lesssim 3$) galaxies after masking bright, resolved ones, as predicted by the luminosity function model from Feng et al. (2019). Other sources of emission such as the IHL may also contribute a significant fraction of the total observed fluctuations — though with a lower certainty, making the component separation even more challenging.

The effect of varying f_* is pronounced for the Pop III contribution, whereas the fluctuations sourced by Pop II stars themselves are barely affected. As discussed in Section 7.2.1.2 (see also discussion in Mebane et al. 2018), once formed in sufficient number, Pop II stars can play an important role in shaping the Pop III SFH by lifting the minimum mass of Pop III haloes through their LW radiation. The contrast between the `steep` and `floor` models suggests that, for a fixed Pop III model,

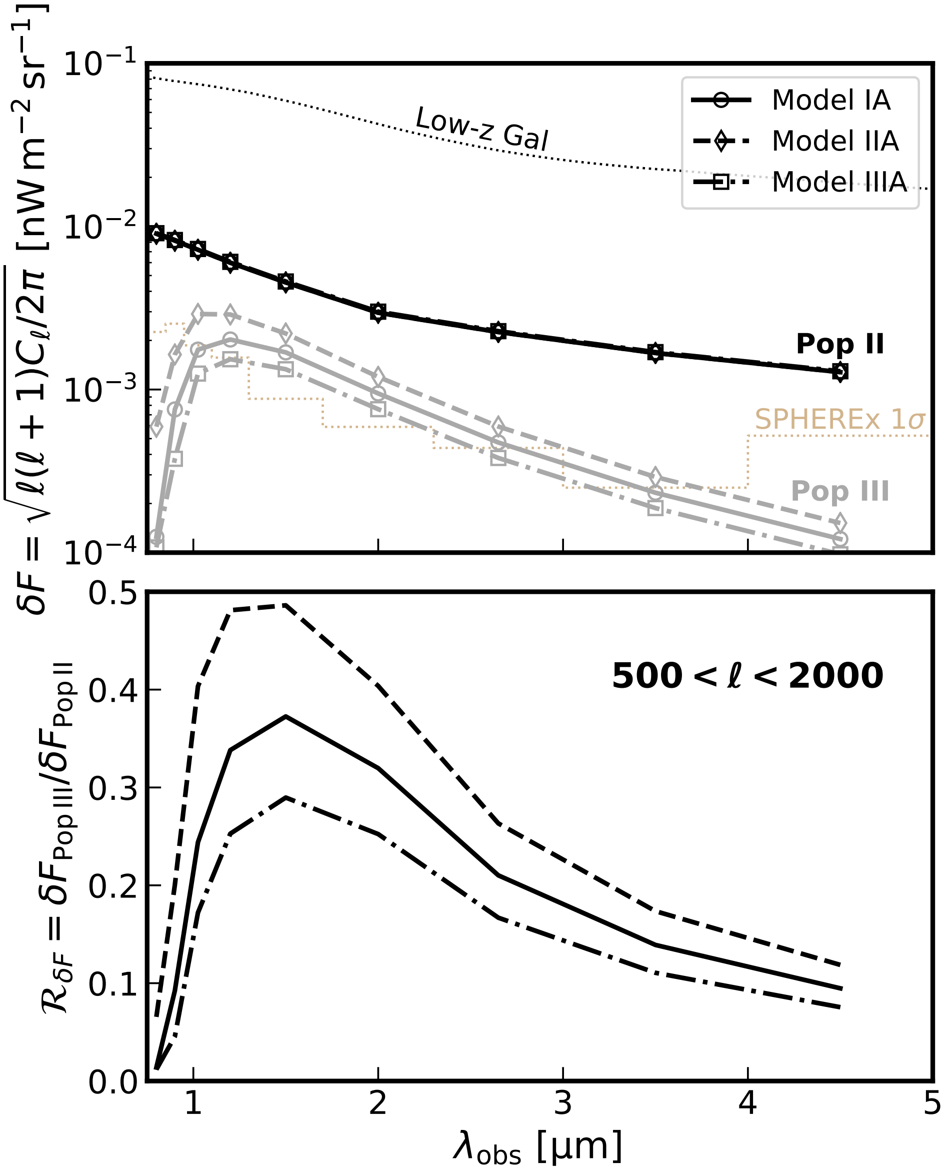

Figure 7.6: Spectra of NIRB intensity fluctuations from Pop II and Pop III stars and their ratio, with varying Pop II prescriptions. Top: spectra of NIRB intensity fluctuations sourced by $z > 5$ star-forming galaxies in the angular bin $500 < \ell < 2000$ predicted by the three variations of the Pop II SFE f_* defined in Table 8.1, compared with the broad-band uncertainties of the forthcoming survey in the 200 deg^2 SPHEREx deep field. Also shown is the expected NIRB fluctuations contributed by low-z galaxies after masking bright resolved sources, taken from Feng et al. (2019). Bottom: the ratio of NIRB intensity fluctuations sourced by Pop III and Pop II stars. The strong evolution with wavelength is driven by the efficient production of Lyα emission by massive Pop III stars.

changing f_* within the range of uncertainty in UVLF measurements can vary the Pop III signature on the NIRB by up to a factor of two. Unlike the Pop III SFRD, whose dependence on f_* grows over time as the LW background accumulates, the dependence of $\mathcal{R}_{\delta F}$ on f_* shows only modest evolution with wavelength since Pop III stars formed close to the peak redshift dominate the fluctuation signal at all wavelengths. On the contrary, the Pop II contribution remain almost unaffected by variations of f_* because the majority of the fluctuation signal is contributed by Pop II stars at $z \sim 5$–6, which formed mostly in more massive haloes not sensitive to the low-mass end of f_* (see Fig. 7.1).

7.3.2.2 Effects of variations in the Pop III SFH

Apart from the influence of the LW background from Pop II stars, the Pop III SFH is also, and more importantly, determined by the physics of Pop III star formation in minihaloes under the regulation of all sources of feedback. As specified in Table 8.1, we consider an additional set of three variations of the Pop III star formation prescription and quantify how the imprint on the NIRB may be modulated.

Similar to Fig. 7.6, Fig. 7.7 shows the NIRB intensity fluctuations for the four different Pop III models considered, each of which yields a possible Pop III SFH fully regulated by the LW feedback and physical arguments about metal enrichment, as described in Section 7.2.1.2. Compared with the reference model (Model IA), which implies an extremely high Pop III star formation efficiency of order 0.1–1 by comparing rates of star formation and mass accretion, approximations to the semi-analytic models from Mebane et al. (2018) imply less efficient Pop III star formation and thus predict Pop III SFRDs that are at least one order of magnitude smaller, as illustrated in Fig. 7.1. Nevertheless, the fluctuation signals in Model IB and ID are only a factor of 2–3 smaller than what Model IA predicts, due to the high mass of Pop III stars assumed in these models which yields a high photoionization rate of $Q(\mathrm{H}) = 10^{51}\,\mathrm{s}^{-1}$. Involving neither a high star formation efficiency ($\dot{M}_*^{\mathrm{III}} = 3\times10^{-6}\,M_\odot\,\mathrm{yr}^{-1}$) nor a very top-heavy IMF ($Q(\mathrm{H}) = 10^{50}\,\mathrm{s}^{-1}$), Model IC represents a much less extreme picture of Pop III star formation favoured by some recent theoretical investigations (e.g., Xu et al. 2016a; Mebane et al. 2018), which is unfortunately out of reach for any foreseeable NIRB measurement.

The correspondence between the Pop III SFHs and their spectral signatures on the NIRB can be easily seen by comparing the shapes of $\dot{\rho}_*^{\mathrm{III}}(z)$ in Fig. 7.1 and $\mathcal{R}_{\delta F}$ in the bottom panel of Fig. 7.7, which suggests that the latter can be exploited

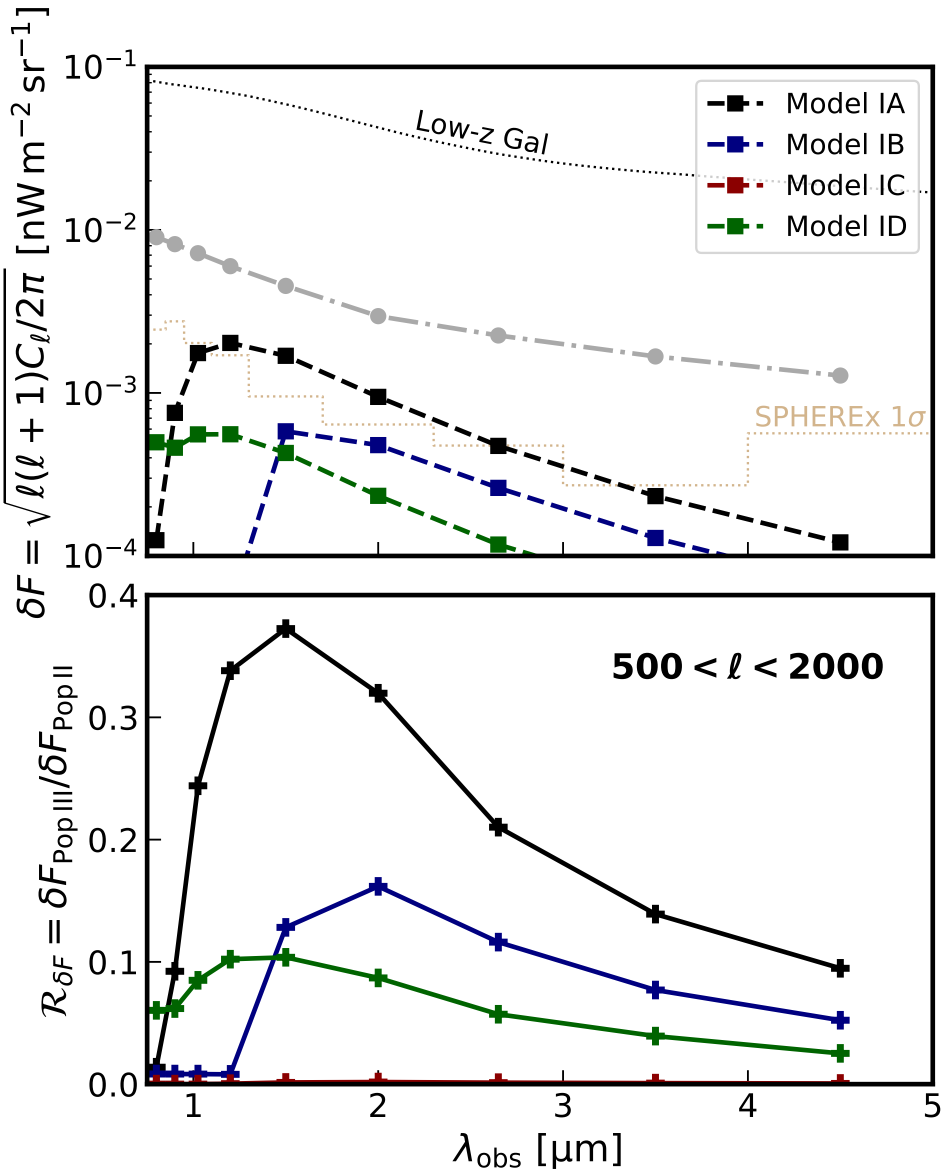

Figure 7.7: Same as Fig. 7.6 but for the four variations of the Pop III SFHs. For comparison, the grey dash-dotted curve shows the Pop II contribution to the fluctuations.

Table 7.2: Survey and instrument parameters for SPHEREx deep field and CDIM medium field. Survey and instrument parameters for SPHEREx deep field and CDIM medium field. Note that the surface brightness sensitivities are quoted at $1.5\,\mu$m for the $500 < \ell < 2000$ bin in the last row. The numbers inside the parentheses are the raw surface brightness sensitivities per ℓ mode per spectral resolution element, whereas the numbers outside are after spectral and spatial binning.

Parameter	Description	SPHEREx	CDIM
$A_{\rm s}(\deg^2)$	survey area	200	30
R	resolving power	40	300
$f_{\rm sky}$	sky coverage	0.005	0.0007
$\Omega_{\rm pix}(\rm sr)$	pixel size	9.0×10^{-10}	2.4×10^{-11}
$\sigma_{\rm pix}(\rm nW/m^2/sr)$	sensitivity (SB)	0.09(1.94)	0.14(24.06)

as a useful probe for the efficiency and persistence of Pop III formation across cosmic time. In particular, the detailed amplitude of $\mathcal{R}_{\delta F}$ is subject to astrophysical uncertainties associated with, e.g., the stellar SED and escape fraction, which are highly degenerate with the SFH as pointed out by FZ13. However, the contrast between spectra showing turnovers at different redshifts (Model IA vs Model IB), or with or without a spectral break (Model IB vs Model ID), is robust, provided that the aforementioned astrophysical factors do not evolve abruptly with redshift. Any evidence for the existence of such a spectral signature from future facilities like SPHEREx would therefore be useful for mapping the landscape of Pop III star formation. We further elaborate on the prospects for detecting the NIRB signal of Pop III stars in the next subsection.

7.3.3 Detecting Pop III stars in the NIRB with SPHEREx and CDIM

To this point, we have elucidated how massive Pop III stars might leave a discernible imprint on the observed NIRB when formed at a sufficiently high rate $\dot{M}_*^{\rm III} \gtrsim 10^{-3}\,M_\odot\,{\rm yr}^{-1}$ per minihalo whose minimum mass $M_{h,\rm min}^{\rm III}$ is set by the LW feedback, as well as how effects of varying Pop II and Pop III star formation physics can affect such a spectral signature. It is interesting to understand how well the NIRB signal contributed by high-z, star-forming galaxies may be measured in the foreseeable future, and more excitingly, what scenarios of Pop III star formation may be probed. For this purpose, we consider two satellites that will be able to study the NIRB in detail, namely SPHEREx (Doré et al. 2014), a NASA Medium-Class Explorer (MIDEX) mission scheduled to be launched in 2024, and CDIM (Cooray et al. 2019a), another NASA Probe-class mission concept. It is useful to point out that other experiments/platforms also promise to probe the NIRB signal from galaxies

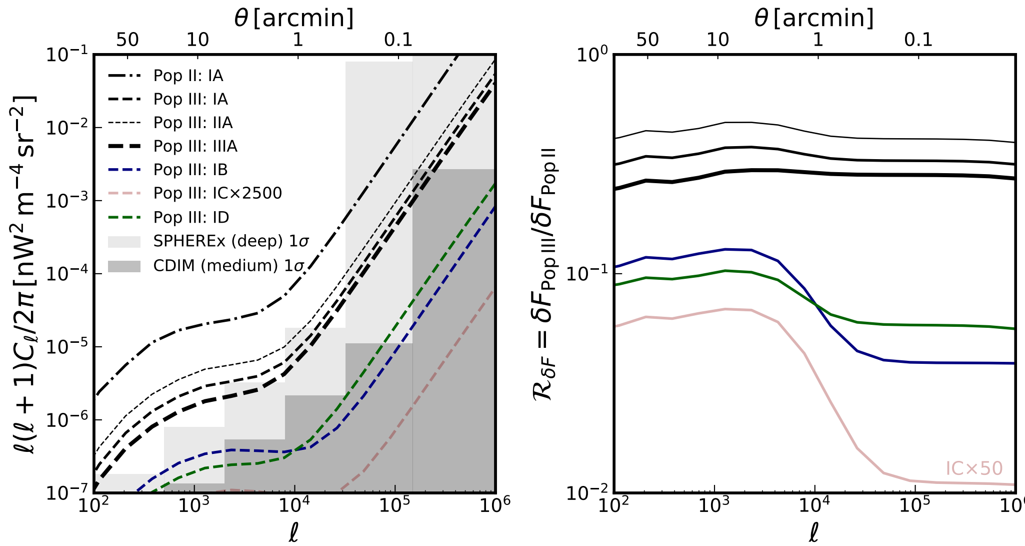

Figure 7.8: Angular power spectra of the NIRB from Pop II and Pop III stars and their ratio. Left: the angular auto-power spectrum C_ℓ of the NIRB at 1.5 μm predicted by different combinations of Pop II and Pop III models. Contributions from Pop II and Pop III stars are shown by dash-dotted and dashed curves, respectively. Variations of Pop II model with `steep`, `dpl`, and `floor` SFE are represented by the thin, intermediate, and thick curves, respectively, whereas different colors represent different Pop III variations. The prediction of Model IC is raised by a factor of 2500 (50) to fit in the left (right) panel. The light and dark shaded regions indicate the expected band uncertainties of SPHEREx deep and CDIM medium surveys, respectively, after binning spectral channels and multipoles according to the imaging broadbands and angular bins defined (see text). Note that the band uncertainty of SPHEREx in the largest ℓ bin goes to infinity since such small scales are inaccessible, given the pixel size of SPHEREx. Right: the ratio of NIRB intensity fluctuation amplitudes of Pop III and Pop II stars as a function of multipole moment ℓ.

duration and before the EoR, including the ongoing sounding rocket experiment CIBER-2 (Lanz et al. 2014) and dedicated surveys proposed for other infrared telescopes such as JWST (Kashlinsky et al. 2015b) and Euclid (Kashlinsky et al. 2015a). In what follows, we focus on the forecasts for SPHEREx and CDIM given their more optimal configurations for NIRB observations, and refer interested readers to the papers listed for details of alternative methods. We note, though, that the high spectral resolution of CDIM (see Table 7.2) makes 3D line-intensity mapping a likely more favourable strategy for probing first stars and galaxies than measuring C_ℓ, when issues of foreground cleaning and component separation are considered. While in this work we only focus on the comparison of C_ℓ sensitivities, tomographic

Lyα and Hα observations with CDIM and their synergy with 21-cm surveys have been studied (Heneka et al. 2017; Heneka & Cooray 2021).

Using the Knox formula (Knox 1995), we can write the uncertainty in the observed angular power spectrum C_ℓ measured for any two given bands as

$$\Delta C_\ell = \frac{1}{\sqrt{f_{\rm sky}(\ell + 1/2)}} \left(C_\ell + C_\ell^{\rm noise} \right). \tag{7.36}$$

The first term C_ℓ describes cosmic variance and the second term $C_\ell^{\rm noise} = 4\pi f_{\rm sky} \sigma_{\rm pix}^2 N_{\rm pix}^{-1} e^{\Omega_{\rm pix}\ell^2}$ is the instrument noise (Cooray et al. 2004), where $N_{\rm pix}$ is the number of pixels in the survey. At sufficiently large scales where $\ell \ll \Omega_{\rm pix}^{-1/2}$, we have $C_\ell^{\rm noise} \approx \sigma_{\rm pix}^2 \Omega_{\rm pix}$. The prefactor $[f_{\rm sky}(\ell + 1/2)]^{-1/2}$ accounts for the number of ℓ modes available, given a sky covering fraction of $f_{\rm sky}$. To estimate the instrument noise, we take the surface brightness sensitivity estimates made for a total survey area of 200 deg^2 for SPHEREx and 30 deg^2 for CDIM, corresponding to the deep- and medium-field surveys planned for SPHEREx and CDIM, respectively. The pixel size $\Omega_{\rm pix}$ is taken as 9.0×10^{-10} sr ($6.2'' \times 6.2''$ pixels) and 2.4×10^{-11} sr ($1'' \times 1''$ pixels) for SPHEREx and CDIM, respectively.

Using the same spectral binning scheme as in Feng et al. (2019), we bin native spectral channels of both SPHEREx and CDIM into the following nine broadbands over an observed wavelength range of $0.75 < \lambda_{\rm obs} < 5\,\mu$m: $(0.75, 0.85)$, $(0.85, 0.95)$, $(0.95, 1.1)$, $(1.1, 1.3)$, $(1.3, 1.7)$, $(1.7, 2.3)$, $(2.3, 3.0)$, $(3.0, 4.0)$, and $(4.0, 5.0)$, regardless of their difference in the raw resolving power R per channel. For the spatial binning of ℓ modes, we consider six angular bins over $10^2 < \ell < 10^6$ as follows: $(10^2, 5 \times 10^2)$, $(5 \times 10^2, 2 \times 10^3)$, $(2 \times 10^3, 8 \times 10^3)$, $(8 \times 10^3, 3 \times 10^5)$, $(3 \times 10^4, 1.5 \times 10^5)$, and $(1.5 \times 10^5, 1 \times 10^6)$, which also apply to both SPHEREx and CDIM, although essentially no information is available on scales smaller than the pixel scale of the instrument. The $N = 9$ broadbands specified then allow us to define an angular power spectrum vector $\boldsymbol{C}_\ell^{\bar{\lambda}_1 \bar{\lambda}_2}$ (for each ℓ bin) that consists of $N(N+1)/2 = 45$ noise-included, auto- and cross-power spectra measurable from the broadband images. As shown in Table 7.2, even though the surface brightness (SB) sensitivity per pixel of the CDIM medium field (T.-C. Chang, private communication) is comparable to that of the SPHEREx deep field[7] after binning, its band noise power $C_\ell^{\rm noise}$ is in fact an order of magnitude lower thanks to CDIM's much

[7] See the public product for projected surface brightness sensitivity levels of SPHEREx at `https://github.com/SPHEREx/Public-products/blob/master/Surface_Brightness_v28_base_cbe.txt`.

Table 7.3: The estimated raw S/N of NIRB signals. The estimated raw S/N of NIRB signals sourced by Pop II and Pop III star-forming galaxies at $z > 5$, using only auto-power spectra measured in the 9 broadbands or all 45 available auto- and cross-power spectra combined. For each entry, the first and second numbers represent the S/N estimated for SPHEREx deep survey and CDIM medium survey, respectively.

Model	$(\mathrm{S/N})^{\mathrm{auto}}_{\mathrm{Pop\,II}}$	$(\mathrm{S/N})^{\mathrm{auto}}_{\mathrm{Pop\,III}}$	$(\mathrm{S/N})^{\mathrm{all}}_{\mathrm{Pop\,II}}$	$(\mathrm{S/N})^{\mathrm{all}}_{\mathrm{Pop\,III}}$
IA	68/1100	8.8/86	120/2300	13/110
IB	68/1100	1.9/38	120/2300	2.8/45
IC	68/1100	$0.0/1 \times 10^{-3}$	120/2300	$0.0/2 \times 10^{-3}$
ID	68/1100	0.8/6.0	120/2300	1.4/10

smaller pixel size. For simplicity, we assume that the noise contribution from maps of different bands is uncorrelated, such that entries of the noise-included vector $\tilde{\boldsymbol{C}}_\ell^{\bar{\lambda}_1\bar{\lambda}_2}$ can be expressed as $C_\ell^{\bar{\lambda}_1\bar{\lambda}_2} + \delta_{\bar{\lambda}_1\bar{\lambda}_2} C_\ell^{\bar{\lambda}_1\bar{\lambda}_2,\mathrm{noise}}$, which is distinguished from the signal-only vector $\boldsymbol{C}_\ell^{\bar{\lambda}_1\bar{\lambda}_2}$ by the Kronecker delta $\delta_{\bar{\lambda}_1\bar{\lambda}_2}$.

The resulting signal-to-noise ratio (S/N) of the full-covariance measurement (summed over all angular bins of ℓ)

$$\left(\frac{S}{N}\right)^2 = \sum_\ell \left(\boldsymbol{C}_\ell^{\bar{\lambda}_1\bar{\lambda}_2}\right)^{\mathrm{T}} \left(\boldsymbol{C}_{\ell,\mathrm{COV}}^{\bar{\lambda}_1\bar{\lambda}_2,\bar{\lambda}'_1\bar{\lambda}'_2}\right)^{-1} \left(\boldsymbol{C}_\ell^{\bar{\lambda}'_1\bar{\lambda}'_2}\right) \tag{7.37}$$

is then used to quantify the detectability of the NIRB signals by the two surveys considered. Here, the covariance matrix between two band power spectra $\boldsymbol{C}_\ell^{\bar{\lambda}_1\bar{\lambda}_2}$ and $\boldsymbol{C}_\ell^{\bar{\lambda}'_1\bar{\lambda}'_2}$ can be expressed using Wick's theorem as (Feng et al. 2019)

$$\boldsymbol{C}_{\ell,\mathrm{COV}}^{\bar{\lambda}_1\bar{\lambda}_2,\bar{\lambda}'_1\bar{\lambda}'_2} = \frac{1}{f_{\mathrm{sky}}(2\ell+1)} \left[\tilde{C}_\ell^{\bar{\lambda}_1\bar{\lambda}'_1}\tilde{C}_\ell^{\bar{\lambda}_2\bar{\lambda}'_2} + \tilde{C}_\ell^{\bar{\lambda}_1\bar{\lambda}'_2}\tilde{C}_\ell^{\bar{\lambda}'_1\bar{\lambda}_2}\right], \tag{7.38}$$

which reduces to equation (7.36) when $\bar{\lambda}_1 = \bar{\lambda}'_1 = \bar{\lambda}_2 = \bar{\lambda}'_2$.

In Table 7.3, we summarize the raw sensitivities to C_ℓ in terms of the total S/N that SPHEREx and CDIM are expected to achieve in the four different Pop III star models considered in this work. Since the contribution from Pop II stars dominates over that from Pop III stars at all wavelengths except where the Pop III signature appears ($\sim 1.5\,\mu$m), a significantly higher raw S/N is expected for the former, reaching above 100 when combining all the auto- and cross-correlations available and summing up all angular bins for SPHEREx, similar to what was previously found by Feng et al. (2019). For Pop III stars, our optimistic Model IA predicts a raw S/N greater than 10 for SPHEREx, which is dominated by the first three angular

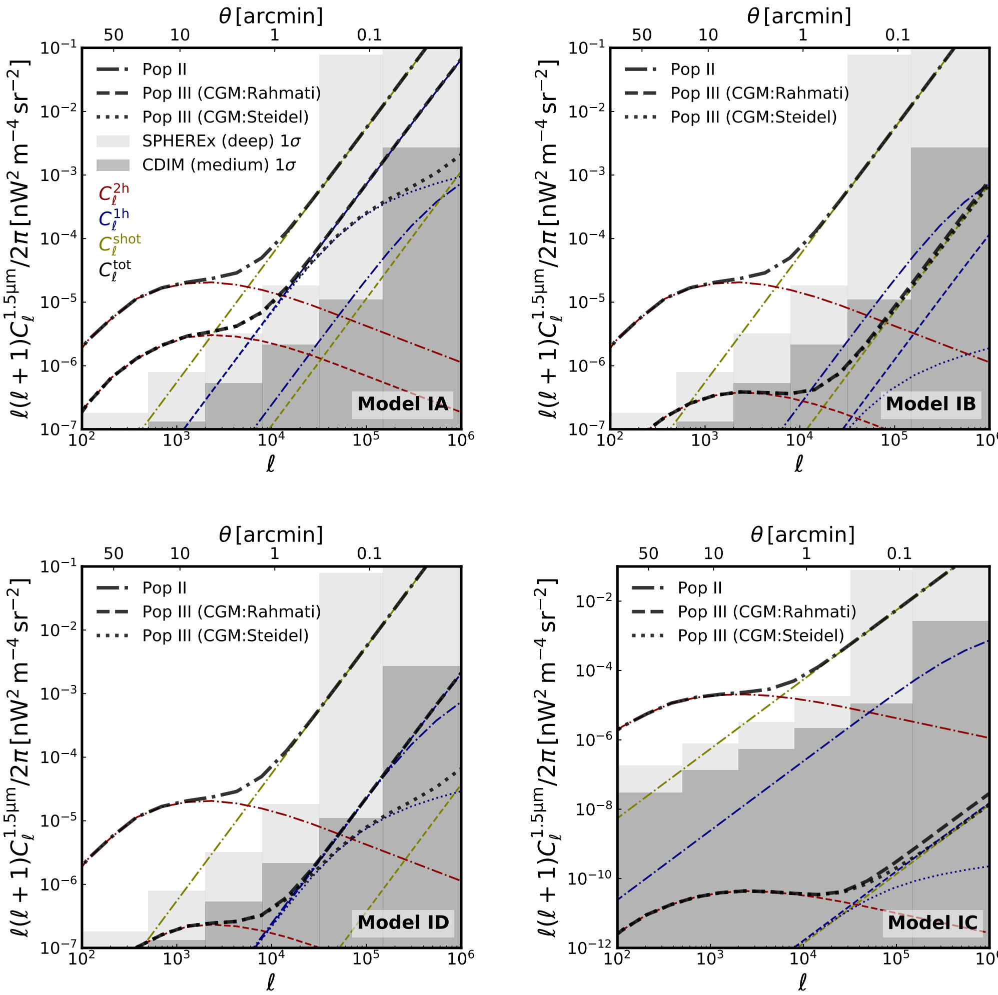

Figure 7.9: Contributions to components of NIRB anisotropies. Contributions from $z > 5$ Pop II and Pop III star-forming galaxies to the two-halo, one-halo and shot-noise components of C_ℓ measured at 1.5 μm. Clockwise from the top left panel: the figures show C_ℓ predicted by Model IA, Model IB, Model IC, and Model ID, defined in Table 8.1. In each panel, the one-halo term is shown for two instances of CGM profile to illustrate the connection between the escape of ionizing photons and the shape of the one-halo term. The light and dark shaded regions indicate the expected band uncertainties of SPHEREx deep and CDIM medium surveys, respectively, after binning spectral channels and multipoles according to the imaging broadbands and angular bins defined (see text). Note the different y-axis scale used in the bottom right panel to show the Pop III signal.

bins with $\ell \lesssim 10^4$, whereas more conservative models assuming lower Pop III SFR per halo predict much smaller raw S/N of only a few. Compared with SPHEREx, CDIM is expected to provide approximately a factor of 20 (10) improvement on the total (Pop III) raw S/N achievable, thanks to the competitive SB sensitivity at its small pixel size. This allows CDIM to measure the Pop III contribution at the same significance (S/N $\sim$ 100) as the Pop II contribution for SPHEREx in Model IA when the full covariance is leveraged. We note, though, that in practice the contribution from high-z, star-forming galaxies must be appropriately separated from all other components of the source-subtracted NIRB, such as unsolved low-z galaxies, the IHL and the diffuse Galactic light (DGL), which lead to a significant reduction of the constraining power on the high-z component (Feng et al. 2019). This component separation issue will be discussed further in Section 7.5.2.

We show in the left panel of Fig. 7.8 a comparison of the auto-correlation angular power spectra C_ℓ of the NIRB predicted by our models in the 1.5 μm band. For clarity, we only show the Pop II signal in Model IA (dash-dotted curve) since it hardly varies with the model variations considered. For Pop III stars, a subset of models yielding NIRB signals potentially detectable for SPHEREx and/or CDIM are shown by the dashed curves with varying thickness and color. The pessimistic Model IC is rescaled and then plotted for completeness. The right panel of Fig. 7.8 illustrates the effect of changing Pop II and Pop III models on the shape of C_ℓ by showing the ratio of intensity fluctuations $\mathcal{R}_{\delta F}$, which is used to characterize the Pop III signature in Section 7.3.2, as a function of ℓ. In all models, $\mathcal{R}_{\delta F}$ peaks at around $\ell \sim 10^3$ or an angular scale of $\sim 10'$, similar to what was found by e.g., Cooray et al. (2004). The fact that in cases like Model IB the fluctuations are preferentially stronger on large angular scales compared to Model IA is because, in the former case, Pop III stars formation completed at much higher redshift and thus was more clustered.

In Fig. 7.9, we further show the halo-model compositions (i.e., one-halo, two-halo and shot-noise terms) of C_ℓ in each Pop III model. Moreover, two possible forms of the one-halo profile motivated by the CGM models, as described in Section 7.2.4 and Fig. 7.3, are displayed for the Pop III contribution.

Three notable features show up from this decomposition of C_ℓ. First, the relative strengths of the one-halo component $C_\ell^{\rm 1h}$ and shot-noise component $C_\ell^{\rm shot}$ are distinct for Pop II and Pop III stars. Because the nebular emission is subdominant to the stellar emission for Pop II stars, on small angular scales their one-halo term is

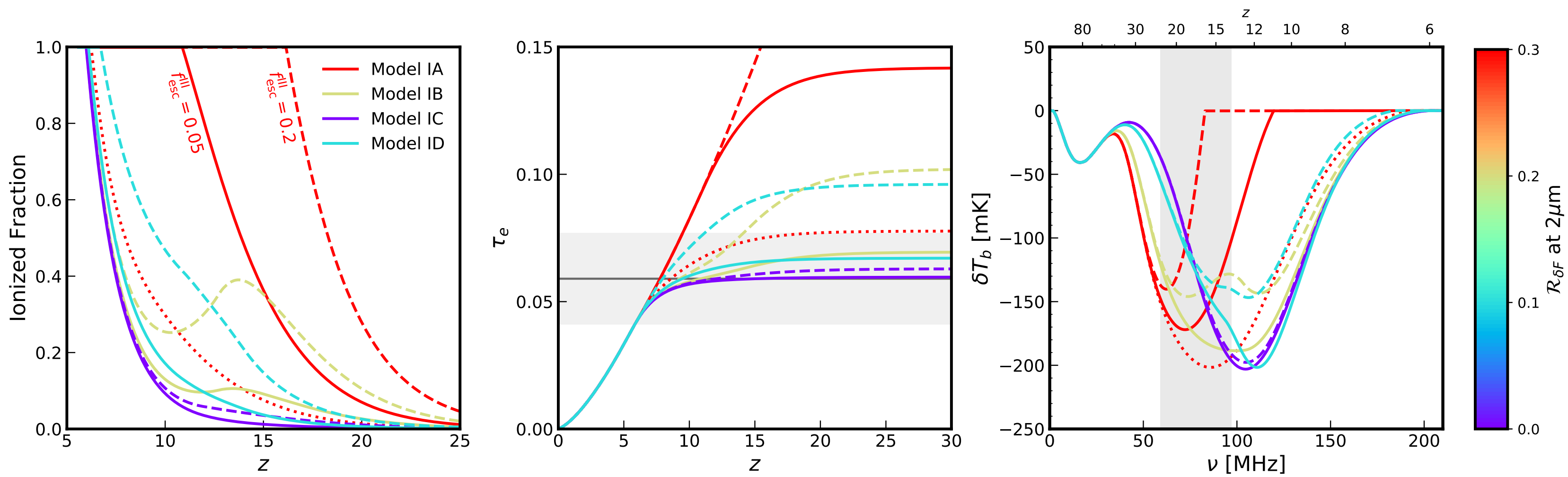

Figure 7.10: Impact of Pop III stars on the reionization history, CMB optical depth, and the 21 cm global signal. Left: impact of Pop III stars on the reionization history and NIRB fluctuations. Different line styles represent different assumptions of $f_{\rm esc}^{\rm III}$, with an additional dotted curve showing the case of $f_{\rm esc}^{\rm III} = 0.01$ for Model IA. Curves are color-coded by the Pop III signature $\mathcal{R}_{\delta F}$ at $2\,\mu$m, where the models can be best distinguished from each other. Middle: the electron scattering optical depth τ_e implied by each model. The horizontal line and grey shaded region indicate the 3σ confidence interval on τ_e inferred from CMB polarization data measured by Planck (Pagano et al. 2020). Right: the 21-cm global signal δT_b implied by each model. The grey shaded region indicates the width of the global signal peaking at 78 MHz as measured by EDGES (Bowman et al. 2018).

negligible compared to the shot-noise term, making C_ℓ of Pop II stars almost scale-invariant at $\ell > 10^4$. On the contrary, Pop III stars can produce very strong nebular emission, especially Lyα, which makes it possible for their one-halo term to dominate on small angular scales. Such an effect can be seen in the left two panels of Fig. 7.9, where the one-halo term is approximately 1.5 dex higher than the shot-noise term.

Second, amplitudes of the one-halo and shot-noise components also depend on the exact SFH, or more specifically, the persistence of Pop III star formation. As shown by the contrast between the left and right two panels of Fig. 7.9, models with an extended Pop III SFH (but not necessarily a later Pop III to Pop II transition, see Fig. 7.1) that persists till $z < 10$ provide the nebular emission with sufficient time to overtake the stellar emission in the contribution to the NIRB, thereby resulting in a stronger one-halo term.

Last but not least, we leverage the physical picture illustrated in Fig. 7.3 to enable additional flexibility in the modelling of the one-halo term by physically connecting its profile with the escape fraction of ionizing photons $f_{\rm esc}^{\rm III}$. Taking the two CGM models considered and described in Section 7.2.4, we get two distinct profiles corresponding to (lower limits on) escape fractions of 5% and 20%, respectively. When the one-halo term is strong enough on scales of $\ell > 10^4$, e.g., in Model IA or ID, such a difference in the radiation profile leads to a clear distinction in the shape of the total power spectrum on these scales. This can be seen by comparing the dashed and dotted curves in black in Fig. 7.9, with a more scale-dependent one-halo term corresponding to a more extended profile of ionizing flux and thus higher escape fraction. It is useful to note that, in most cases considered in this work, an escape fraction of 20% for Pop III stars ends up with a reionization history too early to be consistent with the CMB optical depth constraint from the Planck polarization data, as we will discuss in the next section. Nevertheless, we consider that the two values of $f_{\rm esc}^{\rm III}$ chosen are plausible, allowing us to demonstrate how constraints on small-scale fluctuations, in particular the detailed shape of $C_\ell^{\rm 1h}$, that SPHEREx and CDIM are likely to place may shed light on the escape of ionizing photons from the first ionizing sources at $z \gtrsim 10$.

To this point, we have shown how detectable the high-z contribution from Pop II and Pop III stars to the NIRB would be when compared with sensitivity levels achievable by upcoming/proposed instruments. An important question that follows is how to separate this high-z component from others and, preferably, disentangle the Pop II and Pop III signals. Without the input of external data sets, such as another tracer of star-forming galaxies to be cross-correlated with, the key idea of the solution lies in the utilization of the distinctive spatial and spectral structures of different components. As shown in Fig. 7.4, the high-z component dominated by Pop II stars is characterized by a Lyman break due to the blanketing effect of intergalactic H I. Such a spectral feature has been demonstrated to be useful for isolating the high-z component from sources from lower redshifts (e.g., Feng et al. 2019). Similar ideas apply to the separation of the much weaker Pop III signal from the Pop II signal, thanks to distinctions in their wavelength dependence (due to different types of emission dominating Pop II and Pop III signals, see Fig. 7.7) and angular clustering (due to different halo mass and redshift distributions of Pop II and Pop III signals, see Fig. 7.8). Despite an extremely challenging measurement, these contrasts in spatial and spectral structures make it possible, at least in principle, to distinguish templates of the high-z component as a whole or Pop II and Pop III signals separately. We will elaborate on this component separation issue further in Section 7.5.2, although a detailed study of it is beyond the scope of this chapter and thus reserved for future work.

7.4 Implications for Other Observables

Probing ionizing sources driving the EoR with an integral and statistical constraint like the NIRB has a number of advantages compared to the observation of individual sources, including lower cost of observing time, better coverage of the source population, and importantly, synergy with other observables of the EoR. Taking our models of high-z source populations for the NIRB, we discuss in this section possible implications for other observables, such as the reionization history and 21-cm signal, that can be made from forthcoming NIRB measurements.

7.4.1 Reionization history

In the left panel of Fig. 7.10, we show reionization histories, characterized by the volume-averaged ionized fraction of the IGM, that our models of Pop II/III star formation predict under two different assumptions of the escape fraction $f_{\rm esc}^{\rm III}$, namely 5% and 20% derived from the CGM models by Rahmati et al. (2015) and Steidel et al. (2010), respectively. We note that to compute the reionization history, we assume a constant escape fraction of $f_{\rm esc}^{\rm II} = 10\%$ for Pop II stars, which is known to yield a τ_e in excellent agreement with the best-estimated value based on the latest Planck data (e.g., Pagano et al. 2020) without Pop III contribution. The middle panel of Fig. 7.10 shows contributions to the total τ_e at different redshifts calculated from the reionization histories predicted. Among the four models shown, Model IA forms Pop III stars too efficiently to reproduce the τ_e constraint from Planck, even with $f_{\rm esc}^{\rm III}$ as low as 5%. To reconcile this tension, we include an additional case setting $f_{\rm esc}^{\rm III}$ to 1% as shown by the red dotted curve, which yields a τ_e value marginally consistent with the Planck result. We stress that the LyC escape fraction of Pop III galaxies is poorly understood. A "radiation-bounded" picture of the escape mechanism generally expects an higher escape fraction than Pop II galaxies, due to the extremely disruptive feedback of Pop III stars (Xu et al. 2016b). A "density-bounded" picture, however, requires the ionized bubble to expand beyond the virial radius, and thus predicts significantly lower LyC escape fraction for relatively massive ($M_h \gtrsim 10^{6.5}\,M_\odot$) minihaloes where the majority of Pop III stars formed (e.g., Tanaka & Hasegawa 2021). Therefore, besides τ_e, which is arguably the most trusted observable, NIRB observations provide an extra handle on jointly probing the SFR and escape fraction of minihaloes forming Pop III stars.

In general, earlier reionization is expected for a model that predicts stronger Pop III star signature on the NIRB, and in Model IB, where the Pop III to Pop II transition is early and rapid, unusual double reionization scenarios can even occur. A caveat to keep in mind, though, is that certain forms of feedback, especially photoheating, that are missing from our model can actually alter the chance of double reionization by affecting the mode and amount of star formation in small haloes, making double reionization implausible (Furlanetto & Loeb 2005). As such, we refrain from reading too much into this double reionization feature, which is likely due to the incompleteness of our modelling framework, and focus on the integral measure τ_e instead. While it is challenging to establish an exact mapping between the NIRB signal and reionization history, detecting a Pop III signal as strong as what Model IB or ID predicts would already provide tantalizing evidence for a nontrivial contribution to the progression of reionization from Pop III stars. Such a high-z tail for reionization may be further studied through more precise and detailed measurements of NIRB imprints left by Pop III stars, or via some alternative and likely complementary means such as the kSZ effect (e.g., Alvarez et al. 2021) and the E-mode polarization of CMB photons (e.g., Qin et al. 2020b; Wu et al. 2021). Also worth noting is that, in order not to overproduce τ_e, in cases where the Pop III signature is nontrivial the escape fraction must be either restricted to a sufficiently small upper bound, or allowed to evolve with halo mass and/or redshift. Such constraints on the form of $f_{\rm esc}^{\rm III}$ would become more stringent for a stronger

NIRB signature, as indicated by the curves in different colors and line styles in the middle panel of Fig. 7.10. Combining measurements of $C_\ell^{1\mathrm{h}}$ on sub-arcmin scales with observations of the EoR history, we find it possible to constrain the budget of ionizing photons from Pop III stars, especially $f_{\mathrm{esc}}^{\mathrm{III}}$.

7.4.2 The 21-cm signal

We show in the right panel of Fig. 7.10 the 21-cm global signal, i.e., the sky-averaged differential brightness temperature of the 21-cm line of neutral hydrogen, implied by each of our Pop III star formation models. Similar to what is found by Mirocha et al. (2018), models with efficient formation of massive Pop III stars, which leave discernible imprints on the NIRB, predict qualitatively different 21-cm global signals from that predicted by a baseline model without significant Pop III formation (e.g., Model IC). Except for cases with unrealistically early reionization, Pop III stars affect the low-frequency side of the global signal the most, modifying it into a broadened and asymmetric shape that has a high-frequency tail. The absorption trough gets shallower with increasing Pop III SFR and/or $f_{\mathrm{esc}}^{\mathrm{III}}$, as a result of enhanced heating by the X-rays and a lower neutral fraction.

A tentative detection[8] of the 21-cm global signal was recently reported by the Experiment to Detect the Global Epoch of Reionization Signature (EDGES; Bowman et al. 2018), which suggests an absorption trough centered at 78.1 MHz, with a width of 18.7 MHz and a depth of more than −500 mK. Regardless of the absorption depth, which may only be explained by invoking some new cooling channels of the IGM or some additional radio sources (than the CMB) in the early universe, a peak centering at 78.1 MHz is beyond the expectation of simple Pop II-only models based on extrapolations of the observed galaxy UVLFs (Mirocha & Furlanetto 2019). Additional astrophysical sources such as Pop III stars may help provide the early Wouthuysen–Field (WF) coupling effect and X-ray heating required to explain the absorption at 78.1 MHz, as shown in the right panel of Fig. 7.10 by the shift of curves towards lower frequencies (see also Mebane et al. 2020). Therefore, insights into the Pop III SFH from NIRB observations would be highly valuable for gauging how much the tension between the EDGES signal and galaxy model predictions might be reconciled by including the contribution of Pop III stars.

Besides the global signal, fluctuations of the 21-cm signal also serves as an important

[8] Note, however, that concerns remain about the impact of residual systematics such as foreground contamination on the EDGES results (see e.g., Hills et al. 2018; Draine & Miralda-Escudé 2018; Bradley et al. 2019; Sims & Pober 2020).

probe of reionization. Various physical properties of Pop III stars are expected to be revealed through their effects on cosmic 21-cm power spectrum, especially the timings of the three peaks corresponding to WF coupling, X-ray heating, and reionization (Mebane et al. in prep). On the other hand, the cross-correlation between 21-cm and NIRB observations has been discussed in a few previous works as a way to trace the reionization history (e.g., Fernandez et al. 2014; Mao 2014). We will investigate how to develop a much deeper understanding of Pop III star formation from synergies of 21-cm and NIRB data in future work.

7.5 Discussion

7.5.1 Limitations and the sensitivity to model assumptions

So far, we have described a semi-empirical model of the high-z NIRB signal, based on physical arguments of Pop II and Pop III star formation calibrated against latest observations of high-z galaxies. Our modelling framework, however, is ultimately still simple in many ways. While more detailed treatments are beyond the scope of this chapter and thus left for future work, in what follows, we discuss some major limitations of our model, together with how our findings might be affected by the simplified assumptions.

A key limitation of our model is its relatively simple treatment of the emission spectra of source populations. Despite that (i) the Pop II SED is modelled with the SPS, assuming the simplest possible composite stellar population with a constant SFH, and (ii) the Pop III SED can be reasonably approximated as a blackbody, certain aspects of the complicated problem are unaccounted. These include choices of the IMF, stellar metallicity (for Pop II stars only) and age, etc. and their potential redshift evolution, as well as effects of the stochasticity among galaxies, the extinction by dust, and so forth. We expect our main results about Pop III stars, phrased in terms of a "perturbation" to the Pop II-only baseline scenario, to be robust against these sources of complexity, even though quantifying their exact effects on the shape and amplitude of high-z NIRB signals would be highly valuable in the near future.

Another important limitation is associated with free parameters that are loosely connected to the physics of source populations, such as the nuisance parameters defining the shape of f_*, escape fractions of LyC and LW photons, and parameters $\mathcal{T}_c$ and $\mathcal{E}_c$ used to set the efficiency and persistence of Pop III star formation. While making it easy to explore a wide range of possible scenarios of star formation and reionization, these parameters may not represent an ideal way to parameterize the high-z NIRB signal, meaning that they can be oversimplified or physically related to each other and other implicit model assumptions such as the IMF in practice. Either way, unwanted systematics and degeneracy could arise, making data interpretation with the model challenging and less reliable. Looking ahead, we find it useful to develop a more unified (but still flexible) framework for parameterizing the NIRB, identifying and reflecting the connections among physical quantities/processes of interest. This will be particularly useful for parameter inference in the future.

7.5.2 Component separation of the observed NIRB

As already mentioned at the end of Section 7.3.3, an important challenge in the NIRB data analysis is the separation of its components, which have a broad range of astrophysical origins (Kashlinsky et al. 2018). Failing to perform component separation properly and effectively will make it impossible to constrain a component as weak as the signal from high-z galaxies. Fortunately, as demonstrated in Feng et al. (2019), by measuring the full-covariance angular power spectrum of the observed NIRB, one can reliably separate the major components thanks to their different spatial and spectral structures. In the presence of much stronger low-z components, this approach allows the contribution from EoR galaxies to be recovered and constrained with sufficient significance (S/N $\gtrsim$ 5), without the need for external data sets. To actually reveal the formation histories of the first stars, one must also tell apart the contributions of Pop II and Pop III stars. In addition to the similar full-covariance method discussed in Section 7.3.3, which makes use of the spectral and spatial differences of Pop II and Pop III signals, it can be also promising to consider a joint analysis with ancillary data. External datasets such as 21-cm maps (e.g., Cox et al., in prep) and galaxy distributions (e.g., Scott et al. 2021) can be useful resources for cross-correlation analyses, which are expected to be available from observatories such as HERA (DeBoer et al. 2017), SKA (Mellema et al. 2013), and the Roman Space Telescope (Spergel et al. 2015) in the coming decade. While tracers like the 21-cm signal and photometric galaxies are also complicated by foregrounds and/or survey-specific systematics, which cause loss of information in inaccessible modes, the extra redshift information from cross-correlating the NIRB with these 3D tracers makes the problem of separating the high-z component more tractable.

7.6 Conclusions

In this work, we develop the modelling framework for the NIRB signals sourced by Pop II and Pop III star-forming galaxies at $z > 5$. We leverage a semi-empirical approach to build our model on top of physically-motivated prescriptions of galaxy evolution and star formation under feedback regulation, and calibrate them to observations of high-z galaxies. Using our model, we analyse how the formation histories of first stars may be revealed by measuring the spatial and spectral properties of the NIRB.

Our main findings can be summarized as follows:

1. Using a collection of variations in Pop II and Pop III SFHs derived from our model, we reinforce the modelling of the contribution to the NIRB from high-z star-forming galaxies by characterizing the dependence of its shape and amplitude on physics of star formation and galaxy evolution. We find little difference in the predicted contribution of Pop II stars to the NIRB, given the uncertainty in the SFE allowed by constraints on the faint-end slope of galaxy UVLFs. The Pop III SFH, on the contrary, is highly uncertain and sensitive to the LW feedback from both Pop II and Pop III stars themselves, leading to substantial variations in their imprints on the NIRB.

2. Depending on exact SFHs and detailed properties of Pop III stars such as the IMF, they are expected to leave characteristic spectral signatures on the NIRB at wavelengths redward of 1 μm due to their strong Lyα emission. In our optimistic models with efficient formation of massive Pop III stars, such signatures can be as strong as up to a few tens of percent of the fluctuations sourced by Pop II stars, making the NIRB a promising probe of the first stars. Spatial information of the NIRB, such as the shape of the power spectrum, can also shed light on the physics of the first stars, including effects of various feedback processes and the escape of LyC photons.

3. Forthcoming space missions like SPHEREx and CDIM can quantify the NIRB fluctuations contributed by high-z galaxies, and thereby placing interesting constraints on the Pop III SFH that is difficult to measure by observing individual galaxies. Even though only optimistic models where massive Pop III stars of $\gtrsim 100\,M_\odot$ form at a high efficiency of order 0.1–1 in minihaloes (resulting in a peak Pop III SFRD as high as $\sim 10^{-3}\,M_\odot\,\mathrm{yr}^{-1}\,\mathrm{Mpc}^{-3}$, or $\dot{M}_*^{\mathrm{III}} \sim 10^{-3}\,M_\odot\,\mathrm{yr}^{-1}$ in individual minihaloes) may be probed in the

SPHEREx deep field, ruling out or disfavouring such extremely scenarios with SPHEREx would still be extremely interesting. With better surface brightness sensitivity, the CDIM medium-field survey has the better chance to inspect a larger subset of plausible Pop III models with less efficient star formation and/or less top-heavy IMFs.

4. Any constraints on the first stars from NIRB measurements can have interesting implications for other EoR observables, including the global reionization history, 21-cm signal, and the CMB. In the future, joint analyses of all these probes will provide the best opportunity for overcoming observational systematics such as foreground contamination and studying the first stars from an angle different from, and complementary to, the traditional approach of observing individual galaxies.

Acknowledgments

The authors would like to thank Lluis Mas-Ribas for providing updated models of extended Lyα emission and comments on the early draft, as well as Jamie Bock, Tzu-Ching Chang, Asantha Cooray, Olivier Doré, Chang Feng, Caroline Heneka, and Adam Lidz for helpful discussion about SPHEREx and CDIM instruments and scientific implications. G.S. is indebted to David and Barbara Groce for the provision of travel funds. J.M. acknowledges support from a CITA National fellowship. S.R.F. was supported by the National Science Foundation through award AST-1812458. In addition, S.R.F. was directly supported by the NASA Solar System Exploration Research Virtual Institute cooperative agreement number 80ARC017M0006. S.R.F. also acknowledges a NASA contract supporting the "WFIRST Extragalactic Potential Observations (EXPO) Science Investigation Team" (15-WFIRST15-0004), administered by GSFC.

Chapter 8

COSMOLOGICAL CONSTRAINTS ON THE GLOBAL STAR FORMATION LAW OF GALAXIES: INSIGHTS FROM BARYON ACOUSTIC OSCILLATION INTENSITY MAPPING

Sun, G. (2022). "Cosmological Constraints on the Global Star Formation Law of Galaxies: Insights from Baryon Acoustic Oscillation Intensity Mapping", *Astrophysical Journal*, 931, L29. DOI: 10.3847/2041-8213/ac7138.

Abstract

Originally proposed as a cosmological probe of the large-scale structure, line intensity mapping (LIM) also offers a unique window into the astrophysics of galaxy evolution. Adding to the astrophysical explorations of LIM technique that have traditionally focused on small, non-linear scales, we present a novel method to study the global star formation law using forthcoming data from large-scale baryonic acoustic oscillation (BAO) intensity mapping. Using the amplitude of the percent-level but scale-dependent bias induced by baryon fraction fluctuations on BAO scales, we show that combining auto- and cross-correlation power spectra of two (or more) LIM signals allows to probe the star formation law power index $\mathcal{N}$. We examine the prospect for mapping Hα and [O III] lines across all scales, especially where imprints of the baryon fraction deviation exist, with space missions like SPHEREx. We show that although SPHEREx may only marginally probe $\mathcal{N}$ by accessing a modest number of large-scale modes in its 200 deg^2 deep survey, future infrared all-sky surveys reaching a comparable depth with an improved spectral resolution ($R \gtrsim 400$) are likely to constrain $\mathcal{N}$ to a precision of 10–30%, sufficient for distinguishing models with varying feedback assumptions, out to $z \sim 4$ using BAO intensity mapping. Leveraging this effect, large, cosmic-variance-limited LIM surveys in the far future can scrutinize the physical connection between galaxy evolution and the large-scale cosmological environment, while performing stringent tests of the standard cosmological model.

8.1 Introduction

The coupling between radiation and baryons prior to cosmic recombination drives primordial acoustic waves that leave characteristic imprints on the matter power spectrum through the gravitational effect of baryons. These so-called baryon acoustic oscillations (BAOs) exist on a typical scale of about 100 cMpc, and have become an important standard ruler in cosmology (Eisenstein 2005). Baryons are later on coupled to dark matter through gravity and can be perceived as a (biased) tracer of the matter distribution, with a roughly constant bias factor on large, linear scales. However, a scale-dependent bias is predicted to be induced by fluctuations of the relative baryon fraction measured by the local densities of baryons and dark matter (Barkana & Loeb 2011, hereafter BL11; Angulo et al. 2013; Schmidt 2016; Soumagnac et al. 2016). Detection of this effect has been attempted through BAO measurements using galaxies from the SDSS-III BOSS data, in the aim of testing the standard cosmological paradigm and connecting the light-to-mass ratio of galaxies to their large-scale cosmological environment (Soumagnac et al. 2016, 2019). However, the results remain inconclusive due to the limited sample size and imaging quality of SDSS data.

Given the close connection between the BAO-induced modulation of the baryon fraction and the mass-to-light ratio of galaxies, the scale-dependent modulation is a useful probe of how the star formation activity is related to the gas content of galaxies — a fundamental relation of galaxy evolution often referred to as the global star formation law (Kennicutt 1998; Daddi et al. 2010; Krumholz et al. 2012; Liu et al. 2015; de los Reyes & Kennicutt 2019; Kennicutt & De Los Reyes 2021). Astronomical determination of it relies on accurately measuring multi-wavelength proxies of the ongoing star formation rate (SFR; e.g., rest-frame UV continuum) and the gas mass (e.g., CO line luminosity) from selected galaxy samples, and therefore tends to be demanding and susceptible to various systematics, such as dust obscuration, gas excitation, and selection bias, especially at $z > 2$ (Casey et al. 2014). To date, the state-of-art analysis is still restricted to a relatively small sample of several hundred nearby galaxies (see de los Reyes & Kennicutt 2019; Kennicutt & De Los Reyes 2021), while yet more comprehensive analyses of larger sample sizes and/or at higher redshifts are limited by requirements for high-quality, multi-wavelength data. Statistical constraints from BAO amplitudes thus represent a novel independent way to characterize the global star formation law, including its potential redshift evolution and multi-modality (Santini et al. 2014; Kennicutt & De Los Reyes 2021), without the necessity of detecting individual galaxies.

A concept originating from the field of observational cosmology, the line intensity mapping (LIM) technique has received increasing attention in recent years as a powerful means to study the astrophysics of galaxies and the intergalactic medium (Chang et al. 2019; Kovetz et al. 2019). In particular, the tight connection between the emission-line production and the astrophysics of interstellar gas of galaxies makes LIM a promising statistical probe of galaxy evolution. Historically, large-scale fluctuations of line intensity fields have been mainly considered for cosmological applications, such as probing alternative dark matter models, dark energy, gravitational lensing, neutrino properties, and the primordial non-Gaussianity (e.g., Sitwell et al. 2014; Karkare & Bird 2018; Bernal et al. 2019; Liu & Breysse 2021; Chung 2022; Maniyar et al. 2022; Moradinezhad Dizgah et al. 2022). The majority of astrophysical explorations of LIM have been focusing on small, non-linear scales, where astrophysical processes of galaxy evolution are manifested through their effects on the one-halo or shot-noise components of the LIM power spectrum (e.g., Wolz et al. 2017a; Breysse & Alexandroff 2019; Mas-Ribas & Chang 2020; Schaan & White 2021). Therefore, it is interesting to extend the scope of astrophysical information from LIM to the linear regime by measuring baryon fraction fluctuations with BAO intensity mapping. The wide-bandwidth and coarse-grain averaged nature of LIM also makes it convenient to conduct coherent analysis of large statistical samples at multiple redshifts, thereby constraining any time evolution.

LIM will be a main survey strategy of future space missions such as the Spectro-Photometer for the History of the Universe, Epoch of Reionization, and Ices Explorer (SPHEREx; Doré et al. 2014) and the Cosmic Dawn Intensity Mapper (CDIM; Cooray et al. 2019b), which promise to offer unprecedented surface brightness sensitivity at near-infrared wavelengths that may allow to detect signals as faint as that expected from the first stars in the universe (see e.g., Sun et al. 2021a; Parsons et al. 2021). High signal-to-noise measurements of large-scale LIM signals of optical/UV lines like Hα 6563 Å, [O III] 5007 Å and [O II] 3727 Å are also made possible at $1 \lesssim z \lesssim 4$ (Gong et al. 2017). It is therefore intriguing to understand how BAO imprints of the baryon fraction deviation may be utilized by these future experiments to study galaxy evolution at intermediate redshifts.

In this chapter, we propose a novel method of constraining the global star formation law of galaxies from cosmological measurements of BAO intensity mapping. In Section 8.2, we present the modeling framework of the line intensity field in the presence of baryon fraction fluctuations and how LIM surveys can leverage the scale-dependent bias induced on BAO scales to extract the star formation law power index. In Section 8.3, we use SPHEREx as an example to investigate the observational prospects for our method and forecast the constraining power on the parameters of interest based on the estimated detectability of Hα and [O III] LIM signals. We discuss some limitations and future improvements of our analysis, before concluding in Section 8.4.

Throughout the chapter, all physical quantities related to star formation are normalized to have a Chabrier (2003) initial mass function, and we assume a flat, ΛCDM cosmology consistent with the results from Planck Collaboration et al. (2016b).

8.2 Models

The BAO-induced modulation of the relative clustering of baryons and dark matter is proposed by BL11 as a useful cosmological probe. In this work, we reformulate the original observational proposal, which involves measurements of the (original and luminosity-weighted) number density fields of galaxies, into a framework of multi-tracer LIM observations, which avoids the complications associated with flux-limited samples and alleviates parameter degeneracies.

8.2.1 Intensity Fields and Halo Baryon Fraction

8.2.1.1 Perturbations of Halo Baryon Fraction

Here we briefly review the physical concepts behind the halo baryon fraction perturbations on BAO scales, and interested readers are referred to BL11 for more details.

The scale-dependent modulation of the baryon and dark matter density fields due to primordial acoustic waves can be described as

$$\delta_\gamma = \delta_\mathrm{b} - \delta_\mathrm{tot} = r\delta_\mathrm{tot}, \tag{8.1}$$

where δ_tot is the total matter overdensity. We use CAMB (Lewis et al. 2000) to obtain $r(k, z) = \delta_\mathrm{b}/\delta_\mathrm{tot} - 1$, the fractional deviation of the *global* baryon fraction γ_b whose cosmic mean value is $\bar{\gamma}_\mathrm{b} \equiv \Omega_\mathrm{b}/\Omega_\mathrm{m}$. Relatedly, the *halo* baryon fraction is $f_\mathrm{b} = (\delta_\mathrm{b}/\delta_\mathrm{tot})\bar{\gamma}_\mathrm{b} = [1 + r(k, z)]\bar{\gamma}_\mathrm{b}$. By separating perturbations into large-scale and small-scale effects of the density field and halo collapse, the lowest-order perturbation of the halo baryon fraction f_b is

$$\delta_f = \frac{A_r}{\delta_\mathrm{c}}\,[r(k) - r_\mathrm{LSS}]\,\delta_\mathrm{tot}, \tag{8.2}$$

where $\delta_\mathrm{c} = 1.686$ is the critical density for spherical collapse in linear theory. The mostly constant, small-scale baryon fraction deviation, r_LSS, can be well-approximated by $r(k = 1\,h\,\mathrm{Mpc}^{-1})$, and $A_r \approx 3$ is a constant factor describing the enhancement of gas depletion into halos due to non-linear collapse, which can be characterized by simulations (Naoz et al. 2011; Angulo et al. 2013).

8.2.1.2 Connection to Line Intensity Fields

For a given line tracer of the LSS with line luminosity L, we have (BL11)

$$\delta_L = b_L(k)\delta_{\rm tot} = \left\{b_{L,\rm eff} + b_{L;\Delta}[r(k) - r_{\rm LSS}]\right\}\delta_{\rm tot}, \tag{8.3}$$

where $b_{L,\rm eff}$ is the luminosity-weighted effective bias of the tracer stems from the halo bias[1], which is taken to be scale-independent, and $b_{L;\Delta} = (A_r/\delta_{\rm c})\mathcal{N}\beta$ denotes the additional, scale-dependent bias associated with perturbations of $f_{\rm b}$. Factors $\mathcal{N}$ (the star formation power law index) and β (the L–SFR power law index) for the luminosity weighting of $f_{\rm b}$ are determined by galaxy astrophysics. Both observations and analytic models invoking feedback regulations suggest a universal, power-law relation between star formation activity and the gas content of galaxies, namely the global star formation law. Specifically, the star formation rate surface density is related to the gas surface density by $\dot{\Sigma}_* \propto (\Sigma_{\rm g})^{\mathcal{N}} \propto (f_{\rm b})^{\mathcal{N}}$, where the exact value of $\mathcal{N}$ is sensitive to astrophysical processes like stellar feedback (Dekel et al. 2019). For example, the well-known Kennicutt-Schmidt law suggests $\mathcal{N} \approx 1.4$, whereas Faucher-Giguère et al. (2013) propose a simple model where the galaxy disc is supported entirely by stellar feedback and find $\mathcal{N} \approx 2$. If the L–SFR relation also follows a simple power law with index β (as is usually the case, see Section 8.2.2.2), then

$$L \propto \dot{M}_*^{\beta} \propto (f_{\rm b})^{\mathcal{N}\beta}, \tag{8.4}$$

which implies $b_{L;\Delta} \propto \mathcal{N}\beta$, as discussed above.

BL11 make an initial observational proposal to use the scale dependence from $r(k)$, which modulates the BAO peak amplitudes but barely changes the peak positions, to separate different bias contributions. Specifically, they propose to compare the number density and luminosity density power spectra of the same galaxy sample to cancel out sources of foreground contamination in common. By analogy, we note that LIM data enable a major simplification of observables thanks to their sensitivity to the aggregate line emission (Visbal & Loeb 2010). The (square-rooted) power

[1] Because we work solely with LIM signals in this work, bias contributions from the source number density and the luminosity weighting considered separately in BL11 are combined into a single $b_{L,\rm eff}$.

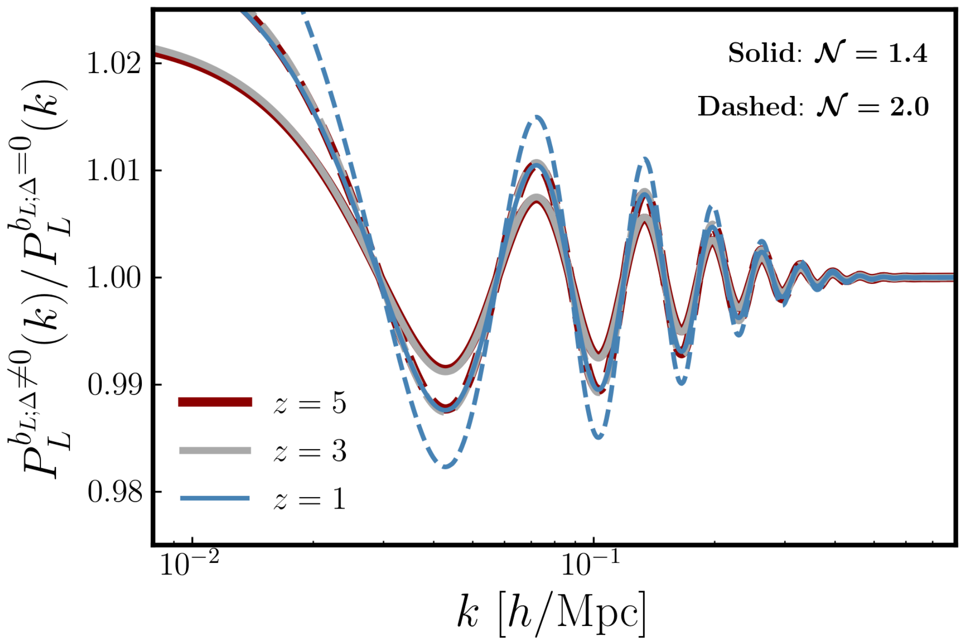

Figure 8.1: Effects of scale-dependent bias on power spectrum ratio. The ratio of the line intensity power spectrum with and without accounting for the scale-dependent bias of a typical LSS tracer with $\beta = 1$ due to baryon fraction fluctuations. The solid and thin curves represent two familiar forms of the star formation law, corresponding to the Kennicutt–Schmidt law ($\mathcal{N} \approx 1.4$, Kennicutt 1998) and a simple feedback-supported disc model ($\mathcal{N} \approx 2$, Faucher-Giguère et al. 2013), respectively.

spectrum ratio of two LIM signals is

$$\mathcal{R} \equiv \left(\frac{P_1}{P_2}\right)^{1/2} = \mathcal{B}_1 \left\{1 + \mathcal{B}_2[r(k) - r_{\rm LSS}]\right\}, \tag{8.5}$$

where we assume the large-scale limit and that the two line tracers share the same $b_{L;\Delta}$ (but see Section 8.2.2.1 for a full treatment), such that the coefficients can be expressed as $\mathcal{B}_1 = b_{L_1,\rm eff}/b_{L_2,\rm eff}$ and $\mathcal{B}_2 = (b_{L;\Delta}/b_{L_2,\rm eff})(\mathcal{B}_1^{-1} - 1)$, respectively. Similar to what BL11 find, we see that the scale dependence of $r(k)$ allows to separately constrain $\mathcal{B}_1$ and $\mathcal{B}_2$ with $\mathcal{R}$, and thereby infer $b_{L;\Delta}$. Nonetheless, several important issues are apparent. First, with $\mathcal{R}$ alone, it is clearly infeasible to decouple individual bias factors $b_{L_1,\rm eff}$, $b_{L_2,\rm eff}$, and $b_{L;\Delta}$ from their ratios. Second, to deduce the global star formation law represented by $\mathcal{N}$ from $b_{L;\Delta}$, the parameter β must be known a priori, though it can actually vary significantly for a single line tracer under different astrophysical conditions, or for different tracers as is relevant here.

Therefore, to ultimately constrain $\mathcal{N}$, some means in addition to the measurement of $\mathcal{R}$ is needed to lift the degeneracies among different bias factors and account for astrophysical uncertainties in the L–SFR relation. In what follows, we investigate and demonstrate a natural extension of Equation (8.5) in the context of multi-tracer LIM. The cross-correlation between the two line tracers and the full shape of the line intensity power spectrum including the small-scale, shot-noise term are incorporated into the analysis, in order to maximally separate the different bias factors and astrophysical parameters.

8.2.2 LIM Observables and Emission Line Models

8.2.2.1 Power Spectrum and Galaxy–Halo Connection

For a given line L, the power spectrum of line intensity fluctuations is

$$P_L(k) = \langle I_L \rangle^2 b_L^2(k) P_{\delta\delta}(k) + P_{L,\mathrm{shot}}, \tag{8.6}$$

where $b_L(k)$ is the net bias factor of the tracer defined in Equation (8.3) and $P_{\delta\delta}(k)$ is the matter power spectrum of δ_{tot}. Scale-independent factors $\langle I_L \rangle$ and $P_{L,\mathrm{shot}}$ represent the mean line intensity and the shot-noise power arising from the Poissonian distribution of discrete line emitters, respectively. We compute them from the L–SFR relation as

$$\langle I_L \rangle = \int dM \frac{dn}{dM} \frac{L[\dot{M}_*(M,z)] y(z) D_A^2}{4\pi D_L^2}, \tag{8.7}$$

and

$$P_{L,\mathrm{shot}} = \int dM \frac{dn}{dM} \left\{ \frac{L[\dot{M}_*(M,z)] y(z) D_A^2}{4\pi D_L^2} \right\}^2, \tag{8.8}$$

where $\langle I_L \rangle$ is related to the line luminosity density by $y(z) = \lambda_{\mathrm{obs}}(1+z)/H(z)$, the comoving angular diameter distance D_A, and the luminosity distance D_L. We adopt the halo mass function dn/dM from Tinker et al. (2008) and evaluate the integrals over $10^9\,M_\odot < M < 10^{15}\,M_\odot$. Figure 8.1 shows how the line intensity power spectra compare with and without including the scale-dependent bias induced by baryon fraction fluctuations.

For simplicity, we assume a one-to-one correspondence between halos and galaxies, and ignore details of the halo occupation distribution (HOD) and the stochasticity in the line luminosity that can have non-trivial effects on small scales (see e.g., Sun et al. 2019; Schaan & White 2021). For each galaxy, we obtain its SFR, $\dot{M}_*(M,z)$, from the Data Release 1 of the `UniverseMachine` code (Behroozi et al. 2019), which semi-empirically models the correlated halo assembly and galaxy growth.

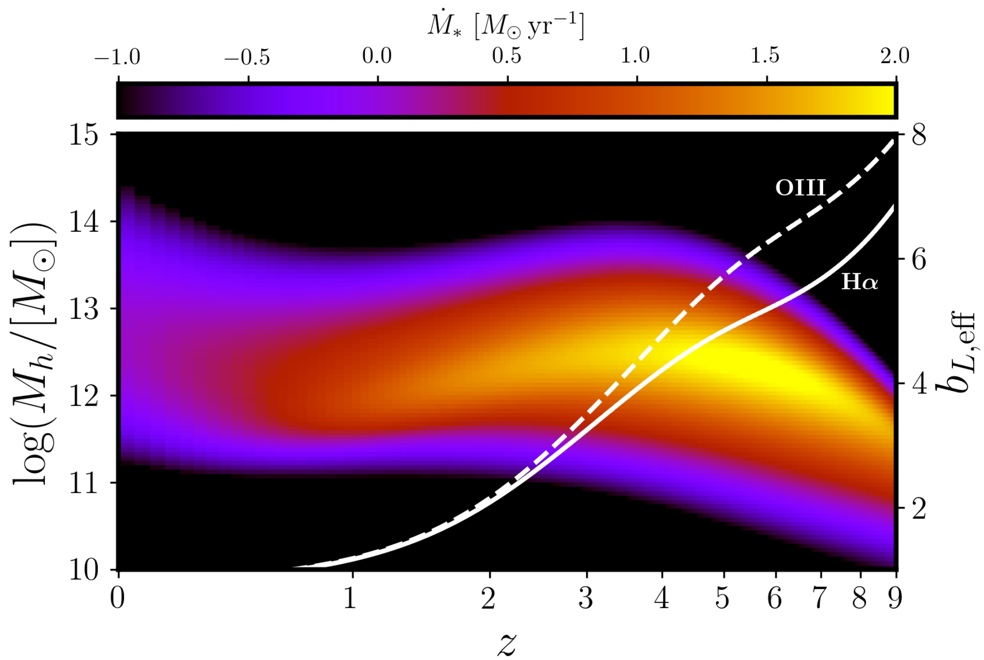

Figure 8.2: Modeling of the star formation rate. The SFR as a function of halo mass and redshift is obtained from the `UniverseMachine` code (Behroozi et al. 2019). Also plotted are the implied luminosity-weighted effective bias factors of the two tracers, $b_{\mathrm{H}\alpha,\mathrm{eff}}(z)$ and $b_{\mathrm{OIII},\mathrm{eff}}(z)$, as labeled by the right axis.

8.2.2.2 L–SFR Relation

As discussed in Section 8.2.1, the line intensity serves as a biased tracer of the local matter density, which is subject to not only the halo occupation and environmental dependence of galaxy evolution but also the relation between the production of line photons and the baryon fraction of galaxies. While $b_{L,\mathrm{eff}}$ accounts for the fluctuations sourced by the dependence of source number density and luminosity on the local matter density, we also need to specify the L–SFR relation to model $b_{L;\Delta}$. Motivated by the well-established correlation observed between the SFR and the luminosity of lines as star formation tracers, we take

$$\log(L/[\mathrm{erg\,s^{-1}}]) = \alpha + \beta \log(\dot{M}_*/[M_\odot\,\mathrm{yr^{-1}}]), \tag{8.9}$$

where for each line we vary both α (affecting the power spectrum amplitude) and β (affecting both the power spectrum amplitude and shape). In Figure 8.2, we plot over the $\dot{M}_*(M, z)$ space the scale-independent, effective bias of two promising target lines for LIM, Hα and [O III], that will be studied by SPHEREx. Note that while we treat $b_{L,\mathrm{eff}}$ as a free parameter in our Fisher matrix analysis (see Section 8.3), we use fiducial values of α and β to obtain the fiducial $b_{L,\mathrm{eff}}$ of our tracers from the scale-independent halo bias. As shown in Figure 8.2, $b_{L,\mathrm{eff}}$ of either line evolves by about a factor of 5 and the different redshift trends are associated with the different fiducial β values taken (see Table 8.1).

Table 8.1: Fiducial model parameters and priors

Parameter	Input Value ($z = 1$)	Prior	Reference
$b_{\mathrm{H}\alpha,\mathrm{eff}}$	1.2	100%	Eq. (8.3)
$b_{\mathrm{OIII},\mathrm{eff}}$	1.2	100%	Eq. (8.3)
$\mathcal{N}$	1.4	100%	Eq. (8.4)
$\alpha_{\mathrm{H}\alpha}$	41.1	100%	Eq. (8.9)
$\beta_{\mathrm{H}\alpha}$	1.0	10%	Eq. (8.4, 8.9)
α_{OIII}	41.0	100%	Eq. (8.9)
β_{OIII}	1.2	50%	Eq. (8.4, 8.9)

8.3 Observational Prospects

8.3.1 Basic Setups

To demonstrate the capability of BAO intensity mapping for probing the global star formation law through the baryon fraction deviation, in this section we envisage a case study to jointly measure Hα and [O III] LIM signals at $z = 1$–5 with $\Delta z = 0.5$ using a SPHEREx-like experiment. We empirically model the LIM signals using the best-fit results to the observed L–SFR relations, assuming $\alpha_{\mathrm{H}\alpha} = 41.1$ and $\beta_{\mathrm{H}\alpha} = 1.0$ for Hα (Ly et al. 2007), and $\alpha_{\mathrm{OIII}} = 41.0$ and $\beta_{\mathrm{OIII}} = 1.2$ for [O III] (Villa-Vélez et al. 2021). Table 8.1 summarizes the fiducial input values and priors (1σ, quoted in percentage of the fiducial value) of model parameters, on which the constraints from mock observations are estimated through the Fisher matrix analysis.

As discussed in Section 8.2.1.2, to explore the parameter constraints that SPHEREx-like experiments can provide, we investigate the observational prospects for measuring together the ratio of Hα and [O III] auto-power spectra, $\mathcal{R} = \sqrt{P_{\mathrm{OIII}}/P_{\mathrm{H}\alpha}}$, and their cross-power spectrum, $\mathcal{P} = P_{\mathrm{OIII}\times\mathrm{H}\alpha}$. There are two main reasons that we choose $\mathcal{R}$ instead of using the auto-power spectra of the respective lines. It preserves the format of the metric proposed in BL11, which can be easily separated into scale-independent and scale-dependent terms. More importantly, given that auto-power spectra are often contaminated by some common sources of foreground such as the atmospheric emission and the extragalactic background light, taking the ratio makes it more justified to use the (propagated) signal-to-noise ratio (S/N) estimated from simple mode counting.

We then adopt the survey specifications of SPHEREx to estimate the detectability of $\mathcal{R}$ and $\mathcal{P}$, following procedures outlined in e.g., Gong et al. (2017). While the all-sky survey of SPHEREx is more advantageous for measuring the BAO amplitudes on large scales, it is too shallow compared to the 200 deg^2 SPHEREx deep survey, which is approximately 7 times deeper in terms of the surface brightness sensitivity and thus more suitable for LIM applications. Thus, we assume a survey area of 200 deg^2 and a spectral resolving power of $R = 40$, consistent with the way Hα and [O III] LIM will be conducted by SPHEREx in its four shortest-wavelength bands. There are, however, two noteworthy differences from Gong et al. (2017). First, for the surface brightness sensitivity that determines the instrument noise power, $P_{\rm n}$, we assume the current best estimate (CBE) performance of SPHEREx[2], which leads to an approximately 100 times lower $P_{\rm n}$. Second, given the relatively low spectral resolution of SPHEREx, we include an extra smoothing factor, $G(k)$, in the sensitivity calculation that accounts for the attenuation of the signal power spectrum on small scales due to finite spatial and spectral resolutions. Although our baseline model predicts Hα and [O III] signal levels similar to those in Gong et al. (2017) and that the total S/N estimates of the power spectra differ only by a factor of 2, the two aforementioned factors imply S/N distributions as a function of k much different from Gong et al. (2017).

8.3.2 Fisher Matrix Analysis

With estimates of the target observables and SPHEREx sensitivities in hand, we calculate the covariance matrix of the model parameters using the Fisher matrix

$$F_{ij} = \sum_k \frac{1}{\mathrm{var}(f)} \frac{\partial f}{\partial \theta_i} \frac{\partial f}{\partial \theta_j}, \tag{8.10}$$

where the summation is over all the k bins for the data vector $f(\theta, k) = (\mathcal{R}(\theta, k), \mathcal{P}(\theta, k))$, and the covariance between the two observables is neglected since auto- and cross-power measurements are subject to generally uncorrelated systematic uncertainties.

Figure 8.3 shows the parameter derivatives of the two observables entering the Fisher matrix analysis, $\mathcal{R}$ and $\mathcal{P}$. The way they are modulated by the model parameters can be perceived from the shape of the curves, which characterizes the scale dependence of the modulation. For instance, from both $\partial\mathcal{R}/\partial b_{L,\mathrm{eff}}$ and $\partial\mathcal{P}/\partial b_{L,\mathrm{eff}}$, it is clear that $b_{L,\mathrm{eff}}$ has a diminishing effect on the observables towards smaller scales, which become increasingly dominated by the shot noise that only depends on α and β. For

[2]See the public product released at `https://github.com/SPHEREx/Public-products/blob/master/Surface_Brightness_v28_base_cbe.txt`

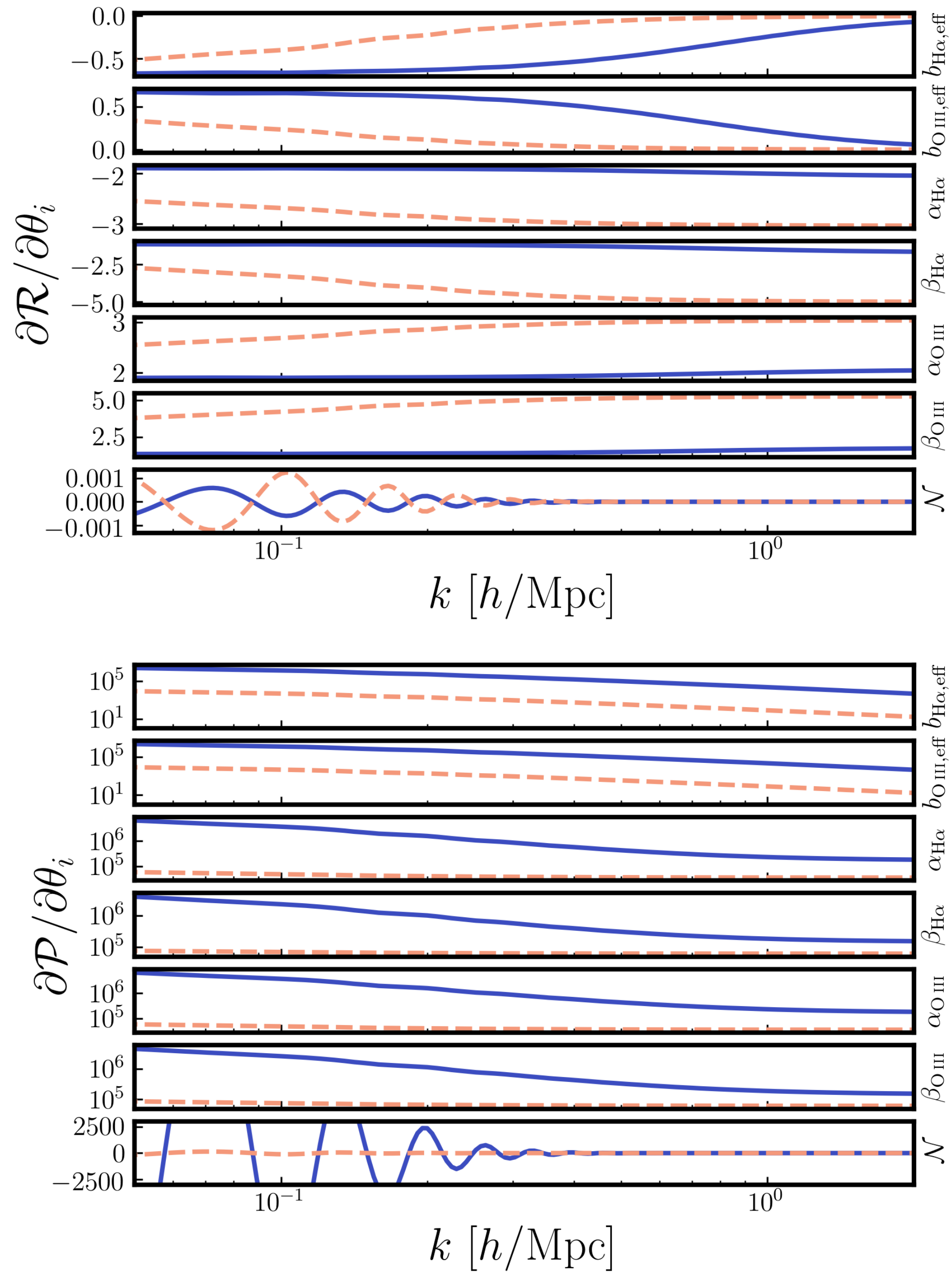

Figure 8.3: Parameter derivatives of the two observables entering the Fisher matrix analysis. From top to bottom, the 7 panels show the derivatives with respect to $b_{\mathrm{H}\alpha,\mathrm{eff}}$, $b_{\mathrm{O\,III},\mathrm{eff}}$, $\alpha_{\mathrm{H}\alpha}$, $\beta_{\mathrm{H}\alpha}$, $\alpha_{\mathrm{O\,III}}$, $\beta_{\mathrm{O\,III}}$, and $\mathcal{N}$, respectively, as a function of the wavenumber at $z = 1$ (blue solid) and $z = 4$ (red dashed).

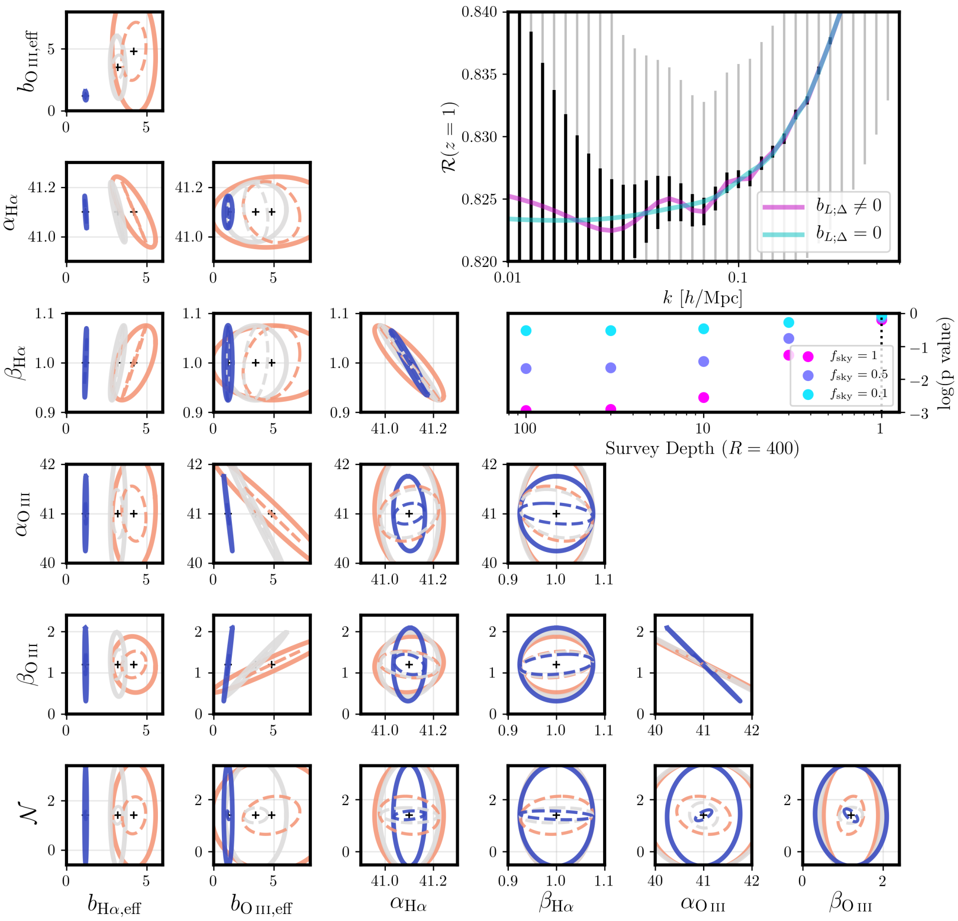

Figure 8.4: Constraints on the model parameters and their degeneracies from the Fisher matrix analysis. The black cross indicates the true input value, with multiple values shown for $b_{L,\mathrm{eff}}$ which increases with redshift. The solid and dashed contours represent constraints from the 200 deg^2 SPHEREx deep fields and a hypothetical all-sky survey reaching the same depth but with $R = 400$, whose constraining power on the power spectrum ratio $\mathcal{R}$ at $z = 1 \pm 0.5$ are shown by the error bars in gray and black in the upper inset, respectively. Note that uncertainties of the SPHEREx deep survey are reduced by 3 times to aid comparison. Models with and without the BAO-induced scale-dependent bias are shown by the magenta and cyan curves, respectively, for comparison. The lower inset shows the distinguishing power (in p value corresponding to the chi-square difference) between models with and without the scale-independent bias, as a function of the sky coverage f_{sky} and the survey depth compared with the nominal depth of the SPHEREx all-sky survey (vertical dotted line), measured by the surface brightness sensitivity.

$\mathcal{N}$, because it only imposes small perturbations on the power spectrum amplitude on BAO scales, the derivatives with respect to it have qualitatively different shapes compared with others. Such distinctions in the scale dependence are key to the capability for separately constraining all free parameters with the two observables. Indeed, as suggested by the close similarity between some curves of derivatives, e.g., with respect to α and β, strong (anti-)correlation and thus degeneracy exist between these parameters.

We show in Figure 8.4 the projected constraints on all the free parameters together with their degeneracy patterns from our Fisher matrix analysis. Overall, jointly measuring $\mathcal{R}$ and $\mathcal{P}$ of Hα and [O III] at high significance makes it possible to robustly constrain the model parameters, including $\mathcal{N}$. Unfortunately, although measurements of the observables are already cosmic-variance limited for the SPHEREx deep survey, it does not have large enough sky coverage and spectral resolution to measure a sufficient number of large-scale modes. With the assumed priors, $\mathcal{N}$ can only be measured to a 80% precision with SPHEREx as shown by solid contours, with insufficient evidence for a scale-dependent bias induced by baryon fraction fluctuations, which we quantify by the p value corresponding to the chi-square difference between best-fit models with and without the scale-dependent bias $b_{L;\Delta}$ (a p value ≈ 0.9 is obtained in this case). While jointly fitting all redshift bins neglecting any redshift evolution improves the constraints, it is still hard to achieve meaningful constraints with the limited size and spectral resolution of the SPHEREx deep survey.

Thus, we also consider a more idealized all-sky survey with $R = 400$ that provides a 10-fold increase in the number of accessible modes required to beat down the sample variance and the same survey depth as the SPHEREx deep survey. With similar instrument specifications but 10 times higher spectral resolution, a much lower system temperature (5 K vs. 80 K for SPHEREx) must be reached via active cooling to achieve a reasonable mission duration of about 2 years. As shown by the dashed contours, such a deep, all-sky survey allows the model parameters to be measured a lot more precisely and the constraints are much less prior-dominated. In this idealized case, a strong evidence for BAO-induced scale-dependent bias is observed (p value ≈ 0.005), and $\mathcal{N}$ can be determined to a precision of 10–30% up to $z \sim 4$, which allows to investigate the physical origin of the global star formation law and reveal any dependence on redshift or the galaxy population. For reference, in the upper inset of Figure 8.4, we show a comparison of the constraints on $\mathcal{R}$ from the two surveys considered, together with best-fit models with and without introducing the scale-independent bias. In the lower inset, we show how the p value of chi-square difference between the best-fit models changes with $f_{\rm sky}$ and the survey depth with respective to the SPHEREx all-sky survey. Consistent with what the dashed contours imply, an all-sky survey reaching the SPHEREx deep survey depth with $R = 400$ is required for obtaining a strong evidence for the scale-dependent bias.

Two other features are noteworthy from the resulting constraint ellipses. First, the degeneracy patterns displayed are generally well-expected from how the model parameters affect the two observables. Clear (anti-)correlations are evident between $\alpha_{\mathrm{H}\alpha}$ and $\beta_{\mathrm{H}\alpha}$, $\alpha_{\mathrm{O\,III}}$ and $\beta_{\mathrm{O\,III}}$, etc. Second, we do see a change of degeneracy direction between $\mathcal{N}$ and other parameters from $z = 1$ to $z = 3$ and 4. This is associated with a change in the dependence of the [O III]–Hα power ratio $\mathcal{R}$ on $\mathcal{N}$, which can be easily seen from the derivative curve of $\partial\mathcal{R}/\partial\mathcal{N}$ shown in the top panel of Figure 8.3, due to the presence of shot-noise contribution $P_{L,\rm shot}$ in $\mathcal{R}$, which can alter the way a nonzero $\mathcal{N}$ impacts $\mathcal{R}$ at sufficiently high redshifts like $z = 4$.

8.4 Discussion and Conclusions

So far, we have assessed how imprints of the baryon fraction deviation on BAO scales can be utilized by future LIM surveys to constrain the fundamental relationship between star formation and the gas content of galaxies. A number of caveats need to be noted though regarding our analysis. First, in practice, LIM data sets ultimately need to be analyzed allowing both astrophysics and cosmology to vary. This is particularly true for large-scale signals such as the BAOs considered in this work, and will inevitably make the extraction and interpretation of astrophysical information like $\mathcal{N}$ more challenging. Meanwhile, although we choose to leave them out of this work for succinctness, observational effects that complicate the target LIM signals, such as redshift-space distortions (RSDs) and line interlopers, are important factors to be accounted for in the actual data analysis. Fortunately, with techniques such as measuring the full multipole moments of redshift-space power spectrum, it is possible to reliably constrain both the astrophysics and cosmology, with effects of RSDs and interloping lines properly included (see e.g., Gong et al. 2020, and references therein). Finally, even on linear scales, astrophysical processes other than what the star formation law encodes may also introduce scale-dependent bias that can further complicate the interpretation of observations, for either astrophysics or cosmology. Some examples of such large-scale modulations include feedback (Coles & Erdogdu 2007), radiative transfer effects (Pontzen 2014), and the impact of galaxy formation physics on halo occupation statistics (Angulo et al. 2014).

In summary, the BAO-induced scale-dependent bias associated with baryon fraction fluctuations provides a useful way to probe astrophysics such as the global star formation law of galaxies on cosmological scales. Our analysis shows that LIM promises to measure this effect and directly constrain the global star formation law power index $\mathcal{N}$, using large-number statistics in a huge cosmic volume rather than zoom-in analyses of individual galaxies. However, such measurements are challenging to make, typically requiring an immense number of modes to achieve a high sensitivity to the BAO amplitudes, which is beyond the capability current-generation surveys like SPHEREx. Future all-sky LIM surveys reaching similar depth but with $\sim$ 10 times better spectral resolving power than SPHEREx will be capable of measuring $\mathcal{N}$ at high significance with BAO intensity mapping. Beyond performing stringent tests on the standard cosmological model, results from such surveys will examine in detail the galaxy evolution theory against the backdrop of large-scale structure formation.

Acknowledgments

We thank Jordan Mirocha, Tzu-Ching Chang, Lluís Mas-Ribas, and Jamie Bock for helpful conversations and comments, as well as the anonymous referee for comments that improved the manuscript. We acknowledge the support from the JPL R&TD strategic initiative grant on line intensity mapping.

Chapter 9

LOOKING FORWARD

In this thesis, I have presented a comprehensive and up-to-date inventory of theoretical perspectives on the applications of the IM technique to better understand galaxy formation and evolution, especially in the high-redshift universe. These applications demonstrate the remarkable potential of the technique for advancing our knowledge of galaxies and the cosmological structure formation in general in the coming age of multi-probe cosmology.

Driven by the persistent experimental effort over decades, represented by experiments such as HERA, CHIME, COMAP, CONCERTO, TIME, TIANLAI, and SPHEREx that have recently started (or will start in the near future) observation, lots of the promised scientific returns of IM will soon be in reach as exciting new data flooded in. It is therefore important for both experimentalists and theorists on this concept to work diligently to comprehend the data, and think collaboratively about how to tease out interesting information from them. Indeed, from the theoretical perspective, there is still much work to be done in all aspects from data analysis methods to the modeling and inference of the signals. Practical challenges like foreground mitigation and component separation in general call for developing and testing out different methods on actual data, whereas realistic modeling, using analytic, semi-empirical, or numerical methods, that captures both observational effects and the physics over wide dynamic ranges will be needed to reliably interpret and maximally extract the physical information from the observed signals.

In the meantime, with the coming online of various new-generation telescopes and experiments, such as eROSITA, JWST, Euclid, Rubin/LSST, Roman/WFIRST, and CMB-S4, that conduct cosmological surveys with other more traditional probes like galaxies and the CMB, investigations of useful cross-correlations between these measurements and IM data sets are extremely worthwhile. Beyond the identification and demonstration of promising synergies to be conducted based on survey specifications and models of the target signals, interesting science cases of astrophysics and cosmology, together with the specific requirements for extracting model constraints with minimal ambiguity, should be explored collaboratively by both theorists and experimentalists.

Bibliography

Abel, T., Bryan, G. L., & Norman, M. L. 2002, Science, 295, 93

Aguirre, J., & STARFIRE Collaboration. 2018, in American Astronomical Society Meeting Abstracts, Vol. 231, American Astronomical Society Meeting Abstracts #231, 328.04

Alvarez, M. A., Ferraro, S., Hill, J. C., Hložek, R., & Ikape, M. 2021, PhRvD, 103, 063518

Amorín, R., Muñoz-Tuñón, C., Aguerri, J. A. L., & Planesas, P. 2016, A&A, 588, A23

Angulo, R. E., Hahn, O., & Abel, T. 2013, MNRAS, 434, 1756

Angulo, R. E., White, S. D. M., Springel, V., & Henriques, B. 2014, MNRAS, 442, 2131

Aravena, M., Decarli, R., Walter, F., et al. 2016, ApJ, 833, 71

Asplund, M., Grevesse, N., Sauval, A. J., & Scott, P. 2009, ARA&A, 47, 481

Atek, H., Richard, J., Jauzac, M., et al. 2015, ApJ, 814, 69

Bakes, E. L. O., & Tielens, A. G. G. M. 1994, ApJ, 427, 822

Bandura, K., Addison, G. E., Amiri, M., et al. 2014, in Proc. SPIE, Vol. 9145, Ground-based and Airborne Telescopes V, 914522

Barkana, R., & Loeb, A. 2001, PhR, 349, 125

—. 2005, ApJ, 626, 1

—. 2011, MNRAS, 415, 3113

Battaglia, N., Natarajan, A., Trac, H., Cen, R., & Loeb, A. 2013, ApJ, 776, 83

Bavouzet, N., Dole, H., Le Floc'h, E., et al. 2008, A&A, 479, 83

Beane, A., Villaescusa-Navarro, F., & Lidz, A. 2019, ApJ, 874, 133

Becker, G. D., D'Aloisio, A., Christenson, H. M., et al. 2021, MNRAS, 508, 1853

Beckwith, S. V. W., Stiavelli, M., Koekemoer, A. M., et al. 2006, AJ, 132, 1729

Behroozi, P., Wechsler, R. H., Hearin, A. P., & Conroy, C. 2019, MNRAS, 488, 3143

Behroozi, P. S., Conroy, C., & Wechsler, R. H. 2010, ApJ, 717, 379

Behroozi, P. S., Wechsler, R. H., & Conroy, C. 2013, ApJL, 762, L31

Belokurov, V., & Kravtsov, A. 2022, arXiv e-prints, arXiv:2203.04980

Benson, A. J. 2010, PhR, 495, 33

Bernal, J. L., Breysse, P. C., & Kovetz, E. D. 2019, PhRvL, 123, 251301

Béthermin, M., Wu, H.-Y., Lagache, G., et al. 2017, A&A, 607, A89

Béthermin, M., Fudamoto, Y., Ginolfi, M., et al. 2020, A&A, 643, A2

Bethermin, M., Gkogkou, A., Van Cuyck, M., et al. 2022, arXiv e-prints, arXiv:2204.12827

Bhattacharya, S., Habib, S., Heitmann, K., & Vikhlinin, A. 2013, ApJ, 766, 32

Bhowmick, A. K., Campbell, D., DiMatteo, T., & Feng, Y. 2018, ArXiv e-prints

Bigot-Sazy, M. A., Ma, Y. Z., Battye, R. A., et al. 2016, in Astronomical Society of the Pacific Conference Series, Vol. 502, Frontiers in Radio Astronomy and FAST Early Sciences Symposium 2015, ed. L. Qain & D. Li, 41

Bisbas, T. G., Papadopoulos, P. P., & Viti, S. 2015, ApJ, 803, 37

Blain, A. W., Smail, I., Ivison, R. J., Kneib, J.-P., & Frayer, D. T. 2002, PhR, 369, 111

Blum, R. D., & Pradhan, A. K. 1992, ApJS, 80, 425

Bolatto, A. D., Wolfire, M., & Leroy, A. K. 2013, Annual Review of Astronomy and Astrophysics, 51, 207

Bolmer, J., Ledoux, C., Wiseman, P., et al. 2019, A&A, 623, A43

Bond, J. R., Cole, S., Efstathiou, G., & Kaiser, N. 1991, ApJ, 379, 440

Boselli, A., Cortese, L., Boquien, M., et al. 2014, A&A, 564, A66

Bothwell, M. S., Wagg, J., Cicone, C., et al. 2014, MNRAS, 445, 2599

Bourne, N., Dunlop, J. S., Merlin, E., et al. 2017, MNRAS, 467, 1360

Bouwens, R. J., Illingworth, G. D., Oesch, P. A., et al. 2015a, ApJ, 811, 140

Bouwens, R. J., Oesch, P. A., Illingworth, G. D., Ellis, R. S., & Stefanon, M. 2017, ApJ, 843, 129

Bouwens, R. J., Illingworth, G. D., Oesch, P. A., et al. 2014, ApJ, 793, 115

—. 2015b, ApJ, 803, 34

Bouwens, R. J., Oesch, P. A., Stefanon, M., et al. 2021, AJ, 162, 47

Bowman, J. D., Rogers, A. E. E., Monsalve, R. A., Mozdzen, T. J., & Mahesh, N. 2018, Nature, 555, 67

Boylan-Kolchin, M., Springel, V., White, S. D. M., Jenkins, A., & Lemson, G. 2009, MNRAS, 398, 1150

Bradač, M., Garcia-Appadoo, D., Huang, K.-H., et al. 2017, ApJL, 836, L2

Bradford, C. M., Kenyon, M., Holmes, W., Bock, J., & Koch, T. 2008, in Society of Photo-Optical Instrumentation Engineers (SPIE) Conference Series, Vol. 7020, Proc. SPIE, 70201O

Bradford, C. M., Cameron, B., Moore, B., et al. 2018, in Society of Photo-Optical Instrumentation Engineers (SPIE) Conference Series, Vol. 10698, Proc. SPIE, 1069818

Bradley, R. F., Tauscher, K., Rapetti, D., & Burns, J. O. 2019, ApJ, 874, 153

Brauher, J. R., Dale, D. A., & Helou, G. 2008, ApJS, 178, 280

Brennan, R., Pandya, V., Somerville, R. S., et al. 2015, MNRAS, 451, 2933

Breysse, P. C., & Alexandroff, R. M. 2019, MNRAS, 490, 260

Breysse, P. C., Kovetz, E. D., Behroozi, P. S., Dai, L., & Kamionkowski, M. 2017, MNRAS, 467, 2996

Breysse, P. C., Kovetz, E. D., & Kamionkowski, M. 2014, MNRAS, 443, 3506

—. 2015, MNRAS, 452, 3408

Breysse, P. C., Chung, D. T., Cleary, K. A., et al. 2021, arXiv e-prints, arXiv:2111.05933

Bromm, V. 2013, Reports on Progress in Physics, 76, 112901

Bromm, V., & Larson, R. B. 2004, ARA&A, 42, 79

Bromm, V., & Yoshida, N. 2011, ARA&A, 49, 373

Bull, P., Ferreira, P. G., Patel, P., & Santos, M. G. 2015, ApJ, 803, 21

Byler, N., Dalcanton, J. J., Conroy, C., & Johnson, B. D. 2017, ApJ, 840, 44

Cai, Z., Fan, X., Jiang, L., et al. 2011, ApJL, 736, L28

Cain, C., D'Aloisio, A., Gangolli, N., & Becker, G. D. 2021, ApJL, 917, L37

Capak, P. L., Carilli, C., Jones, G., et al. 2015, Nature, 522, 455

Cappelluti, N., Kashlinsky, A., Arendt, R. G., et al. 2013, ApJ, 769, 68

Carilli, C. L., & Walter, F. 2013, ARA&A, 51, 105

Carilli, C. L., Chluba, J., Decarli, R., et al. 2016, ApJ, 833, 73

Casey, C. M., Narayanan, D., & Cooray, A. 2014, PhR, 541, 45

Casey, C. M., Chen, C.-C., Cowie, L. L., et al. 2013, MNRAS, 436, 1919

Cataldo, G., Ade, P. A. R., Anderson, C. J., et al. 2020, in Society of Photo-Optical Instrumentation Engineers (SPIE) Conference Series, Vol. 11445, Society of Photo-Optical Instrumentation Engineers (SPIE) Conference Series, 1144524

Chabrier, G. 2003, PASP, 115, 763

Chang, T. C., Gong, Y., Santos, M., et al. 2015, in Advancing Astrophysics with the Square Kilometre Array (AASKA14), 4

Chang, T.-C., Pen, U.-L., Bandura, K., & Peterson, J. B. 2010, Nature, 466, 463

Chang, T.-C., Pen, U.-L., Peterson, J. B., & McDonald, P. 2008, PhRvL, 100, 091303

Chang, T.-C., Beane, A., Dore, O., et al. 2019, BAAS, 51, 282

Chapman, E., Zaroubi, S., Abdalla, F. B., et al. 2016, MNRAS, 458, 2928

Chary, R., & Elbaz, D. 2001, ApJ, 556, 562

Chen, C.-C., Cowie, L. L., Barger, A. J., et al. 2013, ApJ, 776, 131

Chen, Z., Xu, Y., Wang, Y., & Chen, X. 2019, ApJ, 885, 23

Cheng, S., Ting, Y.-S., Ménard, B., & Bruna, J. 2020a, MNRAS, 499, 5902

Cheng, Y.-T., Chang, T.-C., Bock, J., Bradford, C. M., & Cooray, A. 2016, ApJ, 832, 165

Cheng, Y.-T., Chang, T.-C., & Bock, J. J. 2020b, ApJ, 901, 142

Chluba, J., & Thomas, R. M. 2011, MNRAS, 412, 748

Choudhury, T. R., & Ferrara, A. 2007, MNRAS, 380, L6

Chung, D. T. 2022, arXiv e-prints, arXiv:2203.12581

Chung, D. T., Viero, M. P., Church, S. E., & Wechsler, R. H. 2020, ApJ, 892, 51

Chung, D. T., Viero, M. P., Church, S. E., et al. 2019, ApJ, 872, 186

Cleary, K. A., Borowska, J., Breysse, P. C., et al. 2021, arXiv e-prints, arXiv:2111.05927

Clegg, P. E., Ade, P. A. R., Armand, C., et al. 1996, A&A, 315, L38

Cohen, A., Fialkov, A., Barkana, R., & Lotem, M. 2017, MNRAS, 472, 1915

Coles, P., & Erdogdu, P. 2007, JCAP, 2007, 007

Comaschi, P., & Ferrara, A. 2016, MNRAS, 455, 725

Concerto Collaboration, Ade, P., Aravena, M., et al. 2020, A&A, 642, A60

Cooray, A., Bock, J. J., Keatin, B., Lange, A. E., & Matsumoto, T. 2004, ApJ, 606, 611

Cooray, A., Gong, Y., Smidt, J., & Santos, M. G. 2012a, ApJ, 756, 92

Cooray, A., & Sheth, R. 2002, PhR, 372, 1

Cooray, A., Smidt, J., de Bernardis, F., et al. 2012b, Nature, 490, 514

Cooray, A., Chang, T.-C., Unwin, S., et al. 2019a, in Bulletin of the American Astronomical Society, Vol. 51, 23

Cooray, A., Chang, T.-C., Unwin, S., et al. 2019b, in Bulletin of the American Astronomical Society, Vol. 51, 23

Cormier, D., Abel, N. P., Hony, S., et al. 2019, A&A, 626, A23

Cox, T. A., Jacobs, D. C., & Murray, S. G. 2022, MNRAS, 512, 792

Crain, R. A., Bahé, Y. M., Lagos, C. d. P., et al. 2017, MNRAS, 464, 4204

Crawford, M. K., Genzel, R., Townes, C. H., & Watson, D. M. 1985, ApJ, 291, 755

Crites, A. T., Bock, J. J., Bradford, C. M., et al. 2014, in Proc. SPIE, Vol. 9153, Millimeter, Submillimeter, and Far-Infrared Detectors and Instrumentation for Astronomy VII, 91531W

Crosby, B. D., O'Shea, B. W., Smith, B. D., Turk, M. J., & Hahn, O. 2013, ApJ, 773, 108

Croxall, K. V., Smith, J. D., Pellegrini, E., et al. 2017, ApJ, 845, 96

Cucciati, O., Tresse, L., Ilbert, O., et al. 2012, A&A, 539, A31

Daddi, E., Elbaz, D., Walter, F., et al. 2010, ApJL, 714, L118

D'Aloisio, A., McQuinn, M., Trac, H., Cain, C., & Mesinger, A. 2020, ApJ, 898, 149

Dame, T. M., Hartmann, D., & Thaddeus, P. 2001, ApJ, 547, 792

Davies, F. B., & Furlanetto, S. R. 2022, MNRAS, 514, 1302

Davies, F. B., Hennawi, J. F., Bañados, E., et al. 2018, ApJ, 864, 142

Dayal, P., & Ferrara, A. 2018, PhR, 780, 1

Dayal, P., Ferrara, A., & Gallerani, S. 2008, MNRAS, 389, 1683

De Looze, I., Baes, M., Bendo, G. J., Cortese, L., & Fritz, J. 2011, MNRAS, 416, 2712

De Looze, I., Cormier, D., Lebouteiller, V., et al. 2014, A&A, 568, A62

de los Reyes, M. A. C., & Kennicutt, Robert C., J. 2019, ApJ, 872, 16

DeBoer, D. R., Parsons, A. R., Aguirre, J. E., et al. 2017, PASP, 129, 045001

Decarli, R., Walter, F., Aravena, M., et al. 2016, ApJ, 833, 69

Decarli, R., Walter, F., Gónzalez-López, J., et al. 2019, ApJ, 882, 138

Decarli, R., Aravena, M., Boogaard, L., et al. 2020, ApJ, 902, 110

Dekel, A., & Mandelker, N. 2014, MNRAS, 444, 2071

Dekel, A., Sarkar, K. C., Jiang, F., et al. 2019, MNRAS, 488, 4753

Desjacques, V., Chluba, J., Silk, J., de Bernardis, F., & Doré, O. 2015, MNRAS, 451, 4460

Dessauges-Zavadsky, M., Zamojski, M., Schaerer, D., et al. 2015, A&A, 577, A50

Dewdney, P., Turner, W., R., M., et al. 2013, SKA1 System Baseline Design

Díaz-Santos, T., Armus, L., Charmandaris, V., et al. 2017, ApJ, 846, 32

Dickman, R. L., Snell, R. L., & Schloerb, F. P. 1986, ApJ, 309, 326

Dijkstra, M. 2017, arXiv e-prints, arXiv:1704.03416

Dijkstra, M., & Kramer, R. 2012, MNRAS, 424, 1672

Dodelson, S. 2003, Modern cosmology

Donnari, M., Pillepich, A., Nelson, D., et al. 2021, MNRAS, 506, 4760

Dopita, M. A., & Sutherland, R. S. 2003, Astrophysics of the diffuse universe

Doré, O., Bock, J., Ashby, M., et al. 2014, arXiv e-prints, arXiv:1412.4872

Doré, O., Werner, M. W., Ashby, M., et al. 2016, arXiv e-prints, arXiv:1606.07039

Doré, O., Werner, M. W., Ashby, M. L. N., et al. 2018, arXiv e-prints, arXiv:1805.05489

Draine, B. T. 2011, Physics of the Interstellar and Intergalactic Medium (Princeton, NJ: Princeton University Press)

Draine, B. T., & Miralda-Escudé, J. 2018, ApJL, 858, L10

Draine, B. T., Dale, D. A., Bendo, G., et al. 2007, ApJ, 663, 866

Driver, S. P., Popescu, C. C., Tuffs, R. J., et al. 2007, MNRAS, 379, 1022

Dumitru, S., Kulkarni, G., Lagache, G., & Haehnelt, M. G. 2019, MNRAS, 485, 3486

Dunne, L., Gomez, H. L., da Cunha, E., et al. 2011, MNRAS, 417, 1510

Dutton, A. A., van den Bosch, F. C., & Dekel, A. 2010, MNRAS, 405, 1690

Eide, M. B., Ciardi, B., Graziani, L., et al. 2020, MNRAS, 498, 6083

Eide, M. B., Graziani, L., Ciardi, B., et al. 2018, MNRAS, 476, 1174

Eisenstein, D. J. 2005, NewAR, 49, 360

Eldridge, J. J., & Stanway, E. R. 2009, MNRAS, 400, 1019

Eldridge, J. J., Stanway, E. R., Xiao, L., et al. 2017, PASA, 34, e058

Ellis, R. S., McLure, R. J., Dunlop, J. S., et al. 2013, ApJL, 763, L7

Endo, A., Karatsu, K., Tamura, Y., et al. 2019, Nature Astronomy, 3, 989

Fan, X., Carilli, C. L., & Keating, B. 2006a, ARA&A, 44, 415

Fan, X., Strauss, M. A., Becker, R. H., et al. 2006b, AJ, 132, 117

Faucher-Giguère, C.-A., Quataert, E., & Hopkins, P. F. 2013, MNRAS, 433, 1970

Feng, C., Cooray, A., Bock, J., et al. 2019, ApJ, 875, 86

Ferland, G. J. 1980, PASP, 92, 596

Ferland, G. J., Porter, R. L., van Hoof, P. A. M., et al. 2013, RMxAA, 49, 137

Ferland, G. J., Chatzikos, M., Guzmán, F., et al. 2017, RMxAA, 53, 385

Fernandez, E. R., & Komatsu, E. 2006, ApJ, 646, 703

Fernandez, E. R., Komatsu, E., Iliev, I. T., & Shapiro, P. R. 2010, ApJ, 710, 1089

Fernandez, E. R., & Zaroubi, S. 2013, MNRAS, 433, 2047

Fernandez, E. R., Zaroubi, S., Iliev, I. T., Mellema, G., & Jelić, V. 2014, MNRAS, 440, 298

Ferrara, A., Vallini, L., Pallottini, A., et al. 2019, MNRAS, 489, 1

Fialkov, A., Barkana, R., Pinhas, A., & Visbal, E. 2014, MNRAS, 437, L36

Fialkov, A., Barkana, R., Tseliakhovich, D., & Hirata, C. M. 2012, MNRAS, 424, 1335

Fialkov, A., Barkana, R., Visbal, E., Tseliakhovich, D., & Hirata, C. M. 2013, MNRAS, 432, 2909

Finkelstein, S. L., Ryan, Jr., R. E., Papovich, C., et al. 2015, ApJ, 810, 71

Fontanot, F., Cristiani, S., & Vanzella, E. 2012, MNRAS, 425, 1413

Foreman-Mackey, D., Hogg, D. W., Lang, D., & Goodman, J. 2013, Publications of the Astronomical Society of the Pacific, 125, 306

Frayer, D. T., Sanders, D. B., Surace, J. A., et al. 2009, AJ, 138, 1261

Fu, J., Kauffmann, G., Huang, M.-l., et al. 2013, MNRAS, 434, 1531

Furlanetto, S. R. 2006, MNRAS, 371, 867

—. 2021, MNRAS, 500, 3394

Furlanetto, S. R., & Lidz, A. 2007, ApJ, 660, 1030

Furlanetto, S. R., & Loeb, A. 2005, ApJ, 634, 1

Furlanetto, S. R., & Mirocha, J. 2022, MNRAS, 511, 3895

Furlanetto, S. R., Mirocha, J., Mebane, R. H., & Sun, G. 2017, MNRAS, 472, 1576

Furlanetto, S. R., & Oh, S. P. 2008, ApJ, 681, 1

Furlanetto, S. R., Oh, S. P., & Briggs, F. H. 2006, PhR, 433, 181

Furlanetto, S. R., & Stoever, S. J. 2010, MNRAS, 404, 1869

Furlanetto, S. R., Zaldarriaga, M., & Hernquist, L. 2004, ApJ, 613, 1

Furlong, M., Bower, R. G., Theuns, T., et al. 2015, MNRAS, 450, 4486

Gagnon-Hartman, S., Cui, Y., Liu, A., & Ravanbakhsh, S. 2021, MNRAS, 504, 4716

Gao, L., Frenk, C. S., Boylan-Kolchin, M., et al. 2011, MNRAS, 410, 2309

Genzel, R., Tacconi, L. J., Combes, F., et al. 2012, ApJ, 746, 69

Glover, S. C. O., Clark, P. C., Micic, M., & Molina, F. 2015, MNRAS, 448, 1607

Goldsmith, P. F., Yıldız, U. A., Langer, W. D., & Pineda, J. L. 2015, ApJ, 814, 133

Gong, M., Ostriker, E. C., & Kim, C.-G. 2018, ApJ, 858, 16

Gong, Y., Chen, X., & Cooray, A. 2020, ApJ, 894, 152

Gong, Y., Cooray, A., Silva, M., et al. 2012, ApJ, 745, 49

Gong, Y., Cooray, A., Silva, M. B., Santos, M. G., & Lubin, P. 2011, ApJL, 728, L46

Gong, Y., Cooray, A., Silva, M. B., et al. 2017, ApJ, 835, 273

Gong, Y., Silva, M., Cooray, A., & Santos, M. G. 2014, ApJ, 785, 72

Gorce, A., Douspis, M., & Salvati, L. 2022, arXiv e-prints, arXiv:2202.08698

Graham, J. F., & Fruchter, A. S. 2017, ApJ, 834, 170

Greif, T. H., Springel, V., White, S. D. M., et al. 2011, ApJ, 737, 75

Greig, B., Mesinger, A., & Bañados, E. 2019, MNRAS, 484, 5094

Greig, B., Mesinger, A., Haiman, Z., & Simcoe, R. A. 2016, Monthly Notices of the Royal Astronomical Society, 466, 4239

Greig, B., Ting, Y.-S., & Kaurov, A. A. 2022, MNRAS, 513, 1719

Greve, T. R., Leonidaki, I., Xilouris, E. M., et al. 2014, ApJ, 794, 142

Griffin, M. J., Abergel, A., Abreu, A., et al. 2010, A&A, 518, L3

Grisdale, K., Thatte, N., Devriendt, J., et al. 2021, MNRAS

Grogin, N. A., Kocevski, D. D., Faber, S. M., et al. 2011, ApJS, 197, 35

Gruppioni, C., Pozzi, F., Rodighiero, G., et al. 2013, MNRAS, 432, 23

Gullberg, B., De Breuck, C., Vieira, J. D., et al. 2015, MNRAS, 449, 2883

Gurvich, A. B., Stern, J., Faucher-Giguère, C.-A., et al. 2022, arXiv e-prints, arXiv:2203.04321

Haardt, F., & Madau, P. 1996, ApJ, 461, 20

Hailey-Dunsheath, S., Shirokoff, E., Barry, P. S., et al. 2014, in Society of Photo-Optical Instrumentation Engineers (SPIE) Conference Series, Vol. 9153, Proc. SPIE, 91530M

Haiman, Z., Abel, T., & Rees, M. J. 2000, ApJ, 534, 11

Haiman, Z., Rees, M. J., & Loeb, A. 1997, ApJ, 476, 458

Hamilton, A. J. S. 1998, in Astrophysics and Space Science Library, Vol. 231, The Evolving Universe, ed. D. Hamilton, 185

Harikane, Y., Ouchi, M., Ono, Y., et al. 2018, PASJ, 70, S11

Harikane, Y., Ouchi, M., Inoue, A. K., et al. 2020, ApJ, 896, 93

Harikane, Y., Ono, Y., Ouchi, M., et al. 2022, ApJS, 259, 20

Harker, G., Zaroubi, S., Bernardi, G., et al. 2009, MNRAS, 397, 1138

Hashimoto, T., Inoue, A. K., Mawatari, K., et al. 2019, PASJ, 71, 71

Hayatsu, N. H., Matsuda, Y., Umehata, H., et al. 2017, PASJ, 69, 45

Helgason, K., Ricotti, M., & Kashlinsky, A. 2012, ApJ, 752, 113

Helgason, K., Ricotti, M., Kashlinsky, A., & Bromm, V. 2016, MNRAS, 455, 282

Heneka, C., & Cooray, A. 2021, MNRAS, 506, 1573

Heneka, C., Cooray, A., & Feng, C. 2017, ApJ, 848, 52

Herrera-Camus, R., Bolatto, A. D., Wolfire, M. G., et al. 2015, ApJ, 800, 1

Herrera-Camus, R., Bolatto, A., Smith, J. D., et al. 2016, ApJ, 826, 175

Hills, R., Kulkarni, G., Meerburg, P. D., & Puchwein, E. 2018, Nature, 564, E32

Hivon, E., Górski, K. M., Netterfield, C. B., et al. 2002, ApJ, 567, 2

Ho, P. T. P., Altamirano, P., Chang, C.-H., et al. 2009, ApJ, 694, 1610

Hoag, A., Bradač, M., Huang, K., et al. 2019, ApJ, 878, 12

Holzbauer, L. N., & Furlanetto, S. R. 2012, MNRAS, 419, 718

Hopkins, A. M., & Beacom, J. F. 2006, ApJ, 651, 142

Hopkins, P. F., Wetzel, A., Kereš, D., et al. 2018, MNRAS, 480, 800

Hughes, T. M., Foyle, K., Schirm, M. R. P., et al. 2015, A&A, 575, A17

Hui, L., & Haiman, Z. 2003, ApJ, 596, 9

Hummel, J. A., Stacy, A., Jeon, M., Oliveri, A., & Bromm, V. 2015, MNRAS, 453, 4136

Hunacek, J., Bock, J., Bradford, C. M., et al. 2016, Journal of Low Temperature Physics, 184, 733

—. 2018, Journal of Low Temperature Physics, 193, 893

Hunacek, J. R. 2020, PhD thesis, California Institute of Technology, doi: http://doi.org/10.7907/hp2n-849510.7907/hp2n-8495

Ihle, H. T., Chung, D., Stein, G., et al. 2019, ApJ, 871, 75

Inayoshi, K., Visbal, E., & Haiman, Z. 2020, ARA&A, 58, 27

Inoue, A. K., Tamura, Y., Matsuo, H., et al. 2016, Science, 352, 1559

Israel, F. P., Rosenberg, M. J. F., & van der Werf, P. 2015, A&A, 578, A95

Ivison, R. J., Papadopoulos, P. P., Smail, I., et al. 2011, MNRAS, 412, 1913

Jaacks, J., Thompson, R., Finkelstein, S. L., & Bromm, V. 2018, MNRAS, 475, 4396

Jenkins, A., Frenk, C. S., White, S. D. M., et al. 2001, MNRAS, 321, 372

Jensen, H., Datta, K. K., Mellema, G., et al. 2013, MNRAS, 435, 460

Ji, X., & Yan, R. 2022, A&A, 659, A112

Jiao, Q., Zhao, Y., Zhu, M., et al. 2017, ApJL, 840, L18

Jose, C., Srianand, R., & Subramanian, K. a. 2013, MNRAS, 435, 368

Kamenetzky, J., Rangwala, N., Glenn, J., Maloney, P. R., & Conley, A. 2016, ApJ, 829, 93

Kannan, R., Garaldi, E., Smith, A., et al. 2022a, MNRAS, 511, 4005

Kannan, R., Marinacci, F., Vogelsberger, M., et al. 2020, MNRAS, 499, 5732

Kannan, R., Smith, A., Garaldi, E., et al. 2022b, MNRAS

Karkare, K. S., & Bird, S. 2018, PhRvD, 98, 043529

Karkare, K. S., Barry, P. S., Bradford, C. M., et al. 2020, Journal of Low Temperature Physics, 199, 849

Kashlinsky, A., Arendt, R., Gardner, J. P., Mather, J. C., & Moseley, S. H. 2004, ApJ, 608, 1

Kashlinsky, A., Arendt, R. G., Ashby, M. L. N., et al. 2012, ApJ, 753, 63

Kashlinsky, A., Arendt, R. G., Atrio-Barandela, F., et al. 2018, Reviews of Modern Physics, 90, 025006

Kashlinsky, A., Arendt, R. G., Atrio-Barandela, F., & Helgason, K. 2015a, ApJL, 813, L12

Kashlinsky, A., Arendt, R. G., Mather, J., & Moseley, S. H. 2005, Nature, 438, 45

Kashlinsky, A., Mather, J. C., Helgason, K., et al. 2015b, ApJ, 804, 99

Katz, H., Galligan, T. P., Kimm, T., et al. 2019, MNRAS, 487, 5902

Keating, G. K., Marrone, D. P., Bower, G. C., & Keenan, R. P. 2020, ApJ, 901, 141

Keating, G. K., Marrone, D. P., Bower, G. C., et al. 2016, ApJ, 830, 34

Keenan, R. P., Marrone, D. P., & Keating, G. K. 2020, ApJ, 904, 127

Kelson, D. D. 2014, ArXiv 1406.5191

Kennicutt, Robert C., J., & De Los Reyes, M. A. C. 2021, ApJ, 908, 61

Kennicutt, Jr., R. C. 1998, ARA&A, 36, 189

Keres, D., Yun, M. S., & Young, J. S. 2003, ApJ, 582, 659

Kewley, L. J., Nicholls, D. C., & Sutherland, R. S. 2019, ARA&A, 57, 511

Kittiwisit, P., Bowman, J. D., Murray, S. G., et al. 2022, arXiv e-prints, arXiv:2204.01124

Knox, L. 1995, PhRvD, 52, 4307

Konno, A., Ouchi, M., Shibuya, T., et al. 2018, PASJ, 70, S16

Koopmans, L., Pritchard, J., Mellema, G., et al. 2015, in Advancing Astrophysics with the Square Kilometre Array (AASKA14), 1

Kovetz, E., Breysse, P. C., Lidz, A., et al. 2019, BAAS, 51, 101

Kovetz, E. D., Viero, M. P., Lidz, A., et al. 2017, arXiv e-prints

Kravtsov, A. V., Berlind, A. A., Wechsler, R. H., et al. 2004, ApJ, 609, 35

Kravtsov, A. V., Vikhlinin, A. A., & Meshcheryakov, A. V. 2018, Astronomy Letters, 44, 8

Krumholz, M. R., Dekel, A., & McKee, C. F. 2012, ApJ, 745, 69

Krumholz, M. R., McKee, C. F., & Tumlinson, J. 2009, ApJ, 693, 216

Kuhlen, M., & Faucher-Giguère, C.-A. 2012, MNRAS, 423, 862

La Plante, P., Lidz, A., Aguirre, J., & Kohn, S. 2020, ApJ, 899, 40

Lacey, C., & Cole, S. 1993, MNRAS, 262, 627

Lagache, G. 2018, in IAU Symposium, Vol. 333, Peering towards Cosmic Dawn, ed. V. Jelić & T. van der Hulst, 228–233

Lagache, G., Cousin, M., & Chatzikos, M. 2018, A&A, 609, A130

Laigle, C., McCracken, H. J., Ilbert, O., et al. 2016, ApJS, 224, 24

Lanz, A., Arai, T., Battle, J., et al. 2014, in Society of Photo-Optical Instrumentation Engineers (SPIE) Conference Series, Vol. 9143, Space Telescopes and Instrumentation 2014: Optical, Infrared, and Millimeter Wave, ed. J. Oschmann, Jacobus M., M. Clampin, G. G. Fazio, & H. A. MacEwen, 91433N

Laporte, N., Katz, H., Ellis, R. S., et al. 2019, MNRAS, 487, L81

Lee, K.-G., Krolewski, A., White, M., et al. 2018, ApJS, 237, 31

Lenkić, L., Bolatto, A. D., Förster Schreiber, N. M., et al. 2020, AJ, 159, 190

Lewis, A., Challinor, A., & Lasenby, A. 2000, ApJ, 538, 473

Lewis, J. S. W., Ocvirk, P., Sorce, J. G., et al. 2022, arXiv e-prints, arXiv:2202.05869

Li, Q., Narayanan, D., & Davé, R. 2019, MNRAS, 490, 1425

Li, T. Y., Wechsler, R. H., Devaraj, K., & Church, S. E. 2016, ApJ, 817, 169

Lidz, A., Furlanetto, S. R., Oh, S. P., et al. 2011, ApJ, 741, 70

Lidz, A., & Taylor, J. 2016, ApJ, 825, 143

Lidz, A., Zahn, O., Furlanetto, S. R., et al. 2009, ApJ, 690, 252

Liu, A., & Shaw, J. R. 2020, PASP, 132, 062001

Liu, A., & Tegmark, M. 2011, PhRvD, 83, 103006

Liu, B., & Bromm, V. 2020, MNRAS, 497, 2839

Liu, L., Gao, Y., & Greve, T. R. 2015, ApJ, 805, 31

Liu, R. H., & Breysse, P. C. 2021, PhRvD, 103, 063520

Livermore, R. C., Finkelstein, S. L., & Lotz, J. M. 2017, ApJ, 835, 113

Loeb, A., & Furlanetto, S. R. 2013, The First Galaxies in the Universe (Princeton University Press)

Loiacono, F., Decarli, R., Gruppioni, C., et al. 2020, arXiv e-prints, arXiv:2006.04837

Lotz, J. M., Koekemoer, A., Coe, D., et al. 2017, ApJ, 837, 97

Ly, C., Malkan, M. A., Kashikawa, N., et al. 2007, ApJ, 657, 738

Madau, P. 1995, ApJ, 441, 18

—. 2017, ApJ, 851, 50

Madau, P., & Dickinson, M. 2014, ARA&A, 52, 415

Madau, P., Meiksin, A., & Rees, M. J. 1997, ApJ, 475, 429

Madau, P., & Silk, J. 2005, MNRAS, 359, L37

Maio, U., Ciardi, B., Dolag, K., Tornatore, L., & Khochfar, S. 2010, MNRAS, 407, 1003

Malhotra, S., Helou, G., Stacey, G., et al. 1997, ApJL, 491, L27

Maniyar, A. S., Béthermin, M., & Lagache, G. 2018, A&A, 614, A39

Maniyar, A. S., Schaan, E., & Pullen, A. R. 2022, PhRvD, 105, 083509

Mao, X.-C. 2014, ApJ, 790, 148

Mao, Y., Shapiro, P. R., Mellema, G., et al. 2012, MNRAS, 422, 926

Marsden, G., Ade, P. A. R., Bock, J. J., et al. 2009, ApJ, 707, 1729

Mas-Ribas, L., & Chang, T.-C. 2020, PhRvD, 101, 083032

Mas-Ribas, L., & Dijkstra, M. 2016, ApJ, 822, 84

Mas-Ribas, L., Dijkstra, M., & Forero-Romero, J. E. 2016, ApJ, 833, 65

Mas-Ribas, L., Dijkstra, M., Hennawi, J. F., et al. 2017a, ApJ, 841, 19

Mas-Ribas, L., Hennawi, J. F., Dijkstra, M., et al. 2017b, ApJ, 846, 11

Mashian, N., Oesch, P. A., & Loeb, A. 2016, MNRAS, 455, 2101

Mashian, N., Sternberg, A., & Loeb, A. 2015a, JCAP, 2015, 028

Mashian, N., Sturm, E., Sternberg, A., et al. 2015b, ApJ, 802, 81

Mason, C. A., Trenti, M., & Treu, T. 2015, ApJ, 813, 21

Mason, C. A., Treu, T., Dijkstra, M., et al. 2018, ApJ, 856, 2

Mason, C. A., Fontana, A., Treu, T., et al. 2019, MNRAS, 485, 3947

Matthee, J., Sobral, D., Boogaard, L. A., et al. 2019, ApJ, 881, 124

McAlpine, S., Helly, J. C., Schaller, M., et al. 2016, Astronomy and Computing, 15, 72

McBride, J., Fakhouri, O., & Ma, C.-P. 2009, MNRAS, 398, 1858

McCracken, H. J., Wolk, M., Colombi, S., et al. 2015, MNRAS, 449, 901

McGreer, I. D., Mesinger, A., & D'Odorico, V. 2015, MNRAS, 447, 499

McKee, C. F., & Krumholz, M. R. 2010, ApJ, 709, 308

McKee, C. F., & Tan, J. C. 2008, ApJ, 681, 771

McQuinn, M., Hernquist, L., Zaldarriaga, M., & Dutta, S. 2007, MNRAS, 381, 75

McQuinn, M., Zahn, O., Zaldarriaga, M., Hernquist, L., & Furlanetto, S. R. 2006, ApJ, 653, 815

Mebane, R. H., Mirocha, J., & Furlanetto, S. R. 2018, MNRAS, 479, 4544

—. 2020, MNRAS, 493, 1217

Mellema, G., Koopmans, L. V. E., Abdalla, F. A., et al. 2013, Experimental Astronomy, 36, 235

Ménard, B., & Fukugita, M. 2012, ApJ, 754, 116

Ménard, B., Scranton, R., Fukugita, M., & Richards, G. 2010, MNRAS, 405, 1025

Mesinger, A., & Furlanetto, S. 2007, ApJ, 669, 663

Mesinger, A., Furlanetto, S., & Cen, R. 2011, MNRAS, 411, 955

Mesinger, A., Greig, B., & Sobacchi, E. 2016, MNRAS, 459, 2342

Mészáros, P., & Rees, M. J. 2010, ApJ, 715, 967

Metha, B., Cameron, A. J., & Trenti, M. 2021, MNRAS, 504, 5992

Meurer, G. R., Heckman, T. M., & Calzetti, D. 1999, ApJ, 521, 64

Mirocha, J. 2014, MNRAS, 443, 1211

—. 2020, MNRAS, 499, 4534

Mirocha, J., & Furlanetto, S. R. 2019, MNRAS, 483, 1980

Mirocha, J., Furlanetto, S. R., & Sun, G. 2017, MNRAS, 464, 1365

Mirocha, J., Harker, G. J. A., & Burns, J. O. 2015, ApJ, 813, 11

Mirocha, J., La Plante, P., & Liu, A. 2020, arXiv e-prints, arXiv:2012.09189

—. 2021, MNRAS, 507, 3872

Mirocha, J., Mebane, R. H., Furlanetto, S. R., Singal, K., & Trinh, D. 2018, MNRAS, 478, 5591

Mo, H., van den Bosch, F. C., & White, S. 2010, Galaxy Formation and Evolution (Cambridge University Press)

Moncelsi, L., Ade, P. A. R., Chapin, E. L., et al. 2011, ApJ, 727, 83

Moradinezhad Dizgah, A., Keating, G. K., Karkare, K. S., Crites, A., & Choudhury, S. R. 2022, ApJ, 926, 137

More, S., van den Bosch, F. C., Cacciato, M., et al. 2009, MNRAS, 392, 801

Moriwaki, K., Filippova, N., Shirasaki, M., & Yoshida, N. 2020, MNRAS, 496, L54

Mostek, N., Coil, A. L., Cooper, M., et al. 2013, ApJ, 767, 89

Moster, B. P., Somerville, R. S., Maulbetsch, C., et al. 2010, ApJ, 710, 903

Muñoz, J. A., & Furlanetto, S. R. 2013, MNRAS, 435, 2676

Muñoz, J. A., & Oh, S. P. 2016, MNRAS, 463, 2085

Muñoz, J. B., Qin, Y., Mesinger, A., et al. 2022, MNRAS, 511, 3657

Murray, S., Greig, B., Mesinger, A., et al. 2020, The Journal of Open Source Software, 5, 2582

Murray, S. G., Power, C., & Robotham, A. S. G. 2013, Astronomy and Computing, 3, 23

Muzzin, A., Marchesini, D., Stefanon, M., et al. 2013a, ApJ, 777, 18

—. 2013b, ApJS, 206, 8

Nagao, T., Motohara, K., Maiolino, R., et al. 2005, ApJL, 631, L5

Naidu, R. P., Tacchella, S., Mason, C. A., et al. 2020, ApJ, 892, 109

Naoz, S., Yoshida, N., & Barkana, R. 2011, MNRAS, 416, 232

Naoz, S., Yoshida, N., & Gnedin, N. Y. 2012, ApJ, 747, 128

Narayanan, D., & Krumholz, M. R. 2014, MNRAS, 442, 1411

Navarro, J. F., Frenk, C. S., & White, S. D. M. 1997, ApJ, 490, 493

Nesvadba, N. P. H., Cañameras, R., Kneissl, R., et al. 2019, A&A, 624, A23

Newburgh, L. B., Bandura, K., Bucher, M. A., et al. 2016, in Society of Photo-Optical Instrumentation Engineers (SPIE) Conference Series, Vol. 9906, Ground-based and Airborne Telescopes VI, 99065X

Newman, A. B., Rudie, G. C., Blanc, G. A., et al. 2020, ApJ, 891, 147

Nguyen, H. T., Schulz, B., Levenson, L., et al. 2010, A&A, 518, L5

Obreschkow, D., Heywood, I., Klöckner, H.-R., & Rawlings, S. 2009a, ApJ, 702, 1321

Obreschkow, D., Klöckner, H.-R., Heywood, I., Levrier, F., & Rawlings, S. 2009b, ApJ, 703, 1890

Oesch, P. A., Bouwens, R. J., Illingworth, G. D., et al. 2015, ApJ, 808, 104

Oesch, P. A., Bouwens, R. J., Illingworth, G. D., Labbé, I., & Stefanon, M. 2018, ApJ, 855, 105

Oesch, P. A., Bouwens, R. J., Illingworth, G. D., et al. 2014, ApJ, 786, 108

Oesch, P. A., Brammer, G., van Dokkum, P. G., et al. 2016, ApJ, 819, 129

Oh, S. P., & Haiman, Z. 2002, ApJ, 569, 558

Okamoto, T., Gao, L., & Theuns, T. 2008, MNRAS, 390, 920

Oliver, S. J., Bock, J., Altieri, B., et al. 2012, MNRAS, 424, 1614

O'Shea, B. W., & Norman, M. L. 2007, ApJ, 654, 66

Osterbrock, D. E. 1989, Astrophysics of gaseous nebulae and active galactic nuclei

Osterbrock, D. E., & Ferland, G. J. 2006, Astrophysics of gaseous nebulae and active galactic nuclei

Ouchi, M., Harikane, Y., Shibuya, T., et al. 2018, PASJ, 70, S13

Padmanabhan, H. 2018, MNRAS, 475, 1477

—. 2019, MNRAS, 488, 3014

Padmanabhan, H., Breysse, P., Lidz, A., & Switzer, E. R. 2021, arXiv e-prints, arXiv:2105.12148

Padmanabhan, H., Refregier, A., & Amara, A. 2017, MNRAS, 469, 2323

Padoan, P., & Nordlund, Å. 2002, ApJ, 576, 870

Pagano, L., Delouis, J. M., Mottet, S., Puget, J. L., & Vibert, L. 2020, A&A, 635, A99

Pallottini, A., Ferrara, A., Gallerani, S., Salvadori, S., & D'Odorico, V. 2014, MNRAS, 440, 2498

Pallottini, A., Ferrara, A., Decataldo, D., et al. 2019, MNRAS, 487, 1689

Palmerio, J. T., Vergani, S. D., Salvaterra, R., et al. 2019, A&A, 623, A26

Park, J., Gillet, N., Mesinger, A., & Greig, B. 2020, MNRAS, 491, 3891

Park, J., Mesinger, A., Greig, B., & Gillet, N. 2019, MNRAS, 484, 933

Parsons, A. R., Pober, J. C., Aguirre, J. E., et al. 2012, ApJ, 756, 165

Parsons, J., Mas-Ribas, L., Sun, G., et al. 2021, arXiv e-prints, arXiv:2112.06407

Passot, T., & Vázquez-Semadeni, E. 1998, PhRvE, 58, 4501

Pawlik, A. H., Schaye, J., & van Scherpenzeel, E. 2009, MNRAS, 394, 1812

Pereira-Santaella, M., Spinoglio, L., van der Werf, P. P., & Piqueras López, J. 2014, A&A, 566, A49

Pérez-González, P. G., Rieke, G. H., Villar, V., et al. 2008, ApJ, 675, 234

Planck Collaboration, Aghanim, N., Ashdown, M., et al. 2016a, A&A, 596, A107

Planck Collaboration, Ade, P. A. R., Aghanim, N., et al. 2016b, A&A, 594, A13

Planck Collaboration, Adam, R., Aghanim, N., et al. 2016c, A&A, 596, A108

Planck Collaboration, Ade, P. A. R., Aghanim, N., et al. 2016d, A&A, 594, A13

Planck Collaboration, Aghanim, N., Akrami, Y., et al. 2020, A&A, 641, A1

Planck Collaboration Int. XVII. 2014, A&A, 566, A55

Planck Collaboration XIII. 2016, A&A, 594, A13

Planck Collaboration XXX. 2014, A&A, 571, A30

Pontzen, A. 2014, PhRvD, 89, 083010

Popping, G., Behroozi, P. S., & Peeples, M. S. 2015, MNRAS, 449, 477

Popping, G., Caputi, K. I., Somerville, R. S., & Trager, S. C. 2012, MNRAS, 425, 2386

Popping, G., Narayanan, D., Somerville, R. S., Faisst, A. L., & Krumholz, M. R. 2019, MNRAS, 482, 4906

Popping, G., Somerville, R. S., & Trager, S. C. 2014, MNRAS, 442, 2398

Pritchard, J. R., & Loeb, A. 2010, PhRvD, 82, 023006

—. 2012, Reports on Progress in Physics, 75, 086901

Pullen, A. R., Chang, T.-C., Doré, O., & Lidz, A. 2013, ApJ, 768, 15

Pullen, A. R., Doré, O., & Bock, J. 2014, ApJ, 786, 111

Pullen, A. R., Serra, P., Chang, T.-C., Doré, O., & Ho, S. 2018, MNRAS, 478, 1911

Qin, Y., Mesinger, A., Bosman, S. E. I., & Viel, M. 2021a, MNRAS, 506, 2390

Qin, Y., Mesinger, A., Greig, B., & Park, J. 2021b, MNRAS, 501, 4748

Qin, Y., Mesinger, A., Park, J., Greig, B., & Muñoz, J. B. 2020a, MNRAS, 495, 123

Qin, Y., Poulin, V., Mesinger, A., et al. 2020b, MNRAS, 499, 550

Qin, Y., Mutch, S. J., Poole, G. B., et al. 2017, MNRAS, 472, 2009

Rahmati, A., Schaye, J., Bower, R. G., et al. 2015, MNRAS, 452, 2034

Raiter, A., Schaerer, D., & Fosbury, R. A. E. 2010, A&A, 523, A64

Redford, J., Wheeler, J., Karkare, K., et al. 2018, in Society of Photo-Optical Instrumentation Engineers (SPIE) Conference Series, Vol. 10708, Millimeter, Submillimeter, and Far-Infrared Detectors and Instrumentation for Astronomy IX, ed. J. Zmuidzinas & J.-R. Gao, 107081O

Reis, I., Barkana, R., & Fialkov, A. 2022, MNRAS, 511, 5265

Ricotti, M. 2016, MNRAS, 462, 601

Riechers, D. A., Pavesi, R., Sharon, C. E., et al. 2019, ApJ, 872, 7

Righi, M., Hernández-Monteagudo, C., & Sunyaev, R. A. 2008, A&A, 489, 489

Robertson, B. E. 2021, arXiv e-prints, arXiv:2110.13160

Robertson, B. E., Ellis, R. S., Furlanetto, S. R., & Dunlop, J. S. 2015, ApJL, 802, L19

Rowan-Robinson, M., Oliver, S., Wang, L., et al. 2016, MNRAS, 461, 1100

Rubin, D., Hony, S., Madden, S. C., et al. 2009, A&A, 494, 647

Rybak, M., Calistro Rivera, G., Hodge, J. A., et al. 2019, ApJ, 876, 112

Rydberg, C.-E., Zackrisson, E., Lundqvist, P., & Scott, P. 2013, MNRAS, 429, 3658

Safarzadeh, M., & Scannapieco, E. 2016, ApJL, 832, L9

Safranek-Shrader, C., Agarwal, M., Federrath, C., et al. 2012, MNRAS, 426, 1159

Saintonge, A., Kauffmann, G., Kramer, C., et al. 2011, MNRAS, 415, 32

Salpeter, E. E. 1955, ApJ, 121, 161

Salvaterra, R., & Ferrara, A. 2003, MNRAS, 339, 973

Samui, S., Srianand, R., & Subramanian, K. 2009, MNRAS, 398, 2061

Sanders, D. B., Salvato, M., Aussel, H., et al. 2007, ApJS, 172, 86

Sandstrom, K. M., Leroy, A. K., Walter, F., et al. 2013, ApJ, 777, 5

Santini, P., Maiolino, R., Magnelli, B., et al. 2014, A&A, 562, A30

Santos, M., Bull, P., Alonso, D., et al. 2015, in Advancing Astrophysics with the Square Kilometre Array (AASKA14), 19

Santos, M. R., Bromm, V., & Kamionkowski, M. 2002, MNRAS, 336, 1082

Santos, S., Sobral, D., & Matthee, J. 2016, MNRAS, 463, 1678

Sargent, M. T., Béthermin, M., Daddi, E., & Elbaz, D. 2012, ApJL, 747, L31

Sarkar, A., & Samui, S. 2019, PASP, 131, 074101

Sarmento, R., Scannapieco, E., & Cohen, S. 2018, ApJ, 854, 75

Savaglio, S. 2006, New Journal of Physics, 8, 195

Sayers, J., Golwala, S. R., Ade, P. A. R., et al. 2010, ApJ, 708, 1674

Scalo, J. 1998, in Astronomical Society of the Pacific Conference Series, Vol. 142, The Stellar Initial Mass Function (38th Herstmonceux Conference), ed. G. Gilmore & D. Howell, 201

Schaan, E., & White, M. 2021, JCAP, 2021, 068

Schaerer, D. 2002, A&A, 382, 28

—. 2003, A&A, 397, 527

Schaerer, D., Ginolfi, M., Bethermin, M., et al. 2020, arXiv e-prints, arXiv:2002.00979

Schauer, A. T. P., Drory, N., & Bromm, V. 2020a, ApJ, 904, 145

Schauer, A. T. P., Glover, S. C. O., Klessen, R. S., & Clark, P. 2020b, arXiv e-prints, arXiv:2008.05663

Schauer, A. T. P., Agarwal, B., Glover, S. C. O., et al. 2017, MNRAS, 467, 2288

Schaye, J., Crain, R. A., Bower, R. G., et al. 2015, MNRAS, 446, 521

Schmidt, F. 2016, PhRvD, 94, 063508

Schneider, A., Giri, S. K., & Mirocha, J. 2021, PhRvD, 103, 083025

Schreiber, C., Pannella, M., Elbaz, D., et al. 2015, A&A, 575, A74

Scott, B., Upton Sanderbeck, P., & Bird, S. 2021, arXiv e-prints, arXiv:2104.00017

Scott, D., & Rees, M. J. 1990, MNRAS, 247, 510

Scott, K. S., Austermann, J. E., Perera, T. A., et al. 2008, MNRAS, 385, 2225

Scoville, N., Aussel, H., Brusa, M., et al. 2007, ApJS, 172, 1

Seo, H. J., Lee, H. M., Matsumoto, T., et al. 2015, ApJ, 807, 140

Serra, P., Doré, O., & Lagache, G. 2016, ApJ, 833, 153

Shang, C., Haiman, Z., Knox, L., & Oh, S. P. 2012, MNRAS, 421, 2832

Shekhar Murmu, C., Olsen, K. P., Greve, T. R., et al. 2021, arXiv e-prints, arXiv:2110.10687

Shen, X., Vogelsberger, M., Nelson, D., et al. 2022, MNRAS

Shen, X., Vogelsberger, M., Nelson, D., et al. 2020, Monthly Notices of the Royal Astronomical Society, 495, 4747

Sheth, R. K., & Tormen, G. 1999, MNRAS, 308, 119

Shirasaki, M. 2019, MNRAS, 483, 342

Shull, J. M., Harness, A., Trenti, M., & Smith, B. D. 2012, ApJ, 747, 100

Silva, B. M., Zaroubi, S., Kooistra, R., & Cooray, A. 2017, Monthly Notices of the Royal Astronomical Society, 475, 1587

Silva, B. M., Zaroubi, S., Kooistra, R., & Cooray, A. 2018, MNRAS, 475, 1587

Silva, M., Santos, M. G., Cooray, A., & Gong, Y. 2015, ApJ, 806, 209

Silva, M. B., Santos, M. G., Gong, Y., Cooray, A., & Bock, J. 2013, ApJ, 763, 132

Sims, P. H., & Pober, J. C. 2020, MNRAS, 492, 22

Sitwell, M., Mesinger, A., Ma, Y.-Z., & Sigurdson, K. 2014, MNRAS, 438, 2664

Skinner, D., & Wise, J. H. 2020, MNRAS, 492, 4386

Sobral, D., Matthee, J., Darvish, B., et al. 2015, ApJ, 808, 139

Solomon, P. M., Rivolo, A. R., Barrett, J., & Yahil, A. 1987, ApJ, 319, 730

Somerville, R. S., & Kolatt, T. S. 1999, MNRAS, 305, 1

Soumagnac, M. T., Barkana, R., Sabiu, C. G., et al. 2016, PhRvL, 116, 201302

Soumagnac, M. T., Sabiu, C. G., Barkana, R., & Yoo, J. 2019, MNRAS, 485, 1248

Sparre, M., Hayward, C. C., Springel, V., et al. 2015, MNRAS, 447, 3548

Spergel, D., Gehrels, N., Baltay, C., et al. 2015, arXiv e-prints, arXiv:1503.03757

Spinoglio, L., Dasyra, K. M., Franceschini, A., et al. 2012, ApJ, 745, 171

Stacey, G. J., Geis, N., Genzel, R., et al. 1991, ApJ, 373, 423

Stacey, G. J., Aravena, M., Basu, K., et al. 2018, in Society of Photo-Optical Instrumentation Engineers (SPIE) Conference Series, Vol. 10700, Proc. SPIE, 107001M

Stacy, A., Greif, T. H., & Bromm, V. 2010, MNRAS, 403, 45

—. 2012, MNRAS, 422, 290

Stark, D. P. 2016, ARA&A, 54, 761

Stark, D. P., Schenker, M. A., Ellis, R., et al. 2013, ApJ, 763, 129

Stecher, T. P., & Williams, D. A. 1967, ApJL, 149, L29

Stefanon, M., Bouwens, R. J., Labbé, I., et al. 2021, ApJ, 922, 29

Steidel, C. C., Erb, D. K., Shapley, A. E., et al. 2010, ApJ, 717, 289

Sugimura, K., Matsumoto, T., Hosokawa, T., Hirano, S., & Omukai, K. 2020, ApJL, 892, L14

Suginohara, M., Suginohara, T., & Spergel, D. N. 1999, ApJ, 512, 547

Sun, G., & Furlanetto, S. R. 2016, MNRAS, 460, 417

Sun, G., Hensley, B. S., Chang, T.-C., Doré, O., & Serra, P. 2019, ApJ, 887, 142

Sun, G., Mirocha, J., Mebane, R. H., & Furlanetto, S. R. 2021a, MNRAS, 508, 1954

Sun, G., Moncelsi, L., Viero, M. P., et al. 2018, ApJ, 856, 107

Sun, G., Chang, T. C., Uzgil, B. D., et al. 2021b, ApJ, 915, 33

Susa, H., Hasegawa, K., & Tominaga, N. 2014, ApJ, 792, 32

Switzer, E. 2017, Measuring the Cosmological Evolution of Gas and Galaxies with the EXperiment for Cryogenic Large-aperture Intensity Mapping (EXCLAIM), NASA APRA Proposal

Switzer, E. R., Anderson, C. J., Pullen, A. R., & Yang, S. 2019, ApJ, 872, 82

Switzer, E. R., Masui, K. W., Bandura, K., et al. 2013, MNRAS, 434, L46

Tacchella, S., Bose, S., Conroy, C., Eisenstein, D. J., & Johnson, B. D. 2018, ApJ, 868, 92

Tacconi, L. J., Neri, R., Genzel, R., et al. 2013, ApJ, 768, 74

Tal, T., Dekel, A., Oesch, P., et al. 2014, ApJ, 789, 164

Tanaka, T., & Hasegawa, K. 2021, MNRAS, 502, 463

Tayal, S. S. 2008, A&A, 486, 629

—. 2011, ApJS, 195, 12

Tegmark, M., Silk, J., Rees, M. J., et al. 1997, ApJ, 474, 1

Thacker, C., Cooray, A., Smidt, J., et al. 2013, ApJ, 768, 58

Thomas, R. M., & Zaroubi, S. 2008, MNRAS, 384, 1080

Thöne, C. C., Fynbo, J. P. U., Goldoni, P., et al. 2013, MNRAS, 428, 3590

Tielens, A. G. G. M. 2005, The Physics and Chemistry of the Interstellar Medium (Cambridge University Press)

Tielens, A. G. G. M., & Hollenbach, D. 1985, ApJ, 291, 722

Tinker, J., Kravtsov, A. V., Klypin, A., et al. 2008, ApJ, 688, 709

Tinker, J. L., & Wetzel, A. R. 2010, ApJ, 719, 88

Togi, A., & Smith, J. D. T. 2016, ApJ, 830, 18

Toma, K., Sakamoto, T., & Mészáros, P. 2011, ApJ, 731, 127

Trac, H. 2018, ApJL, 858, L11

Trac, H., Cen, R., & Mansfield, P. 2015, ApJ, 813, 54

Trapp, A. C., & Furlanetto, S. R. 2020, MNRAS, 499, 2401

Trebitsch, M., Volonteri, M., Dubois, Y., & Madau, P. 2018, MNRAS, 478, 5607

Trenti, M., & Stiavelli, M. 2009, ApJ, 694, 879

Trenti, M., Stiavelli, M., & Shull, J. M. 2009, ApJ, 700, 1672

Tseliakhovich, D., & Hirata, C. 2010, PhRvD, 82, 083520

Tumlinson, J., & Shull, J. M. 2000, ApJL, 528, L65

Turk, M. J., Abel, T., & O'Shea, B. 2009, Science, 325, 601

Uzgil, B. D., Aguirre, J. E., Bradford, C. M., & Lidz, A. 2014, ApJ, 793, 116

Uzgil, B. D., Carilli, C., Lidz, A., et al. 2019, ApJ, 887, 37

Valentino, F., Magdis, G. E., Daddi, E., et al. 2018, ApJ, 869, 27

Vallini, L., Pallottini, A., Ferrara, A., et al. 2018, MNRAS, 473, 271

Vieira, J., Aguirre, J., Bradford, C. M., et al. 2020, arXiv e-prints, arXiv:2009.14340

Viero, M. P., Moncelsi, L., Mentuch, E., et al. 2012, MNRAS, 421, 2161

Viero, M. P., Moncelsi, L., Quadri, R. F., et al. 2013a, ApJ, 779, 32

Viero, M. P., Wang, L., Zemcov, M., et al. 2013b, ApJ, 772, 77

Viero, M. P., Moncelsi, L., Quadri, R. F., et al. 2015, ApJL, 809, L22

Villa-Vélez, J. A., Buat, V., Theulé, P., Boquien, M., & Burgarella, D. 2021, A&A, 654, A153

Visbal, E., Haiman, Z., & Bryan, G. L. 2015, MNRAS, 450, 2506

—. 2018, MNRAS, 475, 5246

Visbal, E., Haiman, Z., Terrazas, B., Bryan, G. L., & Barkana, R. 2014, MNRAS, 445, 107

Visbal, E., & Loeb, A. 2010, JCAP, 11, 016

Visbal, E., Loeb, A., & Wyithe, S. 2009, JCAP, 2009, 030

Visbal, E., & McQuinn, M. 2018, ApJL, 863, L6

Visbal, E., Trac, H., & Loeb, A. 2011, JCAP, 8, 010

Vogelsberger, M., Marinacci, F., Torrey, P., & Puchwein, E. 2020, Nature Reviews Physics, 2, 42

Vogelsberger, M., Genel, S., Springel, V., et al. 2014, MNRAS, 444, 1518

Walter, F., Decarli, R., Sargent, M., et al. 2014, ApJ, 782, 79

Walter, F., Carilli, C., Decarli, R., et al. 2019, BAAS, 51, 442

Walter, F., Carilli, C., Neeleman, M., et al. 2020, arXiv e-prints, arXiv:2009.11126

Wardlow, J. L., Cooray, A., Osage, W., et al. 2017, ApJ, 837, 12

Wetzel, A. R., Cohn, J. D., & White, M. 2009, MNRAS, 395, 1376

Whitaker, K. E., van Dokkum, P. G., Brammer, G., & Franx, M. 2012, ApJL, 754, L29

Whitler, L. R., Mason, C. A., Ren, K., et al. 2020, MNRAS, 495, 3602

Williams, C. C., Curtis-Lake, E., Hainline, K. N., et al. 2018, ApJS, 236, 33

Williams, R. J., Quadri, R. F., Franx, M., van Dokkum, P., & Labbé, I. 2009, ApJ, 691, 1879

Willott, C. J., Carilli, C. L., Wagg, J., & Wang, R. 2015, ApJ, 807, 180

Windhorst, R. A., Timmes, F. X., Wyithe, J. S. B., et al. 2018, ApJS, 234, 41

Wise, J. H., & Abel, T. 2007, ApJ, 671, 1559

Wise, J. H., Demchenko, V. G., Halicek, M. T., et al. 2014, MNRAS, 442, 2560

Wolcott-Green, J., Haiman, Z., & Bryan, G. L. 2011, MNRAS, 418, 838

Wolz, L., Blake, C., & Wyithe, J. S. B. 2017a, MNRAS, 470, 3220

Wolz, L., Blake, C., Abdalla, F. B., et al. 2017b, MNRAS, 464, 4938

Wright, E. L., Mather, J. C., Bennett, C. L., et al. 1991, ApJ, 381, 200

Wu, H.-Y., & Doré, O. 2017a, MNRAS, 466, 4651

—. 2017b, MNRAS, 467, 4150

Wu, X., McQuinn, M., Eisenstein, D., & Irsic, V. 2021, arXiv e-prints, arXiv:2105.08737

Xiao, L., Stanway, E. R., & Eldridge, J. J. 2018, MNRAS, 477, 904

Xu, H., Norman, M. L., O'Shea, B. W., & Wise, J. H. 2016a, ApJ, 823, 140

Xu, H., Wise, J. H., Norman, M. L., Ahn, K., & O'Shea, B. W. 2016b, ApJ, 833, 84

Xu, Y., Wang, X., & Chen, X. 2015, ApJ, 798, 40

Yamaguchi, Y., Kohno, K., Tamura, Y., et al. 2017, ApJ, 845, 108

Yan, L., Sajina, A., Loiacono, F., et al. 2020, arXiv e-prints, arXiv:2006.04835

Yang, S., Pullen, A. R., & Switzer, E. R. 2019, MNRAS, 489, L53

Yang, S., Somerville, R. S., Pullen, A. R., et al. 2021, ApJ, 911, 132

Yang, Y. P., Wang, F. Y., & Dai, Z. G. 2015, A&A, 582, A7

Yoshiura, S., Shimabukuro, H., Takahashi, K., & Matsubara, T. 2017, MNRAS, 465, 394

Young Owl, R. C., Meixner, M. M., Fong, D., et al. 2002, ApJ, 578, 885

Yue, B., & Ferrara, A. 2019, MNRAS, 490, 1928

Yue, B., Ferrara, A., Pallottini, A., Gallerani, S., & Vallini, L. 2015, MNRAS, 450, 3829

Yue, B., Ferrara, A., Salvaterra, R., & Chen, X. 2013a, MNRAS, 431, 383

Yue, B., Ferrara, A., Salvaterra, R., Xu, Y., & Chen, X. 2013b, MNRAS, 433, 1556

Yue, B., Ferrara, A., Vanzella, E., & Salvaterra, R. 2014, Monthly Notices of the Royal Astronomical Society: Letters, 443, L20

Yue, B., Castellano, M., Ferrara, A., et al. 2018, ApJ, 868, 115

Yung, L. Y. A., Somerville, R. S., Finkelstein, S. L., Popping, G., & Davé, R. 2019, MNRAS, 483, 2983

Zel'Dovich, Y. B. 1970, A&A, 500, 13

Zemcov, M., Smidt, J., Arai, T., et al. 2014, Science, 346, 732

Zheng, Z., Cen, R., Trac, H., & Miralda-Escudé, J. 2011, ApJ, 726, 38

Zhu, H.-M., Pen, U.-L., Yu, Y., & Chen, X. 2018, PhRvD, 98, 043511